THE SINGLE PHASE TRAVELLING WAVE LINEAR INDUCTION MOTOR

A thesis presented for the degree of
Doctor of Philosophy in Electrical Engineering
in the University of Canterbury,
Christchurch, New Zealand.

by

BIRASAK VARASUNDHAROSOTH

University of Canterbury

1979

This work is dedicated to my father - who was my first engineering teacher.

CONTENTS

CONTENTS (continued)

CONTENTS (continued)

CONTENTS (continued)

CONTENTS (continued)

LIST OF TABLES

LIST OF FIGURES

LIST OF FREQUENTLY USED SYMBOLS

A	propagation constant
a	half coil span for overlap coil model
B	maximum flux density
b	instantaneous flux density
C	shunt capacitance per meter
C'	shunt capacitance per unit section
$\dot{C}$	effective shunt capacitance per meter
d	effective slot pitch for overlap coil model
F	thrust
g	airgap width
G	goodness factor
G	effective shunt conductance per meter
i	stator current
$i_{C'}$	current in capacitance C'
j_1	stator linear current density
j_2	rotor linear current density
L	inductance per meter
l	length of stator block
R	resistance per meter
R'	resistance per unit section
S	slip
T	number of turns per each of stator coil
t	rotor thickness
U	linear velocity of rotor
U_s	velocity of the travelling wave
V	stator voltage
w	effective width of stator block

LIST OF FREQUENTLY USED SYMBOLS (continued)

Z_t	terminating impedance
Z_o	characteristic impedance
α	attenuation function
β	phase function
Δ	slot pitch in non-overlap coil model
Δ	actual unit size for cutoff frequency consideration
Δ	effective distance between single turn coil in overlap coil model
μ_o	permeability of free space
ρ_2	effective rotor resistivity

ABSTRACT

At the time this study was undertaken, linear electric machines(LEMs) were relatively new. Compared with rotating machines, relatively little work had been done on them. Although LEMs are finding ready applications, they concern the polyphase LEMs only. In some applications LEMs have advantages over rotating machines because of an absence of gears or rotary-to-linear converters, a high reliability and the possibility of very high speed of the travelling field. However, problems arise from the undesired characteristics of big airgaps, lossy end-effects, low efficiency, and a low power factor.

This thesis is concerned with a device called a single phase travelling wave linear induction motor(STLIM). Unlike most electrical machines, STLIMs utilise propagating magnetic waves, waves that are obtained by arranging the windings of the linear primary coils and shunt capacitors to simulate a transmission line. The waves drive linear conducting sheet secondaries. The STLIMs have some interesting characteristics: (1) most importantly, the speed of STLIM can be varied by the value of shunt capacitance or series coil inductance; (2) due to the attenuated travelling wave nature, the exit end-effect is self-reduced; (3) the device operates at nearly unity power factor for all ranges of slip; (4) it is a constant current device. Although the experimental efficiency demonstrated in the present work has not been high, it is still compatible with either small single phase induction motors or polyphase linear induction motors of the same physical dimensions.

Original mathematical theories of STLIMs have been presented that have been based on one-dimensional current sheet analysis and adapted transmission line distributed parameter theory. The developed experimental models and the tests that have been carried out substantiate the theories.

CHAPTER 1

GENERAL VIEW OF SINGLE PHASE TRAVELLING WAVE LINEAR INDUCTION MOTORS (STLIMS)

1.1 INTRODUCTION

One of the lines of thought which led to this thesis problem was the realisation that a single phase induction motor and a transmission line are in some respects similar to each other[1].* In a transmission line, the analysis is frequently realised as sinusoidally propagated current and voltage waves in either direction. When comparing these waves with the forward and backward travelling magnetic fields in the airgap of a single phase motor, this resemblance suggests the possibility of utilising the travelling wave property of a transmission line to drive a cage type rotor of the cylindrical motor by arranging the windings of the stator and the shunt capacitors to simulate a transmission line. With the normal single phase induction motor, it is not possible to eliminate the backward rotating field. However with the transmission line arrangement, theoretically a proper terminating impedance can be used to eliminate the backward wave. In a practical arrangement as in Figure 1.1, it is not possible to completely eliminate reflected waves and obtain a pure rotating field. Some reflections occur because the simulated system is lumped rather than continuous.

* Number between brackets refer to references listed at end of manuscript.

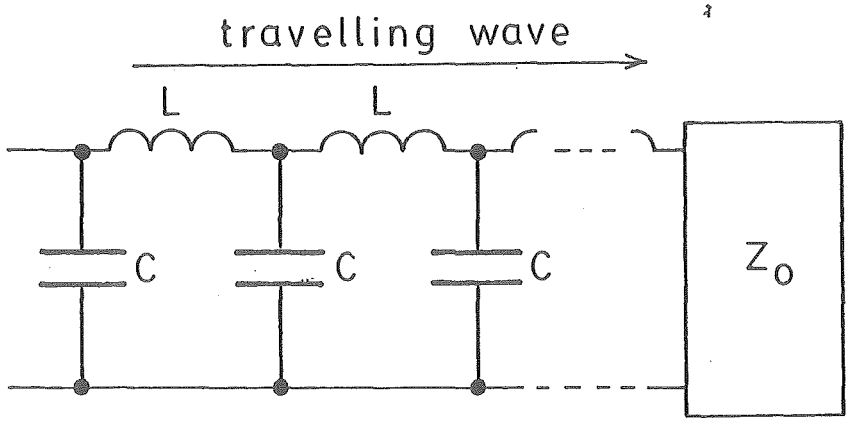

Figure 1.1 Arrangement of coils and shunt capacitors.

By using a large number of coils per wavelength, approximation of the simulated system is improved and thus a reduction in reflections is obtained. Furthermore the power absorbed by the rotor causes the travelling wave to attenuate as it travels down the windings. If the machine is designed so that at rated output, the voltage at the terminated end is small compared to the supply voltage, the end reflected wave is heavily reduced and proper termination may not be necessary. Such an arrangement leads to the advantage of no power dissipated in the terminating impedance but there is an attendent disadvantage that the steel core and the stator windings are not fully utilised, since one end will carry a small current.

The speed of the travelling wave machine is characterised by the velocity of the propagation function. If the excitation frequency is such that the windings may be classified as "low-loss" ones, and if extrapolation of normal transmission line theory is justified, it may be expected that the velocity of propagation is, to the first order,

frequency invariant. The speed of the travelling wave machine can be controlled by means of altering the capacitances or the inductances of the machine. This could lead to a variable-speed single-phase induction motor. However, since speed change implies a change of pole pitch, difficulties may arise in a cylindrical machine when the number of flux waves around the airgap is required to be a non-integral number. Linear motors, both longitudinal and transverse flux types, allow variation in pole pitch: this is therefore the best form in which to investigate the characteristics of the travelling wave machine.

1.2 LITERATURE REVIEW RELATING TO THE DEVELOPMENT OF STLIMS.

Although the recorded work on linear induction motors can be traced back to 1890[4], the first record of a travelling wave machine was not published until 1948[6]. A rotary a.c. power amplifier device using travelling wave principles was investigated in the generating mode. This device was supposed to behave in the manner of a negative-resistance transmission line but, unfortunately, the results of the project were negative. In 1958, Putman carried on the investigation and development of this rotary travelling wave amplifier type machine. It was found that waves of magnetic flux propagated around its periphery could be characterised by a propagation constant just as are the waves of a simple transmission line. The amplifying properties of the device was utilised under certain suitable conditions when the propagation constant of one of the possible waves gave rise to an amplified wave[6]. In 1966, Hiller suggested the

possibility of utilising the travelling wave concept of a transmission line to drive the cage-type rotor of induction motors[1]. The experimental demonstration of variable speed characteristics of the machine was reported by Watson in 1972 [10]. The machine, constructed as a disc motor, had six coils in series and variable shunt capacitors connected to control speed. As the value of shunt capacitors increase, the speed of the machine drops. The change in speed follows closely the theoretical predictions. The maximum speed variation recorded in this experiment is about 2:1. The machine is found to be capable of varying the synchronous speed by very small steps over a fairly wide speed range. This lead to the development of the first experimental STLIM of transverse flux type in 1975 [11]. The device is described as a simple transverse flux linear induction motor. It consists of six stator C cores arranged around the arc of the circle. The width of each core in the direction of rotation is 2,54 cm and the radial depth is 7.62 cm. Each core carries 1000 turns coil. The aluminium disc rotor of 48.62 cm diameter and 0.635 cm thickness revolves in the airgap. Windows have been cut into the rotor leaving a cage-like structure of radial conductors, each 1.27 cm wide and 12.7 cm long, connected at the periphery of the disc by the rim which is 1.905 cm wide. The torque-speed characteristic is recorded. The speed of the field is found to vary approximately as $1/\sqrt{C}$ and the force characteristic is similar to that of a high-rotor-resistance induction motor. The torque increases as an increase in shunt capacitance. The machine tends to have constant power characteristics since the increase in

shunt capacitance also means reduction in speed. By treating the machine as a transmission line, the analysis lead to an expression for starting torque. The starting torque, proportional to capacitance, agrees with the experimental trends. However this method of treatment runs into difficulties when considering the moving rotor, and also because of mutual coupling between stator coils which is not taken into account by the normal transmission line theories. Such a system would result in fourth order differential equations suggesting four possible travelling waves, two forward travelling waves and two backward travelling waves, instead of two travelling waves. Because this machine was small and had poor output characteristics, further work using a larger machine was seen to be necessary.

For further investigations, the overlaping coil STLIM of axial flux type was chosen[12]. It has been found that even if there is very close coupling between coils in this kind of stator, the travelling field can be set up. It is observed to have only two dominant sets of travelling fields, the forward travelling field and the reflected travelling field. When properly terminated only the forward travelling field is observed. When the machine is loaded, the attenuation along the travelling field increases. The speed of the travelling field also drops as the speed of the rotor falls. Speed control is investigated by means of varying the value of shunt capacitances. An attempt on the analysis based on a simplified model using the one-dimensional current-sheet analysis for linear motor was put forward. This gives a useful relationship between physical and electrical parameters.

By engineering deduction, the solution of the dominant forward travelling wave could be obtained. This established the relationship between attenuation function and phase function with different values of shunt capacitance and rotor speed. However, there are many questions of practical importance which have yet to be answered. In particular it is now necessary to take the analysis further to derive expressions for force, input current, power input, power output, power factor, and efficiency. These are the problems that have been investigated by the author. In addition to theoretical work, experiments were to be carried out to check the theoretical predictions.

1.3 SCOPE OF THE THEORY AND DEVELOPMENT OF STLIMS IN THIS THESIS.

Unfortunately, apart form the few references quoted in the previous section, there are no references which deal specifically with this thesis topic or anything closely relating to it. This thesis is concerned with an attempt to further develop the STLIMs. The type of machine that was considered is the two-sided primary, doubly-excited, short-primary and long-conducting sheet secondary type. The analysis is based on the one-dimensional current sheet method[2] and the solution obtained is in the form of realisation of an equivalent circuit comparable with that of the distributed transmission line. This thesis is divided into two parts. Each part consists of theoretical analysis, design and construction of an experimental machine, tests which were carried out, followed by results, discussion and conclusion.

All theoretical calculations were done in FORTRAN IV language.

The first part deals with non-overlap coil arrangement of the stator block. The initial work is the analysis, neglecting the effect of the stator resistance, and design of a model using the avaliable stator block to have a range of measurable speed from about 10 to 20 m/s. The machine has fixed airgap of 1.2 cm and an aluminium secondary of 3 mm thickness. Thrust is then measured for different values of shunt capacitance by a simple rope brake. Preliminary results obtained from tests in some case compared well with the theoretical values, however, some discrepancies occur in the value of thrust and speed characteristics. The motor was described as under-powered and inefficient. Although this experimental model is of little practical value, it did serve its purpose by supporting the idea of the principle of the travelling wave machine. The result of this section has been published [13].

Further investigation is needed and a more complicated model must be realised in order to understand more about the characteristics of the machine. This leads to the modified analysis of the machine taking account of the stator resistance. The analysis shows that the design goodness factor of the machine is independent of the airgap. This suggests the idea of smooth variable speed control from fixed frequency supply without any alterations of the electrical circuit and without penalties in the thrust or efficiency of the machine. The second model is then designed based on this principle, starting from the dimensions of the stator core. The motor has variable airgap and three sets of rotor thickness. The

output at 200 volts constant voltage drive is about 300 watts. The designed value of efficiency is about 30 per cent. Test results confirmed that the variation of speed can be obtained by varying the value of the airgap without change in the thrust or degrading the efficiency of the motor. The result of this section has been published[8]. Also an alternative means of speed control by rearranging the electrical circuit of parallel coils and series capacitances has been investigated. Some preliminary results of this have also been published[9].

The second part of this thesis is concerned with the overlap coil model of the machine. The continuation of the analysis put forward by Watson[12] leads to the realisation of the equivalent circuit. The theoretical values obtained from any given dimensions of the machine are: thrust-speed characteristic; input power; input current; power factor; output power and efficiency. The experimental model is designed to make use of the available stator block of the second model with a chosen coil span of two slots. The efficiency of the model increases to 45 per cent. An offset arrangement of stator blocks is investigated and found to improve the performance of the machine. Variable speed characteristics by means of varying the shunt capacitances and the value of airgaps is investigated. The result of this section has been submitted for publication.

1.4 SOME GENERAL CHARACTERISTICS OF STLIMS COMPARED WITH OTHER TYPES OF INDUCTION MOTORS

From the realisation of the equivalent circuits of the three models, there are some common characteristics

among them. They have no fixed synchronous speed. The synchronous speed falls with increasing slip in the low slip region and then rises again in the high slip region. This implies higher value of theoretical rotor efficiency in the low slip region of operation. Compared with the single phase machine's backward travelling field, the travelling wave motors have the attenuated travelling wave nature and hence the reflected wave is further self-reduced. Because the realisation of the equivalent circuit resembles that of the transmission line, the travelling wave motors have good power factors for all ranges of slip and have low starting current. Even though the maximum efficiency of the experimental models are not high, 29 per cent for the second model and 45 per cent for the third model, they are still within the range compatible with rotary single phase induction motor of similar rating or with 3-phase linear induction machine of the same physical order. They have some merit of variable speed from fixed frequency supply. As the industrial applications of the polyphase linear induction motors continue, the variable speed STLIMs may find some areas of application. Obviously this thesis has not solved all theoretical and practical problems. However, the original idea has been carried another step forward in the conception of the device, the mathematical models and the developments. If this thesis helps to stimulate new areas of thinking toward the industrial applications of STLIMs, then it will have been worthwhile.

PART 1

NON-OVERLAP COIL MODEL OF STLIM

CHAPTER 2

THE MATHEMATICAL MODEL OF SIMPLIFIED NON-OVERLAP COIL STLIM.

2.1 THE CONCEPT OF TRAVELLING-WAVE ON A TRANSMISSION LINE.

The uniform transmission line with unconstrainted value of series inductance, shunt capacitance, series resistance and shunt conductance will propagate sinusoidally varying voltage and current waves in either direction; with proper terminating impedance, only the forward wave exists. These waves are reduced in magnitude as a function of the product of the distance propagated and an attenuation factor. The part of travelling wave function which varies with respect to distance is e^{Ax}. Here A is called the propagation function which consists of real and imaginary part; $A=-\alpha-j\beta$. The real part, α, is called the attenuation function, and the imaginary part, β, is called the phase function. The phase function relates to the phase velocity U_s in the following manner; $U_s = \omega/\beta$ where ω is the angular frequency of the propagated wave or; $U_s = \lambda f$ where λ is the wavelength and f is the frequency of the propagating wave. The terminated or characteristic impedance Z_o of the line relating the current and voltage of the travelling wave is $Z_o = \sqrt{Z/Y}$ where Z is the impedance of the series components, and Y is the admittance of the shunt components of the transmission line. In the following sections it will be shown that the STLIM equations lead to very similar expressions.

2.2 REVIEW OF THE AIRGAP FIELD EQUATION.

In this section, the one-dimensional current-sheet analysis of the airgap field equation will be derived according to the method outlined by Laithwaite [2] or by Yamamura [14].

Consider the STLIM shown in Figure 2.1. The primary current is represented by the two current sheets of infinitesimally small thickness. If a set of rectangular co-ordinate axes is oriented as shown in Figure 2.1, the primary current density $\dot{J}_1$ and the secondary current density $\dot{J}_2$ flow in z direction and travel in the direction of the secondary sheet i.e. in x co-ordinate. The secondary conducting sheet has finite thickness t . Then we can easily obtain an approximate differential expression for the y-component of the magnetic field in the airgap in terms of current density by applying Ampere's Circuital Law around the contour indicated in the developed diagram in Figure 2.2.

$$\left[H(x + \Delta x) - H(x)\right] g = \left[\dot{J}_1(x) + \dot{J}_2(x)\right]\Delta x$$

or

$$\frac{H(x + \Delta x) - H(x)}{\Delta x} = \frac{1}{g}\left[\dot{J}_1(x) + \dot{J}_2(x)\right] \qquad 2 - 1$$

by taking the limit as Δx approaches zero,

$$\frac{\partial H(x)}{\partial x} = \frac{1}{g}\left[\dot{J}_1(x) + \dot{J}_2(x)\right]$$

multiply by permeability of air

$$\frac{\partial b}{\partial x} = \frac{\mu_o}{g}(\dot{J}_1 + \dot{J}_2) \qquad 2 - 2$$

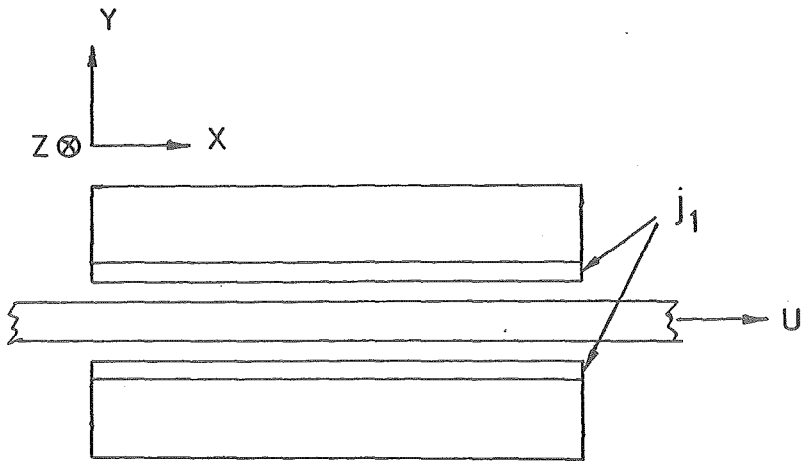

FIGURE 2.1 STLIM with primary windings represented by current sheet.

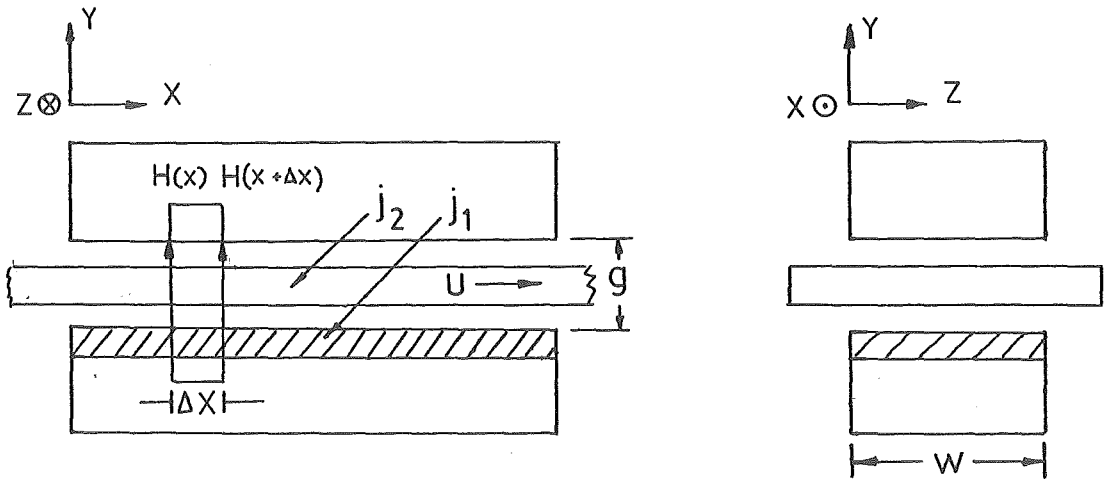

FIGURE 2.2 Developed diagram for one-dimensional analysis of STLIM.

The electromotive force e_2 in the secondary is directed in the Z-coordinate. The line integral of e around the periphery of a rectangle, w long and Δx wide, placed on the secondary sheet located at x is $(\partial e/\partial x)\Delta x w$. The electromotive force has two components; the transformer voltage $(\partial b/\partial t)\Delta x w$, and the speed voltage $U(\partial b/\partial x)\Delta x w$, where U is the speed of the secondary sheet. And hence, we obtain

$$\frac{\partial e_2}{\partial x} = \frac{\partial b}{\partial t} + U\frac{\partial b}{\partial x} \qquad 2 - 3$$

In this present model of analysis, flux density b is directed in the Y-coordinate and has no X-component. This implies that the secondary sheet has no leakage inductance. Therefore the secondary eletromotive force e_2 is completely consumed as resistance drop. Thus we have

$$e_2 = \varsigma_2 j_2 \qquad 2 - 4$$

Where ς_2 is the surface resistivity of the secondary sheet. From Equations 2 - 2, 2 - 3 and 2 - 4 we obtain the general airgap field equation of STLIMs as

$$\frac{\partial^2 b}{\partial x^2} = \frac{\mu_o}{g}\left[\frac{\partial j_1}{\partial x} + \frac{1}{\varsigma_2}\left(\frac{\partial b}{\partial t} + U\frac{\partial b}{\partial x}\right)\right] \qquad 2 - 5$$

Equation 2 - 5 will be used to analyse both cases of STLIMs; non-overlap coil and overlap coil model.

2.3 TYPE AND ASSUMPTIONS OF STLIM USED FOR ANALYSIS

The model of the machine used for analysis is the double-sided, longitudinal-flux, short primary, long conducting sheet secondary, STLIM.

The non-overlap stator coil type is considered first mainly because the electrical circuit resembles more the transmission line than does the overlap coil type which has very large mutual coupling between the coils. However, the overlap coil model will be considered in the second part of this thesis.

Now in order to simplify the mathematical analysis of the machine, the assumptions are as follows. There is one coil on each tooth of the stator block. All defects are neglected, winding resistance, leakage reactance and also mutual inductance between these coils. The inductance of each coil is L'. The active width of the stator block is w, and the active width of airgap is g. Tooth pitch Δ is assumed very small with respect to the wavelength of the travelling field. Each section has shunt capacitor C' connected to the circuit. The primary structure is assumed "smooth" in order to permit the current sheet analysis. The motion of the secondary is in X-direction only. The ferromagnetic material does not saturate. The winding is terminated in its characteristic impedance. The applied voltage varies sinusoidally in time so the flux density at any point is taken to vary in time as $e^{j\omega t}$. All end-effects of the machine, of finite length l, were neglected. The spatial distribution of flux density is assumed to be e^{Ax}, where A is the propagation function of the machine. This very simplified model is shown in Figure 2.3.

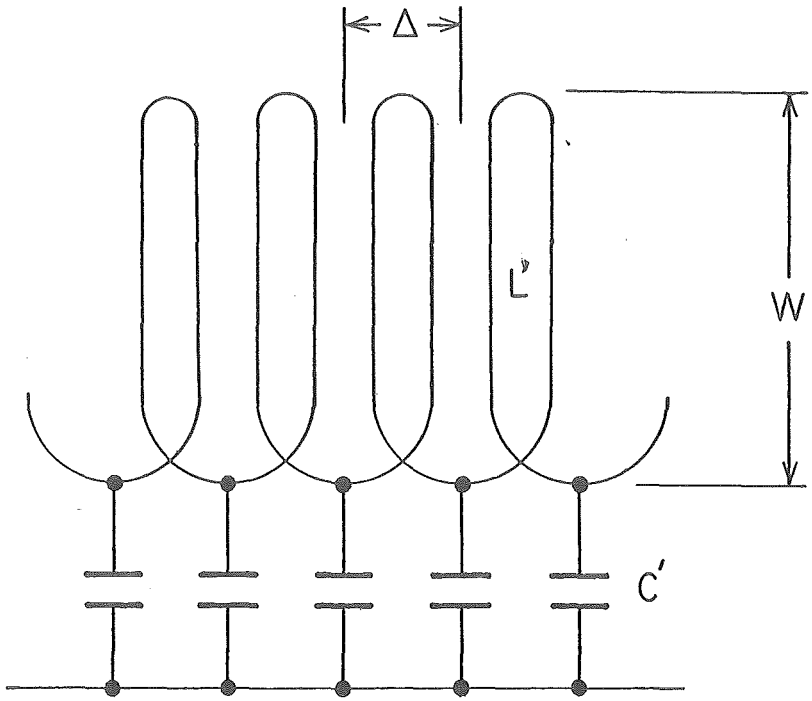

FIGURE 2.3 The simplified model.

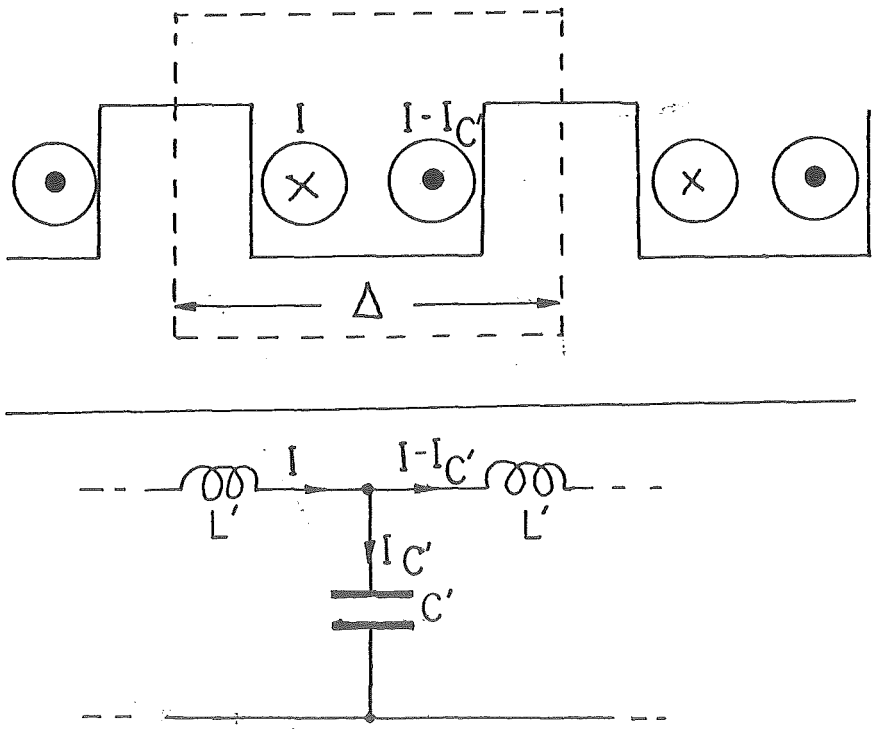

FIGURE 2.4 Sampling section to find the effective slot current.

2.4 EQUATION OF THE PROPAGATION FUNCTION AND REALISATION OF THE EQUIVALENT CIRCUIT.

The flux density b of the machine at distance x along the stator is assumed to be

$$b = B\, e^{j\omega t} e^{Ax} \qquad 2 - 6$$

Now the emf induced in the stator coil of T turns at x is

$$e = w\Delta T \frac{\partial b}{\partial t} \qquad 2 - 7$$

Thus the voltage gradient along the stator winding is given by

$$\Delta \frac{\partial V}{\partial x} = w\Delta T \frac{\partial b}{\partial t} \qquad 2 - 8$$

Hence the voltage at point x in the machine with infinitely long stator or properly terminated in its characteristic impedance is given by

$$\begin{aligned} V(x,t) &= \int dV(x,t) \\ &= \int_{oo}^{x} wT \frac{\partial b}{\partial t}\, dx \\ &= \frac{j\omega wTB\ e^{j\omega t}\ e^{Ax}}{A} \end{aligned} \qquad 2 - 9$$

The current flowing in the capacitor C' at x is

$$i_{C'} = C' \frac{\partial V}{\partial t}$$

From the geometry of the winding as shown in Figure 2.4, the

effective slot current at x is equal to $Ti_{C'}$. Hence the local stator current density is

$$j_1 = Ti_{C'}/\Delta = \frac{TC'}{\Delta}\cdot\frac{\partial V}{\partial t}$$

$$= -\frac{\omega^2 \mu T^2 BC\ e^{j\omega t}\ e^{Ax}}{A} \qquad 2 - 10$$

where $C = C'/\Delta$ is the shunt capacitance per unit length of the machine

The general field equation governing the current sheet analysis of STLIM as reviewed in section 2.2 is

$$\frac{\partial^2 b}{\partial x^2} = \frac{\mu_o}{g}\left[\frac{\partial j_1}{\partial x} + \frac{1}{\rho_2}\left(\frac{\partial b}{\partial t} + U\frac{\partial b}{\partial x}\right)\right]$$

Where, j_1 is the stator current density, ρ_2 is the resistance of the secondary and U is the speed of the secondary.

In this particular model; substitute $\frac{\partial^2 b}{\partial x^2} = A^2 B\ e^{j\omega t} e^{Ax}$, $\frac{\partial b}{\partial x} = AB\ e^{j\omega t} e^{Ax}$, $\frac{\partial b}{\partial t} = j\omega B\ e^{j\omega t} e^{Ax}$ and $\frac{\partial j_1}{\partial x} = -\omega^2 \mu T^2 BC\ e^{j\omega t} e^{Ax}$.

Hence the equation of propagation function becomes,

$$A^2 = \frac{\mu_o}{g}\left[-\omega^2 \mu T^2 C + \frac{1}{\rho_2}(j\omega + UA)\right] \qquad 2 - 11$$

in which the only unknown is the propagation constant A.

Direct solution for A is rather awkward, and will not be attempted at first. Instead, some particular cases are considered to get a feeling for the message embodied in the equation. In the first instance we can put $\rho_2 \to \infty$ to simulate a machine with no conducting sheet rotor. This gives

$$A = \pm j\omega\sqrt{\mu_o w T^2 C/g} \qquad 2 - 12$$

so the flux density becomes

$$b = Be^{j(\omega t \pm \omega x\sqrt{\mu_o w T^2 C/g})} \qquad 2 - 13$$

which represents two sine waves travelling in opposite direction at speed

$$U_{max} = \frac{\partial x}{\partial t} = \pm\sqrt{\frac{g}{\mu_o w T^2 C}} \qquad m/s$$

When properly terminated only the forward wave exists. We now put the rotor back into the machine but concentrate on standstill conditions. When the speed U = 0 we get from equation 2 - 11

$$A^2 = (j\omega w T^2 \mu_o/g)(1/w T^2 \varsigma_2 + j\omega C) \qquad 2 - 14$$

Comparing this with the transmission line propagation constant

$$\gamma^2 = (R + j\omega L)(G + j\omega C)$$

the equivalent circuit which is suggested by this analysis has series inductance $wT^2\mu_o/g$, shunt capacitance C, and shunt conductance $1/wT^2\varsigma_2$.

Again by considering the propagation constant it would be expected that as the resistance ς_2 of the conducting rotor sheet is gradually reduced, an increase should occur in attenuation α and phase function β, analogous to the wave propagating in a lossy medium. The speed of the travelling

field will be lower than the value obtained when the rotor is removed.

Next, the conducting rotor sheet is allowed to move at velocity U, and we enquire into the possibility of zero attenuation. Putting $A = -\alpha - j\beta$ and for $\alpha = 0$, the quadratic expression 2 - 11 gives

$$-\beta^2 = \frac{\mu_0}{g}\left[-\omega^2 w T^2 C + \frac{1}{\rho_2}(j\omega - j\beta U)\right] \qquad 2 - 15$$

From the real part we find

$$\beta = \omega\sqrt{w T^2 C \mu_0 / g}$$

and from the imaginary part

$$U = \omega/\beta$$

This shows that when the attenuation is zero the rotor must be moving at synchronous speed. Thus the highest speed the rotor can attain* is equal to the speed of the travelling wave when the rotor is removed. At speed slightly below U_{max} where the attenuation constant α could be considered relatively small, the propagation constant can be written approximately as

$$A^2 \doteq \frac{\mu_0}{g}\left[-\omega^2 w T^2 C + \frac{j\omega}{\rho_2}(1 - U\beta/\omega)\right] \qquad 2 - 16$$

but since $1 - U\beta/\omega = S$, the slip at speed U, we find

$$A^2 \doteq (j\omega w T^2 \mu_0/g)(S/w T^2 \rho_2 + j\omega C)$$

Hence conditions close to synchronous speed can be investigated using a transmission line equivalent circuit, as

* when operating as a motor

previously described, with ρ_2 replaced by ρ_2/S.

Finally to take the general case, put $A = -\alpha - j\beta$ on the right hand side of 2 - 11 and hence becomes

$$A^2 = \frac{\mu_o}{g}\left[-\omega^2 wT^2 C + \frac{1}{\rho_2}(j(\omega - \beta U) - U\alpha)\right]$$

$$= -\frac{\mu_o \omega^2 wT^2 C}{g} - \frac{U\alpha\mu_o}{\rho_2 g} + \frac{j\omega\mu_o}{\rho_2 g} - \frac{j\beta\mu_o U}{\rho_2 g}$$

the synchronous speed $U_s = \omega/\beta$, and the slip $S = 1 - U/U_s$

$$A^2 = -\frac{\mu_o \omega^2 wT^2 C}{g} - \frac{U\alpha\mu_o}{\rho_2 g} + \frac{j\omega\mu_o S}{\rho_2 g}$$

which can be recast in the form

$$A^2 = (j\omega wT^2\mu_o/g)\cdot\left[j\omega\left[C + \frac{\alpha U}{\omega^2 wT^2 \rho_2}\right] + \frac{S}{wT^2\rho_2}\right] \quad 2 - 17$$

This equivalent circuit is shown in Figure 2.5. It has in per meter values of: series inductance $wT^2\mu_o/g$, shunt capacitance $(C + \frac{\alpha U}{\omega^2 wT^2 \rho_2})$, and shunt conductance $\frac{S}{wT^2\rho_2}$.

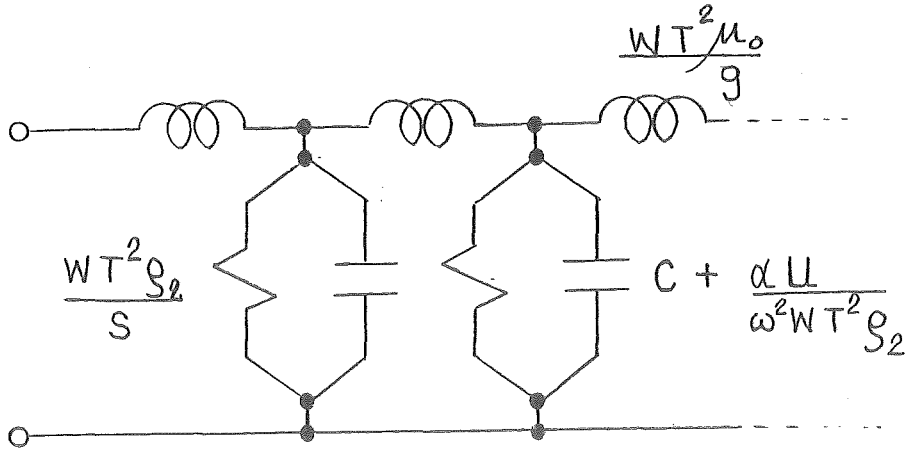

FIGURE 2.5 Equivalent circuit of simplified model: all values are per meter length.

2.5 PROPAGATION CONSTANTS AND SYNCHRONOUS SPEED

The propagation constants can be determined by putting $A = -\alpha - j\beta$ into 2 - 11

$$\alpha^2 - \beta^2 + 2j\alpha\beta = \frac{\mu_o}{g}\left[-\omega^2 wT^2 C + \frac{1}{\rho_2}(j\omega + U(-\alpha - j\beta))\right]$$

from imaginary part we find the attenuation function α

$$2\alpha\beta = \frac{\mu_o \omega}{g\rho_2} - \frac{\mu_o U\beta}{g\rho_2}$$

$$= \frac{\mu_o}{2g\rho_2}(\omega/\beta - U)$$

$$= \frac{\mu_o S U_s}{2g\rho_2} \qquad 2 - 18$$

Where U_s is the synchronous speed at slip S

Now the phase function β and synchronous speed U_s can be found from the real part of the expression i.e.

$$\alpha^2 - \beta^2 = \frac{\mu_o}{g}(\omega^2 wT^2 C + \alpha U/\rho_2)$$

Substitute value of α into equation, giving

$$\frac{\mu_o^2 S^2 U_s^2}{4g^2\rho_2^2} - \frac{\omega^2}{U_s^2} = -\frac{\mu_o \omega^2 wT^2 C}{g} - \frac{\mu_o^2 SUU_s}{2g^2\rho_2^2}$$

giving

$$\left[\frac{\mu_o^2(2S - S^2)}{4g^2\rho_2^2}\right]U_s^4 + \left[\frac{\mu_o \omega^2 wT^2 C}{g}\right]U_s^2 - \omega^2 = 0$$

The solution for the synchronous speed, U_s, has two real roots.

$$U_s = \pm \rho_2 \omega T \sqrt{\left[\frac{2gwC}{\mu_o(2S - S^2)}\right]\cdot\left[\sqrt{1 + \frac{2S - S^2}{\omega^2 w^2 T^4 C^2 \rho_2^2}} - 1\right]} \qquad 2 - 19$$

Equation 2 - 19 represents two waves travelling in opposite direction, the forward travelling wave and the reflected travelling wave. With proper termination and with the attenuated wave characteristic along the length of the stator block, the effect of the reflected wave is neglected and only the dominant forward travelling wave is considered here.

The solution of the phase function is

$$\beta = \omega / U_s \qquad 2 - 20$$

The synchronous speed varies as a function of slip S, decreasing with the increasing slip. The above relationships of equations 2 - 18, 2 - 19 and 2 - 20 can be used tp determine α and β at any value of slip S, and the rotor speed is $\frac{\omega}{\beta}(1-S)$.

For some special cases, where the speed of the rotor approaches synchronous speed, the term $(2S-S^2)/(\omega^2 w^2 T^4 C^2 g_2^2) \ll 1$, therefore

$$\sqrt{1 + \frac{2S - S^2}{\omega^2 w^2 T^4 C^2 g_2^2}} \doteq 1 + \frac{2S - S^2}{2\omega^2 w^2 T^4 C^2 g_2^2} - \frac{(2S - S^2)^2}{8\omega^4 w^4 T^8 C^4 g_2^4}$$

Hence the synchronous speed becomes

$$U_s = \sqrt{\left[\frac{g}{\mu_o w T^2 C}\right] \cdot \left[1 - \frac{(2S - S^2)}{4\omega^2 w^2 T^4 C^2 g_2^2}\right]} \qquad 2 - 21$$

And when the rotor is moving at synchronous speed, the expected synchronous speed at zero slip is $U_s(S=0) = \sqrt{\frac{g}{\mu_o w T^2 C}}$ which is the same as the result obtain from 2 - 15.

At standstill condition, S=1, the synchronous speed becomes

$$U_s(S=1) = g_2 \omega T \sqrt{\frac{2gwC}{\mu_o} \left[\sqrt{1 + \frac{1}{\omega^2 w^2 T^4 C^2 g_2^2}} - 1\right]} \qquad 2 - 22$$

2.6 ANALYSIS OF THRUST AND SUPPLY VOLTAGE.

Having analysed the propagation problem which leads to the equivalent circuit of Figure 2.5, attention is now turned to the calculation of thrust produced by the travelling wave machine. Since the thrust on the stator will be the same as that on the rotor, the total thrust over the entire length l of the machine is given by

$$F = w\int_0^l \text{Real}\left[\frac{j_1 \overset{*}{b}}{2}\right] dx \qquad 2 - 23$$

where from 2 - 10, $j_1 = -\dfrac{\omega^2 w T^2 BC\ e^{j\omega t} e^{Ax}}{A}$, $\overset{*}{b} = B\ e^{-j\omega t} e^{\overset{*}{A}x}$

Here $\overset{*}{A}$ and $\overset{*}{b}$ are the complex conjugate of A and b respectively. Performing the integral gives

$$F = \tfrac{1}{2}w\int_0^l \text{Real}\left[\left[-\frac{\omega^2 w T^2 BC\ e^{j\omega t} e^{Ax}}{A}\right]\cdot(B\ e^{-j\omega t} e^{\overset{*}{A}x})\right] dx$$

$$= -\tfrac{1}{2}\omega^2 w^2 T^2 B^2 C\int_0^l \text{Real}\left[\frac{e^{(A + \overset{*}{A})x}}{A}\right]dx$$

$$= -\frac{\omega^2 w^2 T^2 B^2 C}{4(\alpha^2 + \beta^2)}\left| e^{-2\alpha x}\right|_0^l$$

$$= \frac{\omega^2 w^2 T^2 B^2 C}{4(\alpha^2 + \beta^2)}\cdot(1 - e^{-2\alpha l}) \qquad 2 - 24$$

From 2 - 9, the supply voltage is found by putting x = 0. Thus the r.m.s. value of supply voltage is

$$V = \frac{\omega w T B}{\sqrt{2(\alpha^2 + \beta^2)}} \qquad 2 - 25$$

Equation 2 - 24 can be rewritten in terms of the applied voltage as

$$F = \tfrac{1}{2}V^2C(1 - e^{-2\alpha l}) \qquad 2 - 26$$

and if the product αl is large, as it is at low speed, the starting thrust is approximately $F = \tfrac{1}{2}V^2C$.

The output at any slip S, is the product of thrust and speed. This can be determined by 2 - 18, 2 - 19 and 2 - 26.

$$P_o = FU_s(1 - S) \qquad 2 - 27$$

The characteristic impedance as determined by the realisation of the equivalent circuit is

$$Z_o = \sqrt{\frac{j\omega w T^2 \mu_o / g}{j\omega\left[C + \dfrac{U}{\omega^2 w T^2 g_2^2}\right] + \dfrac{S}{w T^2 g_2}}} \qquad 2 - 28$$

From 2 - 28, the input power, input current and the power factor of the motor at any slip S are;

$$P_i = \left[\frac{V}{Z_o}\right]^2 . \text{Real } Z_o \qquad 2 - 29$$

$$I = \frac{V}{Z_o} \qquad 2 - 30$$

$$P.F. = \frac{\text{Real } Z_o}{|Z_o|} \qquad 2 - 31$$

CHAPTER 3

THE EXPERIMENTAL MACHINE

In the previous chapter of this work, we have developed the simplified model of STLIM. Now an experimental machine designed on this basis is needed to verify the theory.

3.1 PRELIMINARY CONSIDERATIONS OF THE STATOR BLOCK

This is done by rewinding the existing stator block of the axial flux machine [12]. The stator is double-sided, 63.5 cm long and 15 cm wide. Each stator block consists of laminated steel sheets to minimise iron loss. Each stator block has 25 teeth of width 1.27 cm and the slots between teeth are also 1.27 cm wide. The slot depth is 3.8 cm and the stack height is 7.6 cm. The winding is designed in order to get the maximum use of the slot window area. The machine is aimed to have a no-rotor synchronous speed about 10 m/s for the maximum avaliable capacitance, which is 60 μF/coil or 2400 μF/m. For an aluminium rotor of 3 mm thickness, we assumed that the airgap of 10-12 mm is sufficient for smooth operation. The effective stator width is calculated using the fringing at edges of twice the airgap size [5]. Hence from 2 - 15, the approximate number of turns required for this stator block, $\sqrt{g/\mu_o w C U_s^2}$, is 440 turns/coil.

Allowing 0.5 mm slot insulation all around, and 2 mm for slot wedge, the maximum window area for each single layer coil is $(12.7-1)\times(38-2.5)=410$ mm^2. Using space factor of 0.5 for a round conductor, the cross-sectional area of the conductor

is $(0.5 \times 410)/440 = 0.47$ mm^2. Choosing the nearest available size of 21 SWG with cross-sectional area 0.5155 mm^2, this adjusts the maximum number of turns to 383. The coil of 380 turns is chosen, each wound on a former as ten layers of 38 turns. Each layer is separated by paper insulation. The coils are fitted on every second tooth as shown in Figure 3.1. The first stator block has winding on tooth 1, 3, 5, etc. while the opposite stator block has its winding on tooth 2, 4, 6, ... This arrangement was chosen to make the construction easier.

3.2 THE PREDICTED PERFORMANCE

The final value of inductance per meter as shown in the equivalent circuit of Figure 2.5 is

$$L = \frac{\mu_o w T^2}{g} = \frac{4\pi \times 10^{-7} \times 0.194 \times 380^2}{0.011} = 3.2 \text{ H/m}$$

The value of reactance per coil, $\Delta\omega L$, is 28 ohms at 50 Hz. The value of resistance per coil, estimated on average length of 0.4 m/turn, 1.75×10^{-4} ohm-meter resistivity, is 5.2 ohms. This gives a X_L:R ratio of 5:1. The calculated values of no rotor synchronous speeds, $1/\sqrt{LC}$, and characteristic impedances, $\sqrt{L/C}$, are tabulated in table 3.1 for different value of shunt capacitances.

A 3 mm-thickness aluminium secondary disc, of diameter 1.22 m, is used in the airgap. From 2 - 18 and 2 - 20, the value of α and β for this machine can be determined at any slip S, the speed of the rotor is $U_s(1-S)$. These theoretical values are shown in Figure 3.2. It should be mentioned that in

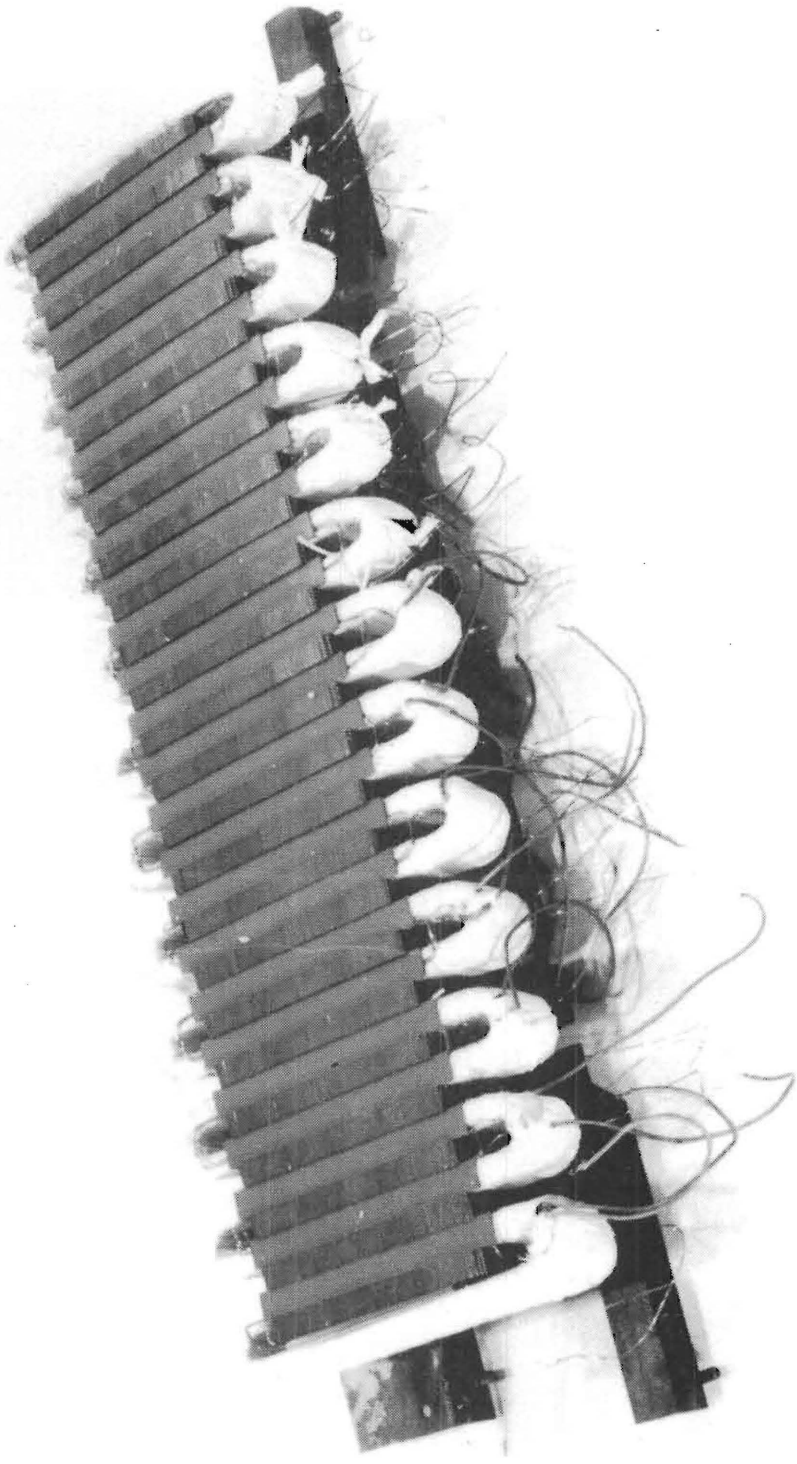

FIGURE 3.1 One side of the stator block

Capacitance per coil μF	20	40	60
Synchronous speed m/s	19.9	14.1	11.5
Characteristic impedance ohms	63	44	36

TABLE 3.1 Calculated values of synchronous speeds and characteristic impedances for shunt capacitances of 20 μF/coil, 40 μF/coil and 60 μF/coil.

carrying out the theoretical calculation of α and β the value of ϱ_2 has to be approximately double the theoretical ϱ/t to take the account of the non-active region of the rotor [2,14]: $\varrho_2 = 2\times10^{-5}$ ohms was used.

Prediction of thrust from constant supply voltage of 200 V, 50 Hz is shown in Figure 3.3. For this voltage, however, the conductor current density of the windings are 10.7 A/mm^2, 8.8 A/mm^2 and 6.2 A/mm^2 for shunt capacitances of 60 μF/coil, 40 μF/coil and 20 μF/coil respectively. Hence it should be noted that, for natural cooling arrangement of the stator block, the machine is not expected to have continuous rating on this voltage.

3.3 EXPERIMENTAL MACHINE ARRANGEMENT

The stator blocksas described in section 3.1 are mounted onto the frame. The windings on one stator block are series connected in sequence with those on the opposite stator block. The complete windings, having total resistance of 130 ohms, is terminated with an adjustable resistor. The rotor, a 3 mm thick aluminium disc of diameter 1.22 m, was

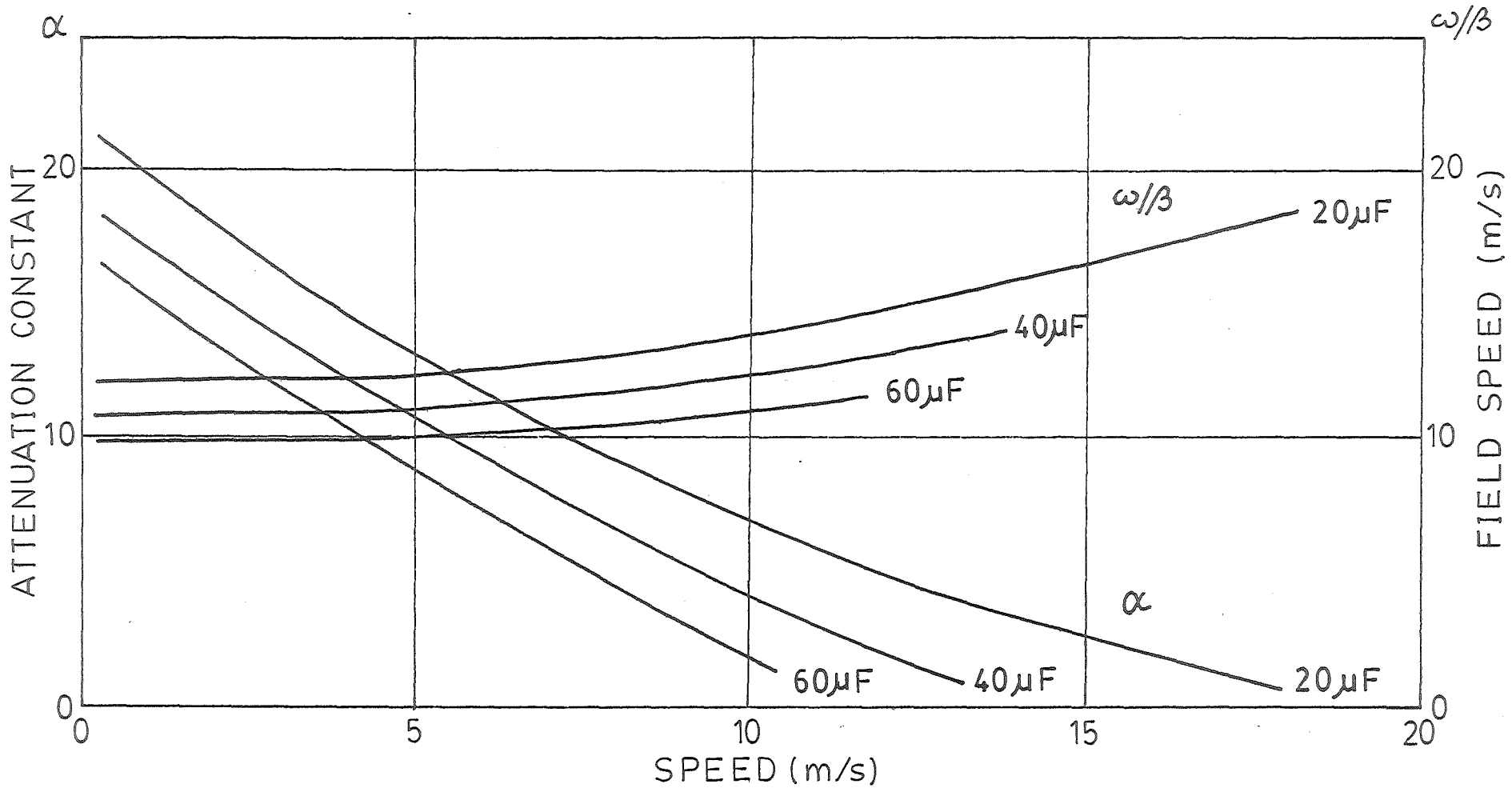

FIGURE 3.2 Behaviour predicted from simple model at 50 Hz.

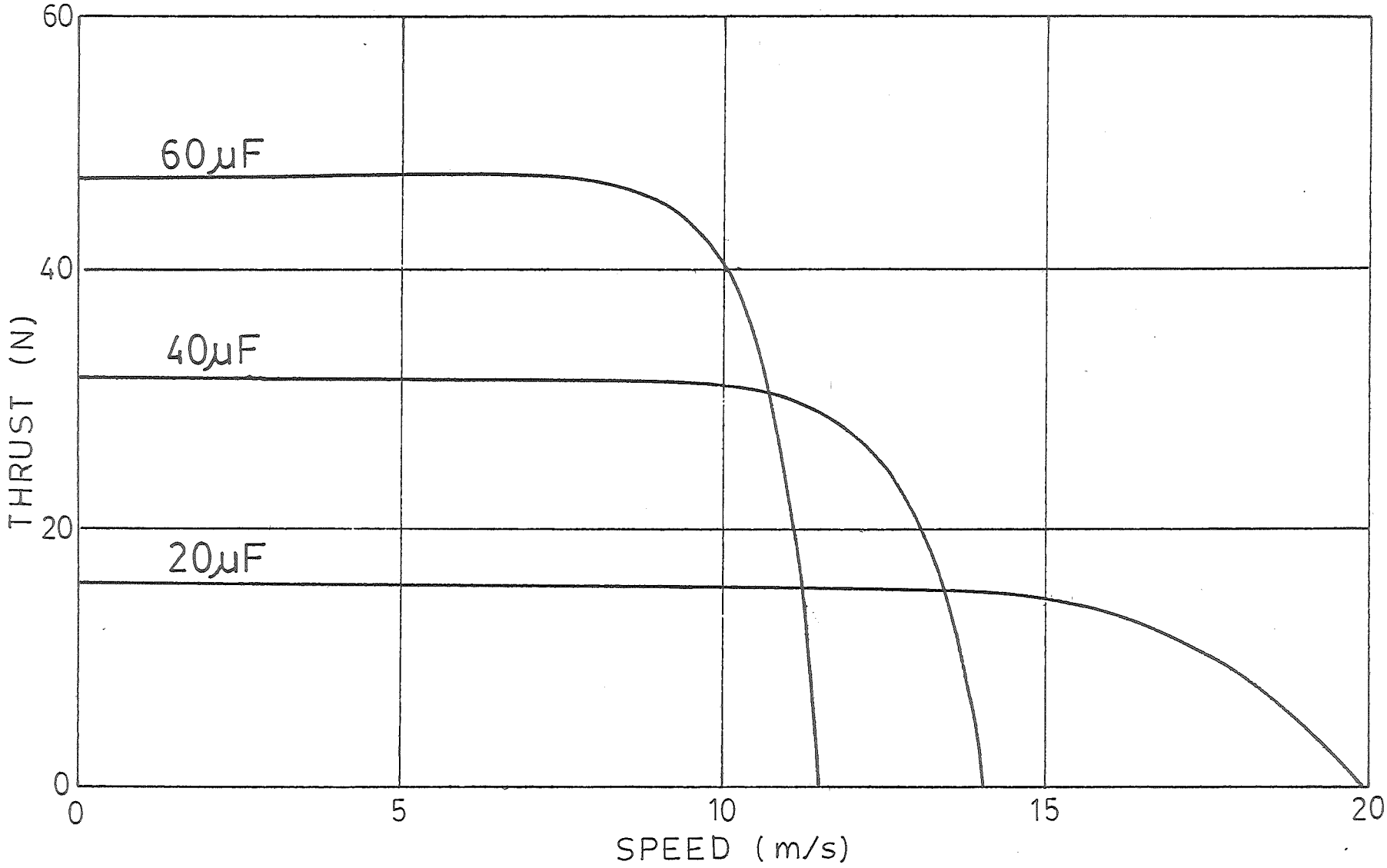

FIGURE 3.3 Thrust predicted from simple model for 200 V at 50 Hz.

run in the airgap. Due to the linear stator and disc rotor arrangement, the linear speed at the inner and outer edges of the stator will not be the same; the mean linear velocity of the disc was chosen as the linear speed of the disc at the middle of the block. This radius distance is 47 cm. When loaded, the disc gets hot and tends to distort. The airgap, as expected, has to extend to 12 mm to allow smooth operation without the disc scraping onto the stator blocks. In addition to the drive windings, one stator block has a search coil of 3 turns on each second tooth. These were used to investigate the phase shift of the travelling field along the length of the stator block. This arrangement is shown in Figure 3.4. When energised from single phase supply, the travelling field is set up. It is noted to have two waves, one in either direction. Both waves have natural attenuation even without the rotor in position due to high value of stator resistance and a fixed resistor of 55 ohms is sufficient to terminate the winding for different value of shunt capacitors. The backward wave is then negligible.

3.4 PERFORMANCE OF THE EXPERIMENTAL MACHINE.

Speed variation was investigated by changing the shunt capacitance. As the capacitance per meter is increased, the speed of the rotor tends to drop. The synchronous speed as observed by the difference in phase shift of the search coil drops when the speed of the rotor drops. Due to the heavily distorted search coil voltage waveform when the machine is loaded, no accurate quantitative value of synchronous speed is recorded, however, the result trends agree with previous

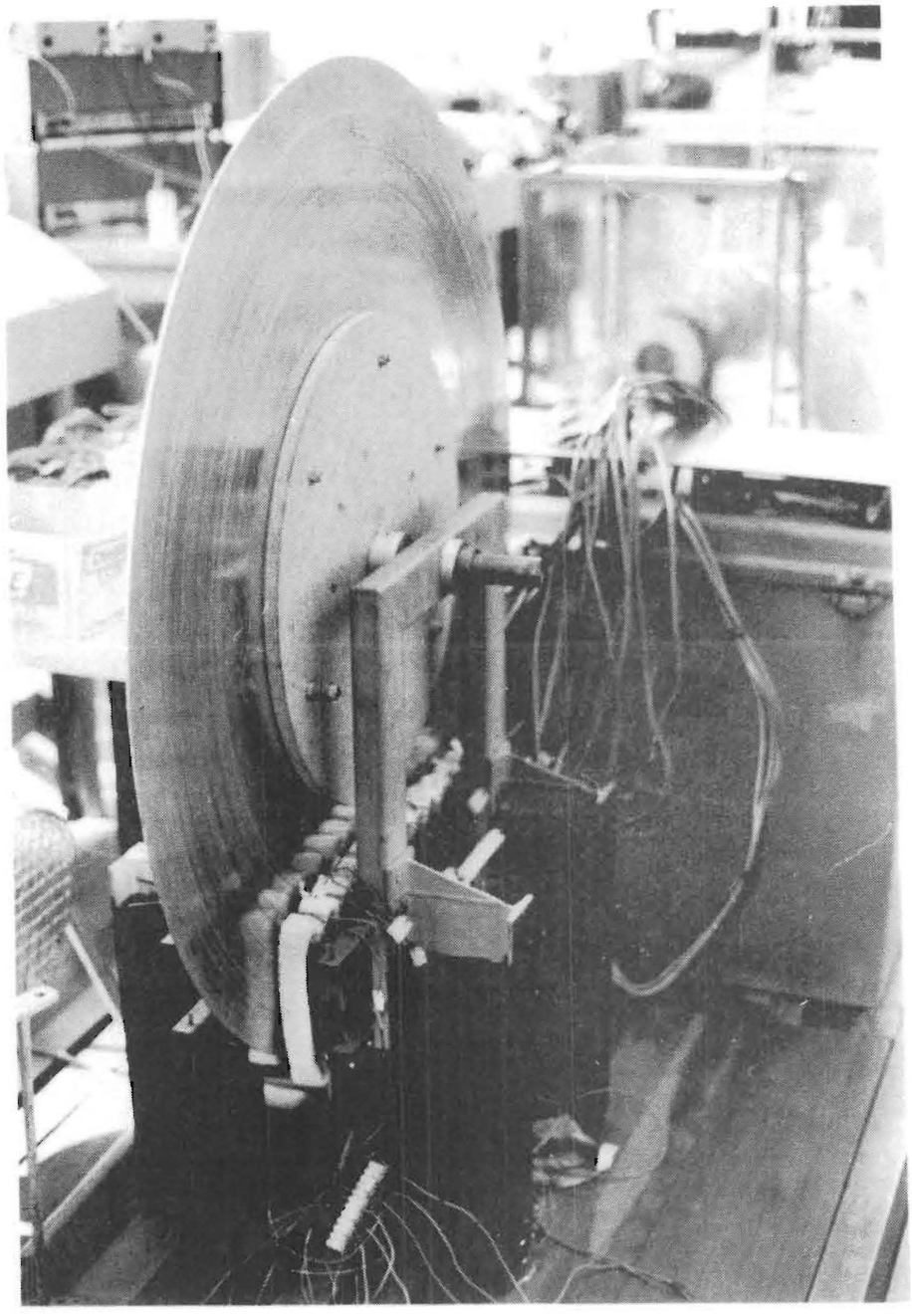

FIGURE 3.4 The experimental motor arrangement

reports[12]. The thrust-speed characteristic for shunt capacitance of 20 μF/coil, 40 μF/coil and 60 μF/coil obtained at constant voltage of 200 V, 50 Hz is shown in Figure 3.5. The thrust was measured by means of a rope brake at a drum radius of 11 cm. The thrust was calculated at mean motor radius of 47 cm neglecting friction and windage. The thrust-speed characteristics are similar to the torque speed characteristic of an induction motor with a high resistance rotor. They also show that the thrust is increased as the capacitance is increased.

The corresponding speed of the magnetic field at maximum disc velocity is shown in Table 3.2. Also included are the field velocity when the rotor is removed and the theoretically predicted synchronous speed. It is found that the maximum linear velocity of the disc under the stator block at mean radius of 47 cm is not as high as that of the travelling field. The reason for this will be discussed in the next section.

Capacitance (μF/coil)	20	40	60
Theoretically predicted synchronous speed (m/s)	19.9	14.1	11.5
Measured field velocity with no rotor (m/s)	17.8	13.2	10.2
Measured field velocity with disc at maximum speed (m/s)	17.8	12.7	10.1
Maximum disc velocity at radius 47 cm (m/s)	14.8	11.1	9.25

TABLE 3.2 Theoretical and measured synchronous speed compared.

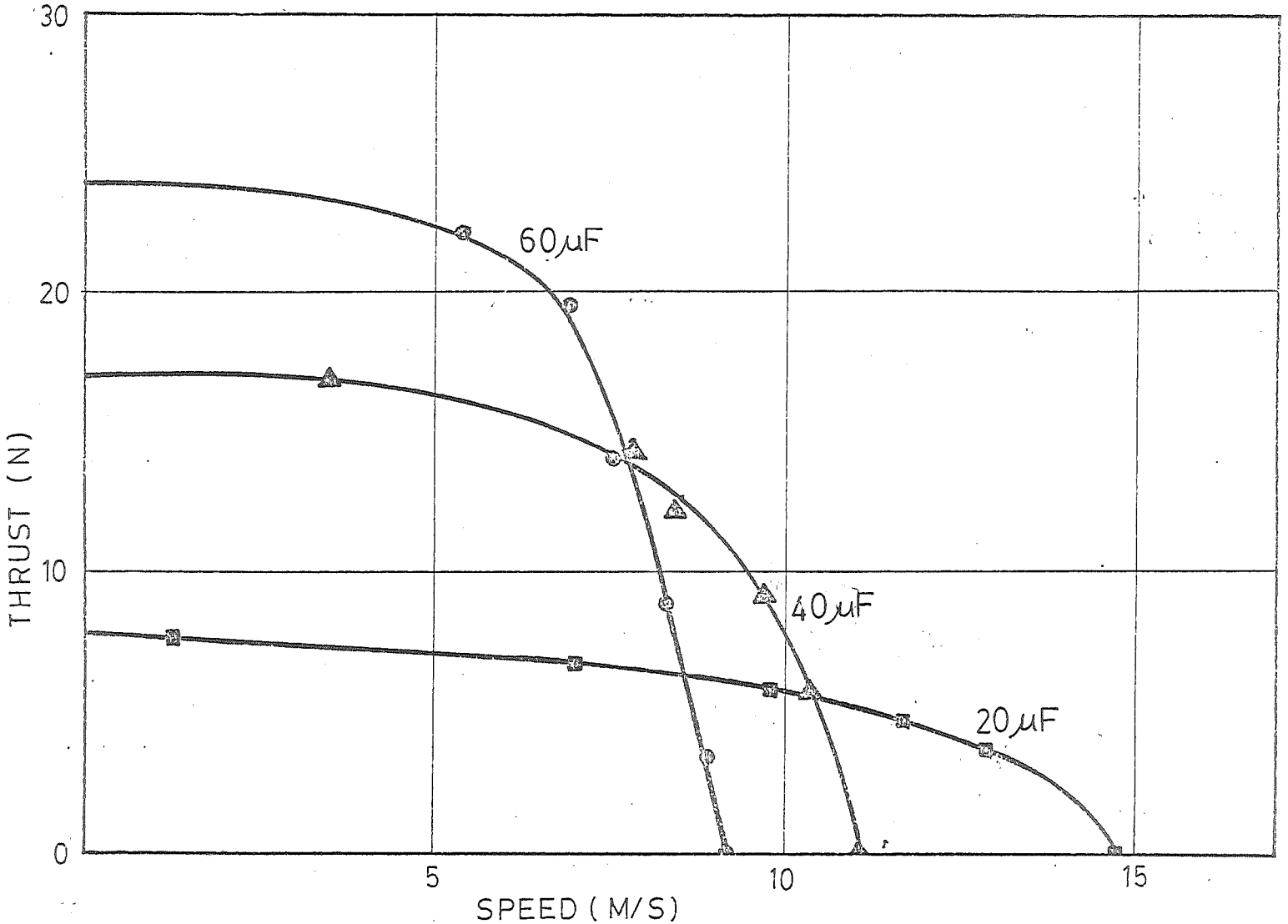

FIGURE 3.5 Measured thrust-speed characteristics at 200 V, 50 Hz

The measured capacitor voltages are heavily attenuated along the winding; in fact the attenuation is so great that it is considered unnecessary to vary the terminating impedance as there would be very little reflected wave. The distribution of capacitor voltage with different rotor speed with coil capacitance of 60 μF is shown in Figure 3.6. In addition to these results, the predicted distribution of the capacitor voltage using the attenuation constant α extracted from Figure 3.2 is superimposed in Figure 3.6.

3.5 DISCUSSION

Although the analysis is based on a very simplified model, it can be used to explain some of the characteristics of the experimental motor in section 3.4.

The expression for synchronous speed, U_s, shows how this is basically related to the physical dimensions of the stator block, the number of turns on the windings, and the capacitance. The measured speed of the travelling field as shown in Table 3.2 is about 10% lower than the theoretical values. This could be a result of high value of stator resistance, flux leakage, and mutual effects which are not included in the theoretical model. Eddy current braking of the disc due to velocity components at right angles to the direction of travel in the field direction could account for the discrepancy between maximum rotor speed and the speed of the travelling field. In addition to this, the linear speed of the rotor at the inner and outer edges of the stator block differ from that at the center by about 15%. Thus for values of slip less than 15% there will be portions of the rotor

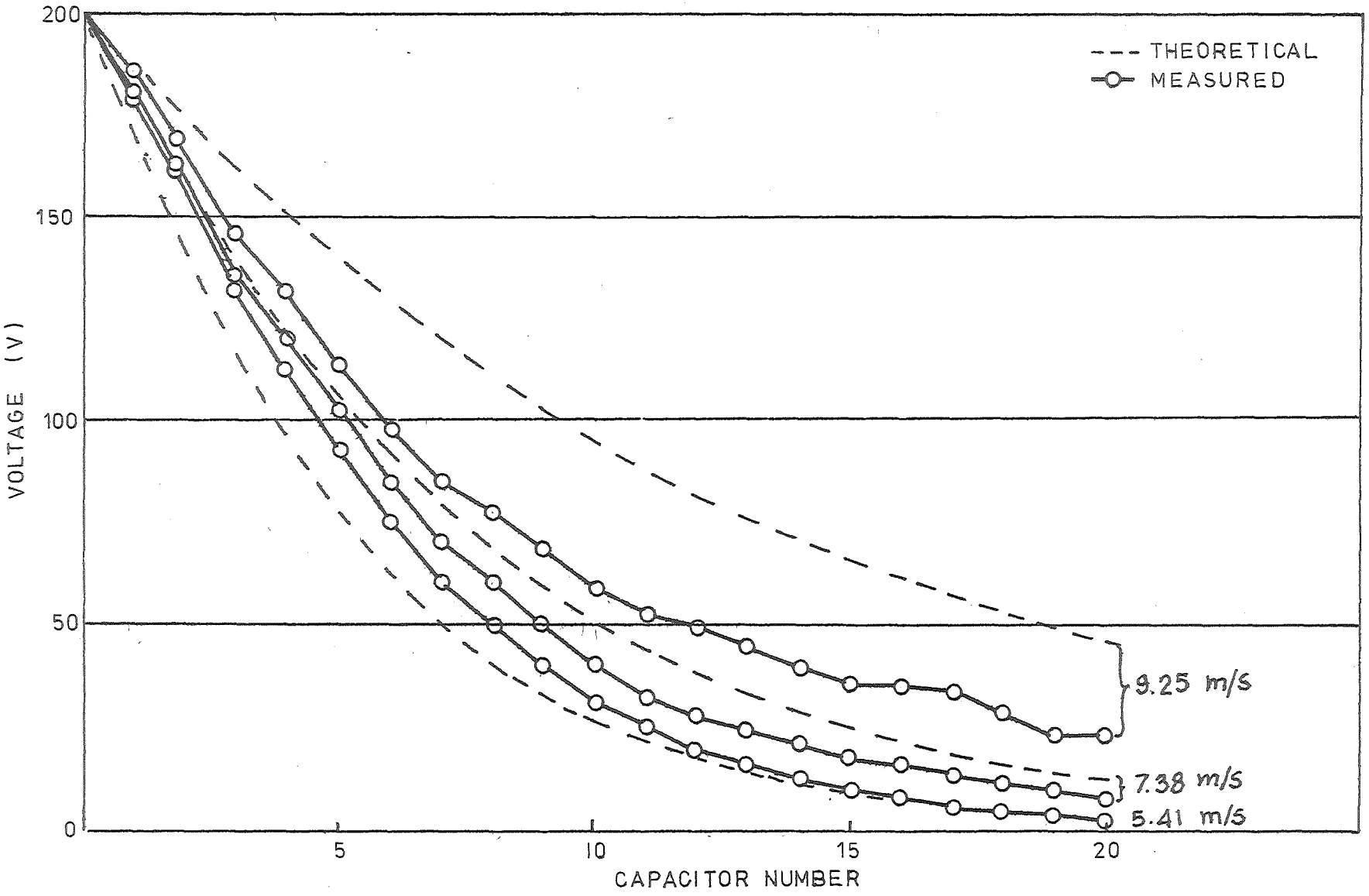

FIGURE 3.6 Distribution of capacitor voltage.

which act in a generating mode and hence limit the maximum speed since the thrust on these portions is in negative direction. This also leads to further reduction in output thrust and extra heat generated in the rotor. Inspite of these adverse factors, the maximum rotor speed does vary as $1/\sqrt{C}$ as predicted from a simple transmission line view point.

Figure 3.2 shows the theoretical field velocity U_s, and attenuation constant α, as functions of linear velocity of the disc under the stator block. It is seen that these values are not constant. As the rotor speed falls the attenuation increases and the speed of the travelling field also falls. Experimentally a slight variation in the field velocity was noted by observing changes in the phase relationships between search coil emfs, but no accurate quantitative changes could be recorded because of harmonic distortion in the search coil emf waves when the motor is heavily loaded. A more measurable change occurs in attenuation as the machine is loaded. The theoretical distribution of capacitor voltage in Figure 3.6, using values of α taken from Figure 3.2 is quite close to the measured distribution.

By comparision of theoretical values of thrust shown in Figure 3.3, the measured thrust from Figure 3.5 is disappointing low. The possible reasons for this are; the windage and friction loss of the machine, stator resistance, the generating effect in some portions of the rotor and that not all the flux from each coil will cross the airgap between stator blocks. It must be remembered that the airgap length is almost as wide as the slot width between teeth. Experiments with reduced gap width are difficult to carry out since with small airgaps the rotor tends to foul the stator block as

previously mentioned. However, for a fixed airgap, the force at low speeds is proportional to the capacitance, as predicted by the theory.

It is interesting to compare the standstill thrust formula with earlier travelling wave machine [11]. In each case the machine is viewed as a transmission line and the predicted thrust is proportional to the product V^2C. The new model in Chapter 2 differs from the previous model [11] in the conducting sheet rotor is now seen as an admittance in parallel with the capacitors where as previously it has been intuitively represented as resistance in series with the stator windings: the earlier model [11] is therefore seen to be in error in this respect.

Up to this point, the experimental machine is of little practical value, the machine described being under-powered and inefficient. However it did serve its purpose to demonstrate the possibility of variable speed operation of STLIM. The transmission line equivalent circuit of Figure 2.5 gives some insight as to the physical operation of the machine.

3.6 CONCLUSION

It has been shown that a travelling wave machine can be used as the basis of a speed change machine. By choosing a relatively simple model of a complex system, the analysis leads to the transmission line equivalent circuit, which can be used to explain the motor characteristics. Measured values of speed and thrust, while varying with capacitance as expected, are lower than predicted. A larger experimental STLIM and more complex model seems to be needed. Much further

work is necessary before the STLIM can be fully understood.

CHAPTER 4

NON OVERLAP COIL MODEL OF STLIM WITH STATOR RESISTANCE.

In the last two chapters, the preliminary investigations of STLIM was presented. It is observed to have natural attenuation even with no rotor in position since part of the power is absorbed by the stator resistance. This also affects the value of thrust. Therefore a new machine with low value of stator resistance and a mathematical model with stator resistance included in the analysis seems to be needed for further work. The following chapters of this part contain a mathematical model of one-dimensional analysis of a non-overlap coil STLIM with the effect of stator resistance, a machine designed and constructed on this basis, and the test results are fully discussed. Some preliminary investigations in these chapters had been published[8].

4.1 ASSUMPTIONS USED FOR NON-OVERLAP COIL STLIM WITH STATOR RESISTANCE.

The assumptions used for the analysis of STLIM in this chapter mostly follow the assumptions made in section 2.3 with the addition of stator resistance. These assumptions are as follow: There are coils on only one of the stator blocks, there is one coil of N turns on each tooth of the stator blocks, all defects are neglected. The resistance of each coil is R'. The active width of the stator block is w and the active width of the airgap is g. Tooth pitch Δ is assumed very small with respect to the wavelength of the

travelling field. Each section has shunt capacitance C' connected to the circuit. The primary structure is assumed "smooth" in order to permit current sheet analysis. The ferro-magnetic material does not saturate. All currents are considered to flow in Z-direction only. All effects of the harmonic components of magnetic field are neglected. The applied voltage varies sinusoidally in time so the flux density at any point is taken to vary in time as $e^{j\omega t}$. The spatial distribution of flux density is assumed to be e^{Ax} where A is the propagation function of the machine. The stator winding has finite length l. The machine is terminated in its characteristic impedance and all the effects associated with discontinuities and reflections are neglected. This model is shown in Figure 4.1

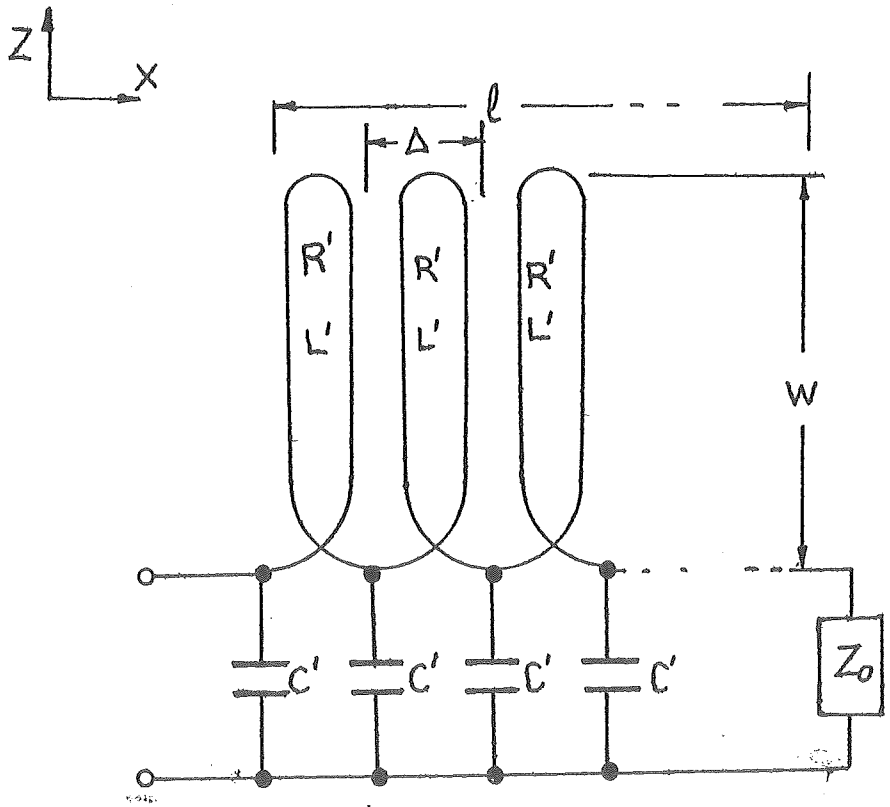

FIGURE 4.1 A simplified model STLIM with stator resistance.

4.2 SOLUTION OF THE VOLTAGE EQUATION.

From the previous section, the flux density of the machine at distance x along the stator can be expressed as

$$b = Be^{j\omega t} e^{Ax} \qquad 2 - 6$$

Now the value of induced emf in the stator coil at x is

$$e = w\Delta T \frac{\partial b}{\partial t} \qquad 2 - 7$$

The voltage gradient along the stator winding including the effect of the stator resistance R' is given by

$$\Delta \frac{\partial V}{\partial x} = e + iR' \qquad 4 - 1$$

Where i is the current in the winding at x which is the total sum of capacitive current, $i_{C'}$, from x onward to the current in the characteristic impedance. When the machine is terminated in its characteristic impedance, it can also be seen as the infinitely long stator machine. By taking the limit of the sum of these capacitive current units, the current in the winding at x becomes

$$i = \frac{1}{\Delta} \int_{\infty}^{x} i_{C'} dx \qquad 4 - 2$$

And from the geometry of the winding in Figure 4.1, the current in the capacitor C' is

$$i_{C'} = \frac{\partial i}{\partial x} \cdot \Delta \quad = C' \frac{\partial V}{\partial t} \qquad 4 - 3$$

From 2 - 7, 4 - 2 and 4 - 3, equation 4 - 1 becomes

$$\frac{\partial V}{\partial x} = wT\frac{\partial b}{\partial t} + RC\int_{\infty}^{x}\frac{\partial V}{\partial t}\,dx \qquad 4-4$$

Where $R = R'/\Delta$ is the stator resistance per unit length of the machine and $C = C'/\Delta$ is the shunt capacitance per unit length of the machine.

The solution of equation 4 - 4 can be obtained by the following deduction;

Usually in a practical machine, the induced emf in stator coil, e, is much bigger than the resistive voltage drop in that coil, iR'. Hence for $e \gg iR'$ the first approximation of 4 - 4 is the same as obtained in 2 - 8

$$\frac{\partial V}{\partial x} \doteqdot wT\frac{\partial b}{\partial t} \doteqdot j\omega wTB\ e^{j\omega t}e^{Ax}$$

This give the first approximate value of voltage $V_{(x,t)}$ at x

$$V_{(x,t)} \doteqdot \int_{\infty}^{x} wT\frac{\partial b}{\partial t}\,dx = \frac{j\omega wTB\ e^{j\omega t}e^{Ax}}{A}$$

and

$$\frac{\partial V}{\partial t} \doteqdot -\frac{\omega^2 wTB\ e^{j\omega t}e^{Ax}}{A}$$

Substitute this approximate value back into 4 - 4

$$\frac{\partial V}{\partial x} \doteqdot wT\frac{\partial b}{\partial t} + RC\int_{\infty}^{x}\frac{-\omega^2 wTB\ e^{j\omega t}e^{Ax}}{A}\,dx$$

Hence the second approximation of $V_{(x,t)}$ equal

$$V_{(x,t)} \doteqdot \frac{j\omega wTB\ e^{j\omega t}e^{Ax}}{A}\left[1 + \frac{j\omega RC}{A^2}\right]$$

and $$\frac{\partial V}{\partial t} = \frac{-\omega^2 wTB\ e^{j\omega t} e^{Ax}}{A}\left[1 + \frac{j\omega RC}{A^2}\right]$$

This result is a closer approximation than the first step. Substitute value of $\frac{\partial V}{\partial t}$ back into 4 - 4 for better approximation still, this gives

$$V_{(x,t)} = \frac{j\omega wTB\ e^{j\omega t} e^{Ax}}{A}\left[1 + \frac{j\omega RC}{A^2} - \frac{\omega^2 R^2 C^2}{A^4}\right]$$

and $$\frac{\partial V}{\partial t} = \frac{-\omega^2 wTB\ e^{j\omega t} e^{Ax}}{A}\left[1 + \frac{j\omega RC}{A^2} - \frac{\omega^2 R^2 C^2}{A^4}\right]$$

By series of approximation of $\frac{\partial V}{\partial t}$, the exact value of voltage is obtained as

$$V_{(x,t)} = \frac{j\omega wTB\ e^{j\omega t} e^{Ax}}{A}\left[1 + \frac{j\omega RC}{A^2} - \frac{\omega^2 R^2 C^2}{A^4} - \frac{j\omega^3 R^3 C^3}{A^6} + \ldots.\right]$$

which can be recognised as

$$V_{(x,t)} = \frac{j\omega wTB\ e^{j\omega t} e^{Ax}}{A\left[1 - \frac{j\omega RC}{A^2}\right]} \qquad 4 - 5$$

From 4 - 5 the supply voltage is the voltage at x = 0 therefore

$$V_{supply} = \frac{j\omega wTBAe^{j\omega t}}{\left[A^2 - j\omega RC\right]}$$

and the r.m.s. value of the supply voltage can be obtained by

$$V = \sqrt{\frac{V_{supply}\ \overset{*}{V}_{supply}}{2}}$$

Where $\overset{*}{V}_{supply}$ is the complex conjugate of V_{supply}.

By taking the dominant forward travelling wave mode, let $A = -\alpha - j\beta$, the r.m.s. value of supply voltage is

$$V = \sqrt{\frac{(j\omega_w TB\ e^{j\omega t}(-\alpha - j\beta))\ (-j\omega_w TB\ e^{-j\omega t}(-\alpha + j\beta))}{2\ (\alpha^2-\beta^2 + j(2\alpha\beta - \omega RC))(\alpha^2-\beta^2 - j(2\alpha\beta - \omega RC))}}$$

$$= \sqrt{\frac{\omega^2 w^2 T^2 B^2 (\alpha^2+\beta^2)}{2\ (\alpha^2-\beta^2)^2+(2\alpha\beta - \omega RC)^2}}$$

$$= \omega_w TB \sqrt{\frac{(\alpha^2+\beta^2)}{2((\alpha^2+\beta^2)^2+2\alpha^2\beta^2-4\alpha\beta\omega RC+\omega^2R^2C^2)}} \qquad 4 - 6$$

4.3 EQUATION OF THE PROPAGATION FUNCTION AND REALISATION OF THE EQUIVALENT CIRCUIT

Similarly to Figure 2.4 of section 2.4, from the geometry of the winding, the effective slot current at x is also equal to $Ti_{C'}$. Hence the local stator current density is

$$j_1 = \frac{Ti_{C'}}{\Delta} = \frac{TC'}{\Delta}\frac{\partial V}{\partial t}$$

which in this case, from 4 - 5

$$\frac{\partial V}{\partial t} = \frac{-\omega^2 w TB\ e^{j\omega t} e^{Ax}}{A\left[1 - \frac{j\omega RC}{A^2}\right]}$$

therefore the local stator current density is

$$j_1 = \frac{-\omega^2 w T^2 BC\ e^{j\omega t} e^{Ax}}{\left[1 - \frac{j\omega RC}{A^2}\right]} \qquad 4 - 7$$

and $$\frac{\partial j_1}{\partial x} = \frac{-\omega^2 \mu T^2 BC \; e^{j\omega t} e^{Ax}}{\left[1 - \frac{j\omega RC}{A^2}\right]}$$

From section 2.2, the general field equation of 2 - 5 still holds in this case giving

$$\frac{\partial^2 b}{\partial x^2} = \frac{\mu_o}{g}\left[\frac{\partial j_1}{\partial x} + \frac{1}{\sigma_2}\left[\frac{\partial b}{\partial t} + U \frac{\partial b}{\partial x}\right]\right]$$

substitute for; $\frac{\partial b}{\partial x} = AB \; e^{j\omega t} e^{Ax}$, $\frac{\partial^2 b}{\partial x^2} = A^2 B \; e^{j\omega t} e^{Ax}$, and $\frac{\partial b}{\partial t} = j\omega B \; e^{j\omega t} e^{Ax}$ into 2 - 5. Hence the general field equation for STLIM with stator resistance R is

$$A^2 = \frac{\mu_o}{g}\left[\frac{-\omega^2 \mu T^2 C}{\left[1 - \frac{j\omega RC}{A^2}\right]} + \frac{1}{\sigma_2}(j\omega + UA)\right] \qquad 4 - 8$$

which involves the fourth power of A.

Thus the coupled transmission line and thin conducting moving sheet together comprise a fourth order system. That is, there are in general four spatial modes having the same frequency as the drive, two propagating in the forward direction and two propagating in the backward direction. Solution of 4 - 8 yields the propagation constant A in terms of the machine parameters and the rotor speed. The solution, however, seems very difficult to obtain in this way. One practical approach is to assume the propagation constant is of the form $A = -\alpha - j\beta$ and then treat α and β as independent variables.

From the real part,

$$\alpha^2-\beta^2 = \frac{\mu_0}{g}\left[\frac{-\omega^2 wT^2 C((\alpha^2-\beta^2)^2+4\alpha^2\beta^2-2\alpha\beta\omega RC)}{(\alpha^2-\beta^2)^2+(2\alpha\beta-\omega RC)^2} - \frac{U\alpha}{g_2}\right] \quad 4-9$$

and from the imaginary part

$$2\alpha\beta = \frac{\mu_0}{g}\left[\frac{-\omega^2 wT^2 C(\alpha^2-\beta^2)\omega RC}{(\alpha^2-\beta^2)^2+(2\alpha\beta-RC)^2} + \frac{1}{g_2}(\omega-U\beta)\right] \quad 4-10$$

From 4 - 9 and 4 - 10 the values of U and C can be found. And the realisation of the equation 4 - 8 compared with that of 2 - 11 is

$$A^2 = \left[\frac{j\omega wT^2\mu_0}{g\left(1-\frac{j\omega RC}{A^2}\right)}\right]\left[j\omega\left[C+\frac{\alpha U\left[1-\frac{j\omega RC}{A^2}\right]}{\omega^2 wT^2 g_2}\right]+\frac{S\left[1-\frac{j\omega RC}{A^2}\right]}{wT^2 g_2}\right] \quad 4-11$$

Comparing 4 - 11 with 2 - 17, the equivalent circuit now has series impedance of $\frac{j\omega wT^2\mu_0}{g\left[1-\frac{j\omega RC}{A^2}\right]}$, and shunt admittance of $j\omega\left[C+\frac{\alpha U(1-j\omega RC/A^2)}{\omega^2 wT^2 g_2}\right]+\frac{S(1-j\omega RC/A^2)}{wT^2 g_2}$

Even from 4 - 9, 4 - 10 and 4 - 11 the solution of 4 - 8 still seems very awkward to recognise as of engineering value. So the direct solution of 4 - 8 has been abandoned in favour of an approximate solution which gives more insight of the operating of the machine. Experimentally only one dominant mode, the forward travelling wave, is observed. The exit end reflection can be suppressed by suitable terminating impedance. The aim of the following analysis is to investigate this mode, others being neglected: approximations

and assumptions are made in order to reach an engineering solution for the dominant mode.

First consider the case of no rotor. Since $1/\rho_2 = 0$ the propagation function becomes

$$A^2 = \frac{\mu_0}{g}\left[\frac{-\omega^2 wT^2 C}{1 - \frac{j\omega RC}{A^2}}\right]$$

$$A^2 - j\omega RC = -\omega^2 wT^2 C\mu_0/g$$

$$A^2 = (R + j\omega wT^2\mu_0/g)(j\omega C) \qquad 4 - 12$$

The form of 4 - 12 is more familiar, there are now only two modes, one propagating forward and the other propagating backwards as in a transmission line. The equivalent circuit suggested by 4 - 12 has per unit length a series resistance R, series inductance $L = wT^2\mu_0/g$, and shunt capacitance C.

The rotor is now replaced but in order to maintain a quadratic expression for the propagation function, the stator resistance R is assumed negligible. The propagation function is now the same as 2 - 17.

$$A^2 = \left[\frac{j\omega wT^2\mu_0}{g}\right]\left[j\omega\left[C + \frac{\alpha U}{\omega^2 wT^2\rho_2}\right] + \frac{S}{wT^2\rho_2}\right] \qquad 2 - 17$$

The equivalent circuit suggested by 2 - 17 has per unit length series inductance $wT^2\mu_0/g$, shunt capacitance $C + \alpha U/(\omega^2 wT^2\rho_2)$, and shunt conductance $S/(wT^2\rho_2)$.

Thus if R is negligible then 2 - 17 applies and there is only one forward travelling wave and one backward travelling

wave. Even if R is not negligible as in 4 - 12 the same conclusion is drawn provided the influence of the rotor is negligible: this will apply when the conducting sheet moves at or near synchronous speed. Since in general we are interested in the behaviour of the machine near synchronous speed, and in any practical machine the stator resistance should be small, the approximate equivalent circuit of Figure 4.2 is proposed. This has all the components derived from 2 - 17 but includes the stator resistance R as a series element as suggested by 4 - 12. While this circuit does not exactly represent 4 - 8, it is believed to predict the behaviour of the travelling wave machine sufficiently accurately for most practical purposes.

Using Figure 4.2 the propagation function becomes

$$A^2 = (R + j\omega L)(G + j\omega \overset{*}{C}) \qquad 4 - 13$$

where the per unit length values are $L = w\tau^2\mu_o/g$, $\overset{*}{C} = C + \alpha U/(\omega^2 w\tau^2 \rho_2)$ and $G = S/(w\tau^2\rho_2)$ as from 2 - 17, while R is the stator winding resistance per unit length. Thus by making the previous assumptions this form of approximate solution concentrates on only the dominant modes.

Now the solution of the attenuation function α and the phase function β can be given by

$$\alpha = \text{Real } \{(R + j\omega L)(G + j\omega \overset{*}{C})\}^{1/2} \qquad 4 - 14$$

$$\beta = \text{Imaginary } \{(R + j\omega L)(G + j\omega \overset{*}{C})\}^{1/2} \qquad 4 - 15$$

From 4 - 12 the initial values of α and β are obtained. These values are associated with zero slip. By increasing the value of slip by small steps and substituting into 4 - 13 the series of α and β at progressive values of slip is obtained. This numerical method of analysis was developed and the computer programme is shown in Appendix I.

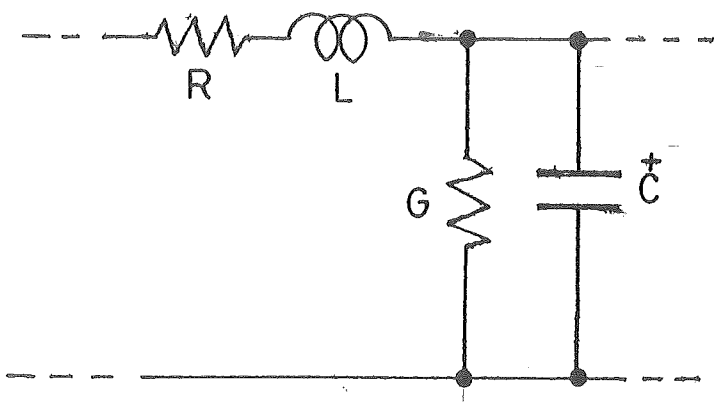

FIGURE 4.2 Proposed equivalent circuit.

4.4 THE SYNCHRONOUS SPEED

From 4 - 15 the synchronous speed of the machine is given by

$$U_s = \omega/\beta$$

When $R \ll \omega L$ and $G \ll \omega C$, the synchronous speed approaches $1/\sqrt{LC}$ as expected. This indicates the possibility of speed control either by varying the capacitance or by changing the inductance. As the latter is inversely proportional to gap width it would seem feasible to vary the speed by changing the airgap.

The theoretical synchronous speed is not fixed. Starting from approximately $1/\sqrt{LC}$ at slip S = 0 the synchronous

speed starts to decrease with increasing slip since the value of $\alpha U/(\omega^2 w T^2 g_2)$ increases as the speed drops. The term αU reaches a maximum and decreases again and hence we expect the synchronous speed to increase at slower rotor speed and to be approximately $1/\sqrt{LC}$ again at standstill.

4.5 ANALYSIS OF THRUST

The total value of thrust over the entire length l of the machine is given by

$$F = w\int_0^l \text{Real}\left[\frac{j_1 \overset{*}{b}}{2}\right]dx \qquad 2 - 23$$

where $\overset{*}{b}$ is the complex conjugate of b

From 4 - 7 the current density is

$$j_1 = \frac{-\omega^2 w T^2 BC\ e^{j\omega t} e^{Ax} A}{A^2 - j\omega RC}$$

hence 2 - 23 becomes

$$F = \tfrac{1}{2}w\int_0^l \text{Real}\left[\frac{-\omega^2 w T^2 BC\ e^{j\omega t} e^{Ax} A}{A^2 - j\ RC}\right] B\ e^{-j\omega t} e^{\overset{*}{A}x}\ dx$$

$$= -\tfrac{1}{2}\omega^2 w^2 T^2 B^2 C\int_0^l \text{Real}\left[\frac{A\ e^{-2\alpha x}}{A^2 - j\omega RC}\right]dx$$

$$= -\tfrac{1}{2}\omega^2 w^2 T^2 B^2 C\int_0^l \text{Real}\left[\frac{(-\alpha - j\beta)\ e^{-2\alpha x}}{(-\alpha - j\beta)^2 - j\omega RC}\right]dx$$

$$= -\frac{\omega^2 w^2 T^2 B^2 C(-\alpha^3 - \alpha\beta^2 + \omega\beta RC)}{2((\alpha^2+\beta^2)^2 + 2\alpha^2\beta^2 - 4\alpha\beta\omega RC + \omega^2 R^2 C^2)}\int_0^l e^{-2\alpha x}dx$$

$$F = -\left[\frac{\omega^2 w^2 T^2 B^2 C\ (\alpha^2+\beta^2)}{4((\alpha^2+\beta^2)^2 + 2\alpha^2\beta^2 - 4\alpha\beta\omega RC + \omega^2 R^2 C^2)}\left[1 - \frac{\omega\beta RC}{2\alpha(\alpha^2+\beta^2)}\right]\right]\int_0^1 -2\alpha\ e^{-2\alpha x}\ dx$$

From 4 - 6 substitute value of voltage

$$F = \frac{V^2 C}{2}\ (\ 1 - e^{-2\alpha l})\left[1 - \frac{\omega\beta RC}{2\alpha(\alpha^2 + \beta^2)}\right] \qquad 4 - 16$$

Compare 4 - 16 with the thrust expression obtained from 2 - 26, the effect of stator resistance reduces the thrust by the factor of $\left[1 - \frac{\omega\beta RC}{2\alpha(\alpha^2 + \beta^2)}\right]$.

4.6 CHARACTERISTIC IMPEDANCE AND OTHER ELECTRICAL PARAMETERS

The characteristic impedance as seen from the equivalent circuit of Figure 4.2 is

$$Z_o = \sqrt{\frac{R + j\omega L}{G + j\omega \overset{*}{C}}}$$

$$= \sqrt[4]{\frac{R^2 + \omega^2 L^2}{G^2 + \omega^2 \overset{*}{C}^2}}\ \angle\theta \qquad 4 - 17$$

where $\theta = \frac{1}{2}(\mathrm{Tan}^{-1}(\omega L/R) - \mathrm{Tan}^{-1}(\omega \overset{*}{C}/G))$

From 4 - 17, the characteristic impedance of STLIM is of very resistive nature since the usually designed parameters $\omega L \gg R$, and $\omega \overset{*}{C} \gg G$. The worst possible case is when the designed value $G \gg \omega \overset{*}{C}$, this give $\theta = \pi/4$ and hence the lowest possible power factor of the machine is still 0.707.

Consider ordinary operation of a STLIM at slip S when the rotor admittance $G = \omega \overset{*}{C}$. Then the power factor becomes $\mathrm{Cos}(\pi/8) = 0.924$ and the magnitude of the characteristic

impedance changes very little. The ratio of the magnitude of the noload characteristic impedance over the characteristic impedance at $G = \omega\overset{*}{C}$ is

$$Z_{o(G=0)} : Z_{o(G=\overset{*}{C})} = \sqrt[4]{2} : 1 = 1.19:1$$

Hence STLIM has a fairly constant input current characteristic for all range of slip. Similar conclusions can be drawn for the power input characteristic. The input power at noload is mainly absorbed by the terminating impedance, and at high slip is mainly absorbed by the rotor circuit. Finally, from constant voltage drive, the other electrical parameters are as follows:

The magnitude of input current is

$$I = V\sqrt[4]{\frac{G^2 + \omega^2\overset{*}{C}^2}{R^2 + \omega^2 L^2}} \qquad 4 - 18$$

The input power is

$$P_i = VI \cos\theta \qquad 4 - 19$$

where the power factor is $\cos\theta = \cos\left[\frac{1}{2}(\tan^{-1}(\omega L/R) - \tan^{-1}(\omega\overset{*}{C}/G)\right]$

The output power is

$$P_o = FU_s(1 - S) \qquad 4 - 20$$

The efficiency is

$$\eta = \frac{P_o}{P_i} \qquad 4 - 21$$

which can be recast in terms of machine parameters as

$$\eta = \frac{\omega\dot{C}(1-S)(1-e^{-2\alpha l})(1-\omega\beta RC/(2\alpha(\alpha^2+\beta^2)))}{\sqrt{(G^2+\omega^2\dot{C}^2)}\ (\mathrm{Sin}\phi_1+\mathrm{Sin}\phi_2)} \qquad 4-21a$$

where $\phi_1 = \mathrm{Tan}^{-1}(\omega L/R)$, and $\phi_2 = \mathrm{Tan}^{-1}(\omega\dot{C}/G)$

Consider the case of ideal design with no stator resistance and total absorbtion of power in the rotor circuit, 4 - 21a becomes

$$\eta = \frac{\omega\dot{C}(1-S)}{\sqrt{(G^2+\omega^2\dot{C}^2)}\ (1+\mathrm{Sin}\phi_2)} \qquad 4-21b$$

For the case $G \ll \omega\dot{C}$, 4 - 21b becomes

$$\eta = 0.5(1-S)$$

and for the case $G > \omega\dot{C}$, 4 - 21b becomes

$$\eta = \frac{\omega\dot{C}}{G}(1-S)$$

This implies that the maximum efficiency can only be 50% on the basis of the assumed theoretical model.

4.7 SOME DESIGN CRITERIA OF STLIM

From the previous analysis of STLIM, some special design criteria must be considered for this type of motor. The following points are considered for assessing the design quality of a STLIM.

4.7.1 Laithwaite's Goodness Factor

For linear induction machines, it has been found that the goodness factor introduced by Laithwaite [2] is a convenient measure of quality of the machine. The goodness factor of a linear induction machine with solid sheet rotor

can be expressed as

$$G = \frac{2f\mu_0 P^2 t}{\pi \rho g}$$

where P is the pole pitch of the machine, ρ is the rotor volume resistivity and t is the thickness of the rotor. This equation can be rewritten in terms of the phase function β by the relationship of the synchronous speed, $U_s = 2Pf = \omega/\beta$. Hence the goodness factor becomes

$$G = \frac{\mu_0 \omega^2 t}{2\pi f \rho_g \beta^2} \qquad 4 - 22$$

Although this relationship is derived from zero attenuation travelling wave of ordinary linear induction motor, it is assumed applicable to STLIM with attenuated travelling wave nature. This can be justified when operating at near synchronous speed, $R \ll \omega L$ and $G \ll \omega \overset{+}{C}$, and the winding can be classified as that of the low loss transmission line situation.

In the case of STLIM with fixed value of capacitance, it is very interesting to see that increasing the airgap also means increase in synchronous speed. For $R < \omega L$ and $G < \omega \overset{+}{C}$, the phase function β is approximately equal to $\omega\sqrt{L\overset{+}{C}}$. Hence the proposed goodness factor of STLIM is

$$G = \frac{\mu_0 t}{2\pi f \rho_g L \overset{+}{C}} = 1/(2\pi f \rho_2 w T^2 \overset{+}{C}) \qquad 4 - 22a$$

where $\rho_2 = \rho/t$ the sheet resistance of the rotor. Equation 4 - 22a suggests that the goodness factor of STLIM varies as

the synchronous speed of the machine vary with capacitance. The change in airgap has very little effect on the goodness factor of the machine. This is unusual for electrical machines and hence implies the possibility of speed control by varying the airgap of the machine without degrading the quality of the machine.

Finally, the fundamental definition of the goodness factor for the secondary, in terms of the equivalent circuit, is given as

$$G = X_m/R_2$$

where X_m is the magnetising reactance and R_2 is the secondary resistance. For STLIM equivalent circuit of Figure 4.2, each unit section has shunt conductance of $S/(w\tau^2 g_2)$, and shunt admittance of $\omega\hat{C}$. Hence the apparent secondary resistance R_2 is $w\tau^2 g_2$, and the apparent magnetising reactance for this equivalent circuit is $1/\omega\hat{C}$. The goodness factor as found from the definition becomes

$$G = 1/(2\pi f g_2 w\tau^2\hat{C})$$

which is equal to that obtained from 4 - 22a

Although the goodness factor is a useful index in preliminary design of linear machine, however, it has been shown that large goodness factor does not ensure maximum machine performance. Nasar and Boldea [5] show that some modification must be met in order to reach better machine performance. The optimum goodness factor is introduced, and it is a function of a number of poles, increasing as an increasing number of poles.

4.7.2 The Noload Cutoff Frequency

From the previous result for the expression of the goodness factor of STLIM, unlike most of the linear machines for which it is proportional to supply frequency, STLIM goodness factor is inversely proportional to supply frequency. This is hardly surprising because as seen from the equivalent circuit that resembles the transmission line, it behaves as a lowpass filter. In the design of STLIM, it is very important to design the value of the natural cutoff frequency to be greater than the supply frequency.

The value of the natural cutoff frequency can be found by the loop cutoff frequency of each section of the actual circuit connections as shown in Figure 4.3.

From any text, the cutoff radian frequency of this ladder network, ω_c, is

$$\omega_c = \frac{2}{\Delta\sqrt{LC}}$$

which in case of STLIM, the noload cutoff frequency, f_c becomes

$$f_c = \frac{1}{\Delta\pi}\sqrt{\frac{g}{w\tau^2\mu_o C}} \qquad 4 - 23a$$

Alternatively in terms of noload synchronous speed, the cutoff frequency is

$$f_c = U_s/\Delta\pi \qquad 4 - 23b$$

Equation 4 - 23b is very useful for preliminary design of STLIM. For any value of the minimum designed value of synchronous speed, there is a minimum unit section which

corresponds physically to the slot pitch, the number of turns per coil, and the maximum value of unit shunt capacitance for variable speed control.

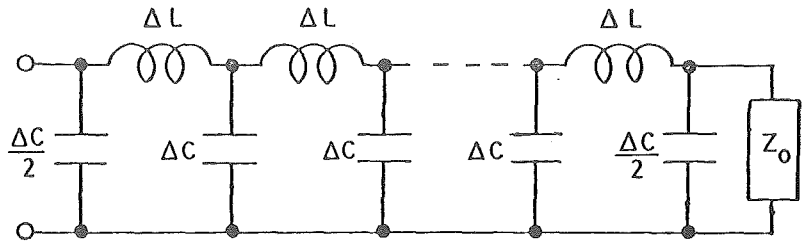

FIGURE 4.3 Actual circuit connection of STLIM.

CHAPTER 5

THE IMPROVED NON-OVERLAP COIL EXPERIMENTAL MOTOR

5.1 SOME PRELIMINARY CONSIDERATIONS

From the analysis of non-overlap coil STLIM in the previous chapter, the performance qualities of the machine are reduced by high value of stator resistance. Using the parameters of the first experimental motor, with stator resistance of 210 ohms/m, and the typical operating condition of 2400 μF/m capacitance, 7 m/s rotor speed: At this point, extract from Figure 3.2, the predicted attenuation function, α, is 5.5 and the predicted phase function, β, is 31. The force predicted neglecting the effect of stator resistance, from Figure 3.3, is about 48 N and the experimental force measured, from Figure 3.5, is about 20 N. Taking account of the stator resistance the corresponding thrust at this point, as calculated from 4 - 16, is 26 N. This results in lower output power and efficiency than the theoretical prediction without stator resistance.

Hence a new machine is needed and one of the primary design parameters is to keep the value of stator resistance per unit length as low as possible. This means that the term $\omega\beta RC/(2\alpha(\alpha^2+\beta^2))$ from 4 - 16 must be much less than unity at all ranges of the designed operational slip.

The second point learnt from the previous experience on the first machine was, when loaded the stator coils at the far end carry very small current and the reflected voltage is

very small. From this point of view, the machine could be designed to have a shorter length of stator block without heavy reduction in the thrust. This can be justified when the design value of the term $(1 - e^{-2\alpha l})$ at full load slip is near unity. As illustrated by the same operating point of the previous example, stator length $l = 0.6$ m, $\alpha = 5.5$, speed $U = 7$ m/s and capacitance $C = 2400\,\mu F/m$, the contribution of the term $(1 - e^{-2\alpha l})$ is 0.998. If the length of the stator is cut in half, the contribution of the term $(1 - e^{-2\alpha l})$ is still 0.963. This means that only 2.5% of extra thrust is obtained at the cost of twice the size of the machine. Therefore the optimum length of the machine must be designed in order to meet the required operating condition. Furthermore for our arrangement of the measuring system by linear stator and disc rotor, the error of the linear velocity at the inner and outer edges of the stator block compared to the middle of the block will be reduced by the reduction in stator length.

Finally the preliminary specifications of the new test machine are as follows; the minimum synchronous speed of about 10 m/s, variable speed control by both change in shunt capacitance and winding inductance via change in airgap, the dimension of the propulsion area not more than 40 cm by 10 cm in order to compare performances with the already available data of the 3-phase machine[3, 14], and to have low stator resistance. A comparision of STLIM and LIMs is given in pp.157-158.

5.2 THE DESIGN OF THE PRIMARY

The propulsion area of the stator block is chosen to be 40 cm long and 9 cm wide. For noload synchronous speed of

10 m/s this corresponds to a 4 pole machine. With the maximum avaliable capacitance per unit length of 2000 μF/m, the value of machine inductance per meter, $L = 1/U_s^2C$, is 5 H/m. Hence the number of turns required for the stator coil for say 1.5 cm airgap is $T = \sqrt{Lg/w\mu_o}$ = 610 turns. The coil of 600 turns is chosen for the final design value.

From the loop cutoff frequency consideration, the value of slot pitch, Δ, at cutoff frequency of the 50 Hz supply from 4 - 23b is $\Delta = U_s/\pi f_c$ = 0.0637 m. This will be the upper limit of the design slot pitch of the machine. The machine is expected to operate as a variable speed device by means of extending the airgap as well as varying the value of shunt capacitance. Due to the arrangement of the stator coil, once the airgap is extended further than the value of the slot width, the heavy increase of the slot leakage flux may interfere with the theoretical model. Hence the slot width must be as big as possible. For the extended airgap of 3 cm, the slot width of 3 cm is chosen and the tooth pitch of 5 cm is needed. At this physical size and the minimum value of 10 m/s synchronous speed, the loop cutoff frequency becomes 63.7 Hz and the machine has low pole pitch:tooth pitch ratio. Although the loop cutoff frequency is close to the supply frequency; as the synchronous speed increases, either by reducing the shunt capacitance or extending the airgap, the loop cutoff frequency will increase linearly with the synchronous speed. The ratio of pole pitch:slot pitch is also increased as the pole pitch increase.

This will result in an eight tooth stator block for the entire length of 40 cm. The machine will have the disadvantage

of a heavily lumped circuit nature. This will result in degrading the performance of the machine which is modeled as distributed parameters. On the other hand, the machine will have a smaller number of connections and allow a wider range of the shunt capacitance value.

Now the designed value of stator resistance must be kept as low as possible. The value chosen is estimated from $\omega\beta RC/(2\alpha(\alpha^2+\beta^2)) \leq 0.1$. The typical value of the phase function, β, is taken as 31.4, which corresponds to 10 m/s synchronous speed. The value of the attenuation function, α, is estimated from the value at slip where 96% theoretical ideal thrust occurs. This will give the value of $\alpha = -(\ln 0.04)/21 = 4$. Hence the minimum value of stator resistance per meter length is $R = 0.1(2\alpha(\alpha^2+\beta^2))/\omega\beta C = 41$ ohms/m for the typical capacitance of 2000 μF/m. This allows the coil resistance of $41 \times 0.05 = 2$ ohms/coil. Using the resistivity of copper conductor, ρ, as 0.018 micro-ohms-m, the minimum cross -sectional area of the conductor of 600 turn coil with mean length per turn of 0.4 m is $A = \rho l/R = 2.17$ mm^2. The conductor of 1.8 mm diameter with the cross-sectional area of 2.545 mm^2 is chosen. The total cross-sectional area of coil, calculated from conductor space factor of 0.5, is equal to $2 \times 600 \times 2.545$ mm^2 = 30.5 cm^2. Allowing 0.5 mm thickness for slot insulation all round, the minimum depth of the slot required is 10.5 cm. The design value of 12 cm is chosen allowing for search coil and slot wedge. For a tooth width of 2 cm and tooth pitch of 5 cm, when operating at maximum designed synchronous speed of about 15 m/s the thickness of the back iron stack must be at least three times the tooth width in order to maintain

operation without any problem of saturation in the back iron stack.

The final dimensions of the stator blocks are: length 40 cm, width 9 cm, total stack height 18 cm, tooth pitch 5 cm, tooth width 2 cm, slot depth 12 cm. There are 8 teeth per stator block. Laminated silicon steel of 0.5 mm sheet thickness is used and the total weight of the magnetic circuit is 60 kg. The measured resistance of the widing is 40 ohms/m.

The coil arrangement is chosen as double layer winding from pre-wound coils. Each stator block has four 450 turn coils and four 150 turn coils alternately placed in slots. The total eight series connected coils of 600 turns is formed by the opposite slot of the double sided stator. The total weight of the coils is 43.5 kg. Three sets of capacitors per coil were used; 60 μF, 80 μF and 100 μF. This corresponds to the capacitance per meter of 1200 μF, 1600 μF and 2000 μF. The complete stator connection is shown in Figure 5.1.

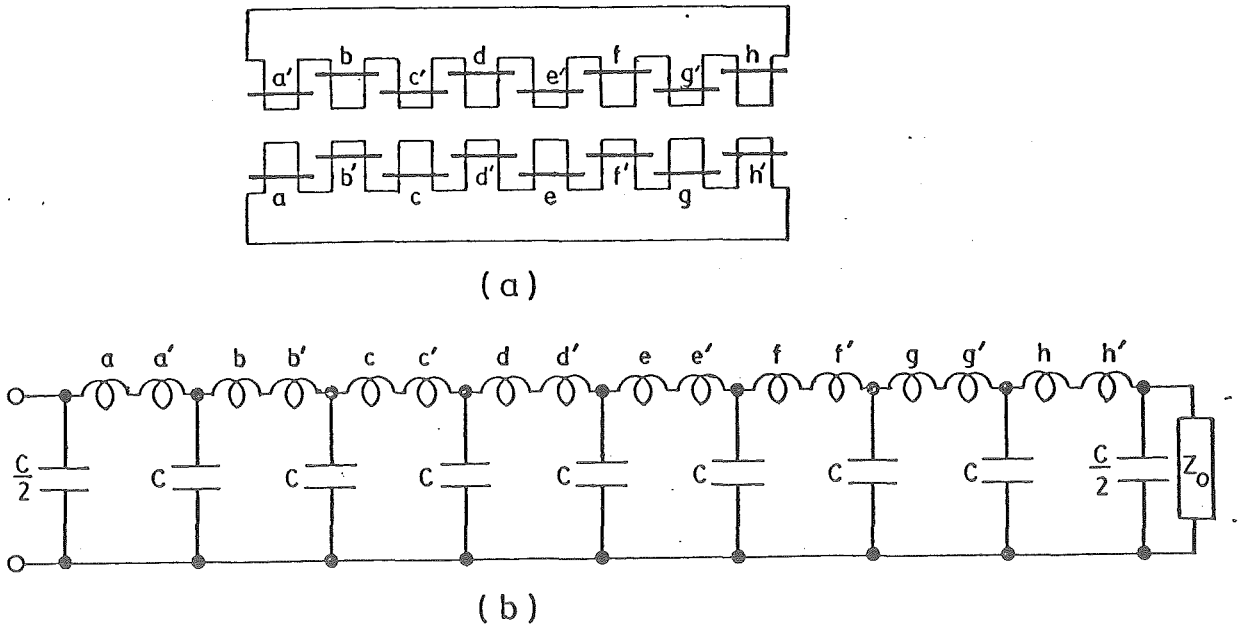

FIGURE 5.1 Stator connections diagram

n denote a 450 turn coil

n' denote a 150 turn coil

5.3 THE DESIGN OF THE SECONDARY

Aluminium disc rotors are used for the secondaries. They are made from the maximum possible diameter of the commercial sheet avaliable. This is aimed to minimise the error effect of the non-uniform linear velocity at different parts under the stator block. Three aluminium sheet rotors are chosen, thickness 3 mm, 5 mm and 10 mm, each forming a disc 1.20 m in diameter. The linear velocity is taken at the mean radius of 0.47 m which corresponds to the distance between the center of the disc and the middle of the stator block.

The calculated goodness factor of the machine, using 4 - 22 with an effective stator width, w, of w+2g, is shown in Table 5.1. The machine has 4 poles when the synchronous speed is 10 m/s, by changing the shunt capacitance and the gap width it is possible to vary the number of poles about this figure. Assuming the optimum goodness factor for 3-phase machine as published by Nasar and Boldea[5] is applicable to STLIM, a goodness factor of around 10 would therefore seem optimum.

5.4 APPARATUS SETUP AND MEASURING EQUIPMENT

The stator was then mounted onto the frame. The rotor shaft is 4 cm diameter and one end of the shaft is connected to a drum-brake of mean radius of 11 cm. Thrust is measured via rope-brake arrangement and the maximum weight that can be put in the weighing pan is 350 N. This corresponds to the machine thrust of 82 N. A search coil of 3 turns is fitted

C(μF/m)		1200			1600			2000		
Secondary thickness(mm)		3	5	10	3	5	10	3	5	10
Airgap(mm)	12	7	11	23	5	8	17	4	7	14
	15	6	11	21	5	8	16	4	7	13
	18	6	10	20	5	8	15	4	6	12
	21	6	10	19	4	7	15	3	6	12
	24	6	9	18	4	7	14	3	6	11
	27	5	9	18	4	7	13	3	5	11
	30	5	8	17	4	6	13	3	5	10

TABLE 5.1 The goodness factor of the machine.

on each tooth to investigate the amplitude and phase of the flux along the stator. Because when on load the rotor distorted due to heating, there has to be large clearance between the rotor and the stator block: the airgap has to be at least 7 mm wider than the thickness of the disc. The airgap is adjustable from 12 to 30 mm. The machine is fed by variac at the supply end and terminated with a 55 ohms resistor at the far end. It will be remembered that 4 - 8 implies two forward moving fields and two backward moving fields, and therefore the machine should be terminated so as to eliminate not one, but two reflected waves. In addition the termination should vary as the slip changes since the propagating constant is a function of rotor speed. In practice, however, there is one dominant forward travelling field and its corresponding reflection, while because of attenuation the amplitude of this reflected wave is extremely low. It is found that it is possible to minimise the reflected wave by terminating the machine in a resistance and that a fixed resistor is suitable. The motor assembly is shown in Figure 5.2 and the measuring apparatus is shown in Figure 5.3

5.5 ELECTRICAL CAPACITY OF THE EXPERIMENTAL MACHINE

From section 5.2, the cross-sectional area of the stator comductor is $2\frac{1}{2}$ mm^2. Taking the maximum current density of stator conductor as 5 A/mm^2, the maximum allowable current on stator winding will be about 12 amps. For a typical case as selected in Section 5.2, the characteristic impedance is about 50 ohms. The value of input voltage at

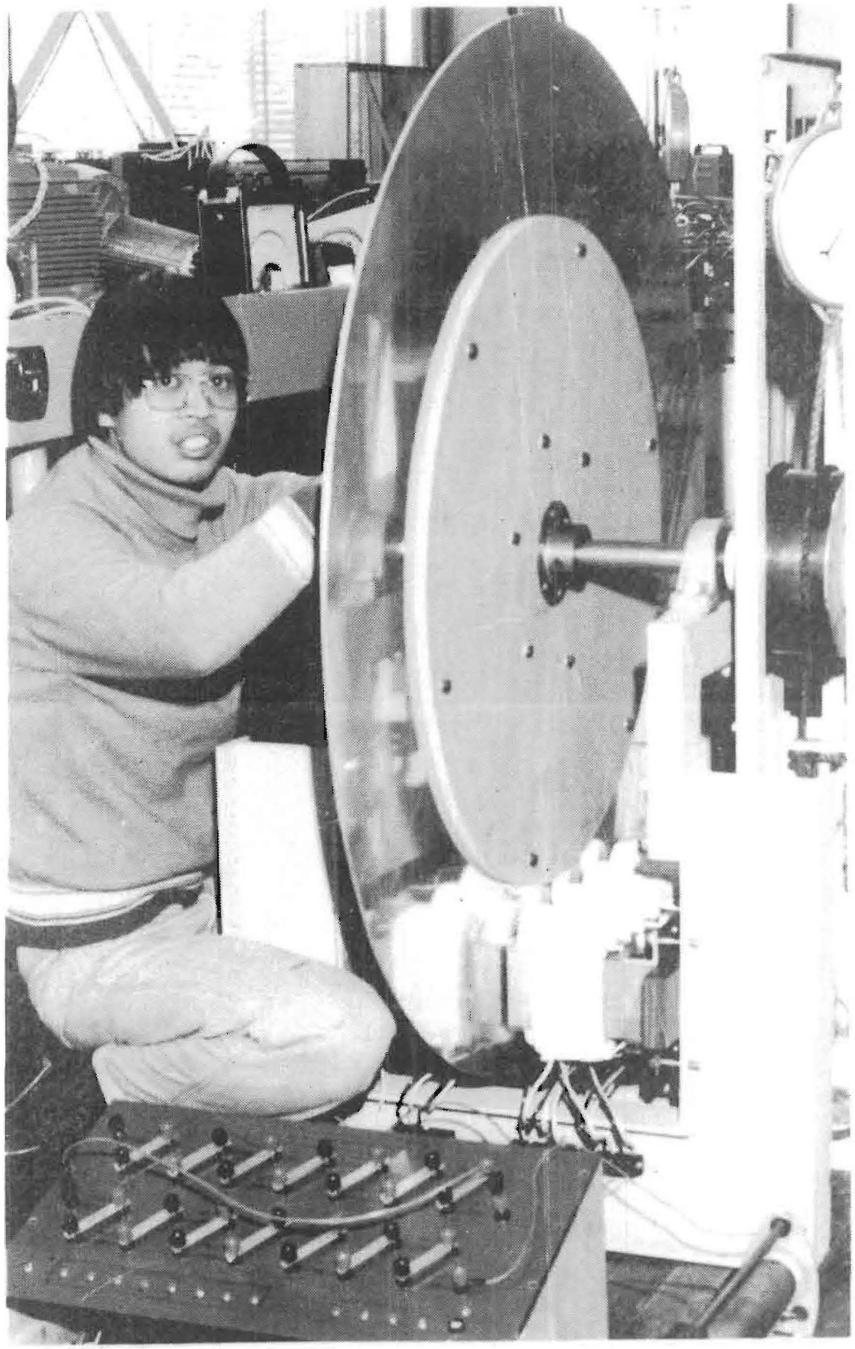

FIGURE 5.2 The experimental machine assembly

FIGURE 5.3 The measuring apparatus

12 amps. input current is V = IR = 600 volts. At this voltage, the maximum airgap flux density as calculated from 4 - 6 taking $\alpha = 0$ is $B_{max} = \frac{V}{\omega w T}\sqrt{(2\beta^4+2\omega^2R^2C^2)/\beta^2} = \sqrt{2}\ V\beta/(\omega w T) = 0.88$ T with 50 Hz supply. This value will just saturate the teeth with a flux density of 2.2 T. Hence the machine is designed to have both electric and magnetic upper limit at the supply voltage of around 600 volts. The expected thrust at this voltage will be about 360 N. Due to the rating of the measuring equipment, cooling problem on the disc, the available supply voltage, and the rating of the shunt capacitors, the test results will be measured on the safer low level of supply voltage. The constant supply voltage of 200 V is chosen. It should be noted that, at 200 V, the machine is operating at under voltage rating. This accounts for low value of thrust and power output of the experimental machine.

CHAPTER 6

RESULTS OF THE EXPERIMENTAL MACHINE

6.1 THEORETICAL PREDICTIONS OF THE EXPERIMENTAL MACHINE.

From experimental machine descriptions in the previous chapter and the theoretical model in chapter 4, a computer programme is developed. The programme is shown in Appendix 1. Due to the transverse edge effect and skin effect, the value of the secondary sheet resistance are somewhat bigger than the theoretical value of ρ/t, where t is the thickness of the sheet. In fact the correcting factor of 2 is used in these cases. The theoretical predictions obtained from the computer programme are then presented in graphical form. The chosen performances are: speed of the rotor in X-axis; power input, power output, input current, efficiency and thrust in Y-axis. The supply voltage is calculated at 200 V 50 Hz. The typical case of theoretical prediction is shown in Figure 6.1. Each theoretical case is shown in Appendix 2 from Figure A1 to Figure A54. They are predictions with three sets of rotor thickness 3 mm, 5 mm and 10 mm. With each rotor thickness the airgap is varied from 15 mm to 30 mm at the interval of 3 mm step. The summary of theoretical maximum efficiency for each individual cases is tabulated out in Table 6.1

6.2 SUMMARY OF TEST RESULTS

Initially the experimental machine was set at airgap of 15 mm, shunt capacitance per coil of 60 μF and rotor disc

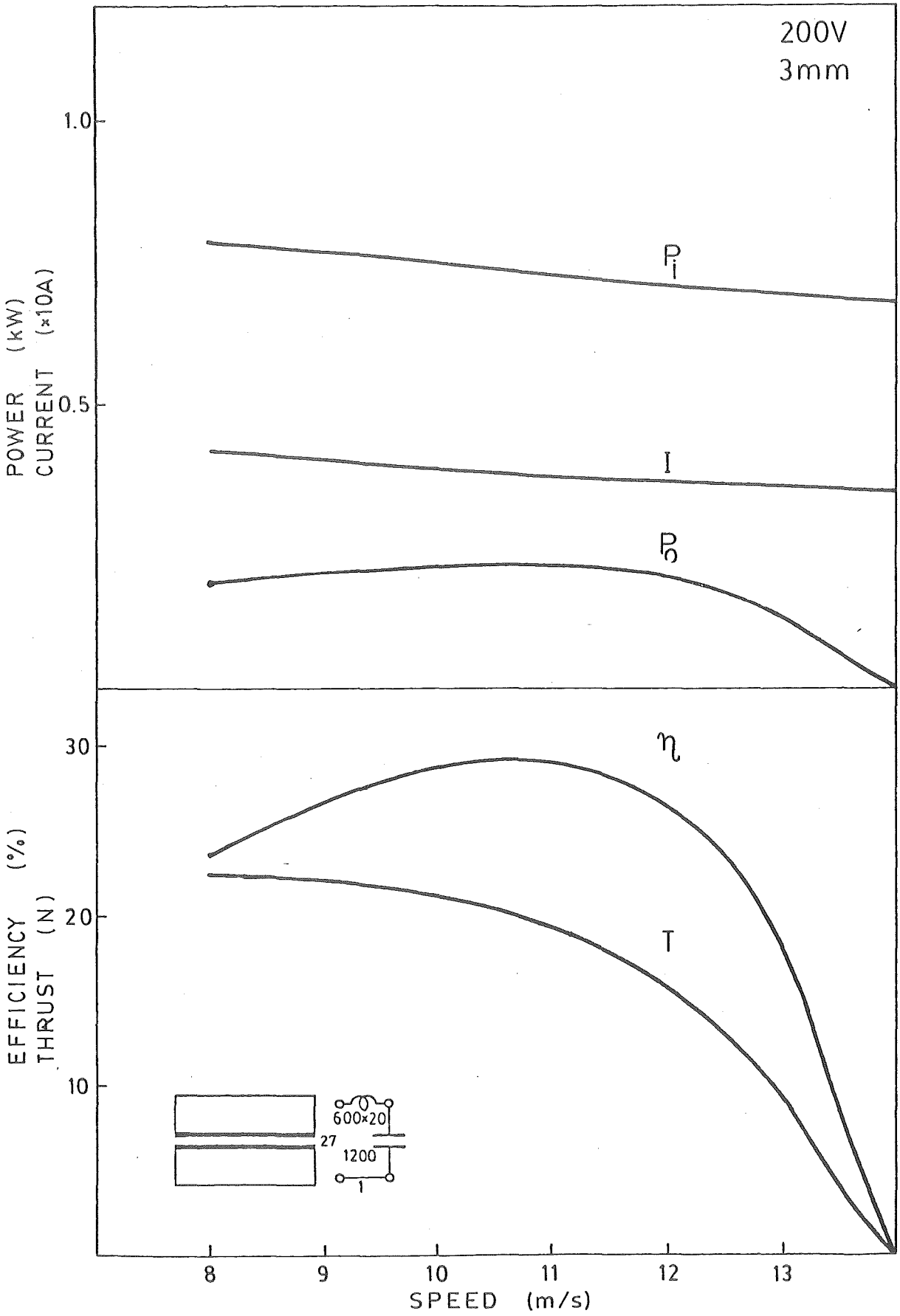

FIGURE 6.1 Theoretical characteristics of STLIM
supply voltage = 200 V, rotor thickness = 3 mm,
airgap = 27 mm and shunt capacitance = 1200 μF/m.

C(μF/m)		1200			1600			2000		
Secondary thickness(mm)		3	5	10	3	5	10	3	5	10
Airgap(mm)	15	31	29	25	32	31	28	32	32	30
	18	30	29	25	31	31	28	31	32	30
	21	30	29	25	30	31	28	30	31	30
	24	29	29	26	30	30	28	29	31	30
	27	29	29	26	29	30	28	29	31	30
	30	29	29	26	29	30	28	28	30	30

TABLE 6.1 Theoretical maximum efficiency in per cent.

of 3 mm thickness. Several preliminary trial runs were made at 50 Hz supply voltage fed from variac up to 300 V. It was noticed that when heavily loaded, the disc tends to distort and hit against the side of the stator block. The attenuated travelling wave was set up and seems to have only one dominant mode. The performance of the machine when loaded was very little dependent of the value of terminating impedance. With fixed value of terminating resistance, there was very small change in power factor for all range of slip and the lowest power factor recorded at standstill was 0.97. The machine inherits very small change in current and input power for all range of slip. The phase shift of the travelling wave along the stator block as observed from oscilloscope was rather uniform except at the terminated impedance end. Different values of terminating impedance gave rise to fluctuation of the end phase shift but due to the attenuated travelling wave nature they seem to have little effect on the overall machine performance. As slip increases the phase shift is increased hence the reduction in synchronous speed as expected from the analysis. The total stator resistance is 16 ohms. This value compared with the estimated value from the design(14ohms) was a bit high. This was due to the number of circuit connection points and the operating temperature of the machine.

Test results are summarised here and then considered in detail in the following sections of this chapter.

The first series of test were chosen at 200 V 50 Hz supply voltage with fixed terminating resistance of 55 ohms, with different values of airgap, shunt capacitance and rotor thickness corresponding to each predicted case in Section 6.1.

In each test, the value of thrust, power input and current were recorded for different values of speed. These data were calculated and presented in graphical form from Figure A55 to Figure A98. Because the value of designed goodness factor for 3 mm rotor and 2000 μF/m shunt capacitance are far lower than the optimum value suggested by Nasar and Boldea[5], none of the experimental results for 3 mm rotor is recorded.

Next, the no rotor synchronous speeds were obtained for each individual case. They are calculated from the avarage phase shift from oscilloscope. The summarised results of the theoretical and experimental no rotor synchronous speed and no load speed of the machine are shown in Table 6.2. Table 6.3 summarises the maximum efficiency obtained from test results of Figure A55 to Figure A98.

After completing these tests some typical experimental cases of different values of terminating resistances, supply frequency, field distributions and losses seperations were investigated.

6.3 GENERAL THEORETICAL AND EXPERIMENTAL RESULTS COMPARED.

From the basic thrust expression, $V^2C/2$, the motor was designed to produce a maximum thrust of 24 N, 32 N and 40 N at 200 V 50 Hz when the capacitance per coils were 60 μF, 80 μF and 100 μF respectively. In most experimental cases, the thrust follows the theoretical predictions table. When comparing the efficiencies of the experimental results of Table 6.3 to the theoretical results from Table 6.1, there are some discrepancies among them. The experimental efficiencies tend to be low at narrow airgap, this is probably due to

Shunt capacitor μF/coil	Linear velocity m/s for rotors of thickness 3 mm, 5 mm, 10 mm.		Airgap mm						
			12	15	18	21	24	27	30
60	no rotor synchronous speed	calculated	11.7	12.4	12.9	13.4	13.7	14.1	14.4
		measured	11.3	12.2	12.6	13.5	13.7	14.0	14.3
	rotor no load speed	3 mm	10.0	11.0	11.7	12.3	12.8	-	-
		5 mm	11.0	11.6	12.2	12.7	13.2	13.5	13.8
		10 mm	-	-	12.5	13.1	13.4	13.5	13.5
80	no rotor synchronous speed	calculated	-	10.7	11.2	11.6	11.9	12.2	12.4
		measured	9.3	10.4	11.0	11.4	11.8	12.0	12.2
	rotor no load speed	3 mm	8.2	9.0	9.7	10.0	10.4	-	-
		5 mm	9.2	9.7	10.3	10.7	10.9	11.1	11.4
		10 mm	-	-	10.7	11.0	11.3	11.6	11.7
100	no rotor synchronous speed	calculated	9.1	9.6	10.0	10.4	10.6	10.9	11.1
		measured	9.0	9.2	9.6	10.0	10.2	10.5	10.7
	rotor no load speed	5 mm	-	8.4	8.9	9.3	9.5	9.9	-
		10 mm	-	-	9.6	9.9	10.2	10.6	10.6

TABLE 6.2 Theoretical and experimental no-rotor synchronous speed, and no-load speed of the machine.

C(μF/m)		1200			1600			2000	
Secondary thickness(mm)		3	5	10	3	5	10	5	10
Airgap(mm)	12	18	18	-	16	18	-	-	-
	15	20	23	-	19	21	-	20	-
	18	24	25	22	21	25	26	22	24
	21	25	27	23	22	26	27	23	27
	24	25	27	24	22	27	28	23	29
	27	-	28	24	-	26	27	23	29
	30	-	27	23	-	25	27	-	28

TABLE 6.3 Experimental maximum efficiency in per cent.

the physical dimension of the slot pitch and slot width which gives the airgap travelling field a very lumpy nature rather than smooth sinusoidally distributed. When the airgap is increased, this effect is reduced. At bigger airgap, in general, the experimental efficiencies compared well with the theoretical predictions but in some cases they do not. The calculated goodness factor of Table 5.1 gives some reason for these discrepancies. Considering the compared cases of Figure 6.2 and Figure 6.3, each figure shows the experimental and the theoretical characteristics of the machine at 27 mm airgap and 60 μF/coil shunt capacitance. The machine has no-rotor synchronous speed of 14.1 m/s and reducing with an increasing slip. This corresponds to about 3 poles at no-load and increasing toward 4 poles with increasing slip. Figure 6.2 with calculated goodness factor of 9 for 5 mm secondary seems to have agreement on the performance. The predicted efficiency of 29% is close to the 28% measured efficiency and the general agreement between theoretical and experimental characteristics is quite good. For Figure6.3 with calculated goodness factor of 18 for 10 mm secondary, a value far beyond the suggested optimum value[5], the predicted efficiency is 26% when the experimental results nearly reach 24%.

For another comparative case Figure 6.4 and Figure 6.5 correspond to the case of 24 mm airgap and 100 uF/coil shunt capacitance for 5 mm secondary and 10 mm secondary respectively. The no-rotor synchronous speed is 10.9 m/s which corresponds to 4 poles machine. The number of poles increase toward 5 poles for an increasing slip hence the goodness factor of 5 for 5 mm secondary is far lower than optimum value and the

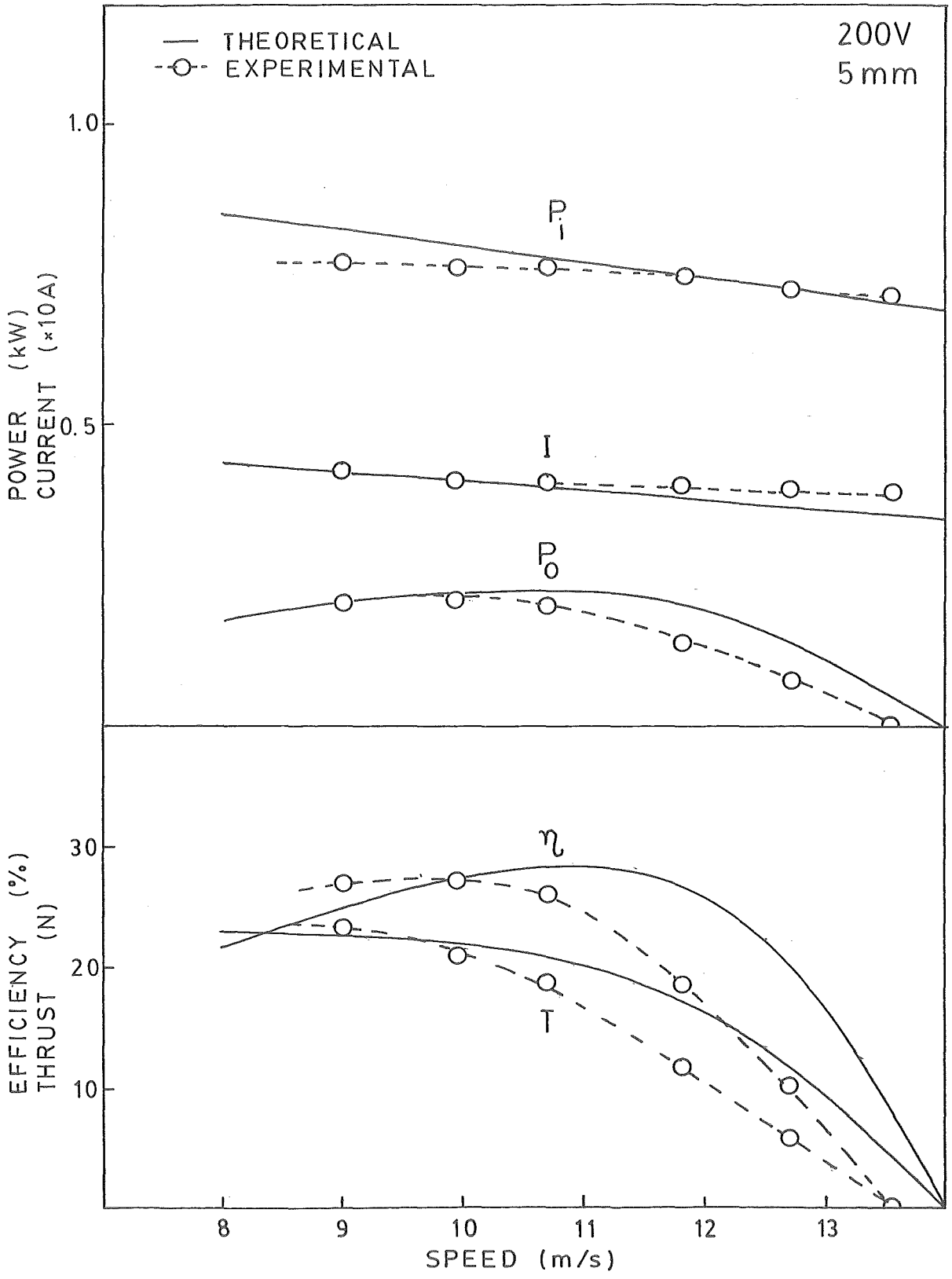

FIGURE 6.2 Typical characteristics of the motor for constant voltage drive; C = 60 μF/coil, g = 27 mm, secondary thickness = 5 mm.

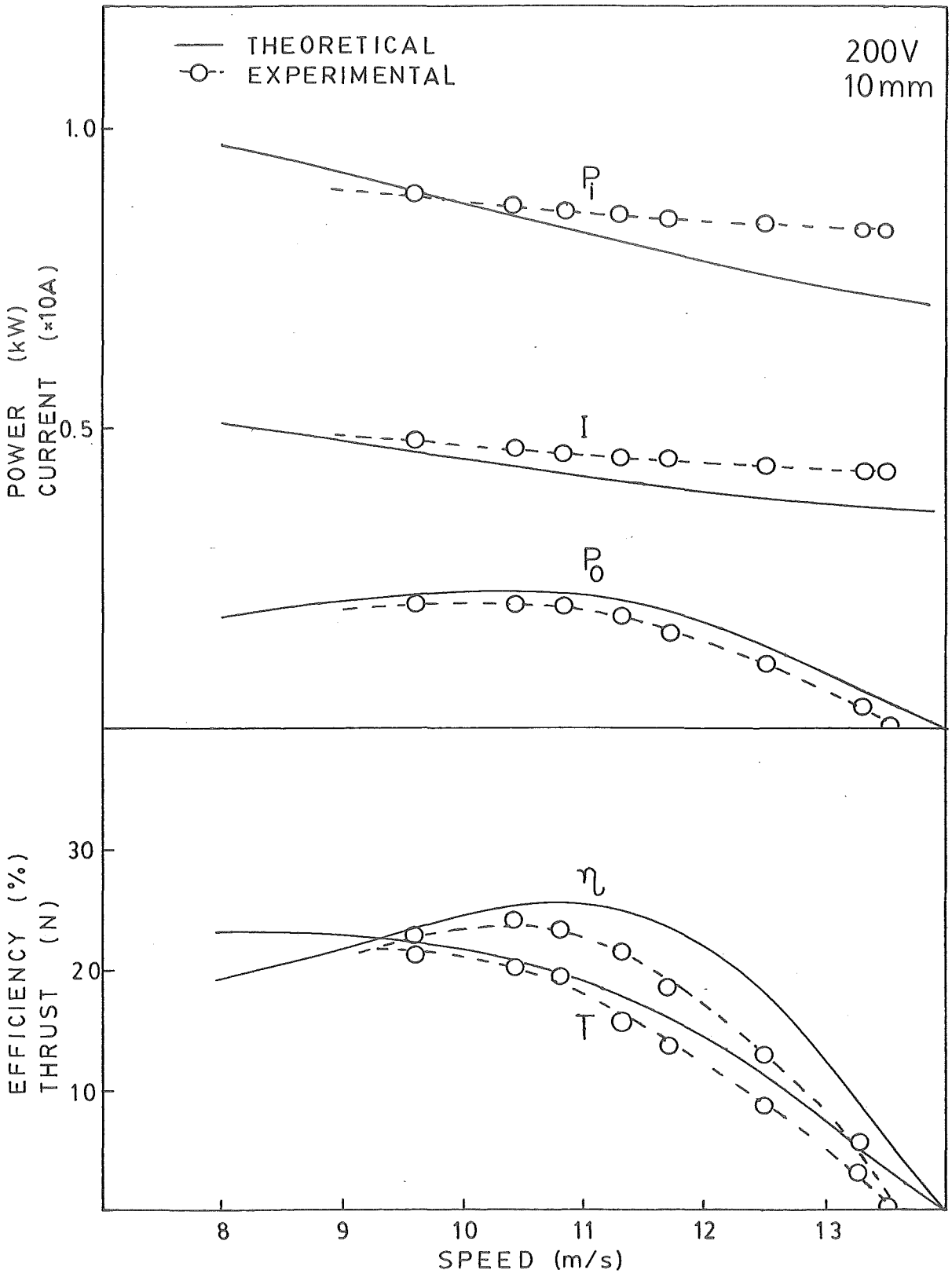

FIGURE 6.3 Typical characteristics of the motor for constant voltage drive; C = 60 μF/coil, g = 27 mm, secondary thickness = 10 mm.

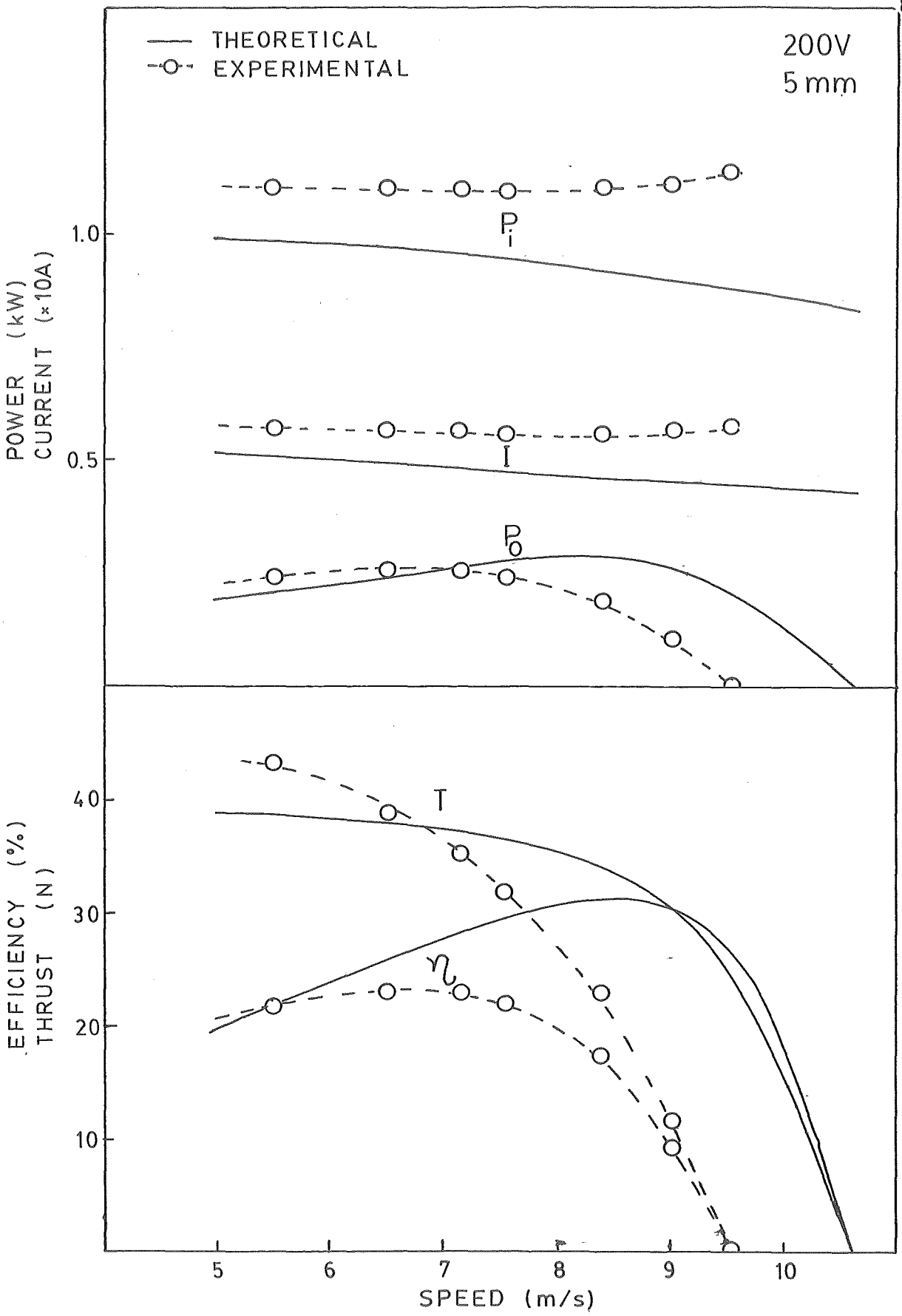

FIGURE 6.4 Typical characteristics of the motor for constant voltage drive; C = 100 μF/coil, g = 24 mm, secondary thickness = 5 mm.

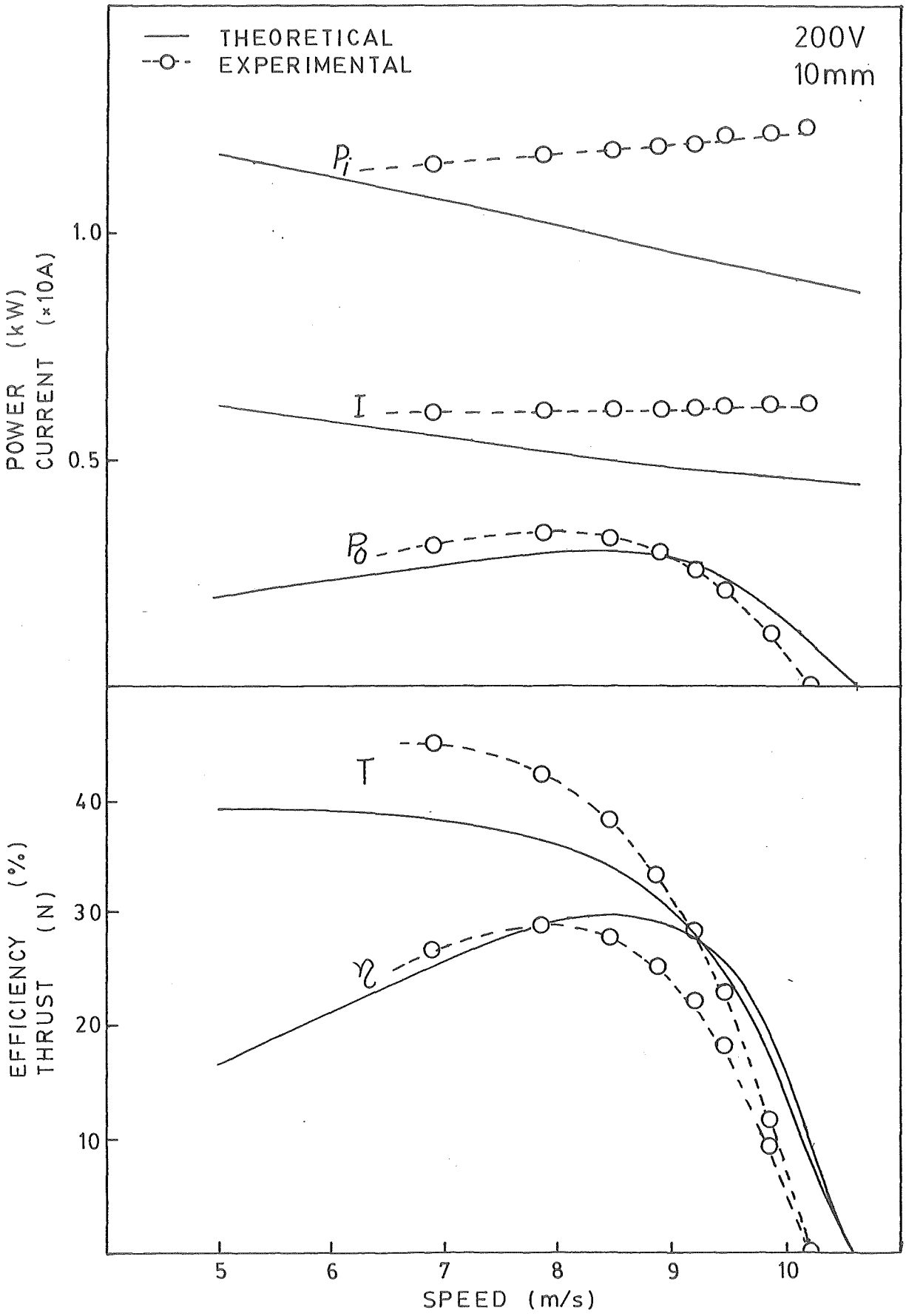

FIGURE 6.5 Typical characteristics of the motor for constant voltage drive; C = 100 μF/coil, g = 24 mm, secondary thickness = 10 mm.

goodness factor of 11 for 10 mm secondary seems to be a better design value. For 5 mm secondary, the predicted maximum efficiency is 31% but the experimental result only reach 23%. But for 10 mm secondary the predicted maximum efficiency of 30% is quite close to the experimental results of 29%.

In general, the disagreement is in the higher speed range where the speed of the rotor never quite reaches its theoretical value, but this is still within the error range of linear stator with rotary type test equipment. Table 6.2 gives information on the difference between no-load speed and the speed of the travelling field when the rotor is removed.

It is also observed that the value of input current and input power at increasing slip for higher values of shunt capacitance increase very little and in some cases drop slightly instead. This is thought to be due to the effect of rotor conductance on the loop cutoff frequency and the effect of the constant termination. For primary design of the loop cutoff frequency the effect of rotor conductance is neglected. In case of Figure 6.3 and Figure 6.4 the no-load cutoff frequency is about 63 Hz and with increasing slip the value of shunt conductance can easily become greater than the value of ωC, hence this will bring further reduction in cutoff frequency. This effect increases when the rotor thickness increases to 10 mm which implies a higher value of shunt conductance for the same rotor speed and hence the power input in this region($G \geq \omega C$) drops further than the case of 5 mm secondary. This effect on the power input will also effect the input current and hence the airgap flux density which will

lead to the reduction in thrust at higher slip region.

6.4 VARIABLE SPEED CHARACTERISTICS

6.4.1 Capacitance Change

Figure 6.6 shows how typical speed change characteristics compared. This is attained by changing the capacitance per coil from 60 μF to 80 μF and 100 μF. As reported previously in Chapter 3, the no-load speed falls and the maximum thrust rises as the capacitance is increased. It is interesting to note here and in Table 6.3 that the maximum efficiency is not greatly effected by change in capacitance. The thrust characteristic is significantly changed, however. When the capacitance is 100 μF the maximum thrust occurs at a slip of about 50%, more like a conventional linear induction motor characteristic.

6.4.2 Inductance Change

The synchronous speed of the travelling wave machine is substantially $U_s = 1/\sqrt{LC}$. Changing the airgap is equivalent to changing the inductance which should cause the speed to vary approximately as $\sqrt{g}$. The advantage of speed change by varying the winding inductance is that there should be no change in basic thrust of the motor, $\frac{1}{2}V^2C$. The winding inductance can be varied by changing the number of turns on the winding. Figure 6.7 shows preliminary investigation for coils of 450 turns compared with 600 turns. Although the no-load speed does not quite vary as 1/T as expected the trend follows the reduction in number of turns implying the reduction in series inductance and hence the speed increases.

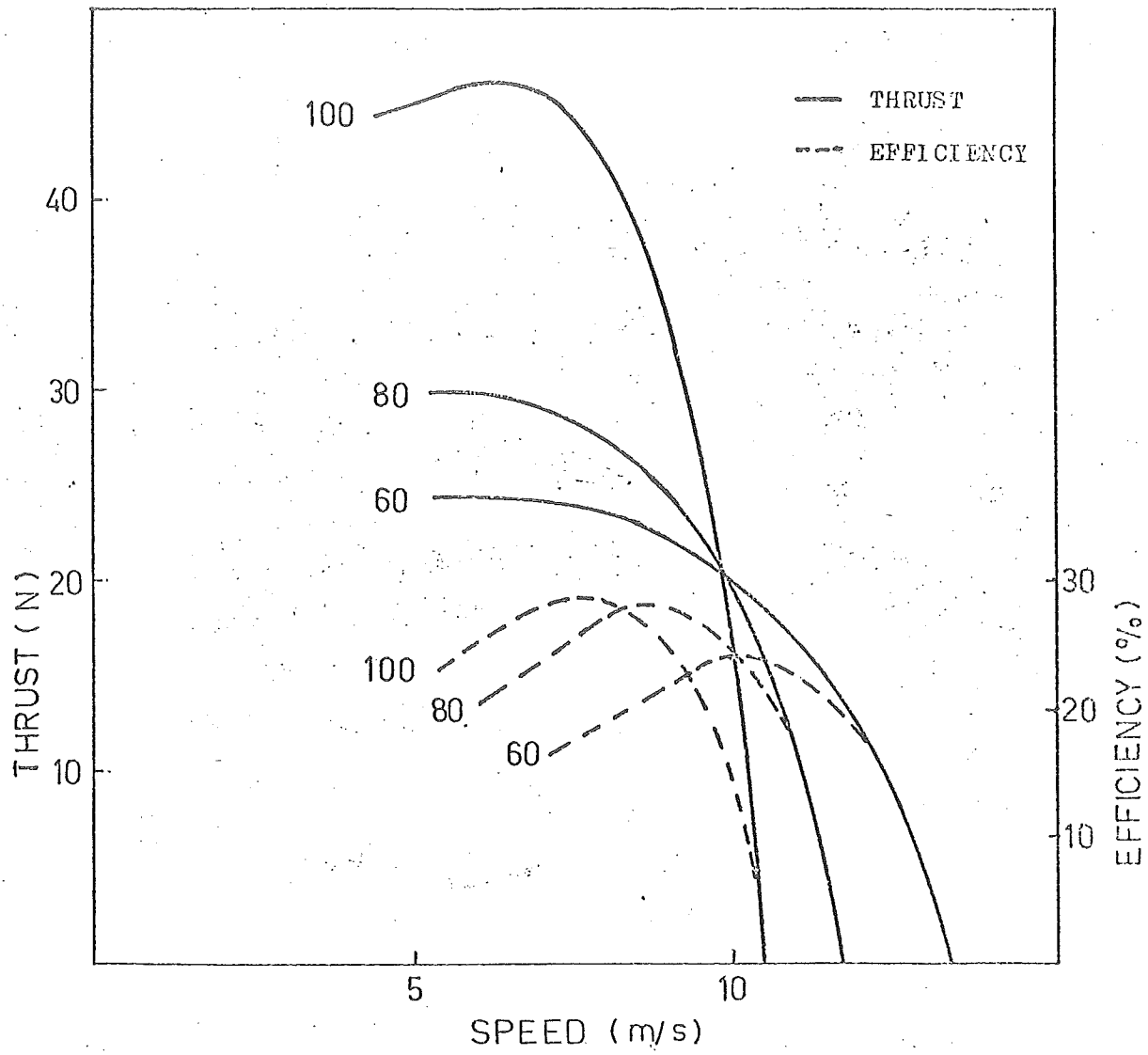

FIGURE 6.6 Typical thrust-speed and efficiency characteristics of the motor with different values of shunt capacitance 60 μF/coil, 80 μF/coil and 100 μF/coil. supply voltage = 200 V, g = 27 mm, thickness = 10 mm.

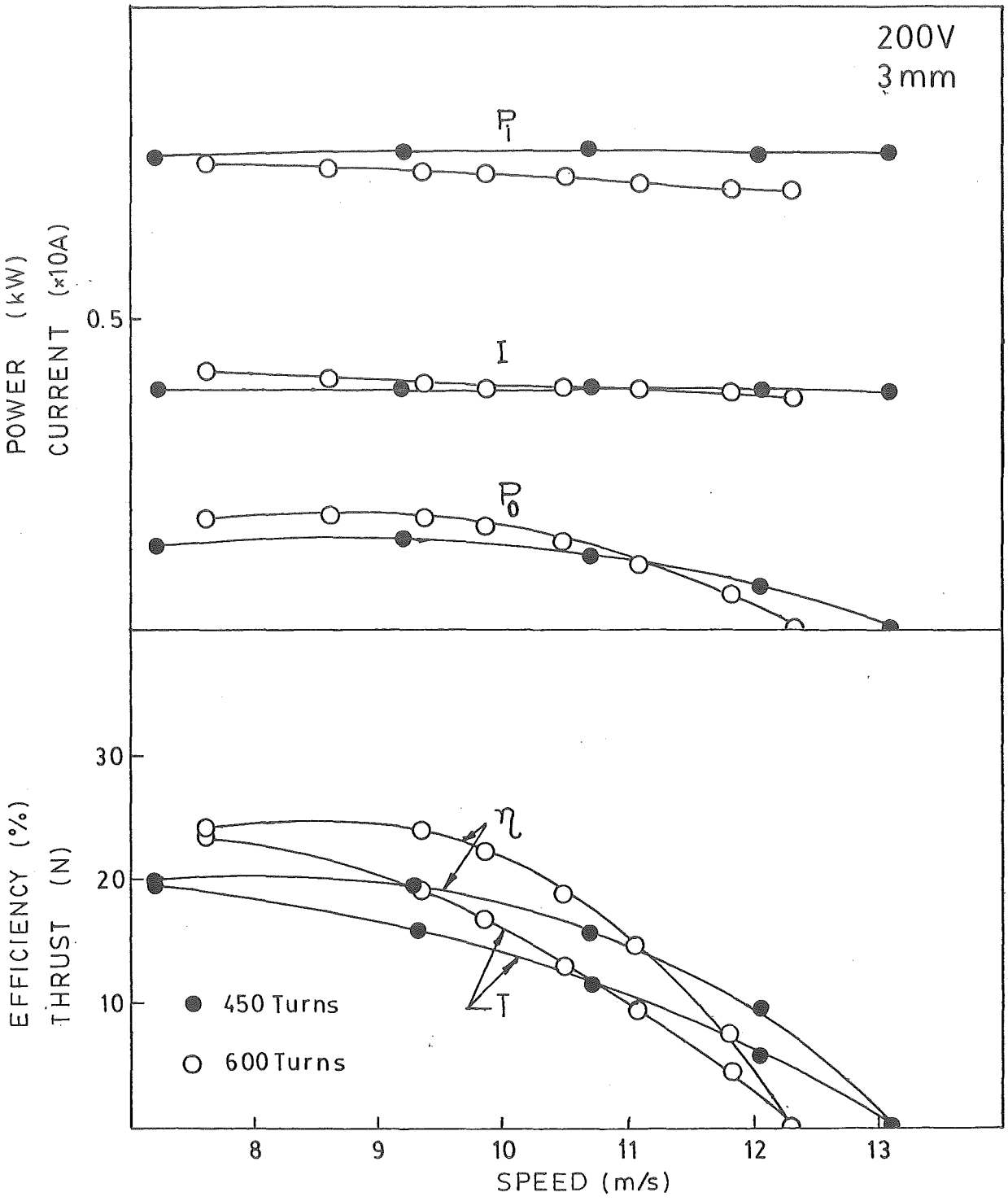

FIGURE 6.7 Experimental characteristics for different number turns. For supply voltage = 200 V, g = 21 mm, secondary thickness = 3 mm, C = 60 μF/coil.

On the other hand variation of the airgap can be carried out smoothly, simply, and without involving the electrical circuit. Figures 6.8, 6.9 and 6.10 show that as expected the no-load speed can be increased without degrading the thrust characteristic; the variation of no-load speed in Table 6.2 follows the theoretical trend quite closely. Table 6.3 shows that the efficiency is considerably affected by the airgap. As the airgap is increased the maximum efficiency rises then falls as the gap passes through an optimum value. In particular it will be noted that the narrower gaps produce the lowest efficiency.

As pointed out previously, the goodness factor is rather less sensitive to changes in the airgap than to changes in capacitance. Although the no-load speed change is roughly similar in each case, Table 5.2 shows that increasing the gap from 15 mm to 30 mm has much smaller effect on the goodness factor than increasing the capacitance from 60 μF to 100 μF.

It is concluded that the technique of increasing the speed by increasing the airgap is preferable to that of reducing the capacitance.

6.5 FLUX DENSITY DISTRIBUTION

Figure 6.11 shows a typical flux density distribution along the airgap. At low speeds the field distributions are fairly well represented by an approximately exponential decay. At higher speeds, however, the fields tend to rise toward the center from each end. This effect is probably due to the entry end effect wave which has not been taken into account in the simplified analysis. This is one of the reasons why

the machine performance does not follow theoretical prediction well outside the region where the value of goodness factor is far from optimum.

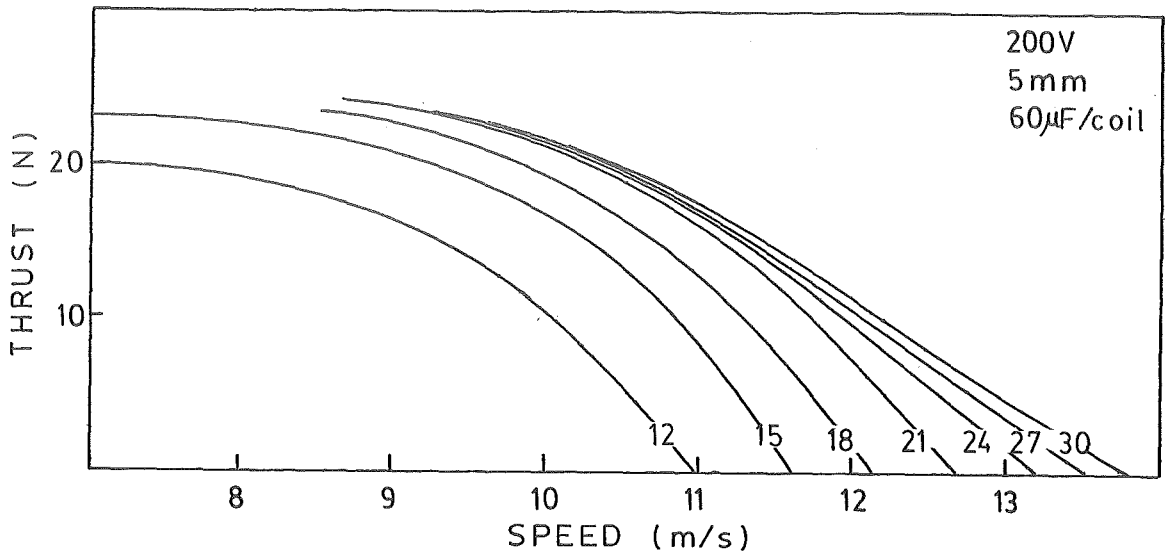

FIGURE 6.8 Thrust-speed characteristics for different values of airgap.

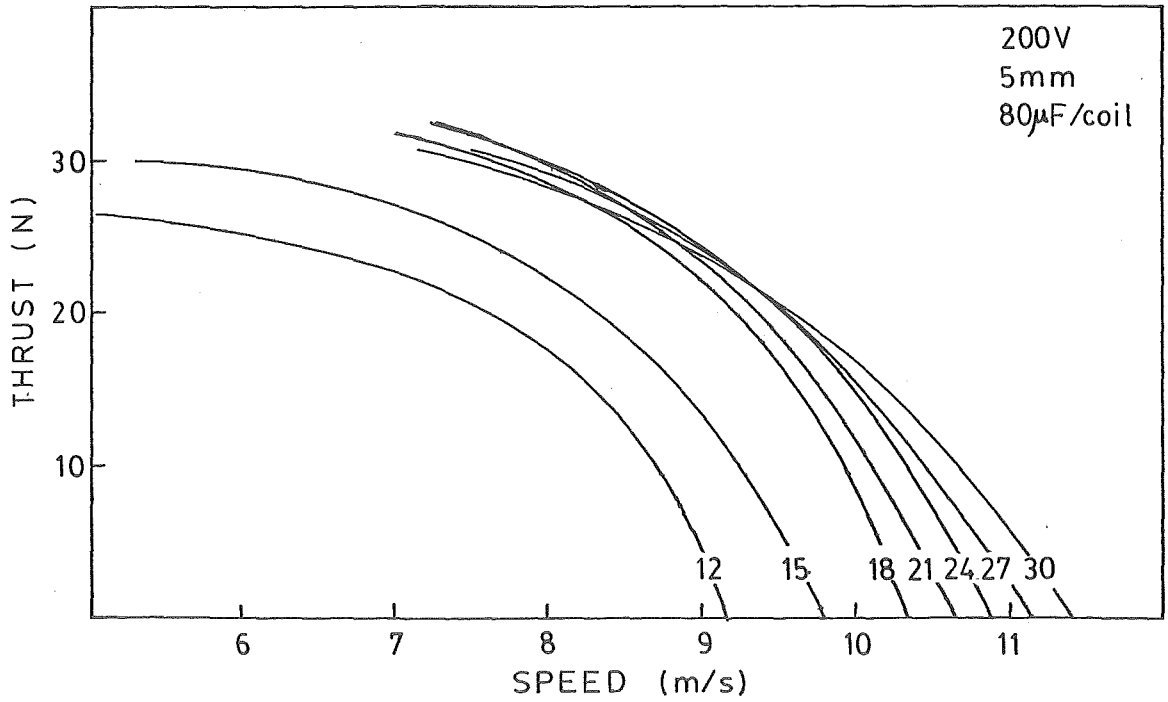

FIGURE 6.9 Thrust-speed characteristics for different values of airgap.

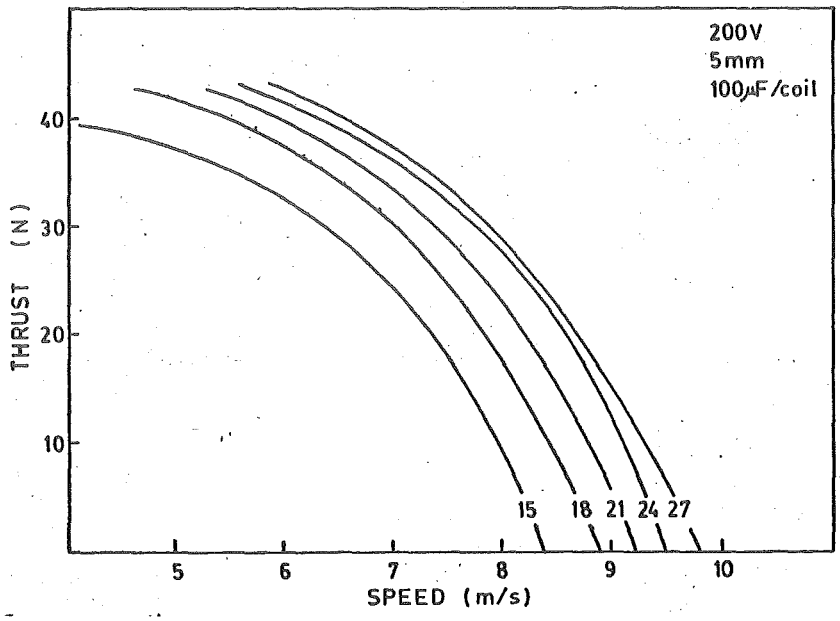

FIGURE 6.10 Thrust-speed characteristics for different values of airgap.

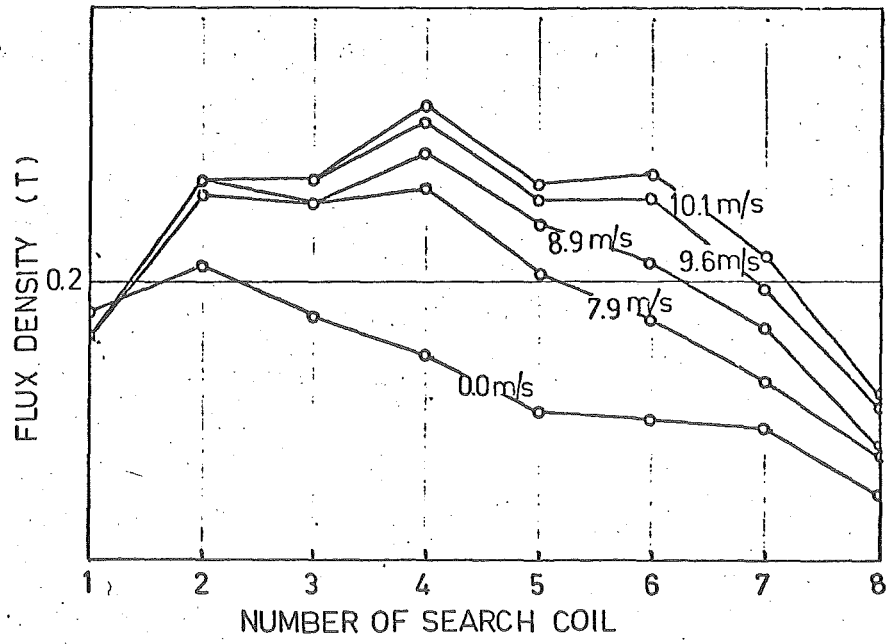

FIGURE 6.11 Typical flux distribution for different rotor speeds; V = 200 V, C = 80 μF/coil, g = 24 mm thickness = 5 mm.

6.6 EFFECT OF TERMINATING RESISTANCES

From previous mathematical analysis, the characteristic impedance of the winding is changing continuously with slip. Therefore, ideally, the terminating impedance of the machine should vary to match the characteristic impedance at different slip values but this proved to be uneconomical for any practical machine. As the characteristic impedance of the machine is of very resistive nature, the terminating resistor is used. The influence of the terminating resistor is now considered. Figure 6.12 shows the influence of terminating resistors of 30 ohms, 55 ohms and 64 ohms. In each case the maximum thrust and efficiency of the machine remains the same. Termination has little effect on these properties. Input current and input power inherit small effects. The overall performance of the machine depends very little on the terminating resistances. When the machine is loaded, the attenuated nature of the travelling field increases because of the absorbtion of power and therefore very small reflection occurs at the far end. Hence the effect of the terminating impedance is minimised. Fixed terminating resistor of 55 ohms is then chosen for each individual case of compared machine performance.

6.7 EFFECT OF SUPPLY FREQUENCY

Generally, the no-load speed of the machine is little affected by supply frequency. However when the frequency of the supply is varied, the machine parameters change. When the frequency is increased the goodness factor falls and the

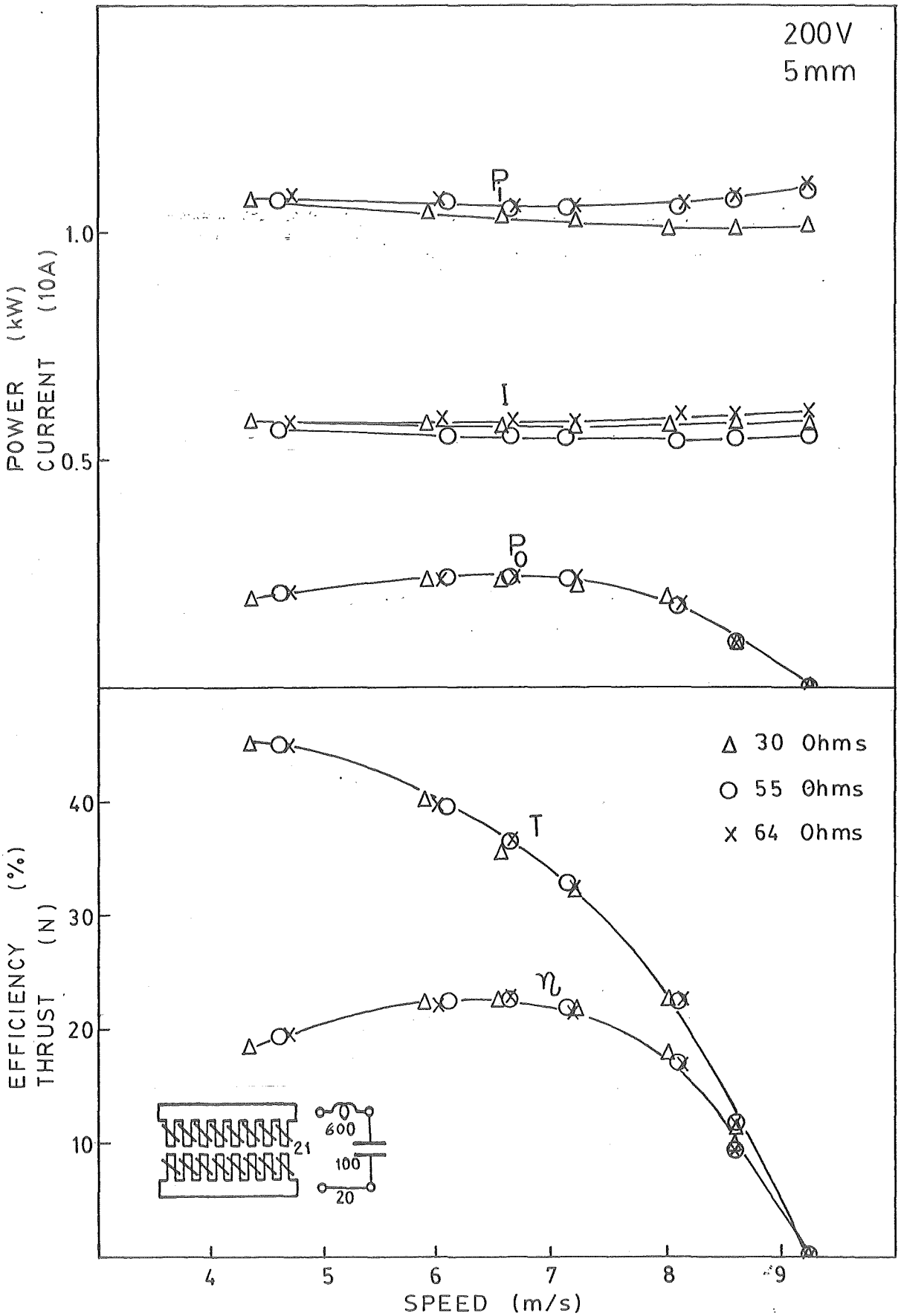

FIGURE 6.12 Motor characteristics for different values of terminating resistor,
C = 100 μF/coil, g = 21 mm, thickness = 5 mm.

number of poles increases. The natural no-load attenuation also increases as the machine behaves like a low pass filter. There is a natural cutoff frequency hence, for any optimum design, when the supply frequency is varied the performance of the machine is degraded. When the supply frequency is reduced, the goodness factor increases and the number of poles falls. This shift leads to an over design goodness factor. Table 6.4 summarises the typical effect of different supply frequency. It is noted that, the cutoff frequency estimated by 4 - 23b is 85 Hz. At normal 50 Hz supply the machine with goodness factor of 19 and 3 poles is over designed and has poor characteristics. As the frequency is increased the number of poles increases. At the same time the goodness factor reduces hence the performance of the machine increase. But to increase the supply frequency also means to approach the natural cutoff frequency of the machine. At 81 Hz supply frequency although the goodness factor for 4.8 poles machine reduced to 12, which compares very favourably to the optimum value suggested[5] of 10 for 4 poles machine and increasing linearly to 40 for 16 poles machine, the performance is degraded again because the estimated cutoff frequency is only 85 Hz. Beyond the cutoff frequency the thrust reduces sharply and the efficiency drops further. The no-load speed of the machine is little effected by supply frequency as expected from the transmission line consideration. Only when the frequency approaches the cutoff region does the no-load speed drop slightly. Figure 6. 13 shows thrust-speed characteristic of the machine at different supply frequencies. The theoretical basic thrust, $V^2C/2$, for these experiments is 24 N.

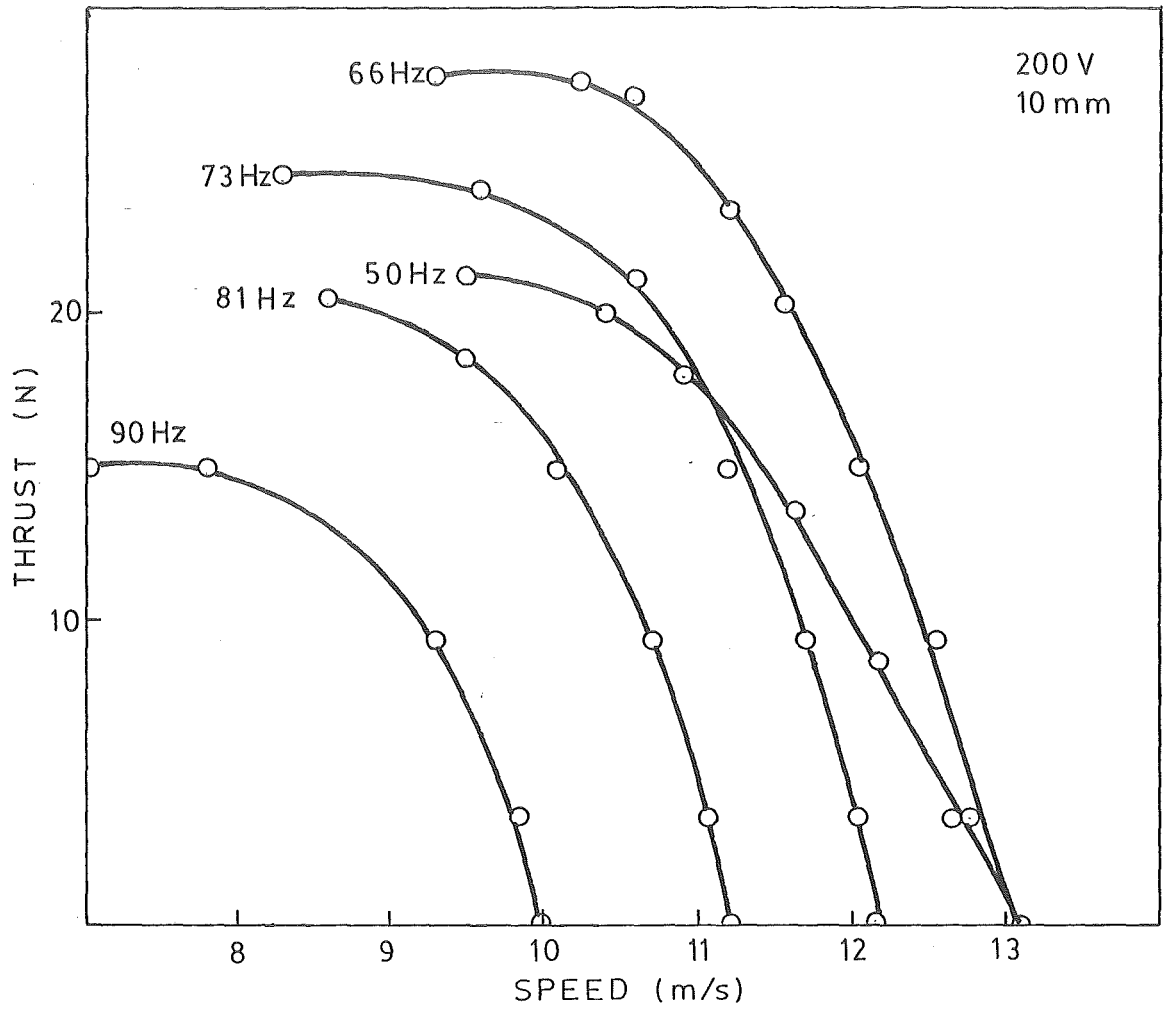

FIGURE 6.13 Thrust-speed characteristics at different values of supply frequency for g = 21 mm, C = 1200 μF/m and thickness = 10 mm.

Frequency (Hz)	50	66	73	81	90
Number of poles	3	3.9	4.4	4.8	5.4
Goodness factor	19	14	13	12	10
No load speed (m/s)	13.1	13.1	12.2	11.2	10.0
Max. efficiency (%)	23	29	29	25	16
Max. thrust (N)	22	27	24	21	16
No load input power (Kw)	0.88	1.0	0.75	0.68	0.76
No load current (A)	4.6	5.0	3.9	3.5	4.2

TABLE 6.4 Comparative performance of motor at different supply frequencies for 1200 μF/m shunt capacitance, 21 mm airgap and 10 mm secondary thickness.

6.8 SEPARATION OF LOSSES AND EFFICIENCY

Figure 6.14 shows the analysis of the losses. Both stator copper loss and termination loss vary with slip; as slip increases these losses reduce in magnitude. With the increase in attenuation function, the smaller the terminating voltage and the smaller the stator current in the subsequent stator coils along the length of the machine. The maximum rotor efficiency, e/c, reach 42% at rotor speed of 8.7 m/s; compared well with 41% calculated from 4 - 21b. However there is a high proportion of the "missing watts" between curve c and curve d. This result is in agreement with the undesired nature of machine efficiency suggested by 4 - 21b which suggests the maximum theoretical efficiency of only 50%.

6.9 CONCLUSIONS

The work on this part describes a non-overlap coil model of STLIM based on transmission line principles in which the coils are connected in series and the travelling field is set up as a result of shunt connected capacitors. The machine has inherent variable speed characteristic which has been realised by changing the shunt capacitors and by varying the airgap. The latter method is simplest and permits smooth speed variation.

It is shown that increasing the airgap of STLIM does not adversely effect its goodness factor, since as the airgap increases the number of poles automatically falls. Also the basic thrust expression, $V^2C/2$, is independent of airgap width. These statements are true for only a limited range

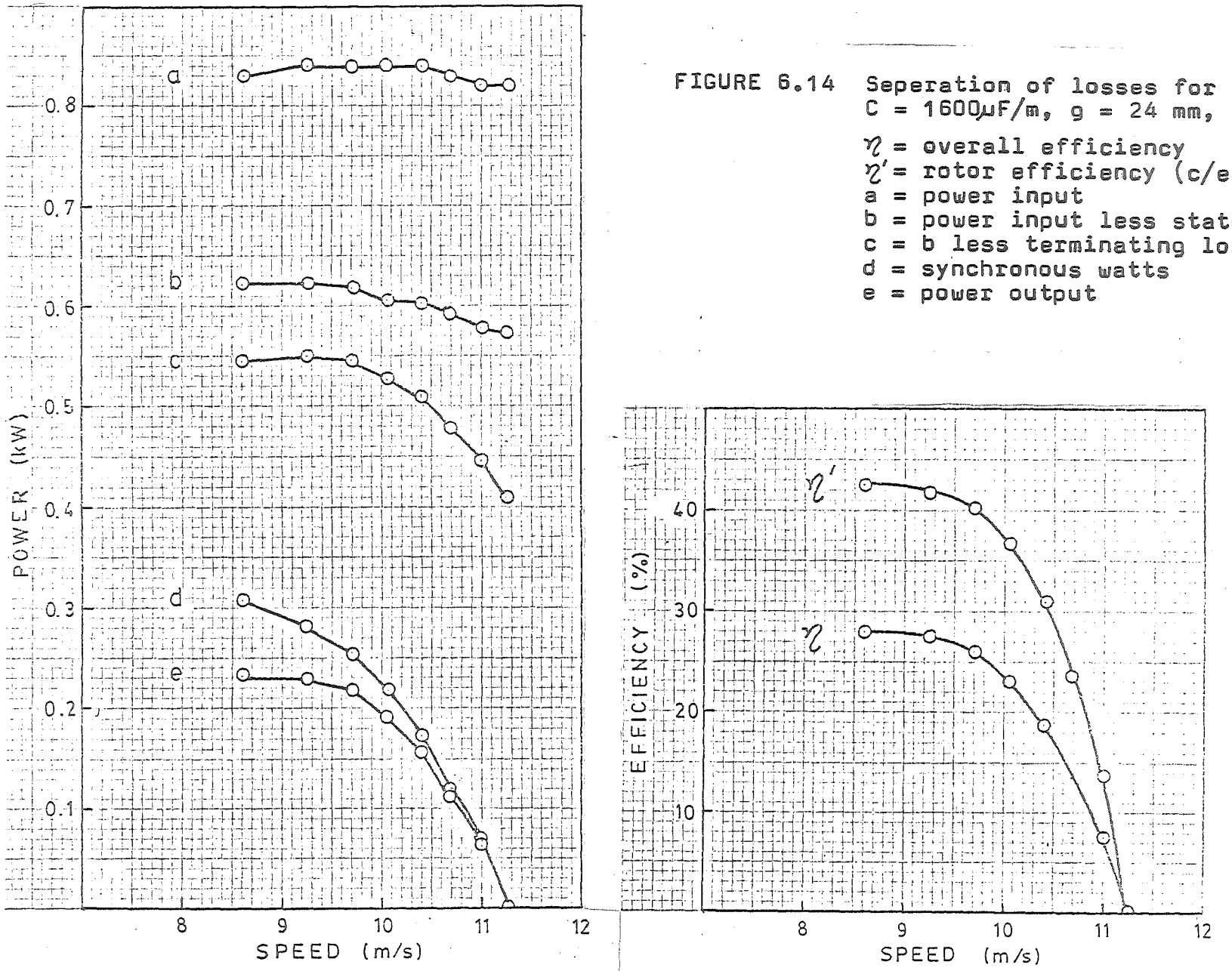

FIGURE 6.14 Seperation of losses for case C = 1600μF/m, g = 24 mm, 10 mm disc

η = overall efficiency
η' = rotor efficiency (c/e)
a = power input
b = power input less stator Cu loss
c = b less terminating loss
d = synchronous watts
e = power output

of airgap in which the adverse affect of leakage is negligible. Within this range, however, STLIM with variable airgap contributes a very robust, simple variable speed linear induction motor which has the advantages of being operable directly from fixed frequency single phase supply and requiring no electronic control.

The most serious practical drawback to STLIM described here is its low efficiency. The non-overlap coil model STLIM seems to have the efficiency ceiling of only 50%. This can only compete with small single phase machines. Further investigations on STLIM with overlap coil type is needed in order to improve the performance of the machine. The following part of this thesis is concentrated on the machine of overlap coil type.

PART 2

OVERLAP COIL MODEL OF STLIM

CHAPTER 7

THE MATHEMATICAL MODEL OF SIMPLIFIED OVERLAP COIL STLIM

7.1 INTRODUCTION

The non-overlap coil STLIM experimental motors described in Part 1 behave largely according to the analysis. However, compared with an ordinary electrical machine, the motor has an unattractive winding pitch. This will lead to lower surface stator current density for a given stator current and hence for the same machine rating the non-overlap coil STLIM seems to need bigger designed dimensions. This will degrade the performance of the motor, and parameters such as cost, power to weight ratio, efficiency and others.

The second type of alternative winding involves coils which span several teeth and therefore overlap. This type of winding, as shown in Figure 7.1, is the general practice for electrical machines. This type of arrangement gives some advantages over the non-overlap coil type. The effective slot current is increased, the pitch factor can be improved and a larger emf is generated by the travelling flux wave in the wide span coil. The disadvantage of the overlap coil is that the first and last few slots on the stator block contain only one coil side. Therefore, the current distribution and the flux distribution at the ends are different from those in the central region.

The analysis of this type of winding is more difficult because there is very large mutual coupling between these

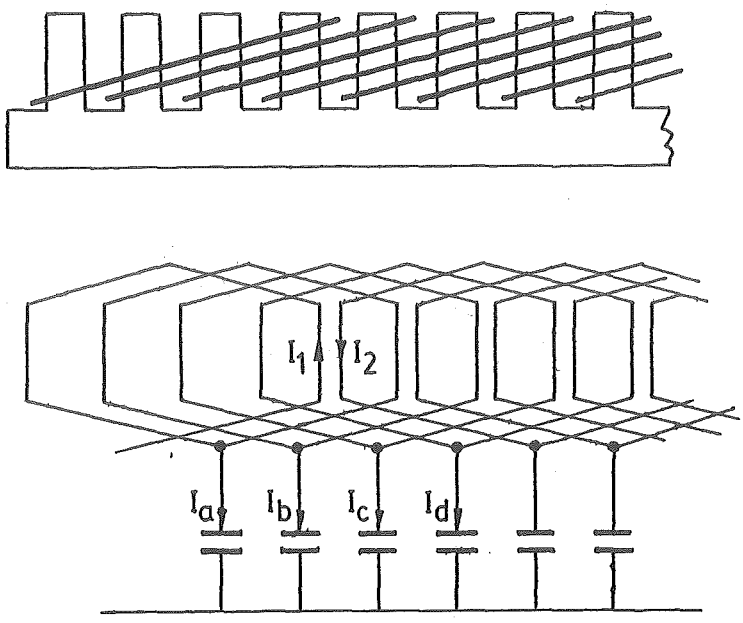

FIGURE 7.1 The overlap coil arrangement of STLIM. Effective slot current $I_1 - I_2$ is the sum of the capacitor current I_a to I_d

overlap coils that is not taken into account in the transmission line analysis. Some preliminary investigations show that the travelling field is easily set up and a method of calculating the propagating function has already been published[12]. The further analysis to reach other expressions such as equivalent circuit, voltage, thrust, current and efficiency is needed. Furthermore an experimental machine of reasonable size is needed to compare the result with the analysis.

This part of the thesis is aimed to investigate further the model of overlap coil STLIM as well as design and test an experimental motor to demonstrate that the STLIM is compatible with the more conventional three phase linear induction motor in the machine performance.

7.2 TYPE AND ASSUMPTIONS OF OVERLAP COIL STLIM USED FOR ANALYSIS

The model of the machine used for analysis is the double-sided, longitudinal-flux, short-primary, long conducting sheet secondary, overlap coil STLIM.

Now in order to simplify the mathematical analysis of the machine, some simplifying approximations are made as follows. The stator winding resistance and leakage reactance are neglected. The magnetic field is assumed to be confined to the regions directly under the stator block of active width w. No allowance is made for entrance and exit end effects. Harmonic components of mmf and flux waves are ignored, and the stator winding is assumed to be either terminated in its characteristic impedance of infinitely long, so that there exists a travelling field in the forward direction only. Consider only one forward dominated travelling field. Reflections due to the lumped nature of the windings are ignored. Hence the actual winding that should be analysed in terms of the sum of finite series is remodeled to enable an integral calculus approach.

A model of the stator winding is proposed in which each concentrated stator coil of T turns and coil span 2a, of Figure 7.1, is replaced by T single turn coils each of span 2a evenly spread over the actual slot pitch d. This arrangement results in a closely wound stator so that the distance between coil $\Delta = d/T$ is very small. This can now be analysed using integral calculus. The applied voltage varies sinusoidally in time so that the flux density at any point is taken to vary in time as $e^{j\omega t}$ and the spatial distribution of flux

density is assumed to be e^{Ax}, where A is the propagation of the machine. This simplified model is now redrawn from Figure 7.1 into Figure 7.2.

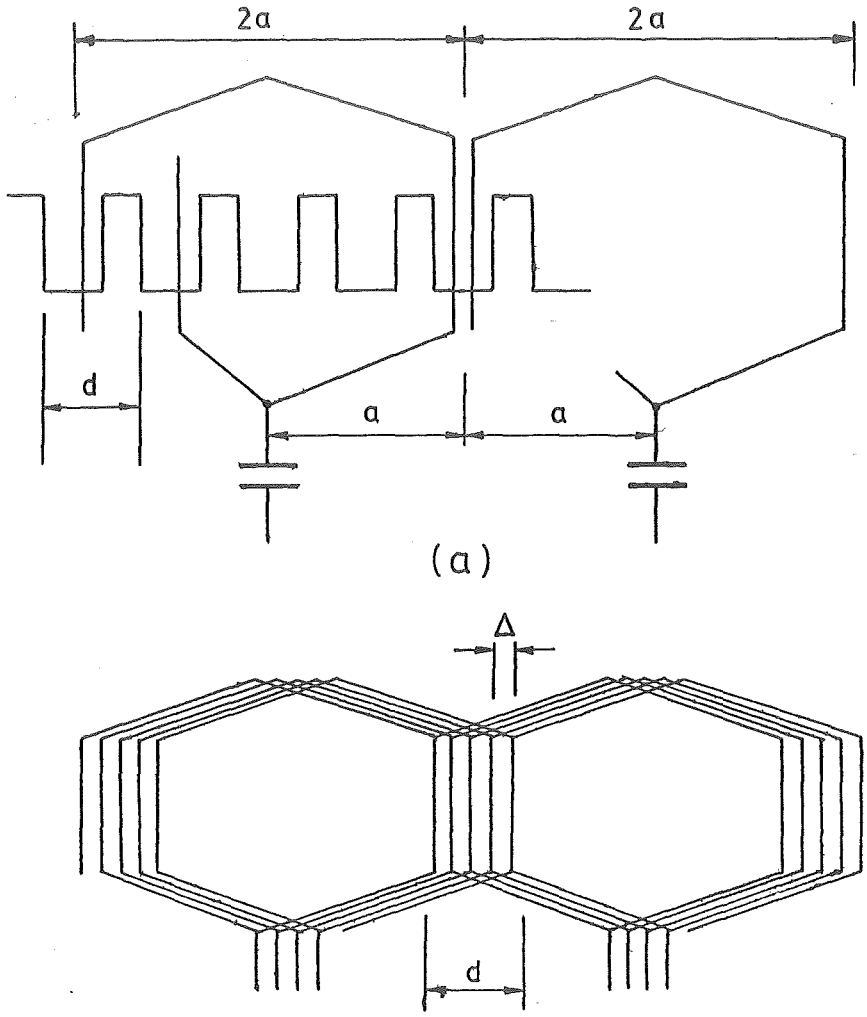

FIGURE 7.2 The model of stator winding of overlap coil STLIM
a) Multiturn coils in stator slots
b) Equivalent surface winding

7.3 SOLUTION OF THE VOLTAGE EQUATION

From the previous section, assuming that an attenuated travelling flux wave is set up, the flux density of the machine at distance x along the stator can be expressed as

$$b = B\, e^{j\omega t} e^{Ax}$$

where ω is the angular frequency of the supply voltage and A is a propagation constant of the machine.

From Figure 7.2 the total magnetic flux linking each turn at distance x is

$$\phi = \int_{x-a}^{x+a} wb\ dx \qquad 7 - 1$$

where w is the effective width of the stator block. The emf per turn e is therefore

$$e = \frac{\partial \phi}{\partial t}$$

$$= \frac{\partial}{\partial t} \int_{x-a}^{x+a} wb\ dx \qquad 7 - 2$$

and the voltage drop along the stator winding neglecting stator resistance, is

$$\frac{\partial V}{\partial x} = e/\Delta$$

$$= \frac{I}{d} \frac{\partial}{\partial t} \int_{x-a}^{x+a} wb\ dx$$

Considering the machine terminated in its characteristic impedance or an infinitely long stator, the voltage at distance x is, then

$$V_x = \int_x^{\infty} \frac{e}{\Delta}\, dx$$

$$= \frac{j\omega w TB}{dA^2} \left(e^{aA} - e^{-aA}\right) e^{j\omega t} e^{Ax} \qquad 7 - 3$$

Hence the supply voltage is when x = 0

$$V_{supply} = \frac{j\omega w TB}{dA^2} \left(e^{aA} - e^{-aA}\right) e^{j\omega t} \qquad 7 - 4$$

For r.m.s. value of supply voltage

$$V = \sqrt{\frac{V_{supply}\, \overset{*}{V}_{supply}}{2}}$$

$$= \sqrt{\frac{\omega^2 w^2 T^2 B^2}{2d^2 A^2 \overset{*}{A}^2} \left(e^{aA} - e^{-aA}\right)\left(e^{a\overset{*}{A}} - e^{-a\overset{*}{A}}\right) e^{j\omega t} e^{-j\omega t}}$$

Where $\overset{*}{V}_{supply}$ and $\overset{*}{A}$ are the complex conjugate of the supply voltage and propagation constant respectively. By taking the dominant forward travelling wave mode, let $A = -\alpha - j\beta$, the r.m.s. value of the supply voltage is

$$V = \sqrt{\tfrac{1}{2}\left[\frac{\omega w TB}{dA\overset{*}{A}}\right]^2 \left(e^{-2a\alpha} - e^{-2ja\beta} - e^{2ja\beta} + e^{2a\alpha}\right)}$$

$$= \sqrt{\tfrac{1}{2}\left[\frac{\omega w TB}{d(\alpha^2+\beta^2)}\right]^2 \left\{\left(e^{2a\alpha} + e^{-2a\alpha}\right) - \left(e^{j2a\beta} + e^{-2ja\beta}\right)\right\}}$$

$$= \sqrt{\left[\frac{\omega w TB}{d(\alpha^2+\beta^2)}\right]^2 \left(\text{Cosh } 2a\alpha - \text{Cos } 2a\beta\right)}$$

$$V = \frac{\omega w T B}{d(\alpha^2+\beta^2)} \sqrt{\text{Cosh } 2a\alpha - \text{Cos } 2a\beta} \qquad 7-5$$

7.4 SOLUTION OF STATOR CURRENT DENSITY

Referring to Figure 7.2, the winding can be considered to be made up of current filaments each filament comprising two coil sides. The coils are seperated by a distance of 2a. If the resultant filament current is i, then the local stator surface current density is

$$j_1 = \frac{i}{\Delta} = iT/d \qquad 7-6$$

Again from Figure 7.2 we find that the filament current i at distance x is the integral of capacitive current from distance x-a to x+a

$$i = \int_{x-a}^{x+a} C \frac{\partial V}{\partial t} dx \qquad 7-7$$

Where $C\frac{\partial V}{\partial t}$ is the capacitive current per unit length. In actual machine the capacitance per coil is C', hence C=C'/d

Therefore the stator current density is

$$j_1 = \frac{I}{d} \int_{x-a}^{x+a} C \frac{\partial V}{\partial t} dx$$

$$= \frac{I}{d} \int_{x-a}^{x+a} C \left[\frac{-\omega^2 w T B}{dA^2}\right] (e^{aA} - e^{-aA})\, e^{j\omega t} e^{Ax}\, dx$$

$$= \frac{-\omega^2 w T^2 B C}{d^2 A^3} (e^{aA} - e^{-aA})\, e^{j\omega t} (e^{A(x+a)} - e^{A(x-a)})$$

$$j_1 = \frac{-\omega^2 w T^2 BC}{d^2 A^3} (e^{aA} - e^{-aA})^2 \, e^{j\omega t} e^{Ax} \qquad 7 - 8$$

7.5 ANALYSIS OF THRUST

The total value of thrust over the entire length l of the machine is given by

$$F = w \int_0^l \text{Real} \left[\frac{j_1 \overset{*}{b}}{2} \right] dx \qquad 7 - 9$$

where $\overset{*}{b}$ is the complex conjugate of b

substitute value of stator current density from 7 - 8 hence

$$F = \frac{-\omega^2 w^2 T^2 B^2 C}{2d^2} \text{Real} \left[\frac{(e^{aA} - e^{-aA})^2}{A^3} \right] \int_0^l e^{-2\alpha x} dx$$

$$= - \frac{\omega^2 w^2 T^2 B^2 C (1 - e^{-2\alpha l})}{4 d^2 (\alpha^2 + \beta^2)^3} \text{Real}((e^{2aA} + e^{-2aA} - 2) \overset{*3}{A}) \qquad 7 - 10$$

Term $\overset{*3}{A} = (-\alpha + j\beta)^3$

$= (-\alpha^3 + 3\beta^2\alpha + 3j\beta\alpha^2 - j\beta^3)$

$= (3\beta^2\alpha - \alpha^3) + j(3\beta\alpha^2 - \beta^3)$

Term $(e^{2aA} + e^{-2aA} - 2)$

$= (-2 + e^{-2a\alpha} e^{-j2a\beta} + e^{2a\alpha} e^{j2a\beta})$

$= -2(1 - \text{Cos}2a\beta \text{Cosh}2a\alpha - j\text{Sin}2a\beta \text{Sinh}2a\alpha)$

Therefore the real part of $(e^{2aA} + e^{-2aA} - 2) \overset{*3}{A}$ is

$-2((3\beta^2\alpha - \alpha^3)(1 - \text{Cos}2a\beta \text{Cosh}2a\alpha) + (3\beta\alpha - \beta^3/\alpha) \text{Sin}2a\beta \text{Sinh}2a\alpha)$

from 7 - 5 substitute for value of supply voltage, hence the thrust becomes

$$F = \tfrac{1}{2}V^2C(1 - e^{-2\alpha l})D \qquad 7 - 11$$

where D equals

$$D = \frac{(3\beta^2-\alpha^2)(1-\text{Cos}2a\beta\text{Cosh}2a\alpha) + (3\alpha\beta-\beta^3/\alpha)\text{Sin}2a\beta\text{Sinh}2a\alpha}{(\alpha^2+\beta^2)(\text{Cosh}2a\alpha-\text{Cos}2a\beta)}$$

From 7 - 11 the value of thrust obtained for the overlap coil model still has the familiar basic thrust unit of $\frac{1}{2}V^2C(1 - e^{-2\alpha l})$ and a new multiplying term D which is a function of pole pitch and attenuation constant.

Consider a special case of fully pitched coil, $2a\beta=\pi$, then the thrust expression becomes

$$F = \tfrac{1}{2}V^2C(1 - e^{-2\alpha l})\left[\frac{3\beta^2 - \alpha^2}{\alpha^2 + \beta^2}\right]$$

Compared with non-overlap coil thrust expression of 4 - 16, equation 7 - 11 has advantage of higher value of thrust than non-overlap coil model for the same value of supply voltage and shunt capacitance.

7.6 EQUATION OF THE PROPAGATION FUNCTION

The relationship between stator surface current density, j_1, and the flux density, b, for a STLIM is given by 2 - 5 as

$$\frac{\partial^2 b}{\partial x^2} = \frac{\mu_o}{g}\left[\frac{\partial j_1}{\partial x} + \frac{1}{g_2}\left[\frac{\partial b}{\partial t} + U\frac{\partial b}{\partial x}\right]\right]$$

Where U is the velocity of the rotor and ρ_2 is the effective rotor sheet resistance.

Now substitute for $\frac{\partial b}{\partial x} = ABe^{j\omega t}e^{Ax}$,

$$\frac{\partial^2 b}{\partial x^2} = A^2 Be^{j\omega t}e^{Ax},$$

$$\frac{\partial b}{\partial t} = j\omega Be^{j\omega t}e^{Ax} \quad \text{and}$$

$$\frac{\partial j_1}{\partial x} = -\frac{\omega^2 \mu T^2 BC}{d^2 A^2}(e^{aA} - e^{-aA})^2 e^{j\omega t}e^{Ax}$$

into 2 - 5. Hence the general field equation for overlap coil model of STLIM is

$$A^2 = \frac{\mu_o}{g}\left[-\frac{\omega^2 \mu T^2 C}{d^2 A^2}(e^{aA} - e^{-aA})^2 + \frac{1}{\rho_2}(j\omega + UA)\right] \qquad 7 - 12$$

This involves the fourth power of A, thus the model comprise a fourth order system that is, there are in general four spatial modes having the same frequency of the drive, two propagating in the forward direction and two propagating in the backward direction. Solution of 7 - 12 yields the propagation constant A in the terms of the machine parameters and the rotor speed. The solution, however, seems very difficult to obtain in this way. The most practical approach is to assume the propagation constants are of the form $A = -\alpha - j\beta$ and then treat α and β as independent variables. From 7 - 12

$$A^4 = \frac{\mu_o}{g}\left[-\frac{2\omega^2 \mu T^2 C}{d^2}(\text{Cos}2a\beta\text{Cosh}2a\alpha + j\text{Sin}2a\beta\text{Sinh}2a\alpha - 1) + j\frac{A^2\omega}{\rho_2} + \frac{UA^3}{\rho_2}\right]$$

7 - 13

and from real part of 7 - 13

$$\alpha^4+\beta^4-6\alpha^2\beta^2 = -\frac{2\mu_o\omega^2 wT^2C}{gd^2}(\text{Cos}2a\beta\text{Cosh}2a\alpha-1) - \frac{2\mu_o\alpha\beta\omega}{g\rho_2} + \frac{\mu_o U}{g\rho_2}(3\alpha\beta^2-\alpha^3)$$

which can be rewritten in terms of

$$C = \frac{gd^2(6\alpha^2\beta^2-\alpha^4-\beta^4-2\alpha\beta\omega\mu_o/(g\rho_2))}{2\mu_o T^2 w\omega^2(\text{Cos}2a\beta\text{Cosh}2a\alpha-1)} + \frac{d^2(3\alpha\beta^2-\alpha^3)}{2\rho_2\omega^2 wT^2(\text{Cos}2a\beta\text{Cosh}2a\alpha-1)}U \qquad 7-14$$

similarly, from imaginary part of 7 - 13

$$4\alpha\beta(\alpha^2-\beta^2) = -\frac{2\mu_o\omega^2 wT^2C}{gd^2}\text{Sin}2a\beta\text{Sinh}2a\alpha + \frac{(\alpha^2-\beta^2)\mu_o}{\rho_2 g} + \frac{\mu_o(\beta^3-3\alpha^2\beta)}{g\rho_2}U$$

which can be rewritten in terms of

$$C = \frac{gd^2(4\alpha\beta(\beta^2-\alpha^2) + \omega\mu_o(\alpha^2-\beta^2)/(g\rho_2))}{2\mu_o\omega^2 wT^2\text{Sin}2a\beta\text{Sinh}2a\alpha} + \frac{d^2(\beta^3-3\alpha^2\beta)}{2\rho_2\omega^2 wT^2\text{Sin}2a\beta\text{Sinh}2a\alpha}U \qquad 7-15$$

From 7 -14 and 7 - 15 the value of rotor speed, U, and shunt capacitance, C, can be found. By series of repeated calculations for different value of α and β, the performance

characteristic curves are obtained.

7.7 THE NO-ROTOR SYNCHRONOUS SPEED

A particular simple case considered here is the possibility of the machine operating with no attenuation, ie $\alpha=0$, hence $A = -j\beta_0$ then 7 - 12 becomes

$$\beta_0^2 = \frac{\mu_0}{g}\left[\frac{4\omega^2 wT^2 CSin^2 a\beta_0}{\beta_0^2 d^2} + \frac{1}{\rho_2}(j\omega - jU\beta_0)\right]$$

Thus, when operating with no attenuation, either $U = \omega/\beta_0 = f\lambda_0$ where λ_0 is the wavelength of the magnetic field at zero attenuation, or $\rho_2 \to \infty$, which means that either the rotor is travelling at the speed of the magnetic field, or the rotor has been removed and the machine is operating on open circuit conditions. Hence the maximum speed the rotor can attain should equal to the speed of the magnetic field when the rotor is removed. The relationship between the no-rotor phase function, β_0, and the machine parameters is

$$\beta_0^4 = \frac{4\mu_0\omega^2 wT^2 CSin^2 a\beta_0}{gd^2}$$

Hence the no-rotor synchronous speed of the machine U_{so} is

$$U_{so} = \omega/\beta_0 \qquad 7 - 16$$

This indicated that the synchronous speed of the machine depends on the supply frequency and vary approximately as $\sqrt{\omega}$ when the coil is fully pitched.

7.8 REALISATION OF THE EQUIVALENT CIRCUIT

From results of the previous section it is now possible to model a distributed parameter equivalent circuit for the machine in terms of α and β which can compare with the transmission line distributed model.

From 7 - 12 put $A = -\alpha - j\beta$ on the right hand side of the expression. Hence 7 - 12 becomes

$$A^2 = \frac{\mu_o}{g}\left[-\frac{2\omega^2 w T^2 C}{d^2(-\alpha-j\beta)^2}(\text{Cosh}2a\alpha\text{Cos}2a\beta + j\text{Sinh}2a\alpha\text{Sin}2a\beta - 1) + \frac{1}{g_2}(j\omega + U(-\alpha-j\beta)) \right]$$

Synchronous speed $U_s = \omega/\beta$, hence term $\frac{1}{g_2}(j\omega + jU\beta)$ can be rewritten in terms as $\frac{j\omega}{g_2}(1-U/U_s) = jS\omega/g_2$ where S is the slip.

$$A^2 = \frac{\mu_o}{g}\left[-\frac{2\omega^2 w T^2 C(-\alpha+j\beta)^2}{d^2(\alpha^2+\beta^2)^2}(\text{Cosh}2a\alpha\text{Cos}2a\beta + j\text{Sinh}2a\alpha\text{Sin}2a\beta) - \frac{U\alpha}{g_2} + j\frac{S\omega}{g_2} \right]$$

$$= \frac{\mu_o}{g}\left[-\frac{2\omega^2 w T^2 C}{d^2(\alpha^2+\beta^2)^2}((\text{Cosh}2a\alpha\text{Cos}2a\beta - 1)(\alpha^2-\beta^2) + 2\alpha\beta\text{Sinh}2a\alpha\text{Sin}2a\beta) - \frac{U\alpha}{g_2} + j\frac{S\omega}{g_2} - j\frac{2\omega^2 w T^2 C((\alpha^2-\beta^2)\text{Sinh}2a\alpha\text{Sin}2a\beta - 2\alpha\beta(\text{Cosh}2a\alpha\text{Cos}2a\beta - 1))}{d^2(\alpha^2+\beta^2)^2} \right]$$

Equation 7 - 17 can be recognised in more familiar terms by taking the factor of

$$\frac{j2\mu_o\omega_w T^2((\beta^2-\alpha^2)(1-\text{Cosh}2a\alpha\text{Cos}2a\beta)+2\alpha\beta\text{Sinh}2a\alpha\text{Sin}2a\beta)}{gd^2(\alpha^2+\beta^2)^2}$$

hence the equation becomes

$$A^2=\left[j\frac{2\mu_o\omega_w T^2}{d^2 g(\alpha^2+\beta^2)^2}((\beta^2-\alpha^2)(1-\text{Cosh}2a\alpha\text{Cos}2a\beta)+2\alpha\beta\text{Sinh}2a\alpha\text{Sin}2a\beta)\right]$$

$$\times\left[j\omega\left[C+\frac{Ud^2(\alpha^2+\beta^2)^2}{2\rho_2\omega^2{}_w T^2((\beta^2-\alpha^2)(1-\text{Cosh}2a\alpha\text{Cos}2a\beta)+2\alpha\beta\text{Sinh}2a\alpha\text{Sin}2a\beta)}\right.\right.$$

$$+S\frac{d^2(\alpha^2+\beta^2)^2}{2\rho_2{}_w T^2((\beta^2-\alpha^2)(1-\text{Cosh}2a\alpha\text{Cos}2a\beta)+2\alpha\beta\text{Sinh}2a\alpha\text{Sin}2a\beta)}$$

$$\left.\left.+C\omega\frac{(\beta^2-\alpha^2)\text{Sinh}2a\alpha\text{Sin}2a\beta-2\alpha\beta(1-\text{Cosh}2a\alpha\text{Cos}2a\beta)}{(\beta^2-\alpha^2)(1-\text{Cosh}2a\alpha\text{Cos}2a\beta)+2\alpha\beta\text{Sinh}2a\alpha\text{Sin}2a\beta}\right]\right]$$

7 - 18

This equation can compare with the transmission line equivalent circuit of

$$\gamma^2 = (R + j\omega L)(G + j\omega C)$$

this gives the overlap coil propagation function of STLIM

$$A^2 = (j\omega L)(G + j\omega \overset{+}{C}) \qquad 7 - 19$$

where $L=\frac{2\mu_o{}_w T^2((\beta^2-\alpha^2)(1-\text{Cosh}2a\alpha\text{Cos}2a\beta)+2\alpha\beta\text{Sinh}2a\alpha\text{Sin}2a\beta)}{gd^2(\alpha^2+\beta^2)^2}$

$$\overset{+}{C}=C+\frac{\alpha Ud^2(\alpha^2+\beta^2)^2}{2\rho_2\omega^2{}_w T^2((\beta^2-\alpha^2)(1-\text{Cosh}2a\alpha\text{Cos}2a\beta)+2\alpha\beta\text{Sinh}2a\alpha\text{Sin}2a\beta)}$$

$$\text{and } G = S\,\frac{d^2(\alpha^2+\beta^2)^2}{2\rho_2\omega^2\mu T^2\left((\beta^2-\alpha^2)(1-\cosh 2a\alpha\cos 2a\beta)+2\alpha\beta\sinh 2a\alpha\sin 2a\beta\right)}$$

$$+\ C\omega\left[\frac{(\beta^2-\alpha^2)\sinh 2a\alpha\sin 2a\beta-2\alpha\beta(1-\cosh 2a\alpha\cos 2a\beta)}{(\beta^2-\alpha^2)(1-\cosh 2a\alpha\cos 2a\beta)+2\alpha\beta\sinh 2a\alpha\sin 2a\beta}\right]$$

Hence the stator inductance can be recognised as L, total effective shunt conductance G, and total effective shunt capacitance $\overset{*}{C}$. And the proposed equivalent circuit is recognised as in Figure 7.3. All values are in per meter.

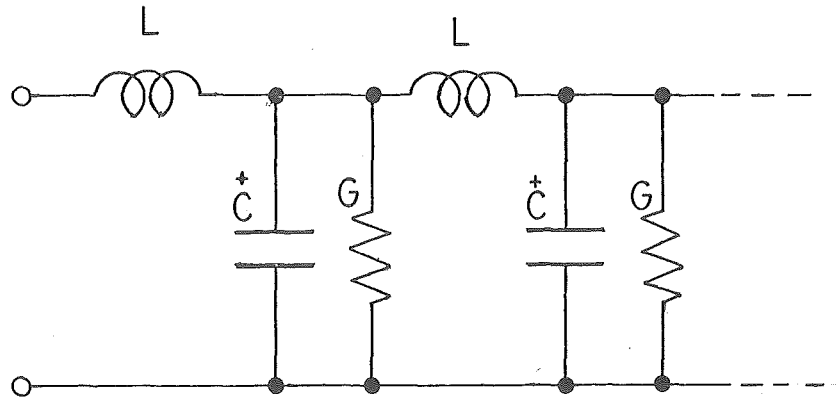

FIGURE 7.3 The proposed equivalent circuit.

7.9 CHARACTERISTIC IMPEDANCE AND OTHER ELECTRICAL PARAMETERS

The characteristic impedance of the machine as seen from the equivalent circuit of Figure 7.3 is

$$Z_o = \sqrt{\frac{j\omega L}{G + j\omega\overset{*}{C}}}$$

$$= \sqrt[4]{\frac{\omega^2 L^2}{G^2 + \omega^2\overset{*}{C}^2}}\ \angle\theta \qquad 7 - 20$$

where $\theta = \frac{1}{2}(\pi/2 - \tan^{-1}(\omega\overset{*}{C}/G))$

Again the nature of the characteristic impedance of overlap coil STLIM is similar to the non-overlap coil model given in 4 - 17. It inherits a very resistive nature ensuring good power factor for all range of slip and the lowest possible power factor is still $\mathrm{Cos}\pi/4$ when $G \gg \omega C$.

The characteristic impedance also has a fairly constant value for all range of slip. Hence similar conclusions can be drawn for the power input and current characteristics.

The magnitude of the current is

$$I = V\sqrt[4]{\frac{G^2+\omega^2\hat{C}^2}{\omega^2 L^2}} \qquad 7 - 21$$

and the power input is

$$P_i = VI\ \mathrm{Cos}\,\theta \qquad 7 - 22$$

where the power factor is $\mathrm{Cos}\theta = \mathrm{Cos}(\frac{1}{2}(\frac{1}{2}\pi - \mathrm{Tan}^{-1}\omega\hat{C}/G))$

The output power is simply the product of thrust and rotor speed

$$P_o = FU = FU_s(1-S) = F\omega(1-S)/\beta \qquad 7 - 23$$

The efficiency of the machine is

$$\eta = \frac{P_o}{P_i}$$

which can be recast in terms of machine parameters as

$$\eta = \frac{\omega C(1-S)(1-e^{-2\alpha l})((3\beta^2-\alpha^2)(1-\mathrm{Cosh}2a\alpha\mathrm{Cos}2a\beta)+\mathrm{Sinh}2a\alpha\mathrm{Sin}2a\beta\left[3\alpha\beta-\beta^3/\alpha\right]}{\sqrt{G^2+\omega^2\hat{C}^2}\,(1+\mathrm{Sin}\phi_2)(\alpha^2+\beta^2)(\mathrm{Cosh}2a\alpha-\mathrm{Cos}2a\beta)}$$

7 - 24

where $\phi_2 = \mathrm{Tan}^{-1}\omega C/G$ as in 4 - 21a

Equation 7 - 24 compares favourably to 4 - 21a of the non-overlap coil model. The theoretical efficiency of the overlap coil model can be improved and depends on attenuation function, winding pitch, and the ratio of shunt capacitance and shunt conductance.

Hence from the developement of the overlap coil model starting from the performance characteristic curves obtained from 7 - 14 and 7 - 15, the results obtained for α and β at certain value of speed U at fixed shunt capacitance per meter C, all theoretical characteristics can be determined from 7 - 11, 7 - 16, 7 - 19 to 7 - 24.

The developed Fortran programmes to compute series of characteristic curves and theoretical performance are shown in Appendix 1. The example of chosen characteristic curves for designed experimental motor are also shown in Appendix 3.

7.10 SOME DESIGN CRITERIA OF OVERLAP COIL STLIM

Again, two basic considerations for the designed quality of the overlap coil model are the Laithwaite's goodness factor and the loop cutoff frequency.

Firstly, as seen from 4 - 22 the goodness factor of STLIM in terms of machine parameters and phase function is

$$G = \frac{\mu_0 \omega^2 t}{2\pi f g \beta^2}$$

For the overlap coil model the goodness factor can be calculated by using the value of phase function β extracted from the performance curve of section 7.6. Generally for

fixed value of machine parameters as the speed of the rotor drops the phase function increases to a maximum value and then begins to drop again at high values of slip. The goodness factor then varies slightly with speed of the rotor starting from no-load speed value, drops slightly with increasing slip and then increases again at high slip region. When the airgap of the machine is opened up for variation of speed control the value of phase function β decreases, but unlike their non-overlap coil counterpart, the goodness factor drops slightly as the airgap g in this case is proportional to approximately β^{-4} instead of β^{-2}. However from the design point of view, the effect of varying the airgap on this type of machine(goodness factor proportional to $1/\sqrt{g}$) is more favourable than the conventional one(proportional to $1/g$).

Secondly when we consider the cutoff frequency-again seen in the light of the equivalent circuit resemblance to that of the distributed transmission line- the machine acts as a lowpass filter. The approximate condition of section 4.7.2 still holds here with different values of parameters. Hence the no-load cutoff radian frequency as seen from the ladder network on page 60 where $L=L_o$ for zero attenuation.

$$\omega_c = \frac{2}{\Delta\sqrt{L_o C}}$$

where Δ is the actual unit size of the ladder network.

Now for the overlap coil model, the total series no-load inductance, L_o, as seen from the equivalent circuit is

$$L_o = \frac{2\mu_o w T^2((\beta^2-\alpha^2)(1-\cosh 2a\alpha \cos 2a\beta)+2\alpha\beta \sinh 2a\alpha \sin 2a\beta)}{gd^2(\alpha^2+\beta^2)^2}$$

when $\alpha = 0$ and $\beta = \beta_o$, this expression reduced to

$$L_o = \frac{2\mu_o w T^2}{gd^2\beta_o^2}(1-\cos 2a\beta_o)$$

then the no-load cutoff frequency is

$$f_o = \frac{d\beta_o}{\Delta\pi T}\sqrt{\frac{g}{2\mu_o C w(1-\cos 2a\beta_o)}} \qquad 7 - 25$$

Equation 7 - 25 is a useful measure for the design parameters in order to choose the individual unit size of the actual ladder network connection of the stator coils.

CHAPTER 8

THE OVERLAP COIL EXPERIMENTAL MOTOR

8.1 PRELIMINARY DESIGN CONSIDERATIONS

From the previous chapter, the mathematical model of STLIM is developed to the point that it is now possible to design an experimental machine to verify the theory. In the theoretical model, however, the effect of stator resistance is neglected. Hence the experimental machine must be designed to have as low stator resistance as possible. The experimental motor is based on the same stator block of non-overlap coil motor which consists of 8 tooth stator of 5 cm tooth pitch and new rewound stator coils. The length of the stator block is 40 cm and the width of 9 cm. Coil span of 2 slot is chosen because of the low number of stator teeth and with two slot coil span, this allows the maximum uniform central region of double sided coils and minimum single sided coils at entry and exit end regions. This arrangement gives the winding pitch of 10 cm which compares favourable to the desired range of synchronous speed of 10 to 15 m/s with 50 Hz supply frequency. The disadvantage of this arrangement is that the slot pitch is as big as half the coil span and in some cases half of the machine pole pitch. This will lead to a very lumpy nature of travelling field and the approximation of smooth sinusoidal travelling field is altered.

The summary of the preliminary designed values are as follow: low stator resistance, synchronous speed of 10

to 15 m/s, chosen coil span of two teeth, hence the winding pitch of 10 cm, variable shunt capacitance per meter of 800 to 2400 μF and the normal supply frequency of 50 Hz. The arrangement of the stator circuit is shown as in Figure 8.1.

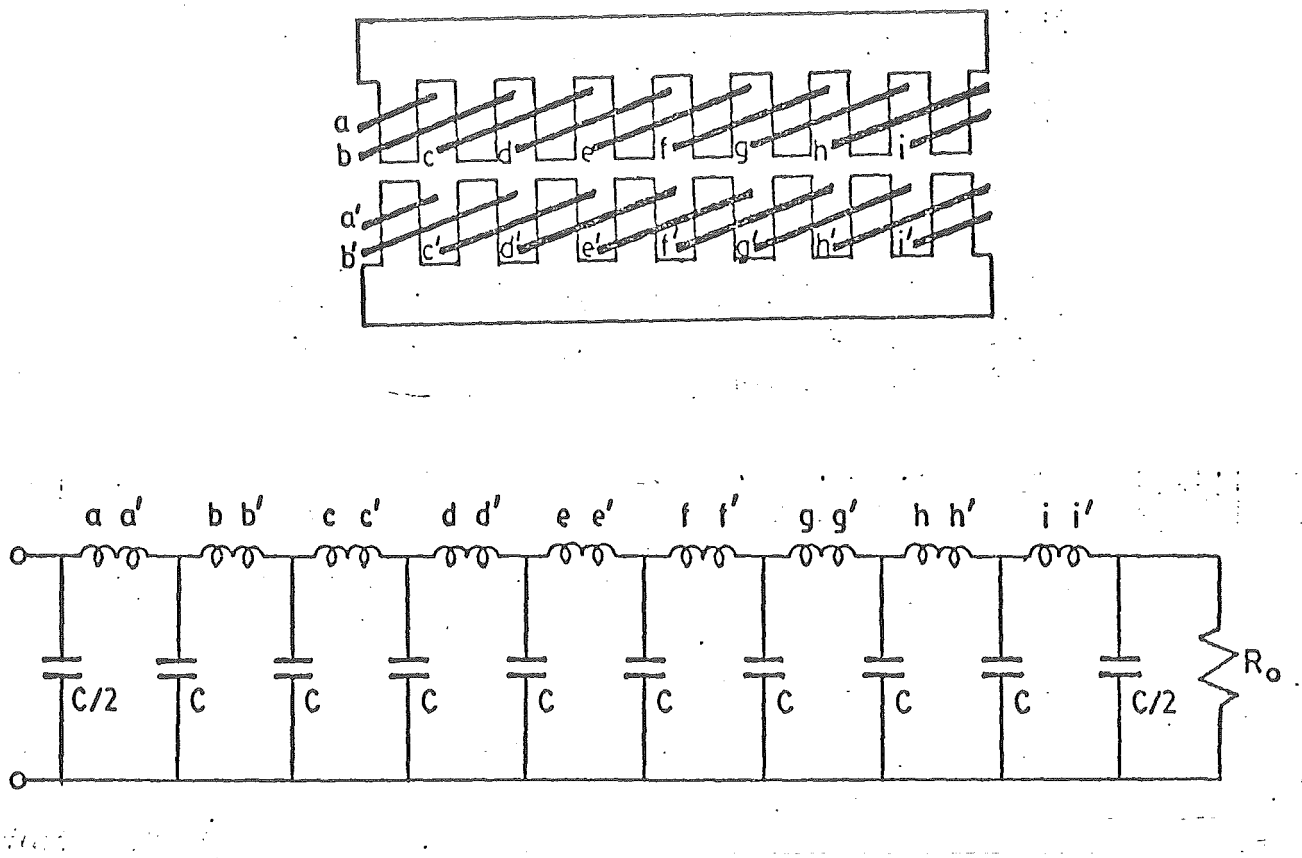

FIGURE 8.1 The arrangement of the stator and circuit connections

8.2 THE DESIGN OF THE STATOR COIL

8.2.1 The Approximate Number of Turns on No-rotor Synchronous Speed Range

From section 7.7 the equation of no-rotor phase function is given by

$$\beta_o^4 = \frac{4\mu_o \omega^2 w T^2 C \sin^2 a\beta_o}{g d^2}$$

For a preliminary design value of number of turns, consider a typical case with airgap of 15 mm, half coil span a of 5 cm, slot pitch d of 5 cm and synchronous speed of 10 m/s. This will give the value of $\beta_o = 31.4$ and $a\beta_o = \frac{1}{2}\pi$. Hence for the value of shunt capacitance of 2000 μF/m, the number of turns per coil is given by

$$T = \sqrt{\frac{g d^2 \beta_o^4}{4\mu_o \omega^2 w C \sin^2 a\beta_o}} = 554 \text{ turns}$$

Choosing 560 turns coil for the motor, this gives the number on each stator block of 280 turns.

8.2.2 Stator Conductor Size

With the designed value of cross-sectional area of coil of 31 cm^2 as used in section 5.2, the estimated value of conductor size that will fit in with the conductor space factor of 0.5 is $0.5 \times 31 \times 100 / 560 = 2.8$ mm^2. This corresponds to the conductor size of about 1.9 mm diameter. It is now necessary to check for the value of coil resistance.

The double layer coil of this physical size must be wound flat on the coil former and stretched out on jig to

form a double layer coil as shown in Figure 8.2. The estimated average length per turn is 0.8 m. Hence, the resistance of the 560 turn coil is therefore $R_{coil} = \rho l/A = 2.9$ ohms/coil. This will give the value of stator resistance per meter of $R_{coil}/d = 2.9/0.05 = 58$ ohms/m. The value is high compared with 40 ohms/m of the non-overlap coil model. With the next conductor size of 2.0 mm diameter, with cross-sectional area of 3.143 mm^2, the resistance/coil will reduce to 2.9X2.84/3.14 = 2.6 ohms/coil. Checking back for the maximum avaliable slot window of 4 cm slot width and 12 cm slot depth the conductor of 3.14 mm^2 cross-sectional area can just fully fill the slot window and hence is the maximum size of conductor that can be used for this experimental motor. This will reduce the value of stator resistance down to 50 ohms/m. This value still appears very high especially when the simplified model does not taken account of this stator resistance.

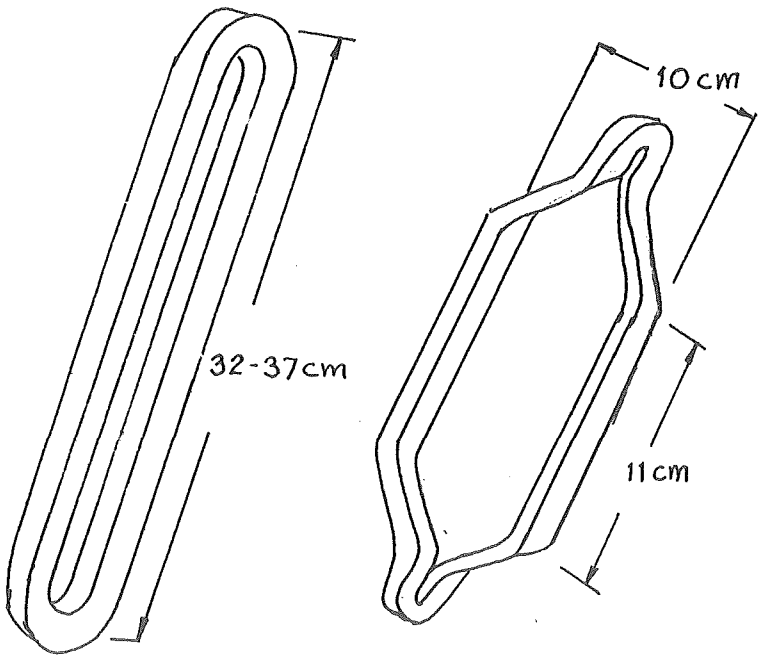

FIGURE 8.2 The estimated mean length of stator coil.

8.3 THE PREDICTED PERFORMANCE OF THE OVERLAP COIL STLIM

From the previous sections, all the machine dimensions are known but there exists the difficulty in the value of rotor resistance ϱ_2. The theoretical value of $\varrho_2 = \rho/t$, where t is the thickness of the aluminium disc, is too low. For the experimental rotor of 10 mm thickness this give $\varrho_2 = 0.3\ 10^{-5}$ ohms. Again as in the first part of this thesis and as previously reported by Watson [12], some correction factor is used. For all theoretical performance predictions the value of $\varrho_2 = 10^{-5}$ ohms is used based on 10 mm secondary thickness. Laithwaite [2] discussed a similar situation in relation to three phase linear induction motor.

From 7 - 14 and 7 - 15, the relationship between rotor speed, shunt capacitance, attenuation, and the speed of the travelling magnetic field can be obtained by assigning values to α and β and treating U and C as dependent variables. The result of the series of calculations is illustrated in Figure 8.3 for the case of 21 mm airgap. The family of performance curves for the values of different airgaps from 18 mm to 30 mm is shown in Appendix 3.

From performance curves of Figure 8.3, for fixed value of capacitance, as the speed of the rotor drops the attenuation function, α, increases and the phase function, β, also increases slightly. The increment of phase function, β, implies the reduction in pole pitch and hence reduction in synchronous speed. As the rotor speed reduces further, the phase function, β, increases to its maximum value and reduces at higher slip region. Hence the synchronous speed starts to increase again in this region. The motor seems to have

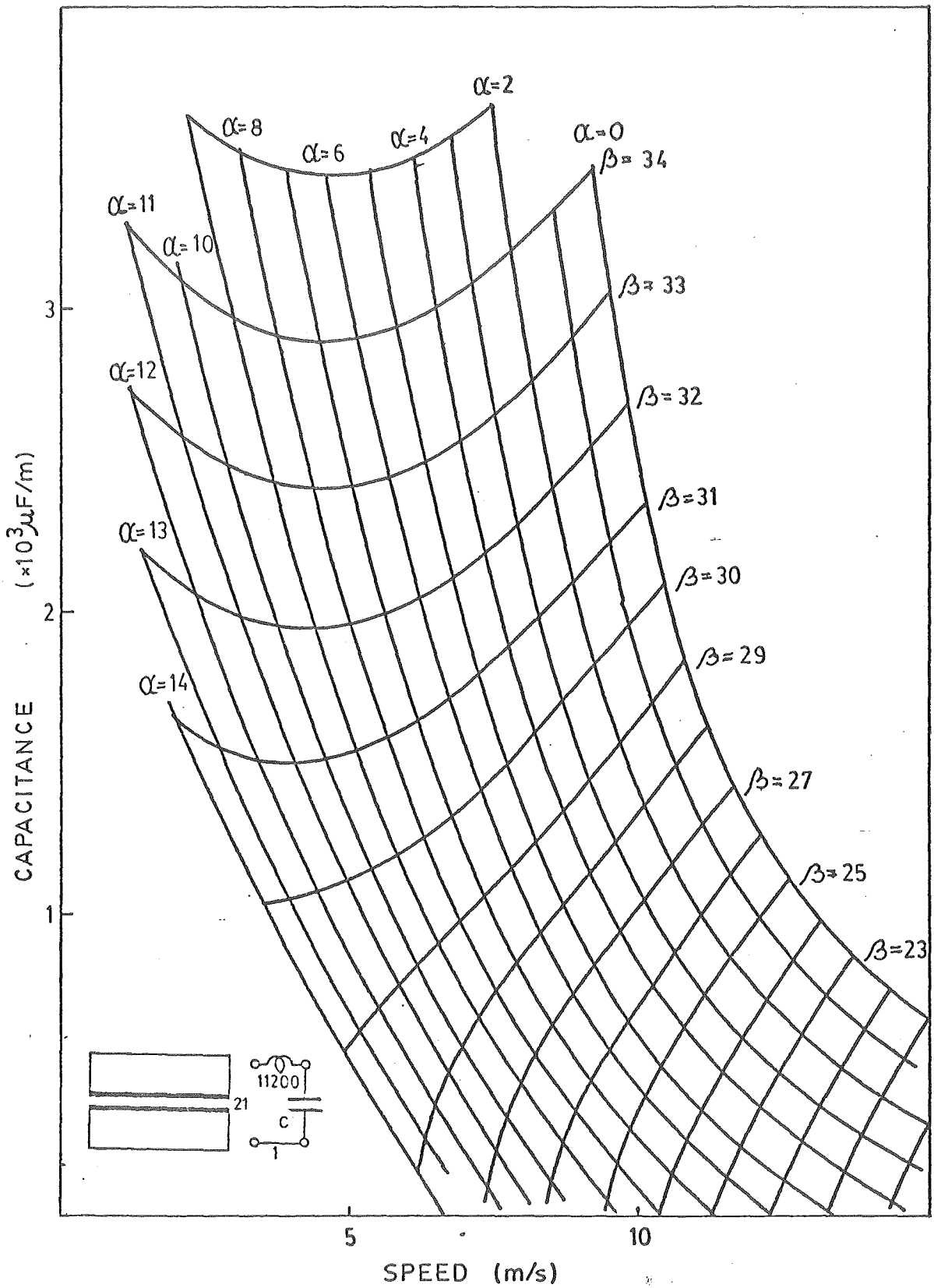

FIGURE 8.3 Typical performance curves of overlap coil STLIM with airgap = 21 mm, T/d = 560/0.05 = 11200 turns/m

no fixed synchronous speed. With the reduction in shunt capacitance the no-load speed increases. The variation of no-load speed is narrow at high value of shunt capacitance region and wider in the low values of shunt capacitance region. Three fixed shunt capacitance values are chosen 800 μF/m, 1600 μF/m and 2400 μF/m. These correspond to the no-load speed as extracted from performance curves of Figure 8.3 of 14 m/s, 11.3 m/s and 10.1 m/s respectively.

At each individual case of shunt capacitance value, a series of phase functions, β, and attenuation functions, α, are extracted out for different values of rotor speed. These values are used in the calculation of all electrical performances of the motor via 7 - 11, 7 - 20 to 7 - 24. The selected illustrations are plotted as; power input, current, power output, thrust and efficiency against the linear speed of the rotor. The typical theoretical characteristic prediction is shown in Figure 8.4. The complete family of these theoretical characteristic predictions for the value of shunt capacitance of 800 μF/m, 1600 μF/m and 2400 μF/m at different airgaps of 18 mm, 21 mm, 24 mm, 27 mm and 30 mm are shown in Appendix 3. The summary of maximum theoretical efficiency is shown in Table 8.1

Shunt capacitance (μF/m)	Airgap (mm)				
	18	21	24	27	30
800	50	47	44	42	39
1600	71	66	62	58	55
2400	84	78	73	68	64

TABLE 8.1 Theoretical efficiency of overlap coil STLIM.

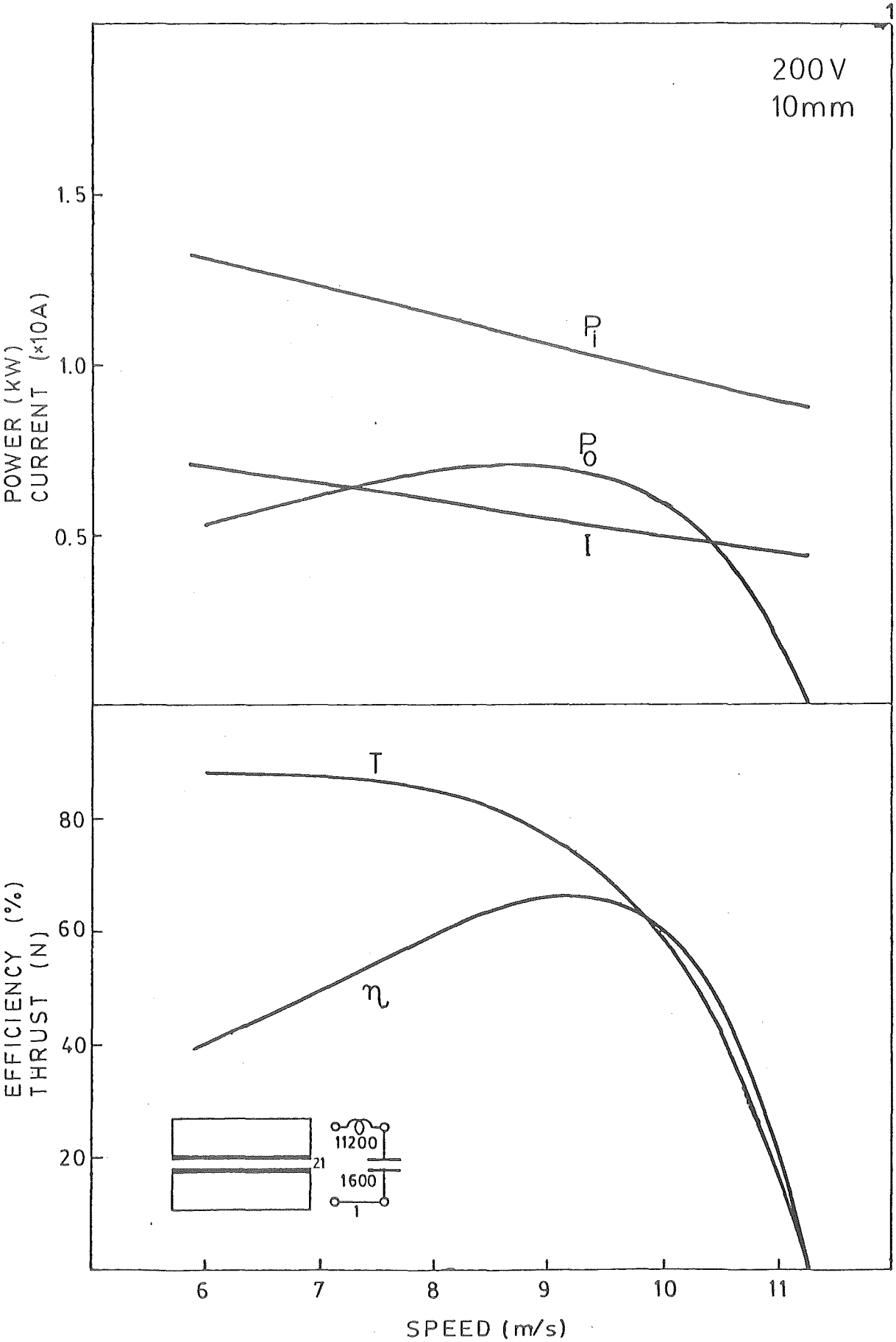

FIGURE 8.4 Theoretical characteristics of overlap coil STLIM with g = 21 mm, C = 1600 uF/m, V = 200 V

8.4 CHECK FOR QUALITY OF DESIGN VALUE

The result of the predicted efficiency for the machine is very high even compared to the conventional single phase machine of the same rating. It is unlikely that the predicted performance will be met at all ranges because of the reasons stated in section 8.1. Furthermore the consideration of the machine qualities of Laithwaite goodness factor and cutoff frequency must be checked.

Firstly, to obtain the Laithwaite goodness factor, machine parameters at no-load were used. From Figure 8.3 the value of β with different values of airgap and shunt capacitance was extracted and the goodness factor of the motor was calculated using 4 - 22. The results are tabulated in Table 8.2. The goodness factor of about 10 seems to compare well with the optimum condition [5] in the lower value of shunt capacitance. Hence from this consideration alone the high value of efficiency in the order of 60-80% in 2400 μF/m shunt capacitance is unlikely. However, there is still some hope in reaching the improved efficiency of 40-60% in the lower range of shunt capacitance. Within this range the value will compare favourably to small single phase conventional motors and three phase linear induction motors of the same number of pole pairs, physical size and rating. Together with the advantages of variable speed at fixed supply frequency and unity power factor characteristic, this machine might prove of some value in linear drive systems.

Secondly, the attention is turned to the basic design quality of cutoff frequency. Using 7 - 25 and the arrangement as in Figure 8.1 the value of unit size Δ is equal to slot

pitch of 5 cm. All other parameters are known and the value of β_0 is obtained from performance curves. The calculated results are summarised in Table 8.3 for values of shunt capacitance 800 μF/m, 1600 μF/m and 2400 μF/m together with with airgap of 18 mm, 21 mm, 24 mm, 27 mm and 30 mm inclusive. The results obtained from the no-load cutoff frequency confirm that at higher values of shunt capacitance the cutoff frequency moves closer to the supply frequency of 50 Hz. In addition with the effect of stator resistance, the performance of the motor will degrade from the predictions especially in the high value of shunt capacitance region.

Shunt capacitance (μF/m)	Airgap (mm)				
	18	21	24	27	30
800	14	12	12	11	10
1600	9	8	7	7	6
2400	7	6	6	5	5

TABLE 8.2 Goodness factor of overlap coil STLIM.

Shunt capacitance (μF/m)	Airgap (mm)				
	18	21	24	27	30
800	86	89	92	94	97
1600	70	72	74	75	76
2400	63	64	66	67	68

TABLE 8.3 Cutoff frequency of overlap coil STLIM.

8.5 ELECTRICAL CAPACITY OF THE EXPERIMENTAL MACHINE

From typical performance curves of Figure 8.3 together with 7 - 5 for selected test voltage of 200 V the maximum flux density in the airgap can be obtained. The flux density varies from about 0.2 Teslas in 800 μF/m shunt capacitance case to about 0.4 Teslas in 2400 μF/m shunt capacitance case. The corresponding characteristic impedance at those conditions, calculated from 7 - 20, varies from 70 ohms to about 30 ohms respectively. This predicts quite a low input current of 200/70 = 3 amperes to 200/30 = 7 amperes. These values of current and flux density are quite low for electrical machine design values. With near maximum saturation flux density in the teeth, which corresponds to about 0.8 to 0.9 Teslas in the airgap, the voltage could rise to about 900 V for 800 μF/m shunt capacitance and 450 V for 2400 μF/m shunt capacitance. Even with higher input voltage the attenuated nature of the flux density along the airgap together with the entry end effect will assist in suppressing the saturation in the airgap. With these voltage levels, the corresponding input current will be about 13 to 15 amperes, which when checked with the value of the stator current density for 2.0 mm diameter conductor is just under the allowable 5 A/mm^2. Hence the estimated full rating of the motor, calculated from say 50% efficiency, will be in the order of $0.5V^2/Z_o = 0.5 \times 900^2/70$ = 5.8 kW for 800 μF/m shunt capacitance and about 3.5 kW for 2400 μF/m shunt capacitance. The corresponding value of thrust at these rating will be about 650 N to 500 N respectively if the maximum thrust reaches the value of the theoretical V^2C newtons.

Similarly to the non-overlap coil cases in Chapter 5, a series of test results of the overlap coil motor is taken at supply voltage of 200 V 50 Hz. However, some special cases of higher supply voltage are added in order to support the predicted full electrical rating of the machine. Generally it should be noted that at 200 V supply, the motor is again operating at under voltage rating which accounts for low values of thrust and power output of the machine.

8.6 THE EXPERIMENTAL MOTOR ASSEMBLY

The main difference between the design of the overlap coil motor and the non-overlap coil motor as described in the first part of the thesis is the rewind of the stator coils. The final value is chosen so that the coil span is two teeth. The coils on each side of the stator block have 280 turns which will be connected in series to give the total number of turns of 560. The connections are shown in Figure 8.1.

A prototype of 280 turns coil was wound on a flat former to test whether the coil could fit into the avaliable slot space. This proved satisfactory for the coil just occupied half the area of slot space. Due to the massive coil shape and the big 2.0 mm conductor diameter several home made jigs, which were designed to pull the coil to form double layer type, failed. The 280 turns coil was then divided into thinner layers of 140 turns coil. After some preliminary trials, a home made jig powered by a car hydraulic jack was used to pull the 140 turn coil into the desired form successfully. Figure 8.5 shows the individual flat coils from the

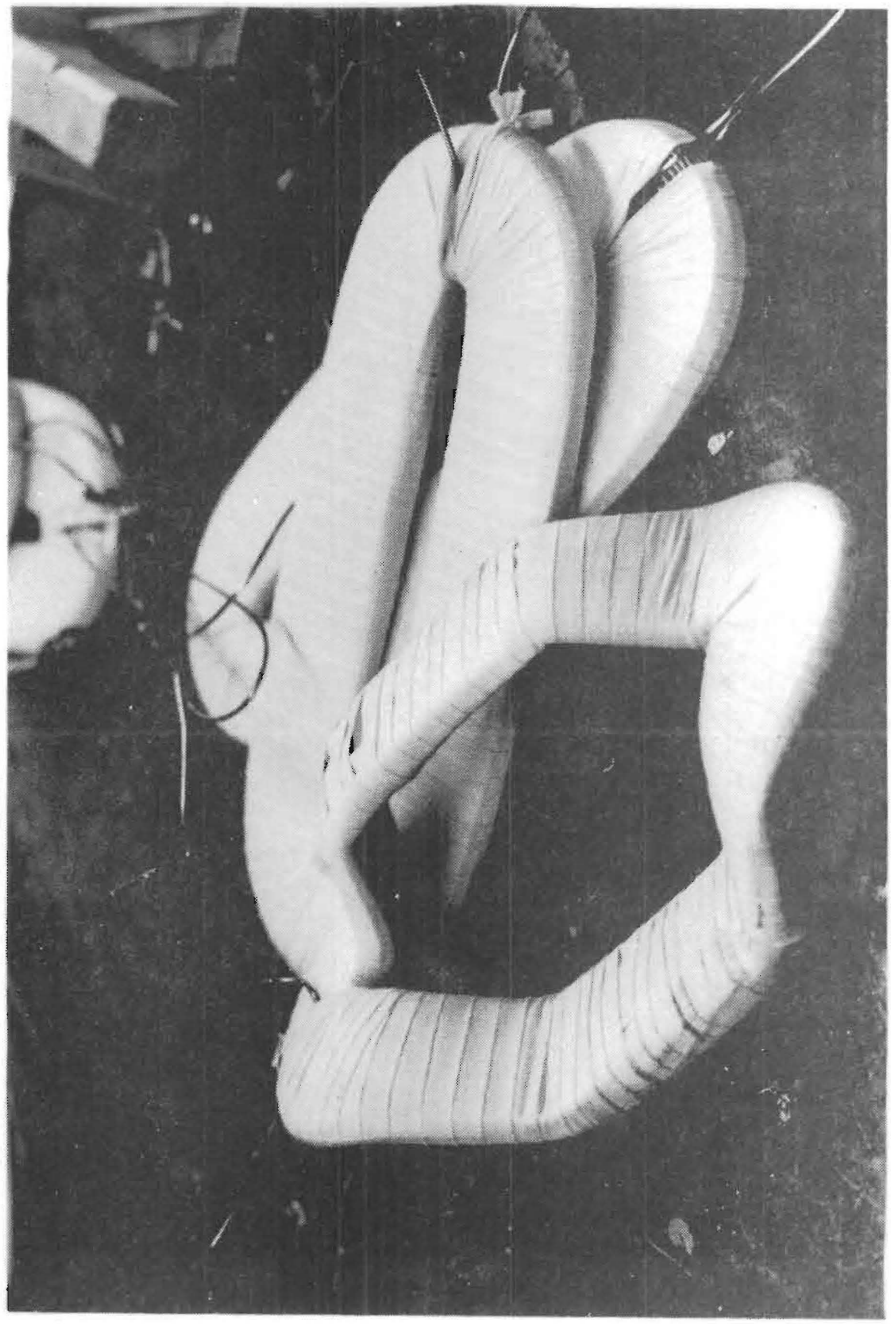

FIGURE 8.5 The prewound flat coils and the double sided coil after being pulled into shape.

former and the processed pulled double layer coil from the jig. The coils are tested individually for damage to insulations. The average record of coil resistance is 0.6 ohms. This bring the total to 2.4 ohms for 560 turns coil, a bit lower than 2.6 ohms predicted. This is due to the shorter average length per turn for the split coil arrangement.

In order to conduct some tests at higher voltage level plastic insulation is used to insulate the slot and coil and between coil sides. Because most of the tests are at lower voltage level of 200 V and the conductor current density is quite low, it was decided not to impregnate the winding and to use rope to hold coils onto the stator block. This proved sufficient to suppress the mechanical vibration at 200 V supply. At both ends a single tooth span coil of 280 turns is added in order to completely fill the slot at both ends and hence help improve the flux distribution in those regions. Each stator block then consists of seven two 140 turn coils which span two slots, and two 280 turn coils spanning one slot at each end. Figure 8.6 shows one side of the stator block after the coils are in place. One stator block is fitted with 5 turns search coil on every tooth in order to investigate the waveform of flux density and synchronous speed.

The rest of the assembly is the same as described in part one. The rope brake thrust measuring apparatus is modified by extending the capacity of the weighing pan in order to measure extra thrust of up to 150 N. The whole motor assembly is illustrated in Figure 8.7 while the arrangement of the stator blocks and the electrical circuit is as shown in Figure 8.1. After a series of preliminary

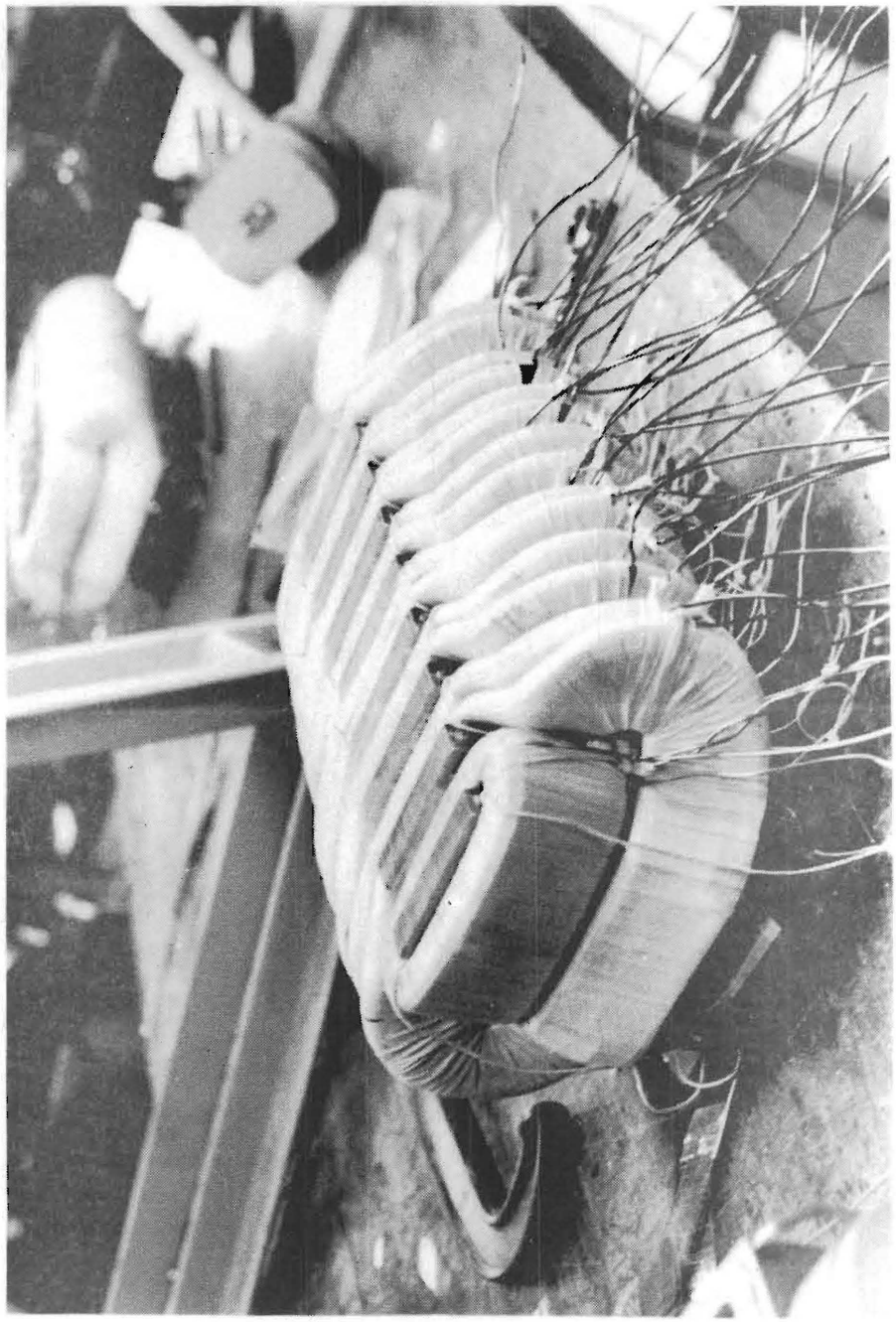

FIGURE 8.6 The stator block assembled

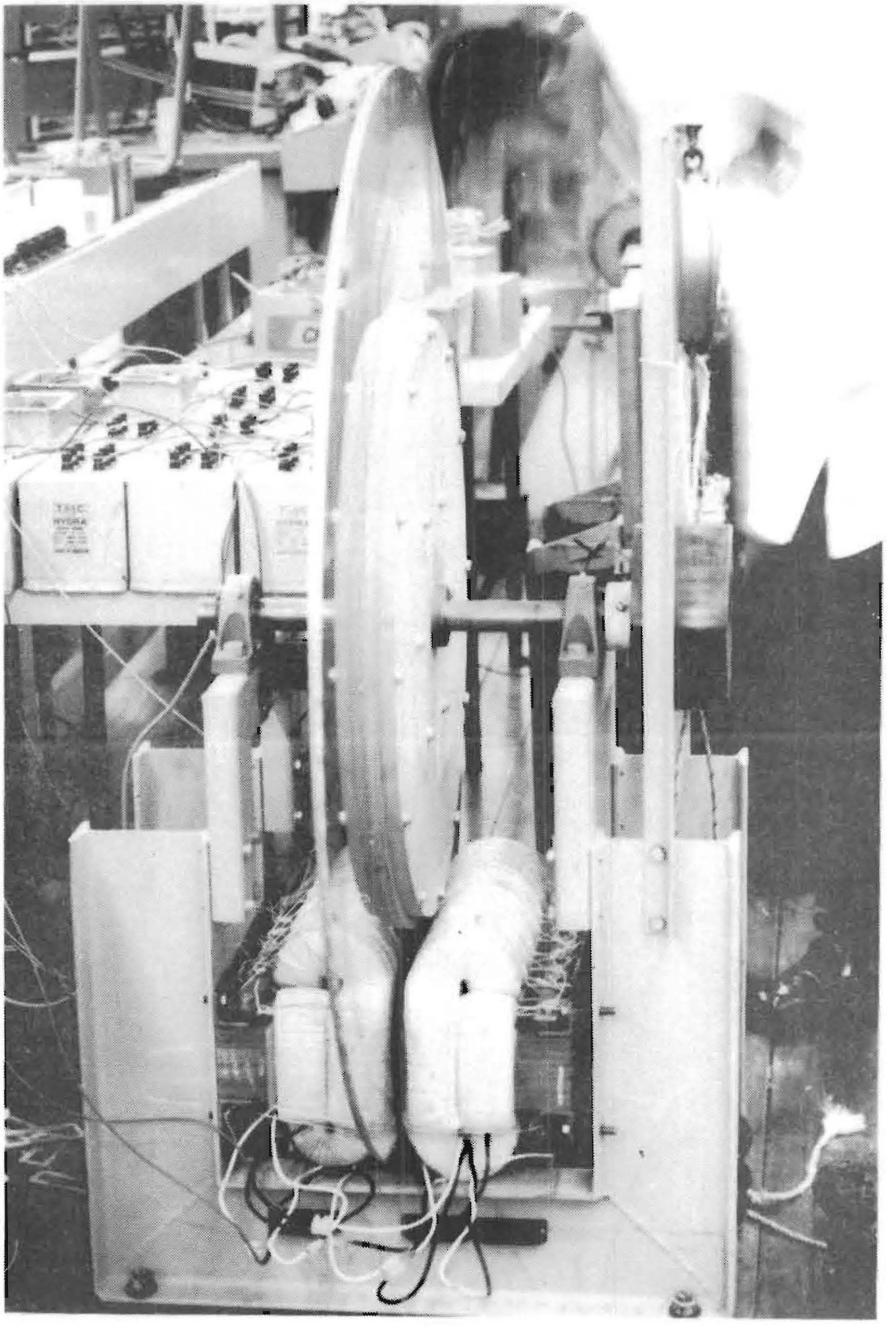

FIGURE 8.7 The overlap coil motor assembly

trial runs, a cooling blower was needed when testing the loaded machine at higher voltage range to prevent excessive heat on the rotor disc which causes the disc to distort and to scrape against the side of the stator block.

CHAPTER 9

RESULT OF THE EXPERIMENTAL OVERLAP COIL STLIM

9.1 SUMMARY OF TEST RESULTS

Initially from the theoretical considerations, the machine's characteristic impedance varies as a function of airgap and shunt capacitance. Furthermore, even with the same set up with fixed value of airgap and capacitance when the rotor speed varies with load the characteristic impedance changes. The typical theoretical value at no-load for shunt capacitance of 800 μF/m, 1600 μF/m and 2400 μF/m are 70 ohms, 45 ohms and 36 ohms respectively. And when the motor is loaded, taking the value of attenuation about 5, the characteristic impedances drop to about 46 ohms, 33 ohms and 26 ohms. In a practical machine the variable terminating impedance to match each particular case and speed would prove too expensive. In preliminary test runs, the termination with fixed resistor seems to be adequate to suppress the exit end reflection wave and the value of terminating resistance is not critical. When loaded, the motor has high natural attenuation and the voltage at the end winding is very small, therefore termination has a very small effect on machine performances. The fixed terminating resistors of 63 ohms, 44 ohms and 38 ohms are chosen in case of shunt capacitance of 800 μF/m, 1600 μF/m and 2400 μF/m respectively. More detail on the effect of terminating impedance will be demonstrated in Section 9.4.

The first series of tests was carried out at 200 V

50 Hz supply for shunt capacitance of 800 μF/m, 1600 μF/m and 2400 μF/m at different airgap of 21 mm, 24 mm and 27 mm. The results show a small improvement over the non-overlap coil STLIM but are far from the predicted values obtained from Chapter 8. The arrangement of stator blocks and electrical connections are as in Figure 8.1. Each individual experimental performance is shown in Appendix 3 from Figure A128 to Figure A142. Although the goodness factor for 3 mm secondary thickness is very small, from 2 to 4, the test results of some cases were obtained. The individual performances are shown in Figure A118 to Figure A127. The summary of maximum efficiency of the experimental motor is shown in Table 9.1. The result for this arrangement will be discussed in more detail in Section 9.2.

shunt capacitance (uF/m)	Airgap(mm)		
	21	24	27
800	34	36	37
1200	35	37	38
1600	33	35	36
2000	30	31	31
2400	28	28	28

TABLE 9.1 Maximum efficiency for symmetrical stator block

Secondly one of the stator blocks is shifted in the longitudinal direction for half the slot pitch and the windings connection of the stator blocks are re-arranged. The reason for this arrangement will be discussed in more detail in Section 9.3. The stator blocks and winding arrangement are as shown in Figure 9.1. Test results were recorded for the value of shunt capacitance of 800 μF/m, 1600 μF/m and 2400 μF/m at the airgap of 18 mm, 21 mm, 24 mm, 27 mm and 30 mm. Each individual experimental performances is shown in Appendix 3 from Figure A143to Figure A157. The maximum efficiency of these results are summarised in Table 9.2

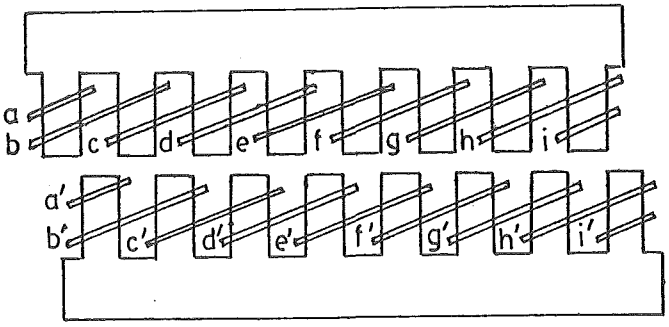

(a)

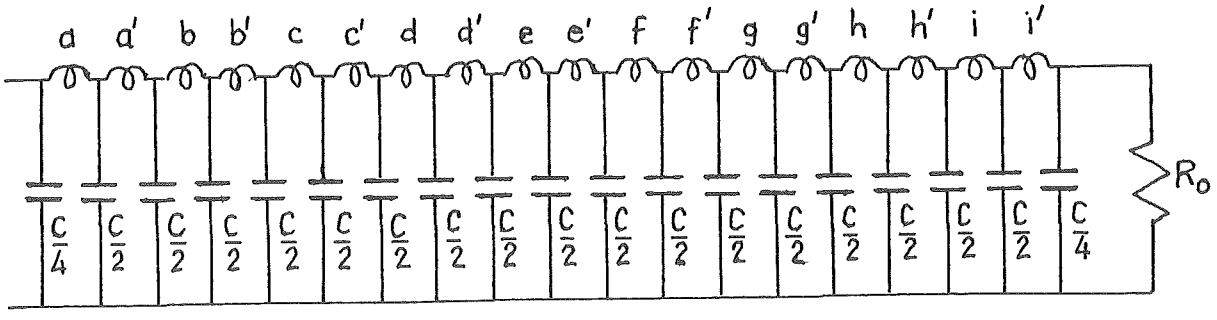

(b)

FIGURE 9.1 (a) Arrangement of stator block with one half offset.
(b) Connections of coils and capacitors.

Next, the no-rotor synchronous speed for each type of arrangement were obtained. As in Part one, they were calculated from the average phase shift from oscilloscope. The summarised results of the theoretical and experimental no-rotor synchronous speed are shown in Table 9.3.

After completing these tests some typical experimental cases of different values of terminating resistances, supply frequency, loss separations and different values of supply voltage were investigated.

shunt capacitance (μF/m)	Airgap(mm)				
	18	21	24	27	30
800	39	41	41	39	40
1600	43	45	44	39	41
2400	39	40	39	34	35

TABLE 9.2 Maximum efficiency for offset stator blocks.

9.2 RESULTS OF THE SYMMETRICAL STATOR BLOCKS

In this series of tests the two halves of the stator blocks were placed symmetrically with their teeth opposite and the coils were connected as in Figure 8.1. Shunt capacitors were connected at the junction of each pair of coils. A typical test result is illustrated in Figure 9.2 for 200 V 50 Hz operation. The overall efficiency as seen from Table 9.1 rise to a maximum value of 28 to 38% depending on the

shunt capacitance (μF/m)	Linear velocity (m/s)	Airgap(mm)				
		18	21	24	27	30
800	calculated	13.5	14.1	14.5	14.8	15.4
	measured(1)	13.0	13.4	14.0	14.2	14.7
	measured(2)	15.1	15.5	15.8	15.9	16.2
1600	calculated	10.9	11.3	11.6	11.8	12.1
	measured(1)	10.3	10.5	10.7	10.9	11.0
	measured(2)	11.1	11.5	11.8	12.0	12.3
2400	calculated	9.8	10.1	10.3	10.5	10.7
	measured(1)	8.7	8.8	9.0	9.1	9.2
	measured(2)	9.9	10.0	10.4	10.5	10.7

Note: measured(1) - symmetrical stator blocks,
measured(2) - offset stator blocks.

TABLE 9.3 Theoretical and experimental no-rotor synchronous speed.

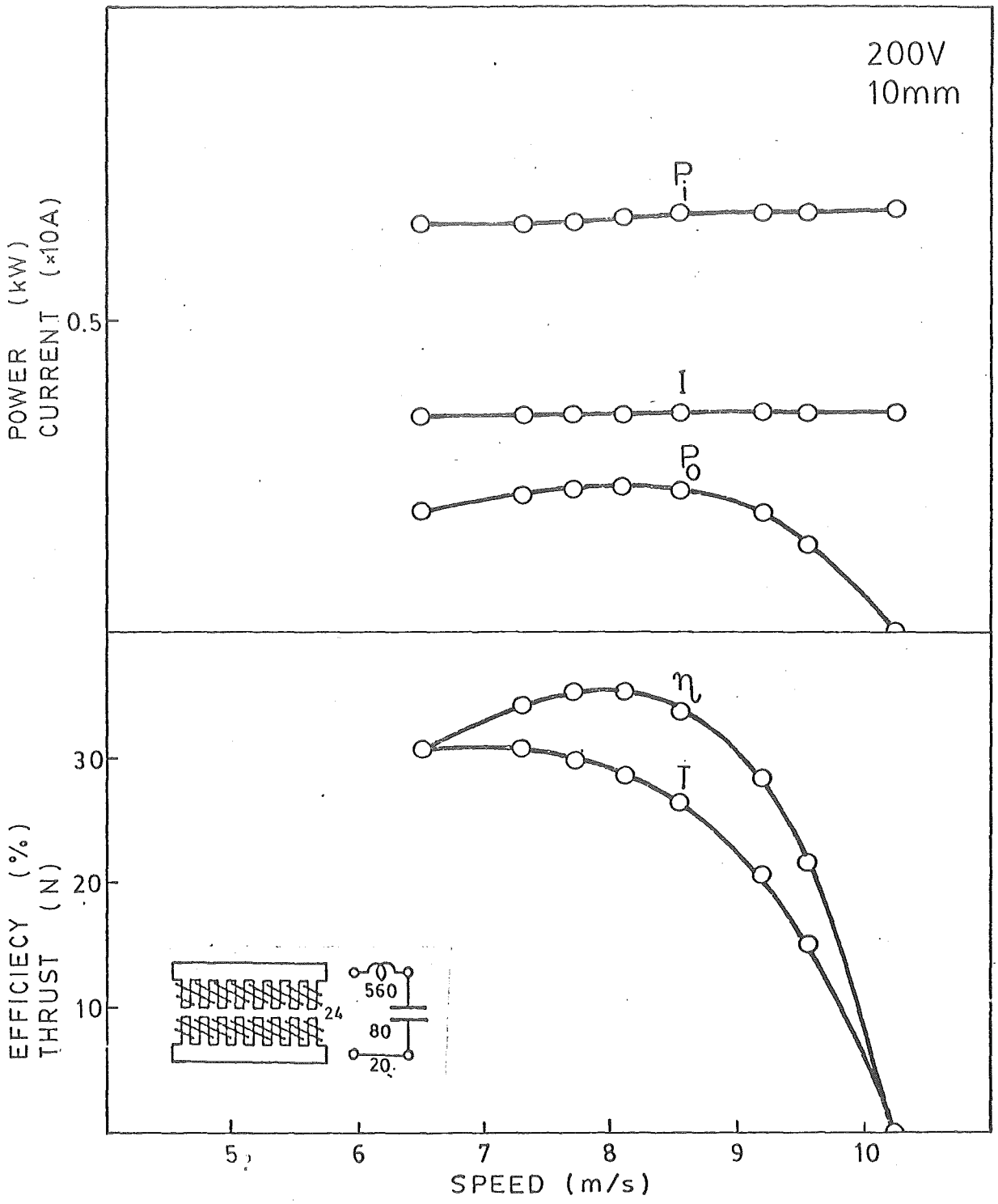

FIGURE 9.2 Characteristic of symmetrical stator blocks g = 24 mm, C = 1600 μF/m, V = 200 V and secondary thickness of 10 mm.

value of airgap and shunt capacitance. These values are low compared to the predicted maximum values in Table 8.1. However, there is a large proportion of stator resistance loss due to the high value of stator resistance that is not taken into account in the model. Additional tests were carried out to find the proportions of these losses, shown in Figure 9.3, assuming negligible iron, friction, windage and capacitors' dielectric losses. By subtracting from the input power the known stator copper losses and termination loss the efficiency of power conversion rises to about 50%. On the other hand the measured maximum thrust, 30 N, is far lower than the predicted 87 N. This disappointing result implies that the simplified theory does not adequately describe the experimental machine though it may possibly give an upper limit for the thrust that could be obtained by an ideal travelling wave machine. The speed variation can be attained by either varying the value of shunt capacitance as shown in Figure 9.4 or by variation of airgap. Table 9.4 show the summary of no-load speed at different value of shunt capacitances and airgaps. Some test results from 3 mm secondary were recorded. The results gave degraded machine performance since the resistance of the 3 mm rotor was more than three times that of 10 mm rotor and hence the goodness factor is too low. The typical case is shown in Figure 9.5.

However, the input power, current and power factor of the machine remain fairly stable for all ranges of slip. The speed variations follow the theoretical trends quite closely.

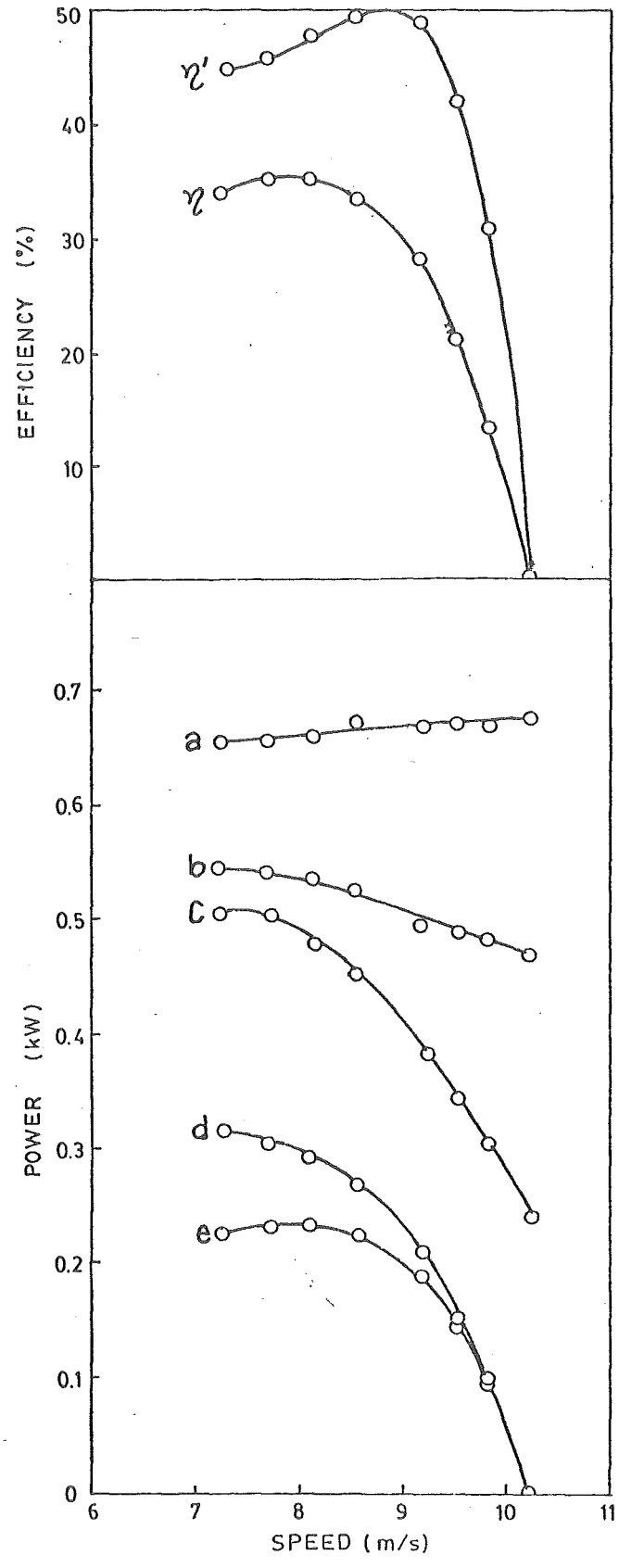

FIGURE 9.3 Analysis of losses for symmetrical stator arrangement. C = 1600 μF/m, 10 mm disc, g =24 mm.

η'= rotor efficiency(e/c), η = overall efficiency(e/a)
a= input power, b = input less stator copper loss,
c= termination loss now subtracted from b,
d= synchronous watts ($F \times U_s$), e = output ($F \times U$).

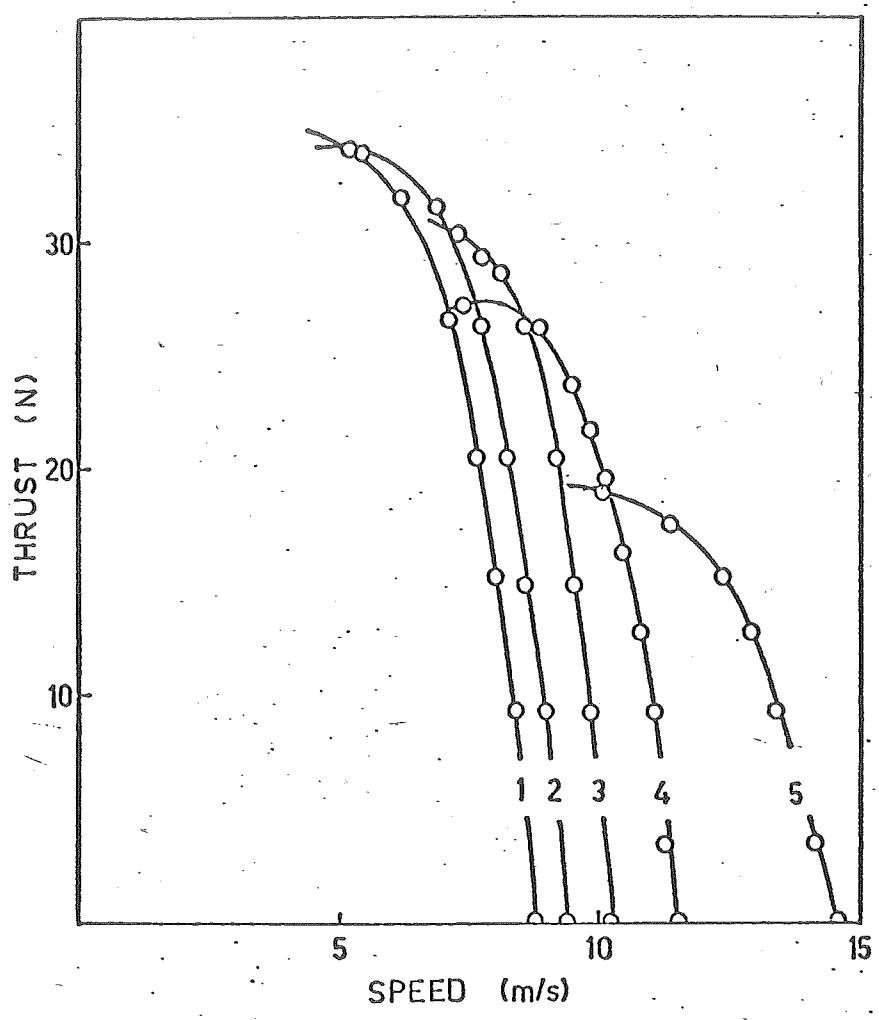

FIGURE 9.4 Thrust as a function of capacitance at 200 V. Symmetrical stator arrangement. g = 24 mm, 10 mm disc, and shunt capacitance of (1) 2400 μF/m, (2) 2000 μF/m, (3) 1600 μF/m, (4) 1200 μF/m and (5) 800 μF/m.

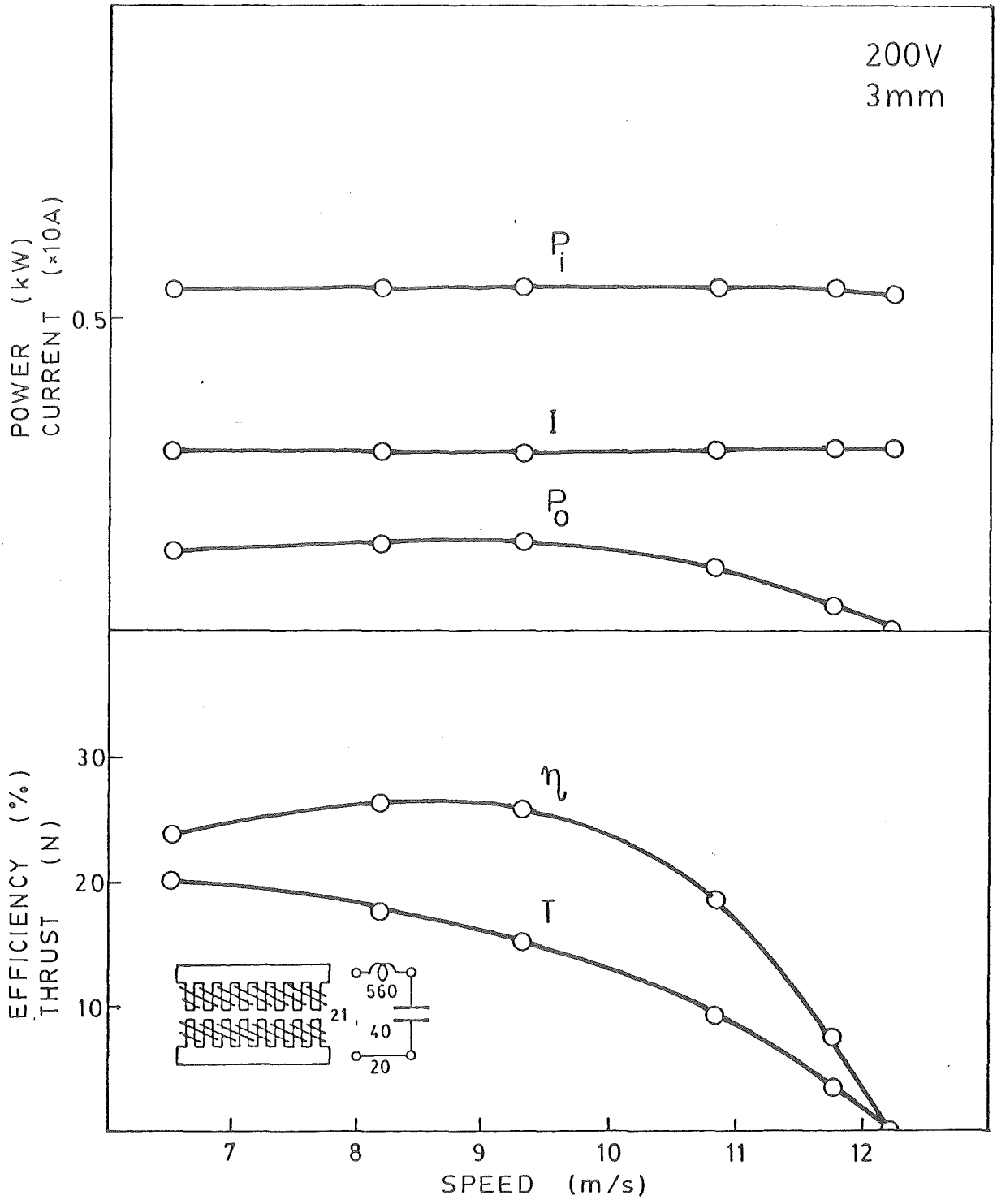

FIGURE 9.5 Typical characteristics of STLIM.
Symmetrical stator blocks arrangement.
3 mm disc, g = 21 mm, C = 800 uF/m.

9.3 RESULTS OF THE OFFSET STATOR BLOCKS

The experimental results of Section 9.2 do not agree very well with the theoretical predictions. Reasons were sought to explain this. One obvious defect in the experimental machine is the very large slot-width to pole pitch ratio which must lead to a very lumpy field distribution. It would seem intuitively that the field would be smoother, i.e. slot harmonic would be reduced, if one half stator block is now moved forward or offset by half a tooth pitch so that each tooth comes opposite a slot in other half stator block as shown in Figure 9.1. This was achieved by moving one half of the stator block forward by 2.5 cm. The windings are series connected as before but the capacitors are more evenly distributed by connecting them at the junction of each coil. From the theoretical prediction the number of turns per coil is reduced by half(280 turns) but the value of effective slot pitch, d, is also half of what had been before. Therefore the ratio T/d for this arrangement is still the same as 560 turns coil and 5 cm slot pitch arrangement and the theoretical predictions were unchanged. Apart from the advantage of more evenly distributed arrangement which will make the experimental motor closer to the approached of integral calculus model, the additional advantage of higher cutoff frequency would be obtained since the individual unit size is now reduced in the value of Δ from 5 cm to 2.5 cm.

The result of offsetting the two halves of the stator blocks were quite surprising. Figure 9.6 shows that for the same applied voltage and total capacitance per meter the

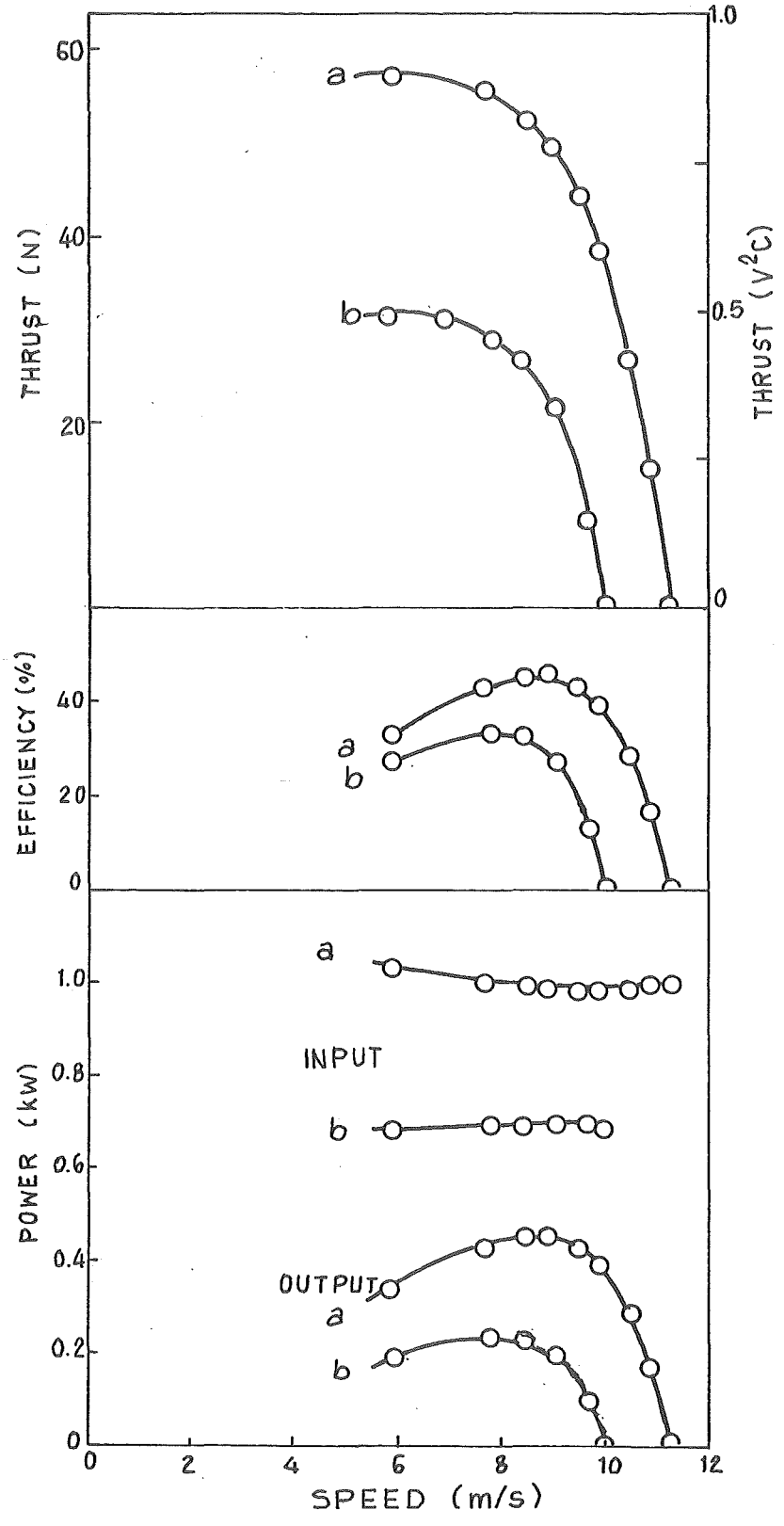

FIGURE 9.6 Improved performance. (a) offset stator blocks (b) symmetrical arrangement. C = 1600 uF/m, g = 21 mm, 10 mm disc, V = 200 V.

maximum thrust is raised from 30 N to 57 N while the overall maximum efficiency raised from 35% to 45%. This pleasing result had occurred as a result of a simple physical re-arrangement.

A series of tests results of the new arrangement were obtained for individual cases of different shunt capacitances 800 μF/m, 1600 μF/m and 2400 μF/m, together with the variable airgaps of 18 mm, 21 mm, 24 mm, 27 mm and 30 mm. These results were shown in Appendix 3 from Figure A143to Figure A157. The overall efficiency as summarised in Table 9.2 improved to the maximum values of 35% to 45% depending on the value of airgap and shunt capacitance.

The rotor is now removed and the phase shift by search coil is investigated. The measured value of no-rotor experimental synchronous speed obtained in this way were higher than the cases of symmetrical arrangement and in some cases more than the value of the predicted ones. The details are summarised in Table 9.3. By offsetting the stator block the series inductances of the coils seems to decrease; this is believed to be caused by the increase in the value of effective airgap which is not taken into account by the theoretical model.

With the experimental thrust still lower than the theoretical values, the overall efficiency was lower than predicted especially in the higher value of shunt capacitance region as discussed in Section 8.4. It is found that quite a proportion of power loss is due to the high value of stator resistance. With the measured values of stator copper loss, termination loss and the estimated dielectric loss of shunt

capacitors, the efficiency of power transfer is raised to the typical maximum value of 65% as shown in Figure 9.7. These values are neglecting iron loss, windage and friction losses.

9.4 THE EFFECT OF TERMINATING IMPEDANCE

The influence of terminating resistor is now considered. Typical analysis of losses, Figure 9.7, shows that a significant percentage of power is wasted in the terminating resistor. It was thought that if the resistor could be reduced or removed without affecting the suppression of the reflected travelling field, the overall efficiency may be raised. This was investigated, using the offset stator block, by terminating the end winding with two extremes of open circuit and then with short circuit. The results compared with the fixed chosen value of 44 ohms resistor are shown in Figure 9.8. With the open circuit and short circuit termination the reflections at the exit end were clearly recognised from the non-uniform phase shift in search coils and the ripple on magnitude of search coils' emf along the length of the stator. This resulted in reductions of power transfer efficiency and the overall efficiency remained the same. In each case the maximum thrust is about 57 N and the maximum overall efficiency of 45%, termination has little effect on these properties. Input current and power were remarkably different. Resistance termination produced a substantially constant input current, open circuit draws a current falling as speed rises, while on short circuit termination the input current rises rapidly as synchronous speed is approached. In the view of these variations of input current and power it is considered that constant resistance termination is best.

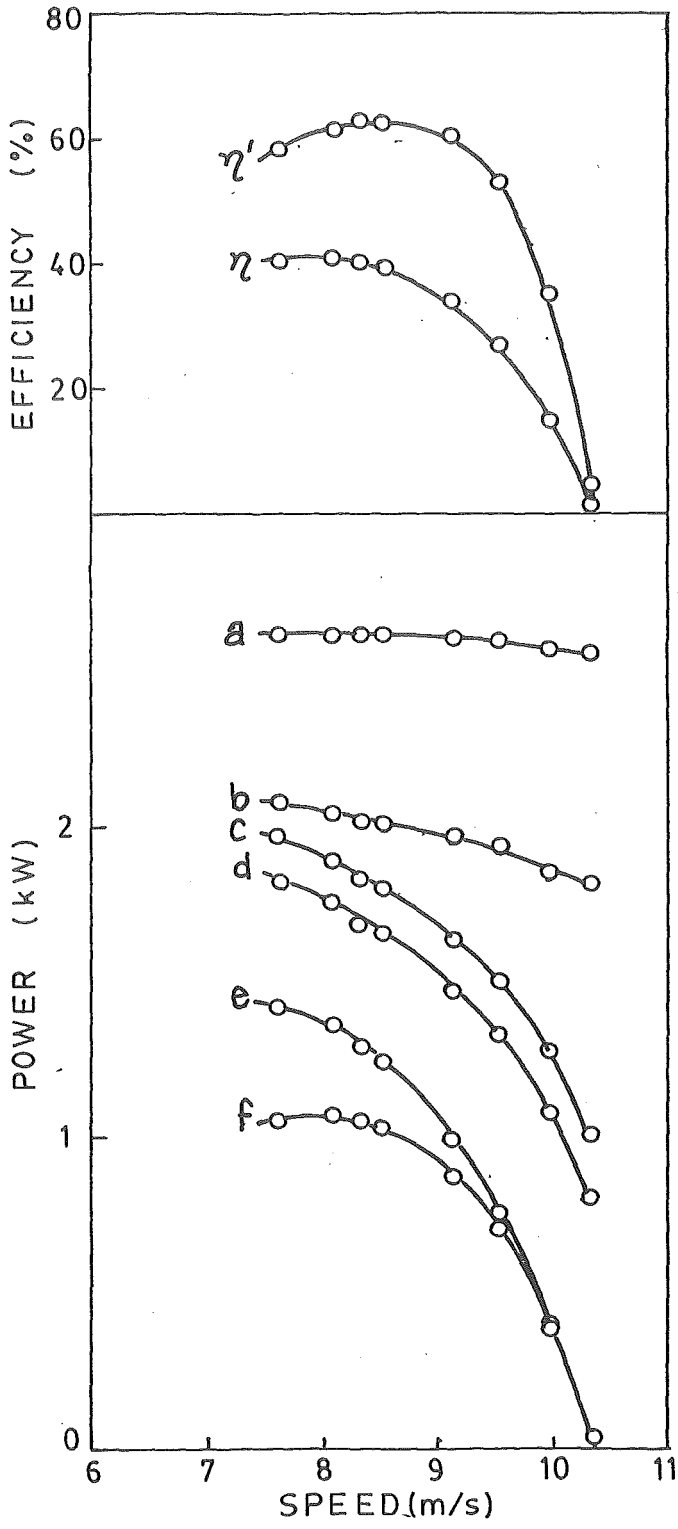

FIGURE 9.7 Analysis of losses in offset stator at 300 V.
(a) input power; (b) input less stator copper losses; (c) termination loss now substracted from b ; (d) capacitor losses substracted from c ; (e) synchronous watts; (f) output;
(η) overall efficiency; (η') rotor efficiency f/d
$C = 2000\,\mu F/m$, $g = 21\,mm$, 10 mm disc

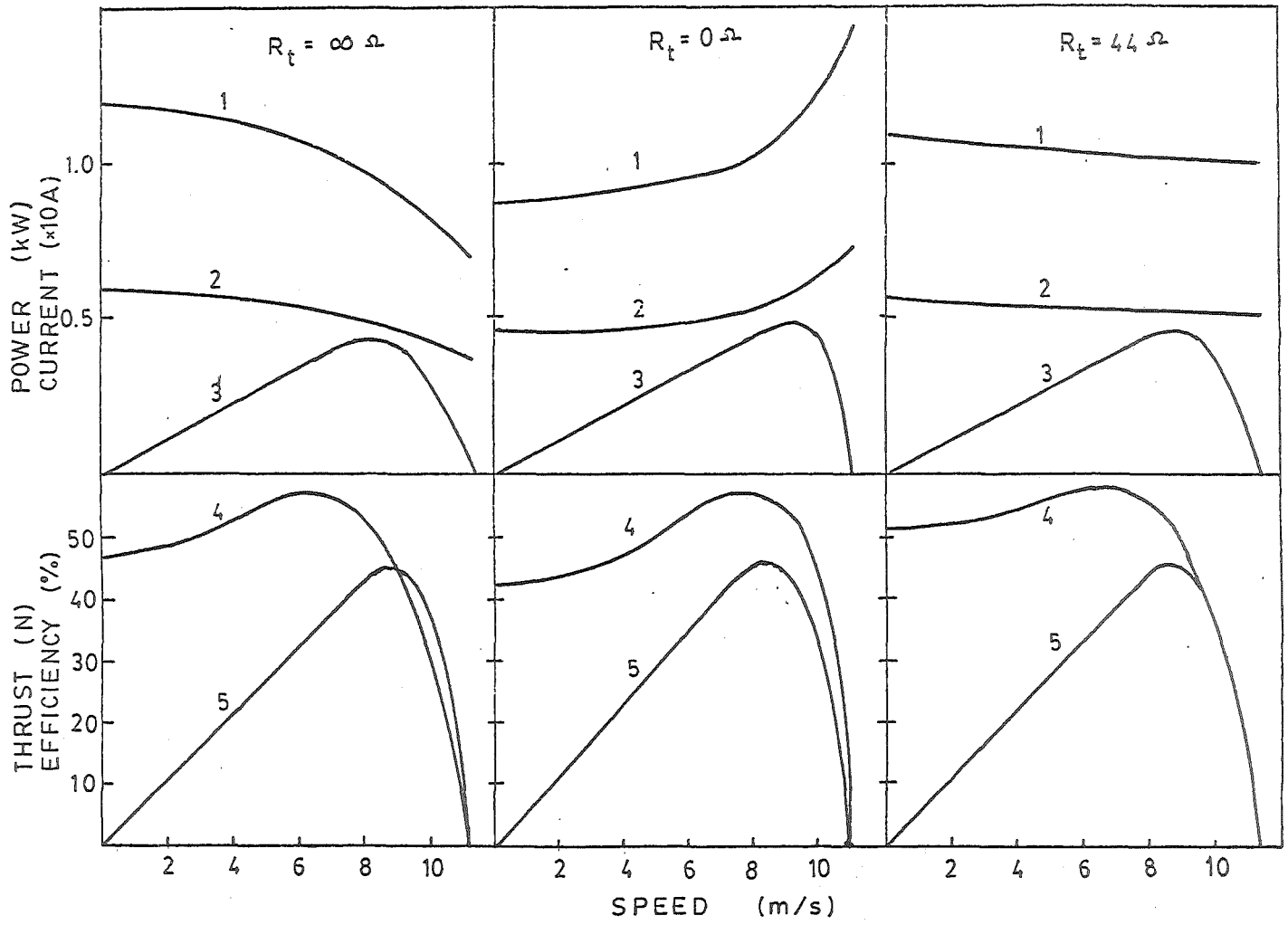

FIGURE 9.8 Influence of terminating resistor. offset stator, g = 21 mm, 10 mm disc, C = 1600 μF/m, V = 200 V. (1) input power (2) current (3) output power (4) thrust (5) efficiency.

9.5 RESULT AT HIGHER VOLTAGE LEVEL

In theory the maximum flux density occurs in the first tooth because of the assumed exponentially flux distribution. Experimentally, however, the maximum flux density is usually recorded at the second or third search coil which corresponds to the distance 7.5 cm or 12.5 cm from the entry edge. Therefore while the theoretical maximum flux density is 0.5 T at 200 V 50 Hz, the measured maximum flux density is only 0.3 T which is well below the normal operating level in electrical machines. In order to achieve the full potential of the experimental machine the value of supply voltage had to be raised; characteristics at various voltages are shown in Figure 9.9. The maximum flux density at 400V 50 Hz for 2000 uf/m shunt capacitance is about 0.6 T, which is still well under the saturation value in the magnetic circuit. Due to heating of the rotor disc, limitation of thrust measuring equipment and capacitors rating no test were carried out above 450 V or above a thrust of 150 N. Some distortion of flux wave was noted at higher voltage suggesting a large third harmonic component which, however, appears to have little effect on the performance characteristics. This was confirmed by rearranging the measured thrust for different supply voltages in terms of a normalised value of V^2C and superimposing into the same graph as shown in Figure 9.10 and Figure 9.11 for the case of shunt capacitance of 1000 μF/m and 2000 μF/m. The value of power input is proportional to V^2 and the no-load characteristic impedance is seen to be stable over the voltage range inspite of the large third

harmonic component of flux density which implies a certain degree of saturation in the magnetic circuit which would lead to the reduction in the series inductance value and hence reduction in characteristic impedance and increase in rotor speed. The summary of characteristics at different voltage for shunt capacitance of 1000 μF/m is shown in Table 9.4.

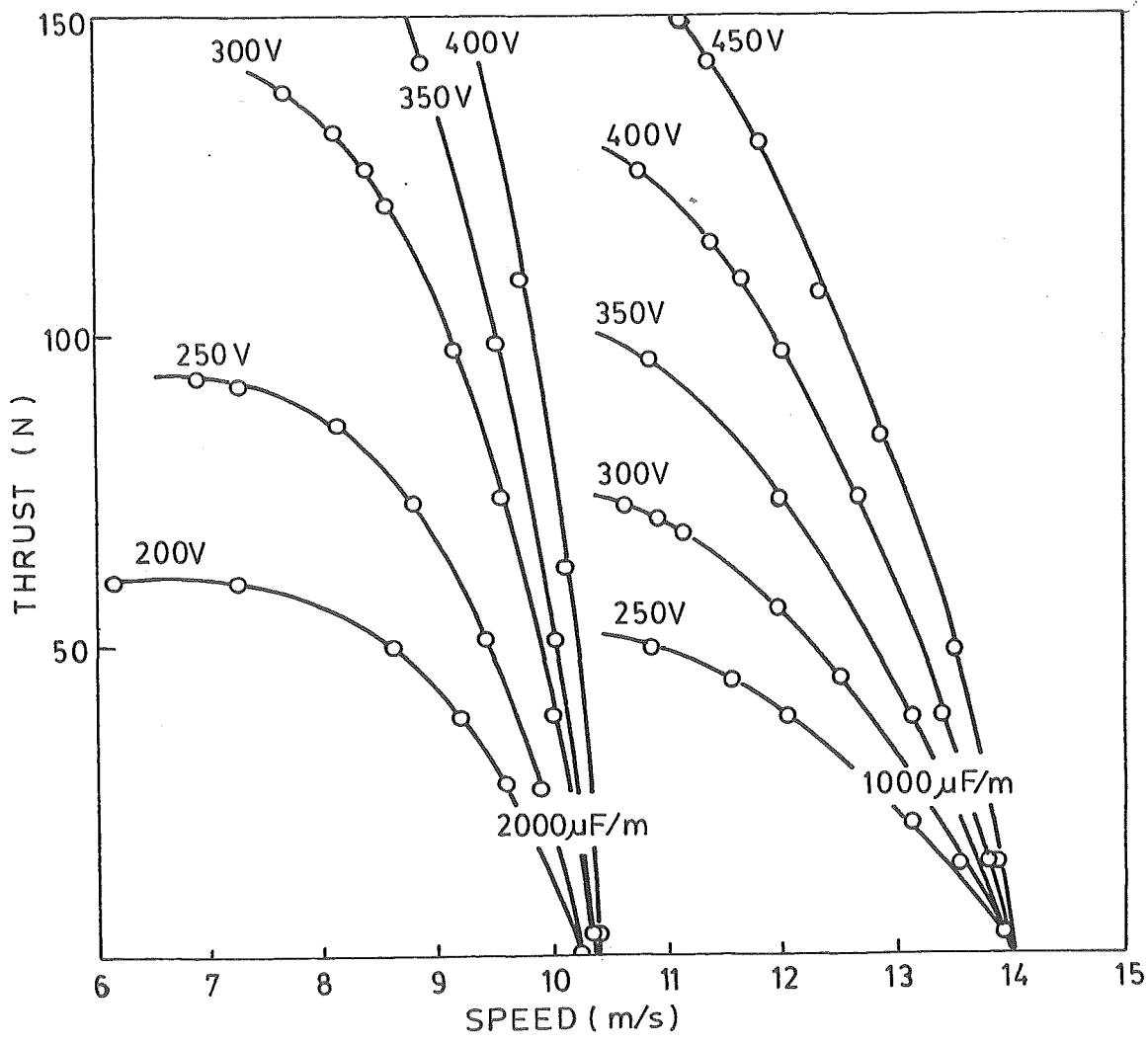

FIGURE 9.9 Performance of offset stator blocks at various voltages; g = 21 mm, 10 mm disc.

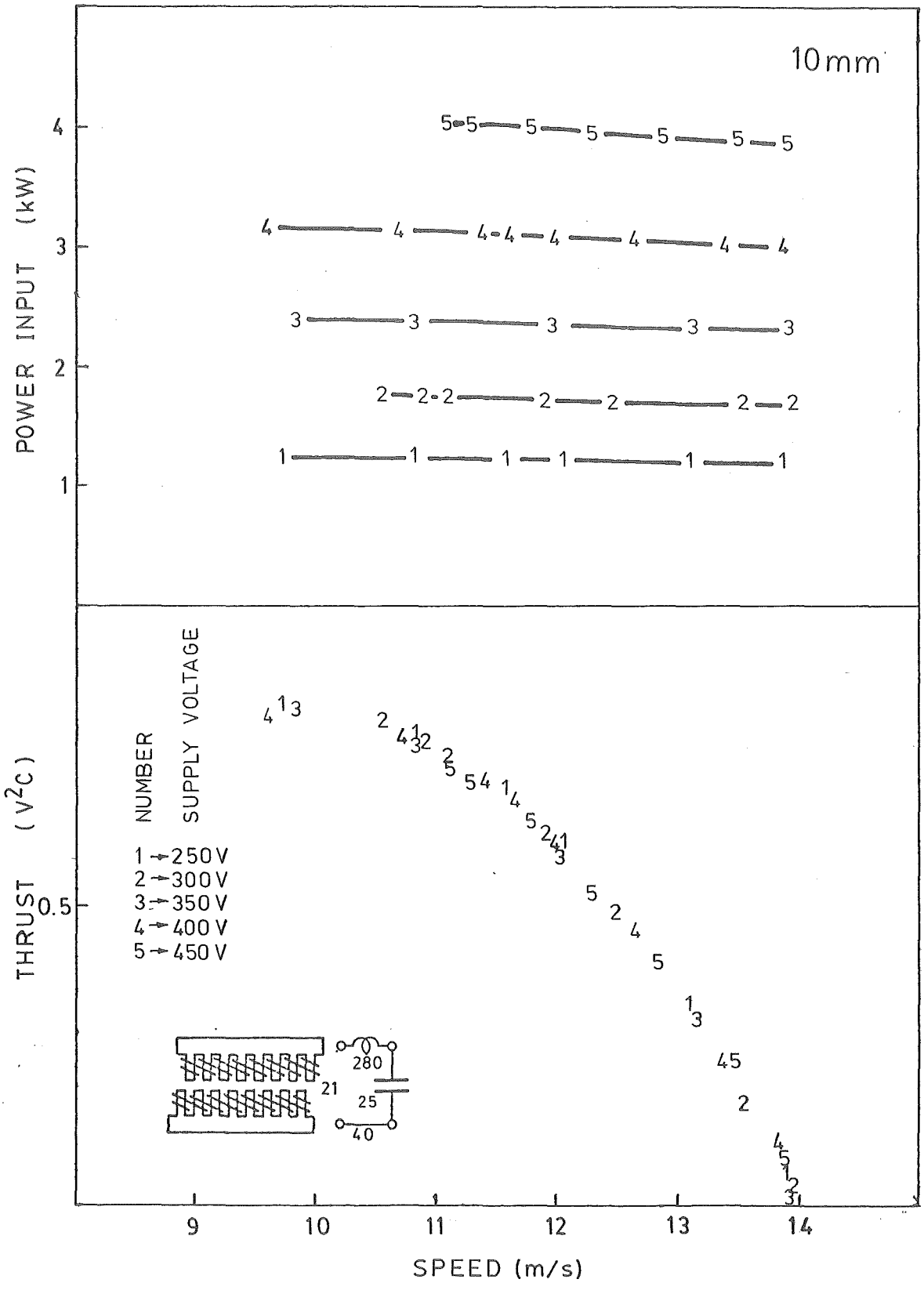

FIGURE 9.10 Power input and normalised thrust-speed characteristics at different supply voltage 1000 μF/m shunt capacitance.

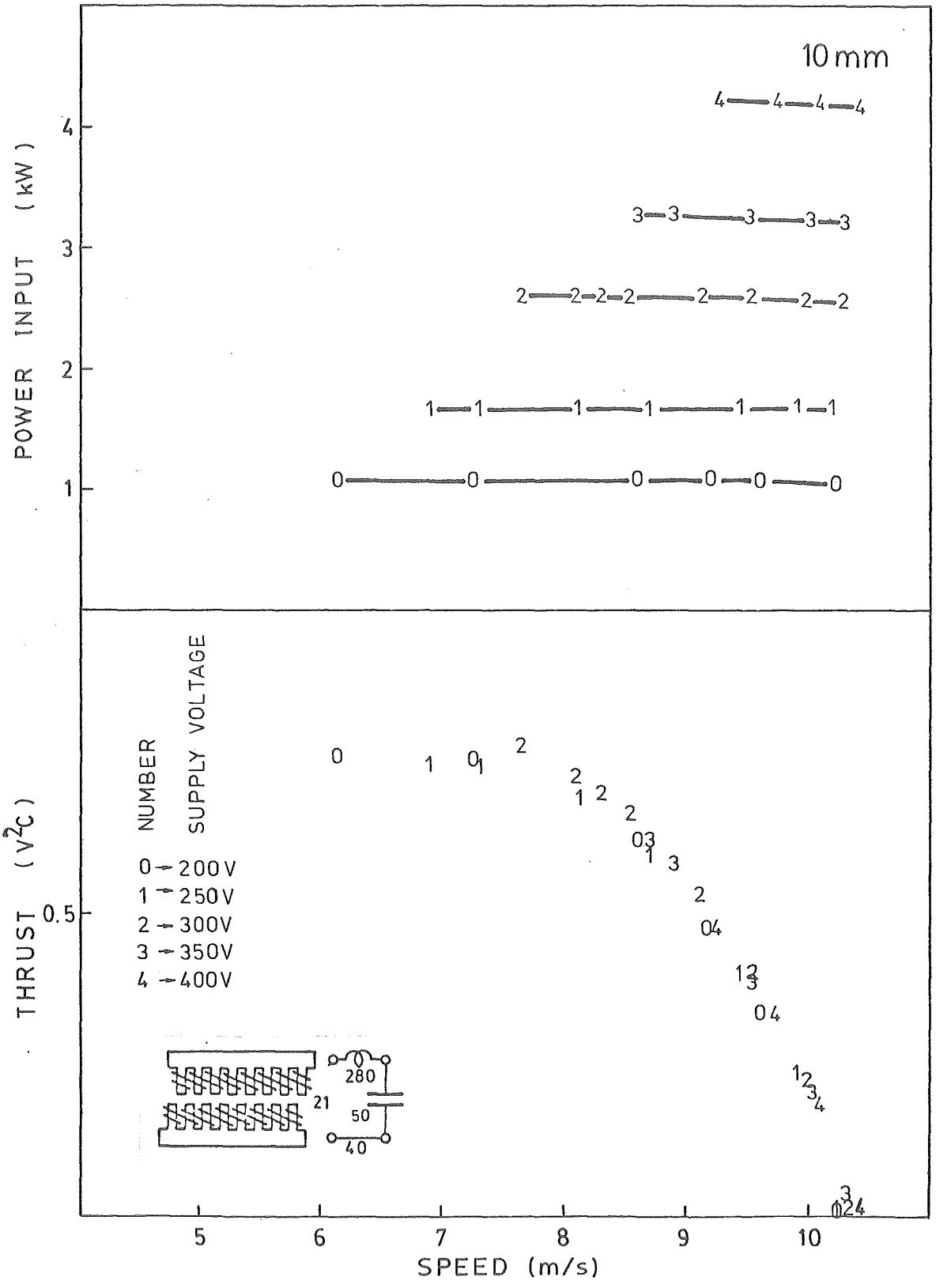

FIGURE 9.11 Power input and normalised thrust-speed characteristics at different supply voltage 2000 μF/m shunt capacitance.

Supply voltage (V)	250	300	350	400	450
*Power input (kW)	1.20	1.71	2.34	3.06	3.88
*Current (A)	4.7	5.6	6.5	7.4	8.3
No-load speed (m/s)	13.9	14.0	14.0	14.0	14.0
*Characteristic impedance (ohms)	53.8	54.0	53.8	54.0	54.1
Maximum thrust (N)	52	73	101	130	-
Maximum thrust (V^2C)	0.84	0.81	0.83	0.81	-
Maximum efficiency (%)	43.0	43.5	43.5	43.0	-
Maximum output (kW)	0.54	0.77	1.04	1.35	-

* denote no-load value

TABLE 9.4 Overlap coil STLIM characteristics at different value of supply voltage for shunt capacitance of 1000 μF/m and airgap of 21 mm.

9.6 EFFECT OF SUPPLY FREQUENCY

From Section 7.7, unlike the non-overlap coil STLIM model, the overlap coil STLIM synchronous speed depends on the value of supply frequency. As the frequency increases the no-load speed of the machine increases. Figure 9.12 shows the thrust-speed characteristic of the motor at supply frequency of 44 Hz, 48 Hz, 50 Hz, 56 Hz and 64 Hz. Generally increasing supply frequency means that the value of no-load attenuation, α_0, increases and the input power decrease

slightly. The overall efficiency and maximum thrust vary slightly. The efficiency is of the order 43 to 44% and the maximum thrust of 50 N to 55 N were recorded.

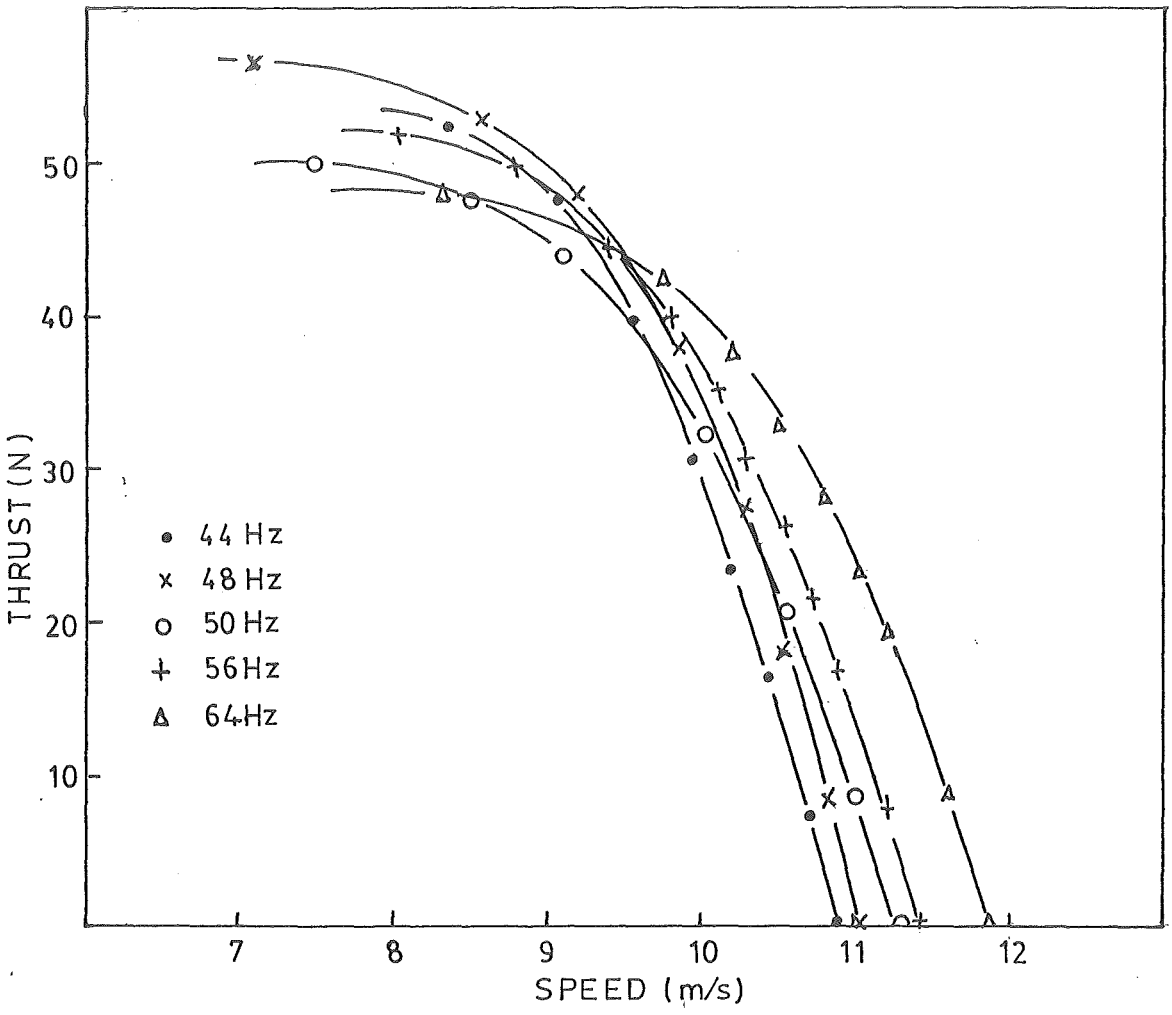

FIGURE 9.12 Thrust-speed characteristic of STLIM with different supply frequency.
10 mm disc; 1600 μF/m shunt capacitance;
18 mm airgap.

9.7 DISCUSSION OF GENERAL CHARACTERISTICS

The experimental results tend to support the view that a winding with overlapping coils is superior to one in which each coil surrounds only a single tooth as described in Part one of this thesis. The maximum efficiency obtained from the single tooth winding on the same stator block, described in Chapter 6, is 29%. Using a double tooth-span winding the efficiency has now been raised to 38%, and by offsetting the stator blocks and re-arranging the capacitors the maximum efficiency has been further raised to 45%. The reason for experimenting with offset stator blocks was to try to minimise the stator slot harmonics.

One of the objects of these experiments is to develop the STLIM to the point where it becomes competitive with the conventional linear induction machine. There are two reasons why comparison of linear motors is rather difficult. One is the very flexibility of the linear induction motor which makes it suitable for an extremely diverse range of applications: a thrust motor can hardly be compared with a high speed traction motor. The other reason is that although a lot of theoretical and experimental work has been published, and linear induction motors are avaliable commercially, it is still difficult to find in the literature the relevant experimental results. However, it is considered that the thrust of the overlap coil STLIM has been raised to a value comparable with that of a three phase linear induction motor. The efficiency is also comparable. For instance in one test the overlap coil STLIM produced a thrust of about 140 N at 2.61 kW drawing 8.7 A at unity power factor from a 300 V 50 Hz supply, Figure 9.7, and

its maximum efficiency is 41% when the output is 1.08 kW. A commercial thrust unit of similar dimensions[3] produces 135 N drawing 6.4 A line current from a 415 V 50 Hz three phase supply. Yamamura's[14] motor A, again of similar dimensions, produced a thrust of about 180 N and a maximum efficiency of about 27% when the output was 1.3 kW. The STLIM compares favourably with each of these examples. In another experimental study of 3-phase linear induction motors carried out on a larger machine 1.4 m long having 6 poles, found published[7] for 60 Hz, the maximum efficiency was just over 50% when driving 20 mm thick aluminium disc. The smaller STLIM with a smaller number of poles(3 to 4 poles) described here is almost as good.

A second objective of these investigations is to develop an analytical model of the machine. In the course of the theoretical work an equivalent circuit is suggested, Figure 7.3, which may give some insight into the behaviour of the machine. In particular it indicates that the machine behaves as a low pass filter; there will be a natural increase in attenuation as the frequency is raised. Unlike the conventional 3-phase linear induction motor, no improvement in goodness factor can be hoped for by raising the supply frequency.

As mentioned in Section 9.2 and 9.3 the calculated thrust is much larger than the measured thrust. The simplified theory in Chapter 7 contains many approximations, notably that an integral form of calculation can be used and that only the forward travelling wave exists; also stator resistance and leakage reactance are ignored. The experimental machine has

a high value of stator resistance and quite a proportion of power is lost in stator resistance(typical values from Figures 9.3 and 9.4 are 20% to 30%). However, the other main reason for the measured thrust falling short of the calculated value is probably slotting harmonics which can be reduced by offsetting the two halves of the stator block.

The experiments have shown that the improved overlap coil STLIM can have thrust and efficiency characteristics equivalent to those of a three phase linear induction motor. Now the virtue of the STLIMs, besides it being a single phase device, is its speed change property. As illustrated in Figure 9.9 the speed can be increased by reducing the shunt capacitance. The result is similar to pole changing except that the pole pitch is determined only by the capacitance so that in theory any synchronous speed can be obtained from one set of stator windings. There will be an upper limit to the designed value of synchronous speed due to magnetic saturation in the back plate when the pole pitch is very large, and the lower limit due to unit cutoff frequency as explained in Section 7.10. Increasing the airgap also increases the speed without adversely affecting the efficiency. Figures 9.13, 9.14 and 9.15 show the variation of speed with different values of airgap. This method could be used to give fine speed adjustment, capacitor change producing the course speed step. Table 9.5 summarised the variable speed characteristics of the STLIM at different values of shunt capacitances and airgaps. While the speed range in Table 9.5 is not very wide, 9.9 m/s to 16.5 m/s, there has always been an interest in close ratio speed change [15]. There is also the possibility

of widening the speed range by interchanging the roles of the coils and capacitors [11].

Shunt capacitance (μF/m)	Airgap (mm)				
	18	21	24	27	30
800	15.4	15.8	16.0	16.1	16.5
1600	11.3	11.6	11.8	11.9	12.1
2400	9.9	10.0	10.2	10.2	10.3

TABLE 9.5 No-load speed in meter per second of the STLIM.

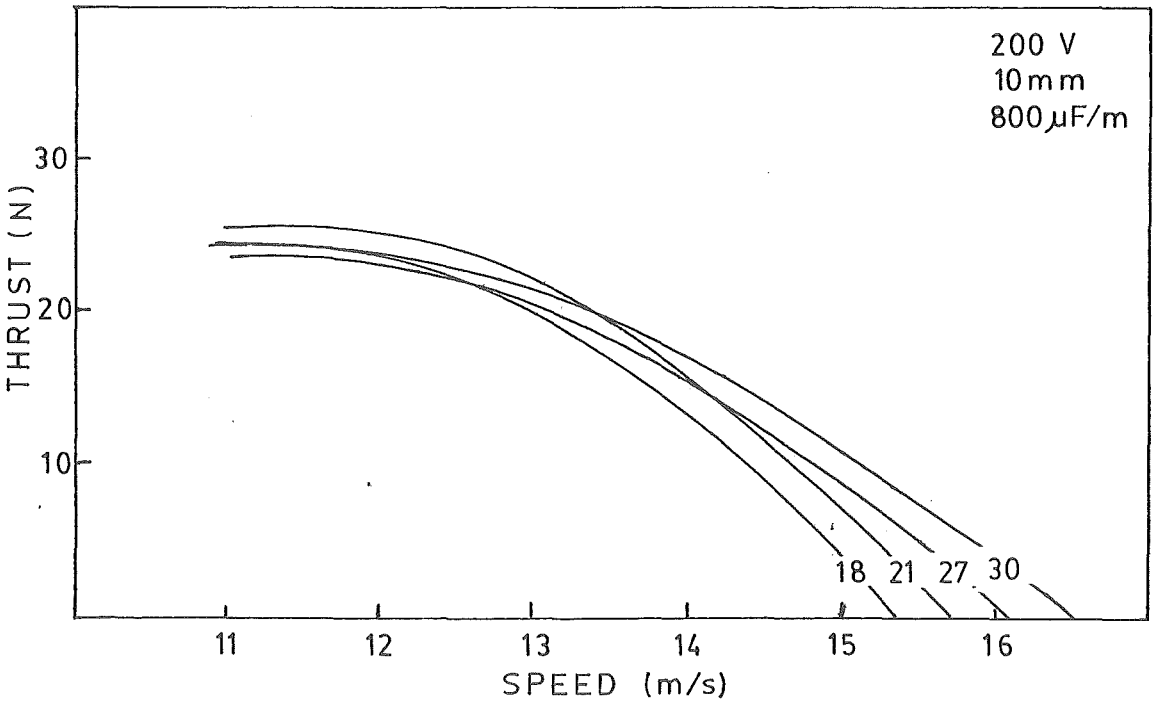

FIGURE 9.13 Variable speed characteristic of STLIM with different valus of airgap, V = 200 V, C = 800 μF/m, 10 mm disc.

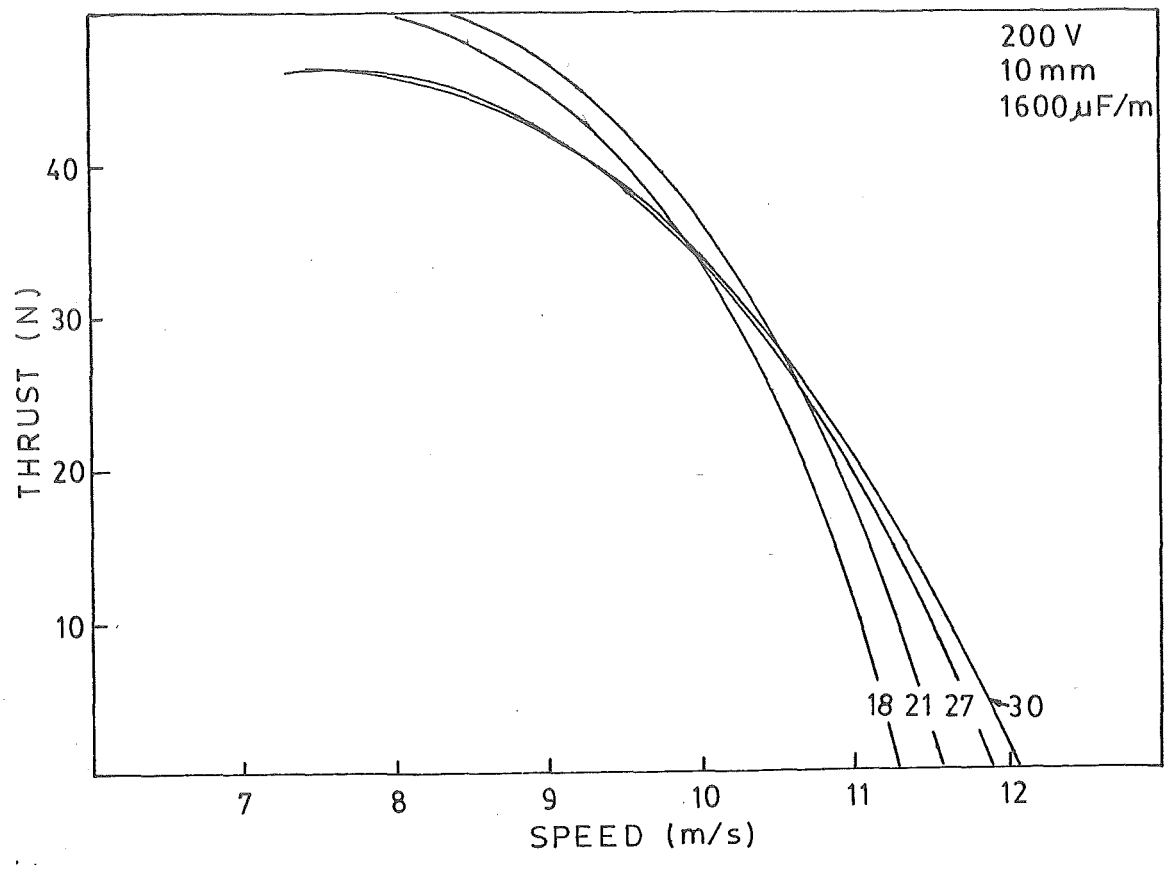

FIGURE 9.14 Variable speed characteristic of STLIM with different values of airgap. V = 200 V, C = 1600 μF/m, 10 mm disc.

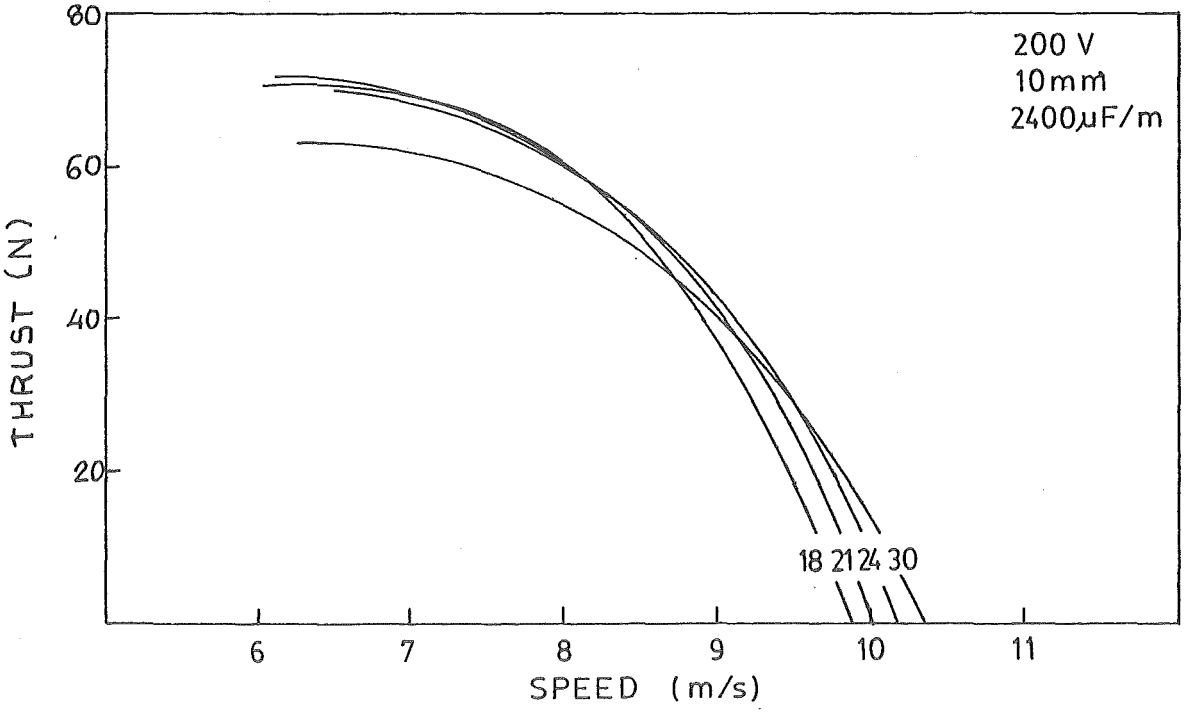

FIGURE 9.15 Variable speed characteristic of STLIM with different values of airgap. V = 200 V, C = 2400 μF/m, 10 mm disc.

CHAPTER 10

CONCLUSIONS AND FURTHER WORK

The purpose of this thesis was to investigate the theory and development of STLIMs. Specifically, the problem concerned the analysis based on a one-dimensional current sheet model and the solution obtained was in the form of an equivalent circuit comparable with that of the distributed transmission line.

The following conclusions were drawn from this research:

General conclusions for both parts: (1) STLIMs equivalent circuit could be realised as that of the distributed transmission line; (2) The cutoff frequency consideration was important to the design quality of STLIM because the machine acted as a low pass filter and increase in supply frequency did not necessary improve the performance of the machine; (3) There was only one dominant mode of travelling wave comprising a forward travelling wave and a reflected travelling wave and although the theoretical characteristic impedance changed with slip a fixed resistor termination was adequate to suppress the reflected wave; (4) Variable speed characteristic was achieved by varying shunt capacitance or coil inductance and the result followed the theoretical trend quite closely.

Conclusions in relation to non-overlap coil model: (1) General agreement between theory and experiment was achieved; (2) From a practical point of view, the first machine was far from successful due to the high value of stator resistance, low efficiency and under-rating; (3) The

effect of stator resistance played an important role, hence an experimental machine with low stator resistance and a theoretical model which included the effect of stator resistance were necessary to obtain accurately predicted performance; (4) Considering that the second motor had a small number of poles(2 to 4 poles), the performance of STLIM was still compatible with the counter part three phase LIM; (5) From theoretical and later experimental points of view the maximum power transfer efficiency of the machine was only as high as 50%.

Conclusions in relation to overlap coil model: (1) The overlap coil STLIM model was found to have a performance superior to the non-overlap coil model; (2) The overall efficiency of the experimental machine improved to 45% and the efficiency of power transfer rose to 65%; (3) Although thrust was lower than predicted it could be raised by simply offsetting the stator blocks and reconnecting the circuit; (4) It is predicted that the overlap coil STLIM could be designed to reach a good efficiency, provided that the machine is designed for a large number of poles, and the stator resistance and the slot harmonics are reduced.

The results of this work suggest some potential applications of STLIM in the following areas: (1) In low speed ground transport. The variable speed characteristic would be extremely useful. Thrust can be attained in either direction by interchanging the supply and terminating resistor. It may be possible to feed power back into the supply instead of absorbing it in a terminating resistor, thus eliminating the termination loss. With natural shrinkage in synchronous

speed when the rotor speed is low, STLIMs may have an additional advantage over conventional polyphase LIMs in reducing the acceleration loss. Electromechanical braking and regenerative power feedback can be achieved (Appendix 5). In the area of linear traction motors, STLIM has the advantage over a polyphase LIM of requiring only one feeder line with an earth return; (2) In providing an end-effect compensation to a conventional three phase LIM as described in Appendix 4; (3) With low speed self excitation characteristic as described in Appendix 5, as a generator this might be an answer to a low cost fixed blade wind turbine.

The area of STLIMs is new and fairly wide open for further investigation. Much more theoretical work is needed in the areas of the entry end-effect, termination, the effect of stator resistance, other modes of travelling waves, slot harmonics, leakage flux, and a modified ladder network consideration instead of a calculus approach.

Obviously this thesis has not considered all possible aspects of the problem. However, the original idea has been carried a long way forward in the concept of the device, the mathematical theory and the development of the machine.

Finally as the industrial development of linear drive systems continues, the Single-phase Travelling-wave Linear Induction Motor might find an area of application which will mean that this research work and this thesis will have been worthwhile.

ACKNOWLEDGEMENTS

I wish to express my sincere gratitude to my supervisor, Dr D.B. Watson, for the kind support he has given me in this work through his supervision and encouragement at critical moments.

I am indebted to Professor J. Arrillaga for his understanding and for giving me the opportunity to do the work.

I would like to thank the following persons: my mother Khunying Sa-ardjit, my wife Took, Khunying S. Chaloryoo and Dr K. Petchsuwan, Dean of Engineering at King Mongkut's Institute of Technology, for their moral support; Mr I. Danson, of the New Zealand Embassy in Bangkok, in relation to the Colombo Plan Scholarship decision; Rev R.G. McCullough, Principal of Christchurch College, for proof-reading the manuscript.

I wish to acknowledge King Mongkut's Institute of Technology for granting me study leave with pay, which made the work possible.

Last, the Colombo Plan Scholarship is also mentioned.

REFERENCES

1. HILLER,J.B. Travelling wave machine. Proc. I.E.E., Vol. 113, No. 8, 1966, pp. 1371-1372.
2. LAITHWAITE,E.R. Induction machine for special purpose. London: George Newnes, 1966.
3. LAITHWAITE,E.R. Experiments with a linear induction motor. Tecquipment, 1972.
4. LAITHWAITE,E.R. and NASAR,S.A. Linear-Motion Electrical Machine. Proc. I.E.E.E., Vol. 58, No. 4, 1970, pp. 531-542.
5. NASAR,S.A. and BOLDEA,I. Linear motion electric machines. John Wiley and Sons, 1976.
6. PUTMAN,T.H. Utilization of Traveling Waves for Energy Conversion. Thesis, Sc. D., M.I.T., U.S.A., 1958.
7. SAKABE,S. and others. Experimental Study of High-Speed Linear Induction Motors. Electr. Eng. Japan, Vol. 95, No. 1, 1975, pp. 87-92.
8. VARASUNDHAROSOTH,B. and WATSON,D.B. A single phase linear travelling wave induction machine. Electric Machines and Electromechanics: An International Quarterly, Vol. 3, No. 1, 1978, pp. 75-88.
9. VARASUNDHAROSOTH,B. and WATSON,D.B. Variable-speed single phase linear induction motor. Proc. I.E.E., Vol. 125, No. 11, 1978, pp. 1273-1274.
10. WATSON,D.B. Variable-speed single-phase induction motor. Proc. I.E.E., Vol. 119, No. 9, 1972, pp. 1360-1361.
11. WATSON,D.B. Speed and torque control of a single-phase linear induction motor. Proc. I.E.E., Vol. 122, No. 2, 1975, pp. 188-189.

12. WATSON,D.B. Some characteristics of the single-phase travelling-wave machine. Proc. I.E.E., Vol. 124, No. 9, 1977, pp. 771-774.

13. WATSON,D.B. and VARASUNDHAROSOTH,B. The travelling wave machine. Elec. Engg. Trans., I.E.Aust., Vol. EE14, No. 1, 1978, pp. 25-30.

14. YAMAMURA,S. Theory of linear induction motor. John Wiley and Sons, 1972.

15. ZAKHAROV,M.K. and others. Comparison of the pole-amplitude and phase modulation methods for forming multispeed windings. Elektrichestvo, U.S.S.R., No. 2, 1977, pp. 78-81.

APPENDIX 1

COMPUTER PROGRAMMES

1. PROGRAMME TO COMPUTE CHARACTERISTICS OF NON-OVERLAP COIL STLIMS.

```
            B6700  F O R T R A N  C O M P I L A T I O N  M A R K  2.9.
                                                        L / M
                                                        = = =
C
C
C       PROGRAMME TO COMPUTE CHARACTERISTICS OF A SINGLE PHASE
C
C       LINEAR INDUCTION MACHINE BY USING MODIFIED SECOND ORDER
C
C       THEORY TAKING ACCOUNT OF THE EFFECT OF THE STATOR RESISTANCE
C
C
C       DEFINE COMPLEX NUMBER FOR PARAMETERS
C
      COMPLEX X1,X2,X3,Y1,Y2,Y3,XSUM1,XSUM2,XFAC1,XFAC2,XFAC
      L=1
C
C       SET LOOP  1  START READING DATA
C
C       READ SUPPLY VOLTAGE (V) AND ANGULAR FREQUENCY (W)
C
   20 READ(5,30)V,W
   30 FORMAT(2(F8.2))
C
C       ARE THERE SOME MORE SET OF DATA ?
      IF(V.LE.0.0.OR.W.LE.0.0) GO TO 5000
C
C       MORE SET OF DATA -- PROCEED
C
C       WRITE RESULT HEADING
C
    5 WRITE(6,10)
   10 FORMAT(1H1,20X,' SINGLE PHASE LINEAR INDUCTION MACHINE CHARACTERIS
     ATICS',//)
      WRITE(6,15)L
   15 FORMAT('    **RUN NUMBER  ',I2,'**'//)
      L=L+1
C
C       WRITE INITIAL SUPPLY VOLTAGE AND ANGULAR FREQUENCY
C
      WRITE(6,40)V,W
   40 FORMAT('    SUPPLY VOLTAGE = ',F8.0,' VOLTS',10X,'ANGULAR FREQUENCY
     A = ',F8.2,' RAD./SEC.'/)
C
C
C       START READ MACHINE'S PARAMETERS FOR THIS SET RUN
C
C       GAP=AIR GAP LENGTH IN METERS
C       W1= STATOR WIDTH IN METERS
C       T= NUMBER OF TURNS OF STATOR COIL IN TURNS
C       R1= STATOR RESISTANCE PER COIL IN OHMS PER COIL
C       D= STATOR BLOCK LENGTH IN METERS
C       C1= SHUNT CAPACITANCE PER COIL IN FARAD PER COIL
C       DEL= SLOT PITCH IN METERS
C       RO= SHEET RESISTANCE OF ROTOR MATERIAL IN OHMS
C
C
      READ(5,50)GAP,W1,T,R1,D,C1,DEL,RO
   50 FORMAT(8F10.0)
      WRITE(6,60)GAP,W1,T,R1,D,C1,DEL,RO
   60 FORMAT(' AIR GAP =',F5.3,' M',' STATOR WIDTH =',F5.3,' M',
     A' NUMBER OF TURNS =',F5.0,' TURNS',/,' STATOR RESISTANCE =',
     AF5.3,' OHM/COIL',' STATOR LENGTH     =',F5.3,' M',' CAPACITANCE='
     AE10.3,'F/M',/,' SLOT PITCH=',F5.3,'M',' SHEET RESISTANCE =',
     AE10.3,'OHM',/)
C
C       DEFINE STARTING SLIP AND INCREMENTAL COMPUTING STEP
C
      READ(5,70)S,H
   70 FORMAT(2F10.0)
      WRITE(6,80)H
   80 FORMAT('  COMPUTE WITH INCREMENTAL STEP =',F6.4,/)
C
C
```

```
C          HEADING OF DATA VALUE
C
C          DEFINE STATOR RESISTANCE PER UNIT METER  (R)
C          DEFINE EFFECTIVE STATOR WIDTH IN METER  (W2)
C          DEFINE STATOR INDUCTANCE PER UNIT METER  (BL)
C          DEFINE ROTOR CONDUCTANCE PER UNIT METER  (G)
C          DEFINE STATOR CAPACITANCE PER UNIT METER  (C2)
C
C
          R=R1/DEL
          W2=W1+6.0*GAP
          BL=W2*T*T*1.257E-6/GAP
          G=S/(W2*T*T*RO)
          C2=C1/DEL
C
C          MAXIMUM FORCE WHEN NEGLECT STATOR RESISTANCE IN NEWTONS (FM)
C
          FM=V*V*C2/2.
C
C          START COMPUTE TO FIND INITIAL CONDITIONS
C
          WC=W*C2
          WL=W*BL
          X1=CMPLX(R,WL)
          X2=CMPLX(G,WC)
C
C          COMPUTE NO ROTOR PROPAGATION FUNCTION (Y1)
C
          Y1=CSQRT(X1*X2)
C  NO ROTOR EXPECTED ATTENUATION FUNCTION
          AL=REAL(Y1)
          AX=AL
          BE=AIMAG(Y1)
          SYN1=W/BE
C
C          WRITE NO ROTOR RESULT
C
          WRITE(6,100)AL,BE,SYN1
  100 FORMAT('   AT SLIP =0.0   ALPHA = ',F5.2,'   BETA = ',F5.2,'   U
         ASYNCHRONOUS = ',F5.2,'  M/S '//)
C
          WRITE(6,90)
   90 FORMAT('  SLIP ',' ALPHA ',' BETA ',' U(SYN)',' S(PU) ',' R  '
         A,'  X  ','CURRENT',' P.F.  ',' INPUT ',' OUTPUT','  T ',
         A'  EFF',/)
C
C          START LOOP 2 HERE
C
  110 N=1
C
C          START LOOP 3 HERE
C
  120 M=1
C
C          COMPUTE EFFECTIVE VALUE OF CAPACITANCE PER UNIT LENGTH
C
  130 C3=C2+AL*(1-S)/(W*W2*T*T*RO*BE)
          G=S/(W2*T*T*RO)
          X3=CMPLX(G,W*C3)
          Y2=CSQRT(X1*X3)
          AL=REAL(Y2)
          BE=AIMAG(Y2)
          S=S+H
          M=M+1
          IF(M.LE.6) GO TO 130
C
          S1=S-H
          IF(S1.GT.0.025)GO TO 360
C
C  VALUE OF SYNCHRONOUS SPEED AT SLIP S  IN METER PER SECOND
  140 SYN=W/BE
C
C  VALUE OF ROTOR SPEED AT SLIP S  IN METER PER SECOND
          SPE=(1.0-S1)*SYN
          SPU=(SYN1-SPE)/SYN1
C
C  FIND TERMINATING IMPEDANCE  IN OHM
          Y3=CSQRT(X1/X3)
C
```

```
C  TOTAL TERMINATING IMPEDANCE IN OHM
      TI=CABS(Y3)
C
C  TOTAL TERMINATING RESISTANCE  IN OHM
      TR=REAL(Y3)
C
C  FIND TERMINATING REACTANCE  IN OHM
      TX=AIMAG(Y3)
C
C  FIND CURRENT IN AMPERE
      EI=V/TI
C
C  FIND POWER FACTOR
      PF=TR/TI
C
C  FIND INPUT POWER  IN WATT
      PI=EI*EI*TR
C
      AY=AL-AX
  320 F=FM*(1.-EXP(-2.*AY*D))*(1.-2.*W*R*C2*AL*BE/(AL*AL+BE*BE)**2)
C
C        FIND OUT PUT POWER      (W)
C
      PO=SPE*E
C
C        FIND EFFICIENCY (P.U.)
C
      EFF=PO/PI
      WRITE(6,350)S1,AL,BE,SYN,SPU,TR,TX,EI,PF,PI,PO,F,EFF
  350 FORMAT(8(F7.2),F5.2,3(F8.2),F7.3)
      GO TO 400
C
  360 N=N+1
      IF(N.LT.5)GO TO 320
C
      GO TO 140
C
  400 IF(S1.LE.0.95) GO TO 110
      GO TO 20
 5000 WRITE(6,5001)
 5001 FORMAT(!    *****END OF DATA**** ')
      STOP
      END
```

2. PROGRAMME TO COMPUTE PREFORMANCE CURVES OF OVERLAP COIL STLIMS.

```
      B6700/B7700  F O R T R A N  C O M P I L A T I O N  M A R K  2.8
C
   40 READ(5,50)G,SA,D,T,W1,R2,W
      IF(G.LE.0.001) GO TO 500
   50 FORMAT(7F10.0)
      WRITE(6,70)
   70 FORMAT(1H1,20X,'CALCULATWD PERFORMANCE CHARACTERISTICS',///)
      WRITE(6,60)W,R2,W1,D,G,T,SA
   60 FORMAT('ANGULAR FREQUENCY  =',F8.2,' RAD./SEC.',/,'EFFECTIVE ROTOR
     A RESISTANCE  =',E10.3,' OHM',/,'STATOR WIDTH  =',F5.3,' METER ',/
     A SLOT PITCH  =',F5.3,' METER ',/  AIR GAP  =',F5.3,' METER',/,'NUM
     ABER OF TURN PER COIL  =',F5.0,' TURNS ',/  WIDTH OF HALF COIL SPAN
     A  =',F5.3,' METER'//)
      A=0.000001
      B=20.0
      WW=W1+2.*G
      U0=4.*3.14159*1.E-07
  100 UU=W/B
      E=D*D/(2.*T*T*WW*W*W)
      C2=(D**3*6*1.E06*B**4)/(2.*U0*SIN(B*SA)*SIN(B*SA))
      WRITE(6,110)A,B,UU,C2
  110 FORMAT(2(F6.1),F8.2,F8.1)
      B=B+1.0
      IF(C2.GT.160.0) GO TO 200
      IF(B.GE.40.0) GO TO 200
      GO TO 100
  200 A=A+1.0
      IF(A.GT.15.0) GO TO 40
      B=20.0
  210 E=D*D/(2.*T*T*WW*W*W)
      AA=COS(2.*SA*B)*COSH(2.*SA*A)-1.0
      BB=SIN(2.*SA*B)*SINH(2.*SA*A)
      F1=(6.*A*A*B*B-A**4-B**4-2.*A*B*W*U0/(R2*G))/AA
      F2=(3.*A*B*B-A**3)/AA
      F3=(4.*A*B*(B*B-A*A)+((A*A-B*B)*W*U0/(R2*G)))/BB
      F4=(B**3-3.*A*A*B)/BB
      U=G*R2*(F3-F1)/((F2-F4)*U0)
      C=G*E*F1/U0+E*F2*U/R2
      C1=C*D*1.E06
      WRITE(6,300)A,B,U,C1
  300 FORMAT(2(F6.1),F8.2,F8.1)
      B=B+1.0
      IF(B.GT.40.0) GO TO 200
      IF(C1.LE.160.0) GO TO 210
      GO TO 200
  500 STOP
      END
```

3. PROGRAMME TO COMPUTE CHARACTERISTICS OF OVERLAP COIL STLIMS.

```
                B6700  F O R T R A N  C O M P I L A T I O N  M A R K  2.
                                                                  L / M
                                                                  = = =
C           PROGRAM TO COMPUTE CHARACTERISTICS OF STLIM
C           OVERLAP COIL MODEL USING REALIZATION OF THE
C           EQUIVALENT CIRCUIT OF DISTRIBUTED PARAMETERS
C
C           DEFINE COMPLEX NUMBER FOR PARAMETERS
          COMPLEX X,Y,Z
C           SET LOOP 1 START READING DATA
C           V=  SUPPLY VOLTAGE                                  VOLTS
C           W=  ANGULAR FREQUENCY                               RADIAN/SECOND
   20   READ(5,22)V,W

   22   FORMAT(2F10.0)
C           CHECK END OF DATA SET     YES-STOP    NO-PROCEED
          IF(V.LE.0.0.OR.W.LE.0.0) GO TO 5000
C           WRITE RESULT HEADING
   10   WRITE(6,11)

   11   FORMAT(1H1,'   ',/////)
   15   WRITE(6,16)
   16   FORMAT(///,10X,' THEORETICAL CHARACTERISTICS OF SINGLE-PHASE TRAVE
         ALLING-WAVE LINEAR INDUCTION MOTOR',//,28X,' DISTRIBUTED PARAMETERS
         A OVERLAP-COIL MODEL',//)
   30   WRITE(6,33)V,W
   33   FORMAT('    SUPPLY VOLTAGE = ',F8.0,'  VOLTS',10X,' ANGULAR FREQUEN
         ACY = ',F8.2,'  RAD./SEC.'/)
C           MACHINE PARAMETERS
C           G   = AIR GAP LENGTH                                METERS
C           W1  = STATOR WIDTH                                  METERS
C           D   = STATOR LENGTH                                 METERS
C           DEL= SLOT PITCH                                     METERS
C           A   = HALF COIL SPAN                                METERS
C           T   = NUMBER OF TURNS ON STATOR COIL                TURNS/COIL
C           C1  = SHUNT CAPACITANCE PER UNIT LENGTH             FARAD/METER
C           R2  = ROTOR SHEET RESISTANCE                        OHMS
   40   READ(5,44)G,W1,D,DEL,A,T,C1,R2
   44   FORMAT(8F10.0)
   50   WRITE(6,55)G,W1,D,DEL,A,T,C1,R2
   55   FORMAT('    AIR GAP = ',F5.3,'  M,  ',' STATOR WIDTH = ',F5.3,'  M
         A,  ',' STATOR LENGTH = ',F5.3,'  M,  ',//,'    SLOT PITCH = ',F5.3,
         A'  M,  ',' HALF COIL SPAN = ',F5.3,'  M,  ',' COIL OF ',F5.0,'  TU
         ARNS',//,'    SHUNT CAPACITANCE =',E10.2,'  F/M,  ',' SHEET RESISTAN
         ACE =',E10.2,'  OHMS,',////)
C           INPUT DATA
C           AL = ALPHA
C           BE = BETA
C           SPE= SPEED
   70   READ(5,77)AL,BE,SPE
   77   FORMAT(3F10.0)
          IF(SPE.LE.0.0)GO TO 20
C           FIND SYNCHRONOUS SPEED (USYN)
        USYN=W/BE
C           FIND SLIP
        S=(USYN-SPE)/USYN
C           FIND MAXIMUM FLUX DENSITY IN THE AIR GAP  B
        TA=2.0*A*AL
        TB=2.0*A*BE
        AA=COSH(TA)-COS(TB)
        BB=COSH(TA)*COS(TB)-1.0
        CC=SINH(TA)*SIN(TB)
        DD=AL*AL+BE*BE
        EE=AL*AL-BE*BE
        WW=W1+2.*G
C
        B=V*DEL*DD/(T*WW*W*SQRT(AA))
C           FIND THRUST IN NEWTONS
        F=V*V*C1*(1.-EXP(-2*AL*D))*((AL*AL-3.*BE*BE)*BB+(3.*BE*AL-BE**3/AL
        A)*CC)/(2.*DD*AA)
C           FIND OUTPUT POWER
        PO=F*SPE
C           FIND VALUE OF STATOR INDUCTANCE PER METER
        AX=EE*BB+2.*AL*BE*CC
        BX=(DEL**2*DD**2)/(WW*T*T)
        BL=1.257E-6*AX/(G*BX)
C           FIND VALUE OF SERIES REACTANCE
```

```
      WL=W*BL
C          FIND VALUE OF SHUNT CAPACITANCE
      C=C1+AL*SPE*BX/(R2*W*W*AX)
      WC=W*C
C          FIND VALUE OF SHUNT CONDUCTANCE
      E=(S*BX/R2+(C1*W*(-EE*CC+2.*AL*BE*BB)))/AX
C          FIND CHARACTERISTICS IMPEDANCE
C          SERIES IMPEDANCE
      X=CMPLX(0.0,WL)
C          SHUNT ADMITTANCE
      Y=CMPLX(E,WC)
      Z=CSQRT(X/Y)
C     TOTAL CHARACTERISTICS IMPEDANCE
      TI=CABS(Z)
C          FIND CURRENT
      EI=V/TI
C          TERMINATED RESISTANCE
      TR=REAL(Z)
C          TERMANATED REACTANCE
      TX=AIMAG(Z)
C          POWER FACTOR
      PF=TR/TI
C          POWER INPUT
      PI=EI*EI*TR
C          EFFICIENCY
      EFF=100.*PO/PI
   80 WRITE(6,88)AL,BE,SPE,S,USYN,TR,TX,F,PI,PO,EI,EFF,PF,B
   88 FORMAT(2F7.1,F7.2,F7.3,3E7.2,F7.1,2F7.0,F7.2,F7.0,2F7.3,/)
      GO TO 70
 5000 STOP
      END
```

APPENDIX 2

THEORETICAL AND EXPERIMENTAL RESULTS OF NON-OVERLAP COIL STLIMS

RESULTS OF NON-OVERLAP COIL STLIMS

In order to recognise individual case of the machine characteristics, the "KEY DIAGRAM" is provided. The similar format also applied to the overlap coil cases shown in Appendix 3.

Figures A1 to A54 show theoretical characteristics of the machine with different shunt capacitance of 1200 μF/m, 1600 μF/m and 2400 μF/m and with different airgap of 15 mm, 18mm, 21 mm, 24 mm, 27 mm and 30 mm together with three sets of rotors 3 mm, 5 mm and 10 mm.

Figures A55 to A97 show experimental characteristics at conditions described above.

KEY DIAGRAM

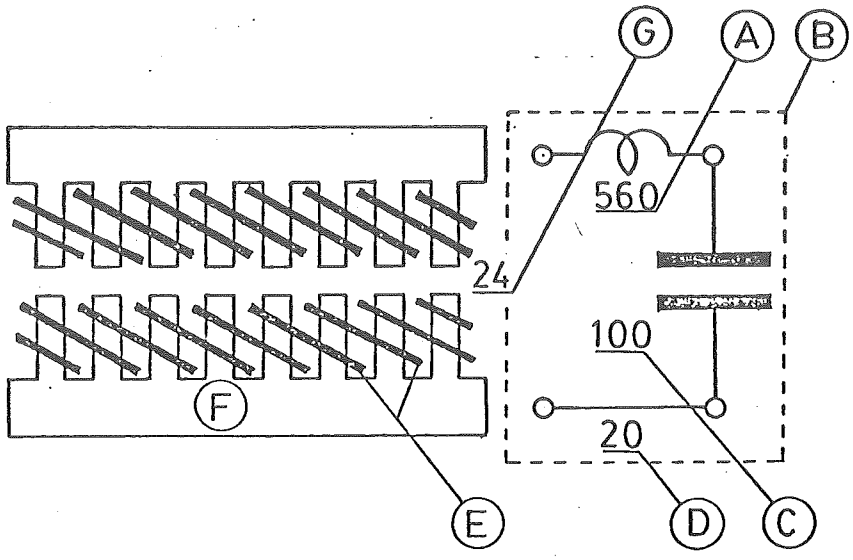

A -number of turns per coil (T)
or theoretical number of turns per meter (T/d)

B -unit section

C -value of capacitance per section (μF)
or theoretical capacitance per meter (μF/m)

D -number of unit section per meter
unity represent theoretical case

E -stator winding arrangement

F -stator magnetic circuit arrangement

G -length of airgap (mm)

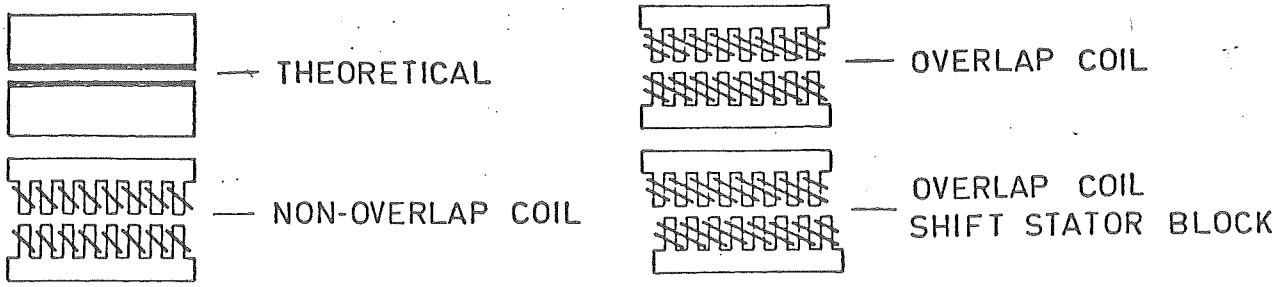

—EXAMPLE—

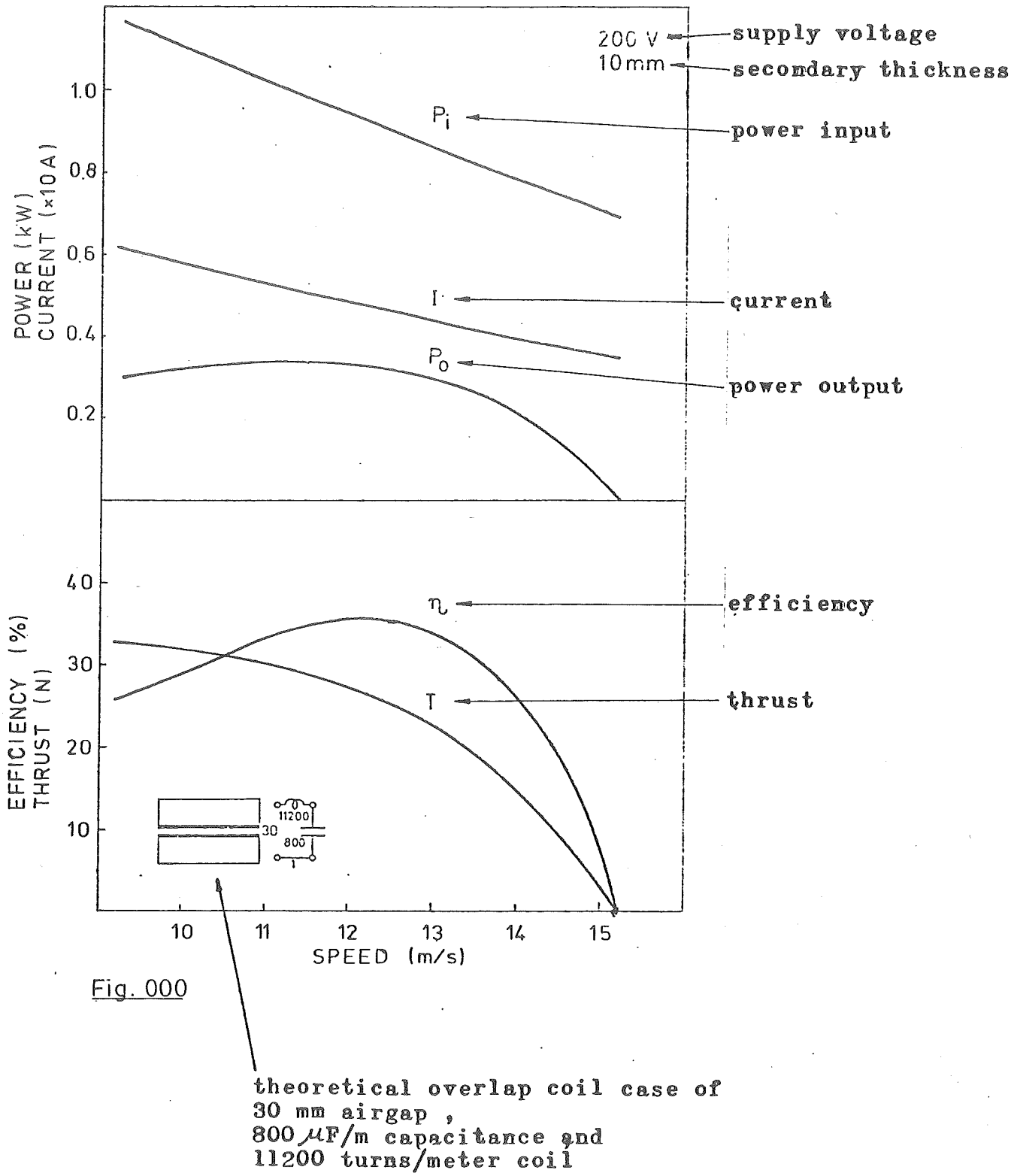

Fig. 000

theoretical overlap coil case of
30 mm airgap ,
800 μF/m capacitance and
11200 turns/meter coil

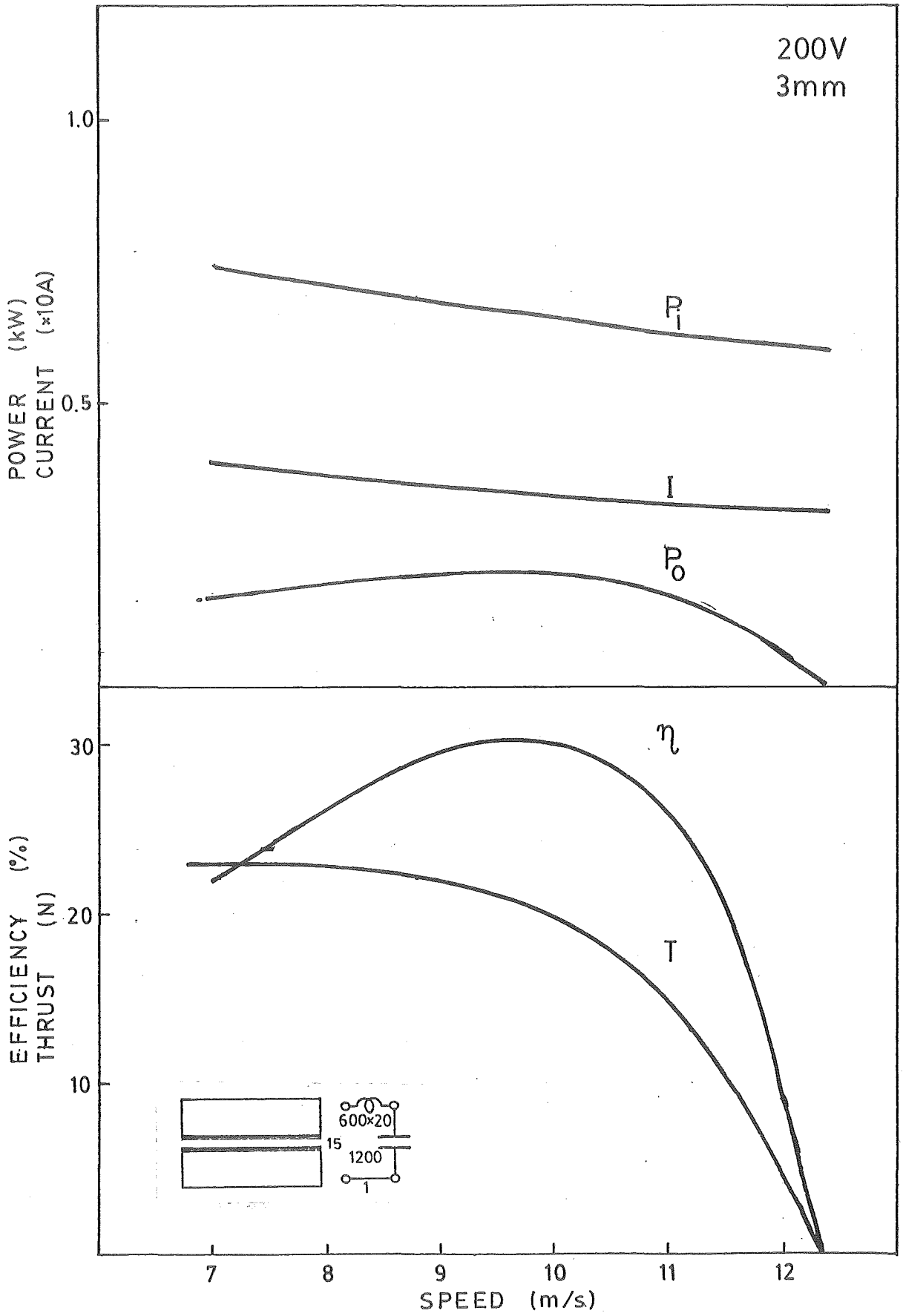
200V
3mm
1.0
0.5
POWER (kW)
CURRENT (×10A)
P_i
I
P_o
30
20
10
EFFICIENCY (%)
THRUST (N)
η
T
600×20
15
1200
1
7
8
9
10
11
12
SPEED (m/s)

Fig. A 1

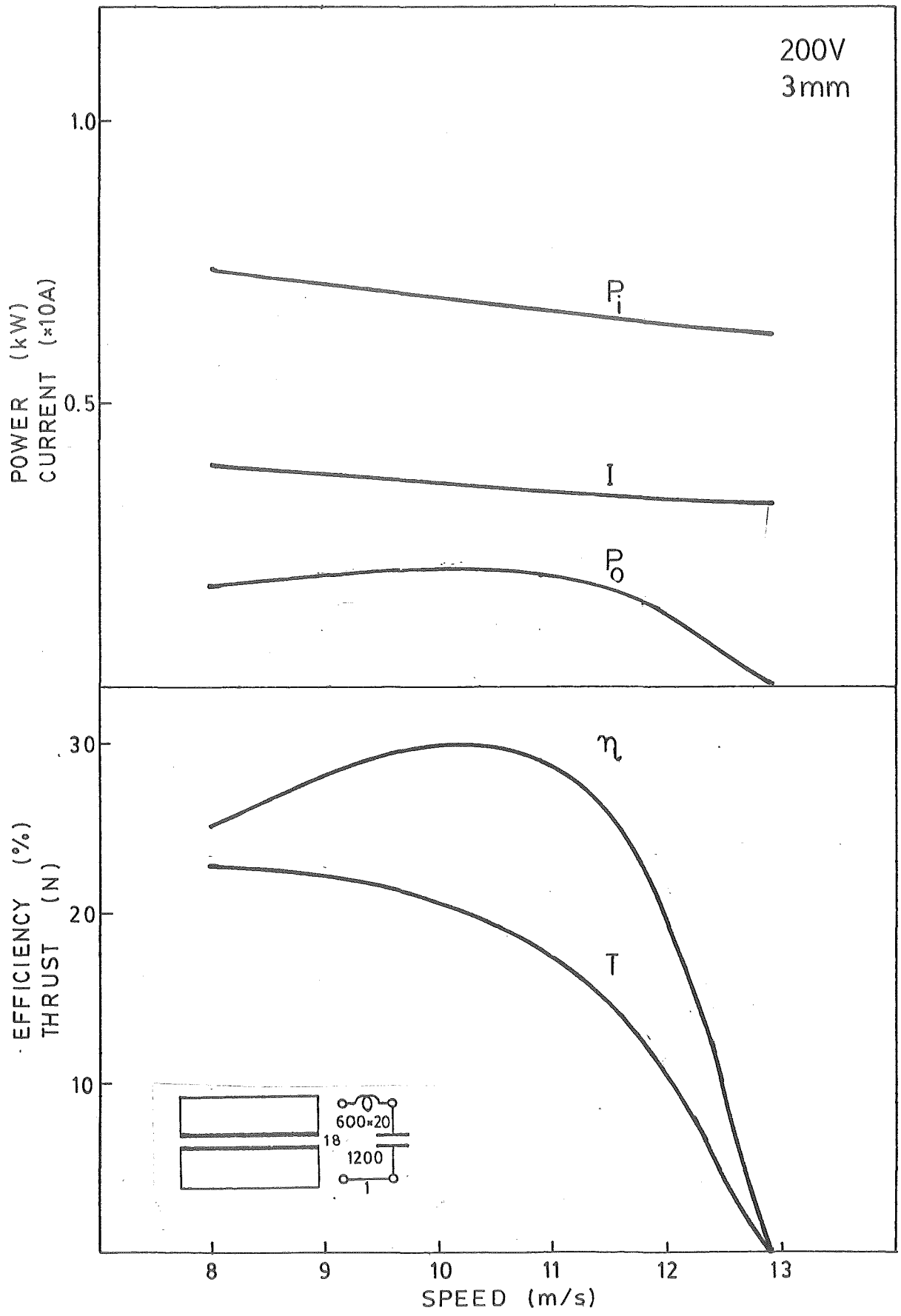
200V
3mm
1.0
0.5
POWER (kW)
CURRENT (×10A)
P_i
I
P_o
30
20
10
EFFICIENCY (%)
THRUST (N)
η
T
600×20
18
1200
1
8
9
10
11
12
13
SPEED (m/s)

Fig. A2

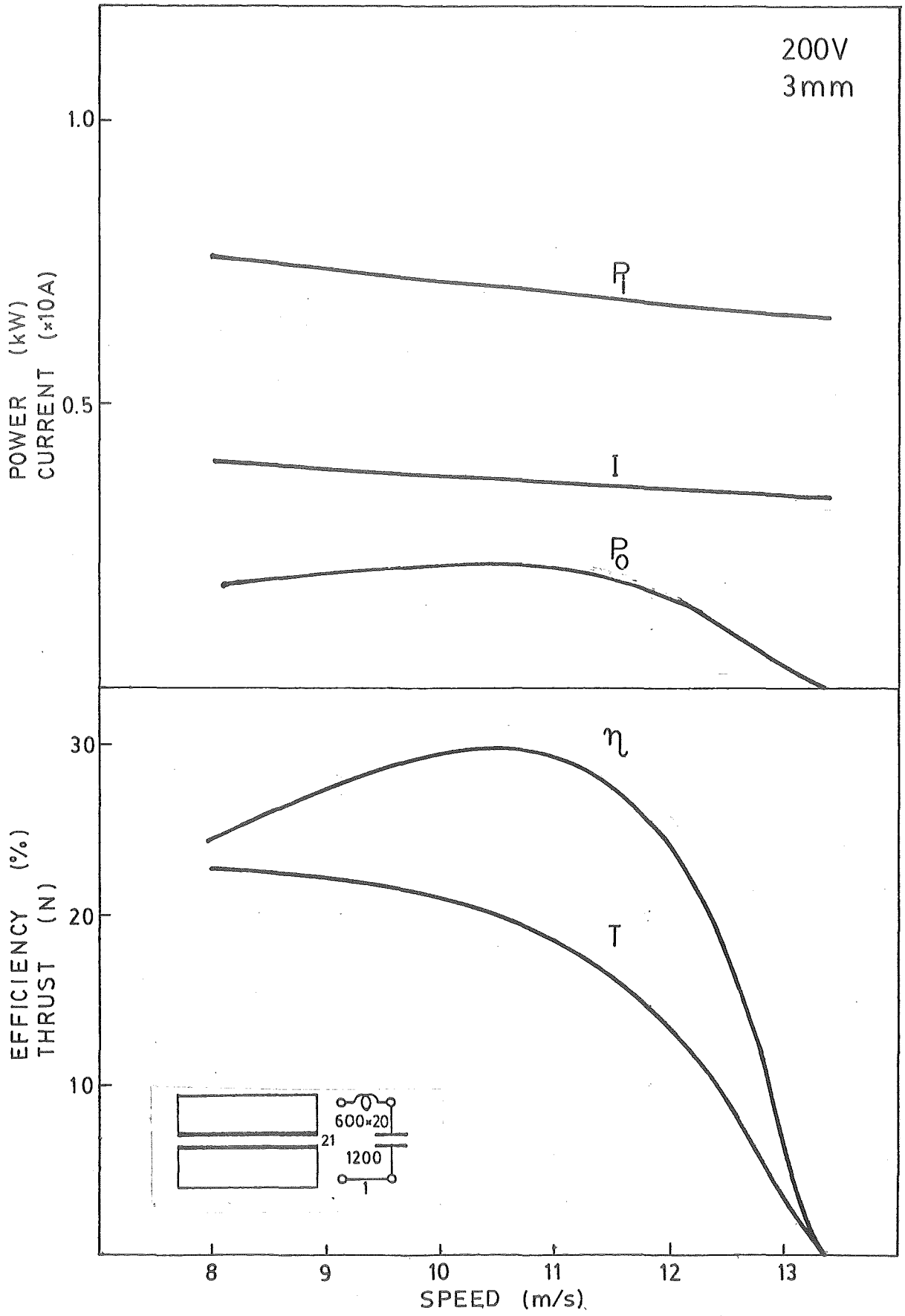
200V
3mm
POWER (kW)
CURRENT (×10A)
1.0
0.5
P_I
I
P_O
EFFICIENCY (%)
THRUST (N)
30
20
10
η
T
600×20
21
1200
1
8
9
10
11
12
13
SPEED (m/s)

Fig. A3

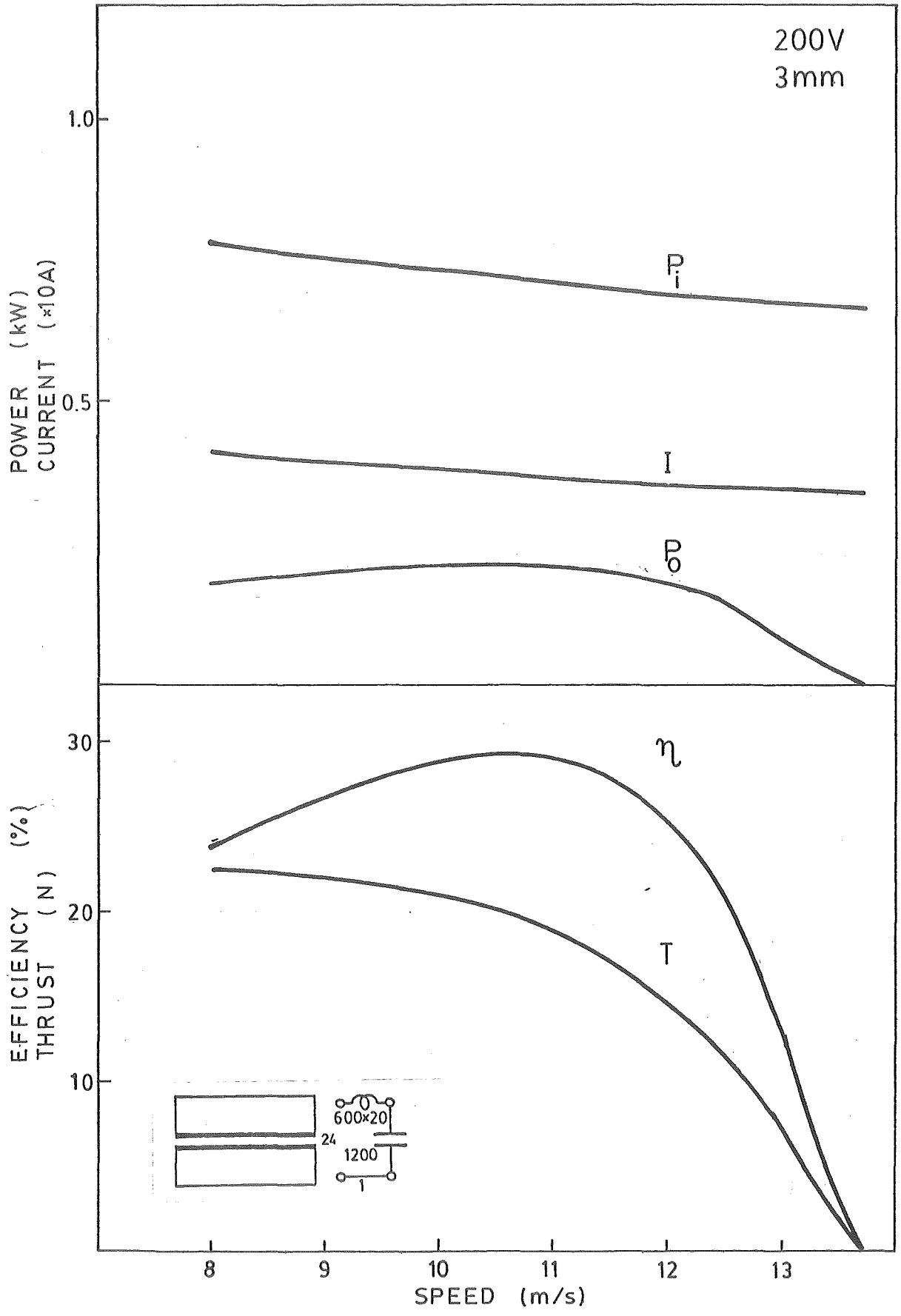
200V
3mm
1.0
0.5
POWER (kW)
CURRENT (×10A)
P_i
I
P_o
30
20
10
EFFICIENCY (%)
THRUST (N)
η
T
600×20
24
1200
1
8
9
10
11
12
13
SPEED (m/s)

Fig. A4

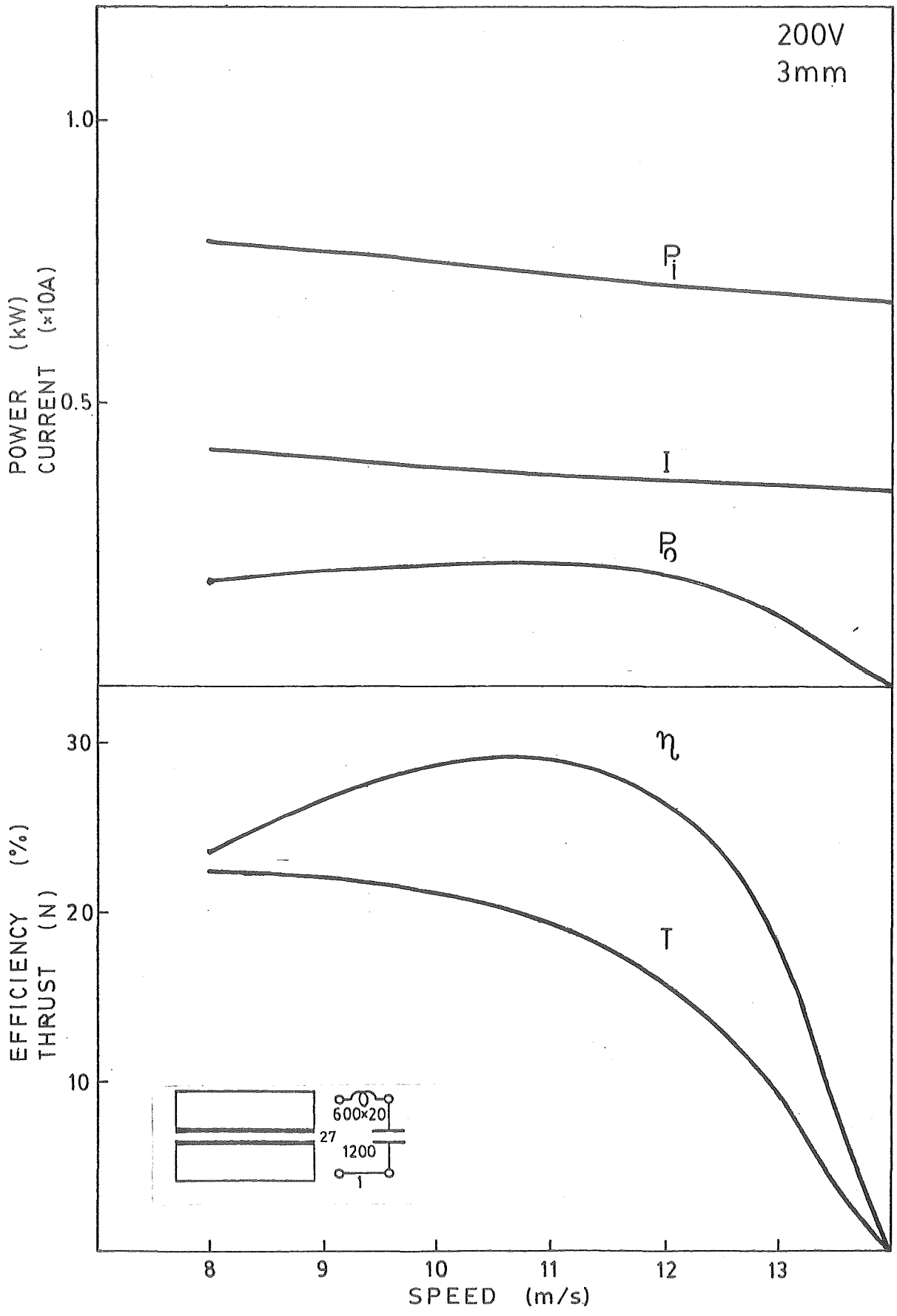
200V
3mm
1.0
0.5
POWER (kW)
CURRENT (×10A)
P_i
I
P_o
30
20
10
EFFICIENCY (%)
THRUST (N)
η
T
600×20
27
1200
1
8
9
10
11
12
13
SPEED (m/s)

Fig. A5

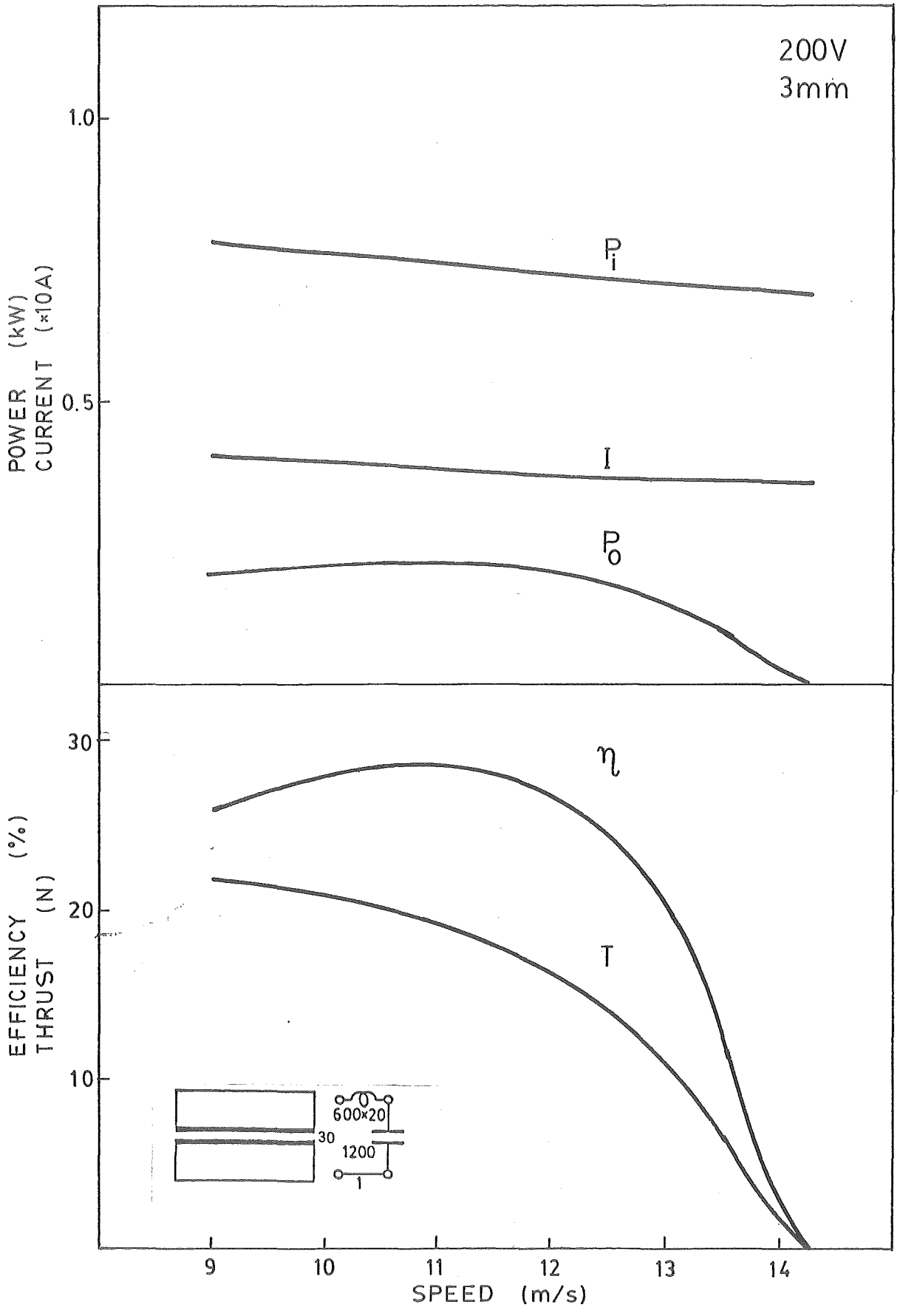
200V
3mm
1.0
0.5
POWER (kW)
CURRENT (×10A)
P_i
I
P_o
30
20
10
EFFICIENCY (%)
THRUST (N)
η
T
600×20
30
1200
9
10
11
12
13
14
SPEED (m/s)

Fig. A 6

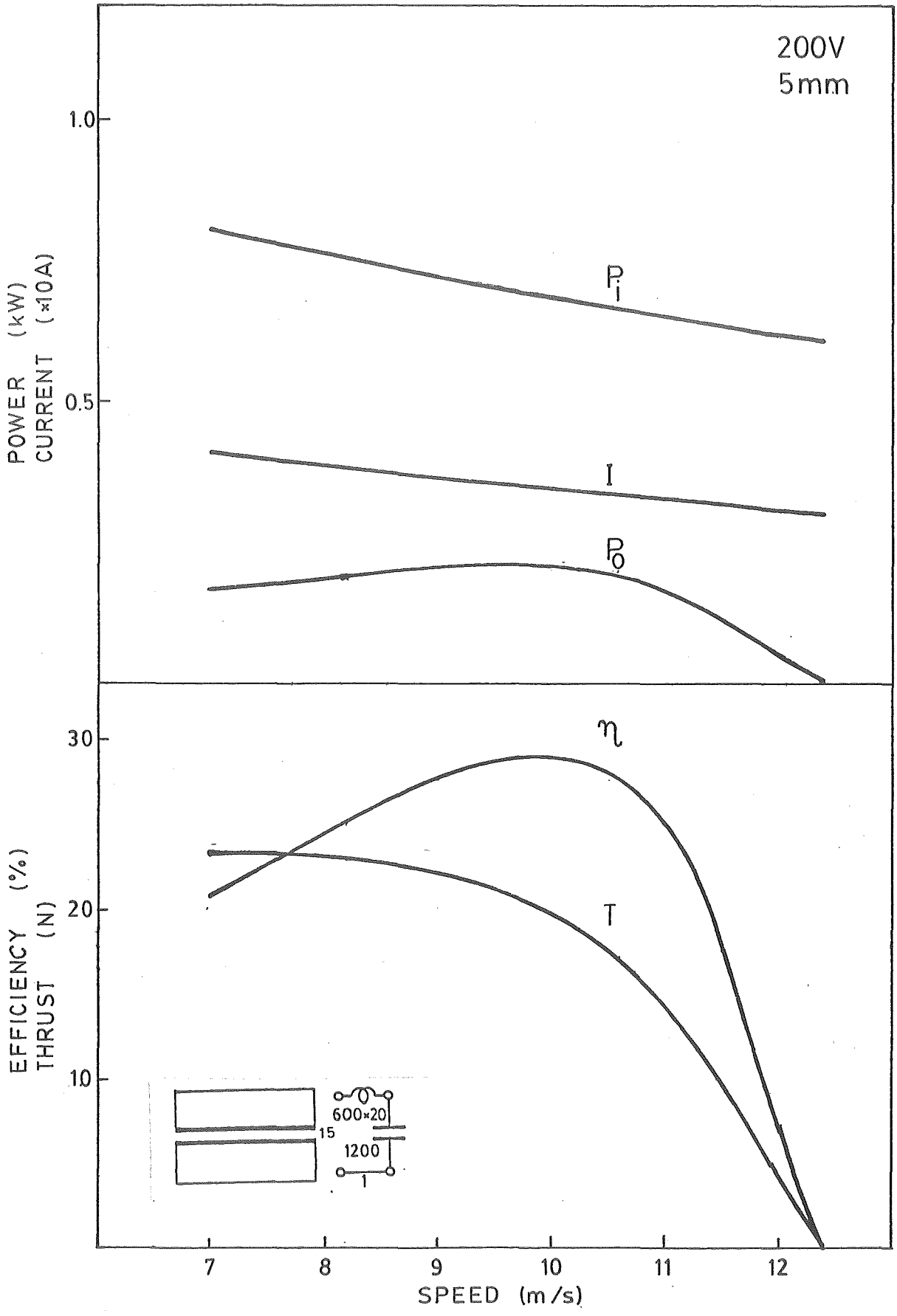
200V
5mm
1.0
0.5
POWER (kW)
CURRENT (×10A)
P_i
I
P_o
30
20
10
EFFICIENCY (%)
THRUST (N)
η
T
600×20
15
1200
1
7
8
9
10
11
12
SPEED (m/s)

Fig. A 7

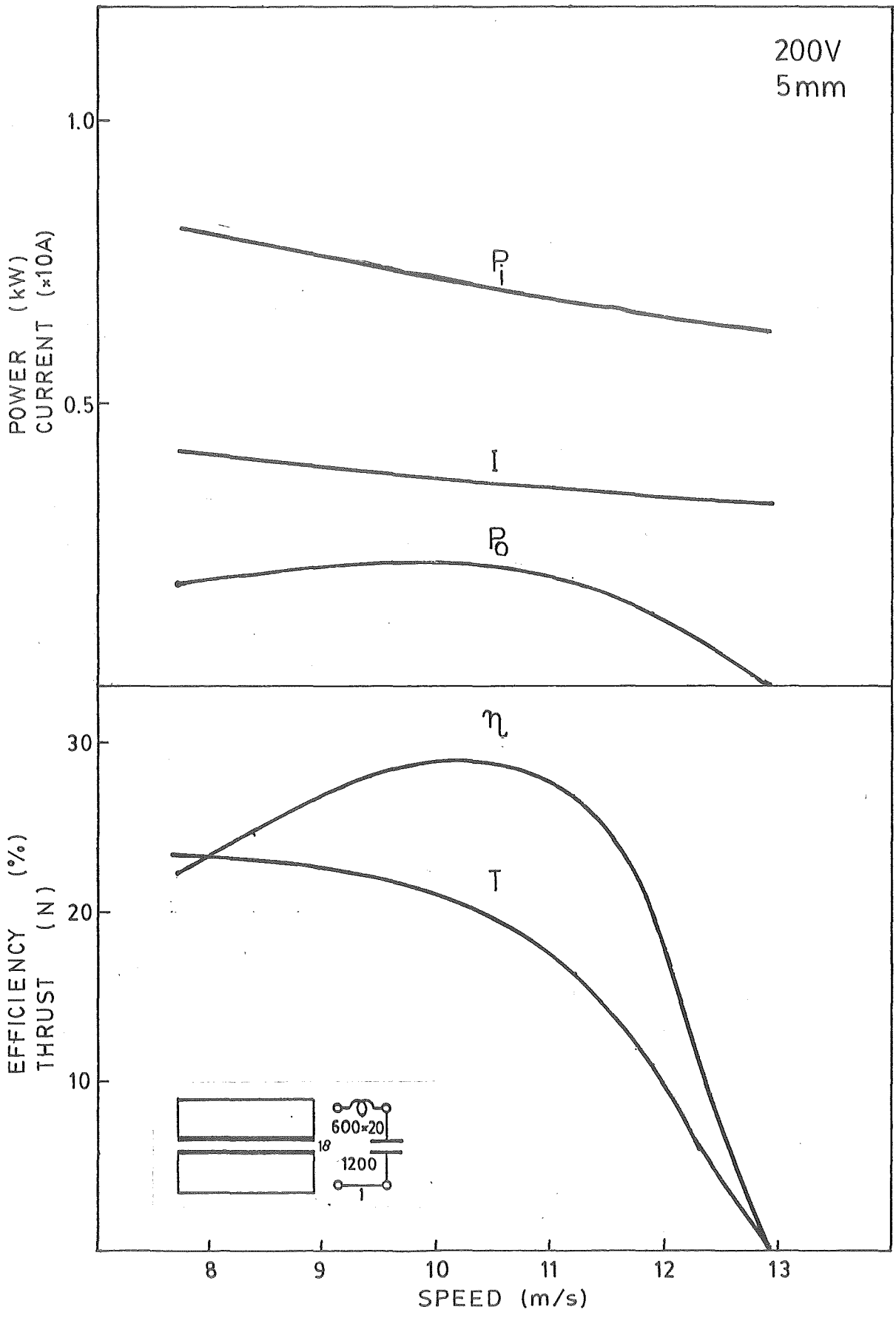
200V
5mm
1.0
0.5
POWER (kW)
CURRENT (×10A)
P_i
I
P_o
η
T
30
20
10
EFFICIENCY (%)
THRUST (N)
600×20
18
1200
1
8
9
10
11
12
13
SPEED (m/s)

Fig. A 8

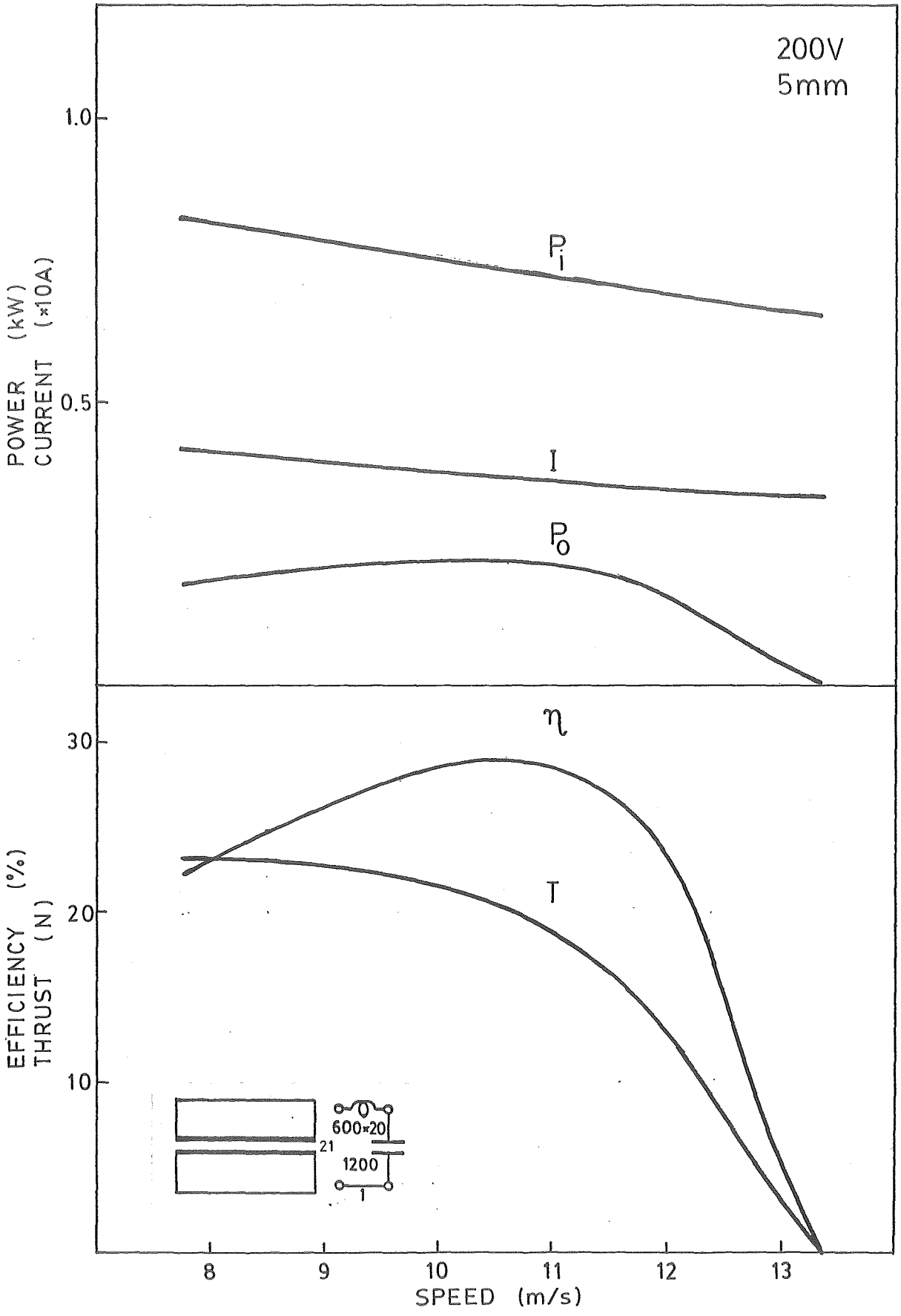
200V
5mm
1.0
0.5
POWER (kW)
CURRENT (×10A)
P_i
I
P_o
30
20
10
EFFICIENCY (%)
THRUST (N)
η
T
600×20
21
1200
1
8
9
10
11
12
13
SPEED (m/s)

Fig. A9

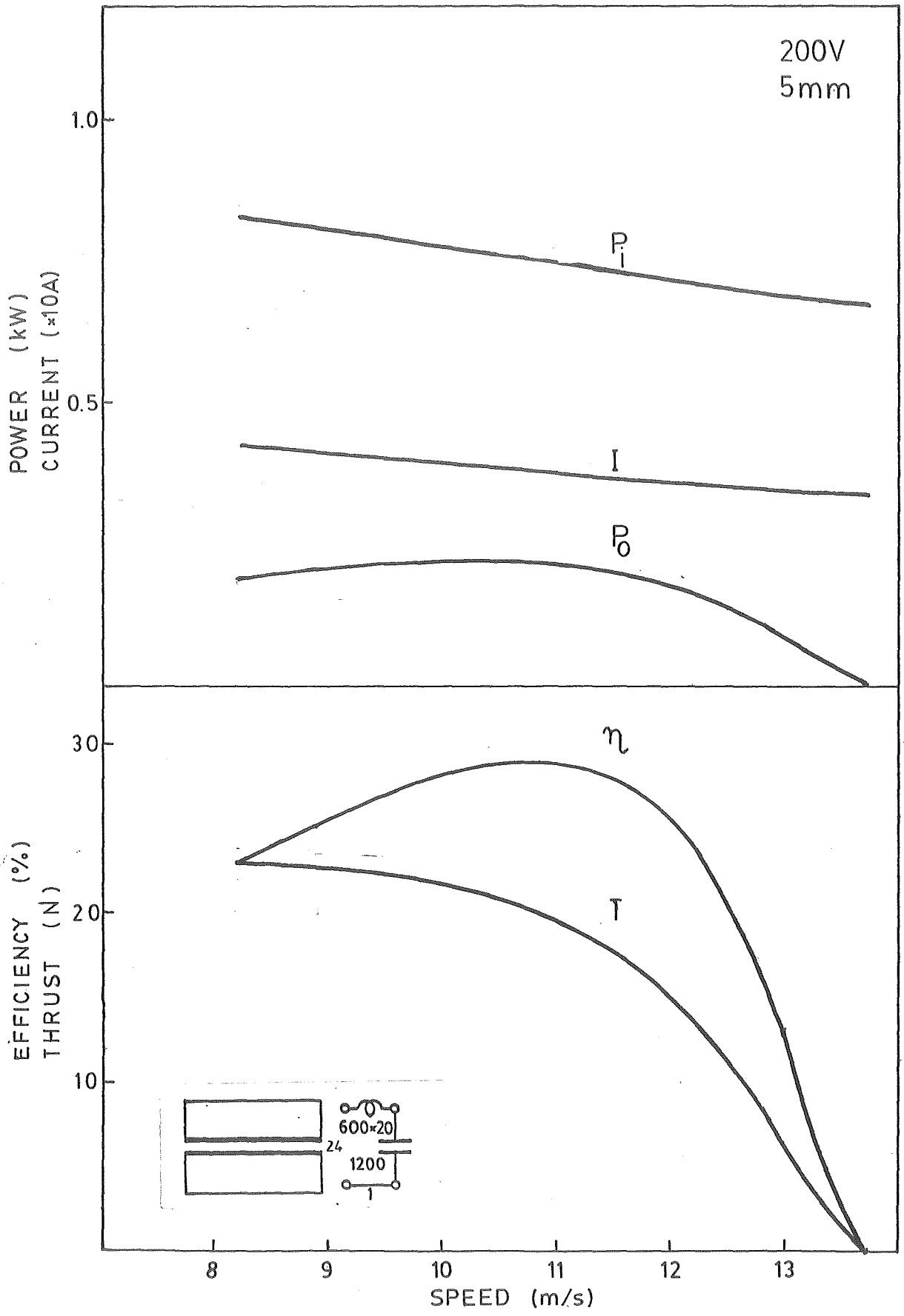
200V
5mm
1.0
0.5
POWER (kW)
CURRENT (×10A)
P_i
I
P_o
30
20
10
EFFICIENCY (%)
THRUST (N)
η
T
600×20
24
1200
1
8
9
10
11
12
13
SPEED (m/s)

Fig. A10

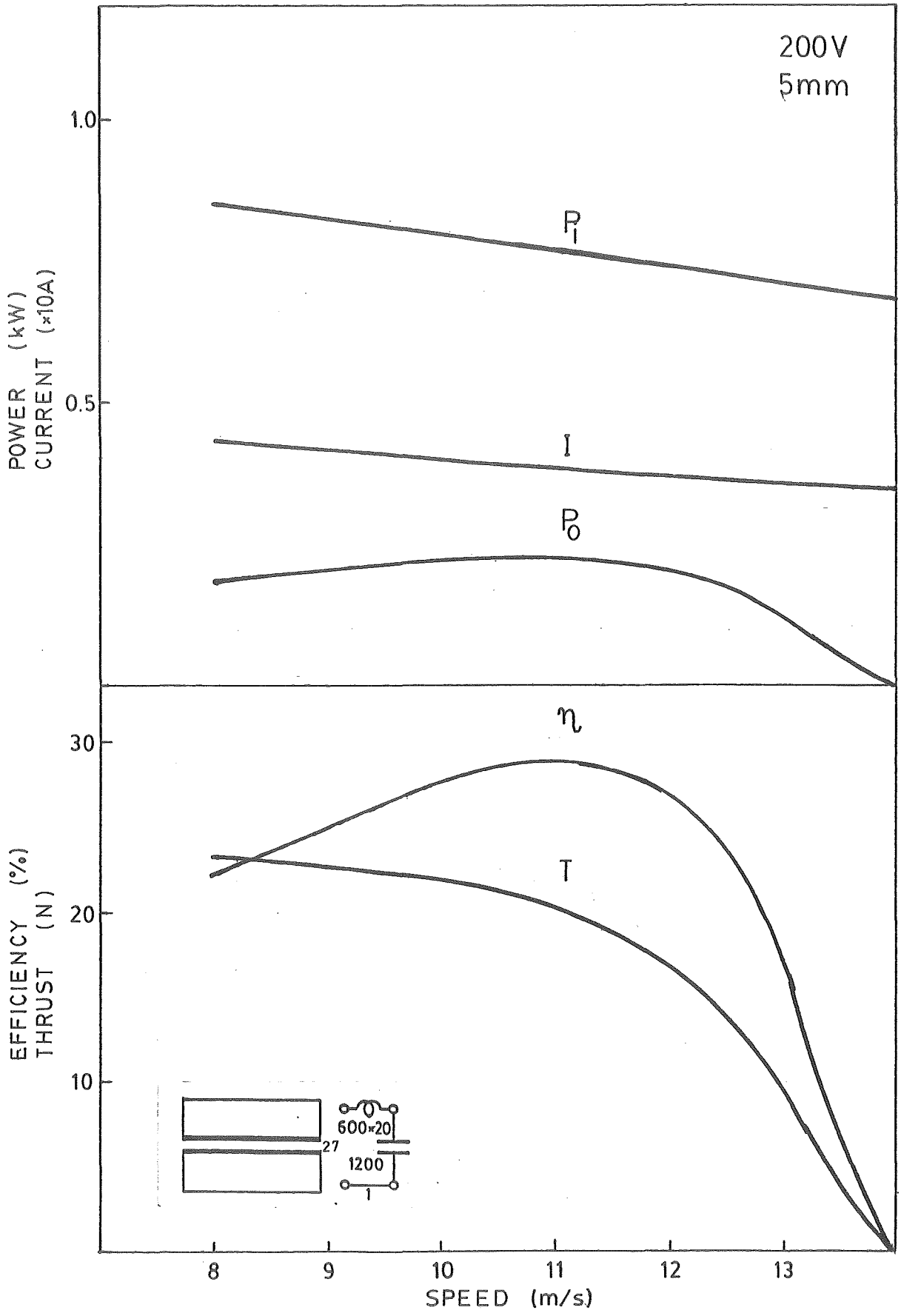
200V
5mm
1.0
0.5
POWER (kW)
CURRENT (×10A)
P_I
I
P_O
η
30
20
10
EFFICIENCY (%)
THRUST (N)
T
600×20
27
1200
1
8
9
10
11
12
13
SPEED (m/s)

Fig. A11

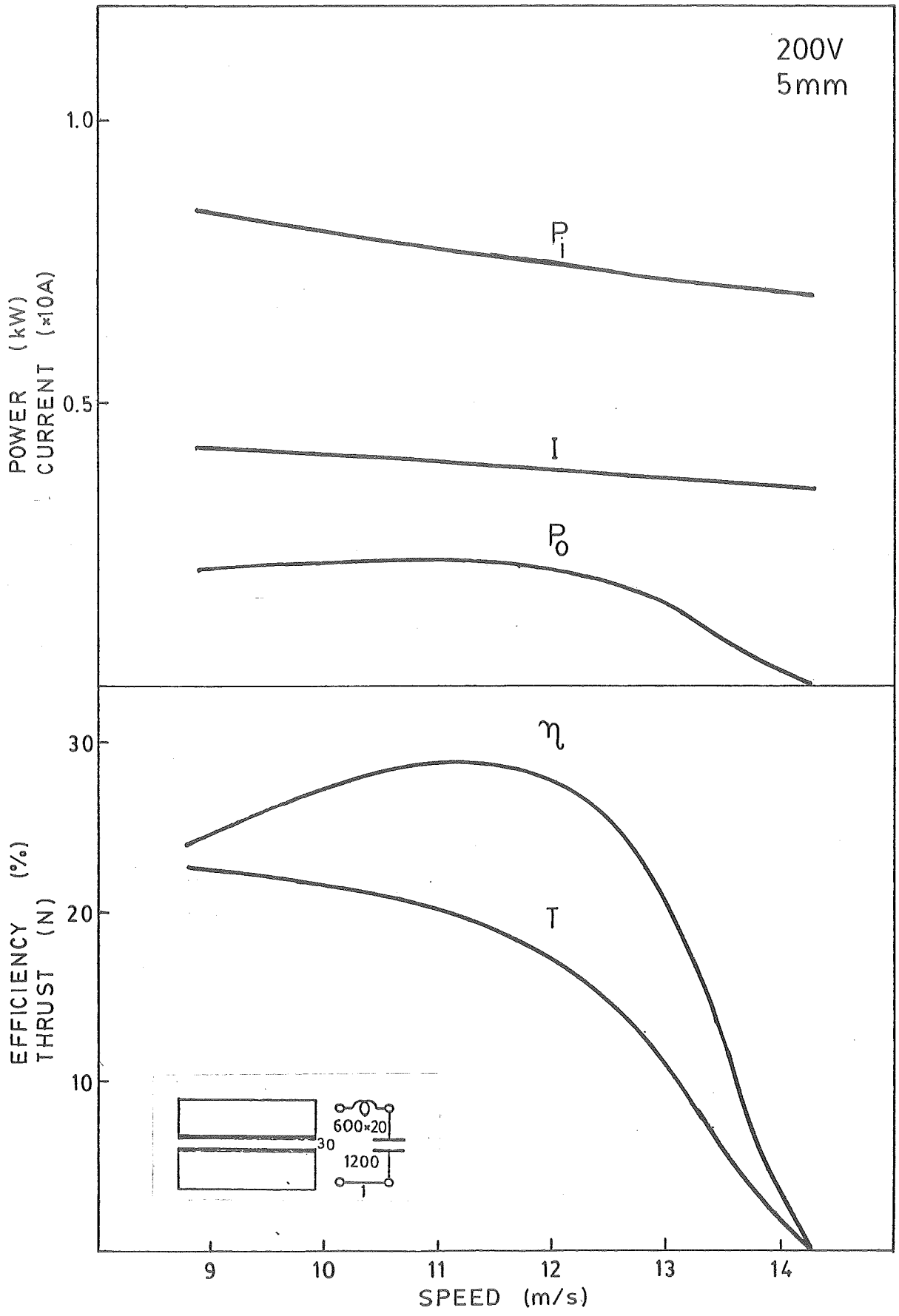
200V
5mm
1.0
0.5
POWER (kW)
CURRENT (×10A)
P_i
I
P_o
30
20
10
EFFICIENCY (%)
THRUST (N)
η
T
600×20
30
1200
1
9
10
11
12
13
14
SPEED (m/s)

Fig. A 12

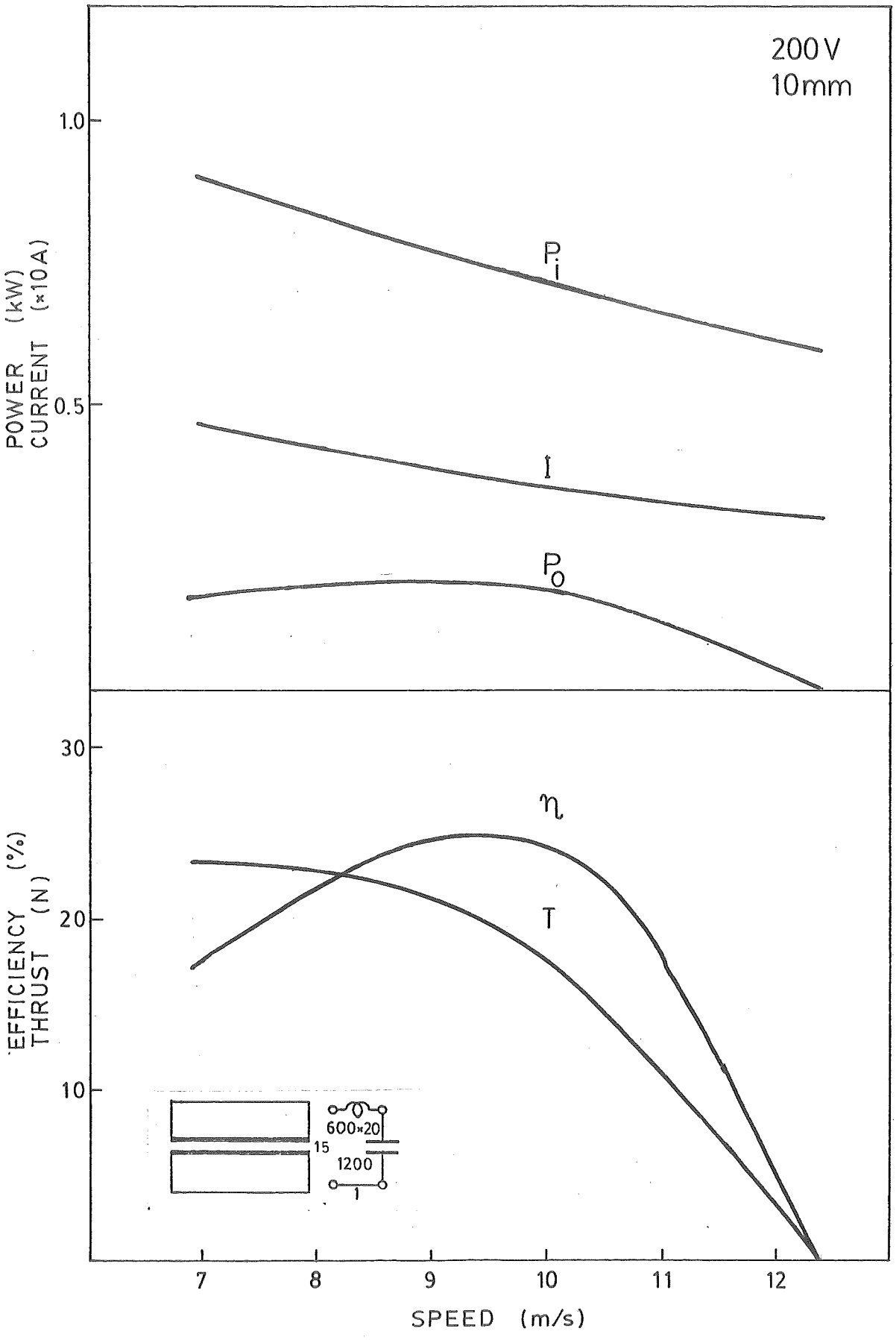
200V
10mm
1.0
0.5
POWER (kW)
CURRENT (×10A)
P_i
I
P_o
30
20
10
EFFICIENCY (%)
THRUST (N)
η
T
600×20
15
1200
1
7
8
9
10
11
12
SPEED (m/s)

Fig. A13

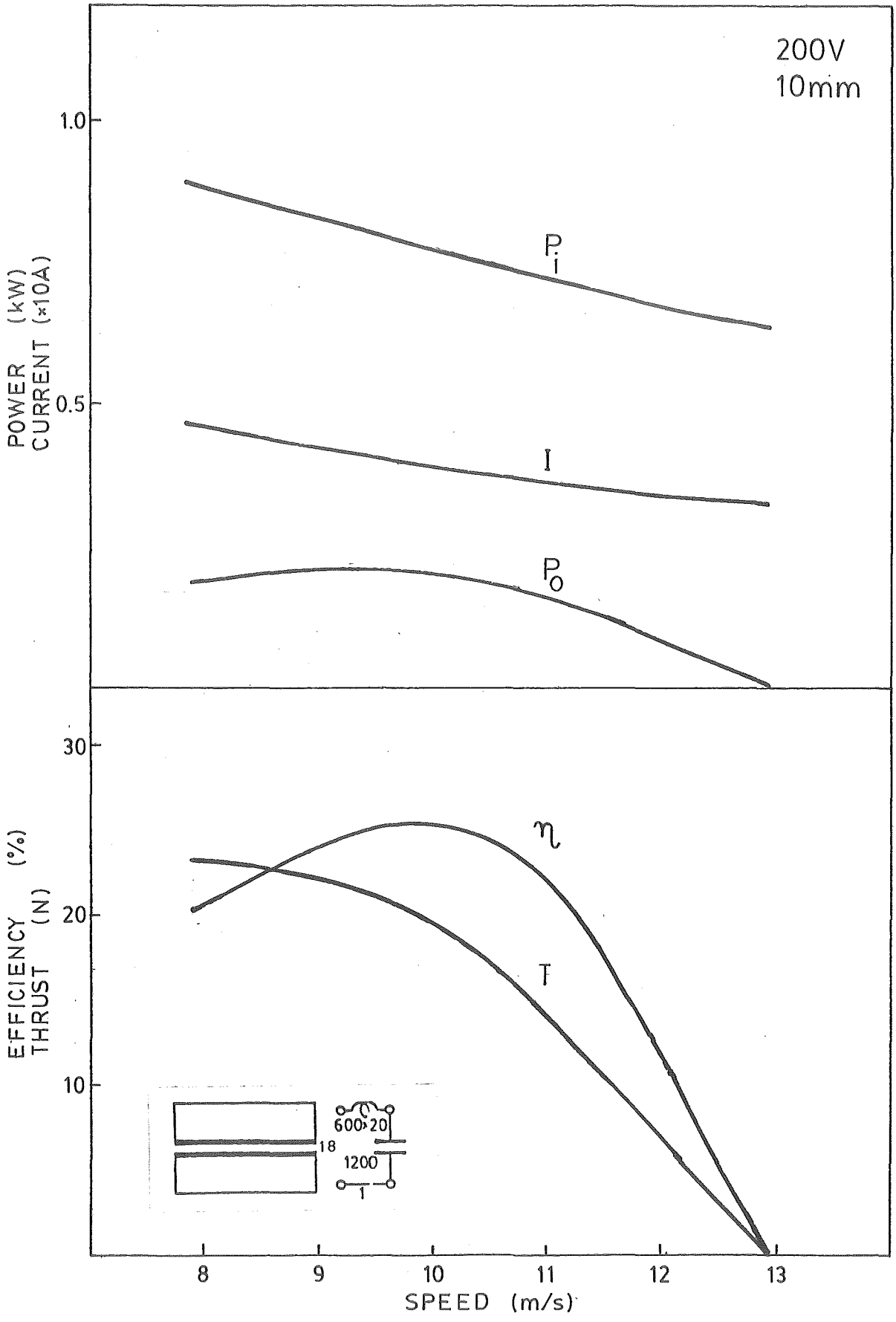
200V
10mm
1.0
0.5
POWER (kW)
CURRENT (×10A)
P_i
I
P_o
30
20
10
EFFICIENCY (%)
THRUST (N)
η
T
600×20
18
1200
1
8
9
10
11
12
13
SPEED (m/s)

Fig. A14

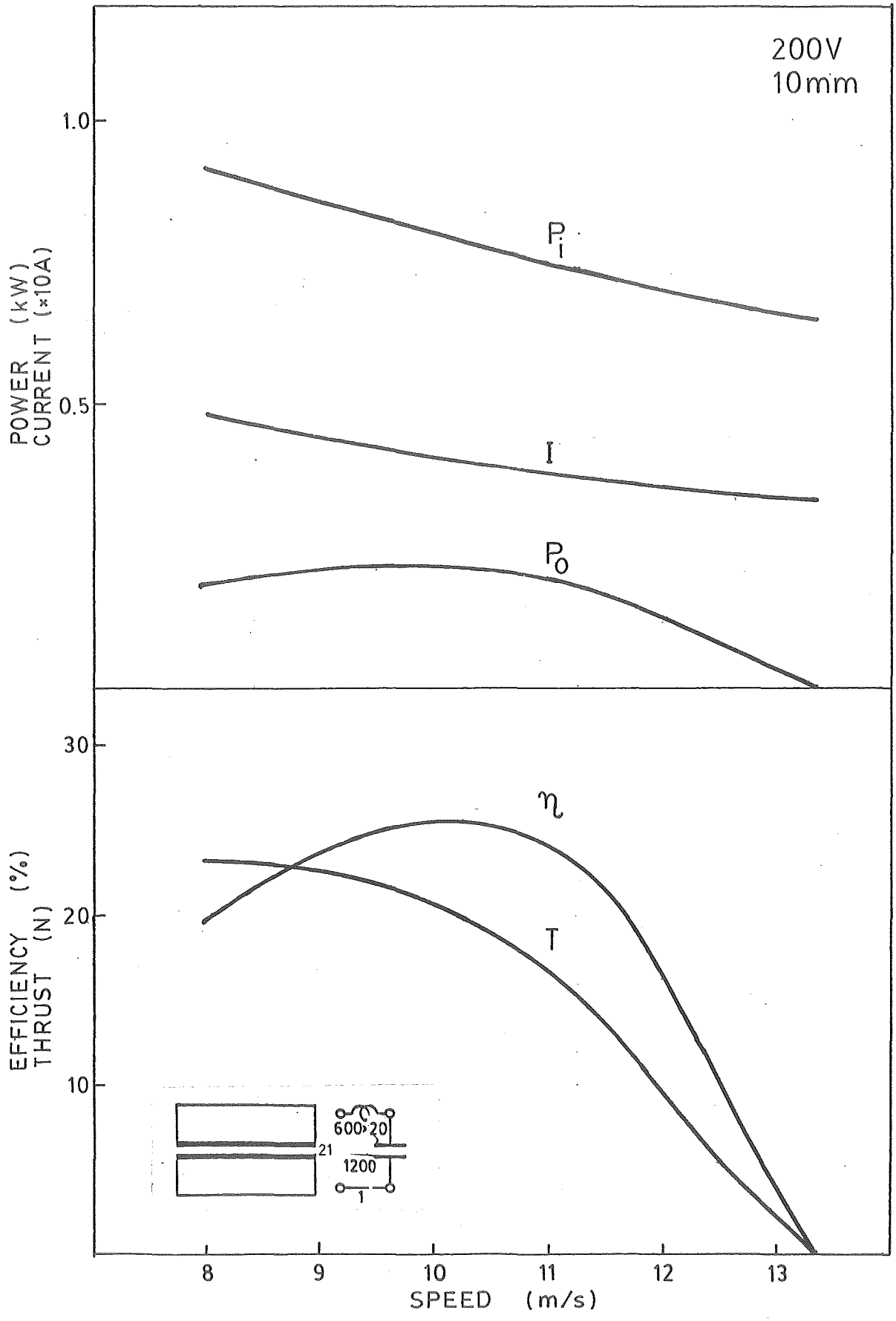
200V
10mm
POWER (kW)
CURRENT (×10A)
1.0
0.5
P_i
I
P_o
EFFICIENCY (%)
THRUST (N)
30
20
10
η
T
600
20
21
1200
1
8
9
10
11
12
13
SPEED (m/s)

Fig. A15

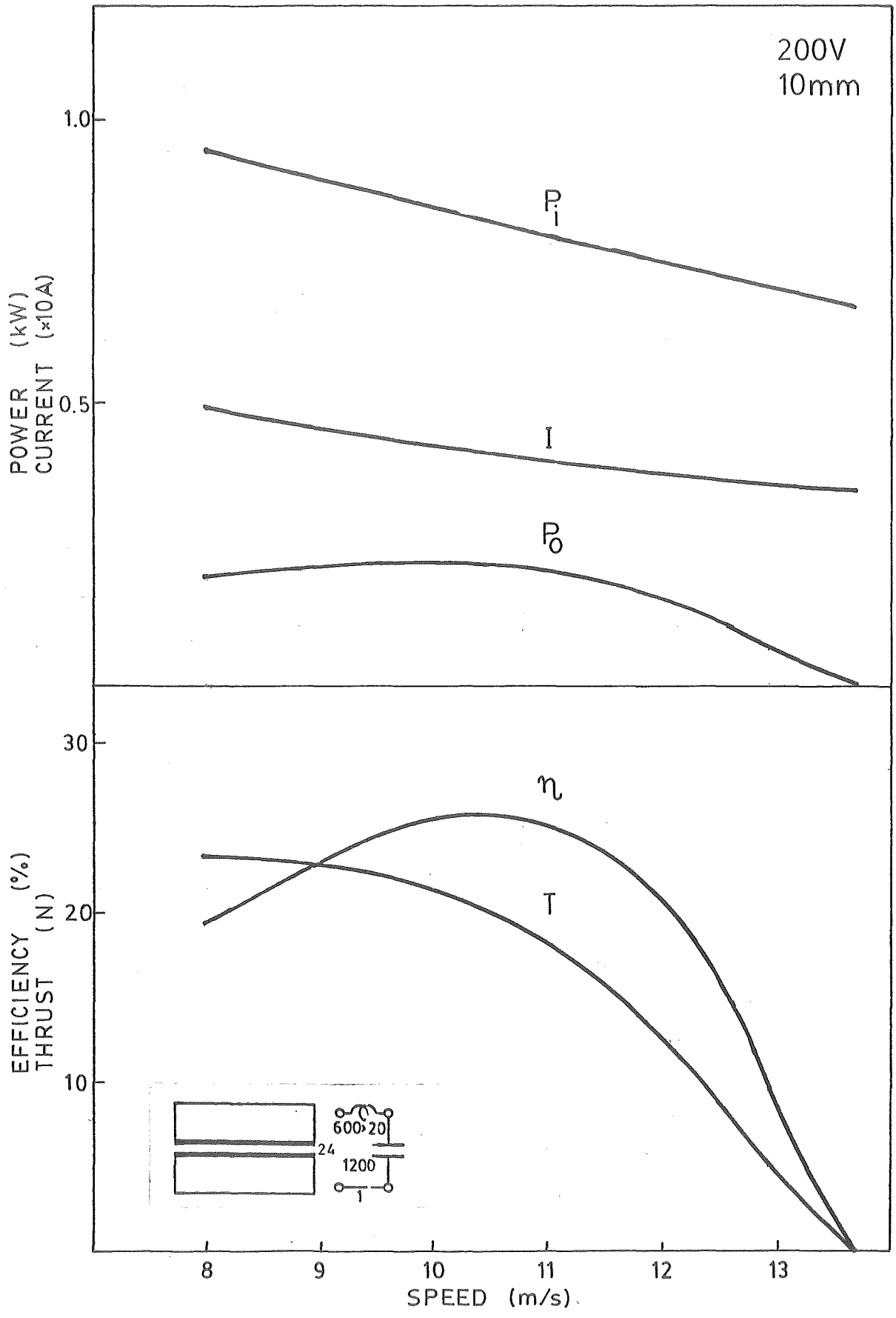
200V
10mm
1.0
0.5
POWER (kW)
CURRENT (×10A)
P_i
I
P_o
30
20
10
EFFICIENCY (%)
THRUST (N)
η
T
600
20
24
1200
1
8
9
10
11
12
13
SPEED (m/s)

Fig. A16

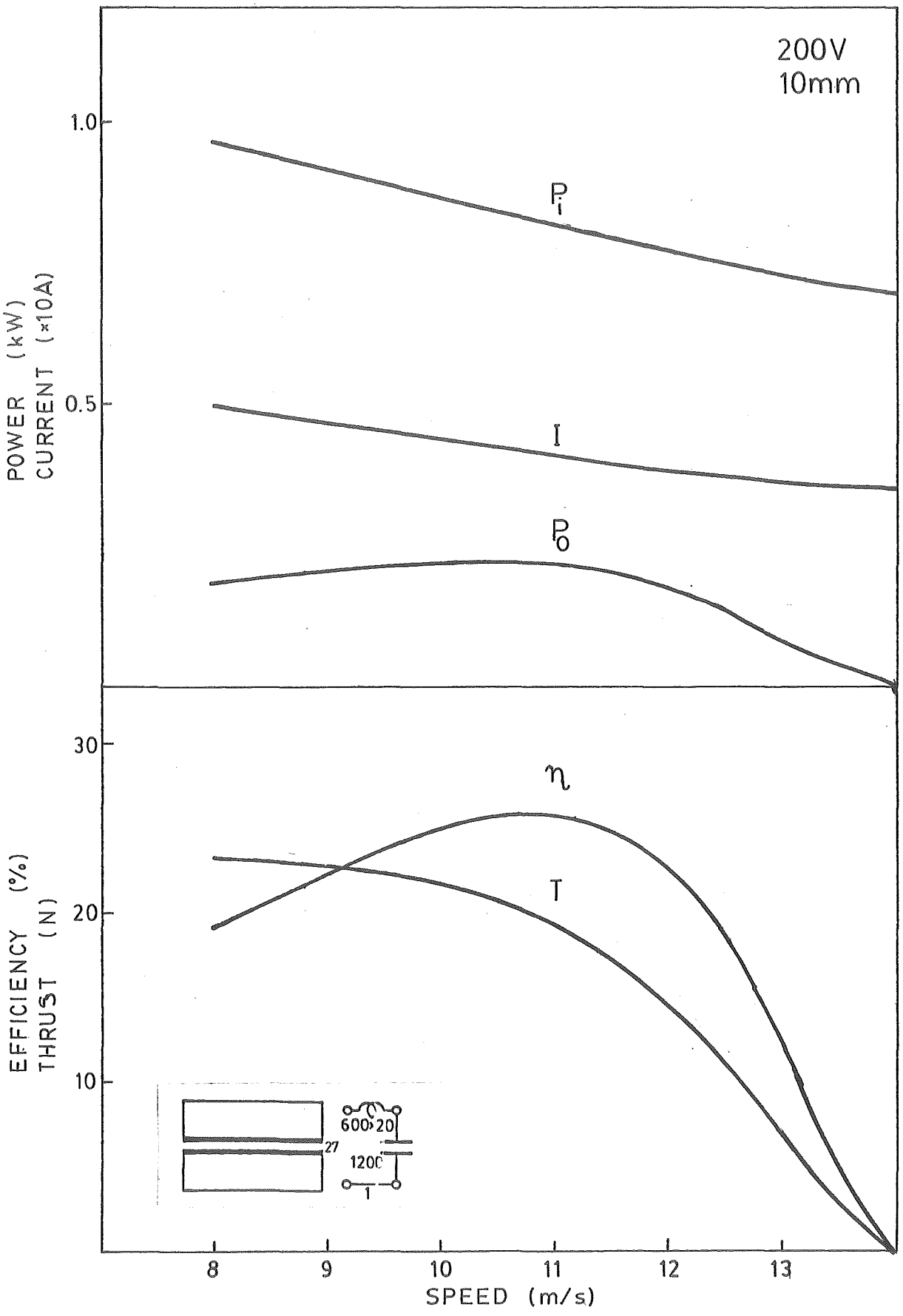
200V
10mm
1.0
0.5
POWER (kW)
CURRENT (×10A)
P_i
I
P_o
30
20
10
EFFICIENCY (%)
THRUST (N)
η
T
600
20
27
1200
1
8
9
10
11
12
13
SPEED (m/s)

Fig. A17

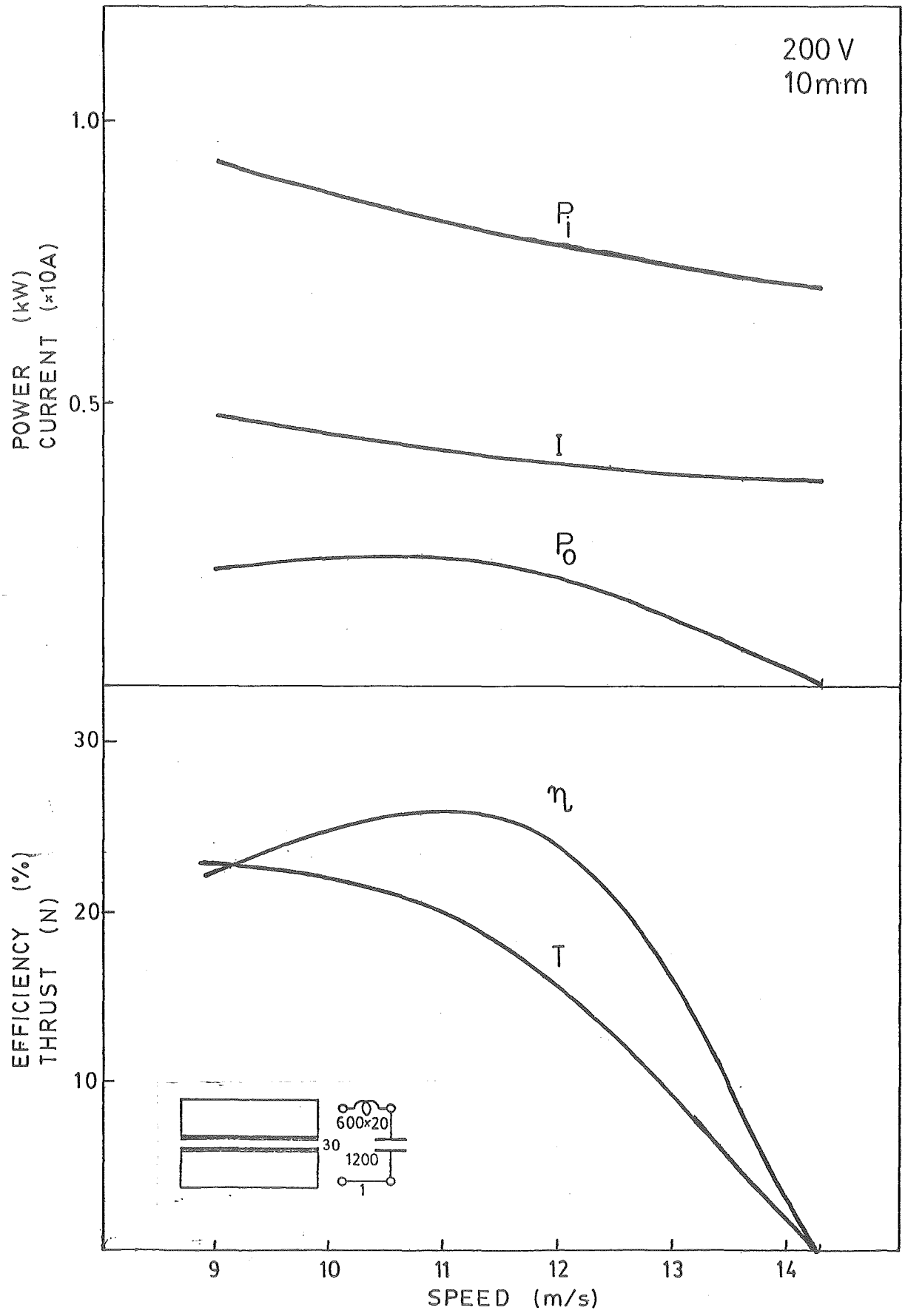
200 V
10mm
POWER (kW)
CURRENT (×10A)
1.0
0.5
P_i
I
P_0
EFFICIENCY (%)
THRUST (N)
30
20
10
η
T
600×20
30
1200
1
9
10
11
12
13
14
SPEED (m/s)

Fig. A18

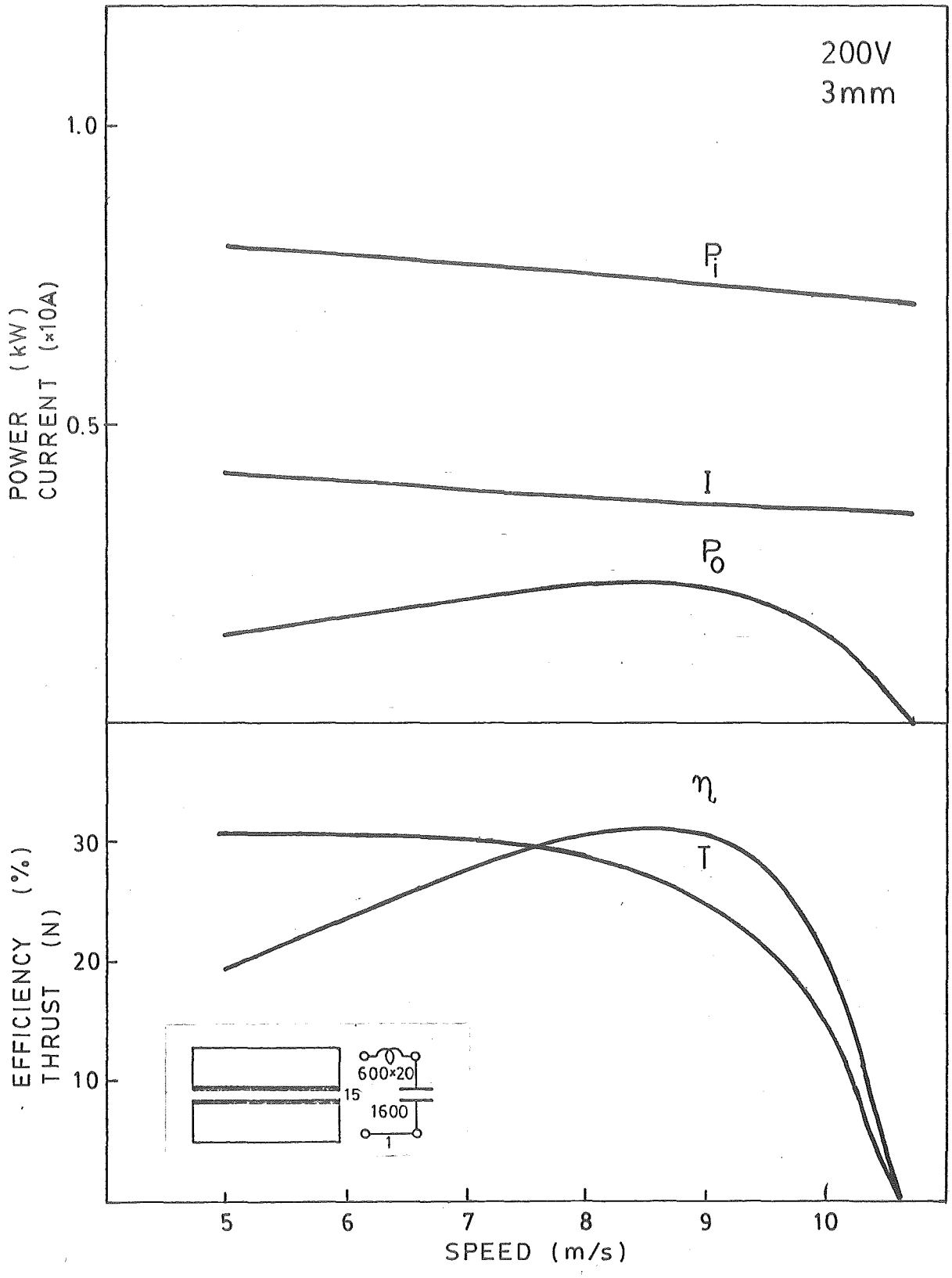
200V
3mm
1.0
0.5
POWER (kW)
CURRENT (×10A)
P_i
I
P_o
η
T
30
20
10
EFFICIENCY (%)
THRUST (N)
600×20
15
1600
1
5
6
7
8
9
10
SPEED (m/s)

Fig. A19

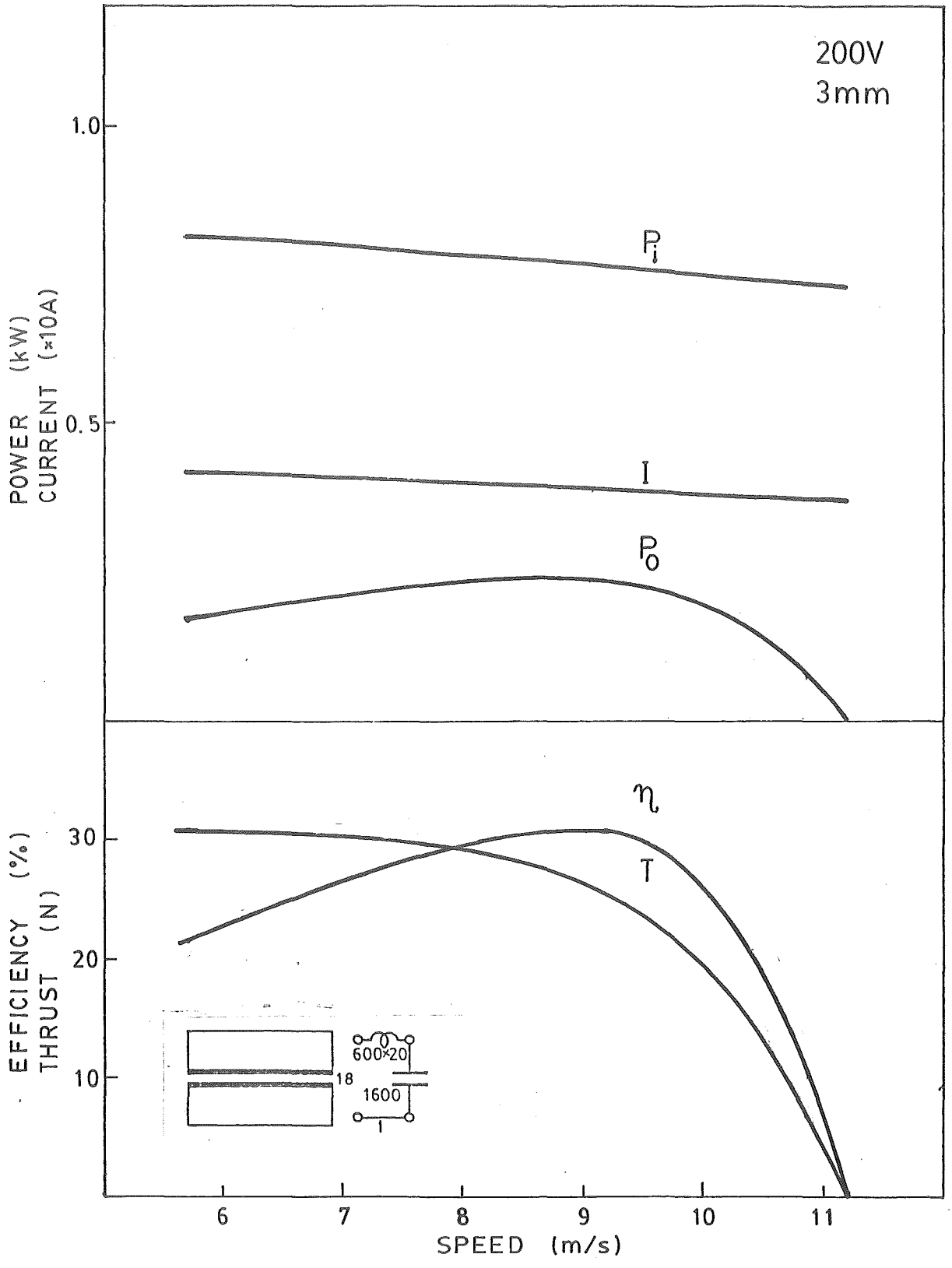
200V
3mm
1.0
0.5
POWER (kW)
CURRENT (×10A)
P_i
I
P_o
η
T
30
20
10
EFFICIENCY (%)
THRUST (N)
600×20
18
1600
6
7
8
9
10
11
SPEED (m/s)

Fig. A20

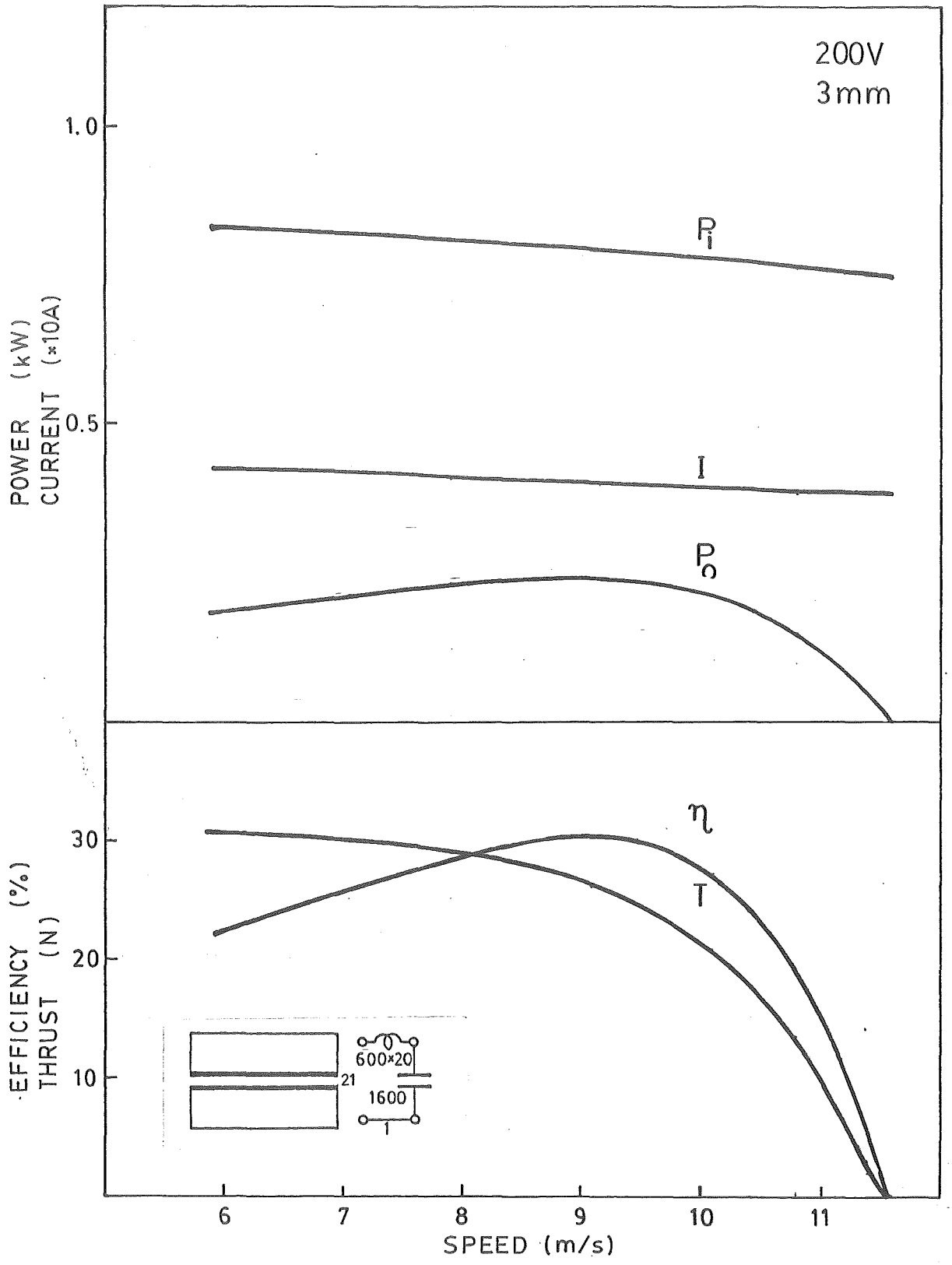
200V
3mm
1.0
0.5
POWER (kW)
CURRENT (×10A)
P_i
I
P_o
30
20
10
EFFICIENCY (%)
THRUST (N)
η
T
600×20
21
1600
1
6
7
8
9
10
11
SPEED (m/s)

Fig. A 21

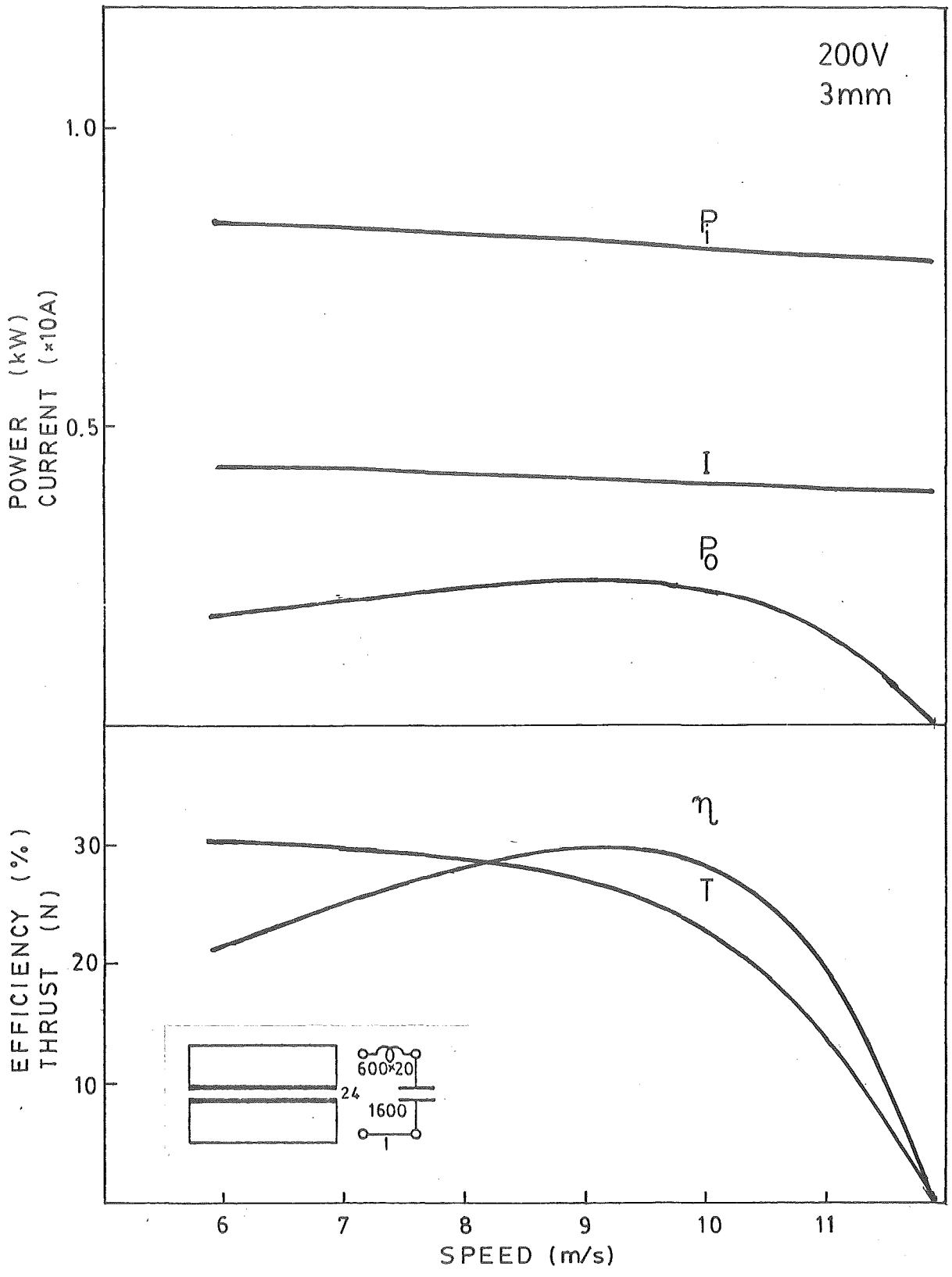
200V
3mm
1.0
0.5
POWER (kW)
CURRENT (×10A)
P_i
I
P_o
η
T
30
20
10
EFFICIENCY (%)
THRUST (N)
600×20
24
1600
6
7
8
9
10
11
SPEED (m/s)

Fig. A22

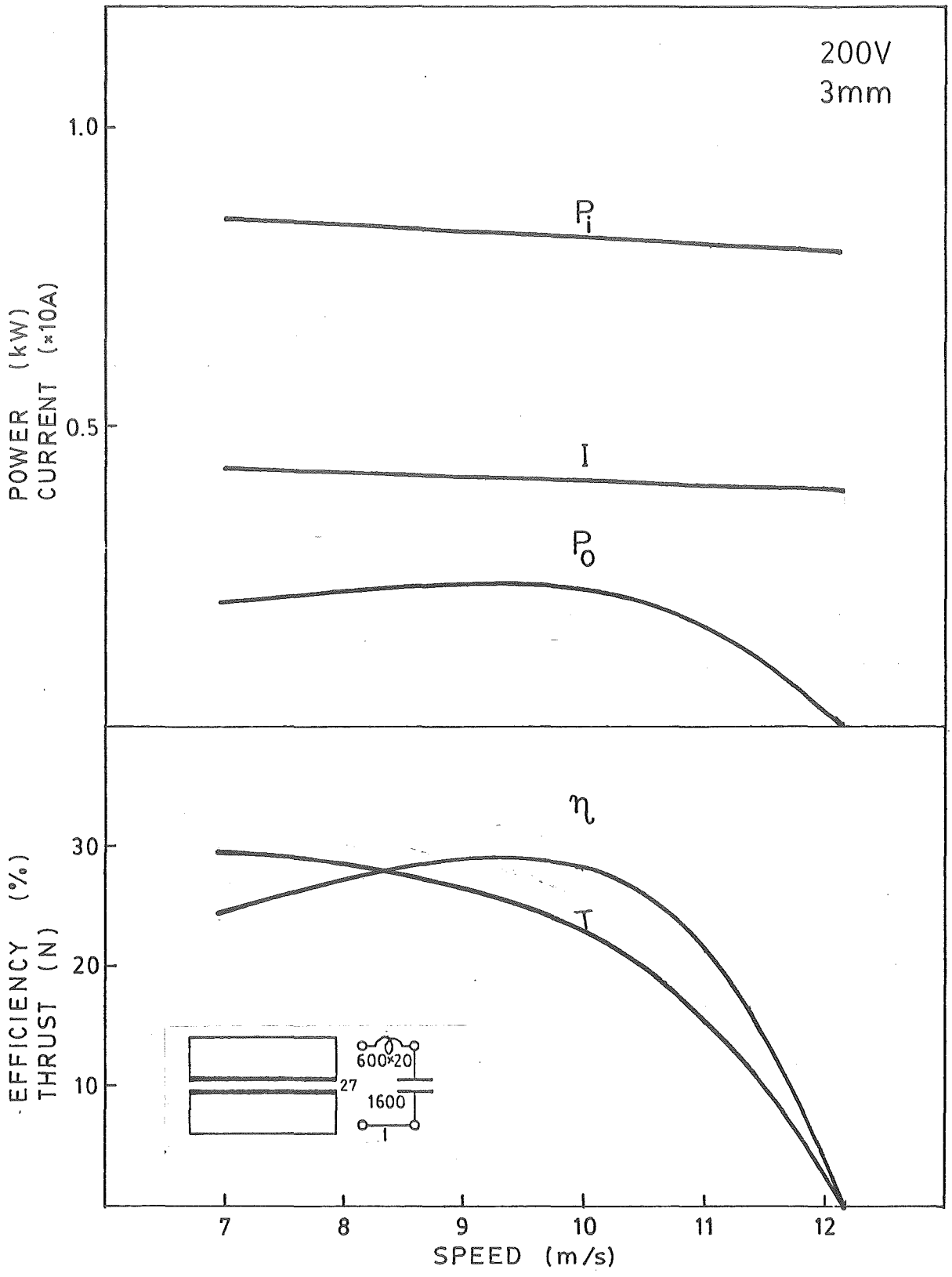
200V
3mm
1.0
0.5
POWER (kW)
CURRENT (×10A)
P_i
I
P_o
η
T
30
20
10
EFFICIENCY (%)
THRUST (N)
600×20
27
1600
7
8
9
10
11
12
SPEED (m/s)

Fig. A 23

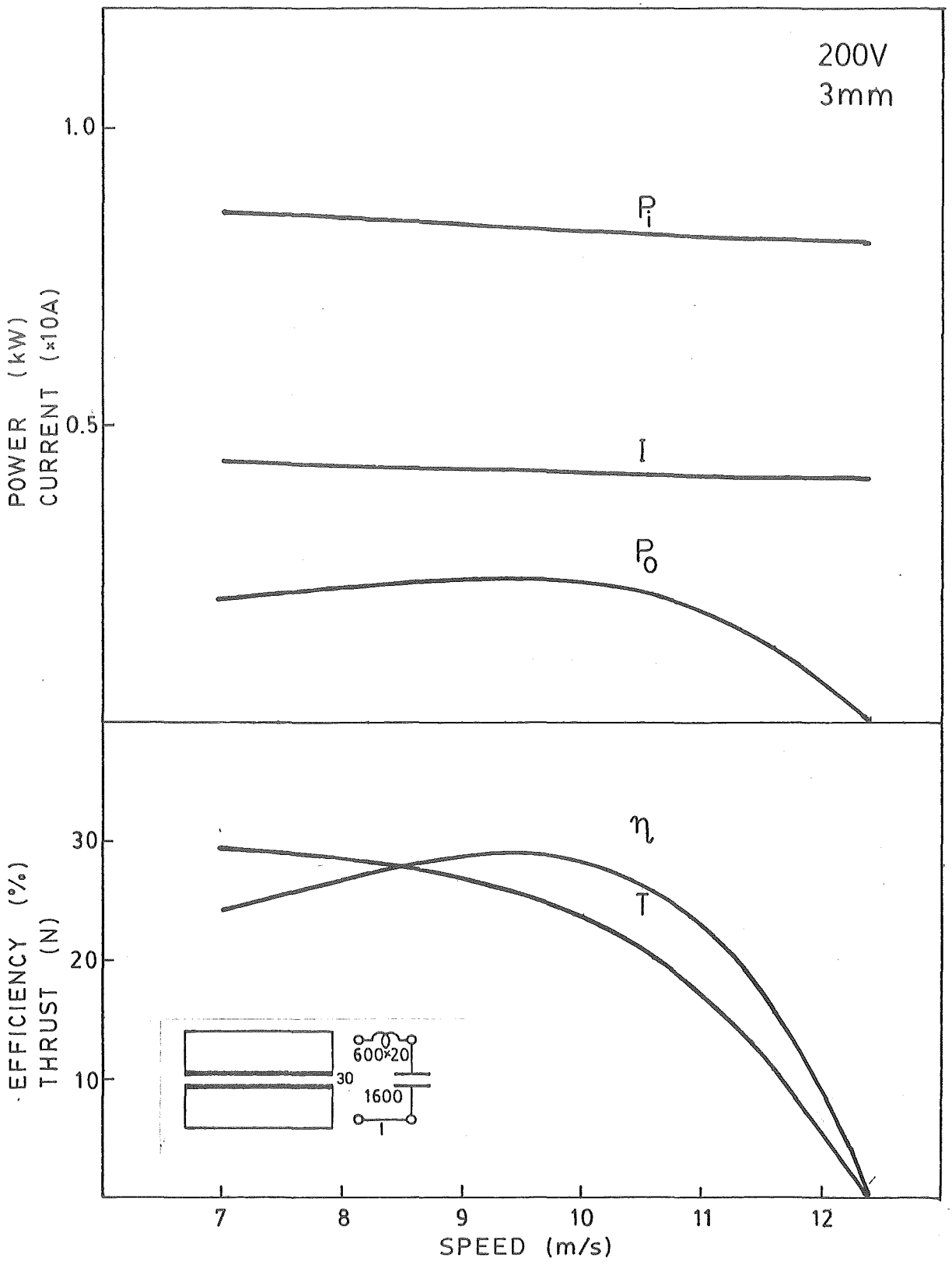
200V
3mm
1.0
0.5
POWER (kW)
CURRENT (×10A)
P_i
I
P_o
30
20
10
EFFICIENCY (%)
THRUST (N)
η
T
600×20
30
1600
7
8
9
10
11
12
SPEED (m/s)

Fig. A 24

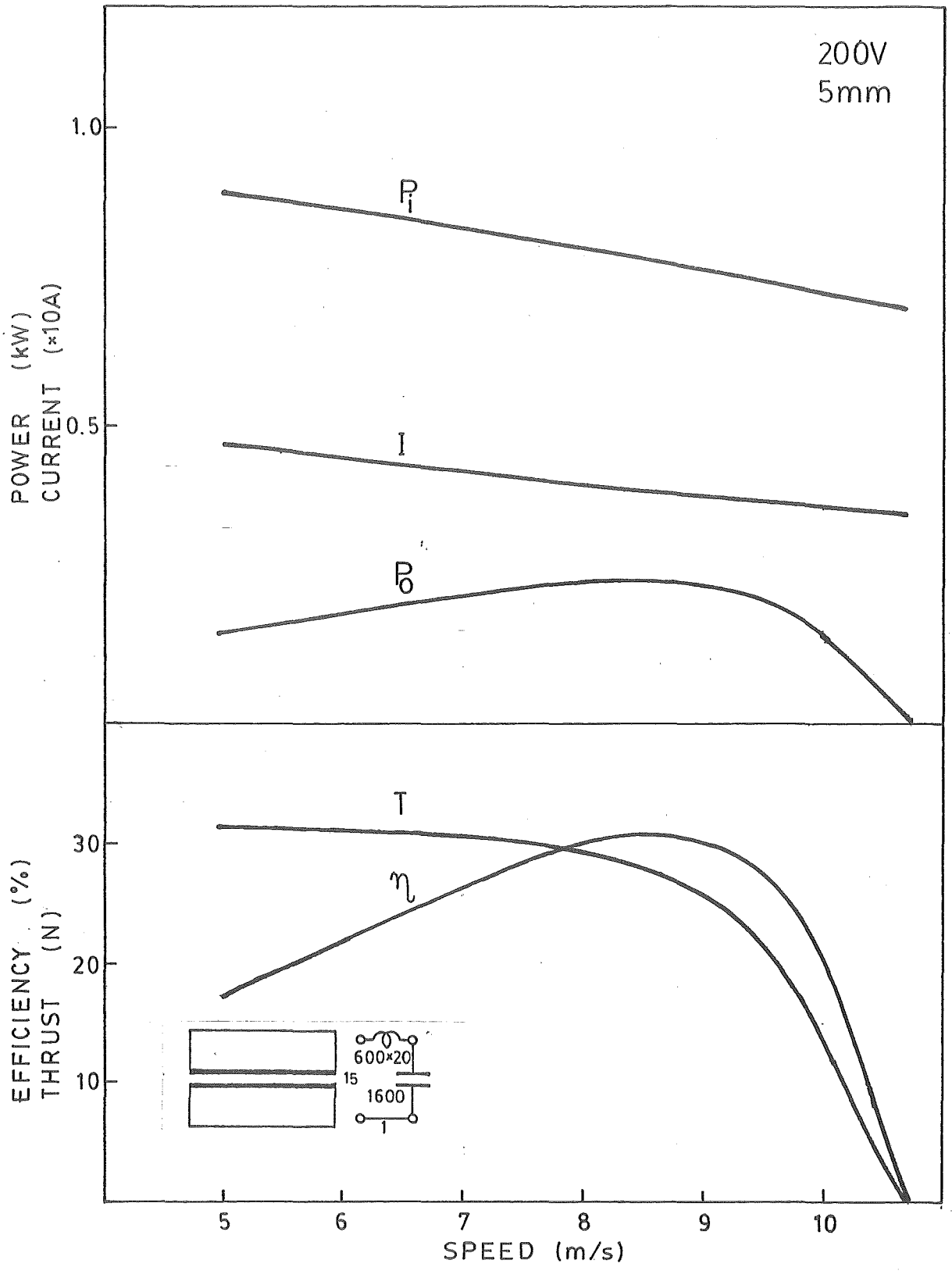
200V
5mm
1.0
0.5
POWER (kW)
CURRENT (×10A)
P_i
I
P_o
T
η
30
20
10
EFFICIENCY (%)
THRUST (N)
600×20
15
1600
1
5
6
7
8
9
10
SPEED (m/s)

Fig.A25

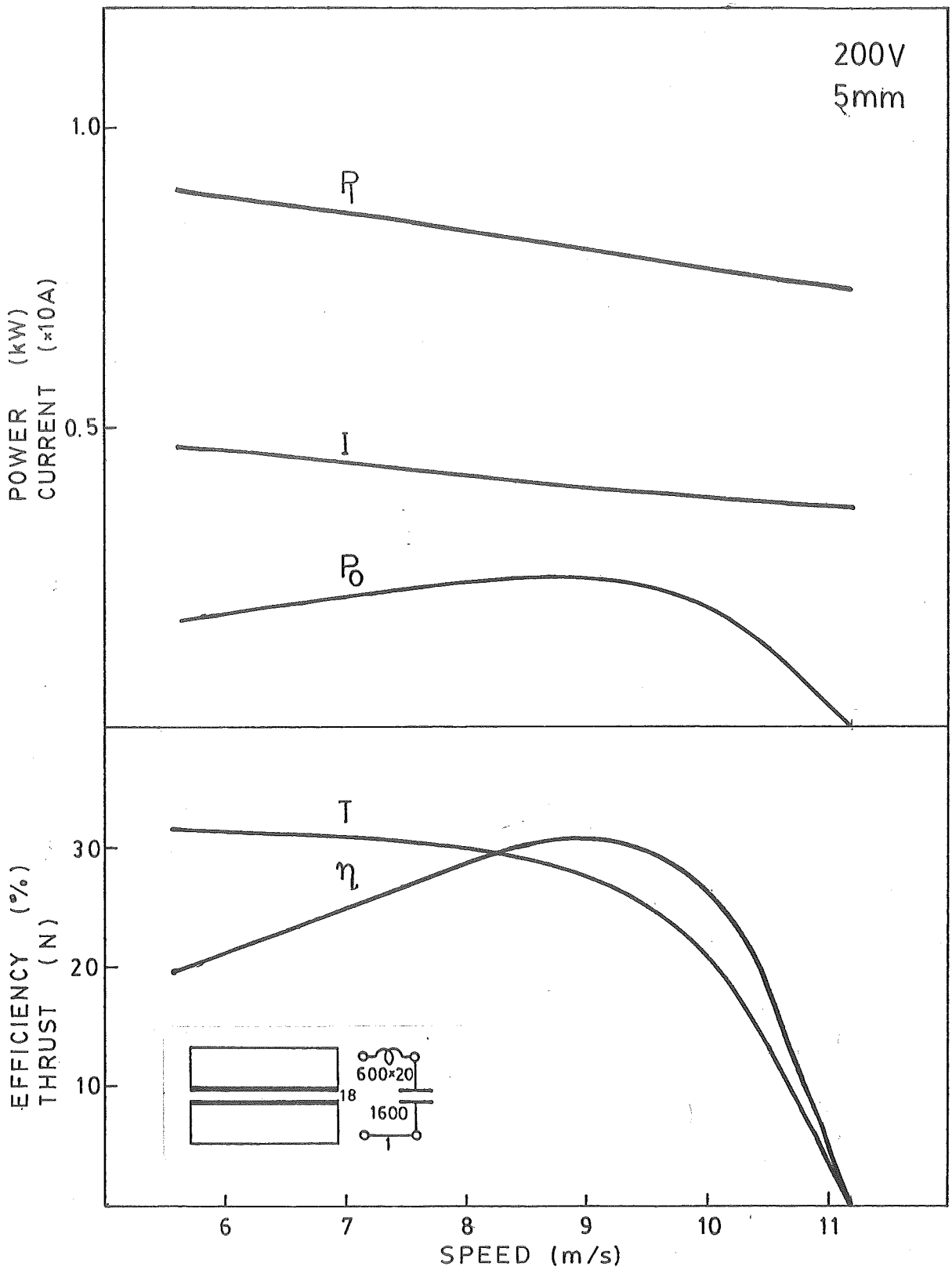
200V
5mm
1.0
0.5
POWER (kW)
CURRENT (×10A)
P_I
I
P_O
T
η
30
20
10
EFFICIENCY (%)
THRUST (N)
600×20
18
1600
1
6
7
8
9
10
11
SPEED (m/s)

Fig. A 26

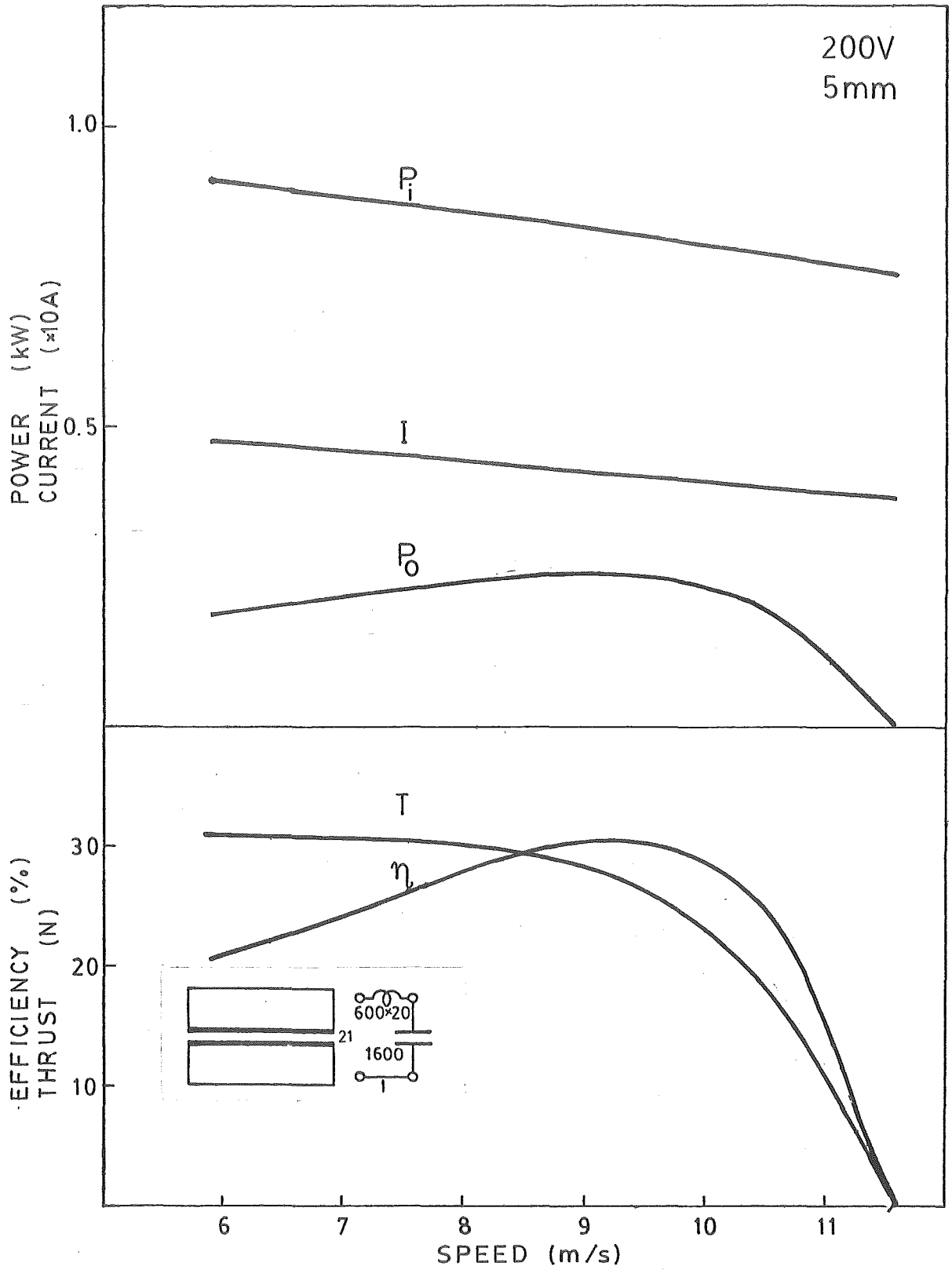
200V
5mm
1.0
0.5
POWER (kW)
CURRENT (×10A)
P_i
I
P_o
T
η
30
20
10
EFFICIENCY (%)
THRUST (N)
600×20
21
1600
6
7
8
9
10
11
SPEED (m/s)

Fig. A 27

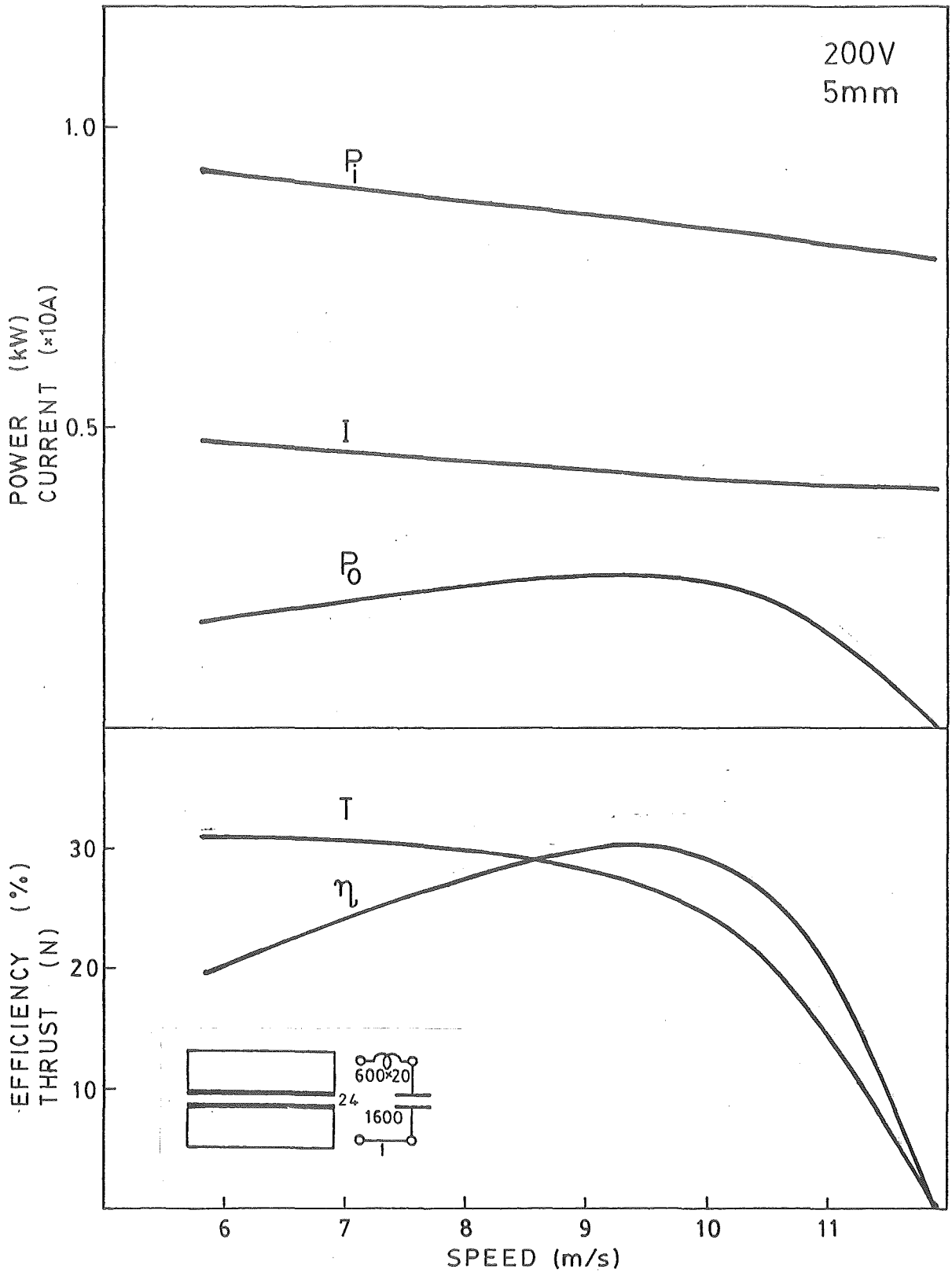
200V
5mm
1.0
0.5
POWER (kW)
CURRENT (×10A)
P_i
I
P_o
T
η
30
20
10
EFFICIENCY (%)
THRUST (N)
600×20
24
1600
6
7
8
9
10
11
SPEED (m/s)

Fig. A 28

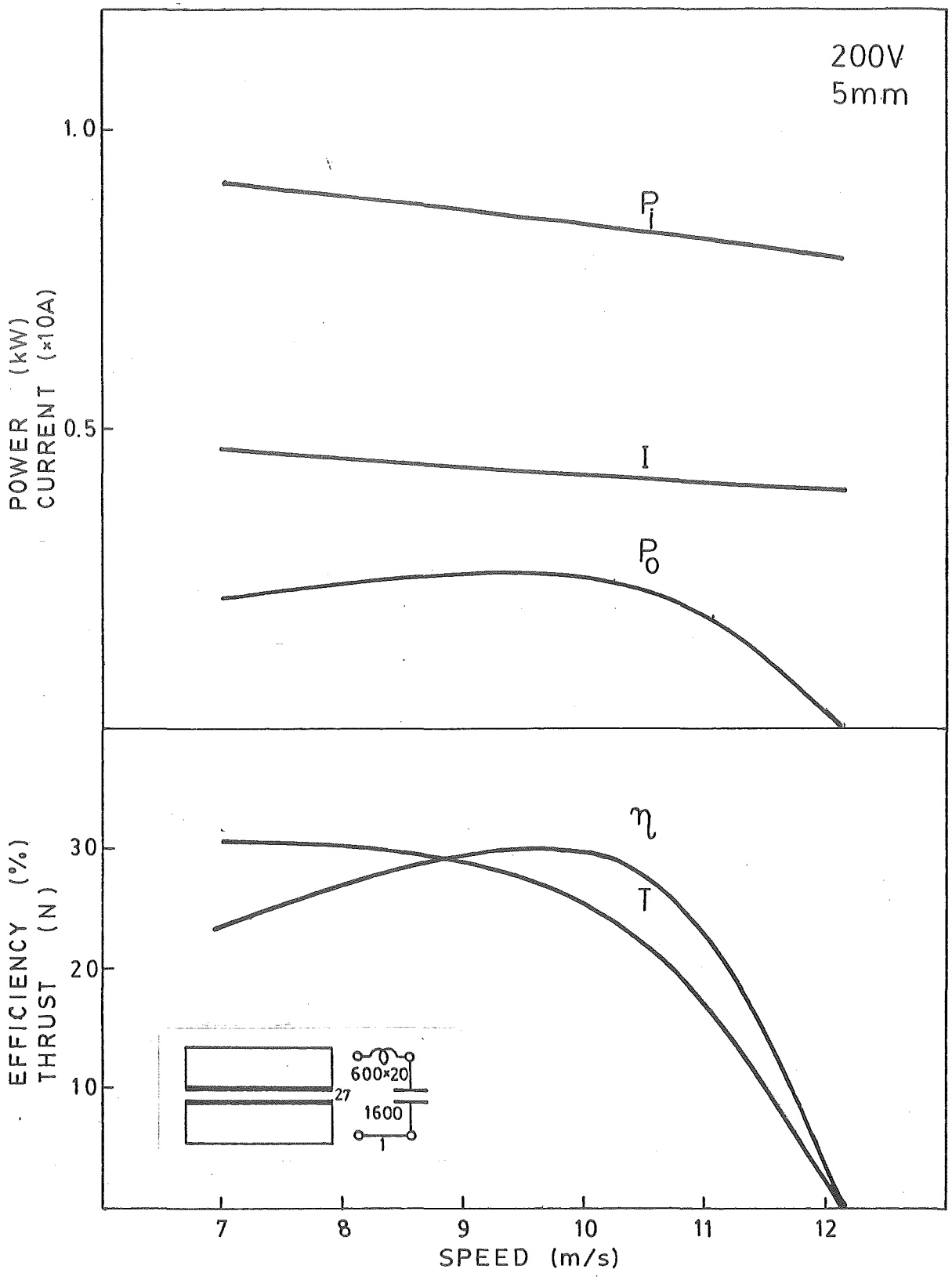
200V
5mm
1.0
0.5
POWER (kW)
CURRENT (×10A)
P_i
I
P_o
30
20
10
EFFICIENCY (%)
THRUST (N)
η
T
600×20
27
1600
7
8
9
10
11
12
SPEED (m/s)

Fig. A29

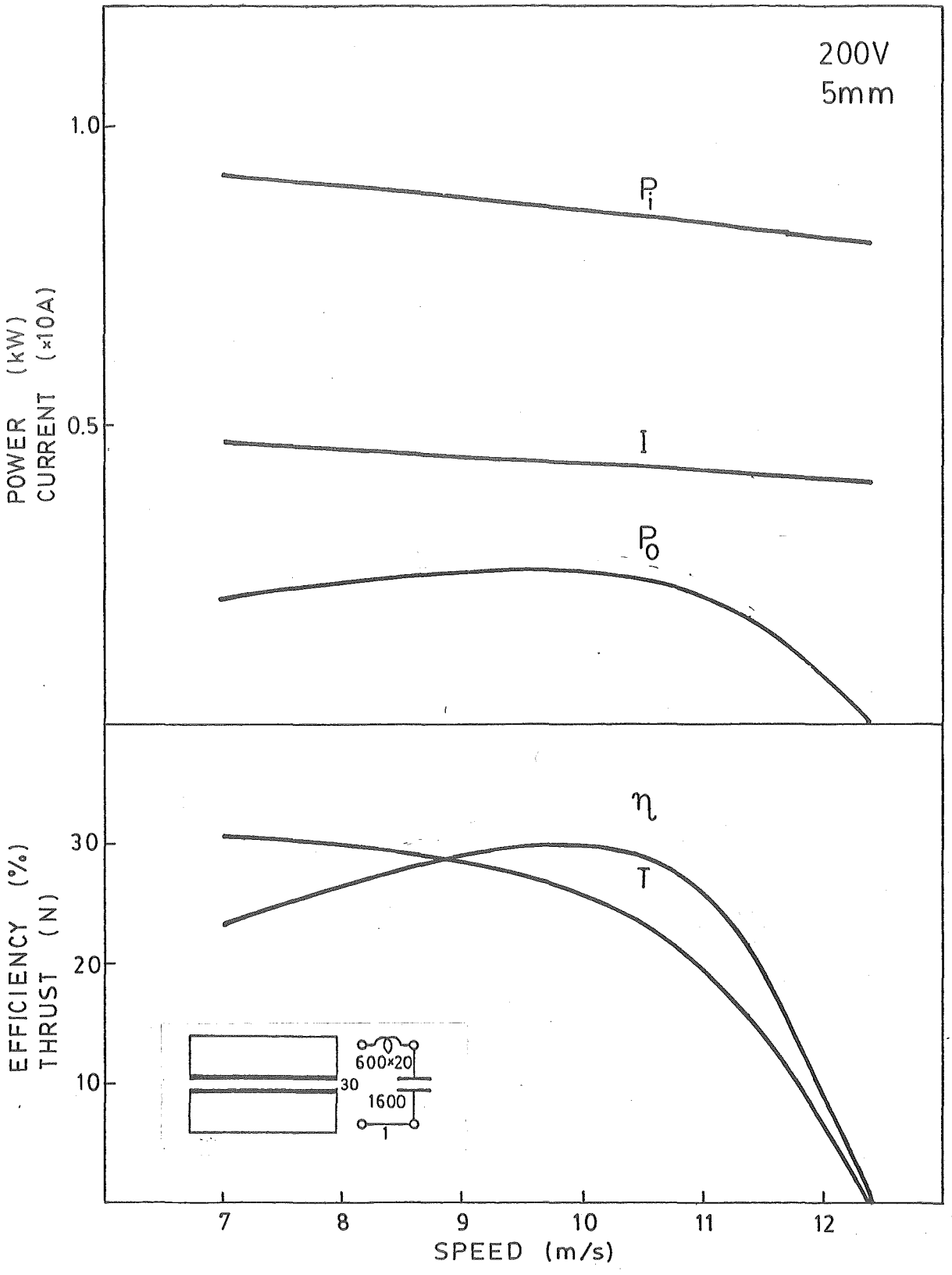
200V
5mm
1.0
0.5
POWER (kW)
CURRENT (×10A)
P_i
I
P_o
η
T
30
20
10
EFFICIENCY (%)
THRUST (N)
600×20
30
1600
1
7
8
9
10
11
12
SPEED (m/s)

Fig. A 30

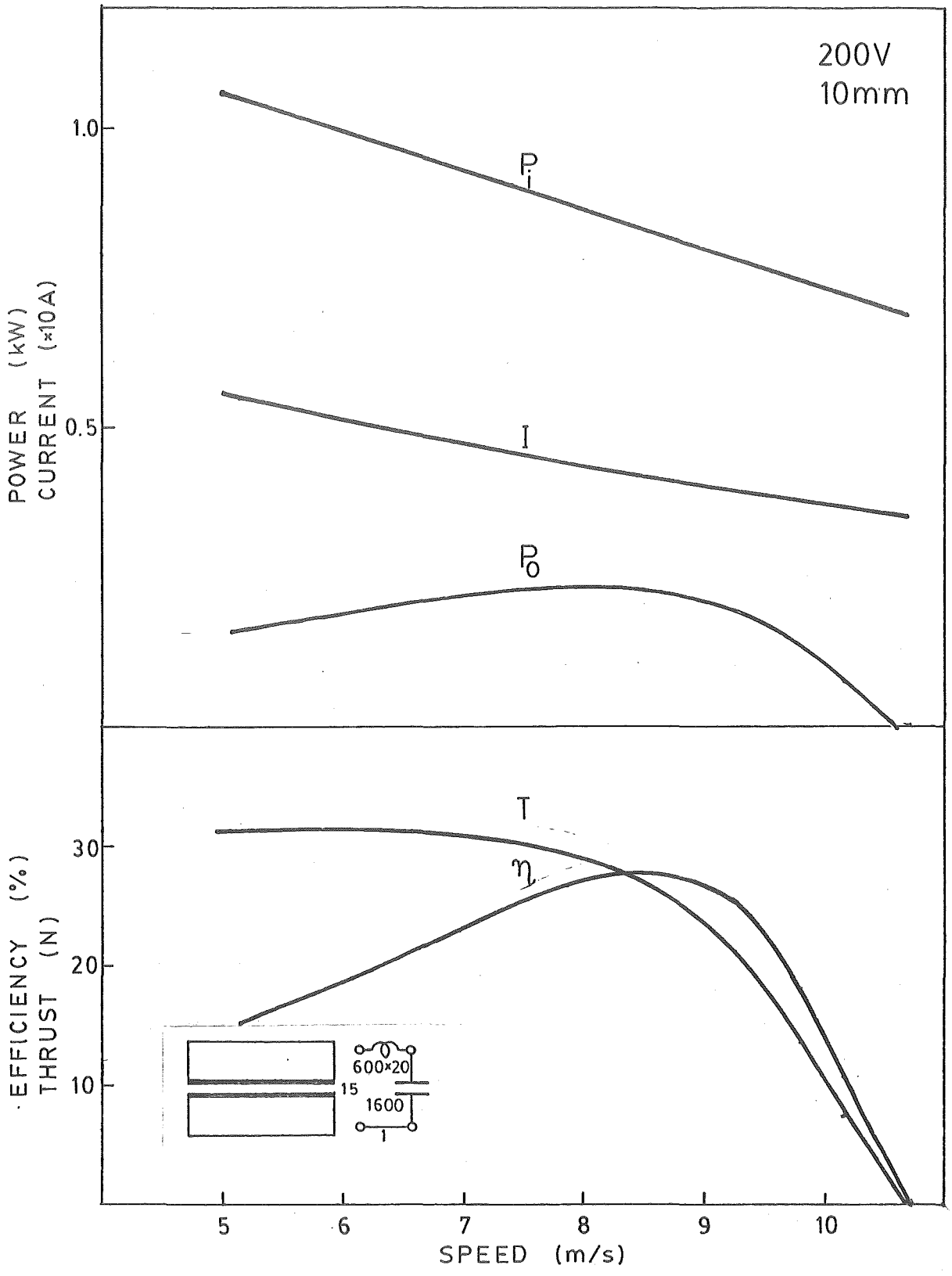
200V
10mm
1.0
0.5
POWER (kW)
CURRENT (×10A)
P_i
I
P_0
T
η
30
20
10
EFFICIENCY (%)
THRUST (N)
600×20
15
1600
1
5
6
7
8
9
10
SPEED (m/s)

Fig. A31

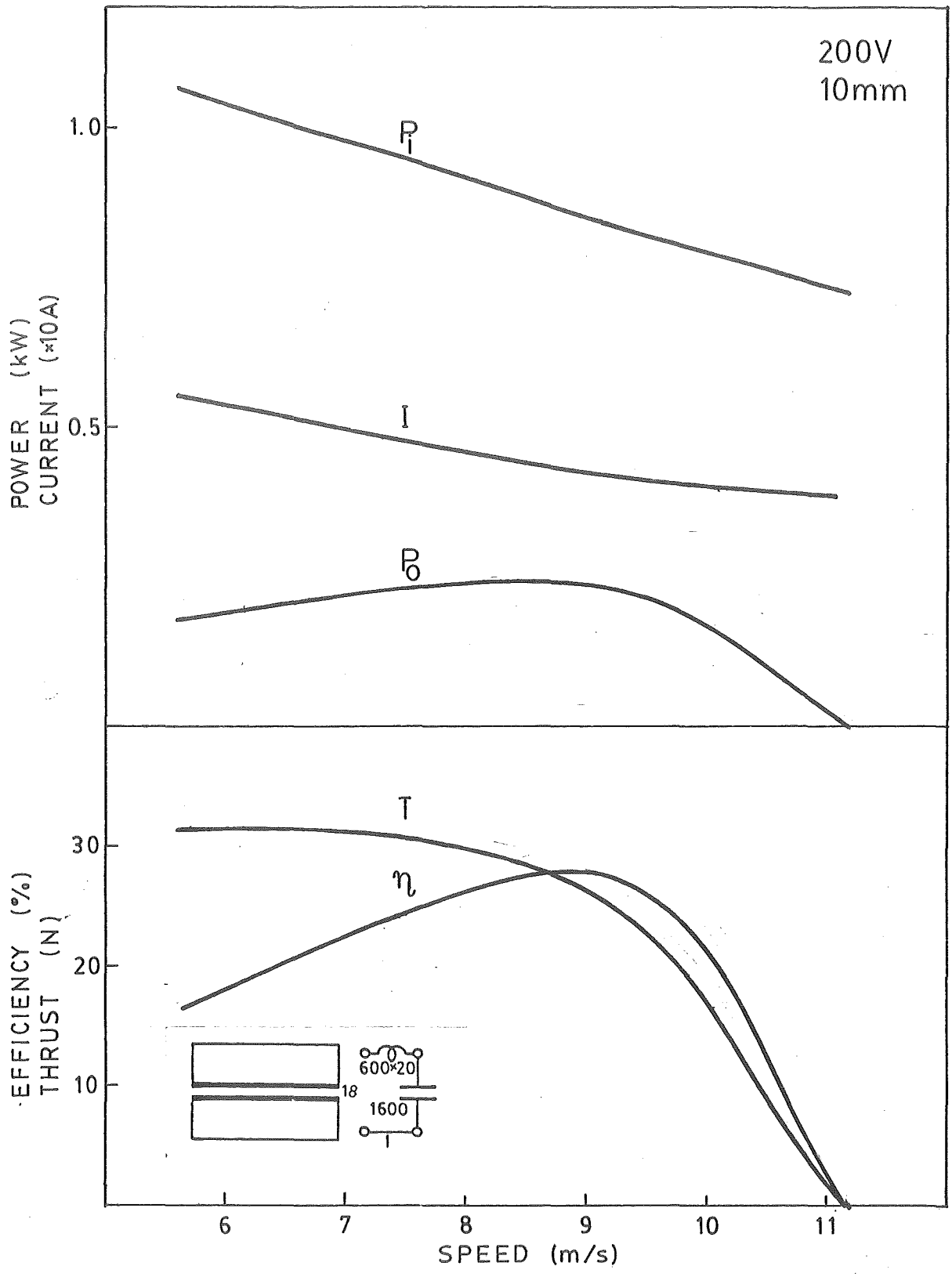
200V
10mm
1.0
0.5
POWER (kW)
CURRENT (×10A)
P_i
I
P_o
T
η
30
20
10
EFFICIENCY (%)
THRUST (N)
600×20
18
1600
6
7
8
9
10
11
SPEED (m/s)

Fig. A32

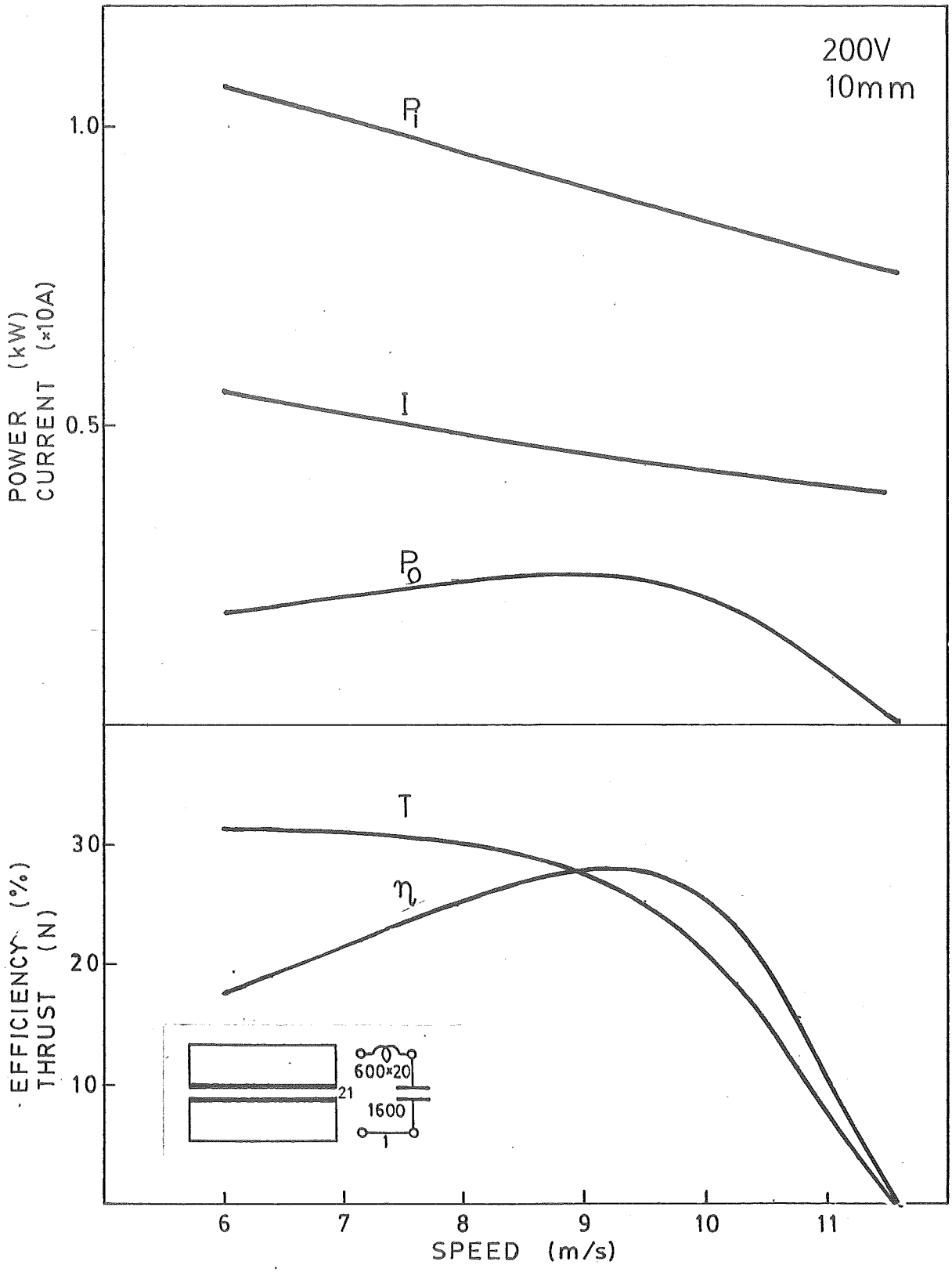
200V
10mm
P_i
I
P_o
POWER (kW)
CURRENT (×10A)
1.0
0.5
T
η
EFFICIENCY (%)
THRUST (N)
30
20
10
600×20
21
1600
1
6
7
8
9
10
11
SPEED (m/s)

Fig. A33

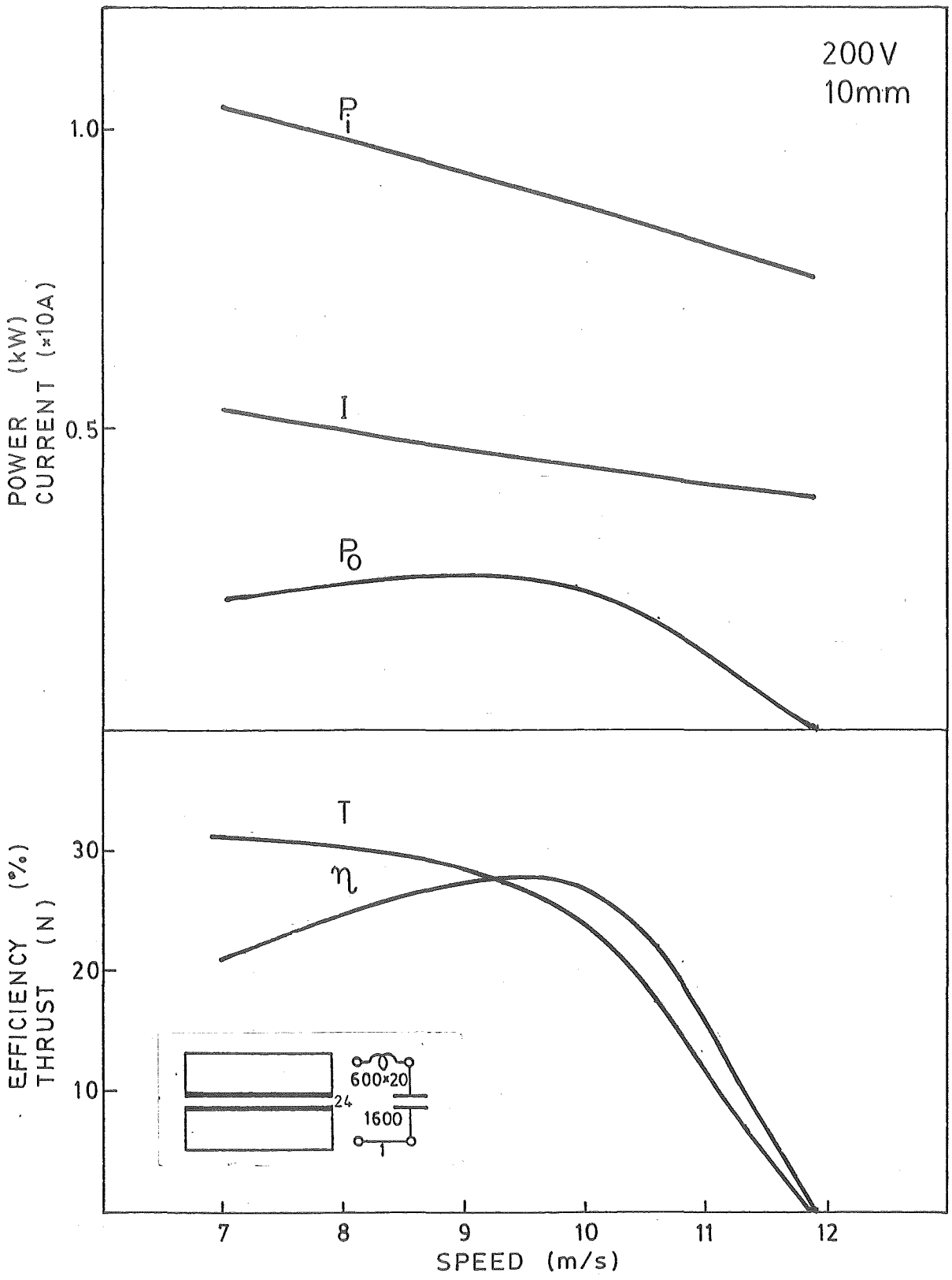
200V
10mm
P_i
I
P_o
POWER (kW)
CURRENT (×10A)
1.0
0.5
T
η
EFFICIENCY (%)
THRUST (N)
30
20
10
600×20
24
1600
1
7
8
9
10
11
12
SPEED (m/s)

Fig.A34

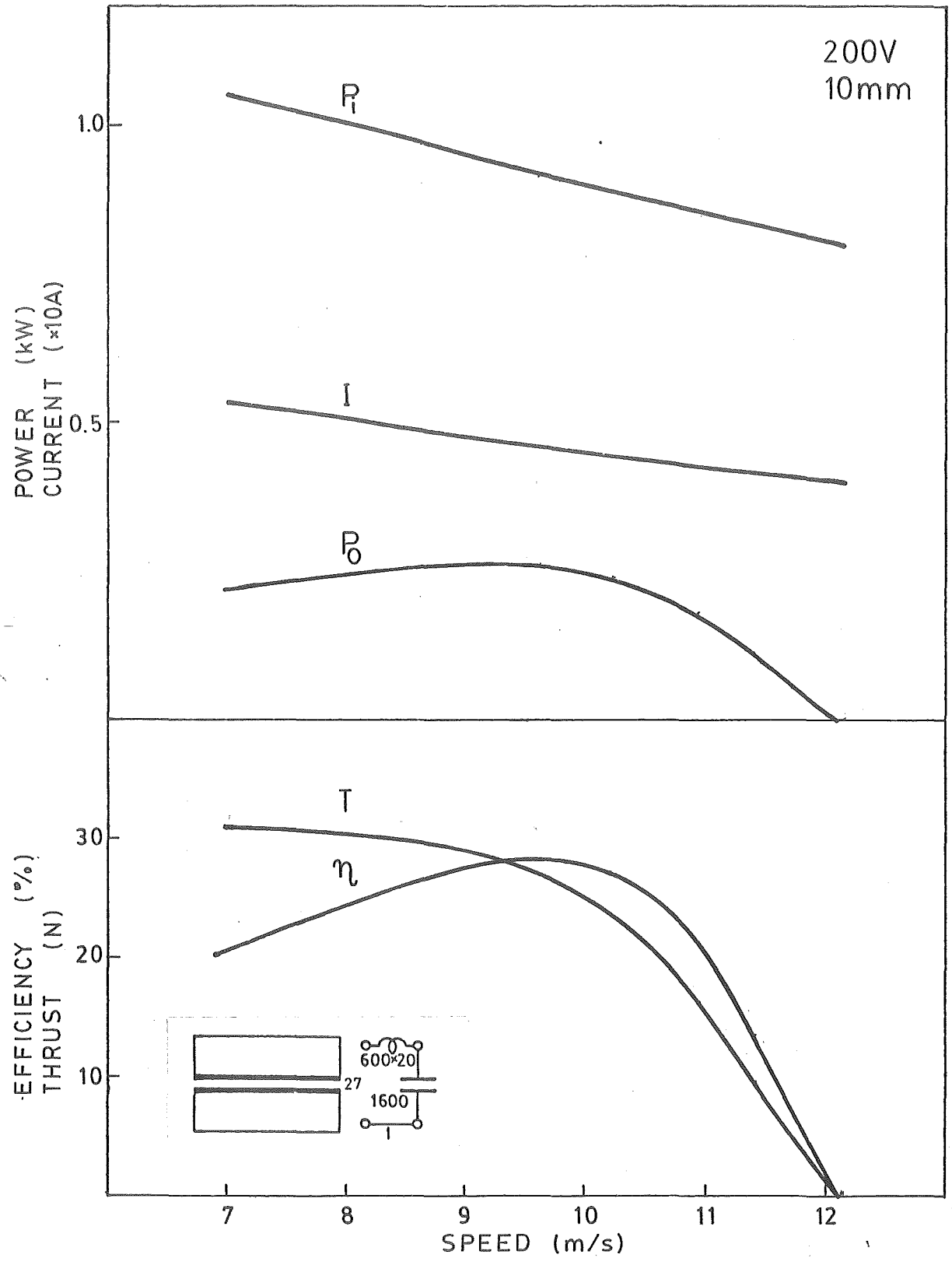
200V
10mm
P_I
I
P_O
1.0
0.5
POWER (kW)
CURRENT (×10A)
T
η
30
20
10
EFFICIENCY (%)
THRUST (N)
600×20
27
1600
7
8
9
10
11
12
SPEED (m/s)

Fig. A35

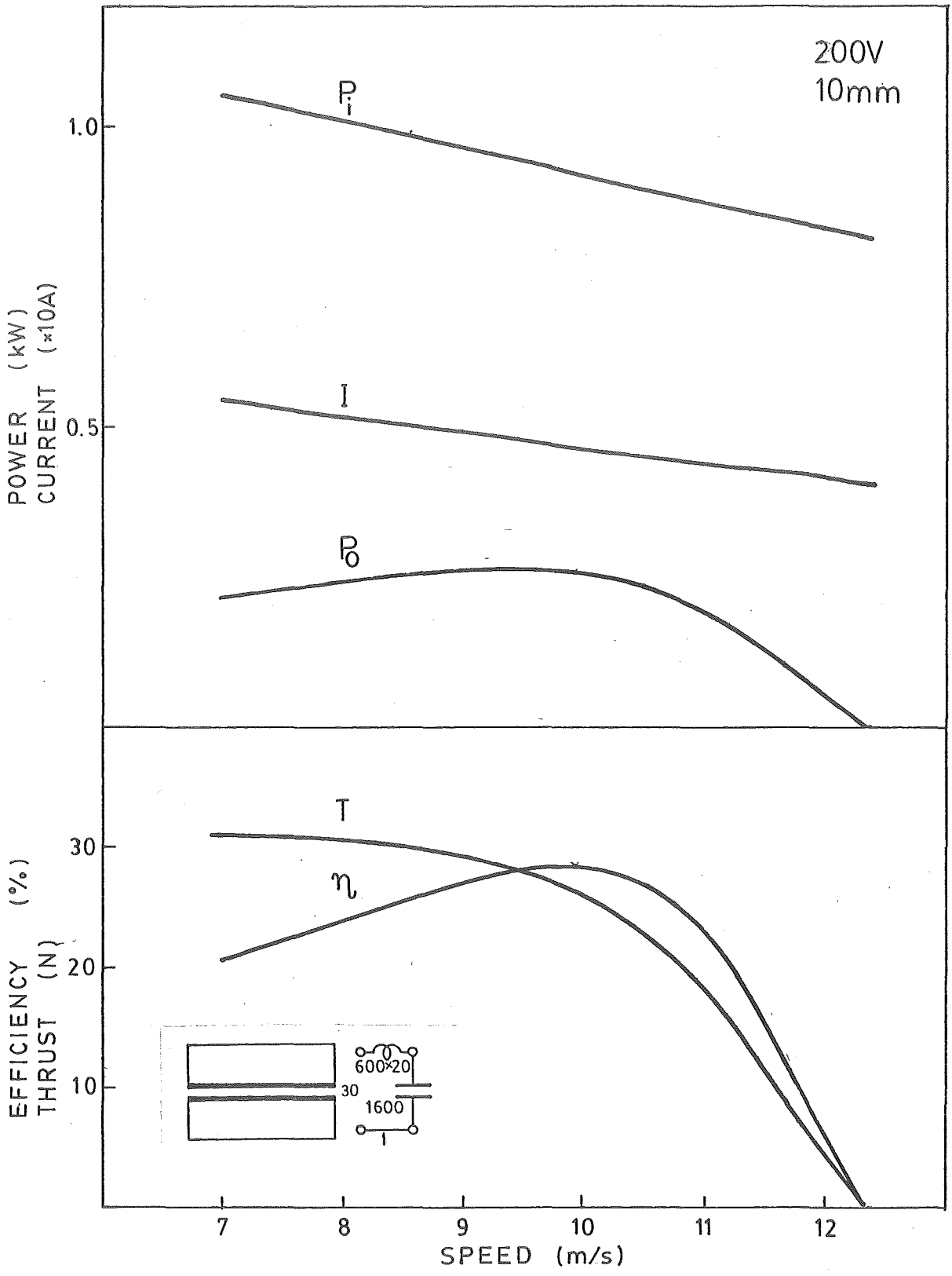
200V
10mm
P_i
I
P_o
POWER (kW)
CURRENT (×10A)
1.0
0.5
T
η
30
20
10
EFFICIENCY (%)
THRUST (N)
600×20
30
1600
1
7
8
9
10
11
12
SPEED (m/s)

Fig.A36

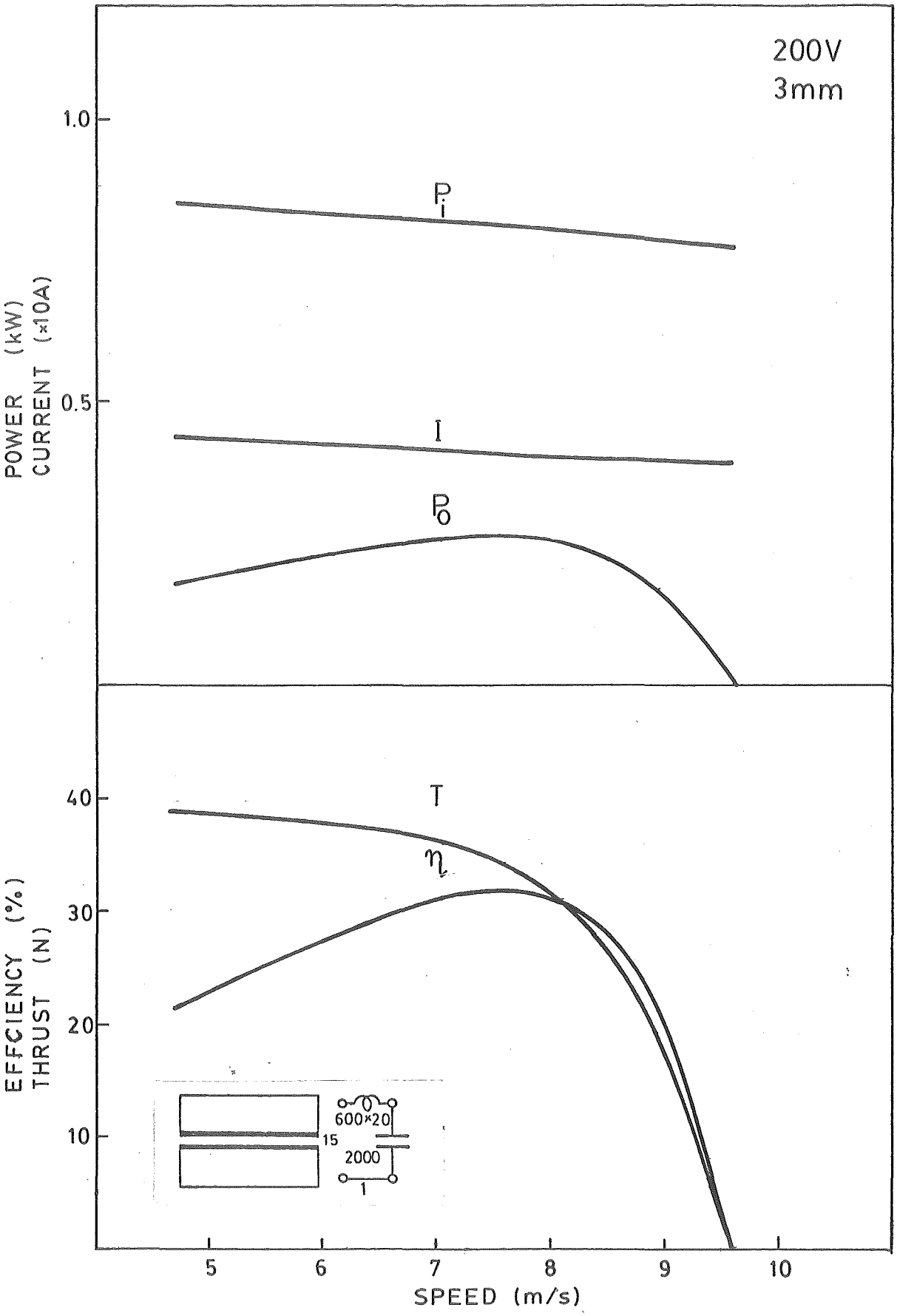
200V
3mm
1.0
0.5
POWER (kW)
CURRENT (×10A)
P_i
I
P_o
40
30
20
10
EFFCIENCY (%)
THRUST (N)
T
η
600×20
15
2000
1
5
6
7
8
9
10
SPEED (m/s)

Fig. A37

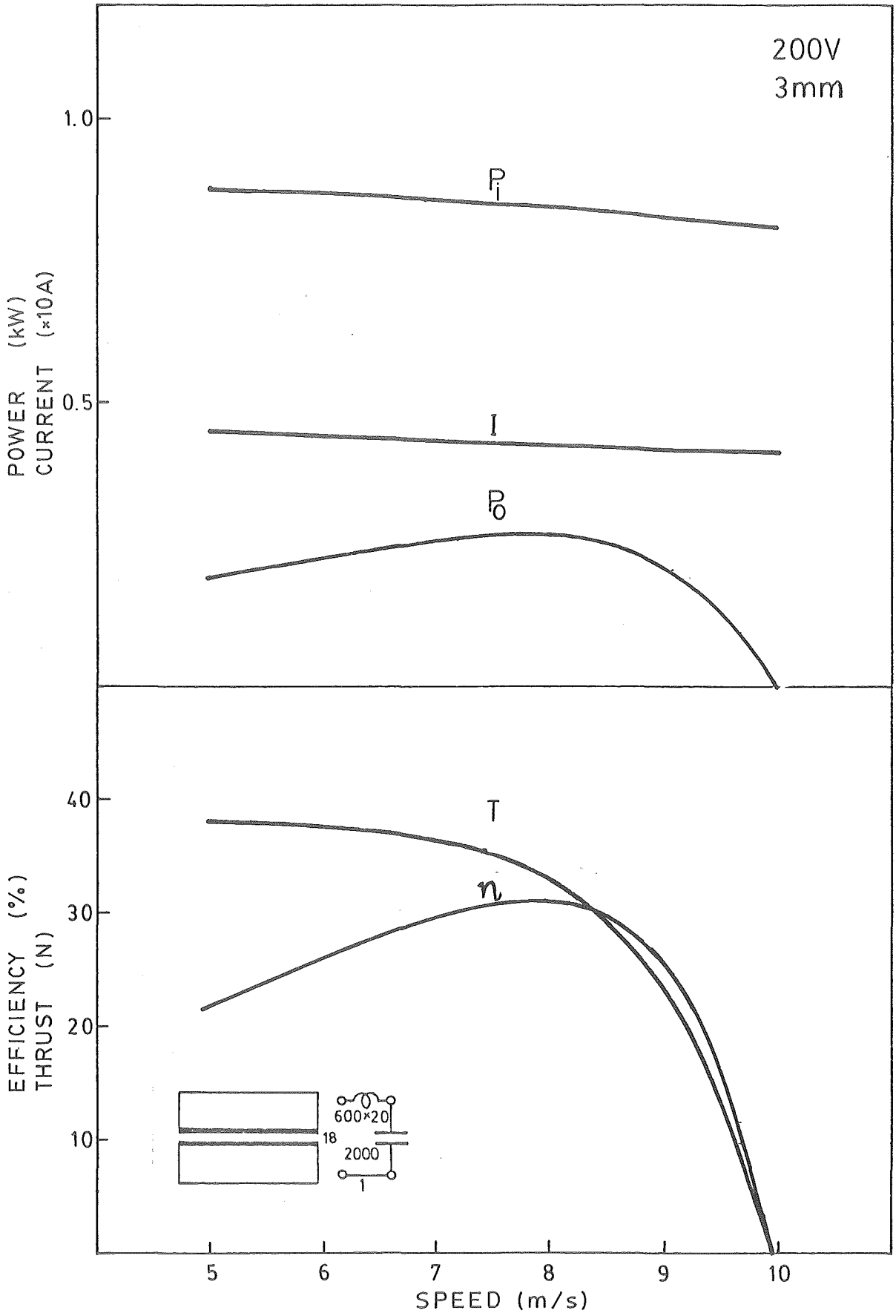
200V
3mm
1.0
0.5
POWER (kW)
CURRENT (×10A)
P_i
I
P_o
40
30
20
10
EFFICIENCY (%)
THRUST (N)
T
η
600×20
18
2000
1
5
6
7
8
9
10
SPEED (m/s)

Fig. A38

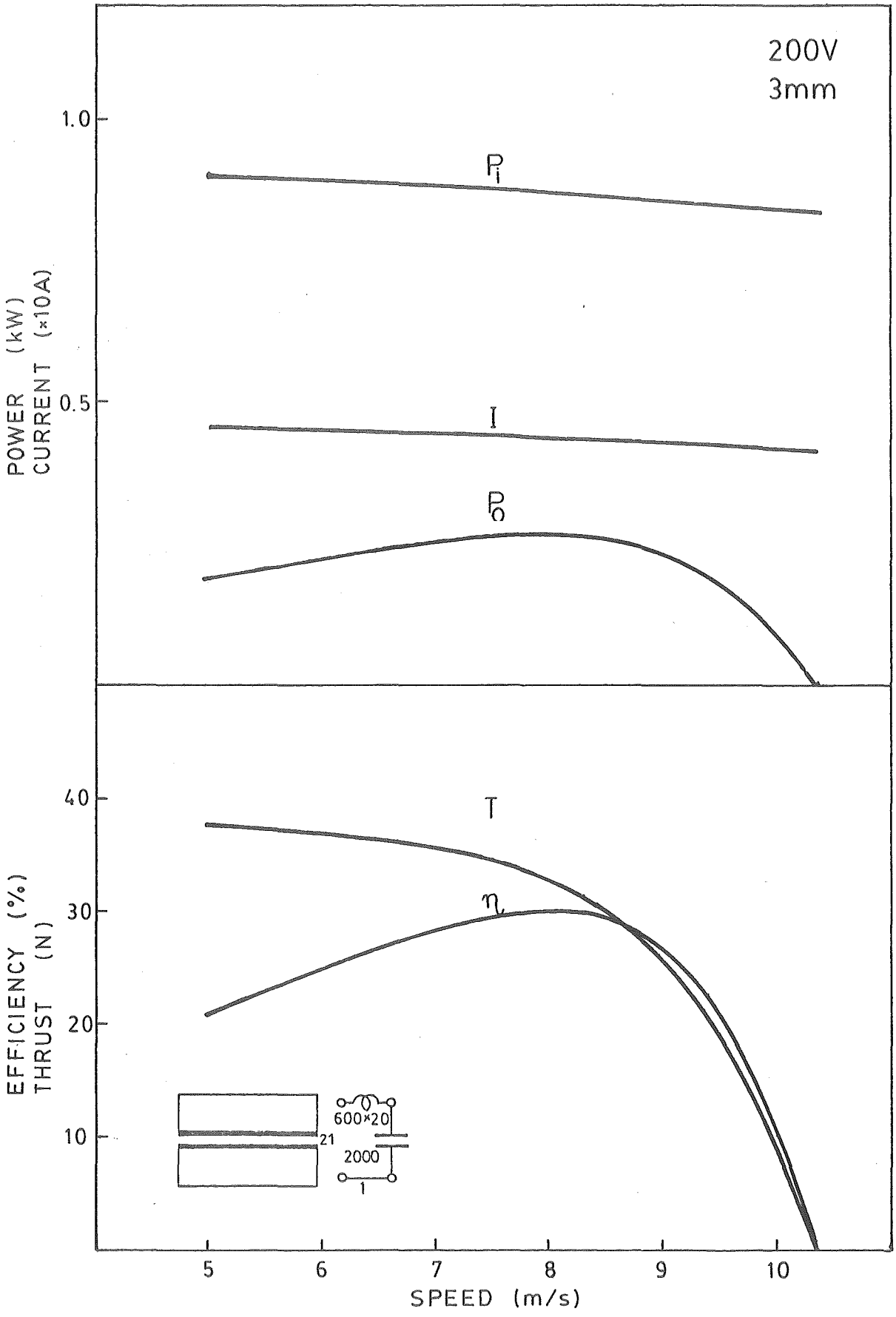
200V
3mm
1.0
0.5
POWER (kW)
CURRENT (×10A)
P_i
I
P_o
40
30
20
10
EFFICIENCY (%)
THRUST (N)
T
η
600×20
21
2000
1
5
6
7
8
9
10
SPEED (m/s)

Fig. A39

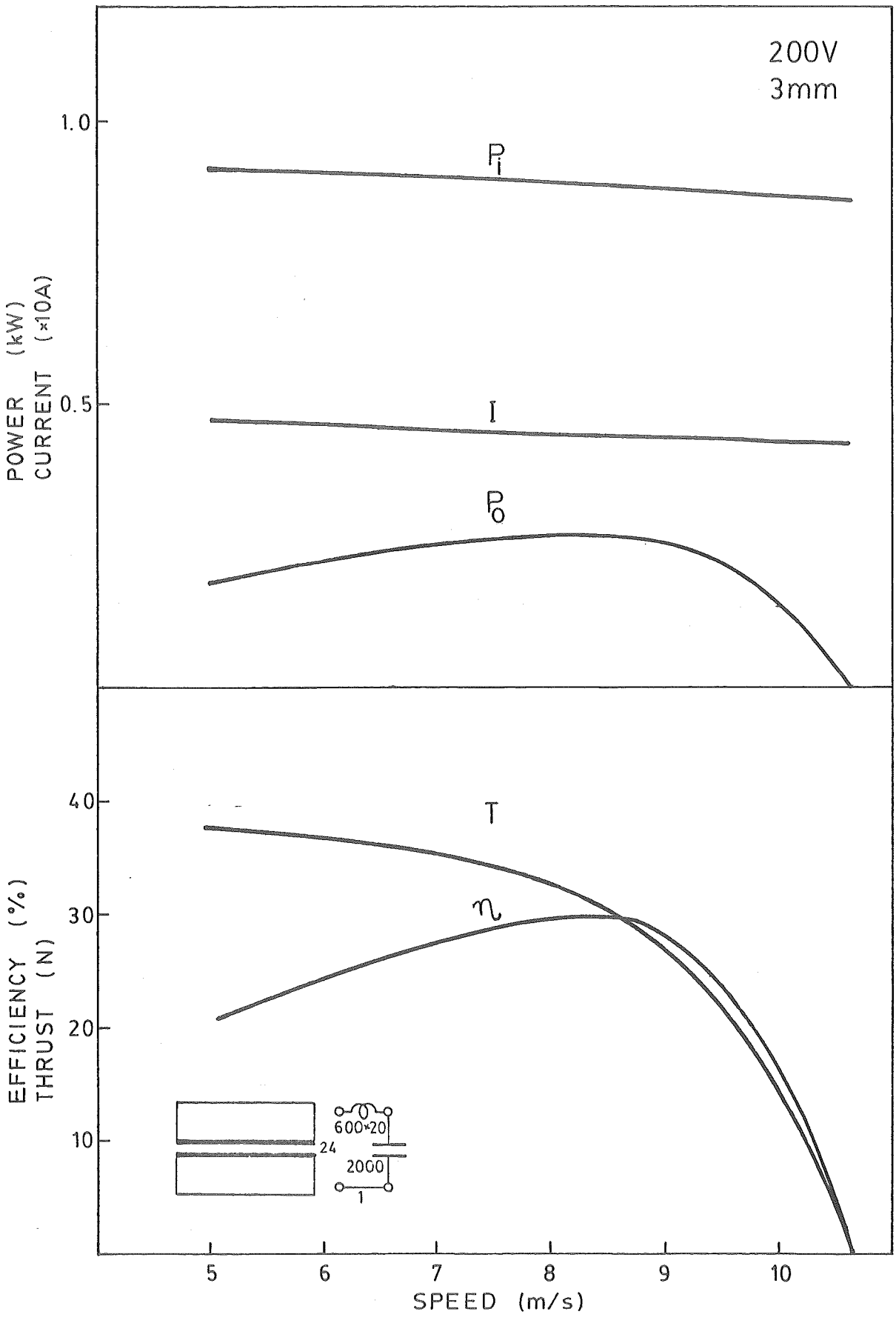
200V
3mm
1.0
0.5
POWER (kW)
CURRENT (×10A)
P_i
I
P_o
40
30
20
10
EFFICIENCY (%)
THRUST (N)
T
η
600×20
24
2000
1
5
6
7
8
9
10
SPEED (m/s)

Fig. A40

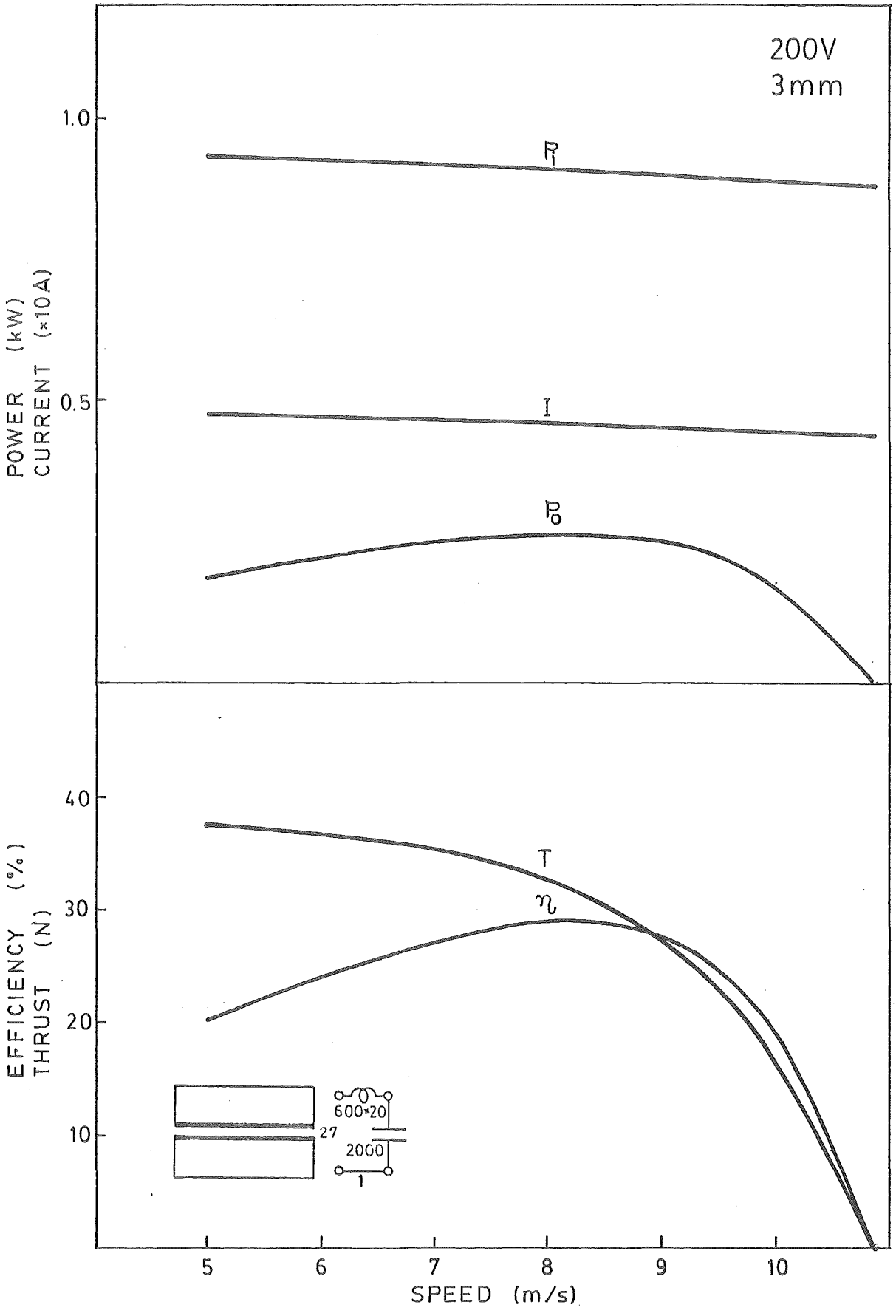
200V
3mm
1.0
0.5
POWER (kW)
CURRENT (×10A)
P_I
I
P_O
40
30
20
10
EFFICIENCY (%)
THRUST (N)
T
η
600×20
27
2000
1
5
6
7
8
9
10
SPEED (m/s)

Fig.A41

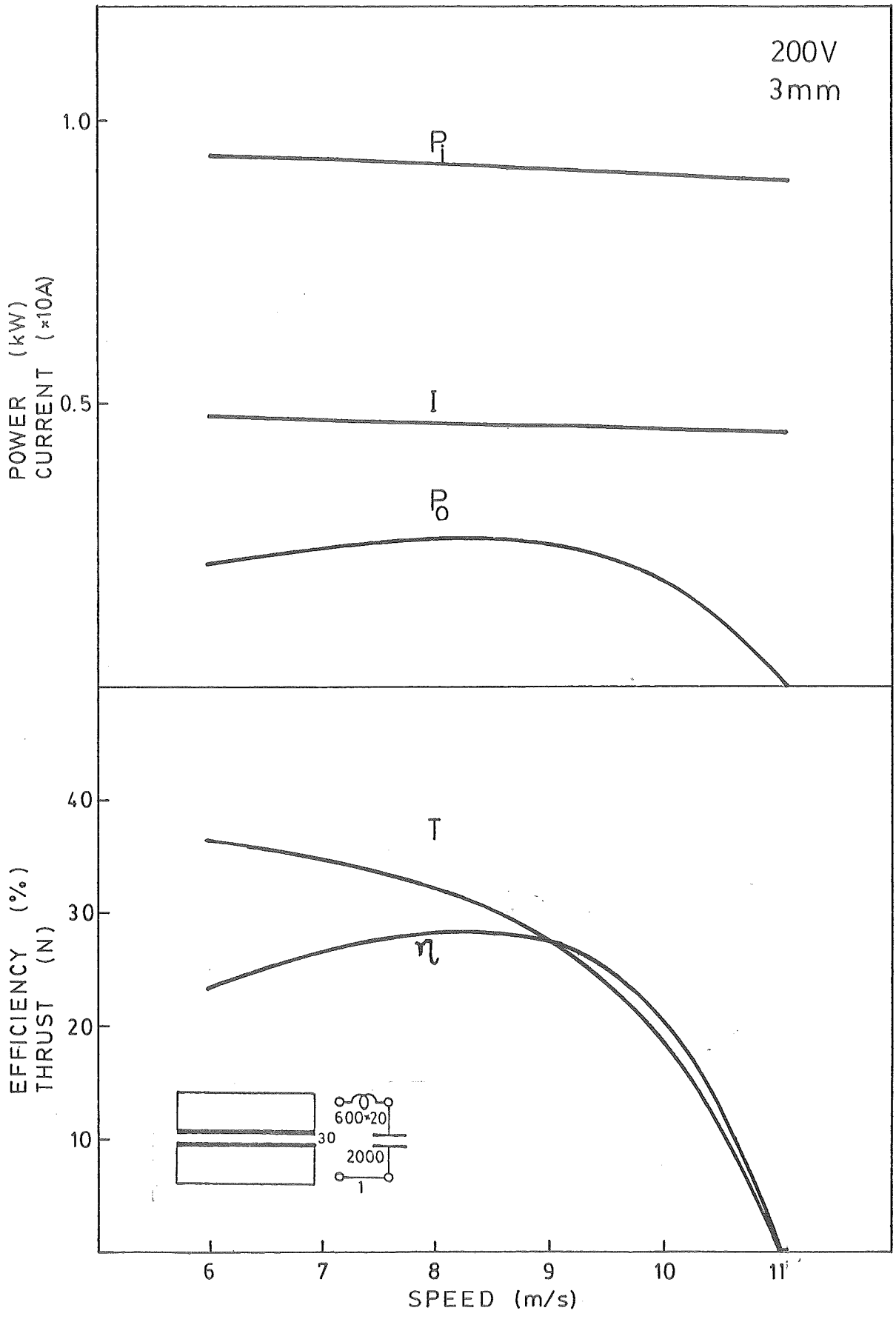
200V
3mm
1.0
0.5
POWER (kW)
CURRENT (×10A)
P_i
I
P_o
40
30
20
10
EFFICIENCY (%)
THRUST (N)
T
η
600×20
30
2000
1
6
7
8
9
10
11
SPEED (m/s)

Fig. A42

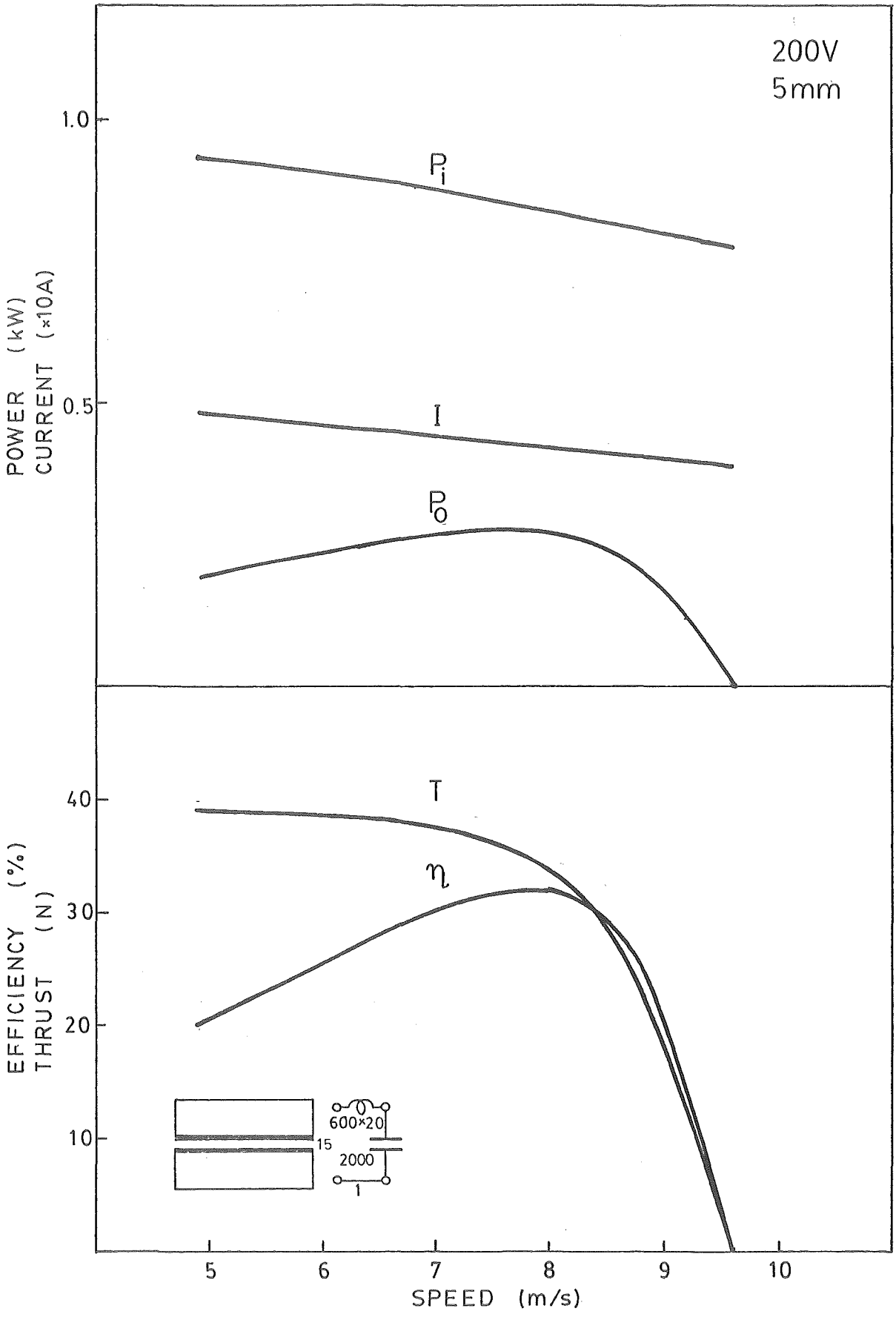
200V
5mm
1.0
0.5
POWER (kW)
CURRENT (×10A)
P_i
I
P_o
40
30
20
10
EFFICIENCY (%)
THRUST (N)
T
η
600×20
15
2000
1
5
6
7
8
9
10
SPEED (m/s)

Fig. A43

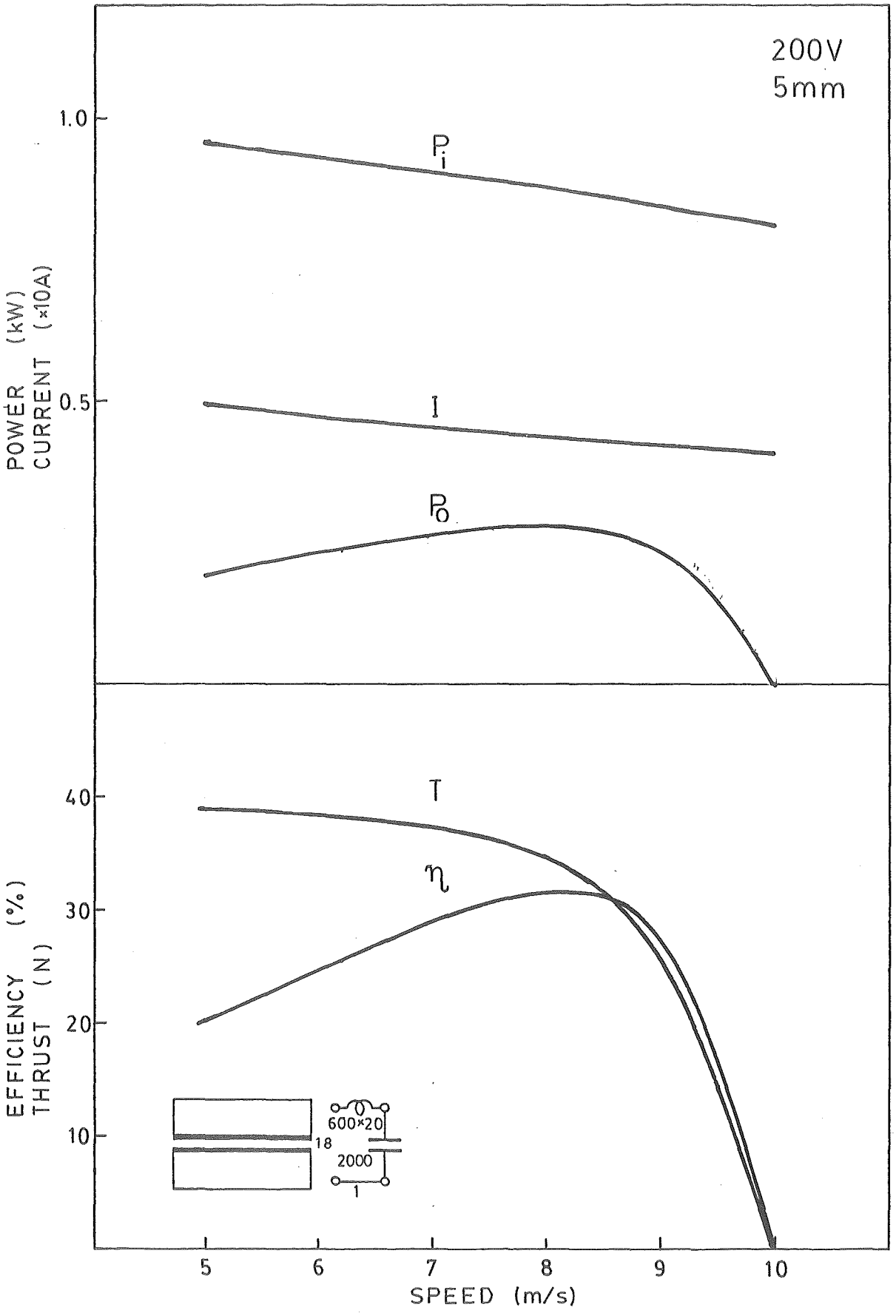
200V
5mm
1.0
0.5
POWER (kW)
CURRENT (×10A)
P_i
I
P_o
40
30
20
10
EFFICIENCY (%)
THRUST (N)
T
η
600×20
18
2000
1
5
6
7
8
9
10
SPEED (m/s)

Fig. A44

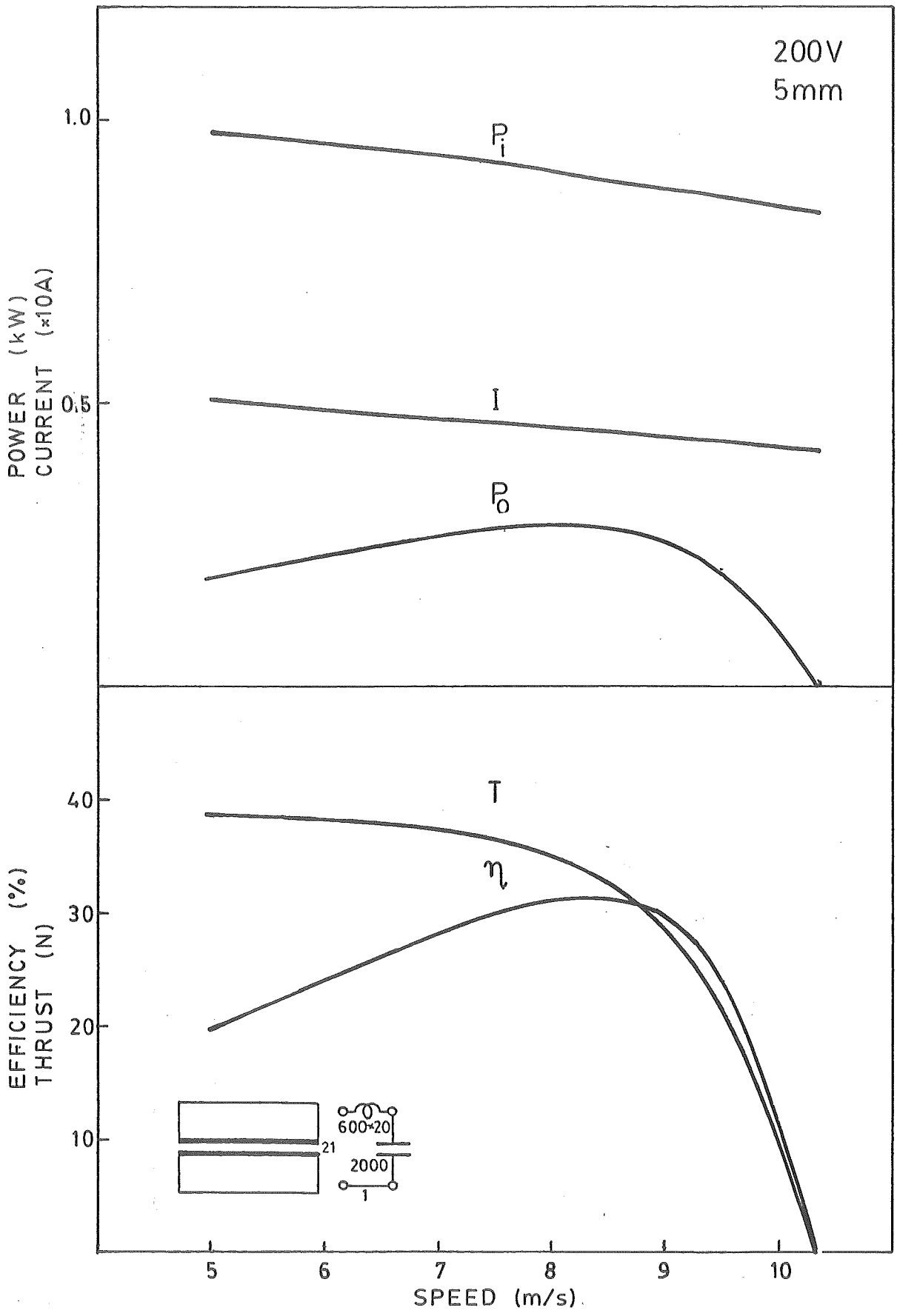
200V
5mm
1.0
0.5
POWER (kW)
CURRENT (×10A)
P_i
I
P_o
40
30
20
10
EFFICIENCY (%)
THRUST (N)
T
η
600×20
21
2000
1
5
6
7
8
9
10
SPEED (m/s)

Fig. A45

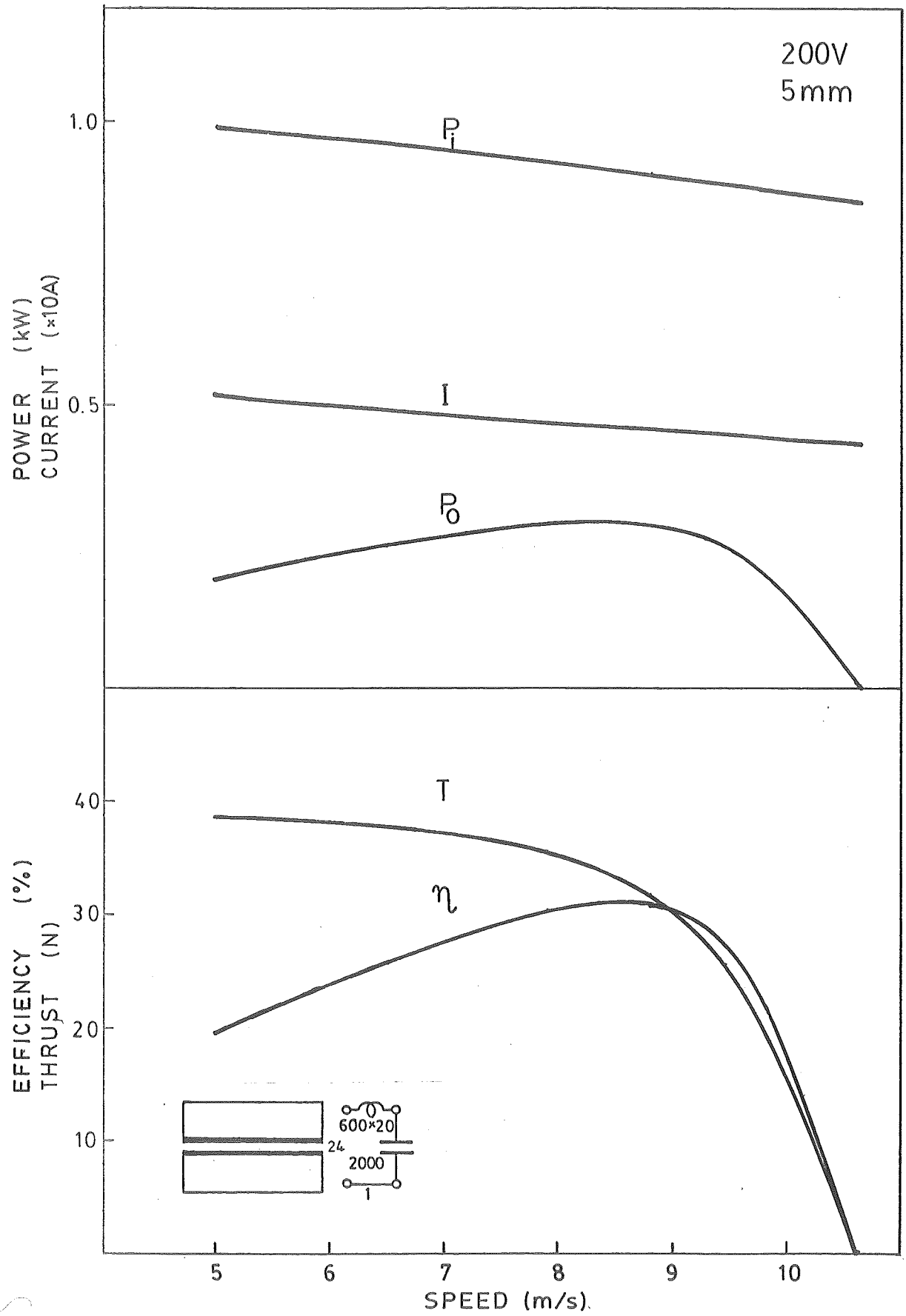
200V
5mm
1.0
0.5
POWER (kW)
CURRENT (×10A)
P_i
I
P_o
40
30
20
10
EFFICIENCY (%)
THRUST (N)
T
η
600×20
24
2000
1
5
6
7
8
9
10
SPEED (m/s)

Fig.A46

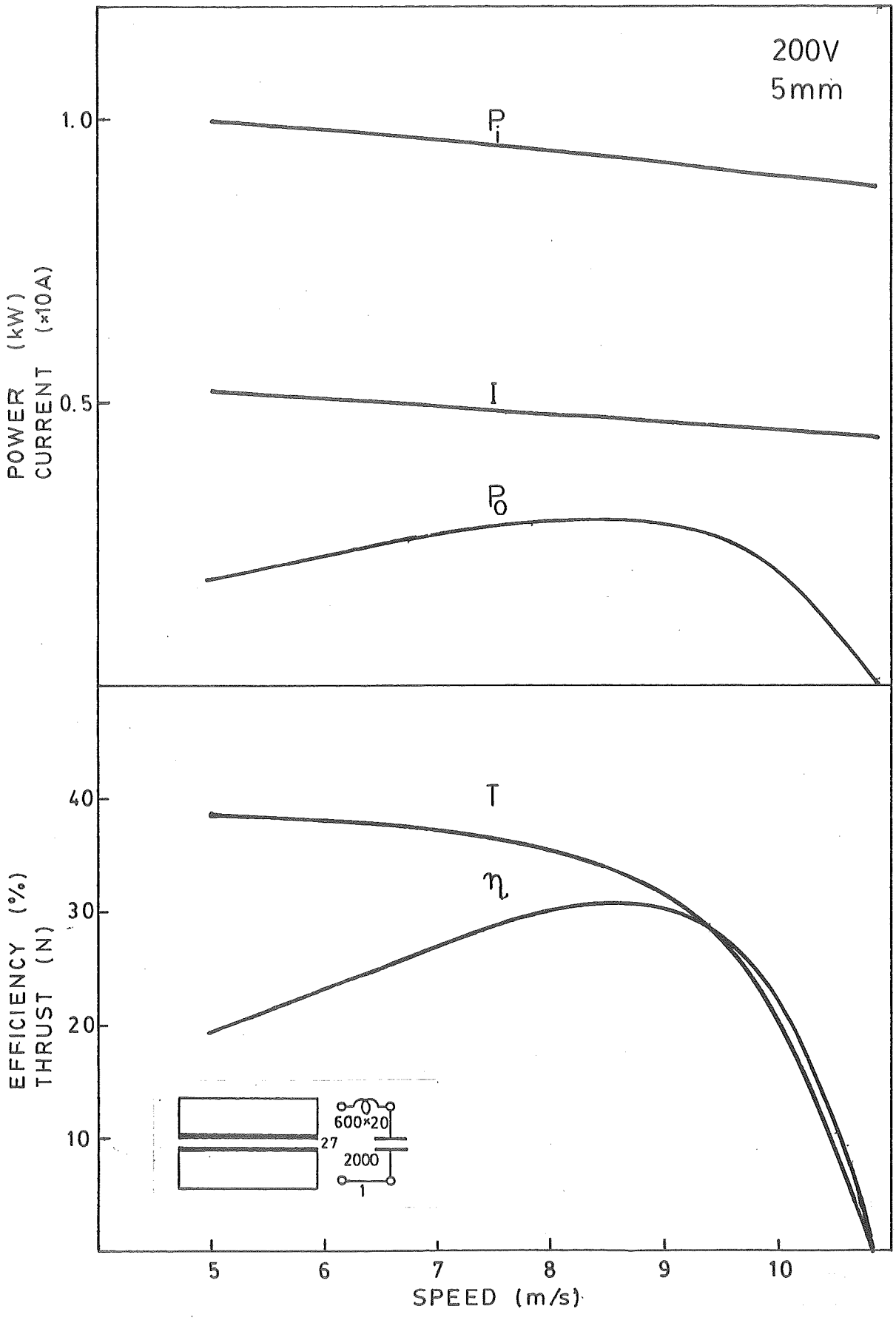
200V
5mm
1.0
0.5
P_i
I
P_o
POWER (kW)
CURRENT (×10A)
40
30
20
10
T
η
EFFICIENCY (%)
THRUST (N)
600×20
27
2000
1
5
6
7
8
9
10
SPEED (m/s)

Fig.A47

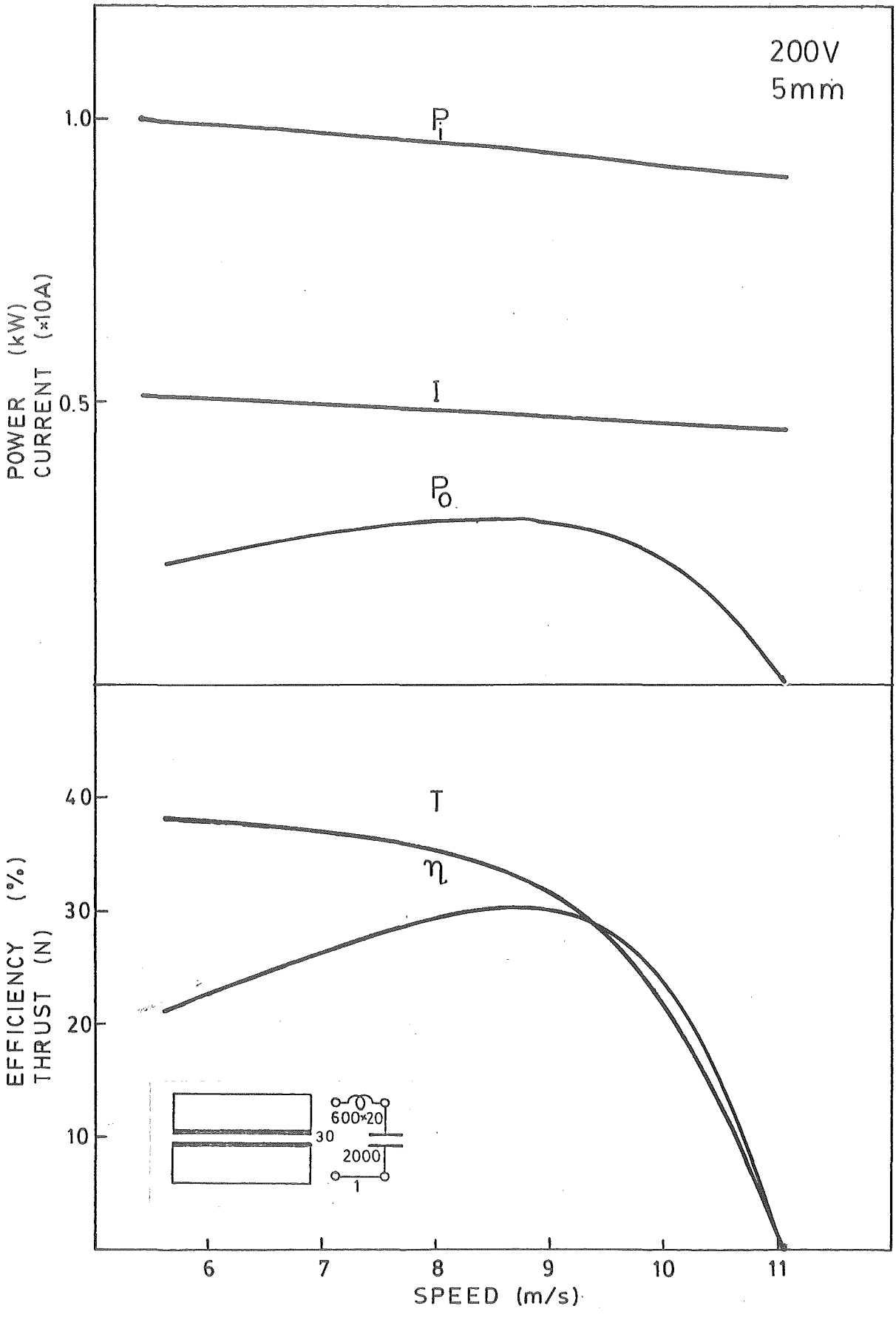
200V
5mm
1.0
0.5
P_i
I
P_o
POWER (kW)
CURRENT (×10A)
40
30
20
10
T
η
EFFICIENCY (%)
THRUST (N)
600×20
30
2000
1
6
7
8
9
10
11
SPEED (m/s)

Fig. A48

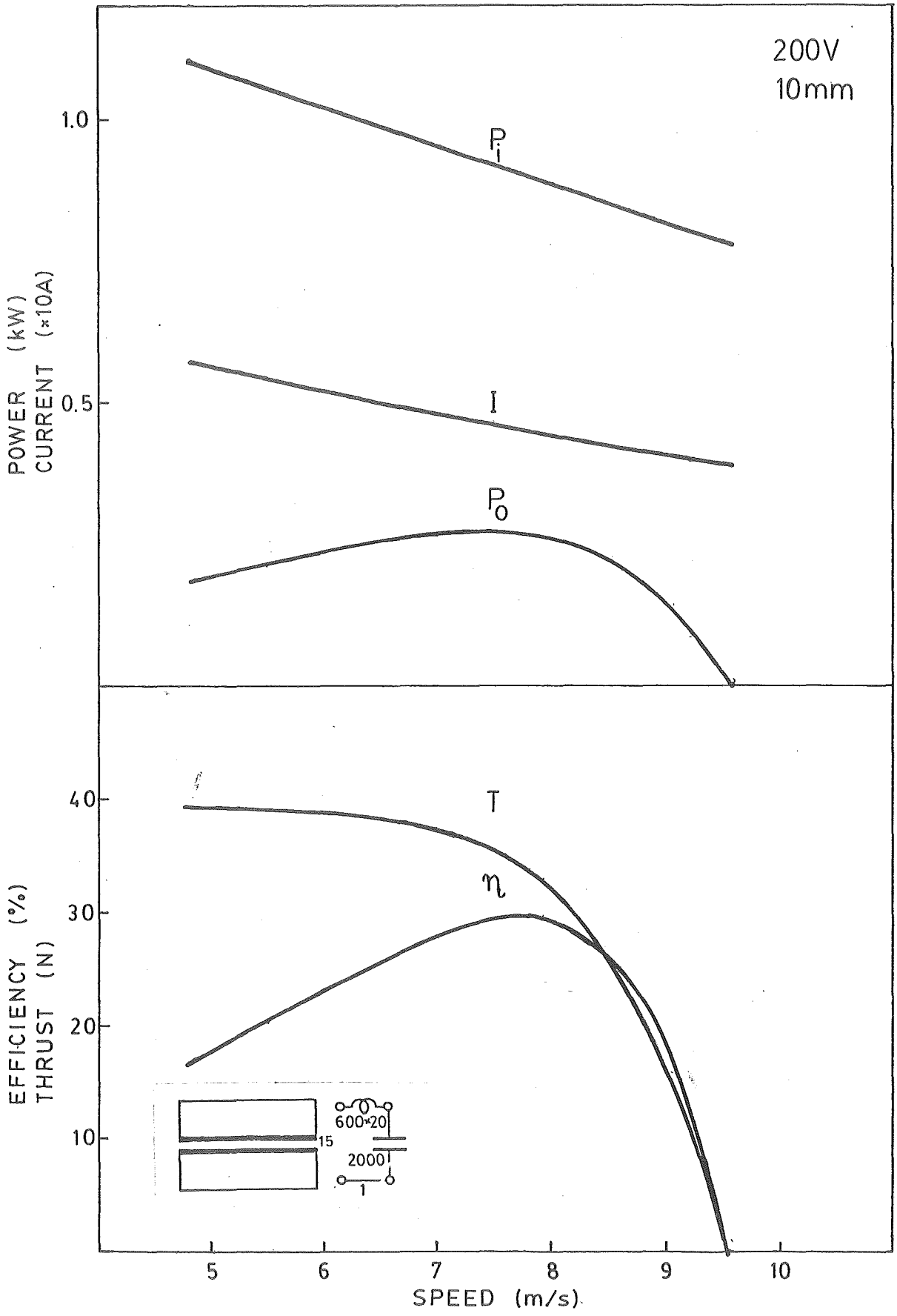
200V
10mm
1.0
0.5
POWER (kW)
CURRENT (×10A)
P_i
I
P_o
40
30
20
10
EFFICIENCY (%)
THRUST (N)
T
η
600×20
15
2000
1
5
6
7
8
9
10
SPEED (m/s)

Fig. A49

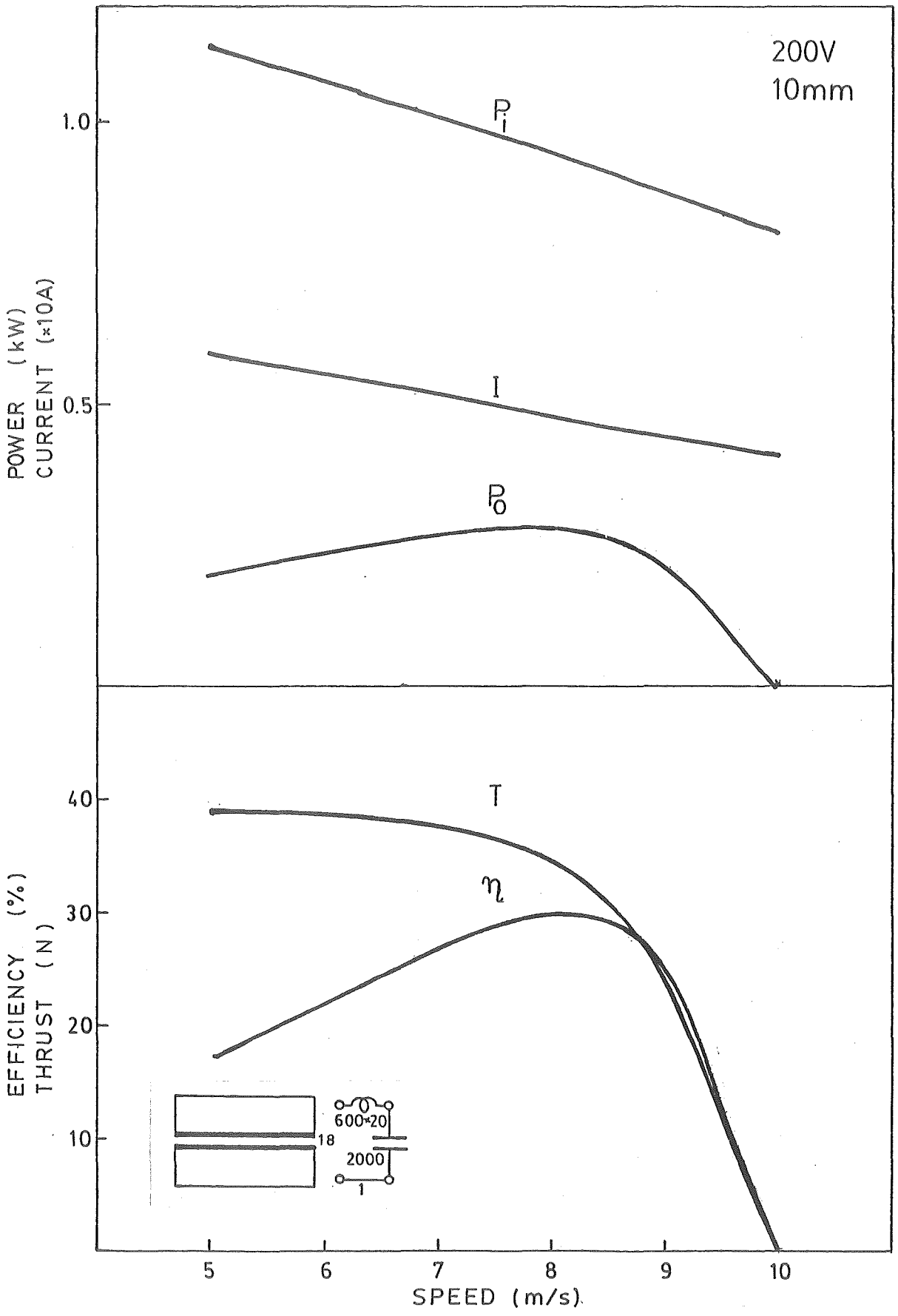
200V
10mm
P_i
I
P_o
POWER (kW)
CURRENT (×10A)
1.0
0.5
T
η
EFFICIENCY (%)
THRUST (N)
40
30
20
10
600×20
18
2000
1
5
6
7
8
9
10
SPEED (m/s)

Fig. A50

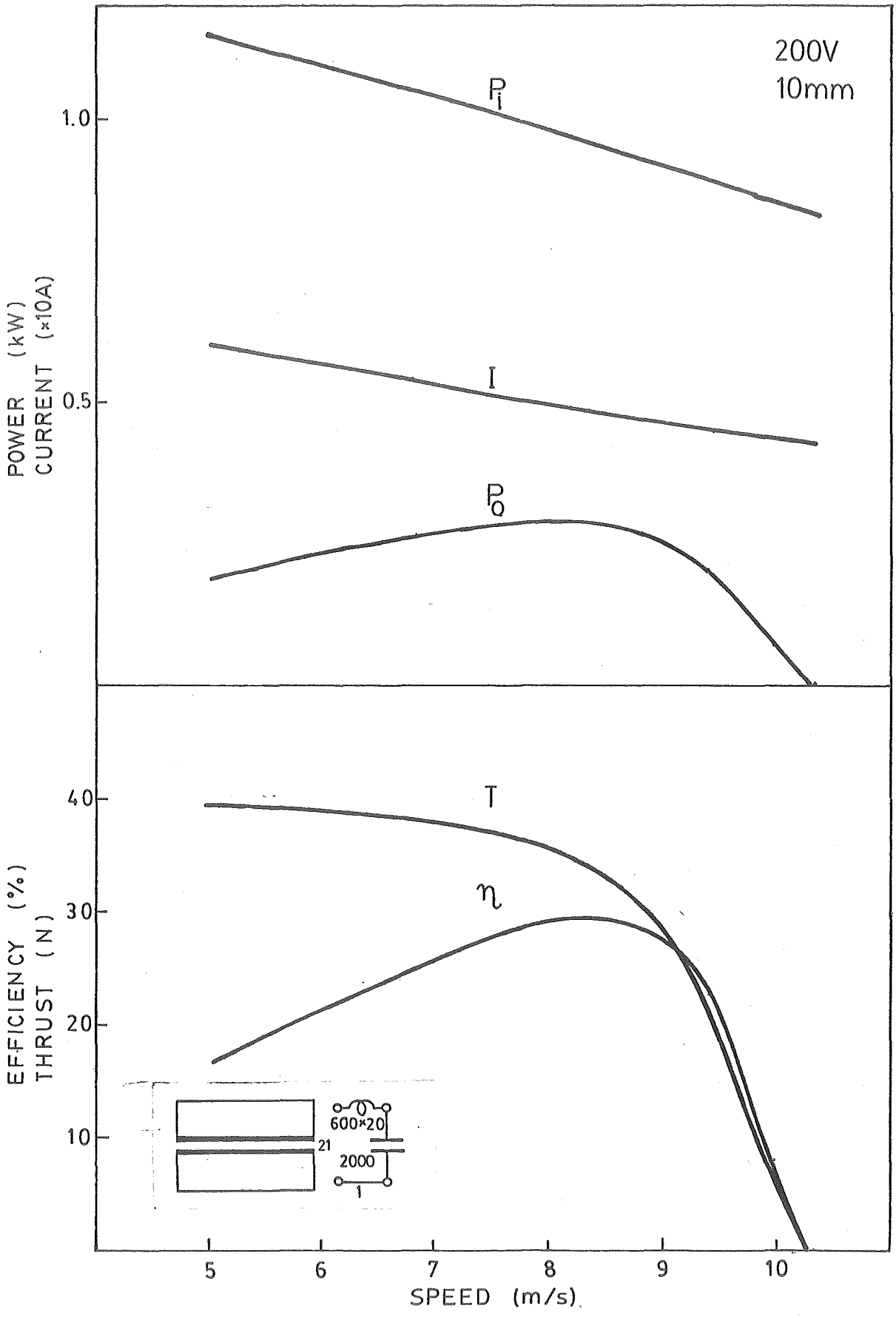
200V
10mm
P_i
I
P_o
POWER (kW)
CURRENT (×10A)
1.0
0.5
T
η
EFFICIENCY (%)
THRUST (N)
40
30
20
10
600×20
21
2000
1
5
6
7
8
9
10
SPEED (m/s)

Fig. A51

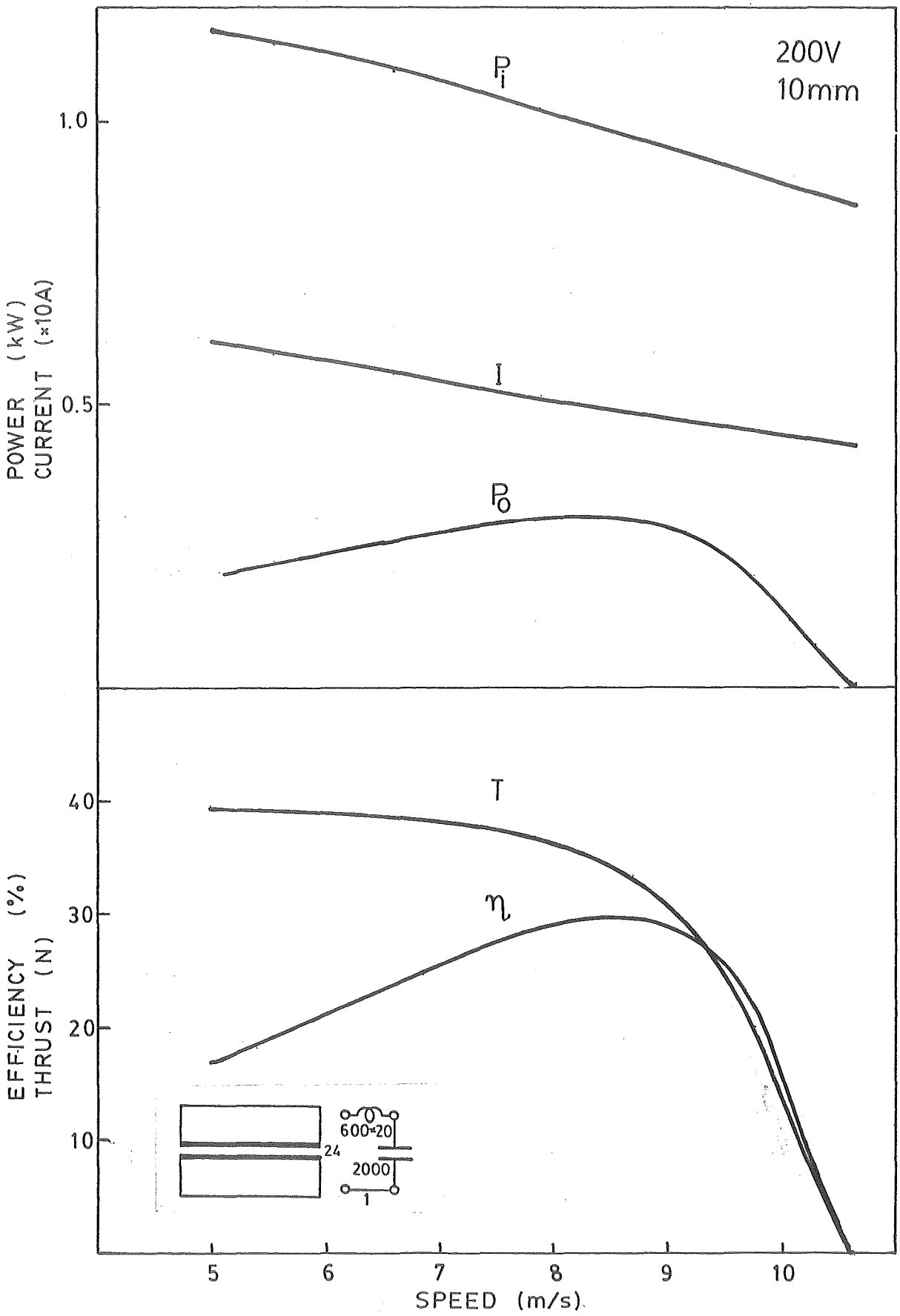
200V
10mm
P_i
I
P_o
POWER (kW)
CURRENT (×10A)
1.0
0.5
T
η
EFFICIENCY (%)
THRUST (N)
40
30
20
10
600×20
24
2000
1
5
6
7
8
9
10
SPEED (m/s)

Fig. A52

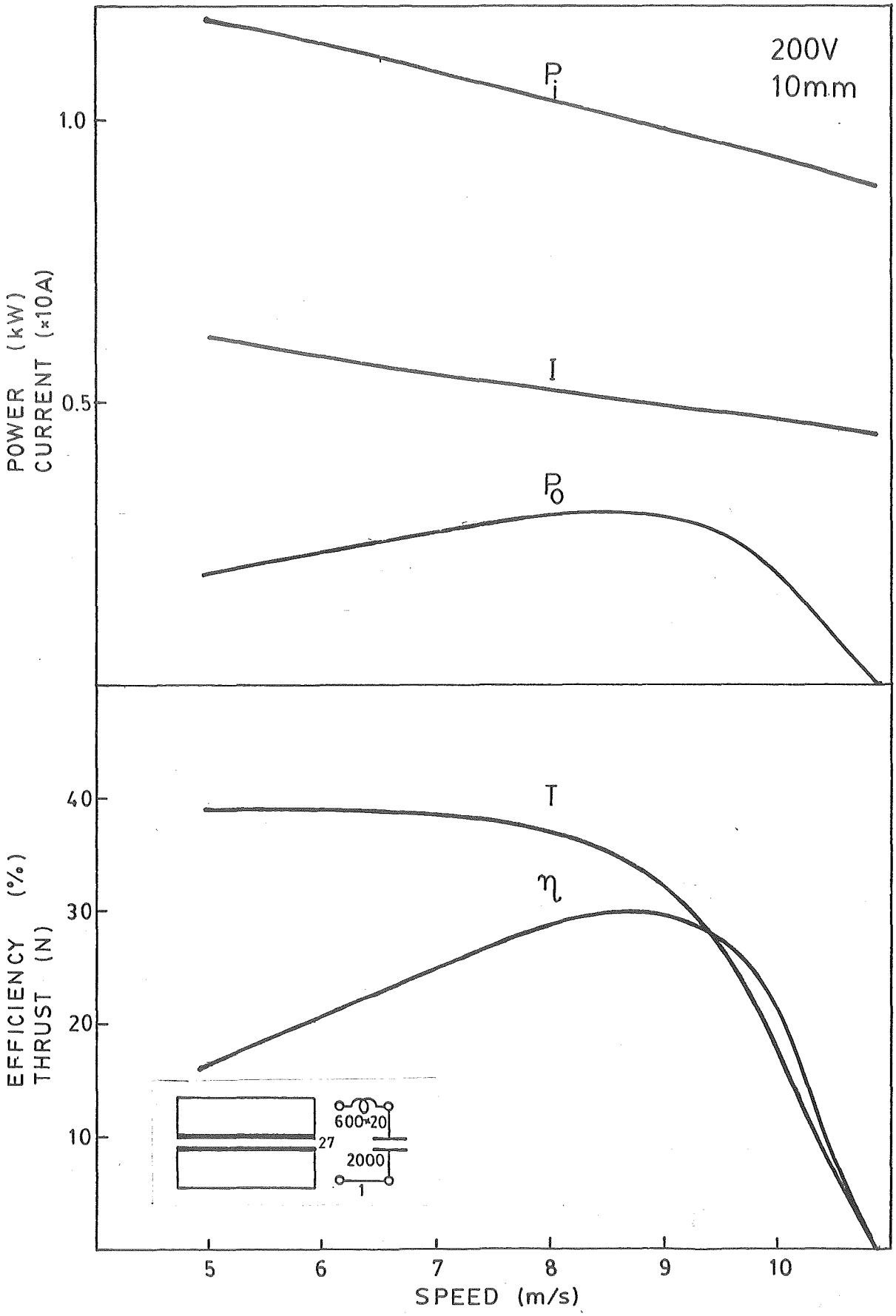
200V
10mm
P_i
I
P_o
POWER (kW)
CURRENT (×10A)
1.0
0.5
T
η
EFFICIENCY (%)
THRUST (N)
40
30
20
10
600×20
27
2000
1
5
6
7
8
9
10
SPEED (m/s)

Fig. A53

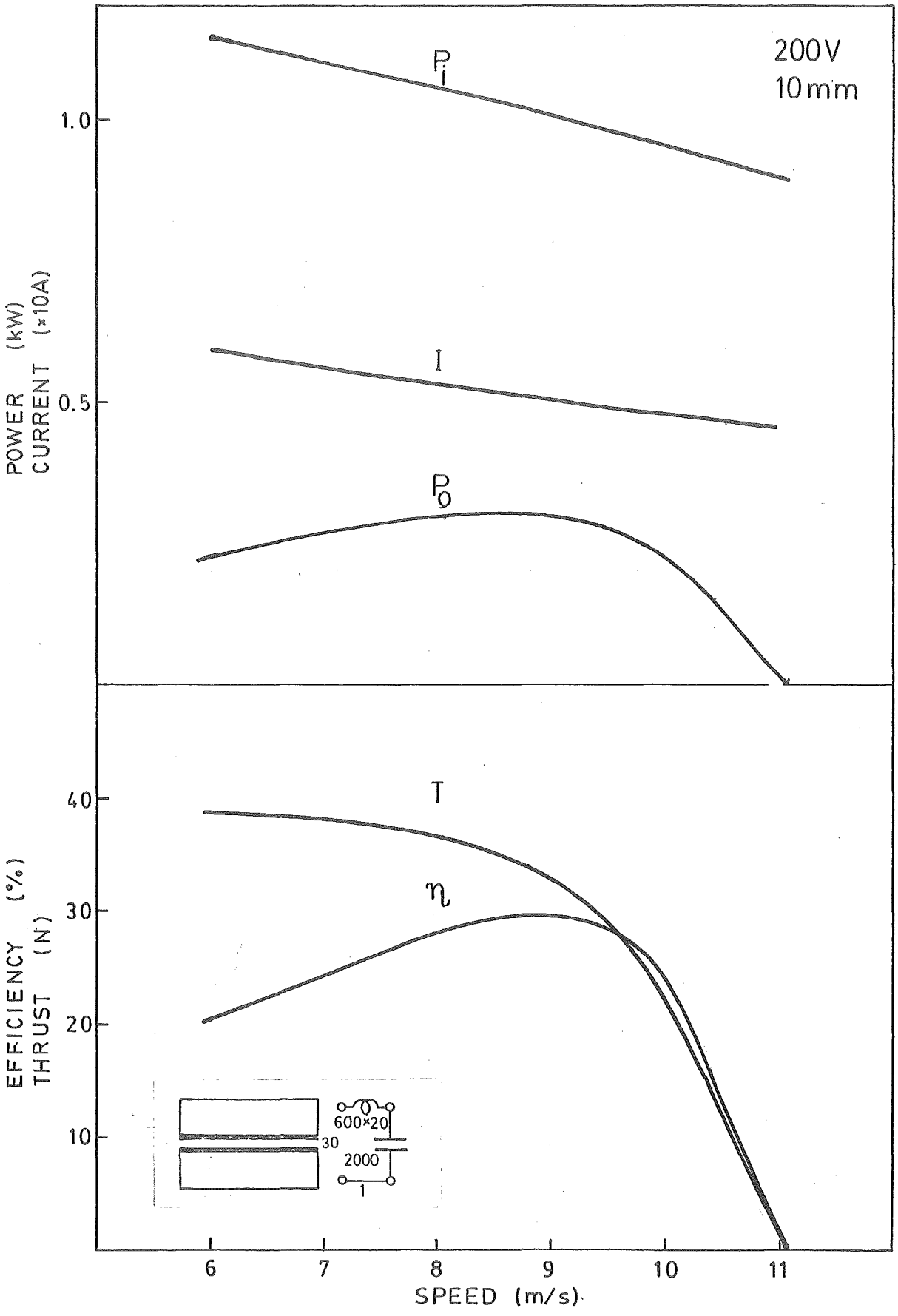
200V
10mm
P_i
I
P_o
POWER (kW)
CURRENT (×10A)
1.0
0.5
T
η
EFFICIENCY (%)
THRUST (N)
40
30
20
10
600×20
30
2000
1
6
7
8
9
10
11
SPEED (m/s)

Fig. A54

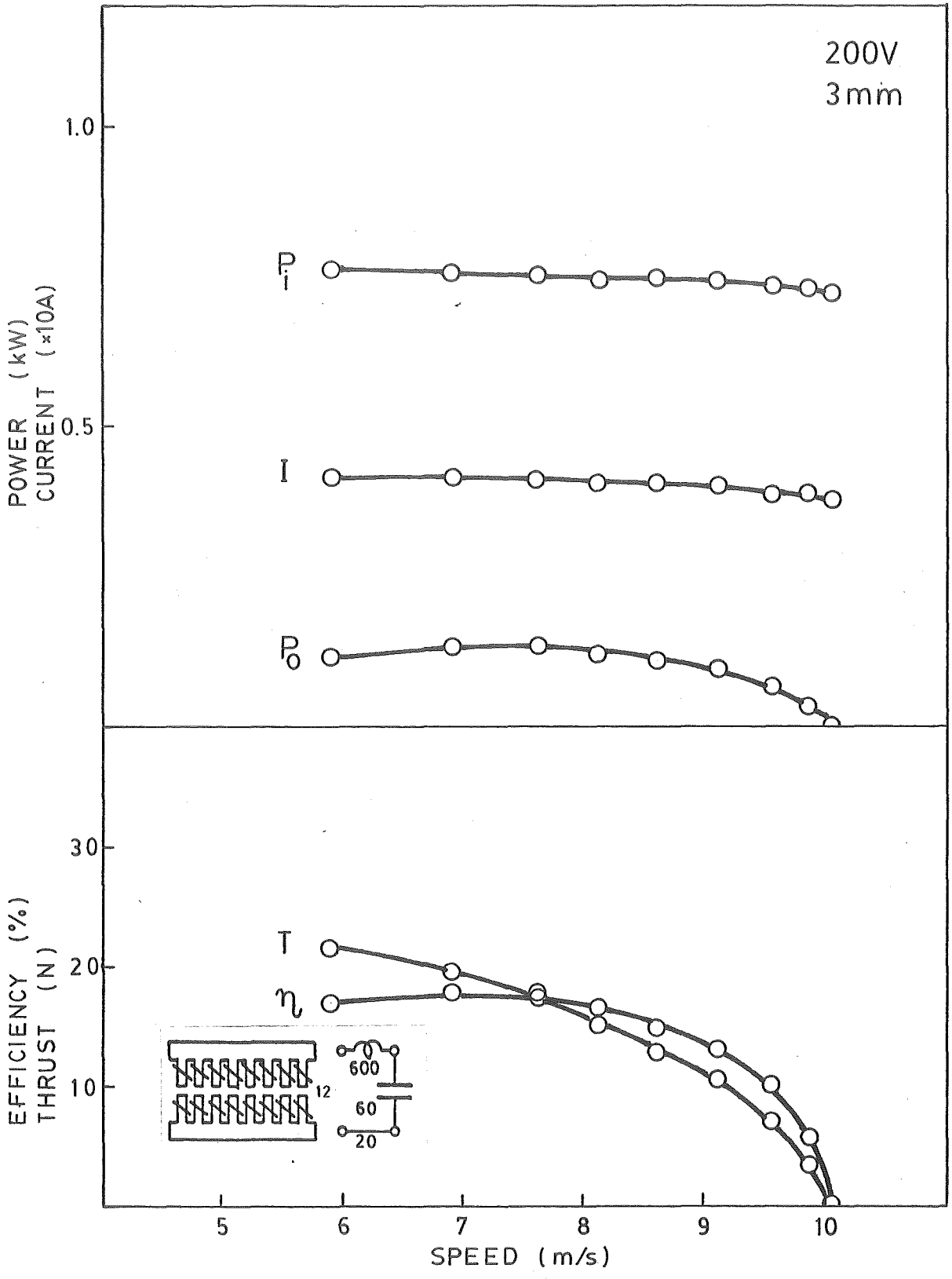
200V
3mm
1.0
0.5
POWER (kW)
CURRENT (×10A)
P_i
I
P_o
30
20
10
EFFICIENCY (%)
THRUST (N)
T
η
600
60
20
12
5
6
7
8
9
10
SPEED (m/s)

Fig. A55

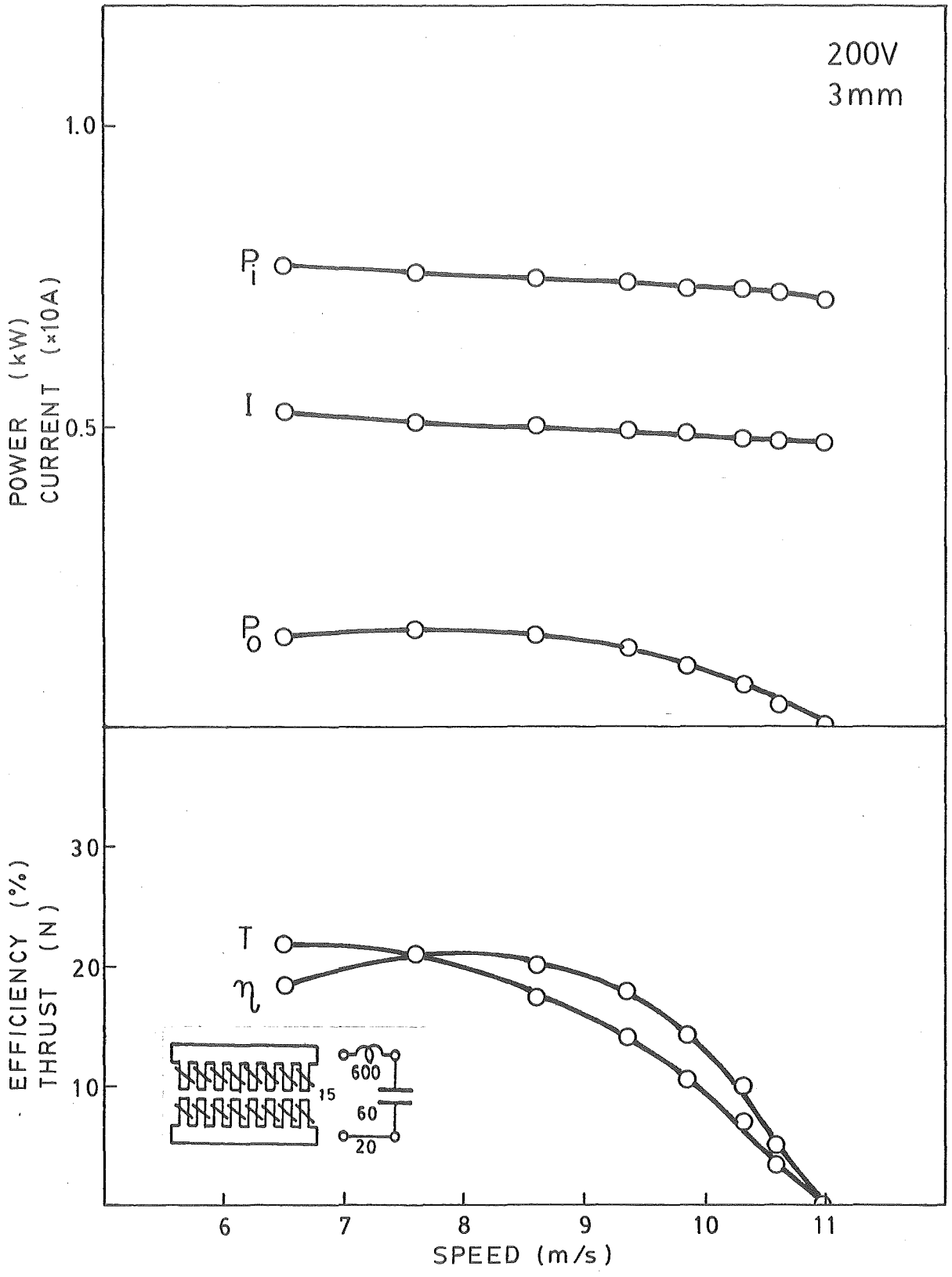
200V
3mm
1.0
0.5
POWER (kW)
CURRENT (×10A)
P_i
I
P_o
30
20
10
EFFICIENCY (%)
THRUST (N)
T
η
600
60
20
15
6
7
8
9
10
11
SPEED (m/s)

Fig. A56

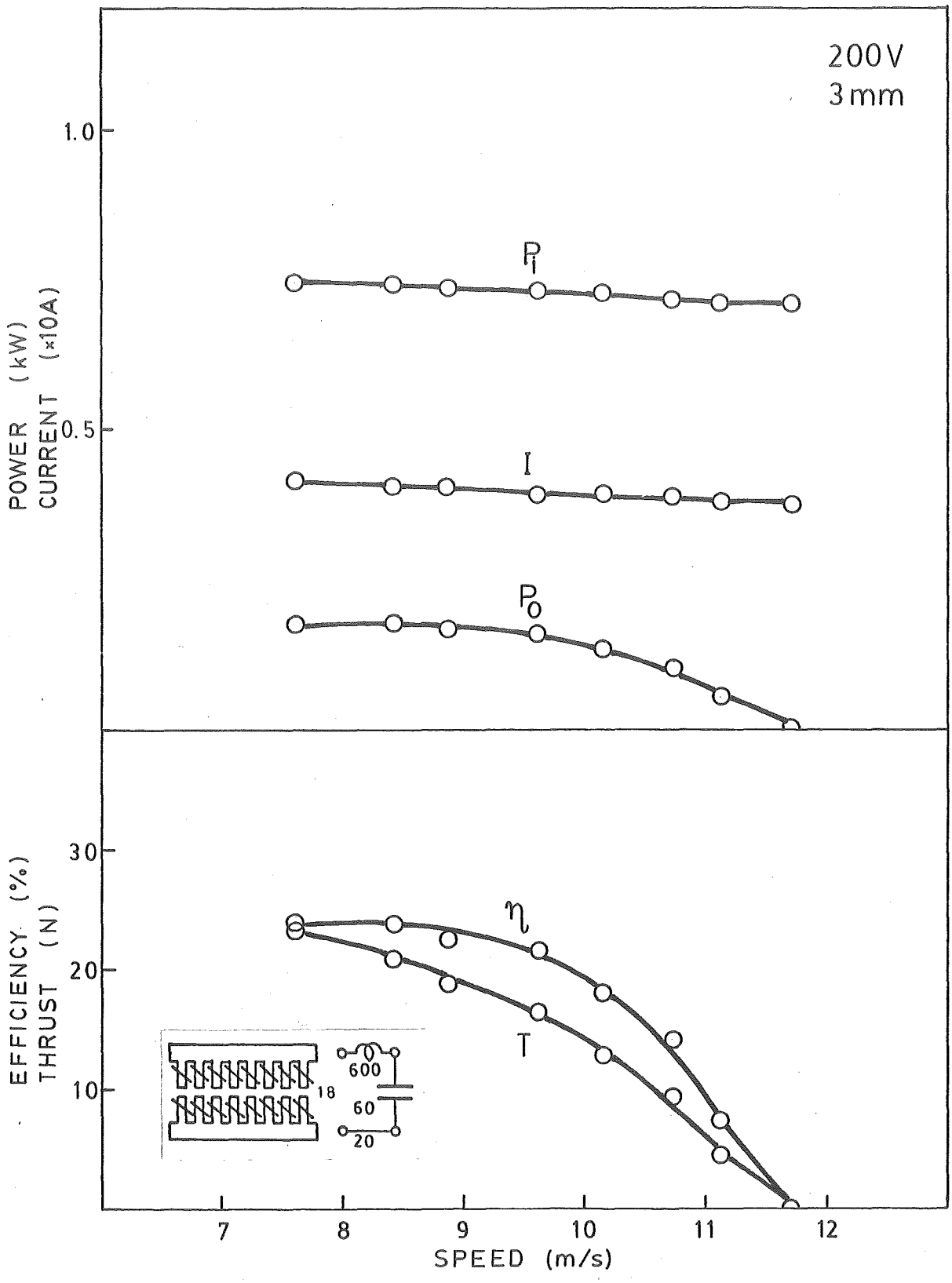
200V
3mm
1.0
0.5
POWER (kW)
CURRENT (×10A)
P_i
I
P_o
30
20
10
EFFICIENCY (%)
THRUST (N)
η
T
600
60
20
18
7
8
9
10
11
12
SPEED (m/s)

Fig. A57

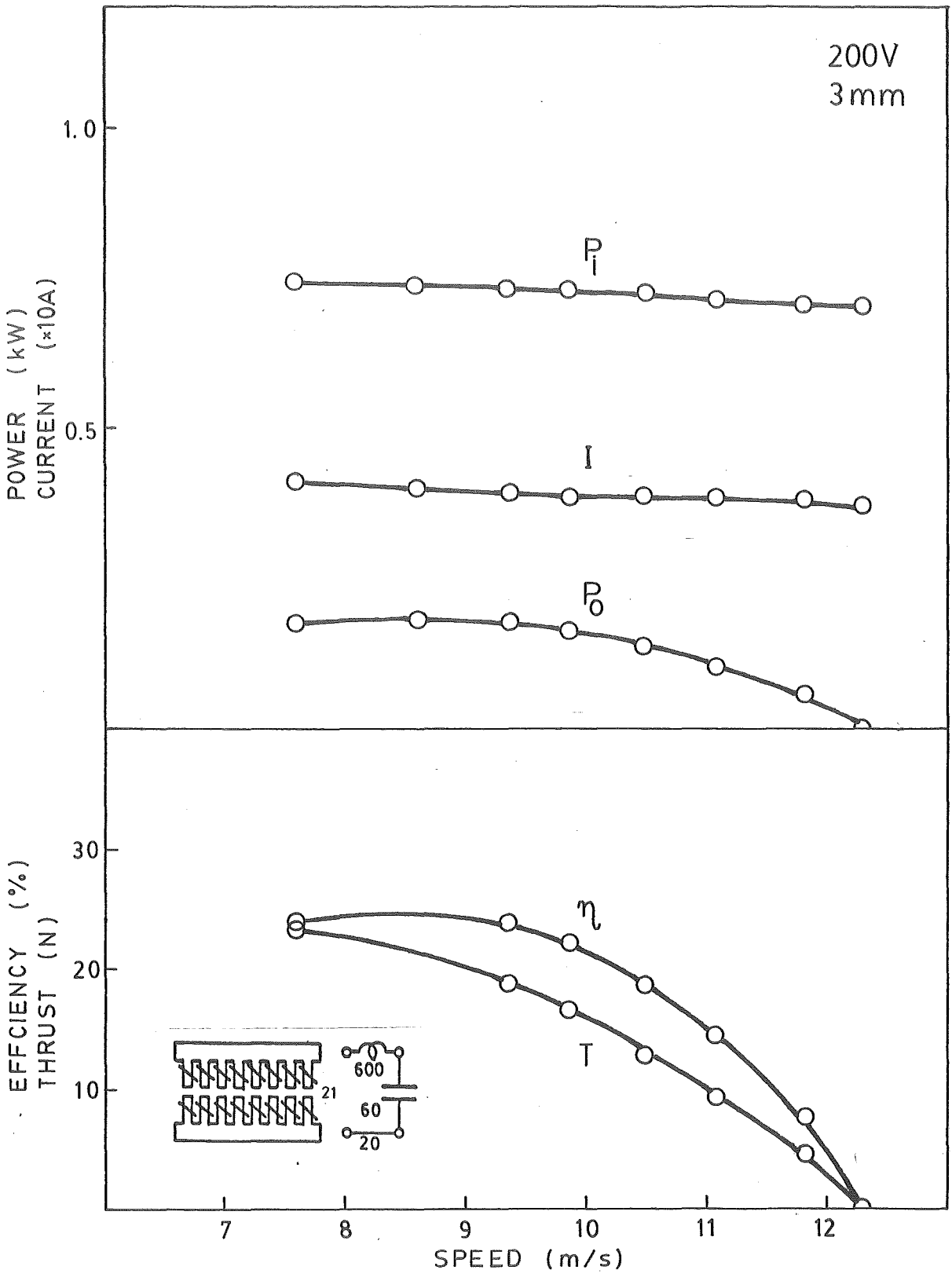
200V
3mm
1.0
0.5
POWER (kW)
CURRENT (×10A)
P_i
I
P_o
30
20
10
EFFCIENCY (%)
THRUST (N)
η
T
0
600
60
20
21
7
8
9
10
11
12
SPEED (m/s)

Fig.A58

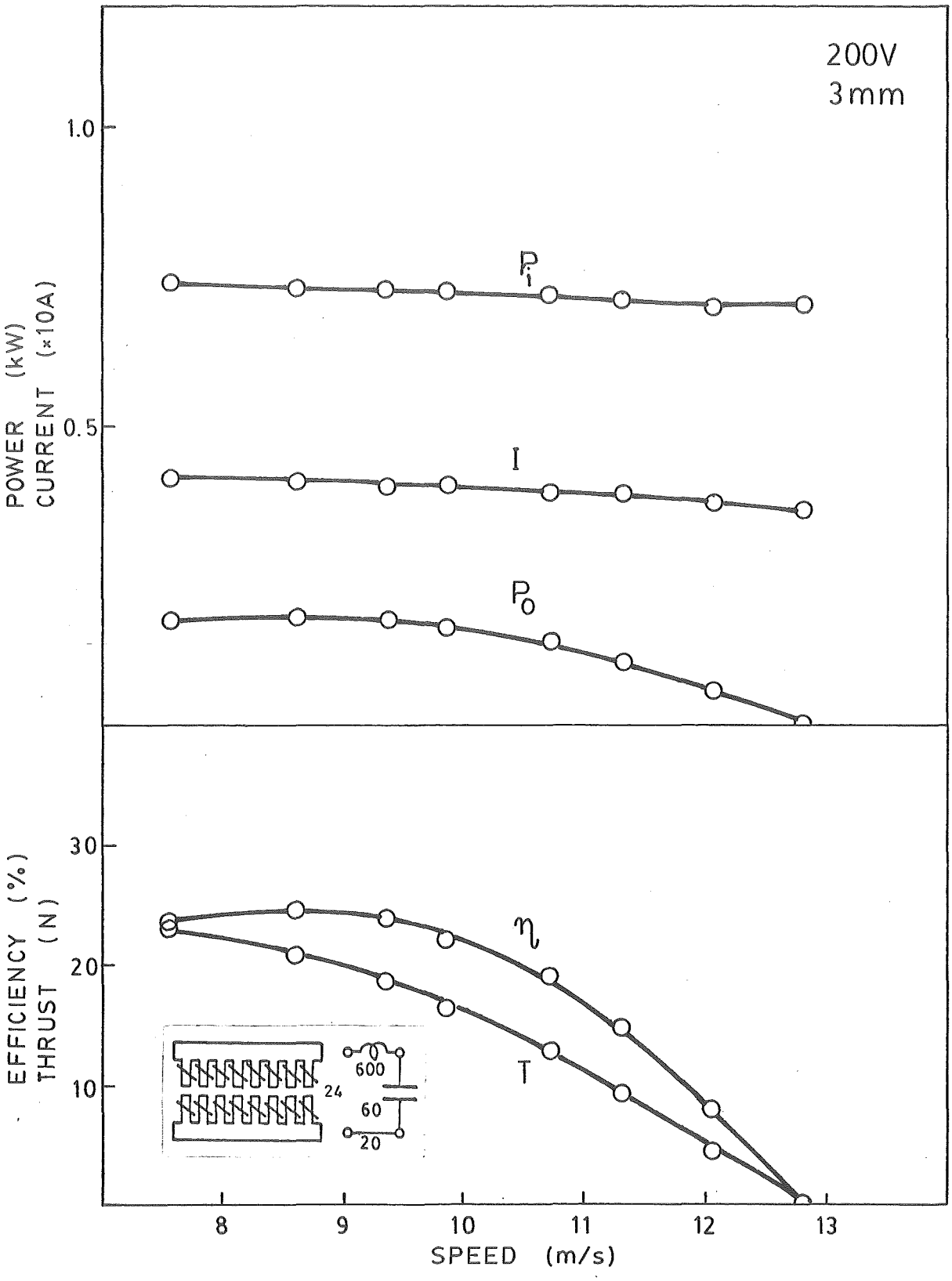
200V
3mm
1.0
0.5
POWER (kW)
CURRENT (×10A)
P_i
I
P_o
30
20
10
EFFICIENCY (%)
THRUST (N)
η
T
600
24
60
20
8
9
10
11
12
13
SPEED (m/s)

Fig. A59

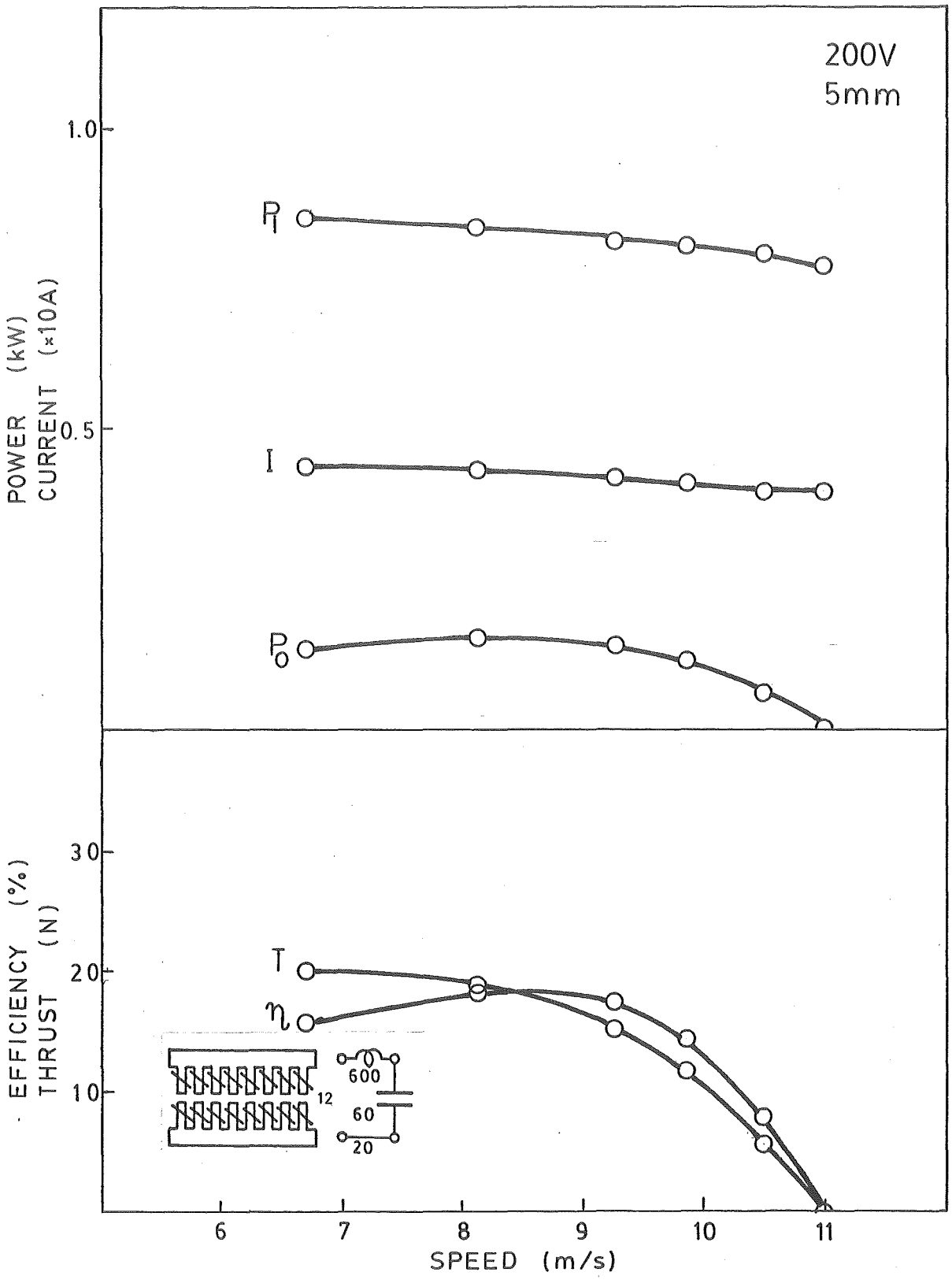
200V
5mm
1.0
0.5
POWER (kW)
CURRENT (×10A)
P_I
I
P_O
30
20
10
EFFICIENCY (%)
THRUST (N)
T
η
600
60
20
12
6
7
8
9
10
11
SPEED (m/s)

Fig. A60

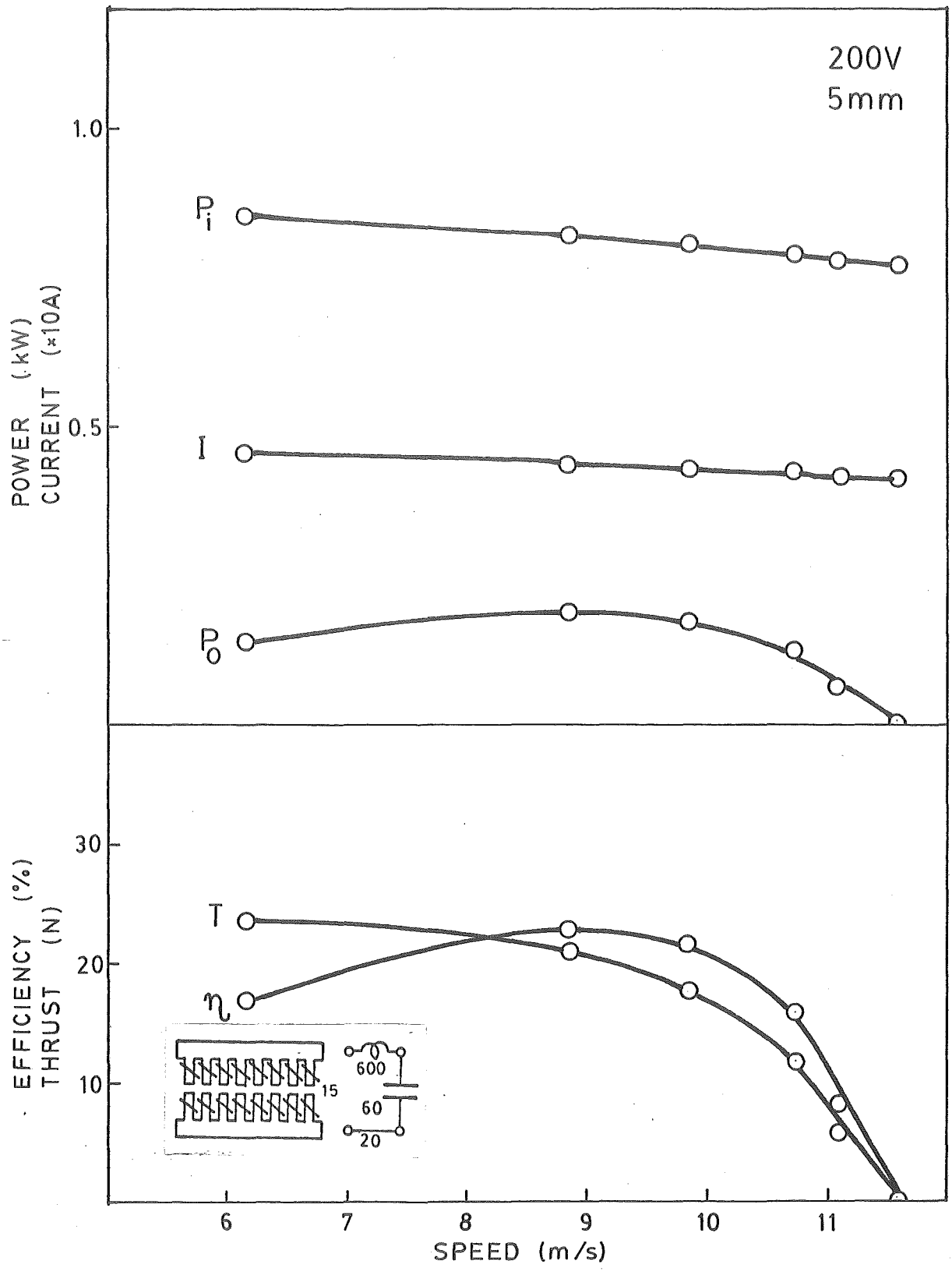
200V
5mm
1.0
0.5
POWER (kW)
CURRENT (×10A)
P_i
I
P_0
30
20
10
EFFICIENCY (%)
THRUST (N)
T
η
600
60
20
15
6
7
8
9
10
11
SPEED (m/s)

Fig.A61

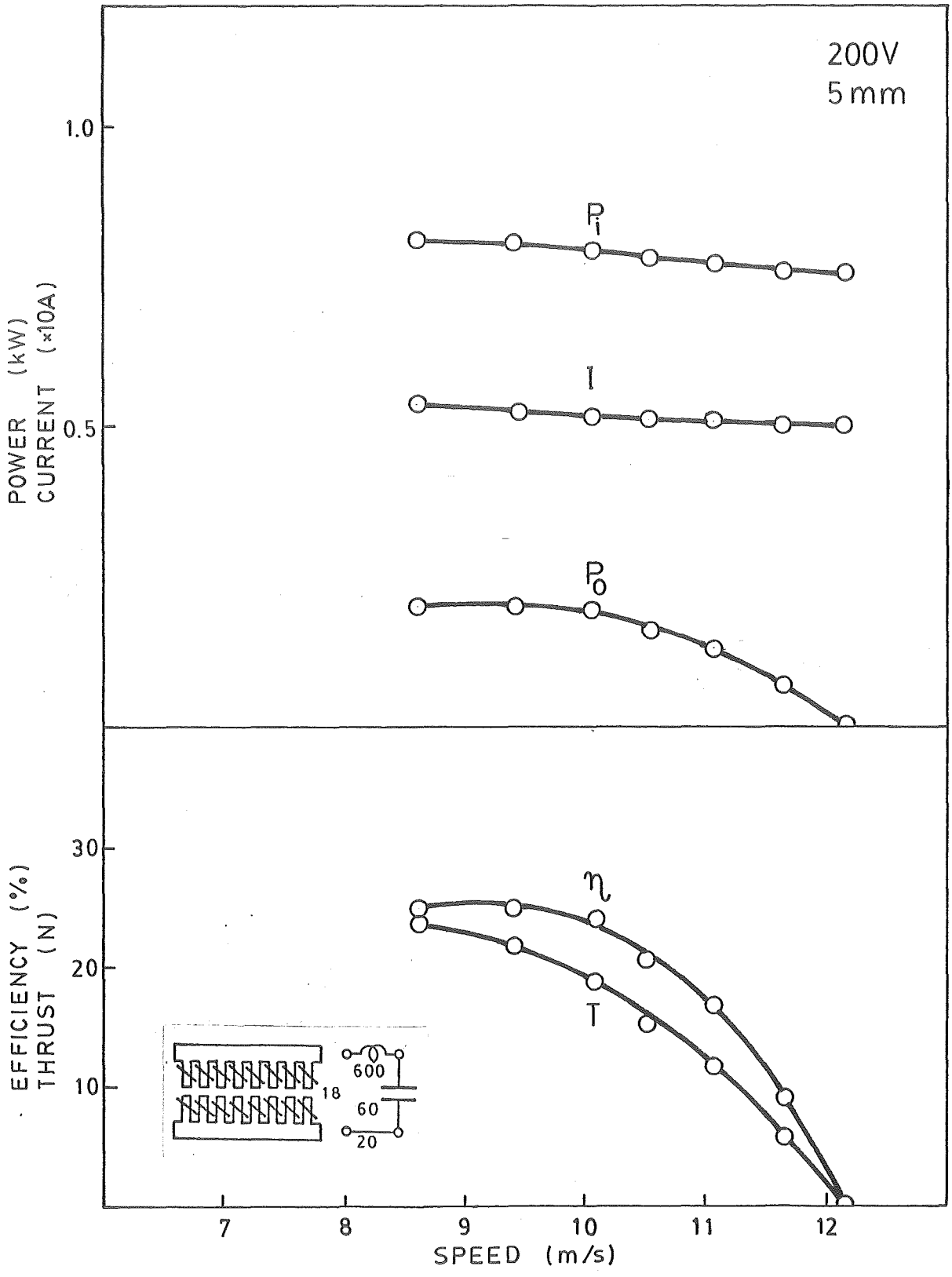
200V
5mm
1.0
0.5
POWER (kW)
CURRENT (×10A)
P_i
I
P_o
30
20
10
EFFICIENCY (%)
THRUST (N)
η
T
600
60
20
18
7
8
9
10
11
12
SPEED (m/s)

Fig. A62

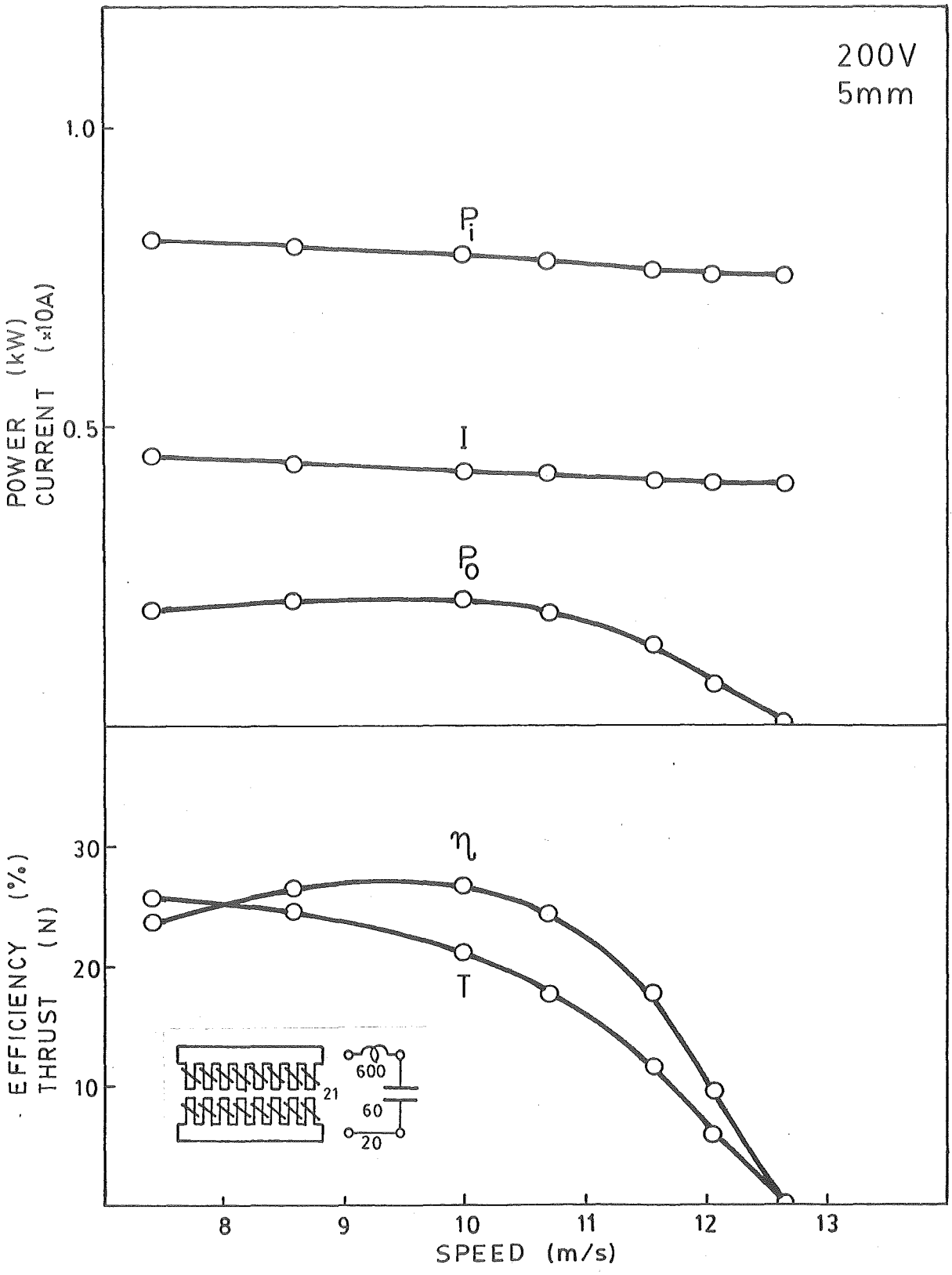
200V
5mm
1.0
0.5
POWER (kW)
CURRENT (×10A)
P_i
I
P_o
30
20
10
EFFICIENCY (%)
THRUST (N)
η
T
600
60
20
21
8
9
10
11
12
13
SPEED (m/s)

Fig.A63

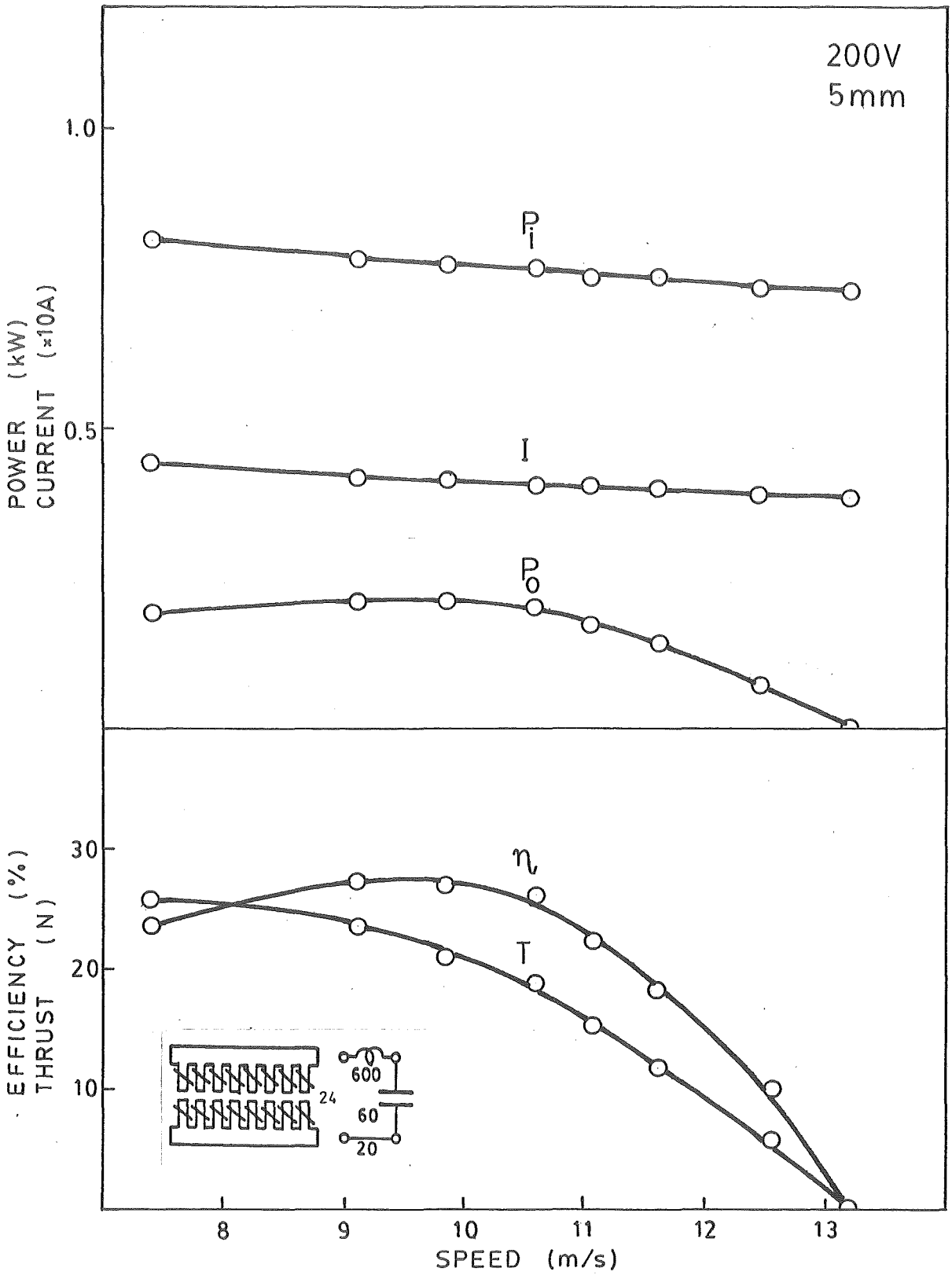
200V
5mm
1.0
0.5
POWER (kW)
CURRENT (×10A)
P_i
I
P_o
30
20
10
EFFICIENCY (%)
THRUST (N)
η
T
24
600
60
20
8
9
10
11
12
13
SPEED (m/s)

Fig. A64

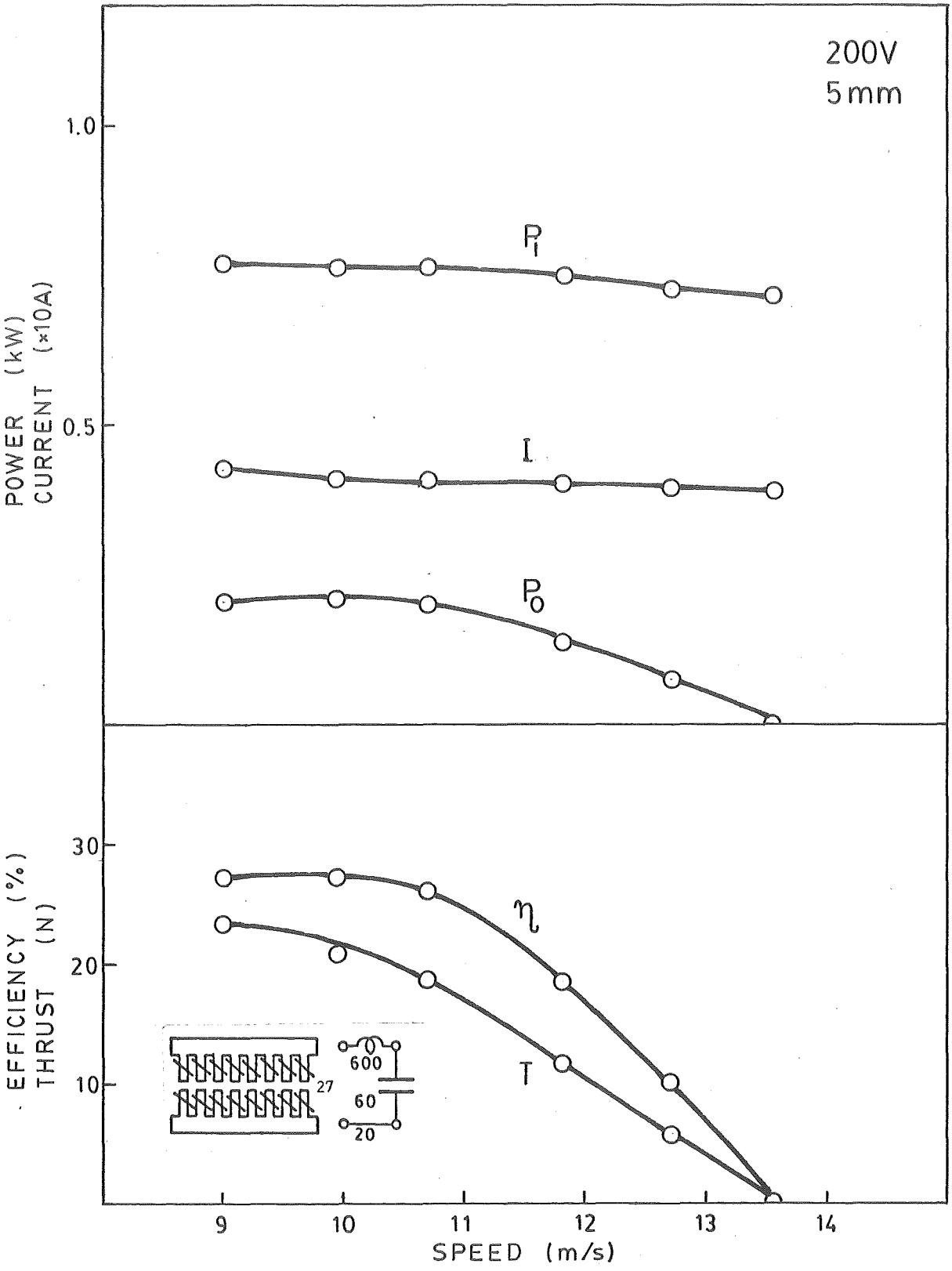
200V
5mm
1.0
0.5
POWER (kW)
CURRENT (×10A)
P_i
I
P_o
30
20
10
EFFICIENCY (%)
THRUST (N)
η
T
600
60
20
27
9
10
11
12
13
14
SPEED (m/s)

Fig. A65

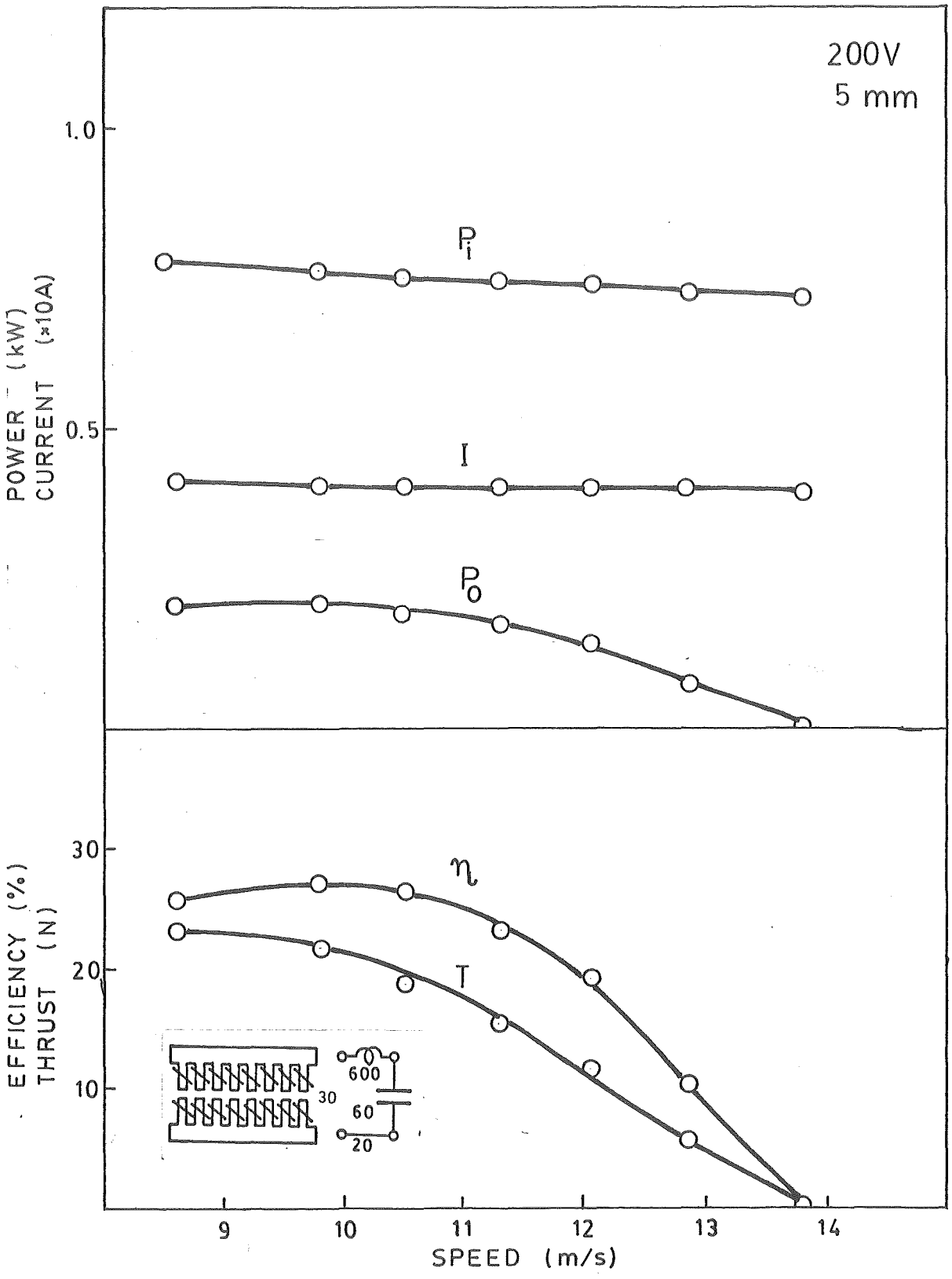
200V
5 mm
1.0
0.5
POWER (kW)
CURRENT (×10A)
P_i
I
P_o
30
20
10
EFFICIENCY (%)
THRUST (N)
η
T
600
60
20
30
9
10
11
12
13
14
SPEED (m/s)

Fig. A66

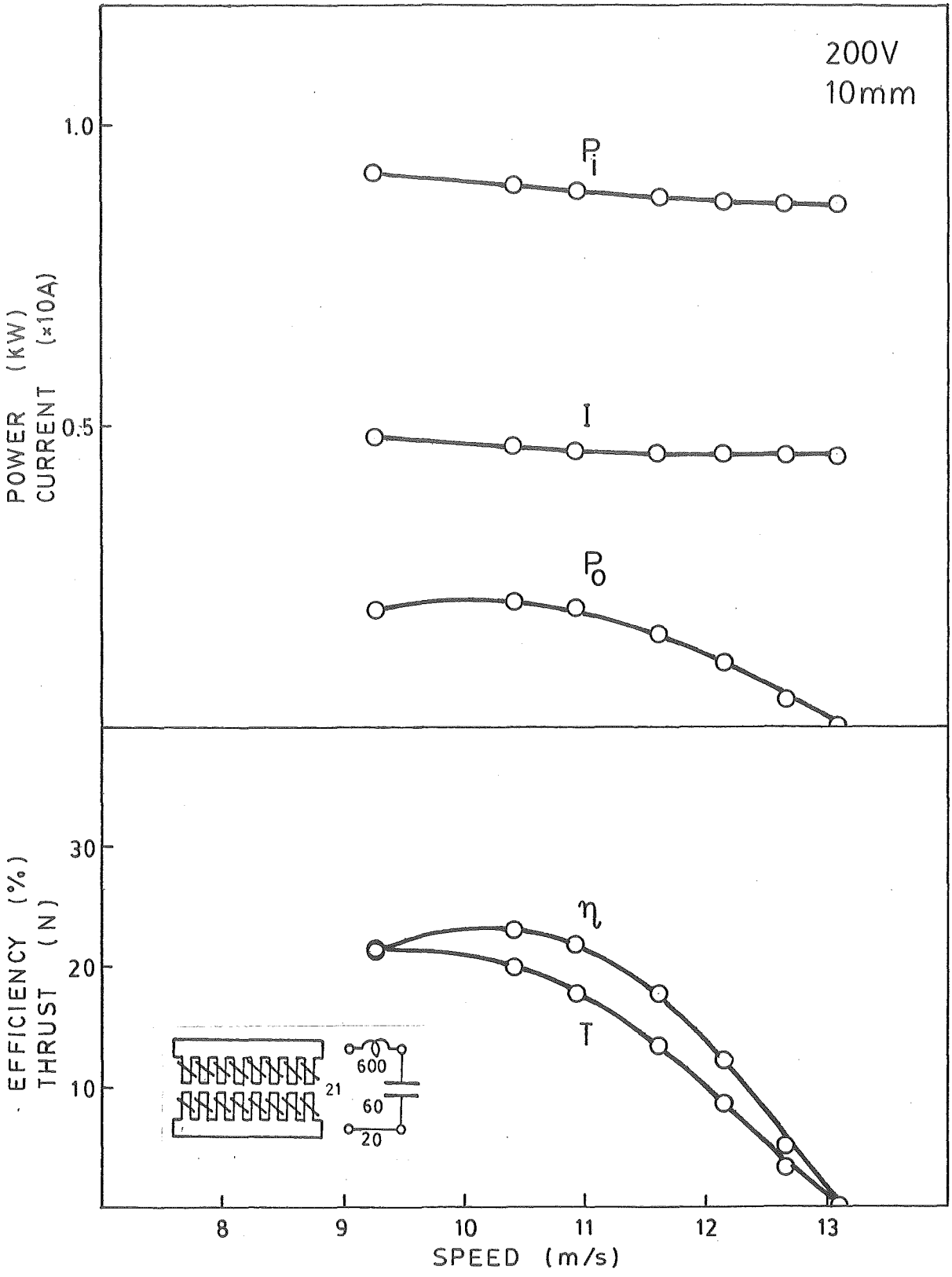
200V
10mm
1.0
0.5
POWER (KW)
CURRENT (×10A)
P_i
I
P_o
30
20
10
EFFICIENCY (%)
THRUST (N)
η
T
600
60
20
21
8
9
10
11
12
13
SPEED (m/s)

Fig. A67

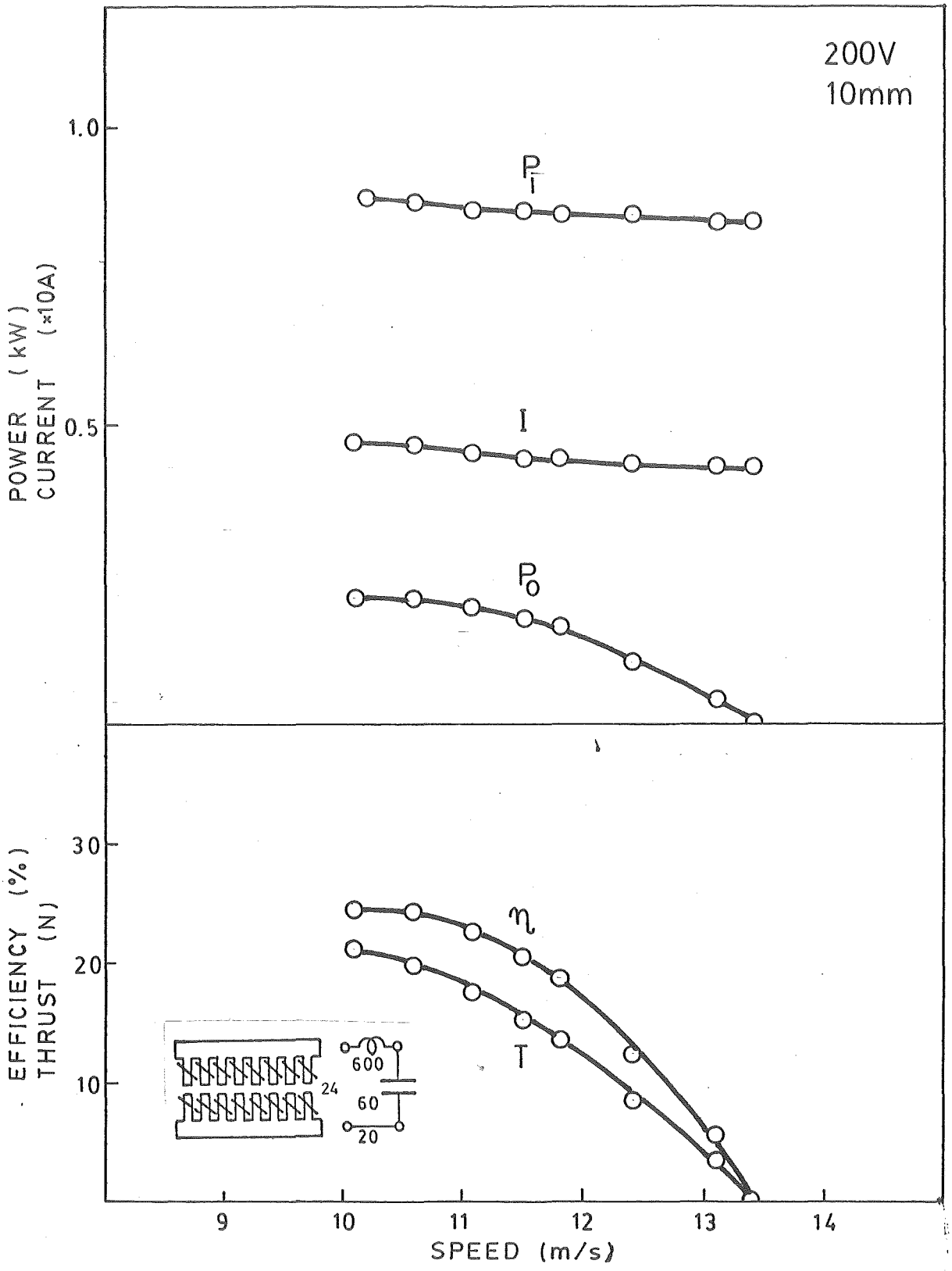
200V
10mm
1.0
0.5
POWER (kW)
CURRENT (×10A)
P_I
I
P_O
30
20
10
EFFICIENCY (%)
THRUST (N)
η
T
600
60
20
24
9
10
11
12
13
14
SPEED (m/s)

Fig. A68

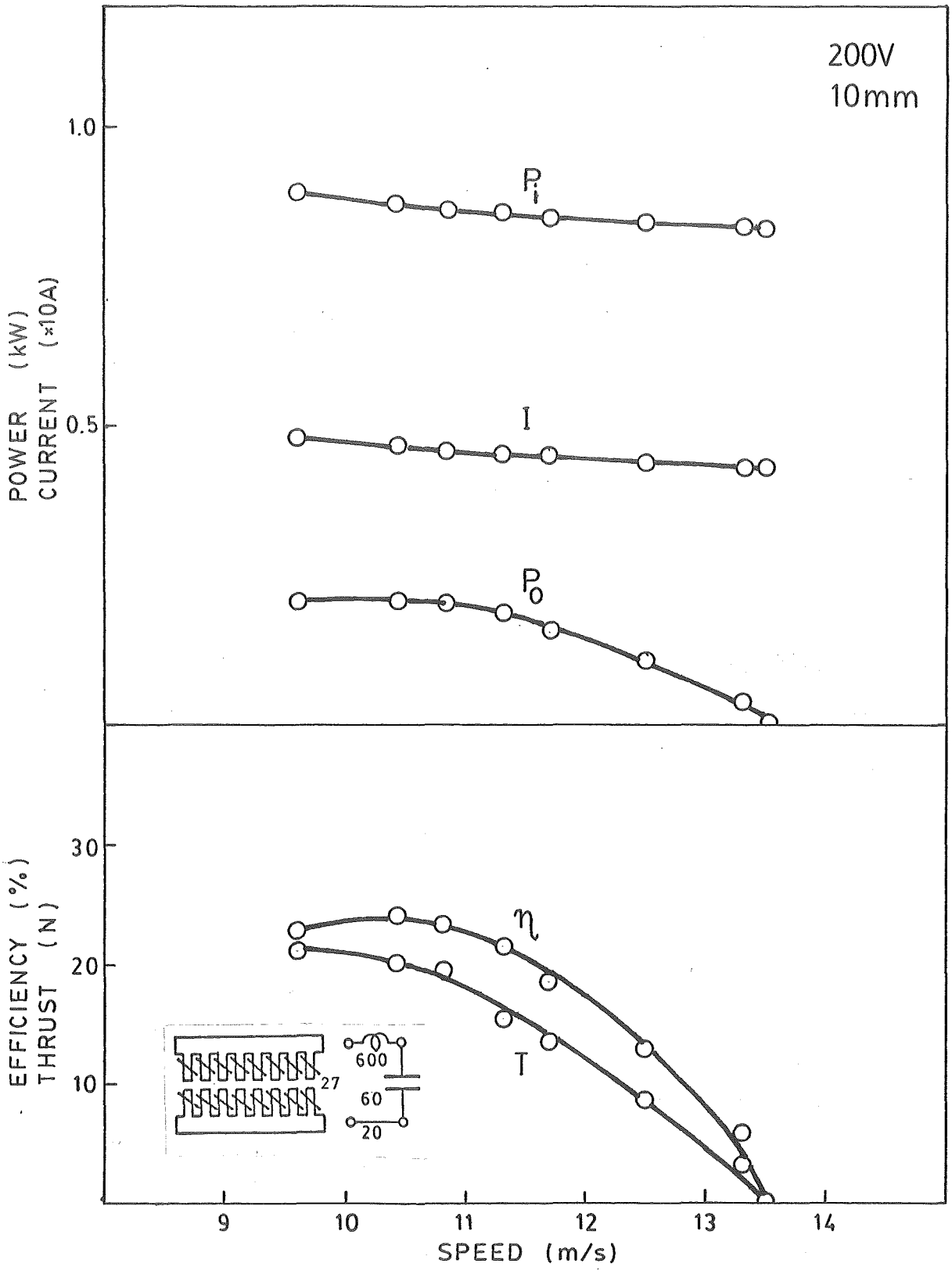
200V
10mm
POWER (kW)
CURRENT (×10A)
1.0
0.5
P_i
I
P_o
EFFICIENCY (%)
THRUST (N)
30
20
10
η
T
600
27
60
20
9
10
11
12
13
14
SPEED (m/s)

Fig. A69

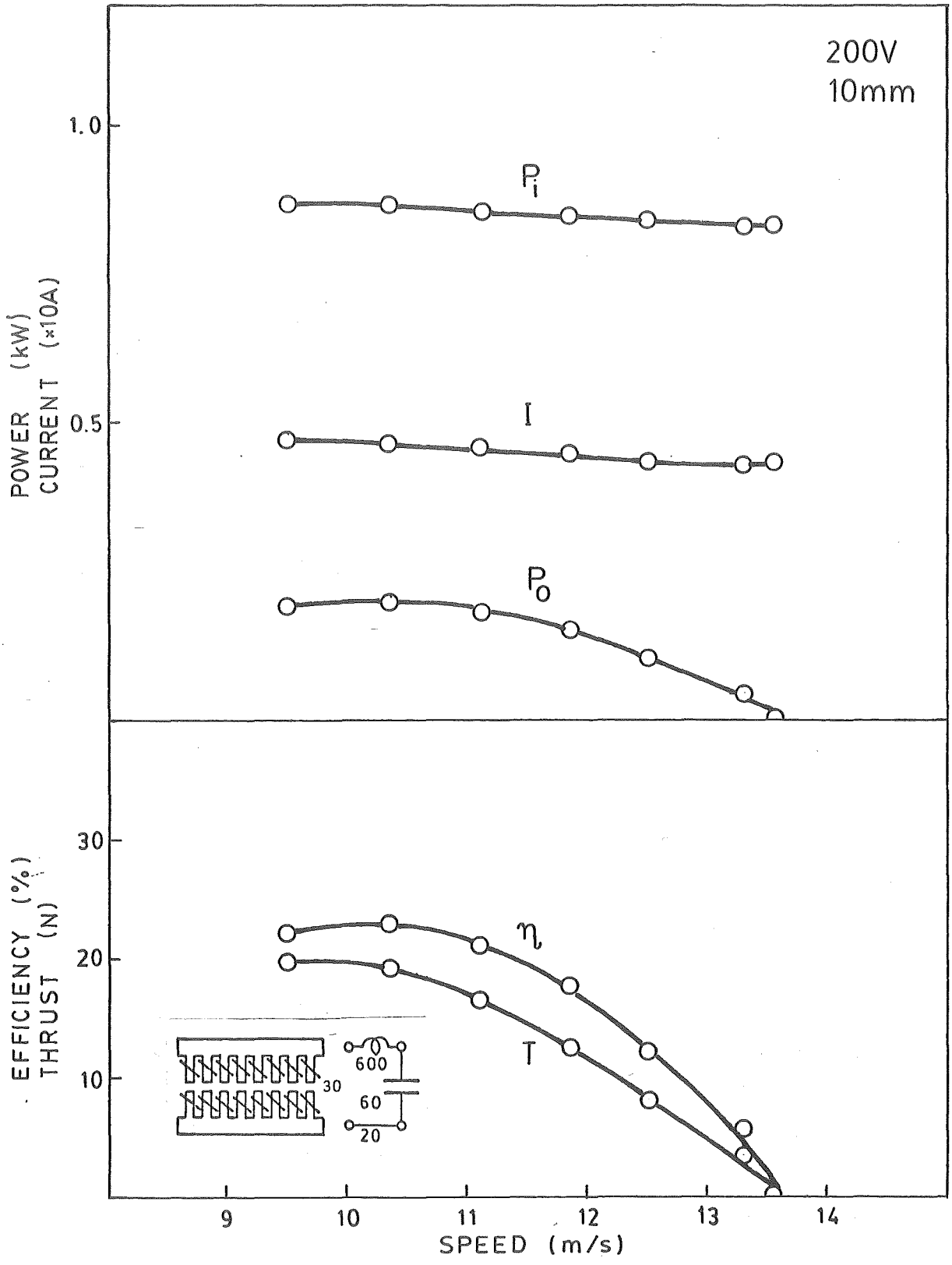
200V
10mm
1.0
0.5
POWER (kW)
CURRENT (×10A)
P_i
I
P_o
30
20
10
EFFICIENCY (%)
THRUST (N)
η
T
600
60
20
30
9
10
11
12
13
14
SPEED (m/s)

Fig. A70

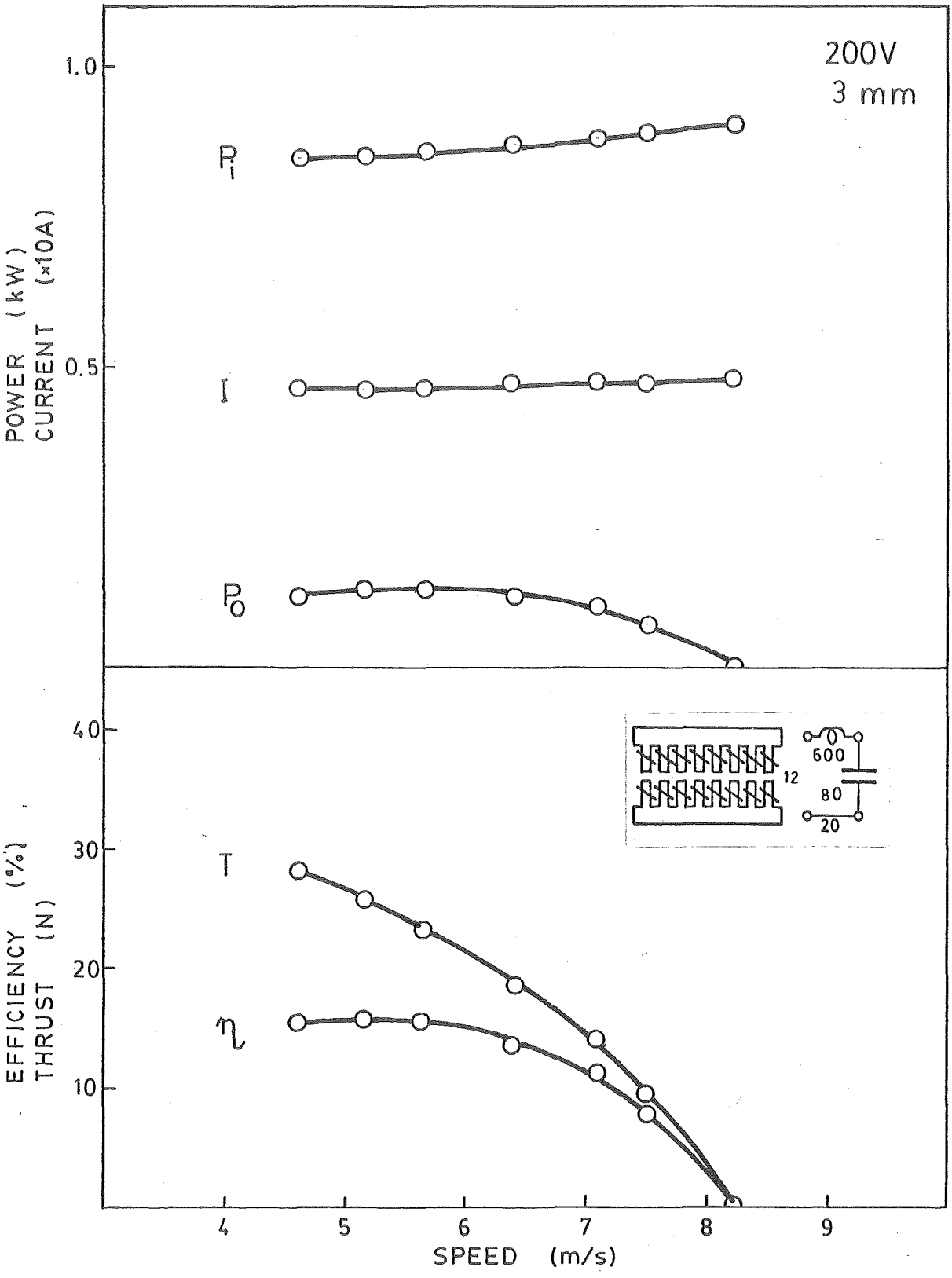
200V
3 mm
1.0
0.5
POWER (kW)
CURRENT (×10A)
P_i
I
P_o
40
30
20
10
EFFICIENCY (%)
THRUST (N)
T
η
12
600
80
20
4
5
6
7
8
9
SPEED (m/s)

Fig. A71

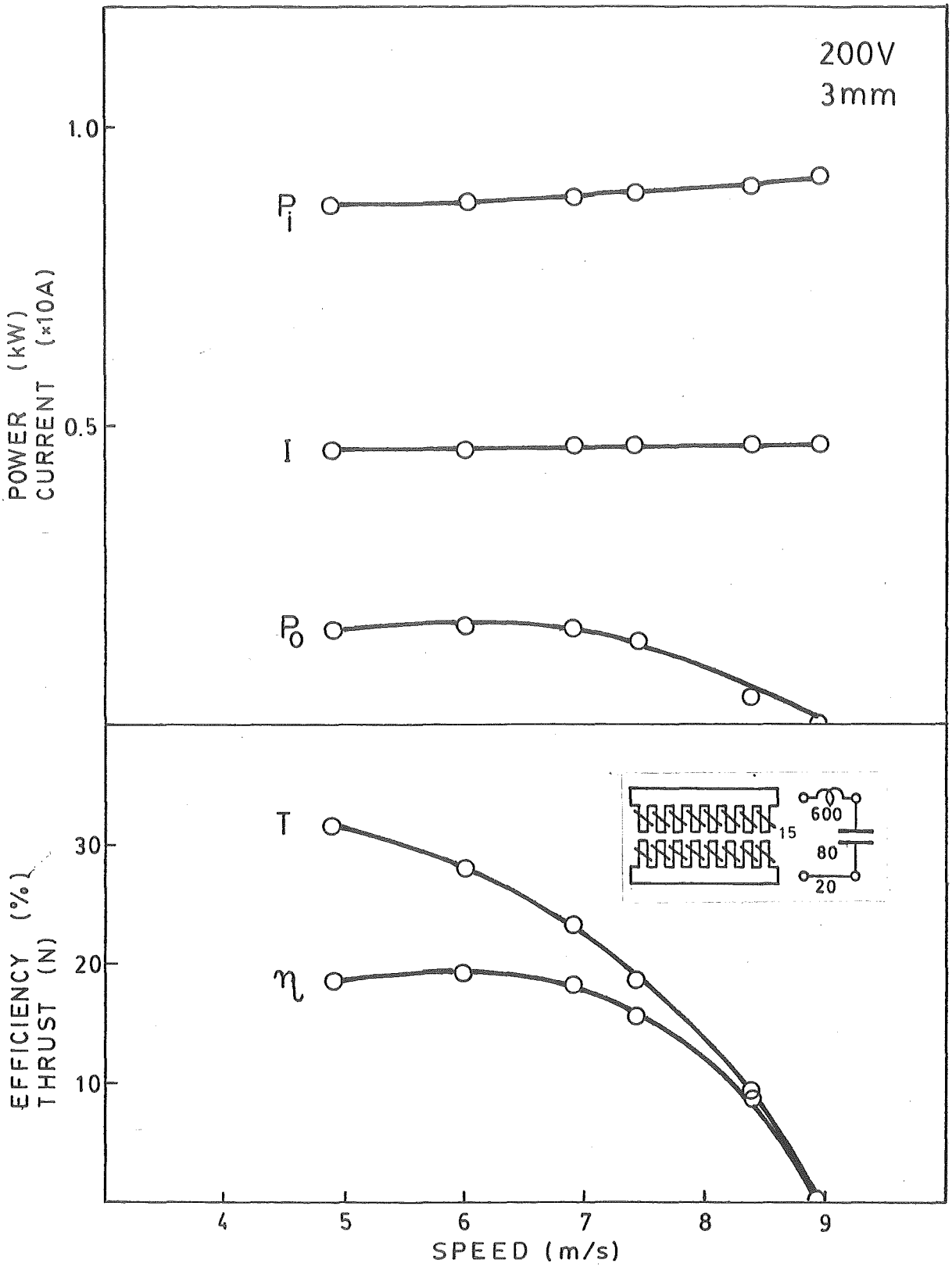
200V
3mm
1.0
0.5
POWER (kW)
CURRENT (×10A)
P_i
I
P_0
T
η
30
20
10
EFFICIENCY (%)
THRUST (N)
15
600
80
20
4
5
6
7
8
9
SPEED (m/s)

Fig. A72

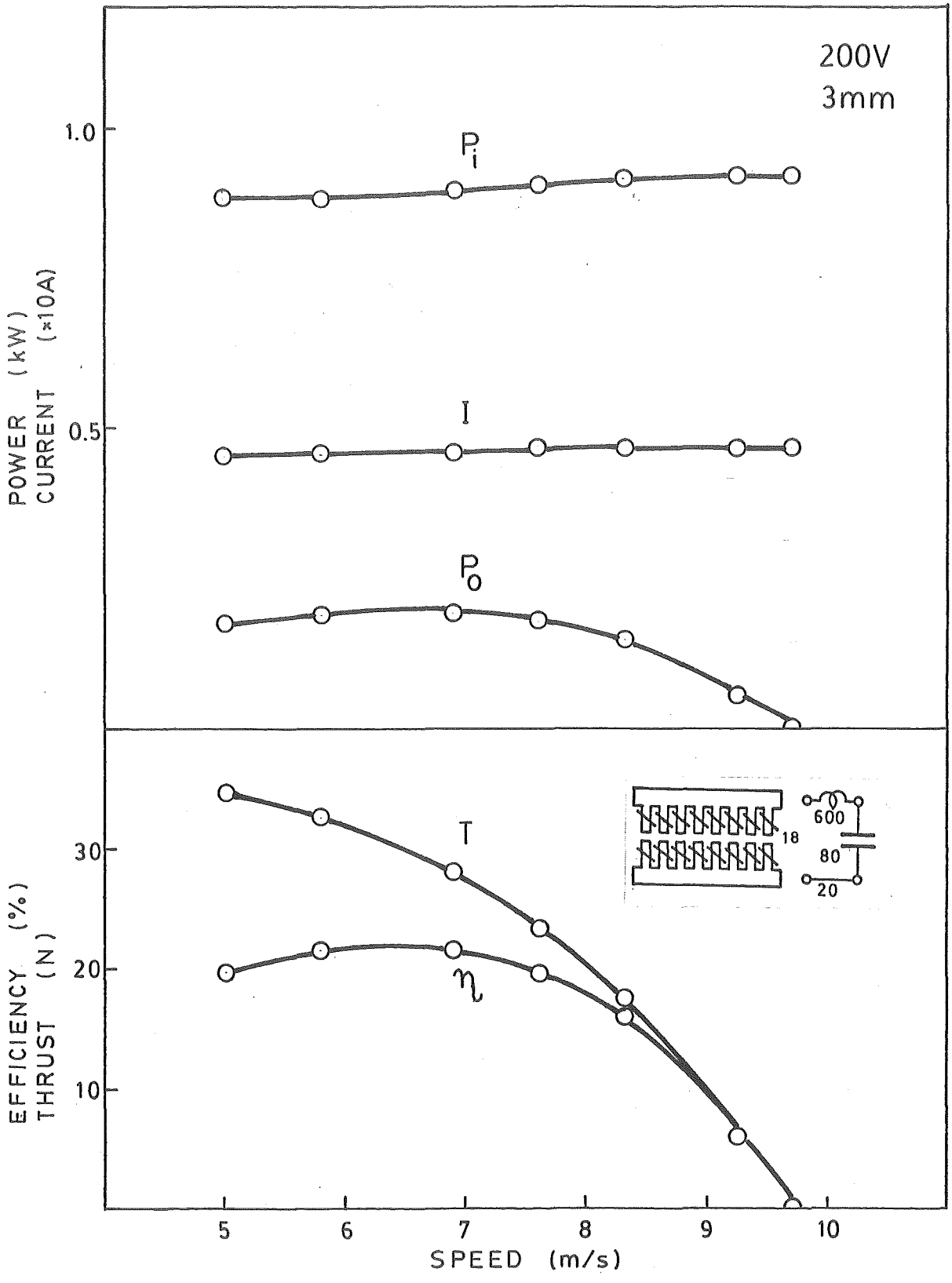
200V
3mm
1.0
0.5
POWER (kW)
CURRENT (×10A)
P_i
I
P_o
30
20
10
EFFICIENCY (%)
THRUST (N)
T
η
18
600
80
20
5
6
7
8
9
10
SPEED (m/s)

Fig. A73

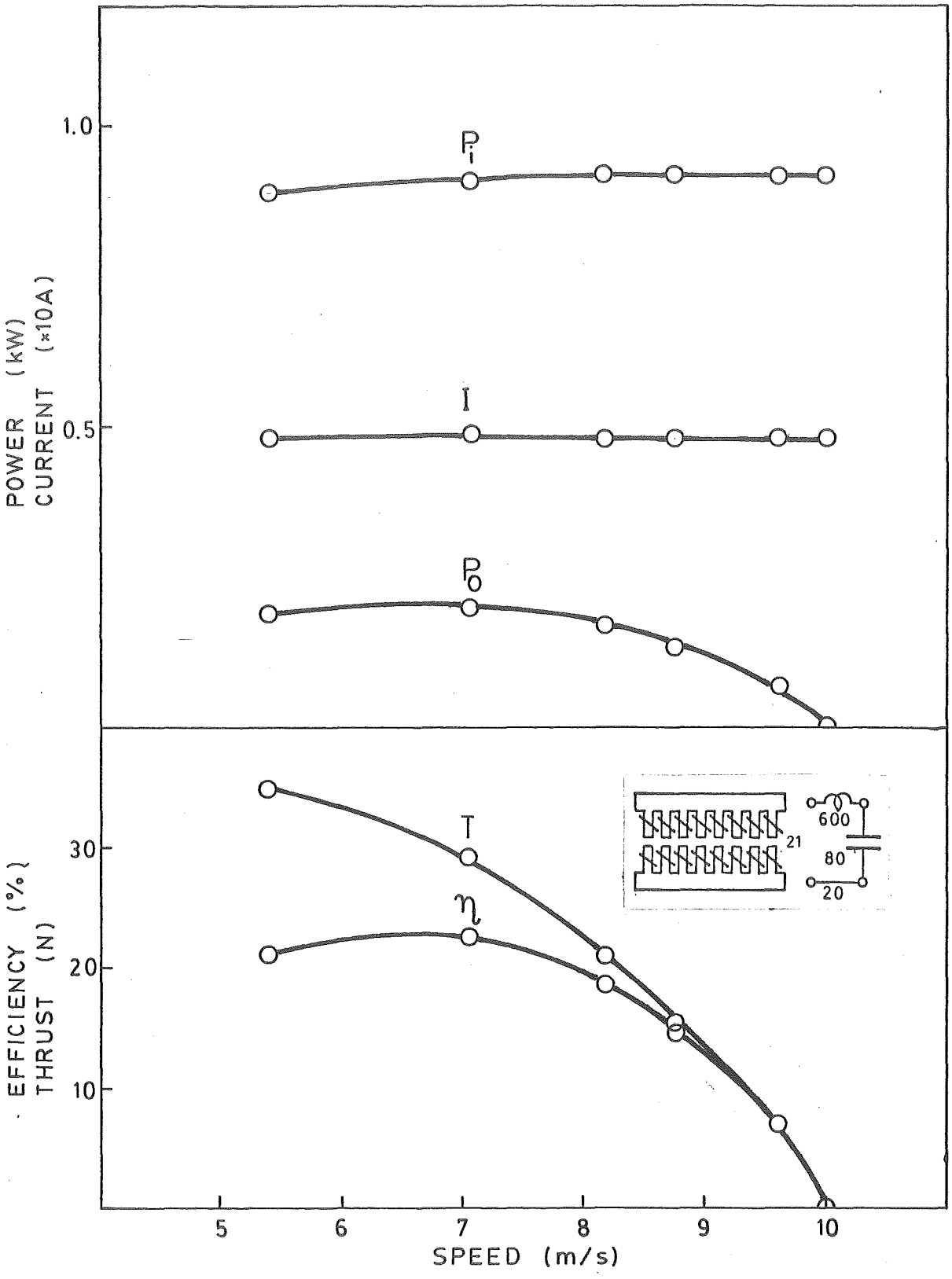
1.0
0.5
POWER (kW)
CURRENT (×10A)
P_i
I
P_o
30
20
10
EFFICIENCY (%)
THRUST (N)
T
η
21
600
80
20
5
6
7
8
9
10
SPEED (m/s)

Fig. A74

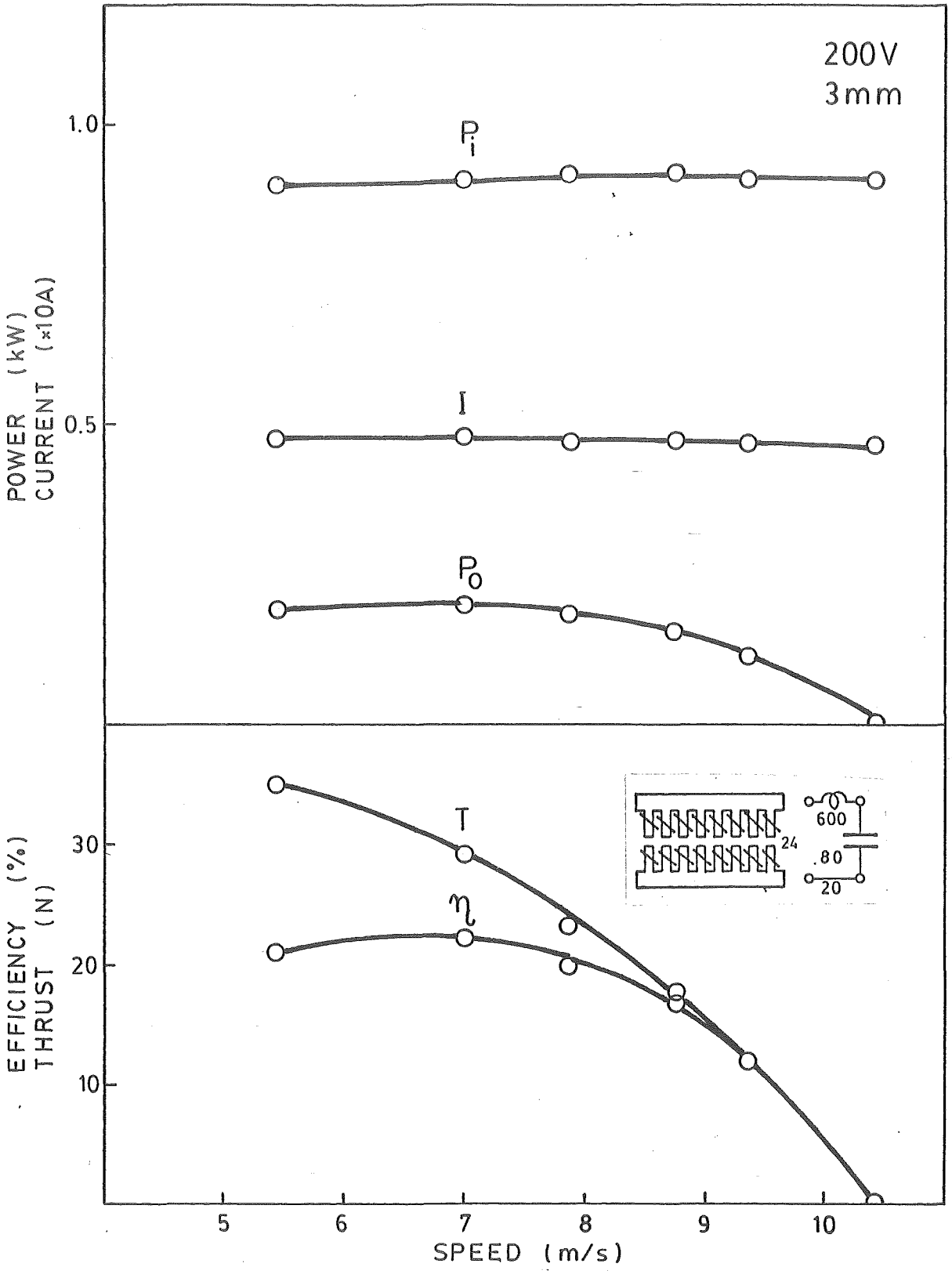
200V
3mm
1.0
0.5
P_i
I
P_o
POWER (kW)
CURRENT (×10A)
30
20
10
T
η
EFFICIENCY (%)
THRUST (N)
24
600
.80
20
5
6
7
8
9
10
SPEED (m/s)

Fig. A75

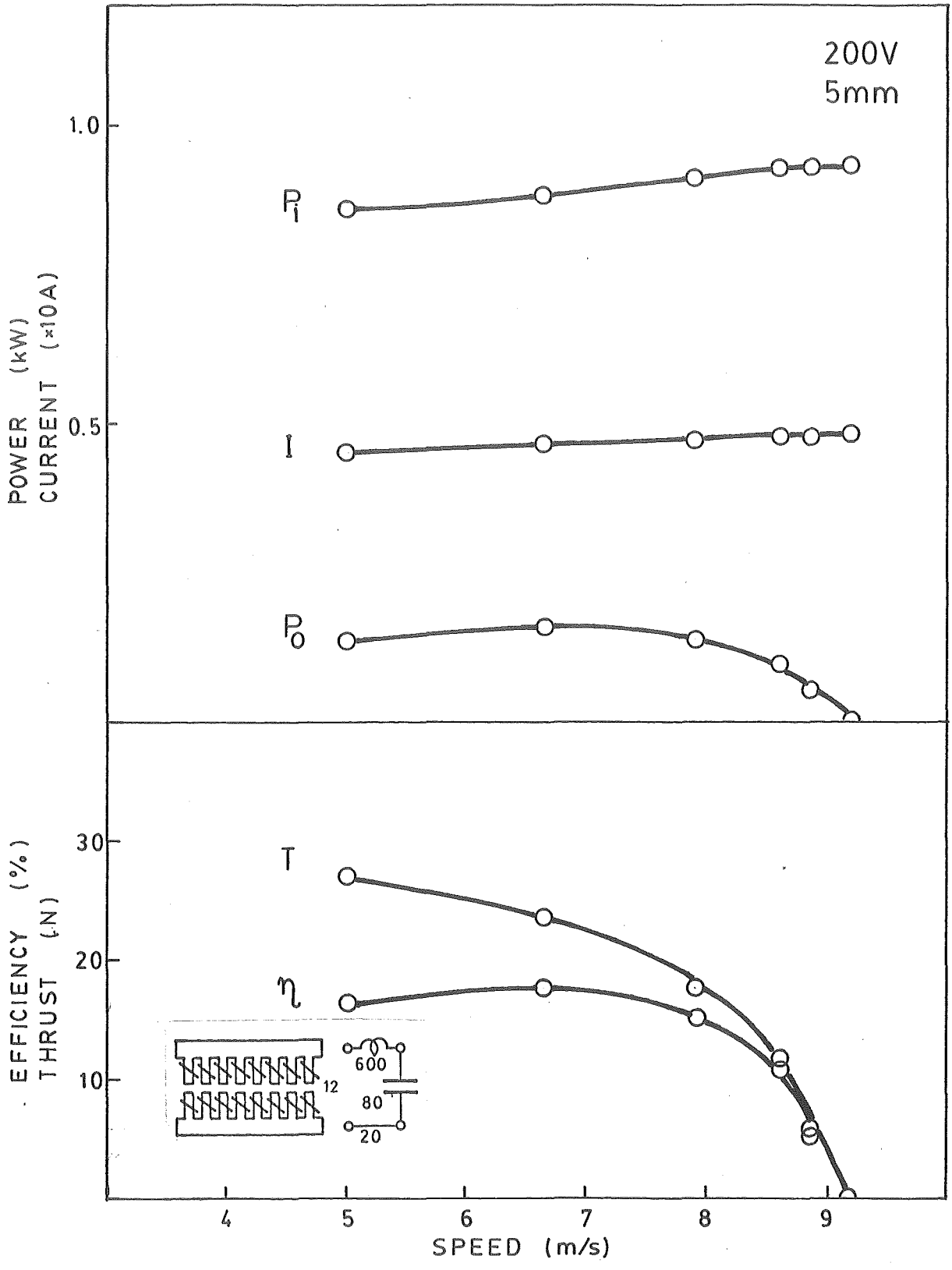
200V
5mm
1.0
0.5
POWER (kW)
CURRENT (×10A)
P_i
I
P_o
30
20
10
EFFICIENCY (%)
THRUST (N)
T
η
600
12
80
20
4
5
6
7
8
9
SPEED (m/s)

Fig. A76

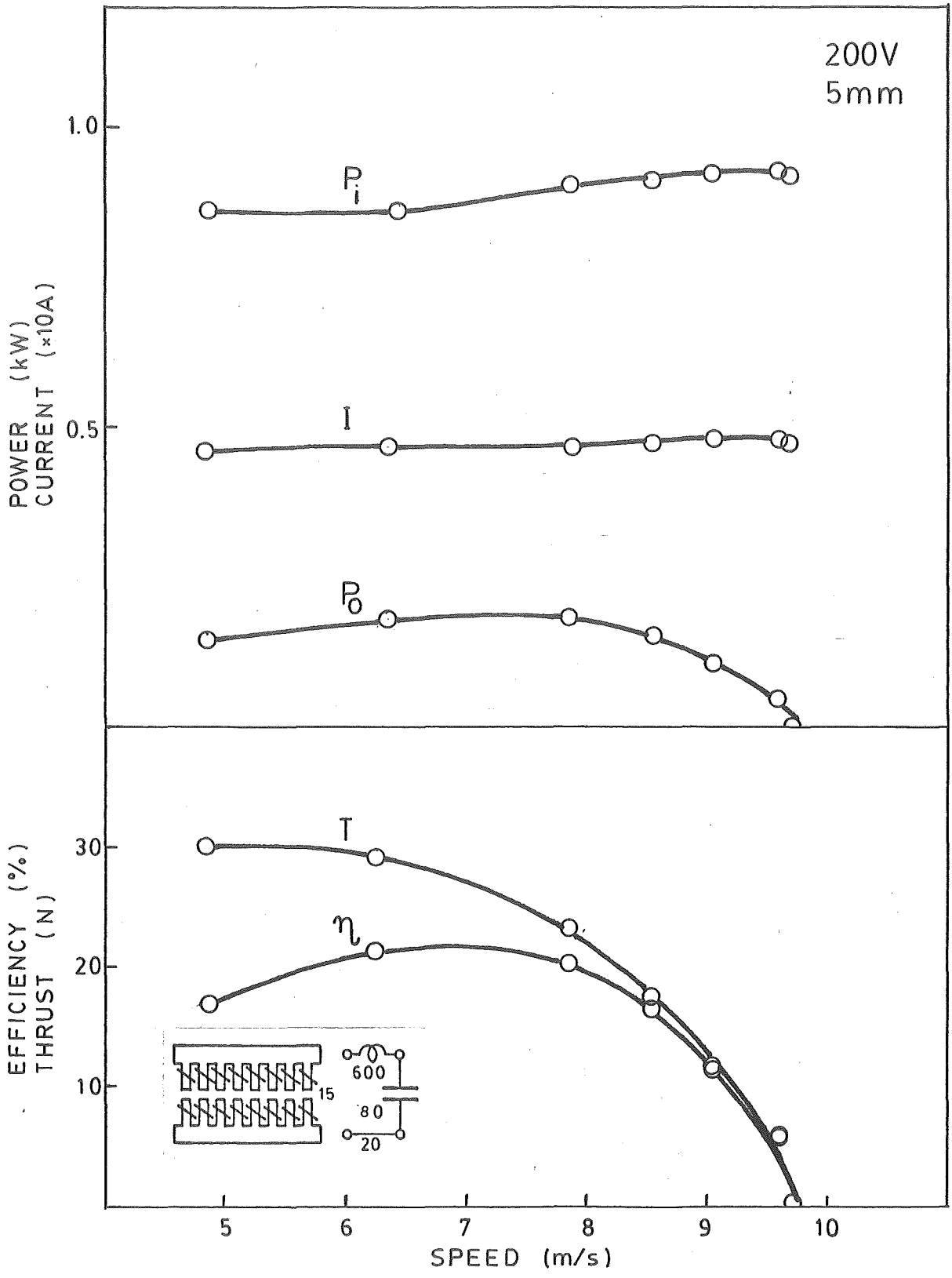
200V
5mm
1.0
0.5
POWER (kW)
CURRENT (×10A)
P_i
I
P_o
30
20
10
EFFICIENCY (%)
THRUST (N)
T
η
600
15
80
20
5
6
7
8
9
10
SPEED (m/s)

Fig.A77

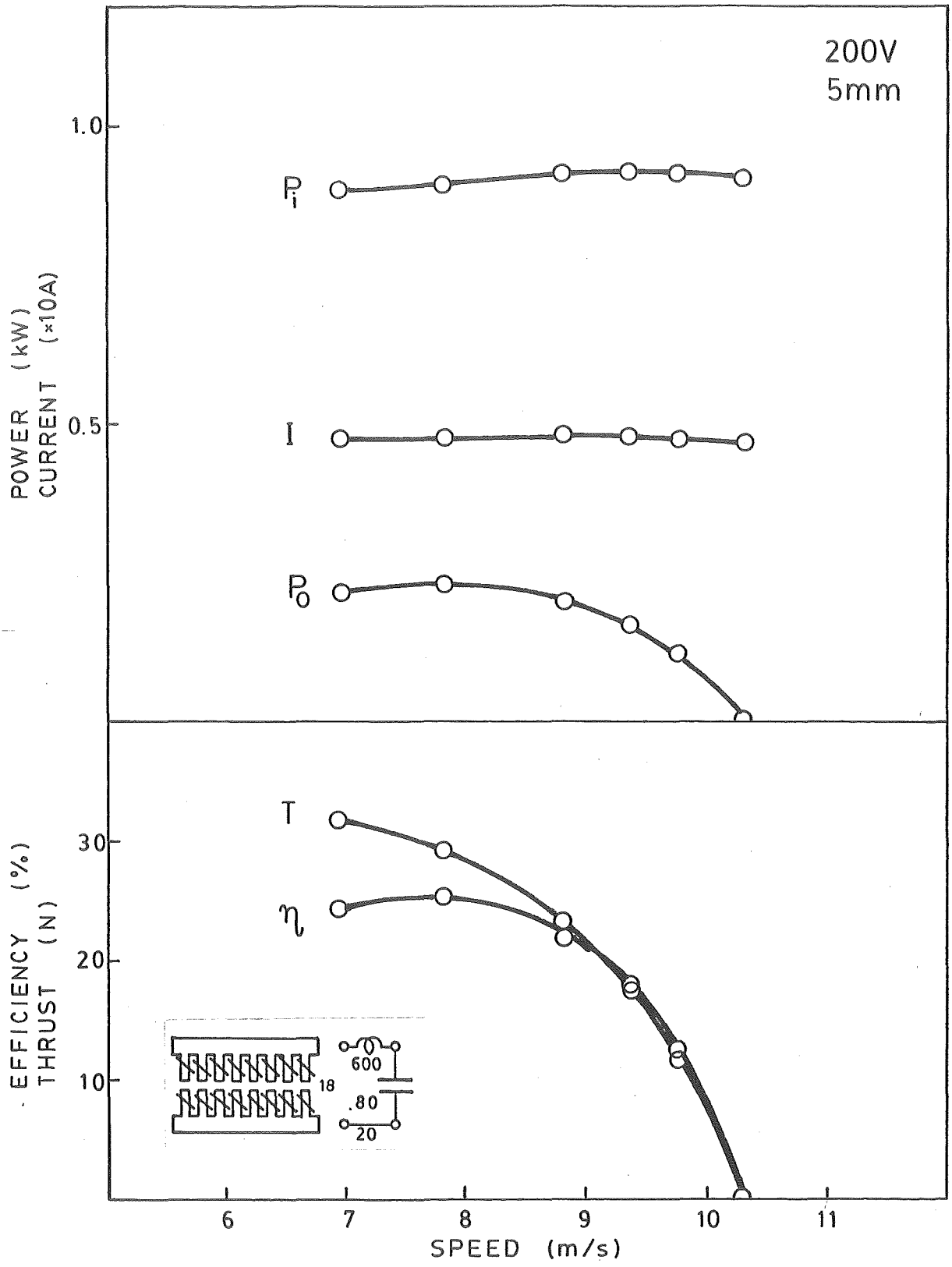
200V
5mm
1.0
0.5
POWER (kW)
CURRENT (×10A)
P_i
I
P_0
T
η
30
20
10
EFFICIENCY (%)
THRUST (N)
600
.80
20
18
6
7
8
9
10
11
SPEED (m/s)

Fig. A78

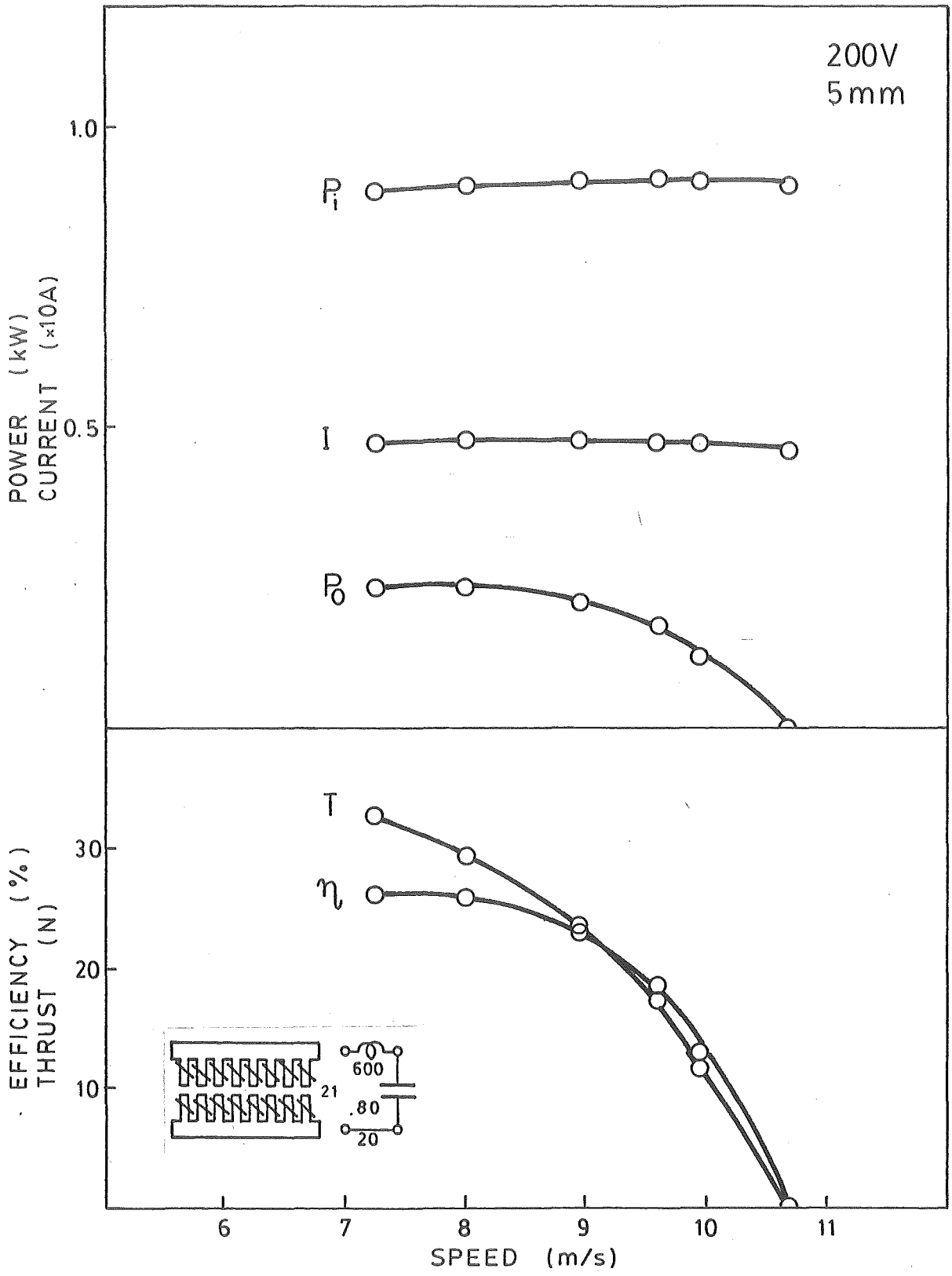
200V
5mm
1.0
0.5
POWER (kW)
CURRENT (×10A)
P_i
I
P_o
30
20
10
EFFICIENCY (%)
THRUST (N)
T
η
0
600
21
.80
20
6
7
8
9
10
11
SPEED (m/s)

Fig. A79

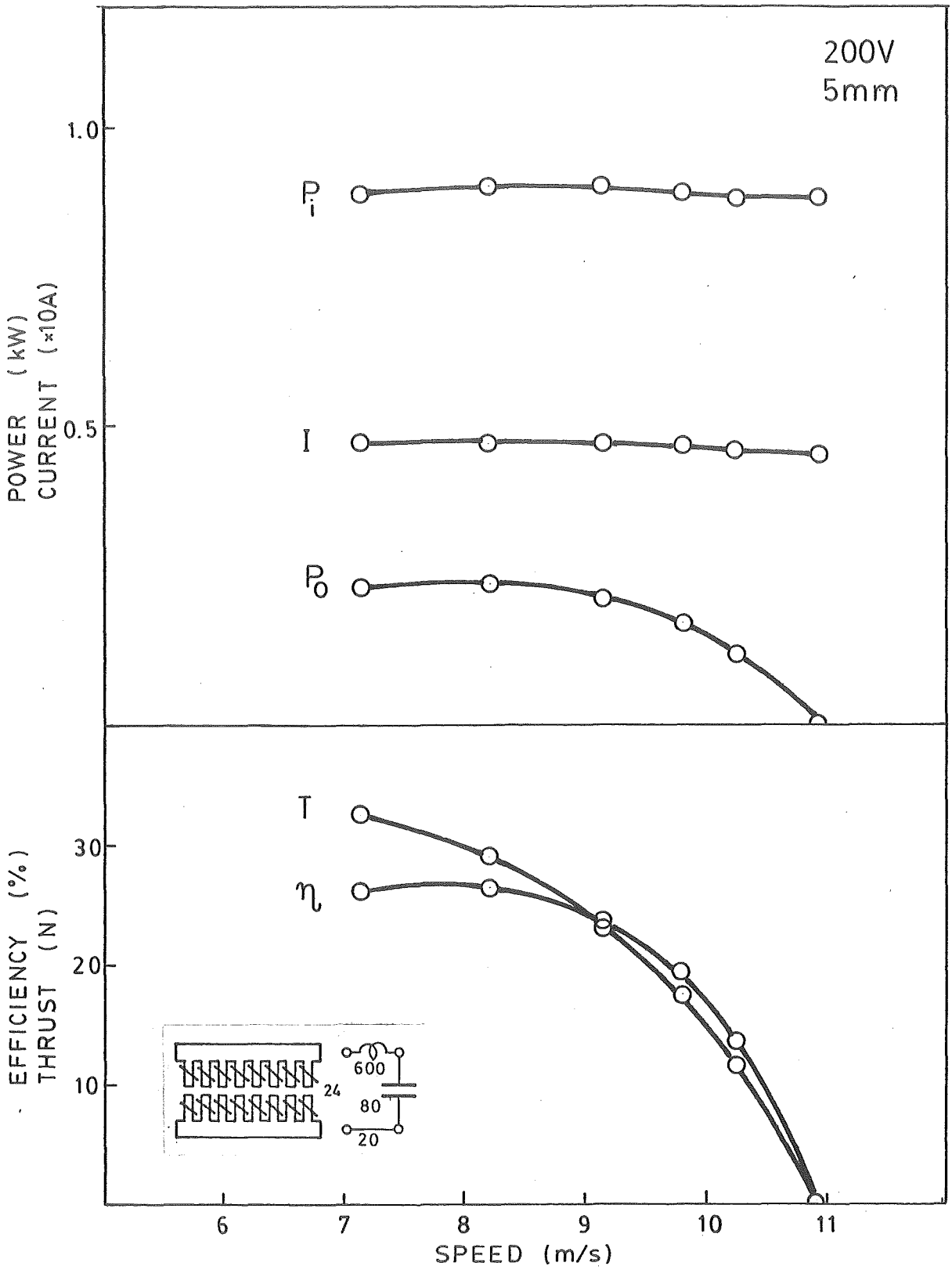
200V
5mm
1.0
0.5
POWER (kW)
CURRENT (×10A)
P_i
I
P_o
T
η
30
20
10
EFFICIENCY (%)
THRUST (N)
600
80
20
24
6
7
8
9
10
11
SPEED (m/s)

Fig. A80

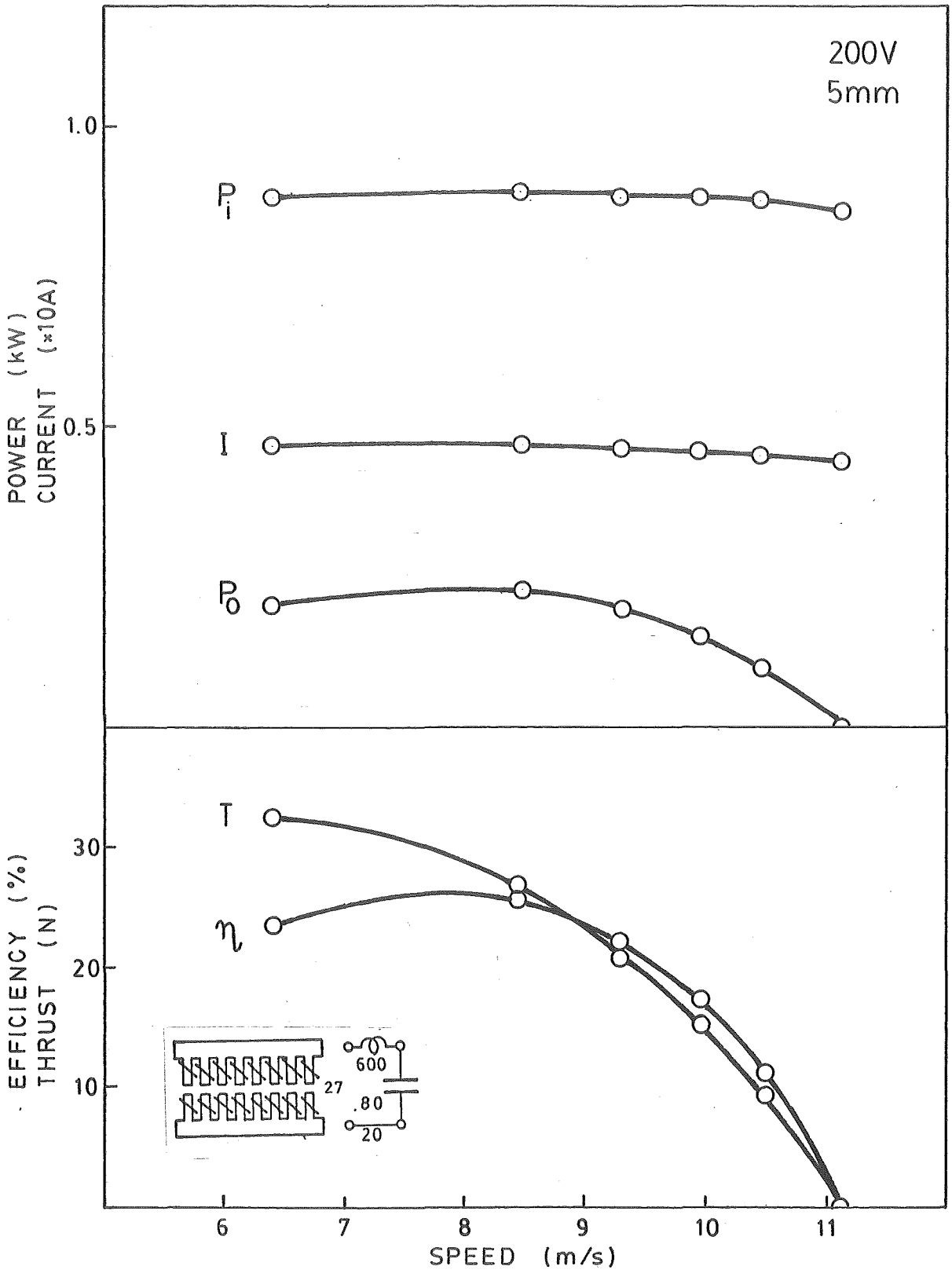
200V
5mm
1.0
0.5
POWER (kW)
CURRENT (×10A)
P_i
I
P_o
T
η
30
20
10
EFFICIENCY (%)
THRUST (N)
600
27
.80
20
6
7
8
9
10
11
SPEED (m/s)

Fig. A81

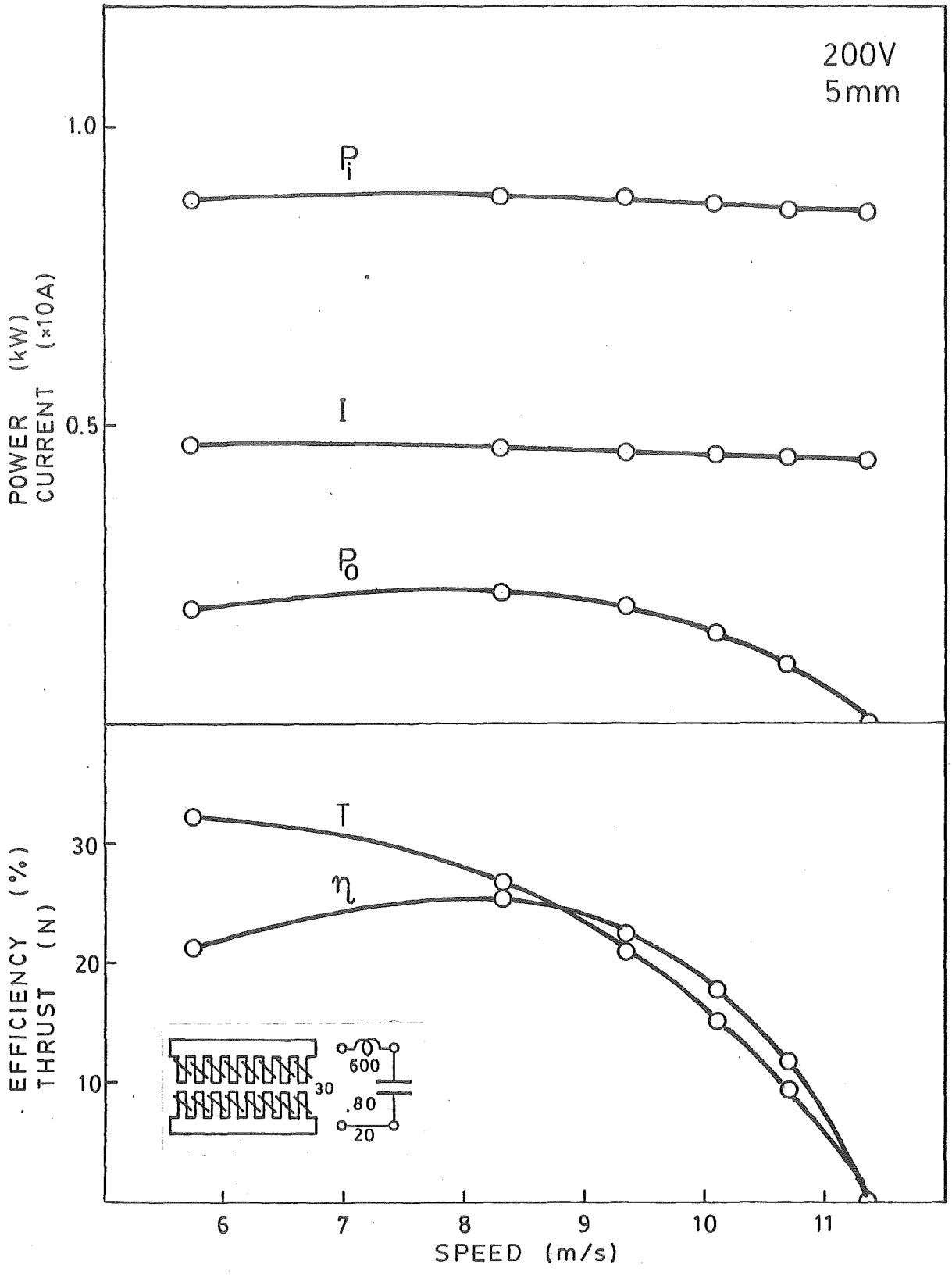
200V
5mm
1.0
0.5
POWER (kW)
CURRENT (×10A)
P_i
I
P_o
T
η
30
20
10
EFFICIENCY (%)
THRUST (N)
600
.80
20
30
6
7
8
9
10
11
SPEED (m/s)

Fig. A82

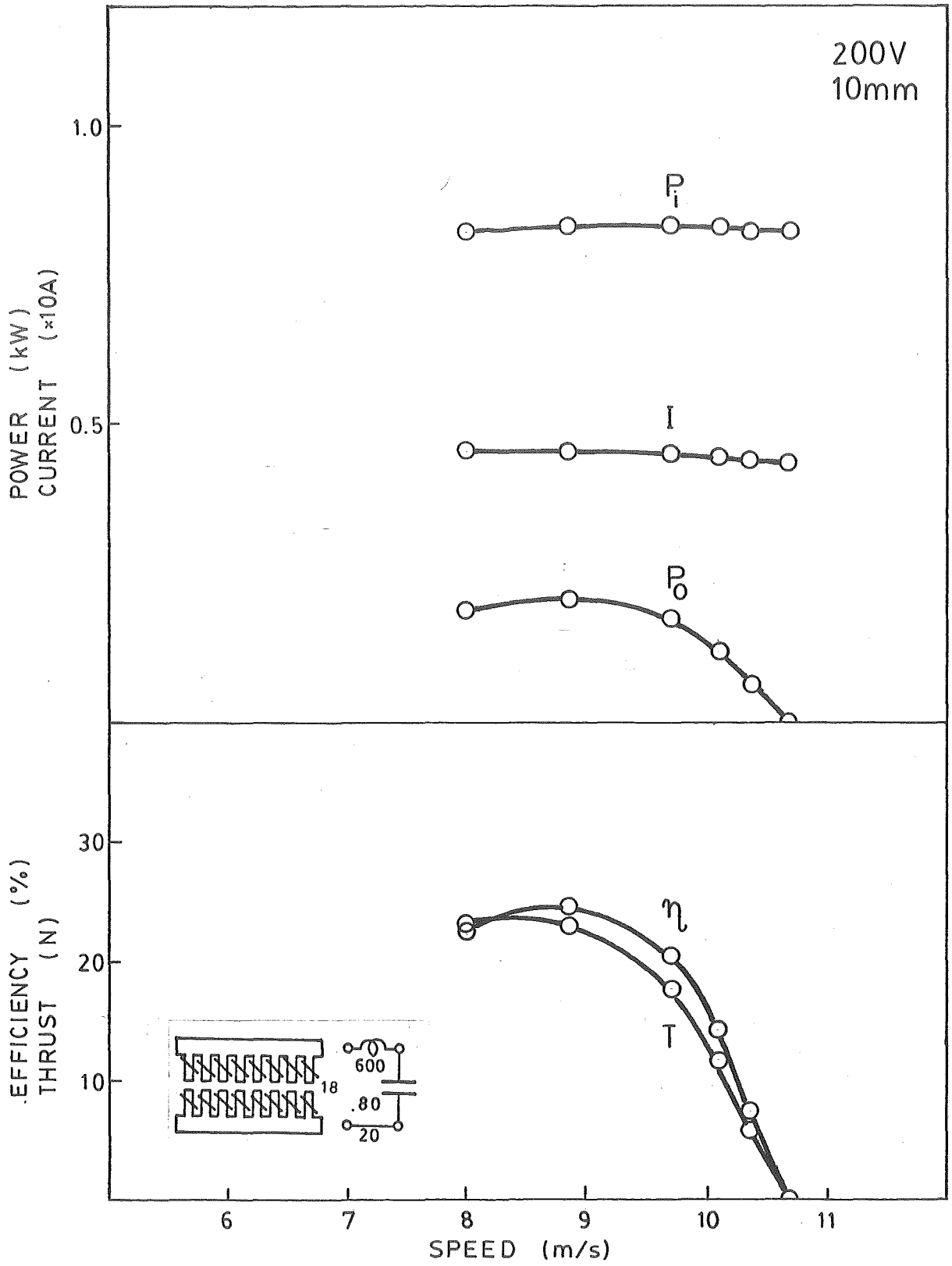
200V
10mm
1.0
0.5
POWER (kW)
CURRENT (×10A)
P_i
I
P_o
30
20
10
EFFICIENCY (%)
THRUST (N)
η
T
18
0
600
.80
20
6
7
8
9
10
11
SPEED (m/s)

Fig. A83

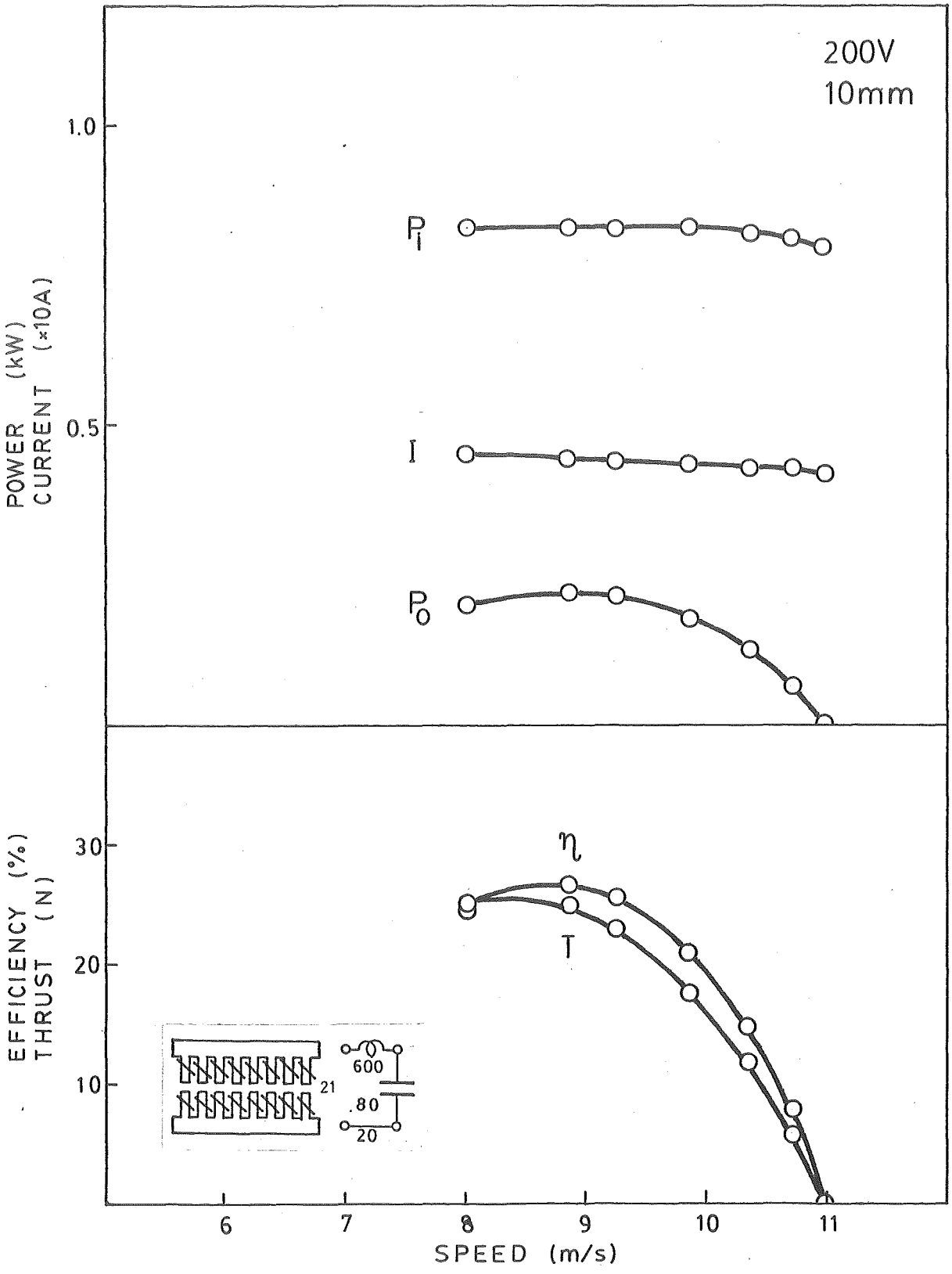
200V
10mm
1.0
0.5
POWER (kW)
CURRENT (×10A)
P_i
I
P_o
30
20
10
EFFICIENCY (%)
THRUST (N)
η
T
600
.80
20
21
6
7
8
9
10
11
SPEED (m/s)

Fig. A84

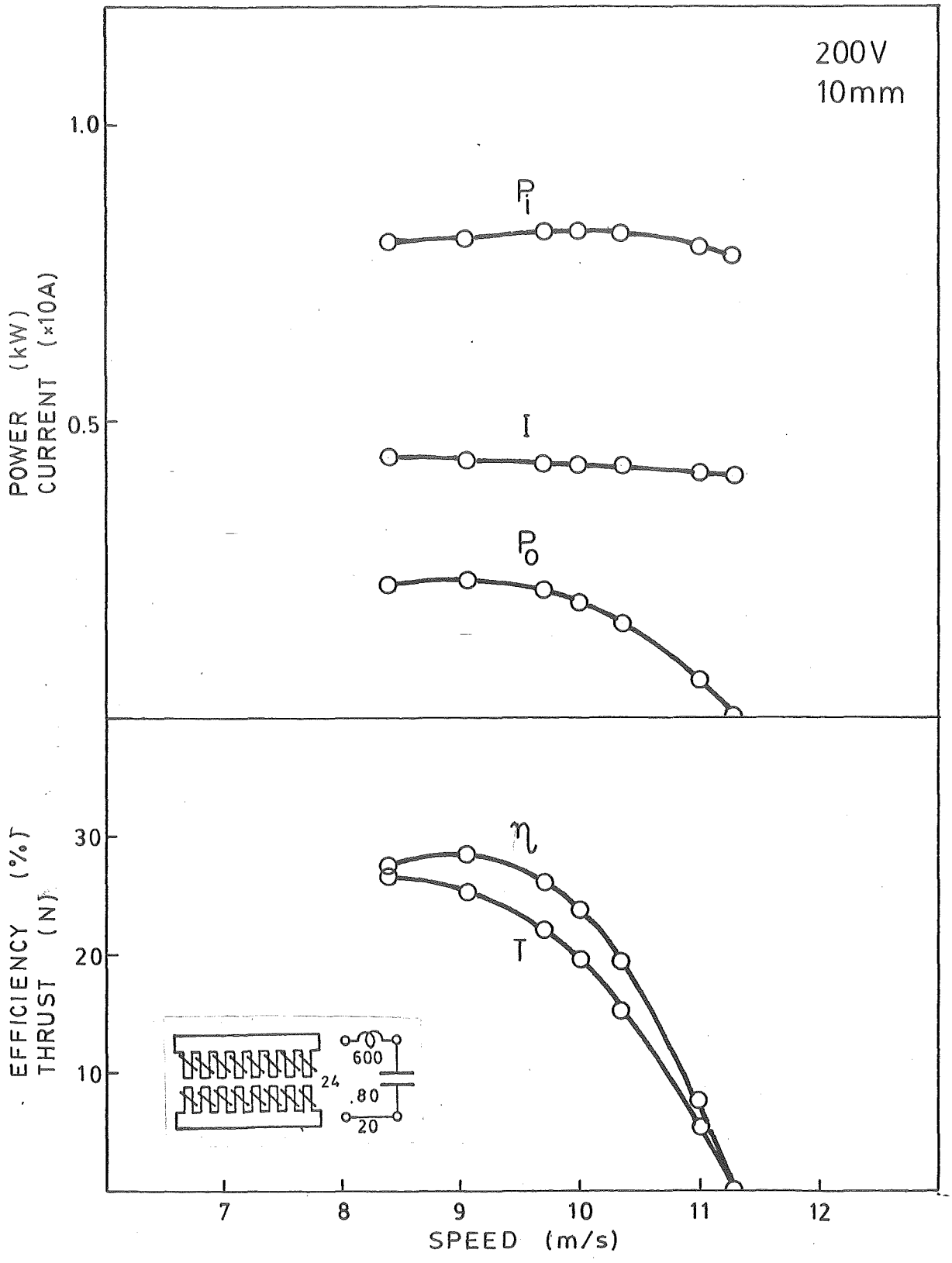
200V
10mm
1.0
0.5
POWER (kW)
CURRENT (×10A)
P_i
I
P_o
30
20
10
EFFICIENCY (%)
THRUST (N)
η
T
600
.80
20
24
7
8
9
10
11
12
SPEED (m/s)

Fig. A85

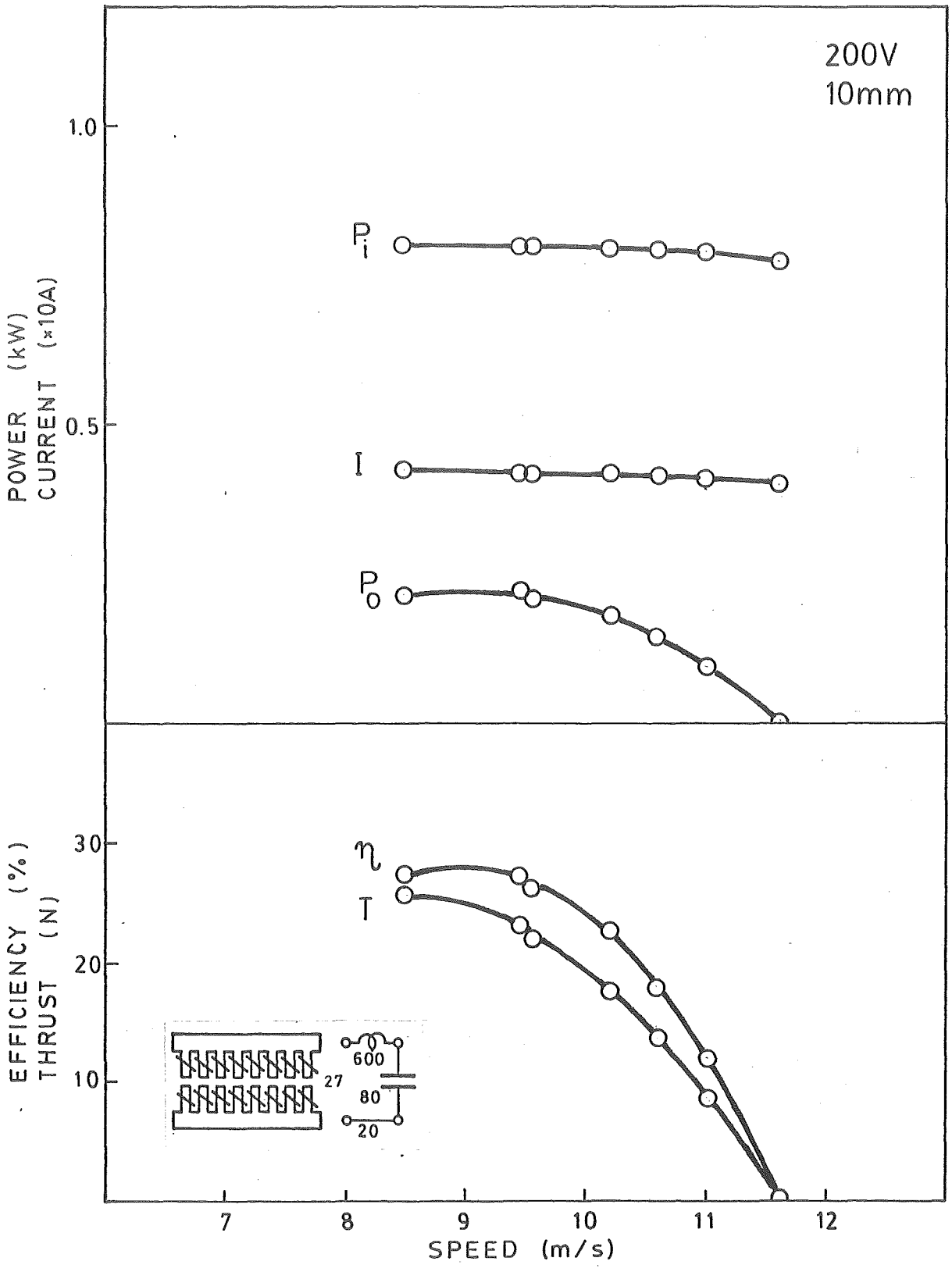
200V
10mm
1.0
0.5
POWER (kW)
CURRENT (×10A)
P_i
I
P_o
30
20
10
EFFICIENCY (%)
THRUST (N)
η
T
600
80
20
27
7
8
9
10
11
12
SPEED (m/s)

Fig. A86

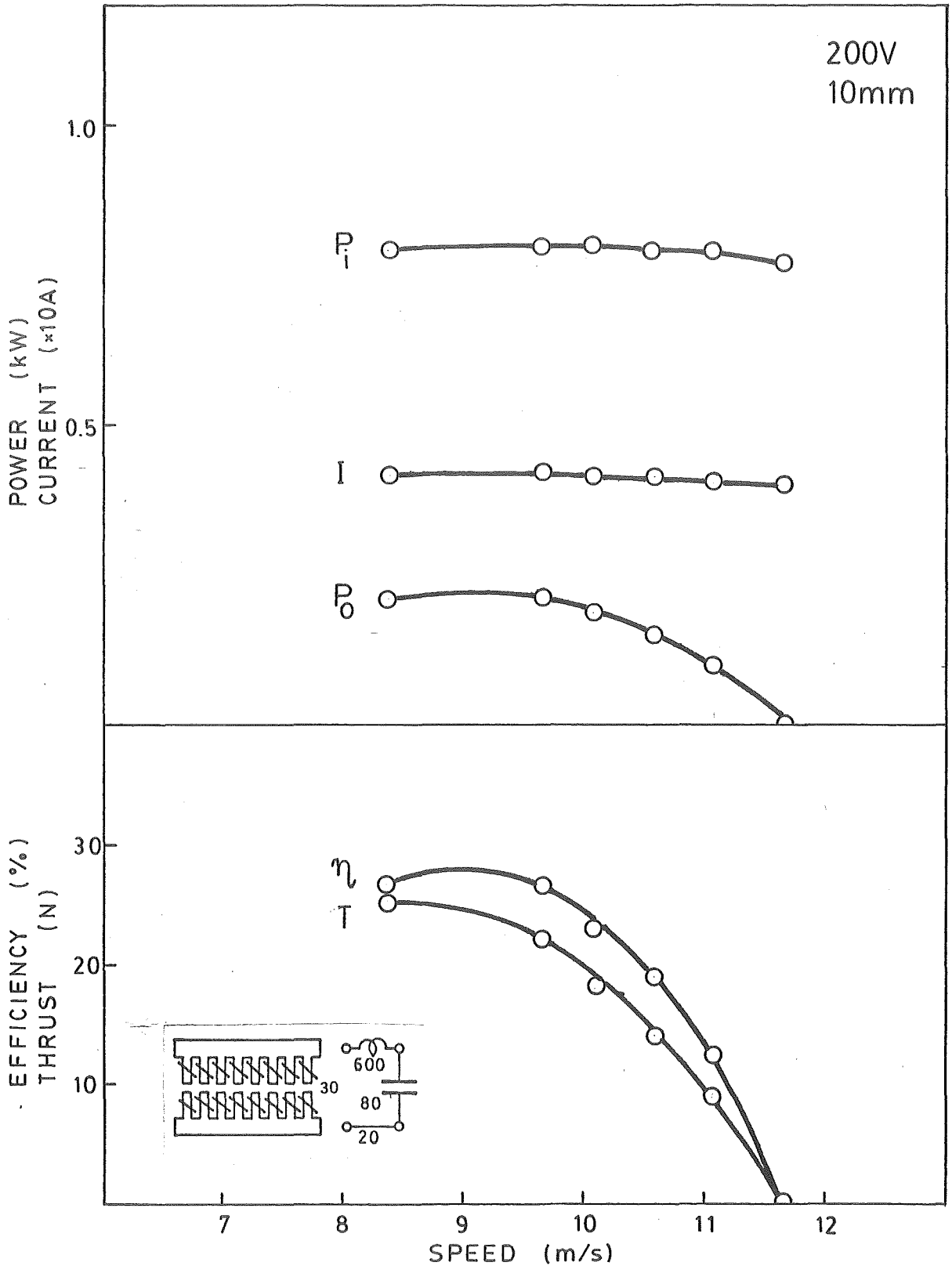
200V
10mm
1.0
0.5
POWER (kW)
CURRENT (×10A)
P_i
I
P_o
30
20
10
EFFICIENCY (%)
THRUST (N)
η
T
600
80
20
30
7
8
9
10
11
12
SPEED (m/s)

Fig. A87

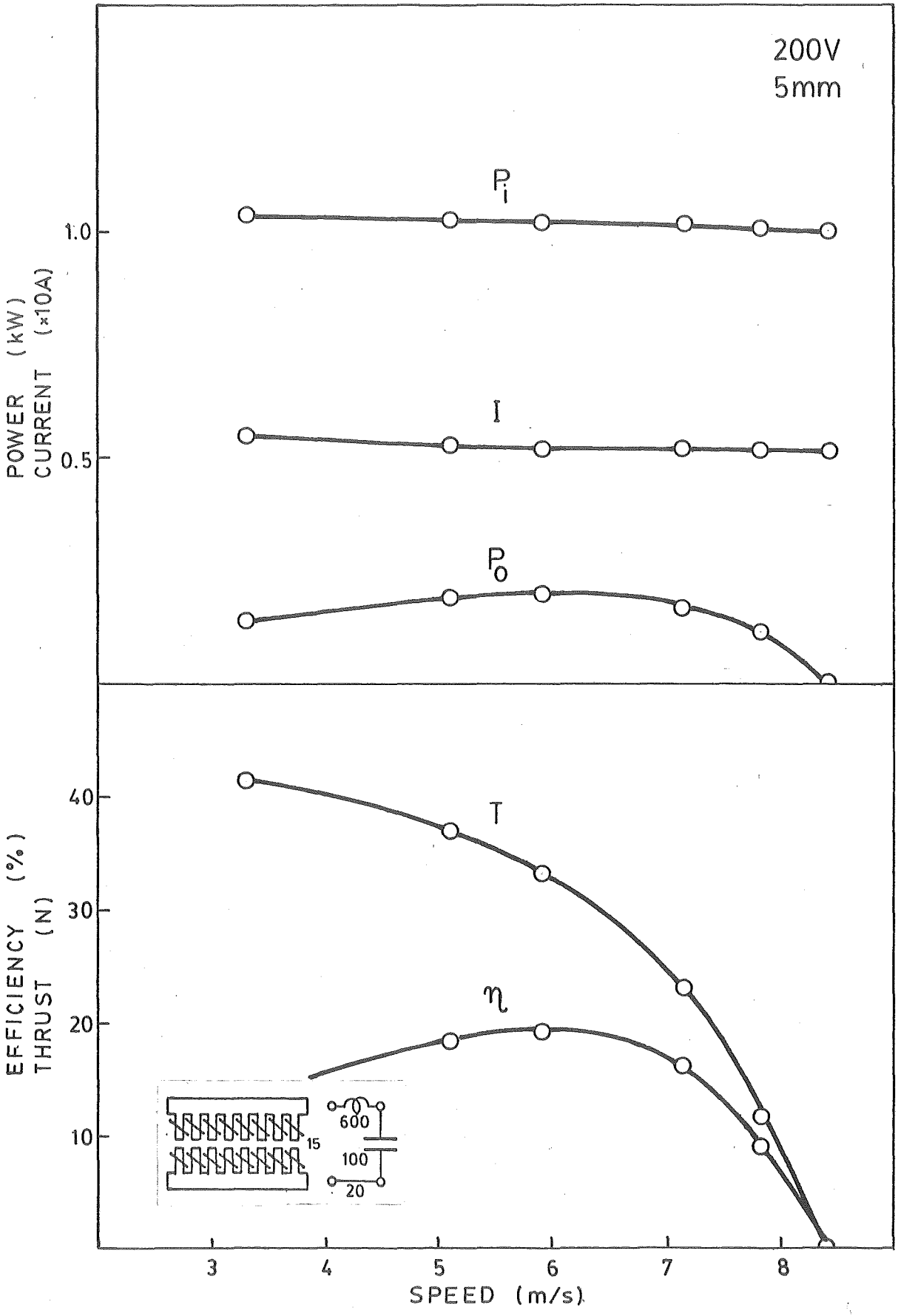
200V
5mm
P_i
I
P_o
1.0
0.5
POWER (kW)
CURRENT (×10A)
T
η
40
30
20
10
EFFICIENCY (%)
THRUST (N)
600
100
20
15
3
4
5
6
7
8
SPEED (m/s)

Fig. A88

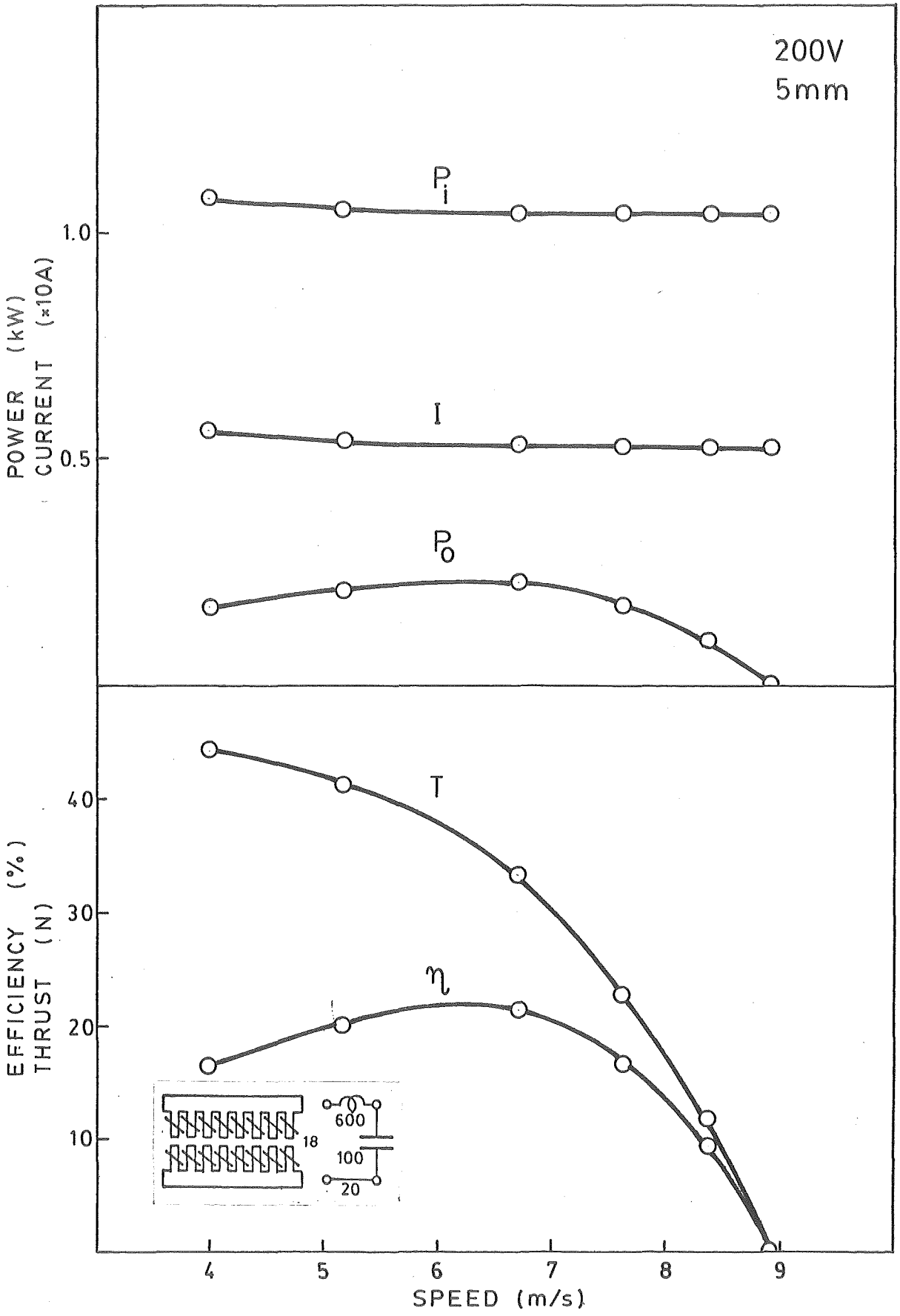
200V
5mm
P_i
I
P_o
POWER (kW)
CURRENT (×10A)
1.0
0.5
T
η
EFFICIENCY (%)
THRUST (N)
40
30
20
10
600
100
20
18
4
5
6
7
8
9
SPEED (m/s)

Fig. A89

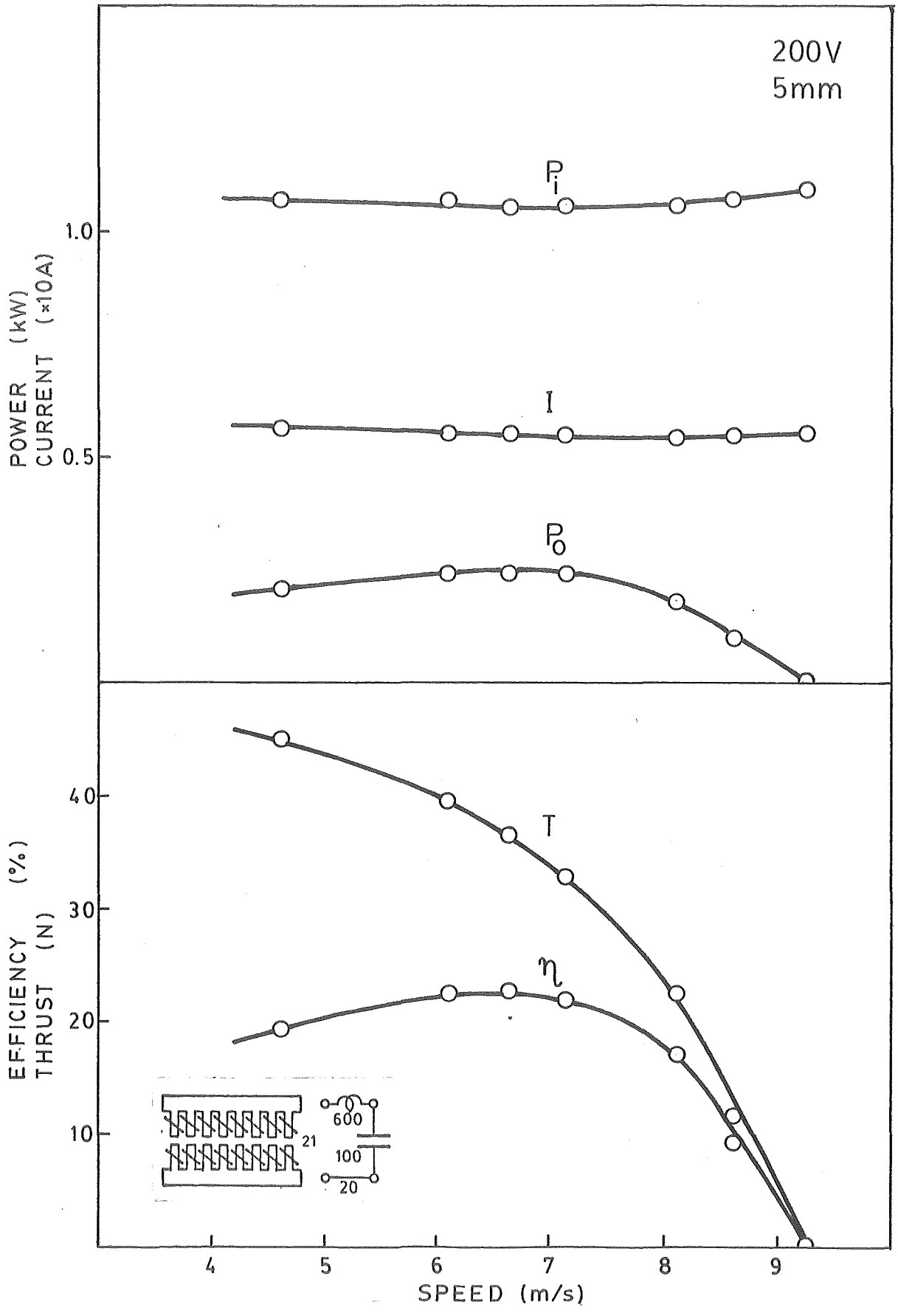
200V
5mm
P_i
I
P_o
POWER (kW)
CURRENT (×10A)
1.0
0.5
T
η
EFFICIENCY (%)
THRUST (N)
40
30
20
10
21
600
100
20
4
5
6
7
8
9
SPEED (m/s)

Fig. A90

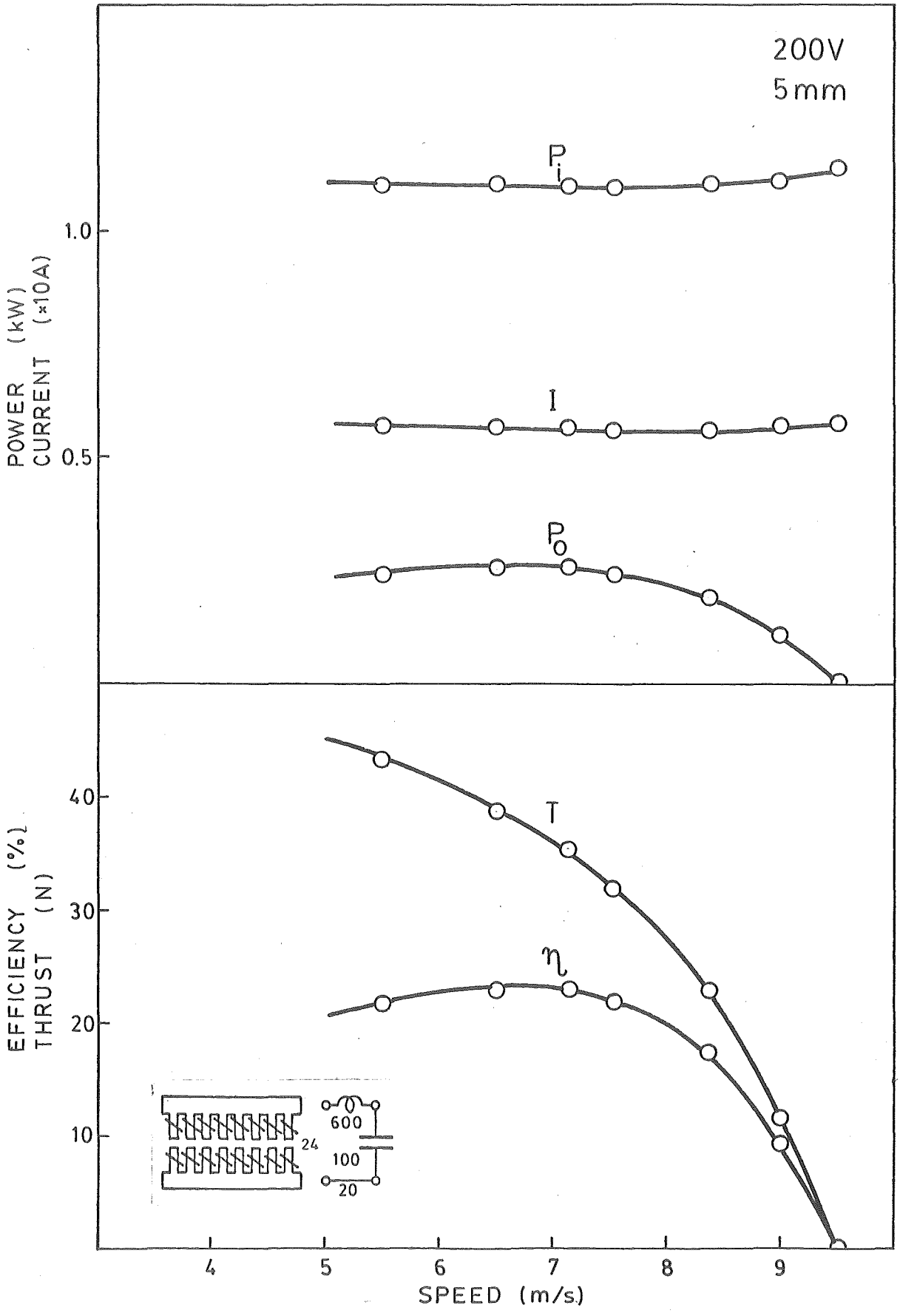
200V
5mm
P_i
I
P_o
POWER (kW)
CURRENT (×10A)
1.0
0.5
T
η
EFFICIENCY (%)
THRUST (N)
40
30
20
10
600
100
20
24
4
5
6
7
8
9
SPEED (m/s)

Fig. A91

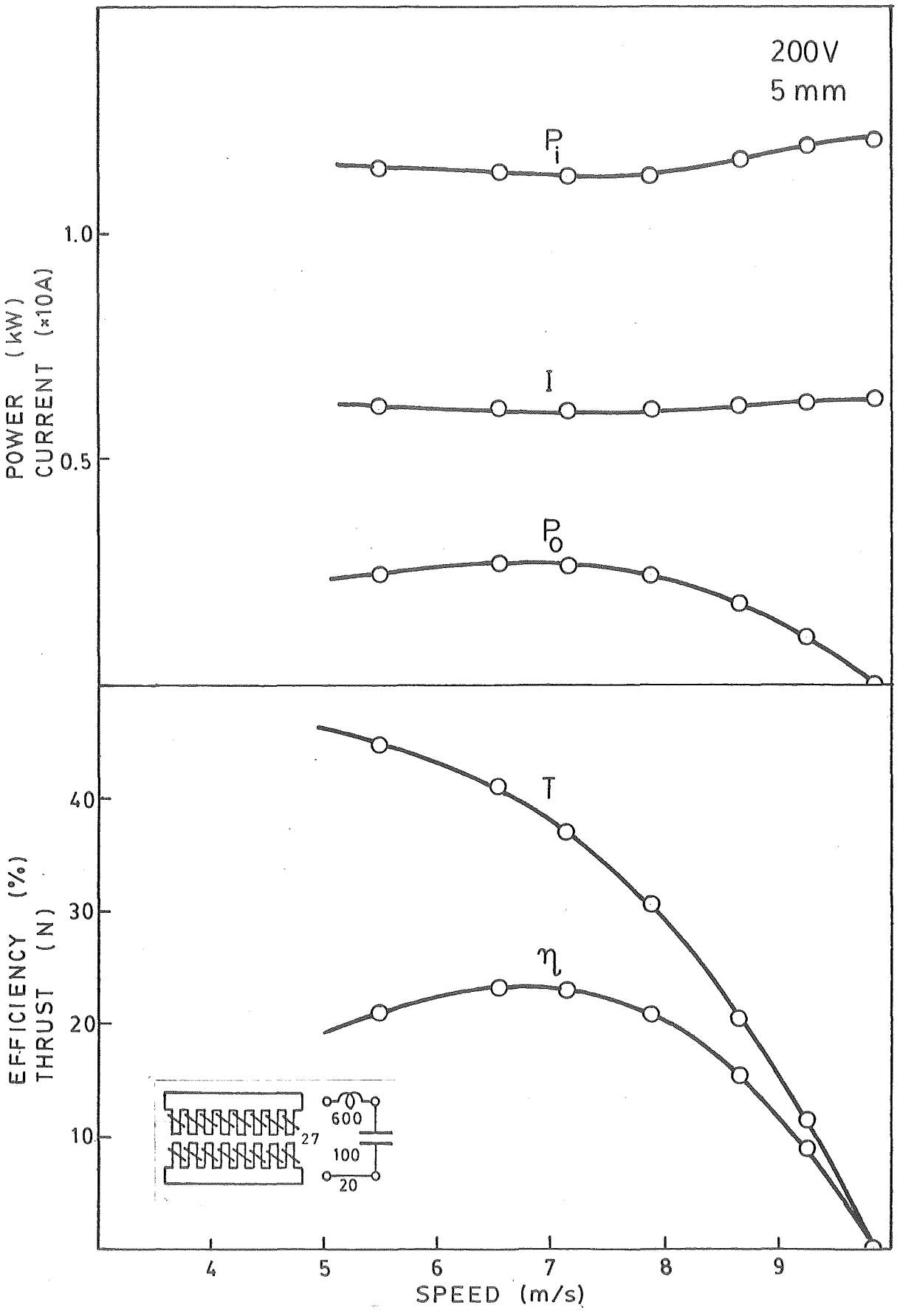
200V
5 mm
P_i
I
P_o
POWER (kW)
CURRENT (×10A)
1.0
0.5
T
η
EFFICIENCY (%)
THRUST (N)
40
30
20
10
27
600
100
20
4
5
6
7
8
9
SPEED (m/s)

Fig. A92

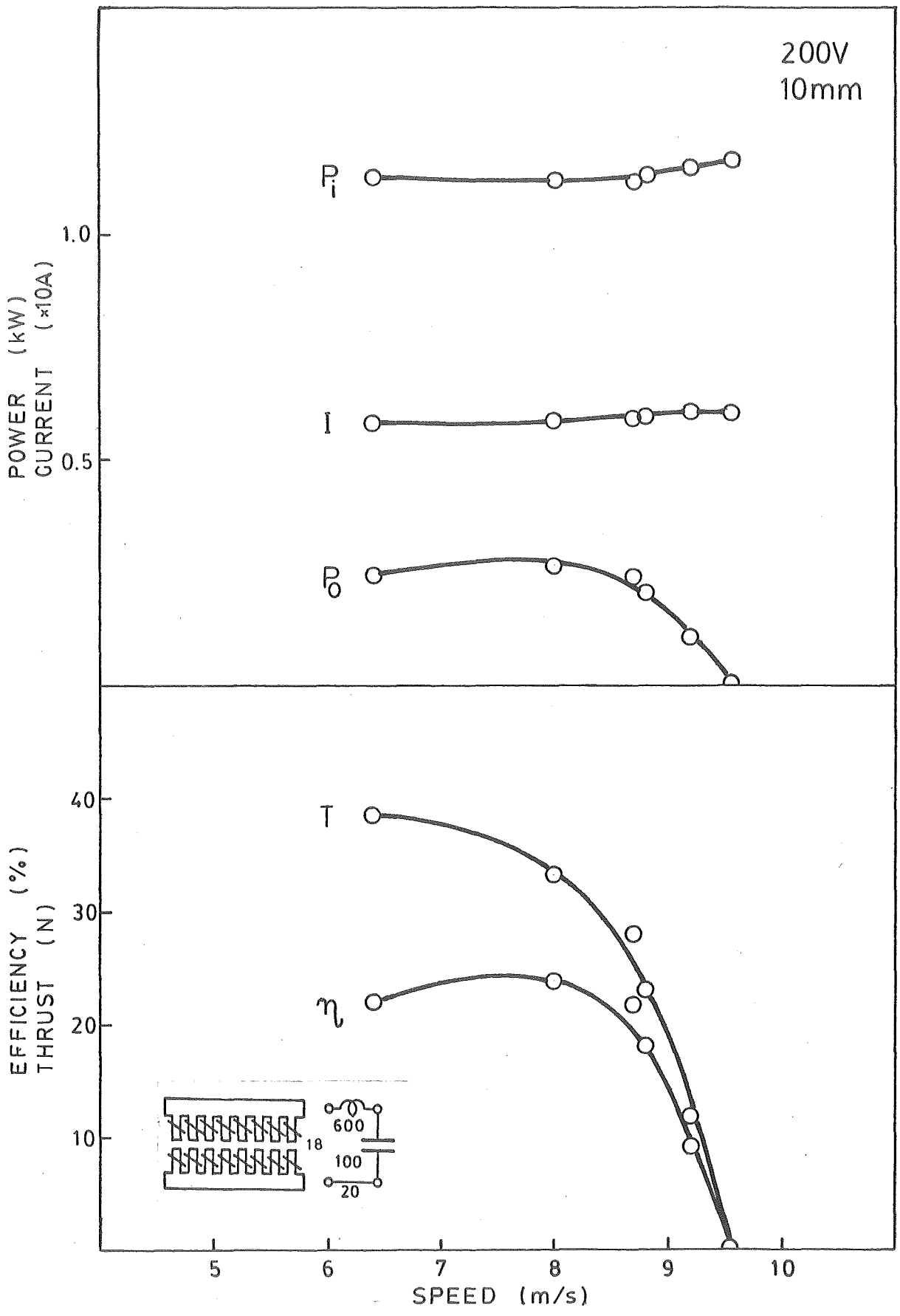
200V
10mm
P_i
I
P_o
POWER (kW)
CURRENT (×10A)
1.0
0.5
T
η
EFFICIENCY (%)
THRUST (N)
40
30
20
10
18
600
100
20
5
6
7
8
9
10
SPEED (m/s)

Fig. A93

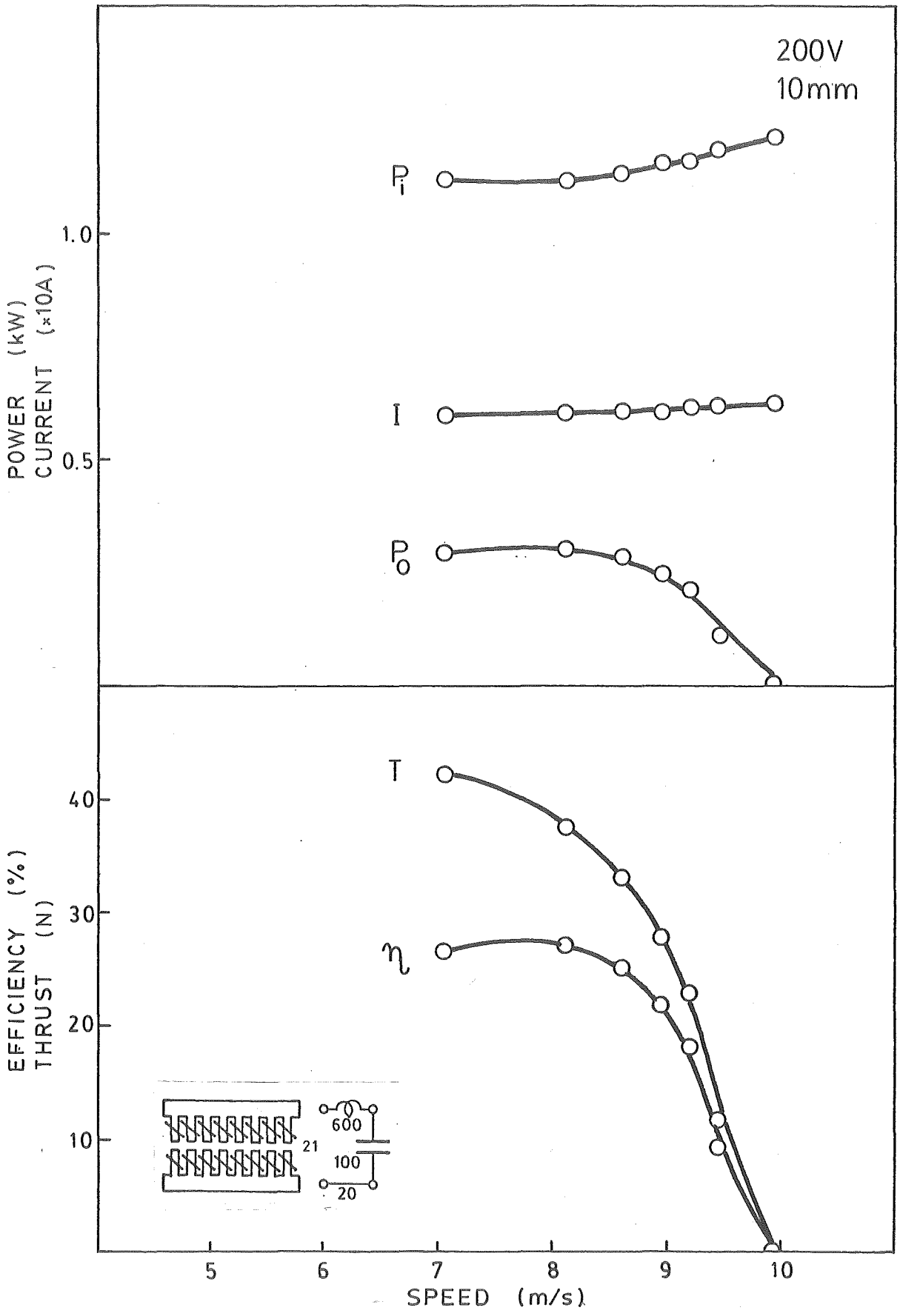
200V
10mm
P_i
I
P_o
POWER (kW)
CURRENT (×10A)
1.0
0.5
T
η
EFFICIENCY (%)
THRUST (N)
40
30
20
10
600
21
100
20
5
6
7
8
9
10
SPEED (m/s)

Fig. A94

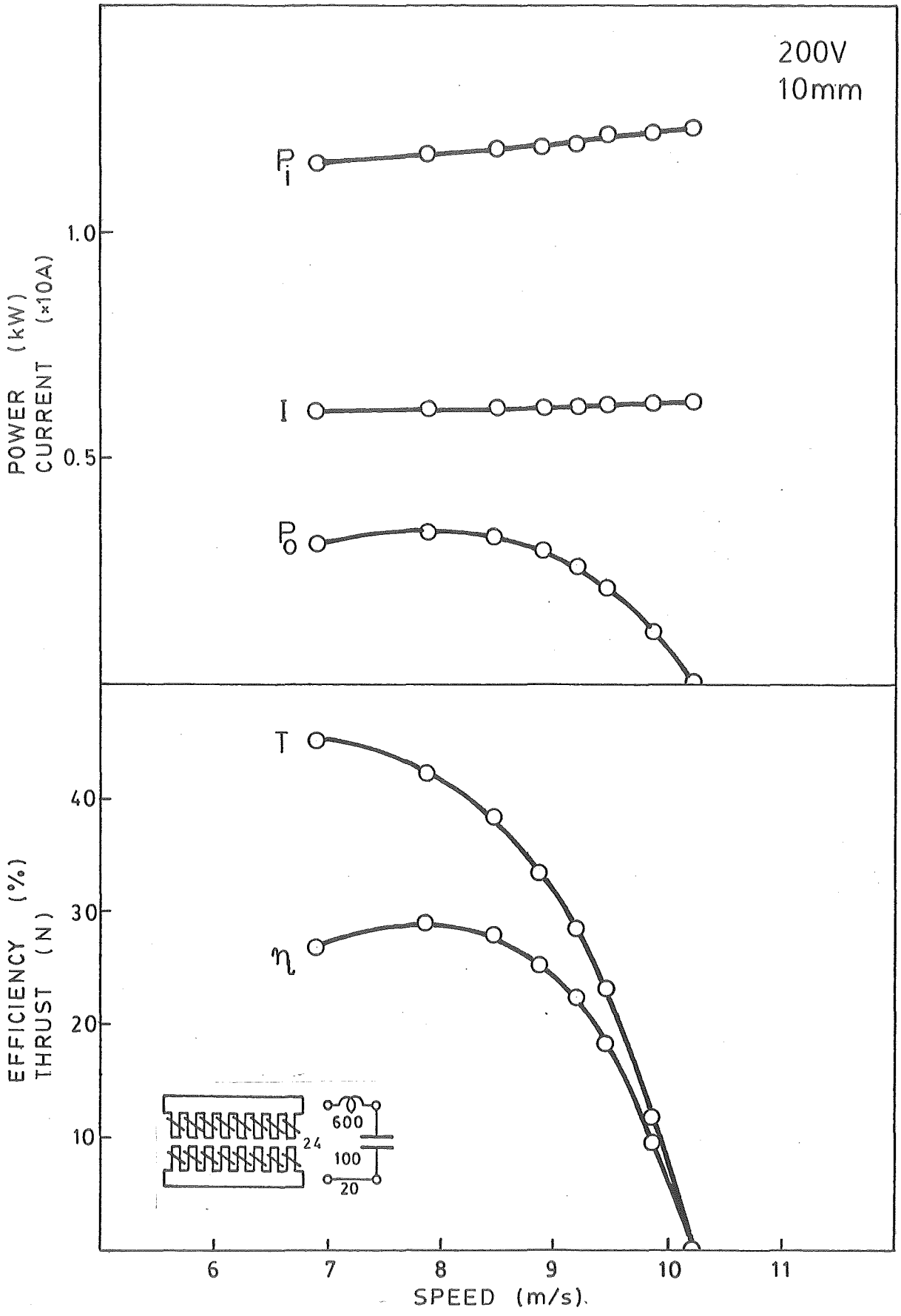
200V
10mm
P_i
I
P_o
POWER (kW)
CURRENT (×10A)
1.0
0.5
T
η
EFFICIENCY (%)
THRUST (N)
40
30
20
10
24
600
100
20
6
7
8
9
10
11
SPEED (m/s).

Fig. A95

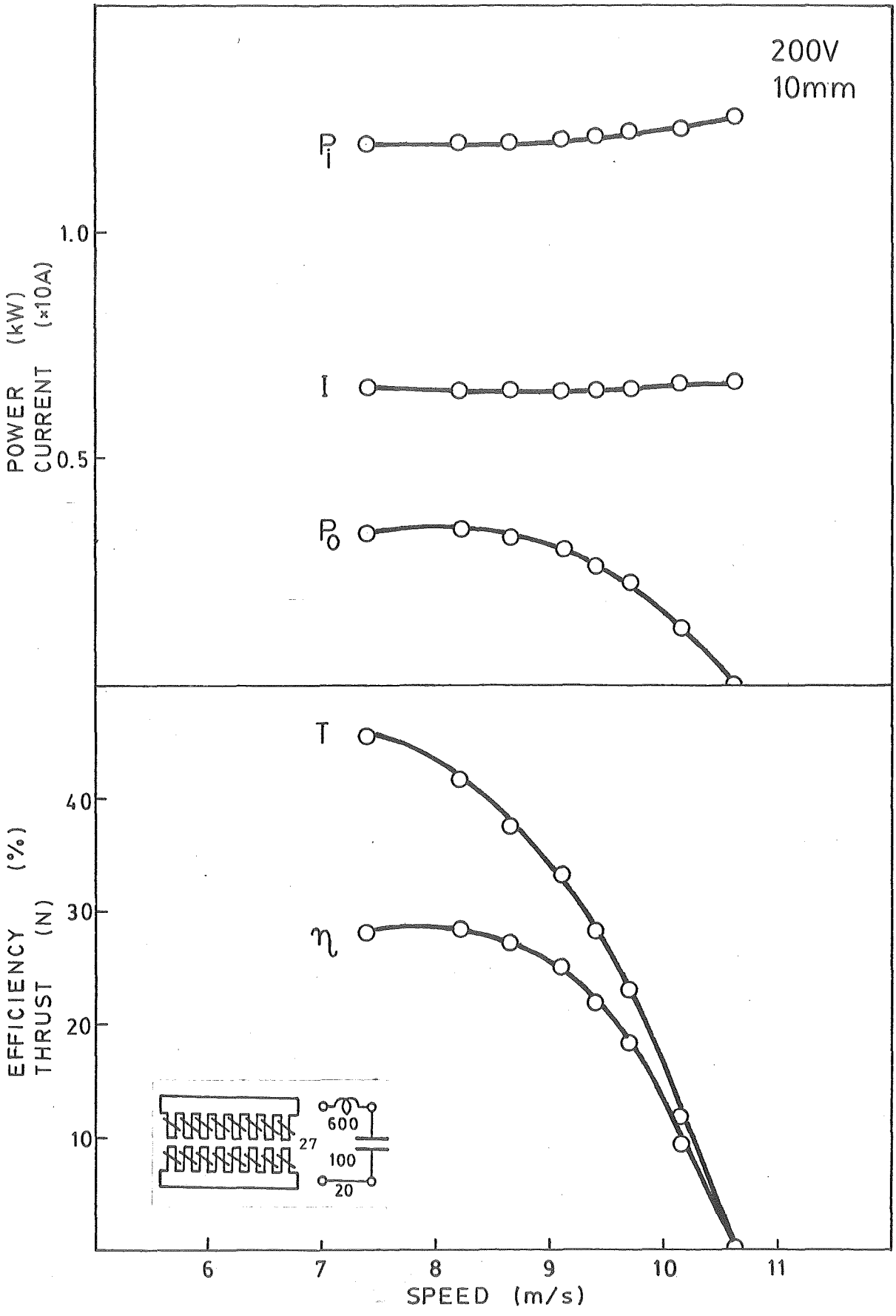
200V
10mm
P_i
I
P_o
POWER (kW)
CURRENT (×10A)
1.0
0.5
T
η
EFFICIENCY (%)
THRUST (N)
40
30
20
10
600
100
20
27
6
7
8
9
10
11
SPEED (m/s)

Fig. A 96

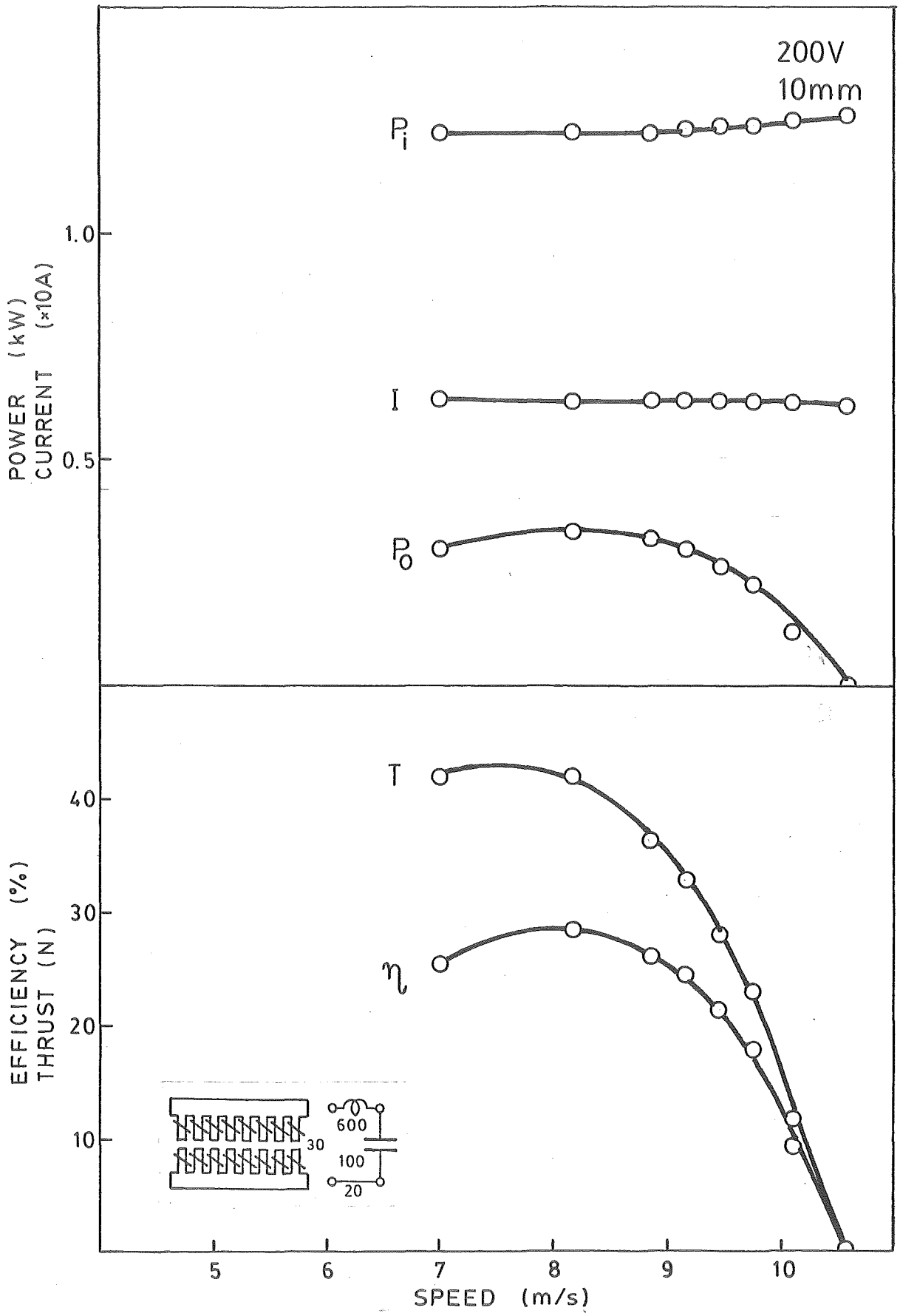
200V
10mm
P_i
I
P_o
POWER (kW)
CURRENT (×10A)
1.0
0.5
T
η
EFFICIENCY (%)
THRUST (N)
40
30
20
10
600
30
100
20
5
6
7
8
9
10
SPEED (m/s)

Fig. A97

APPENDIX 3

THEORETICAL AND EXPERIMENTAL RESULTS OF AN OVERLAP COIL STLIM

RESULT OF AN OVERLAP COIL STLIM

Similarly to Appendix 2, the conditions of each individual case is described by the KEY DIAGRAM illustrated in pages 175-176.

Figures A98 to A102 show theoretical performance curves of the machine at different values of airgap 18 mm, 21 mm, 24 mm, 27 mm and 30 mm.

Figures A103 to A117 show theoretical characteristics of the machine with different values of shunt capacitance of 800 μF/m, 1600 μF/m and 2400 μF/m and with different values of airgaps of 18 mm, 21 mm, 24 mm, 27 mm and 30 mm for 10 mm secondary.

Figures A118 to A127 show experimental characteristics of the motor with shunt capacitance of 800 μF/m, 1200 μF/m, 1600 μF/m, 2000 μF/m and 2400 μF/m and with the airgaps of 21 mm and 24 mm for 3 mm secondary, symmetrical stator blocks arrangement.

Figures A128 to A142 show experimental characteristics of the motor with shunt capacitance of 800 μF/m, 1200 μF/m, 1600 μF/m, 2000 μF/m and 2400 μF/m and with airgaps of 21 mm, 24 mm and 27 mm for 10 mm secondary, symmetrical stator blocks arrangement.

Figures A143 to A157 show experimental characteristics of the offset stator blocks motor corresponding to the theoretical case of Figures A103 to A117.

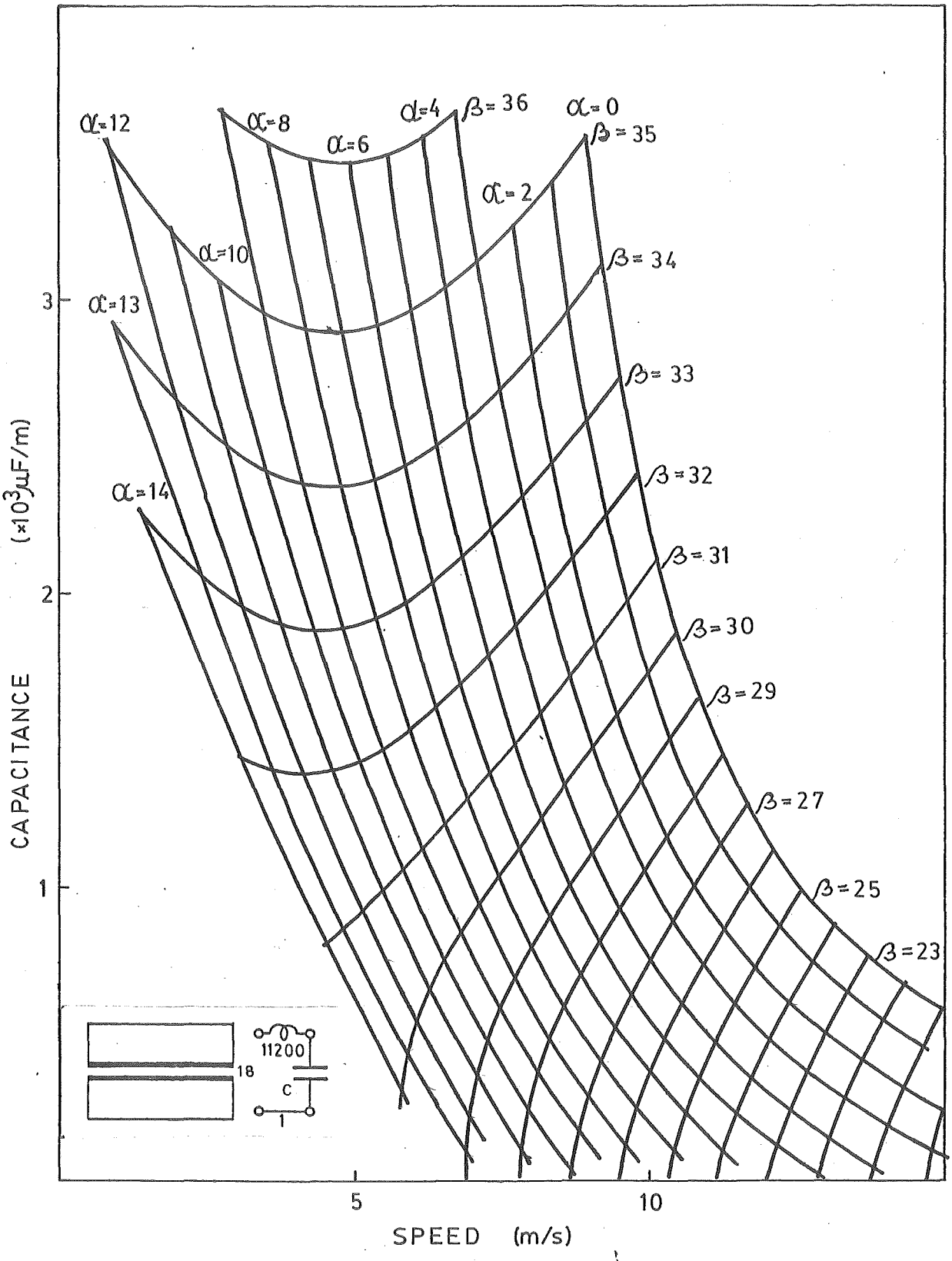
α=12
α=8
α=6
α=4
β=36
α=0
β=35
α=2
α=10
β=34
α=13
β=33
β=32
α=14
β=31
β=30
β=29
β=27
β=25
β=23
3
2
1
CAPACITANCE (×10³μF/m)
5
10
SPEED (m/s)
11200
18
C
1

Fig. A98

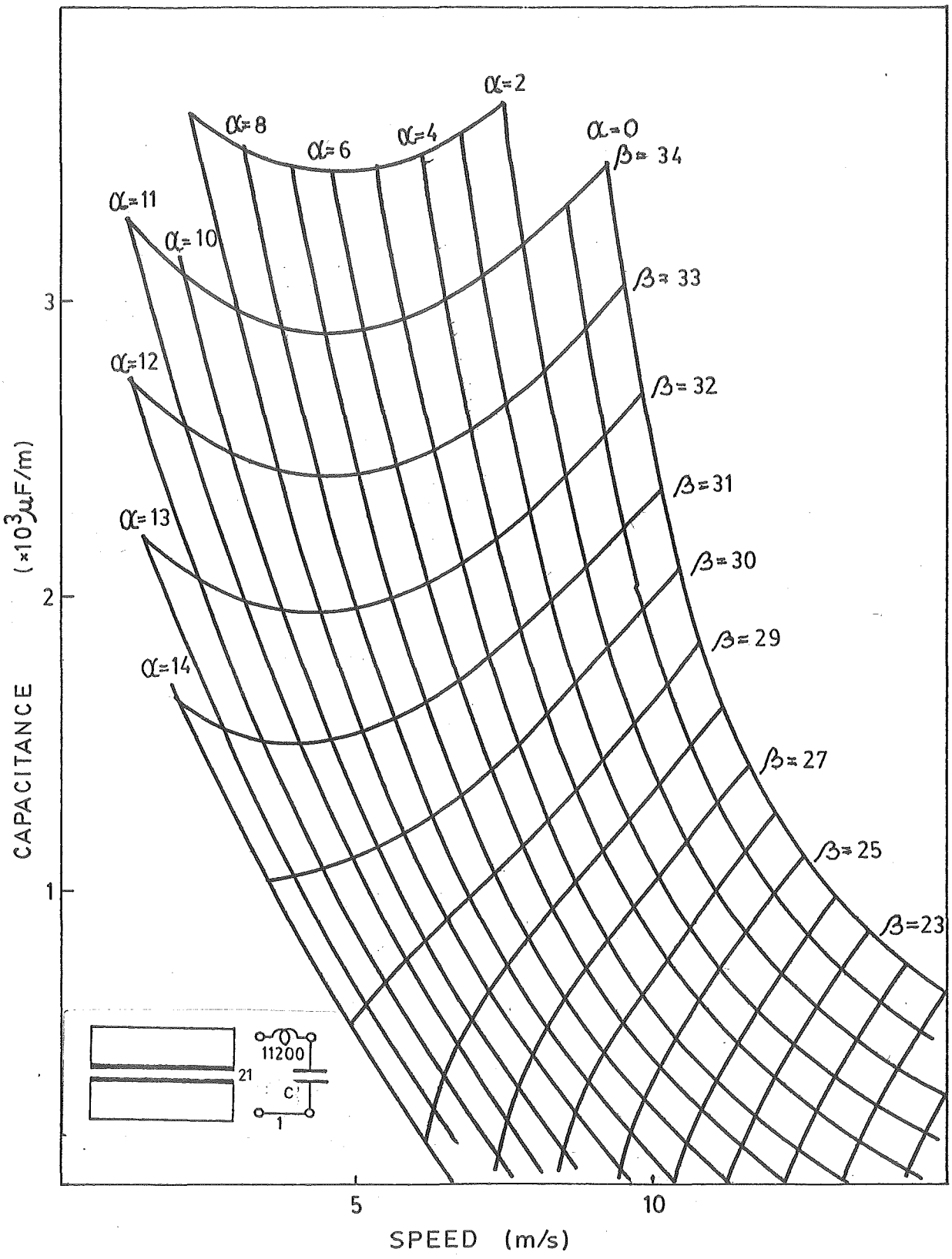
α=2
α=8
α=6
α=4
α=0
β=34
α=11
α=10
β=33
α=12
β=32
β=31
α=13
β=30
β=29
α=14
β=27
β=25
β=23
3
2
1
CAPACITANCE (×10³μF/m)
5
10
SPEED (m/s)
11200
21
C
1

Fig. A99

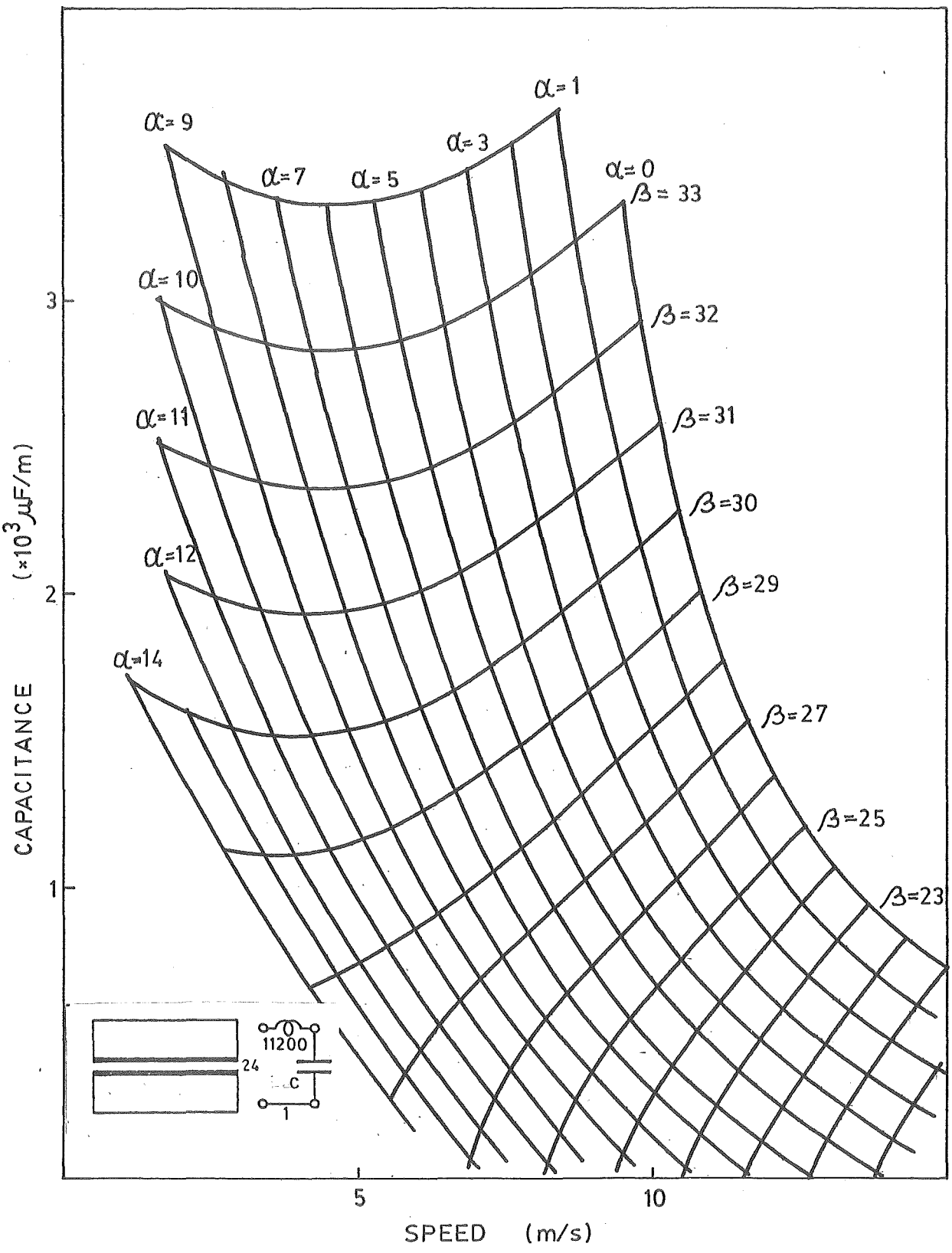
α= 1
α= 9
α= 3
α= 7
α= 5
α= 0
β = 33
α= 10
β=32
α= 11
β=31
β=30
α=12
β=29
α=14
β=27
β=25
β=23
3
2
1
CAPACITANCE (×10³μF/m)
5
10
SPEED (m/s)
0
11200
24
C
1

Fig. A100

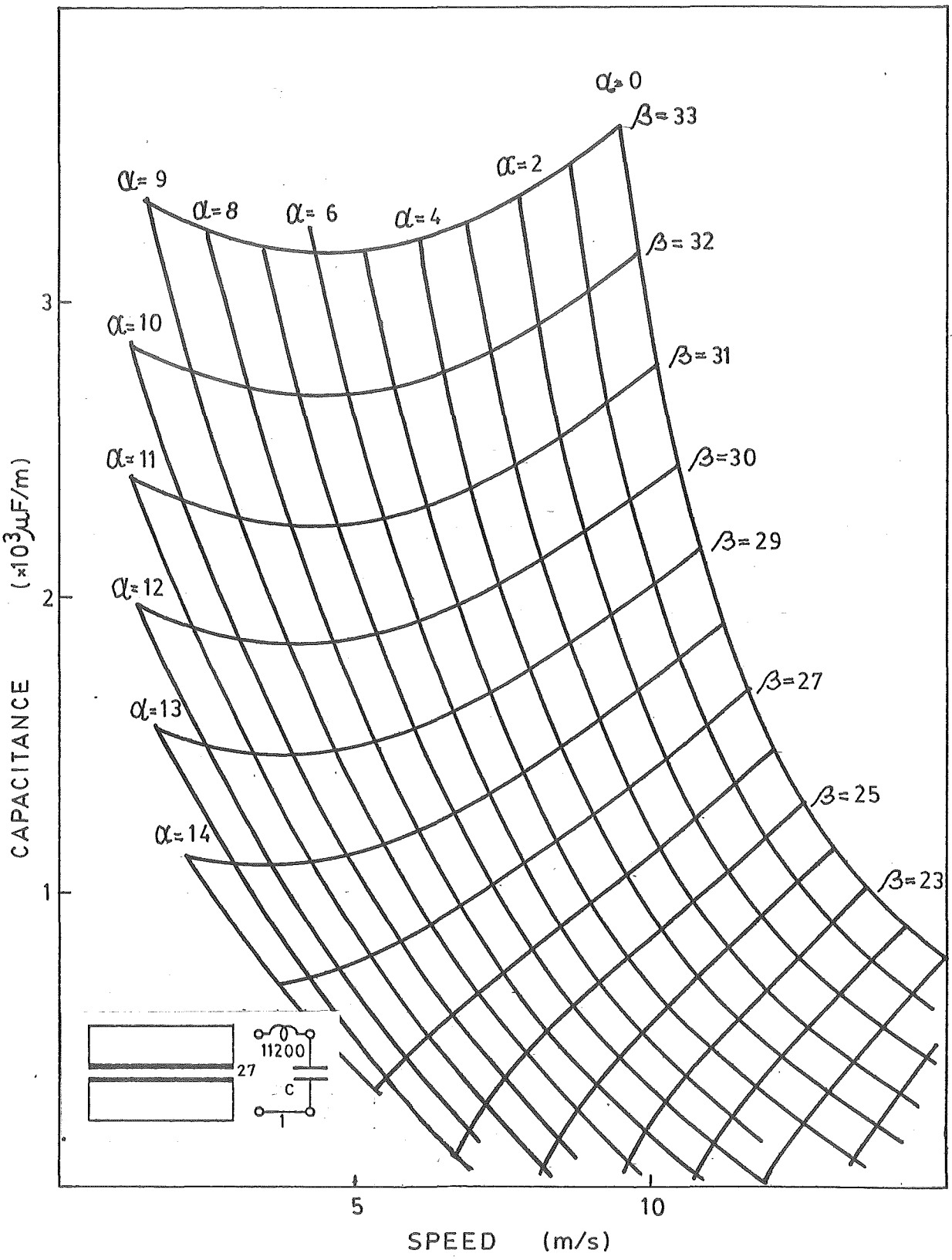
α= 0
β= 33
α= 2
α= 9
α= 8
α= 6
α= 4
β= 32
α=10
β= 31
α=11
β=30
β=29
α=12
β=27
α=13
β=25
α=14
β=23
3
2
1
CAPACITANCE (×10³μF/m)
5
10
SPEED (m/s)
11200
27
C
1

Fig. A101

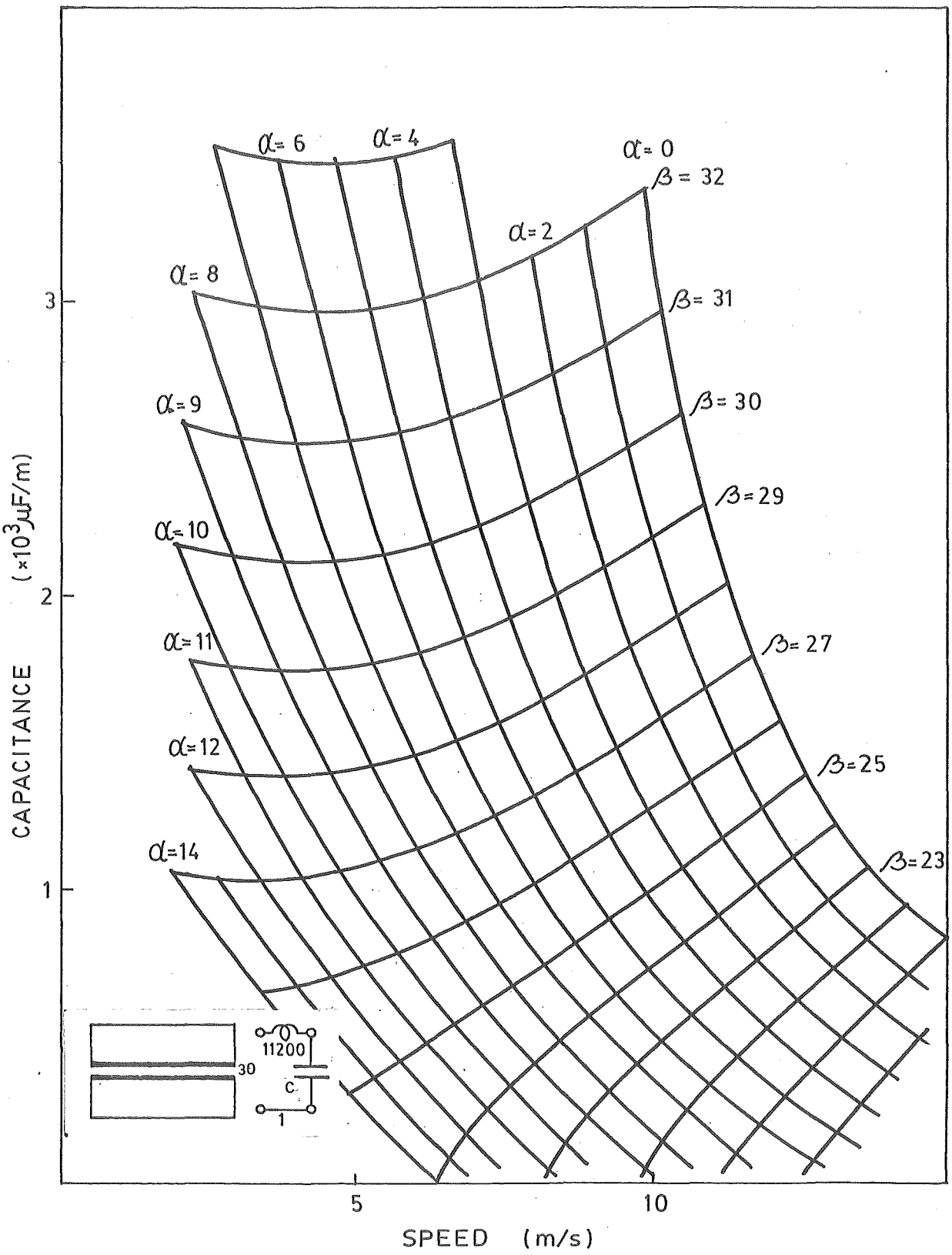
α= 6
α= 4
α= 0
β = 32
α= 2
α= 8
β= 31
α= 9
β= 30
β= 29
α= 10
α= 11
β= 27
α= 12
β= 25
α=14
β= 23
CAPACITANCE (×10³μF/m)
3
2
1
5
10
SPEED (m/s)
11200
30
C
1

Fig.102

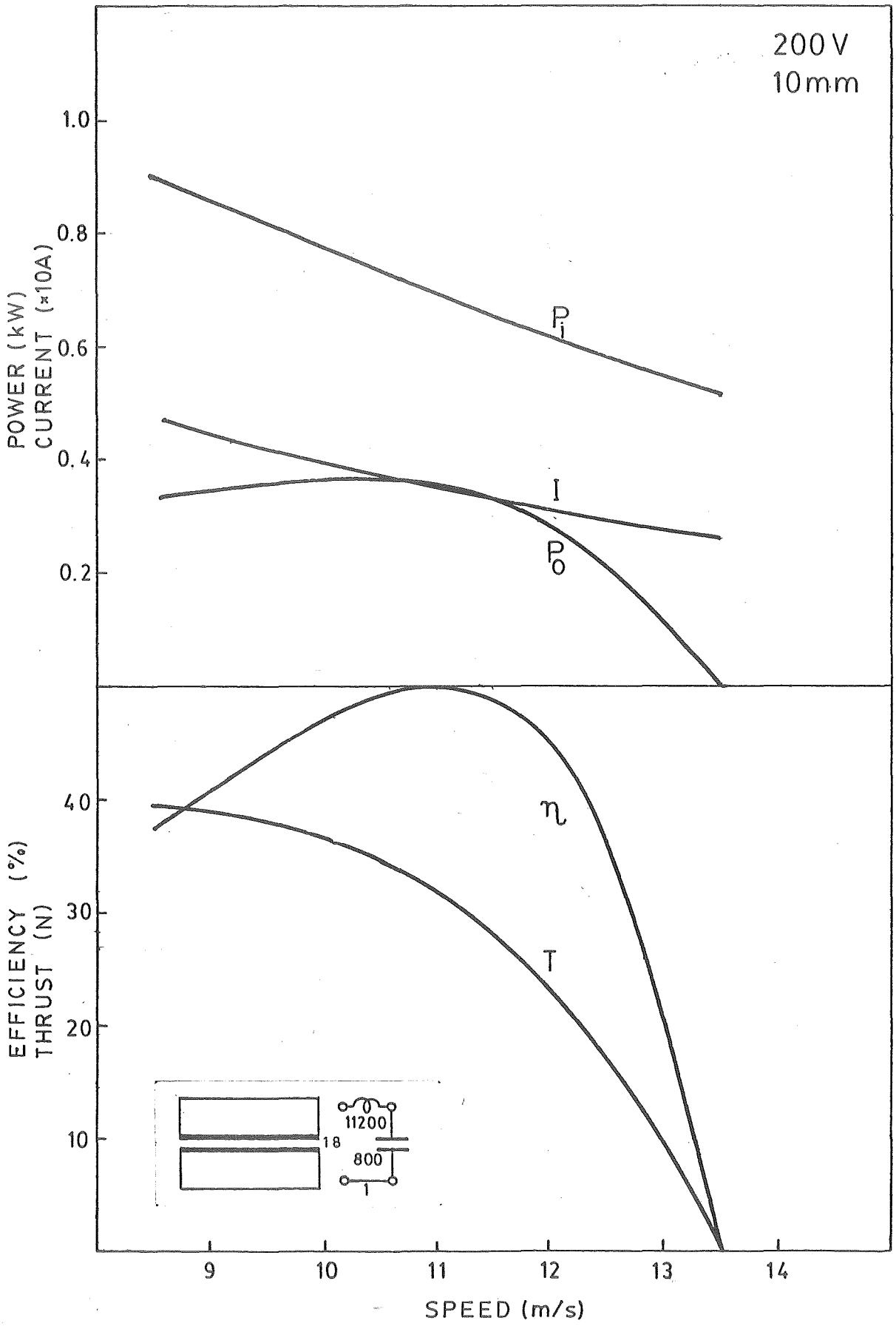
200 V
10 mm
POWER (kW)
CURRENT (×10A)
1.0
0.8
0.6
0.4
0.2
P_i
I
P_o
EFFICIENCY (%)
THRUST (N)
40
30
20
10
η
T
11200
18
800
1
9
10
11
12
13
14
SPEED (m/s)

Fig. A103

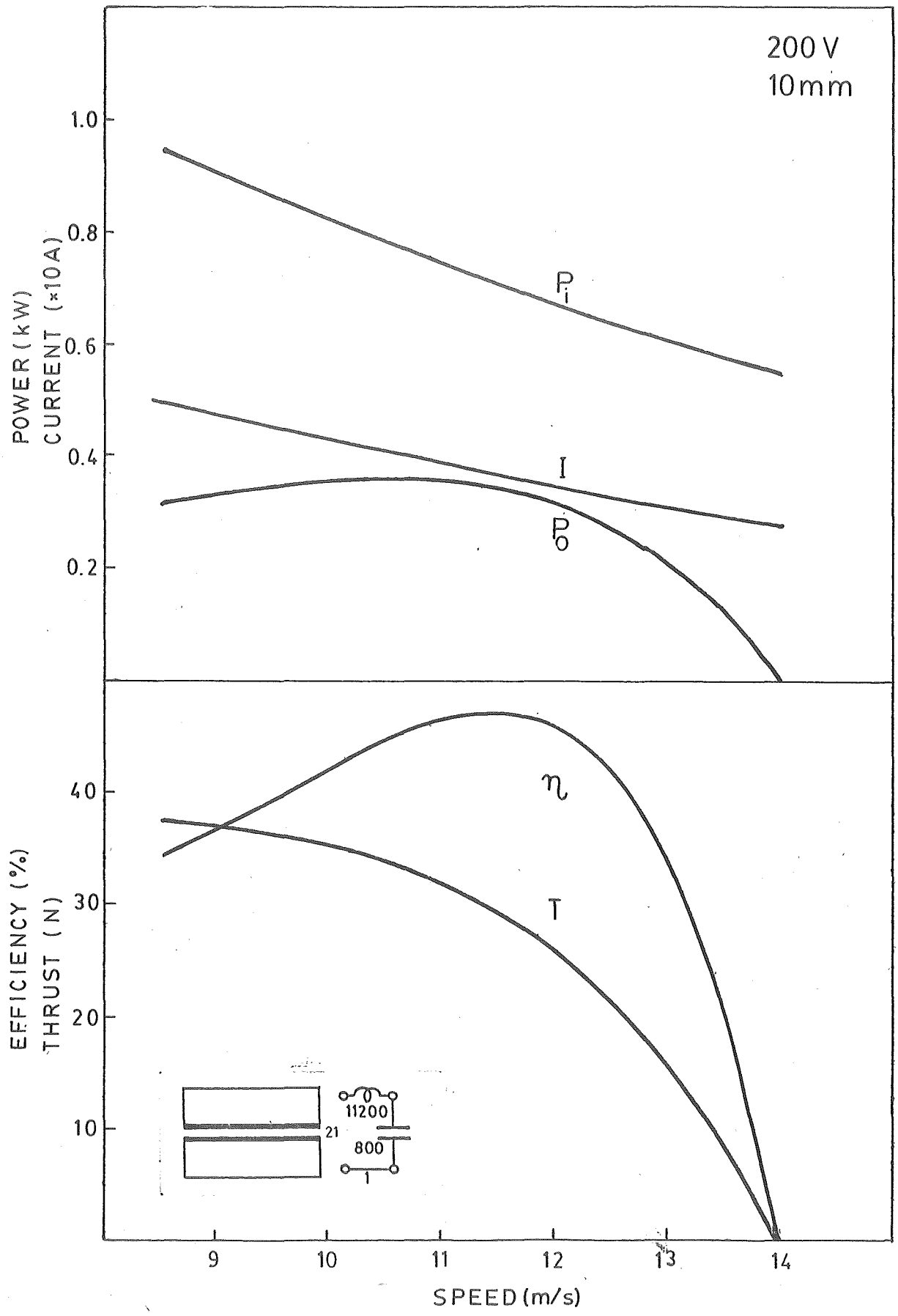
200 V
10 mm
POWER (kW)
CURRENT (×10A)
1.0
0.8
0.6
0.4
0.2
P_i
I
P_o
EFFICIENCY (%)
THRUST (N)
40
30
20
10
η
T
0
11200
21
800
1
9
10
11
12
13
14
SPEED (m/s)

Fig. A104

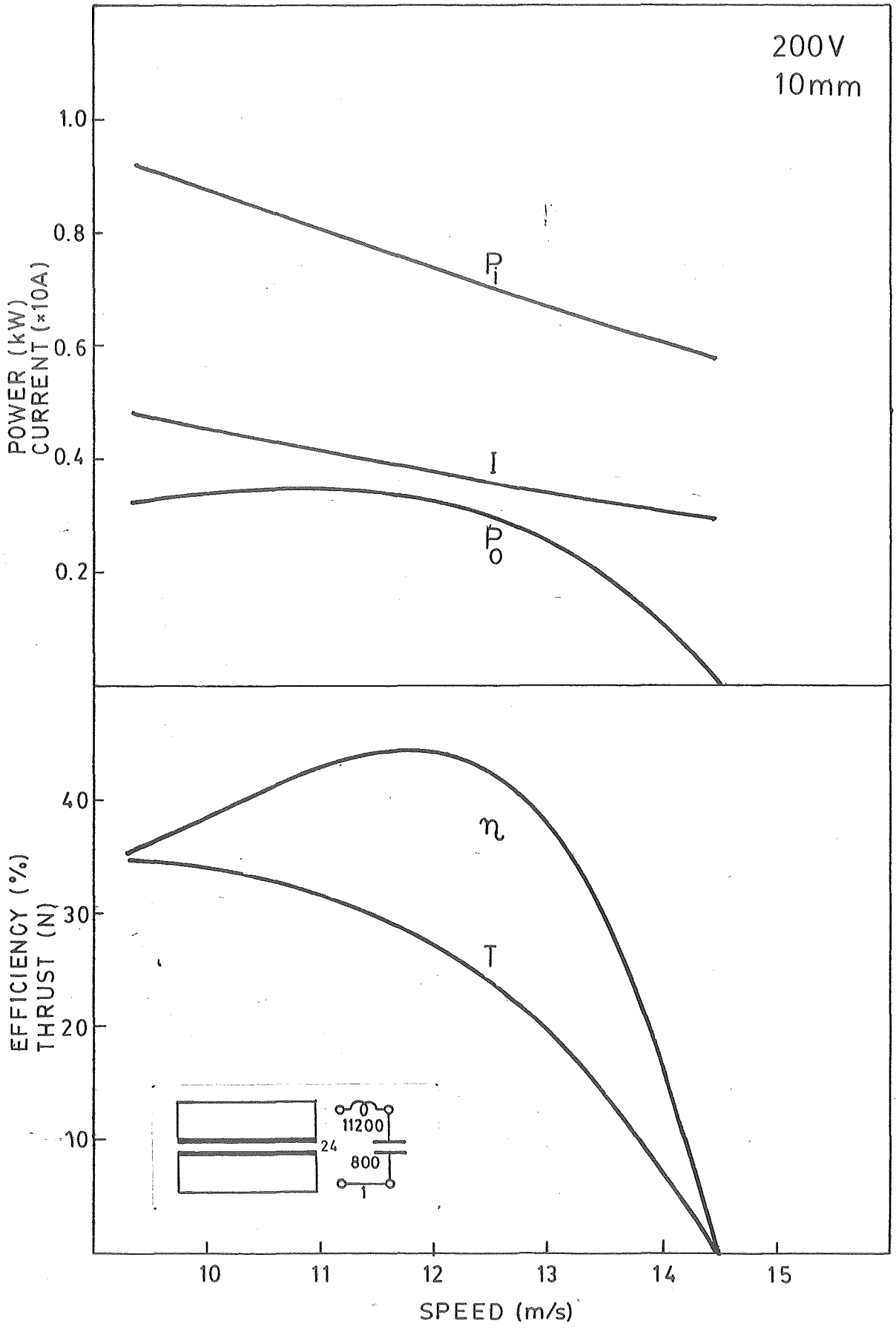
200V
10mm
POWER (kW)
CURRENT (×10A)
1.0
0.8
0.6
0.4
0.2
P_i
I
P_o
EFFICIENCY (%)
THRUST (N)
40
30
20
10
η
T
11200
24
800
1
10
11
12
13
14
15
SPEED (m/s)

Fig. A105

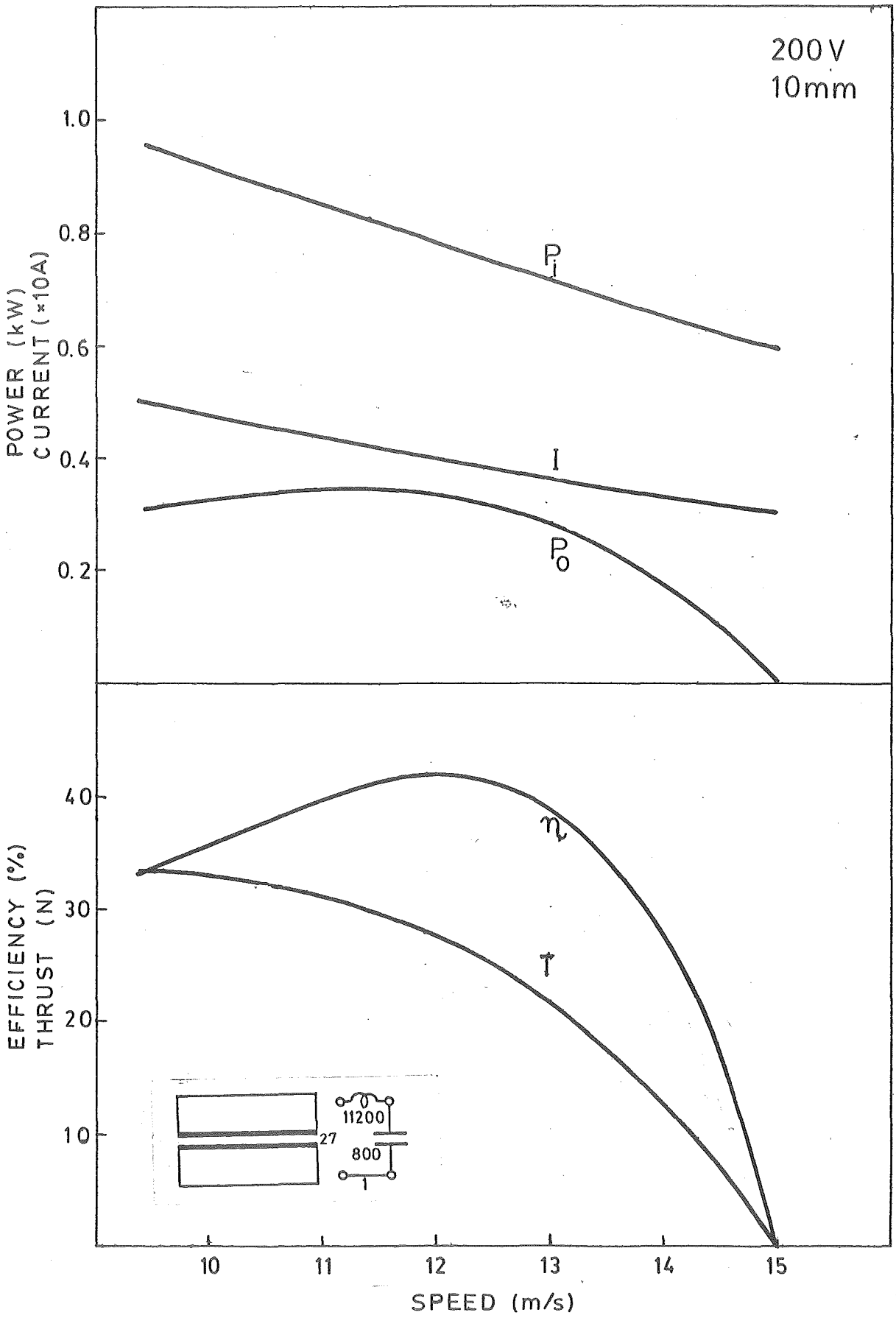
200 V
10mm
POWER (kW)
CURRENT (×10A)
1.0
0.8
0.6
0.4
0.2
P_i
I
P_o
EFFICIENCY (%)
THRUST (N)
40
30
20
10
η
T
11200
27
800
1
10
11
12
13
14
15
SPEED (m/s)

Fig.A106

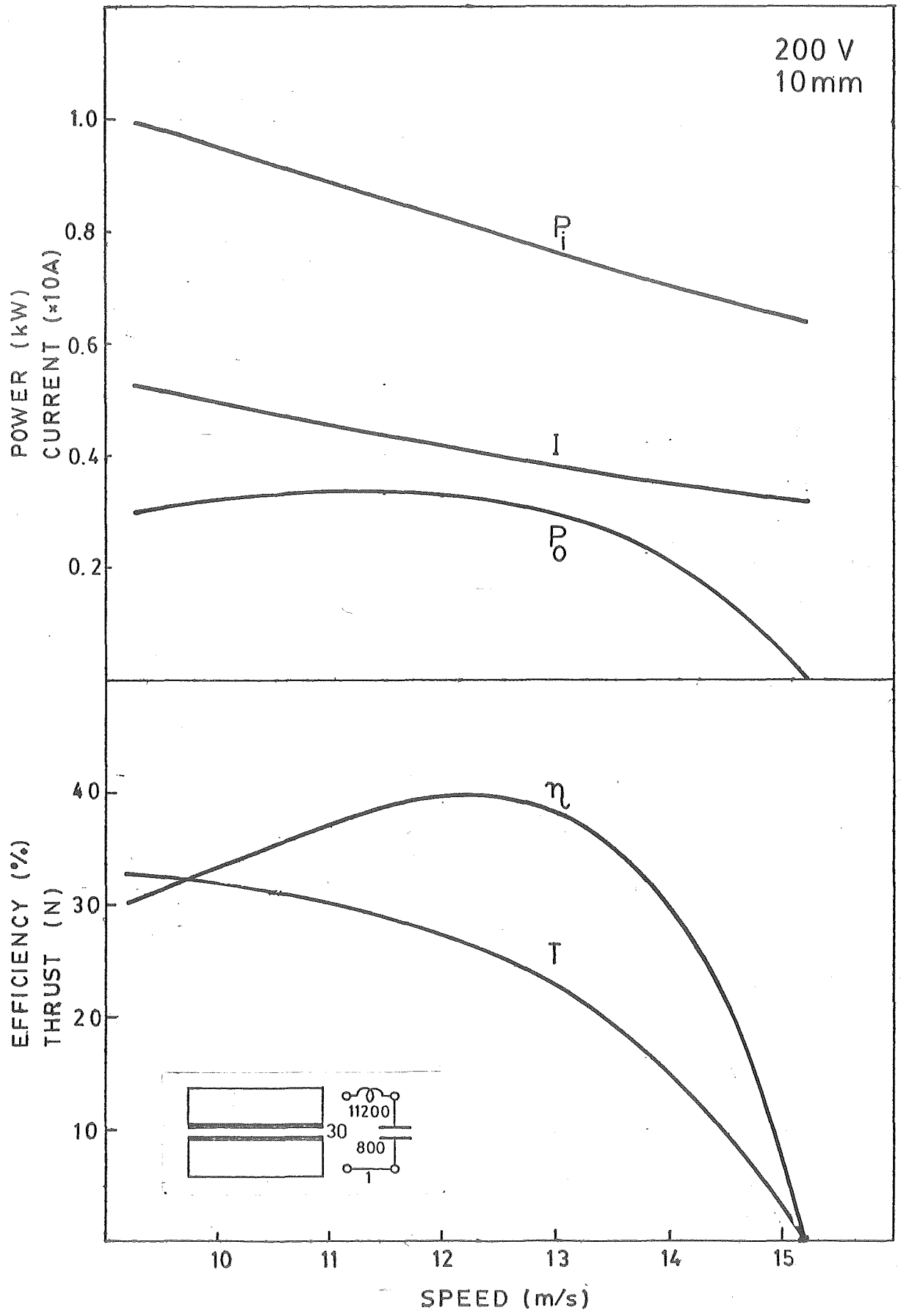
200 V
10mm
POWER (kW)
CURRENT (×10A)
1.0
0.8
0.6
0.4
0.2
P_i
I
P_o
EFFICIENCY (%)
THRUST (N)
40
30
20
10
η
T
11200
30
800
1
10
11
12
13
14
15
SPEED (m/s)

Fig.A107

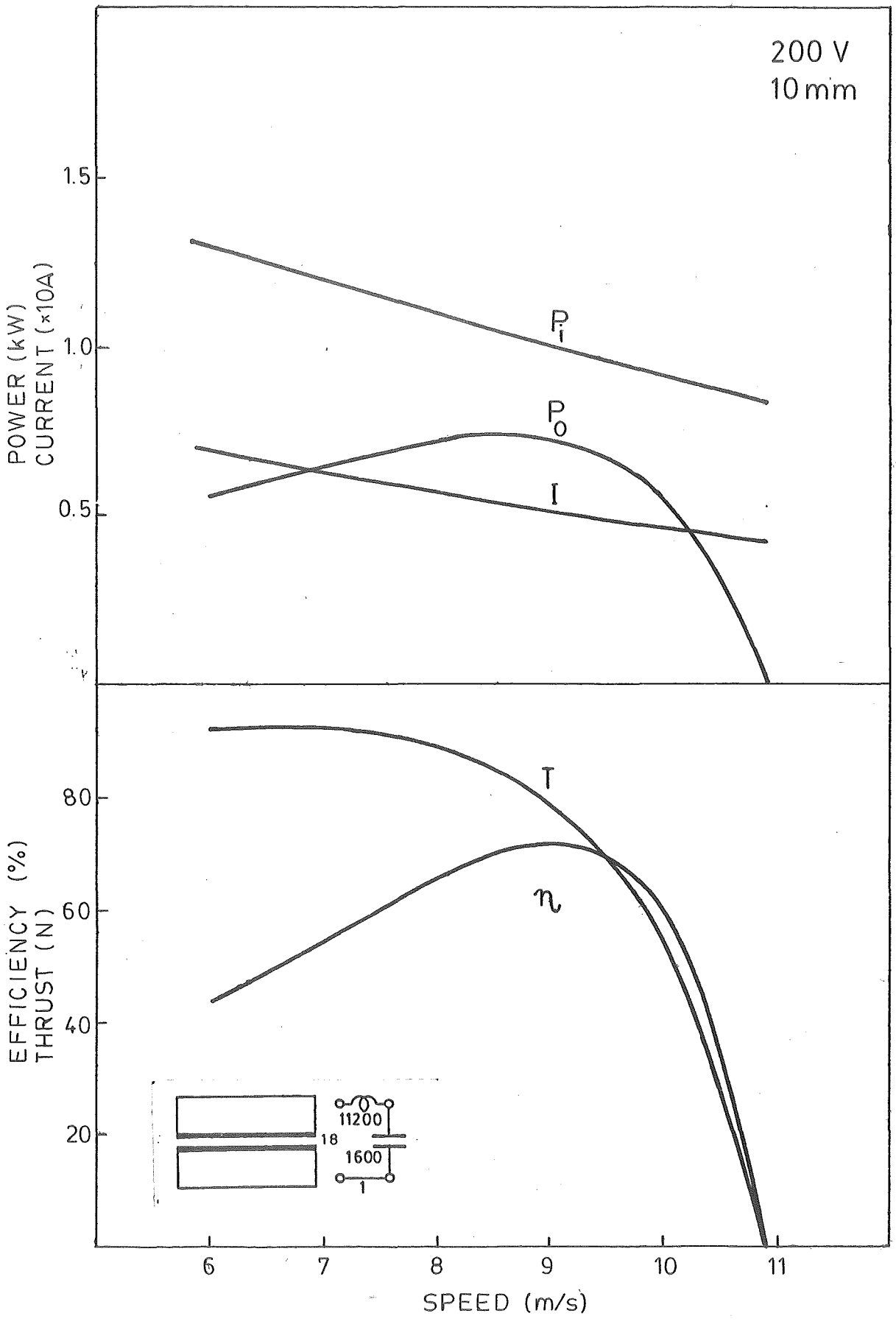
200 V
10 mm
POWER (kW)
CURRENT (×10A)
1.5
1.0
0.5
P_i
P_o
I
EFFICIENCY (%)
THRUST (N)
80
60
40
20
T
η
11200
18
1600
1
6
7
8
9
10
11
SPEED (m/s)

Fig. A108

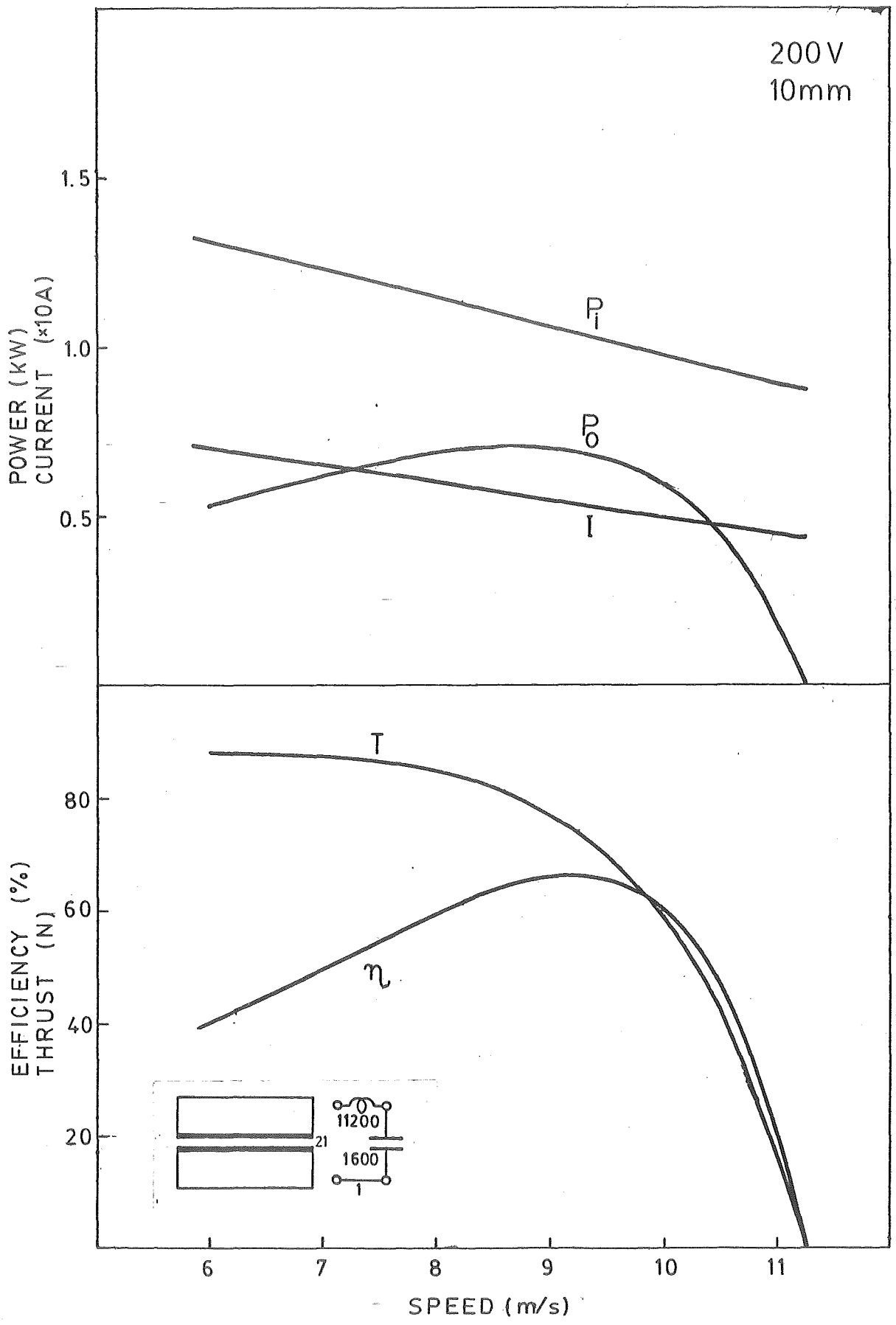
200 V
10mm
POWER (KW)
CURRENT (×10A)
1.5
1.0
0.5
P_i
P_o
I
EFFICIENCY (%)
THRUST (N)
80
60
40
20
T
η
11200
1600
21
1
6
7
8
9
10
11
SPEED (m/s)

Fig. A109

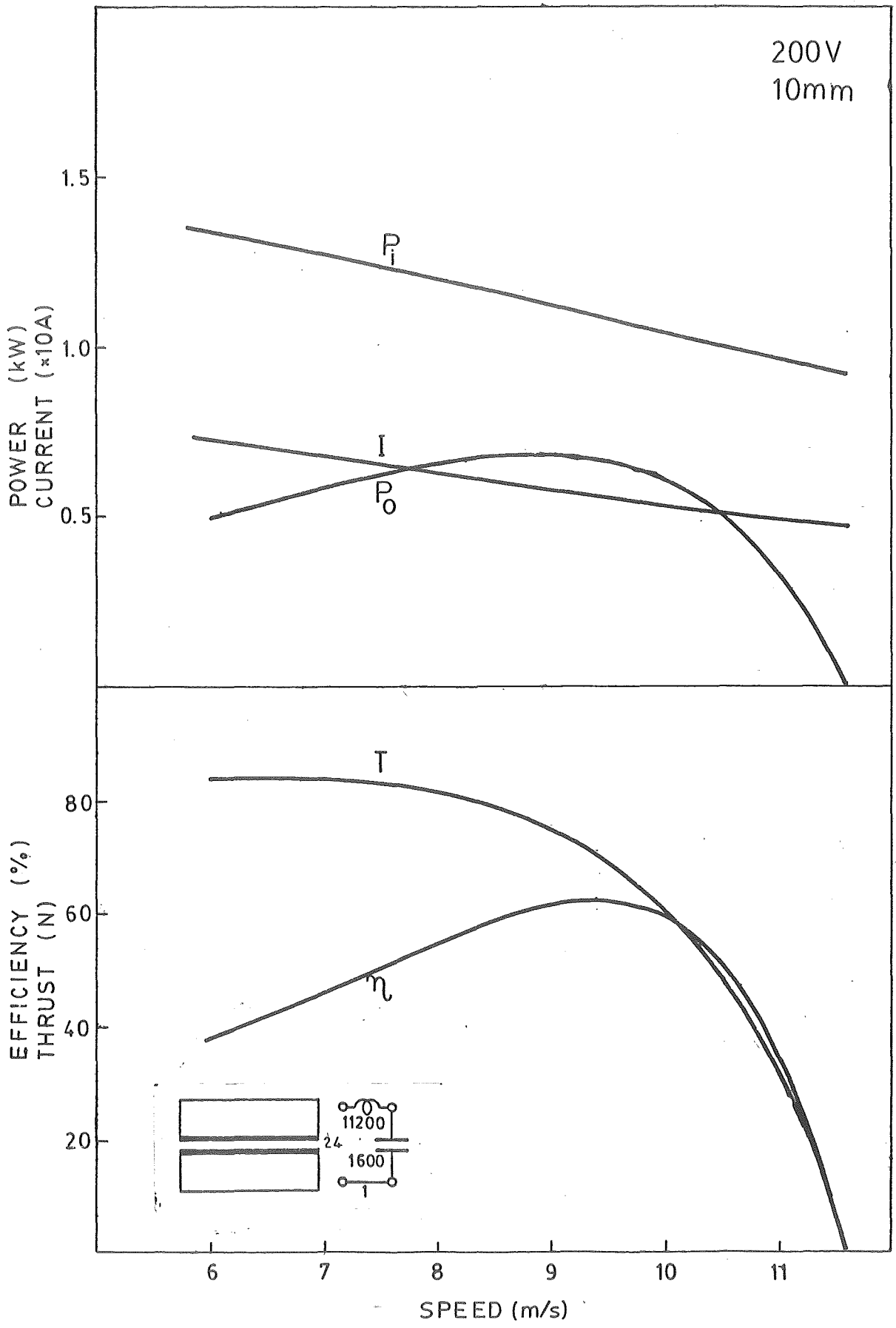
200V
10mm
POWER (kW)
CURRENT (×10A)
1.5
1.0
0.5
P_i
I
P_o
EFFICIENCY (%)
THRUST (N)
80
60
40
20
T
η
11200
24
1600
1
6
7
8
9
10
11
SPEED (m/s)

Fig. A110

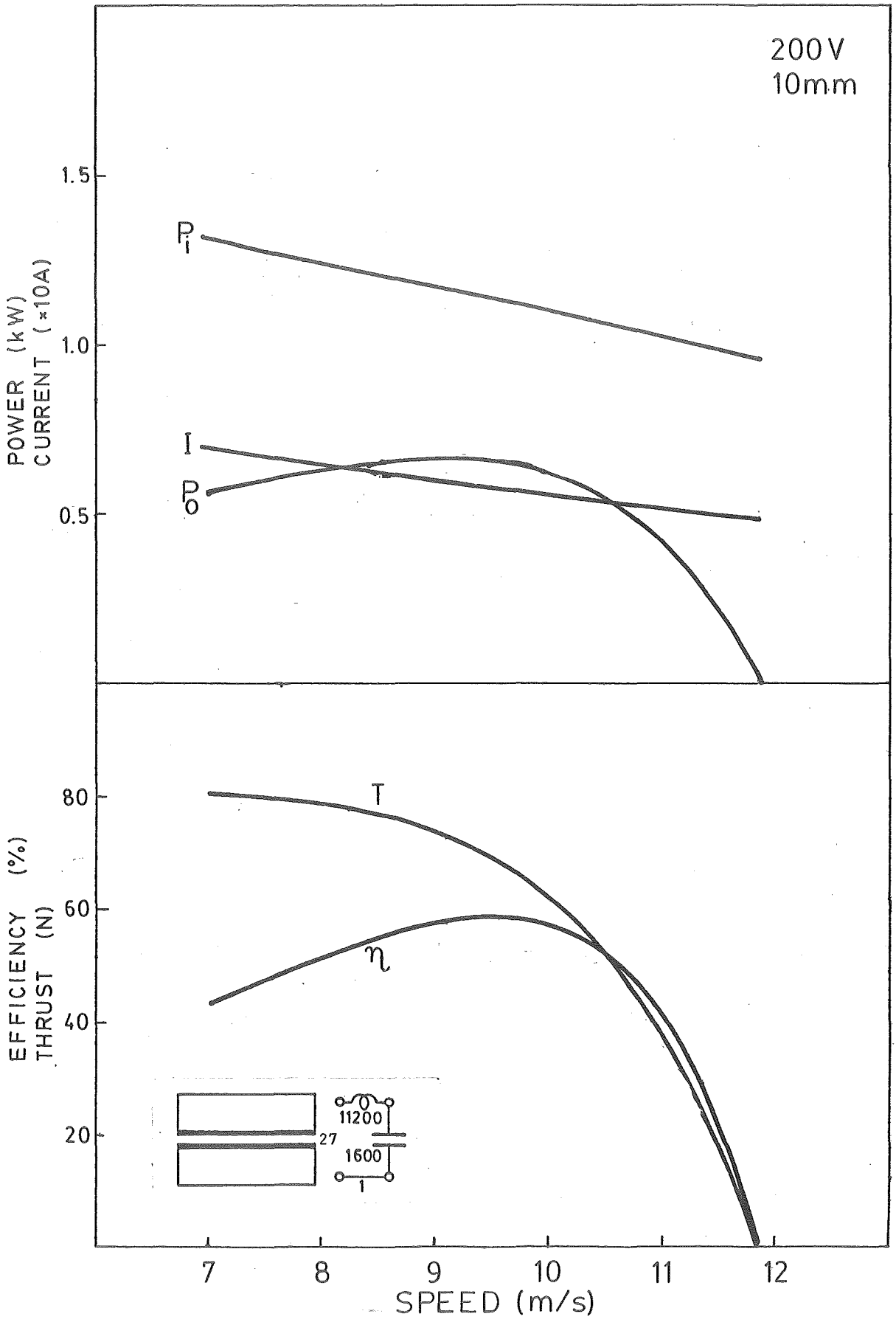
200V
10mm
POWER (kW)
CURRENT (×10A)
1.5
1.0
0.5
P_i
I
P_o
EFFICIENCY (%)
THRUST (N)
80
60
40
20
T
η
11200
27
1600
1
7
8
9
10
11
12
SPEED (m/s)

Fig. A111

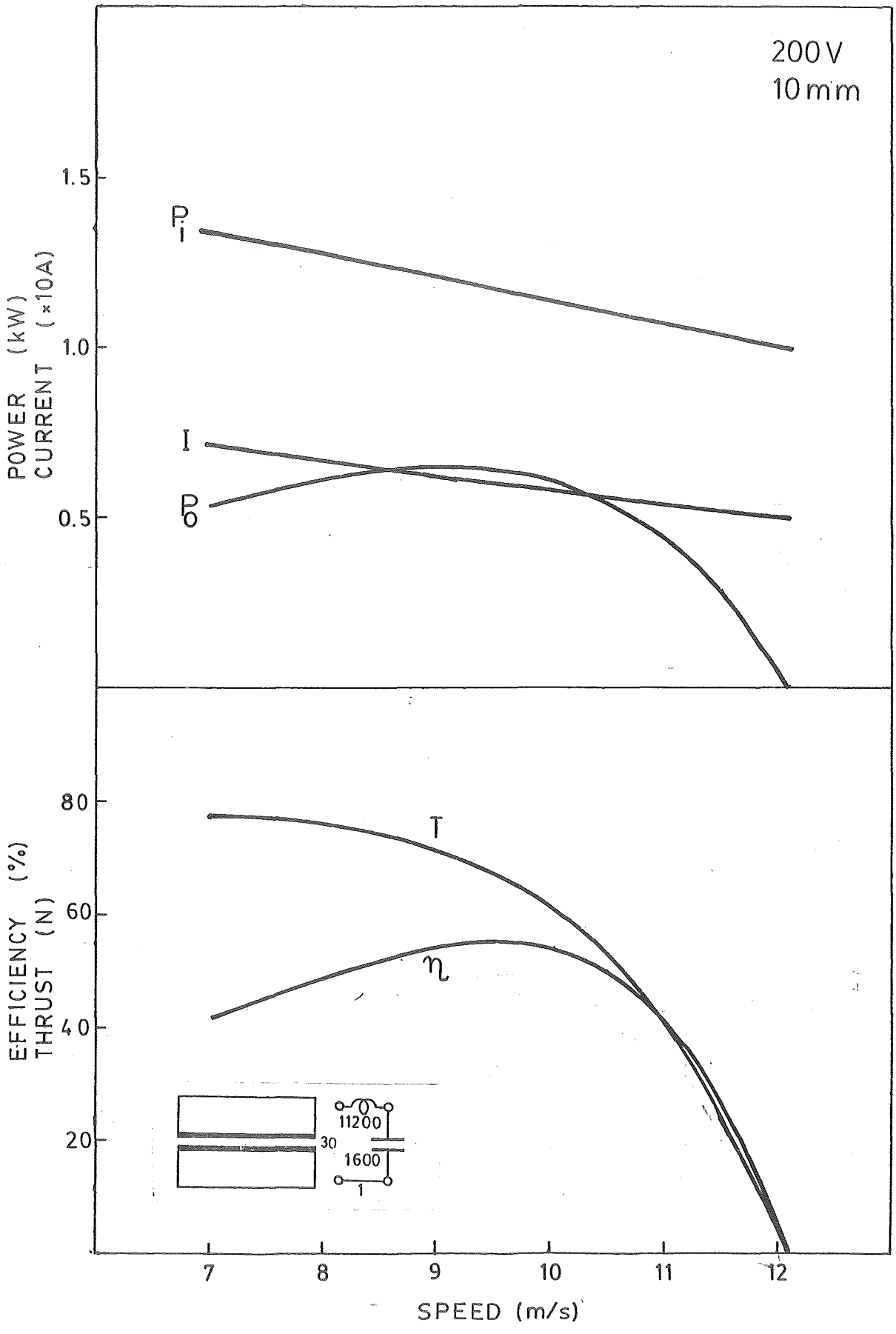
200 V
10 mm
POWER (kW)
CURRENT (×10A)
1.5
1.0
0.5
P_i
I
P_o
EFFICIENCY (%)
THRUST (N)
80
60
40
20
T
η
11200
30
1600
1
7
8
9
10
11
12
SPEED (m/s)

Fig. A.112

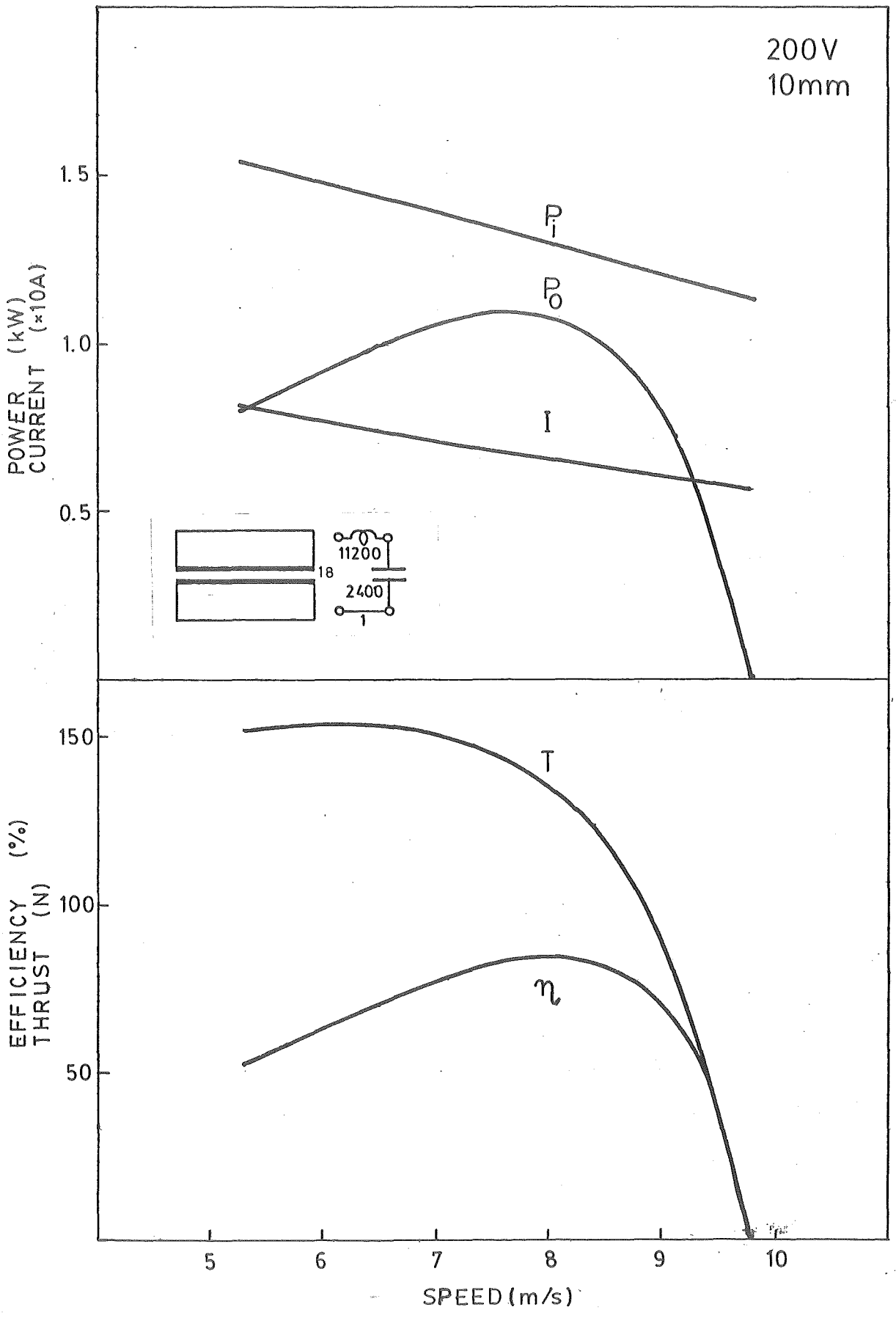
200V
10mm
POWER (kW)
CURRENT (×10A)
1.5
1.0
0.5
P_i
P_o
I
11200
18
2400
1
EFFICIENCY (%)
THRUST (N)
150
100
50
T
η
5
6
7
8
9
10
SPEED (m/s)

Fig. A113

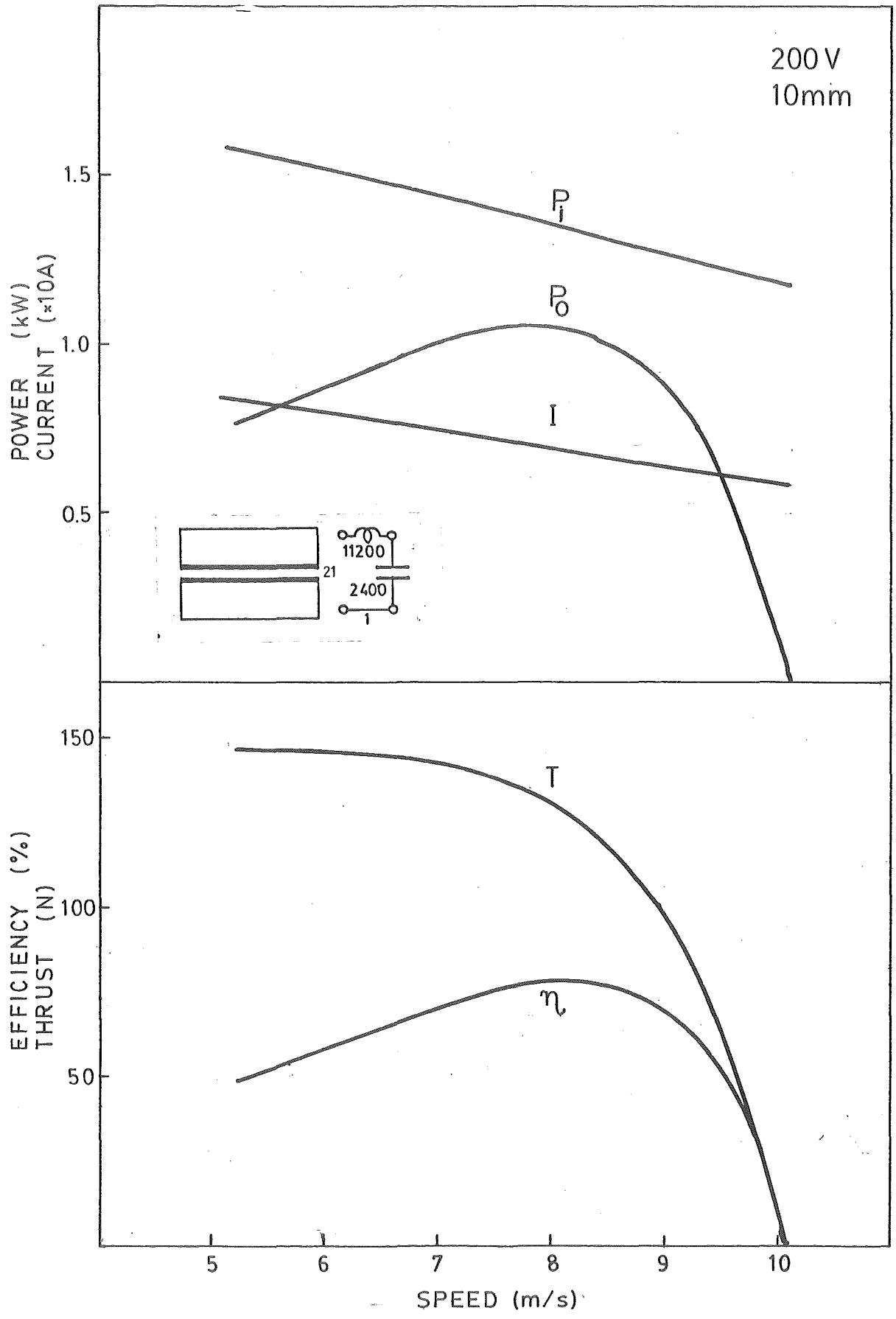
200 V
10mm
POWER (kW)
CURRENT (×10A)
1.5
1.0
0.5
P_i
P_o
I
11200
21
2400
1
EFFICIENCY (%)
THRUST (N)
150
100
50
T
η
5
6
7
8
9
10
SPEED (m/s)

Fig. A114

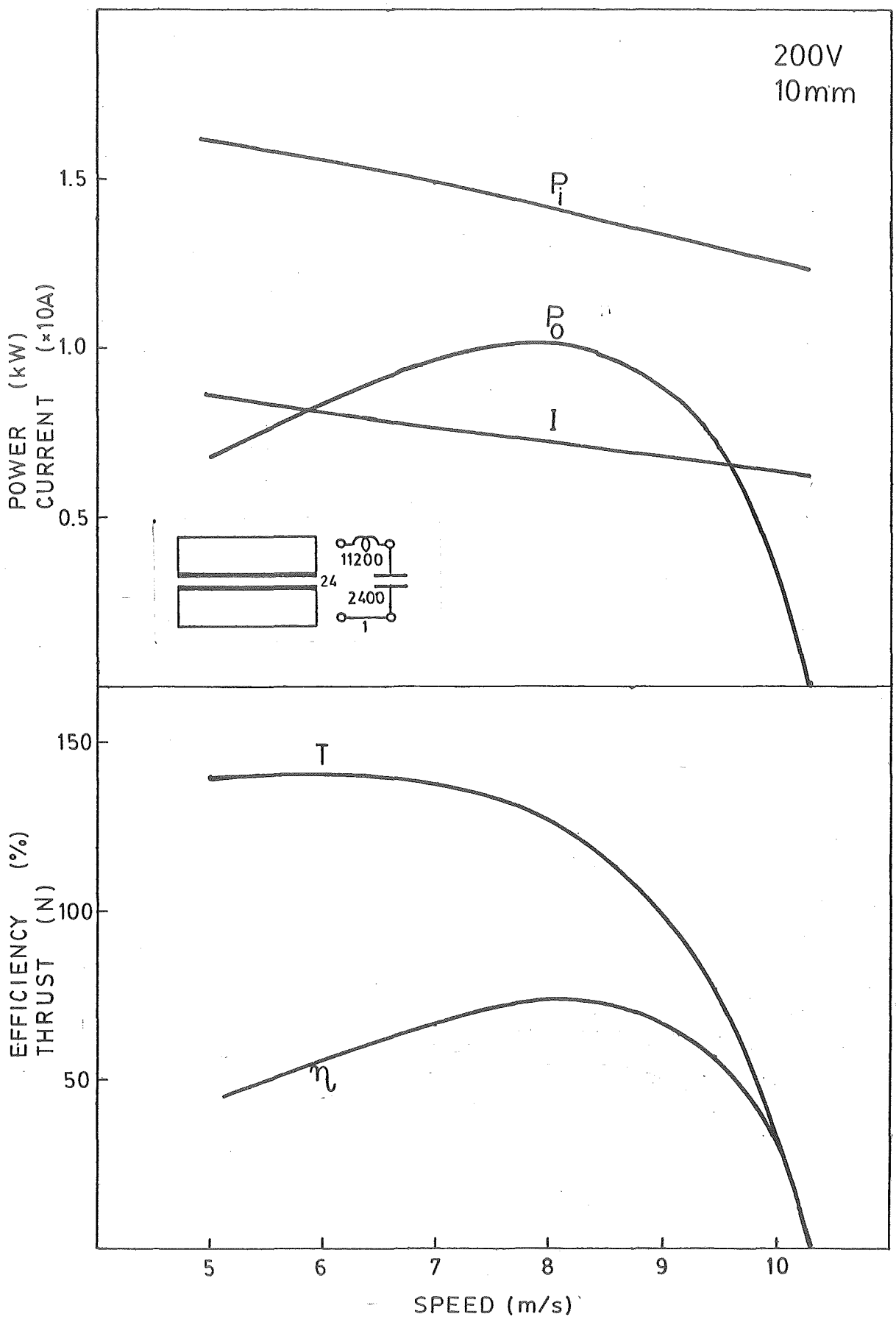
200V
10mm
POWER (kW)
CURRENT (×10A)
1.5
1.0
0.5
P_i
P_o
I
0
11200
24
2400
1
EFFICIENCY (%)
THRUST (N)
150
100
50
T
η
5
6
7
8
9
10
SPEED (m/s)

Fig. A115

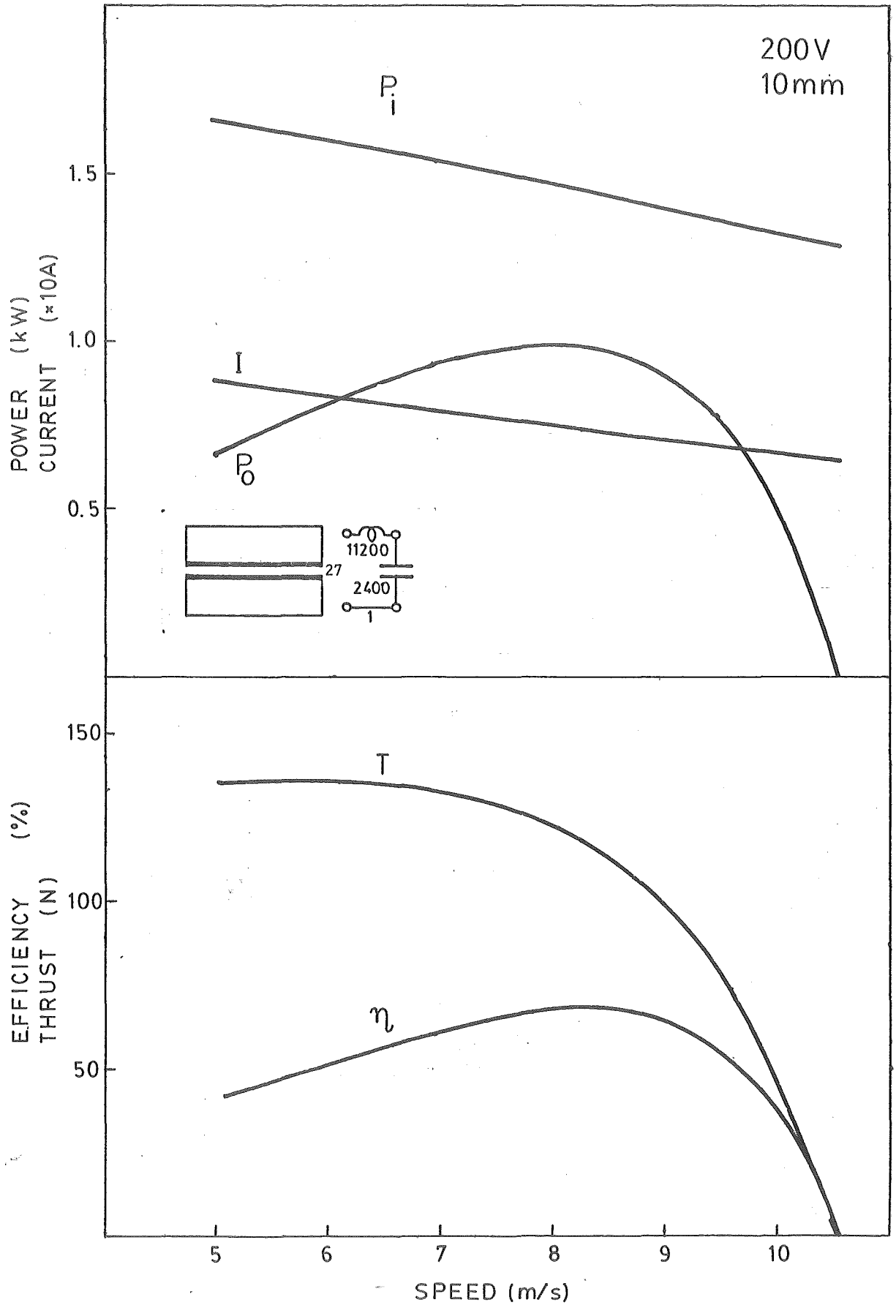
200V
10mm
P_i
I
P_o
POWER (kW)
CURRENT (×10A)
1.5
1.0
0.5
11200
27
2400
1
T
η
EFFICIENCY (%)
THRUST (N)
150
100
50
5
6
7
8
9
10
SPEED (m/s)

Fig. A116

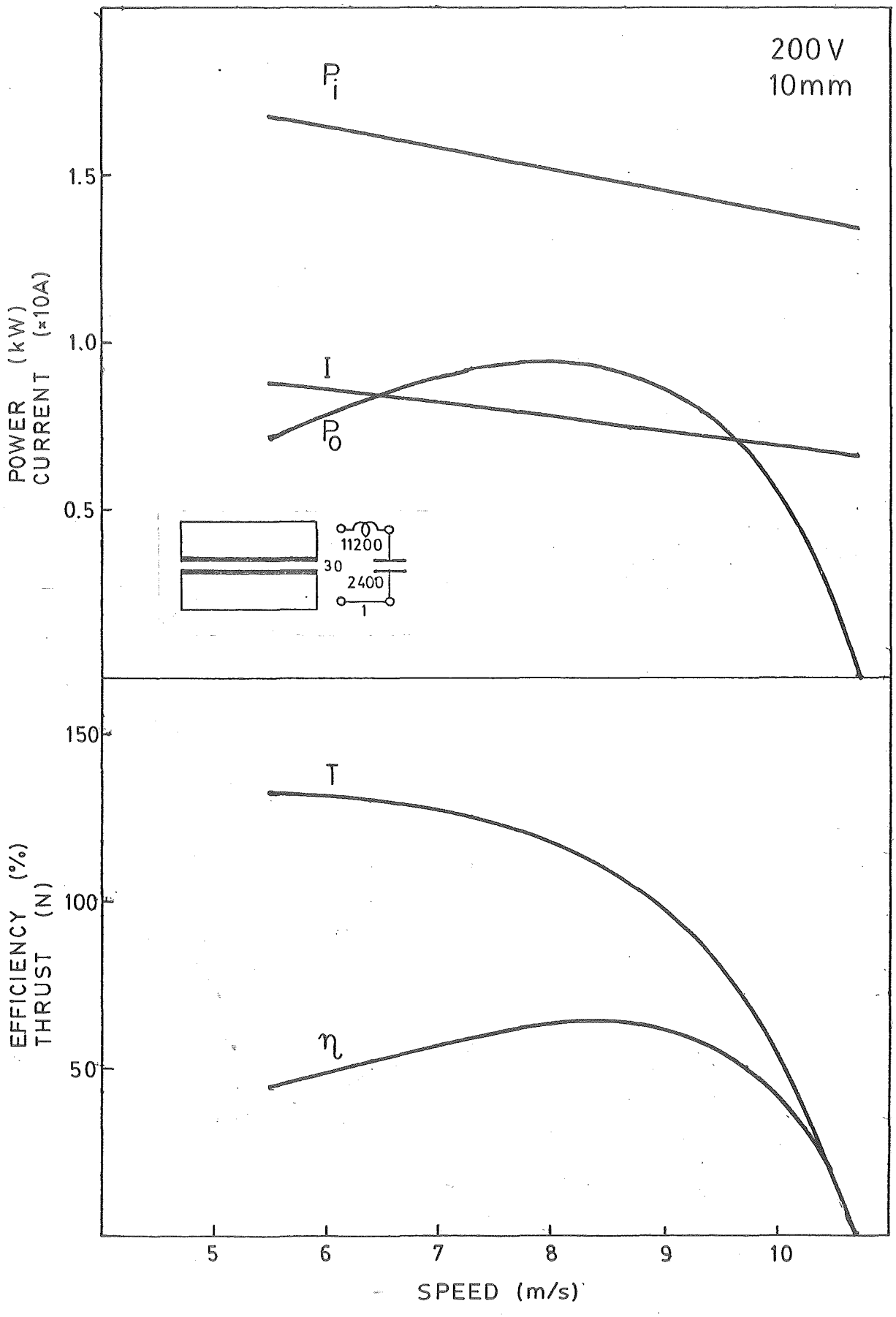
200 V
10mm
P_i
I
P_o
POWER (kW)
CURRENT (×10A)
1.5
1.0
0.5
11200
30
2400
1
T
η
EFFICIENCY (%)
THRUST (N)
150
100
50
5
6
7
8
9
10
SPEED (m/s)

Fig. A117

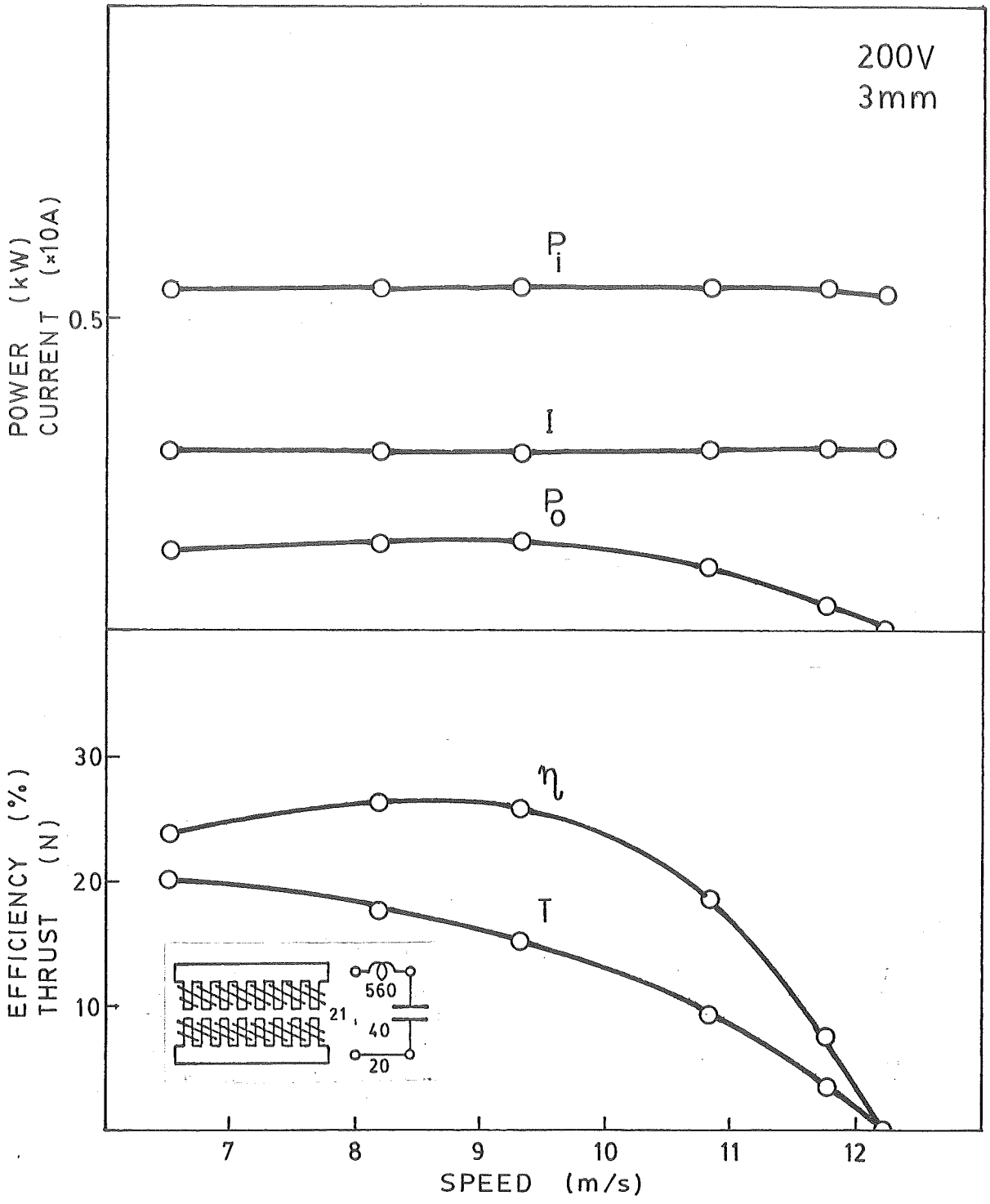
200V
3mm
POWER (kW)
CURRENT (×10A)
0.5
P_i
I
P_o
EFFICIENCY (%)
THRUST (N)
30
20
10
η
T
560
21
40
20
7
8
9
10
11
12
SPEED (m/s)

Fig. A118

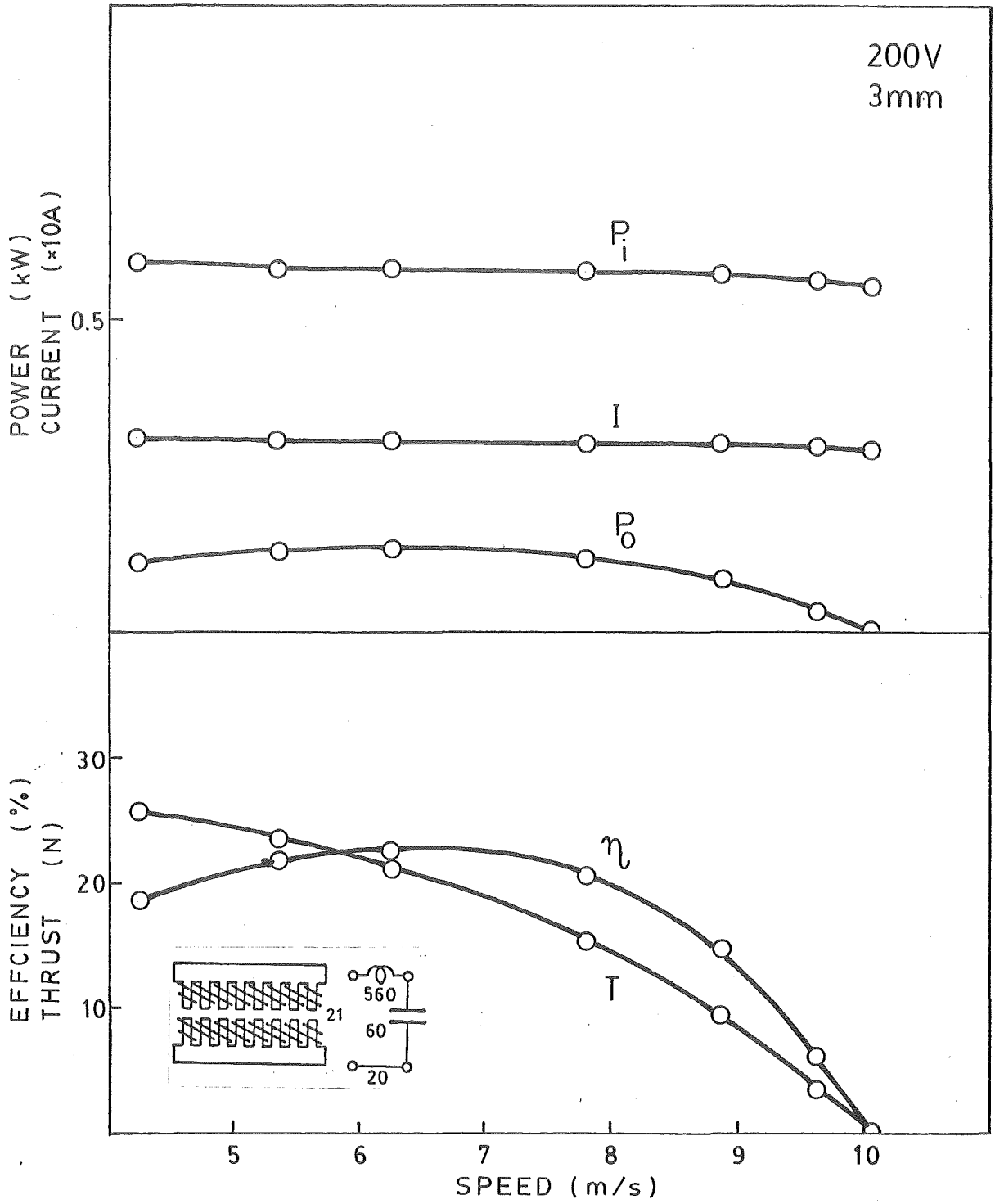
200V
3mm
POWER (kW)
CURRENT (×10A)
0.5
P_i
I
P_o
EFFCIENCY (%)
THRUST (N)
30
20
10
η
T
560
60
20
21
5
6
7
8
9
10
SPEED (m/s)

Fig. A119

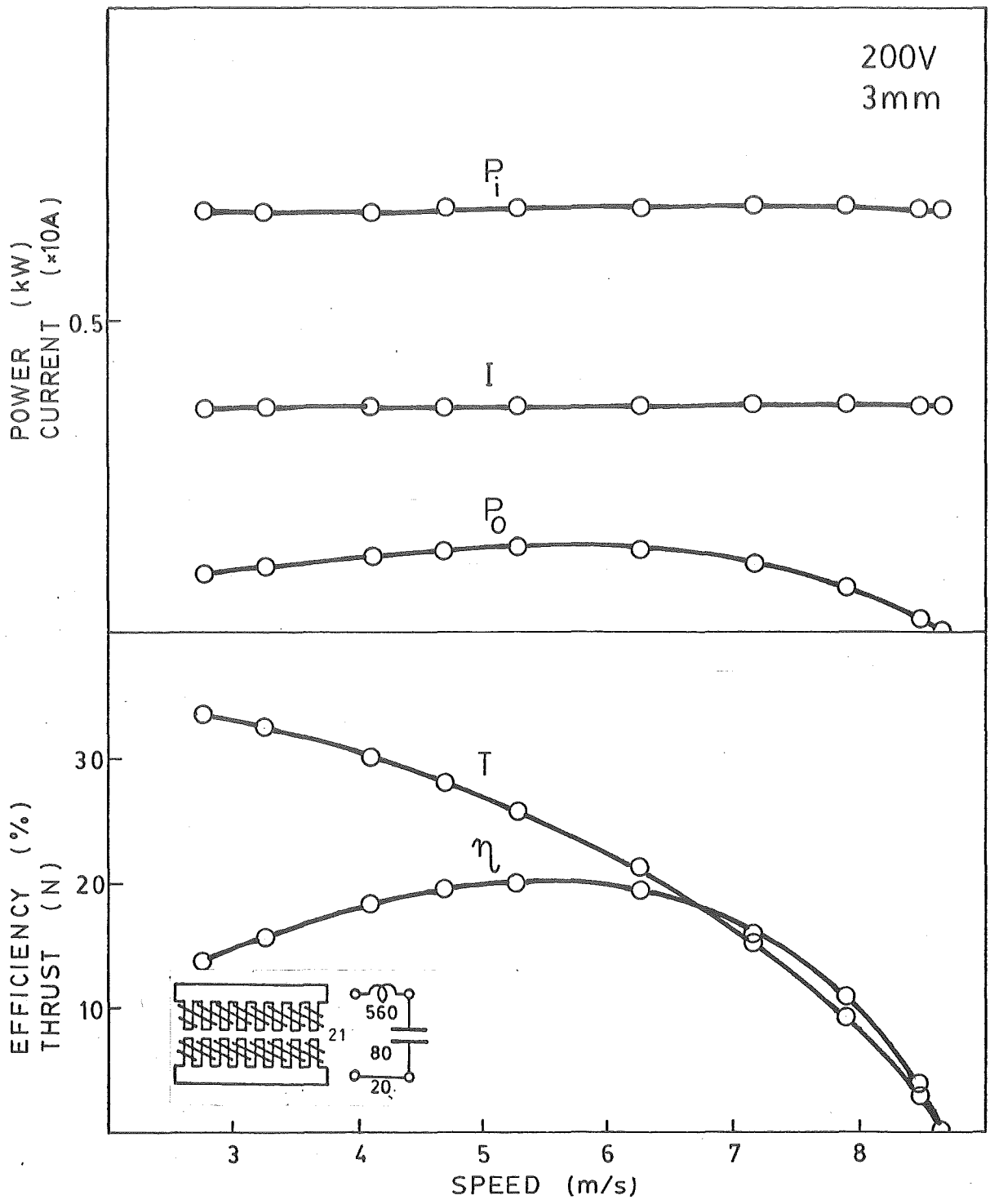
200V
3mm
P_i
I
P_o
POWER (kW)
CURRENT (×10A)
0.5
T
η
EFFICIENCY (%)
THRUST (N)
30
20
10
560
80
20
21
3
4
5
6
7
8
SPEED (m/s)

Fig. A120

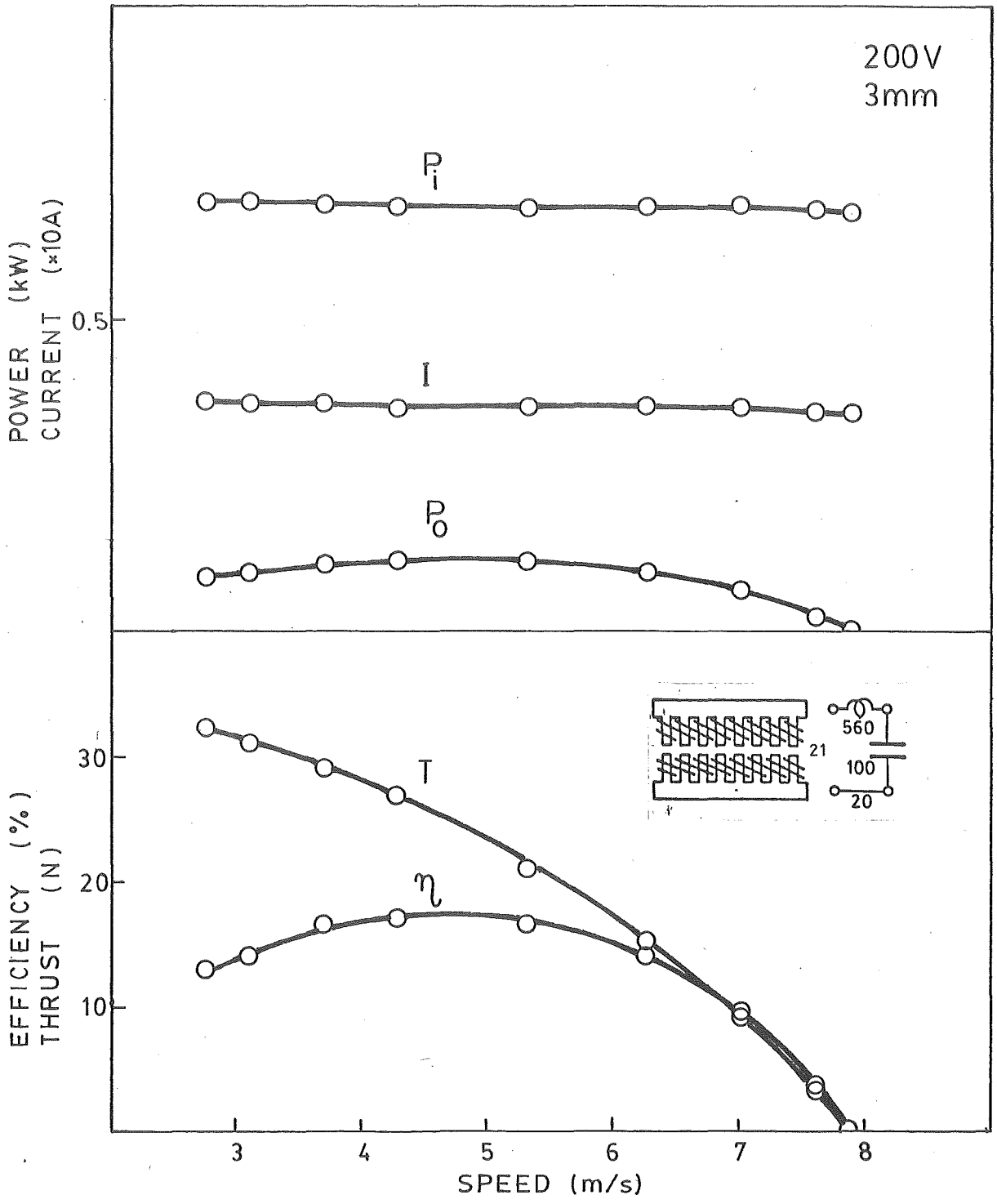
200V
3mm
P_i
I
P_o
POWER (kW)
CURRENT (×10A)
0.5
T
η
EFFICIENCY (%)
THRUST (N)
30
20
10
21
560
100
20
3
4
5
6
7
8
SPEED (m/s)

Fig. A121

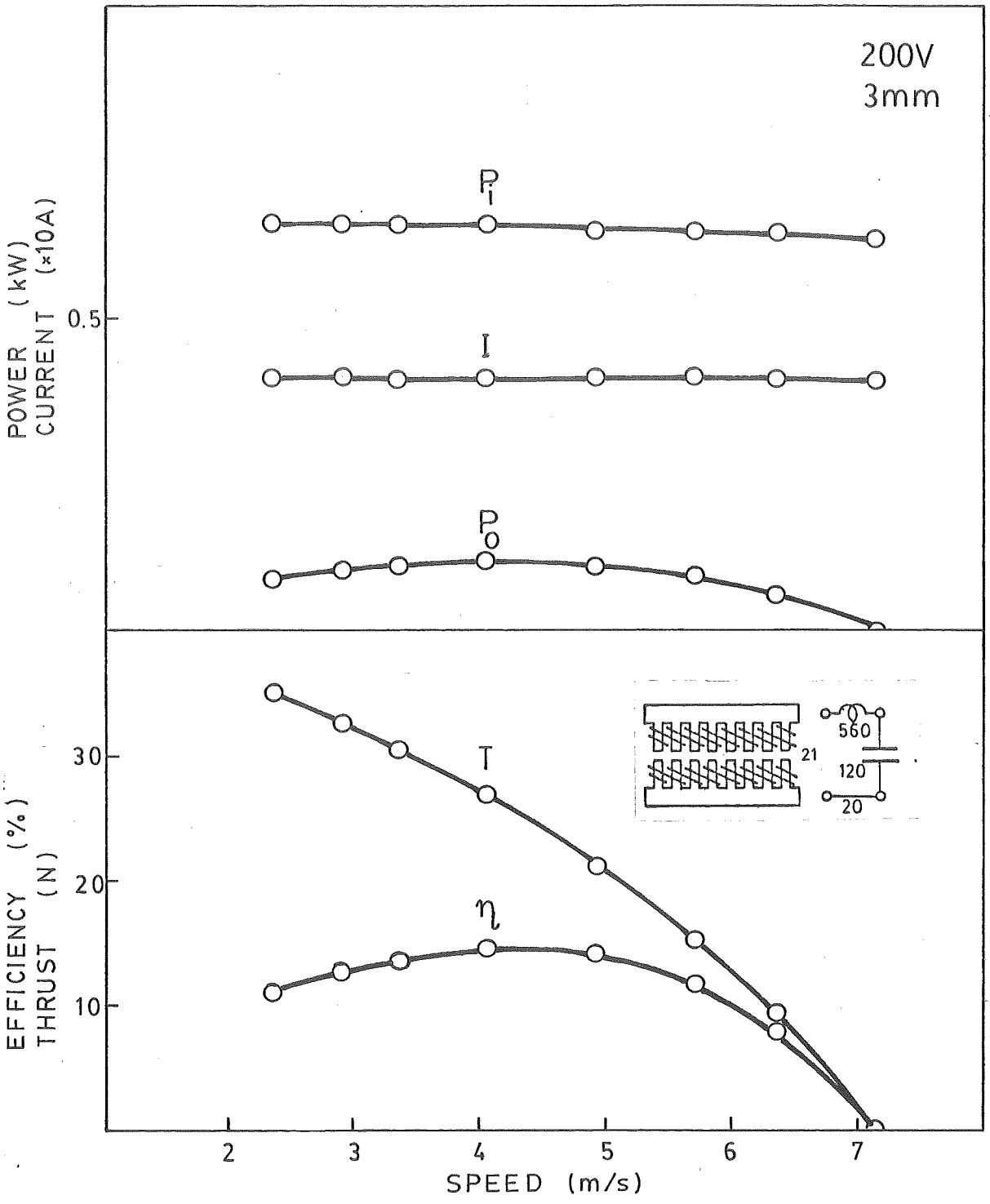
200V
3mm
POWER (kW)
CURRENT (×10A)
0.5
P_i
I
P_o
EFFICIENCY (%)
THRUST (N)
30
20
10
T
η
21
560
120
20
2
3
4
5
6
7
SPEED (m/s)

Fig. A122

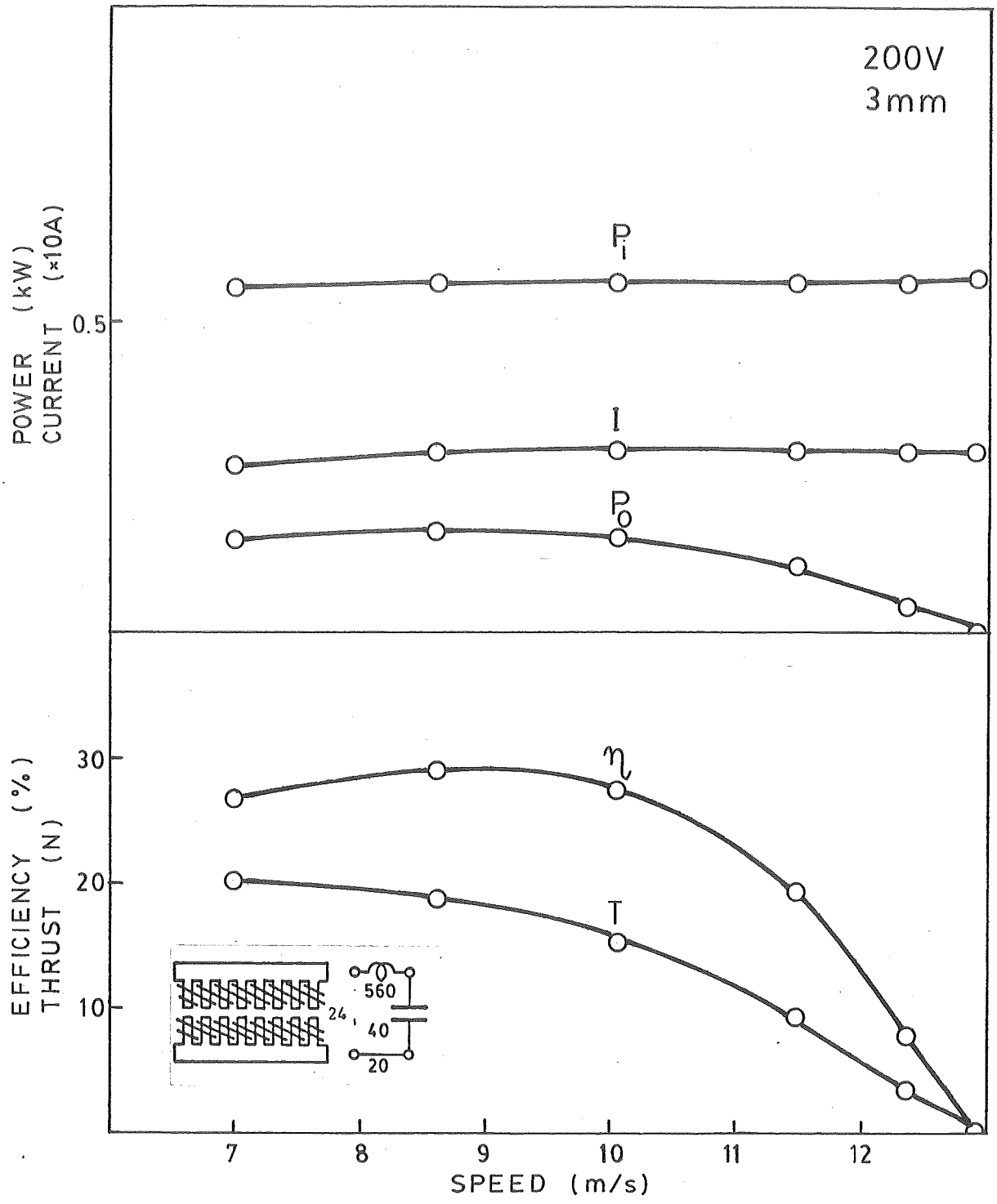
200V
3mm
POWER (kW)
CURRENT (×10A)
0.5
P_i
I
P_o
EFFICIENCY (%)
THRUST (N)
30
20
10
η
T
560
40
20
24
7
8
9
10
11
12
SPEED (m/s)

Fig. A123

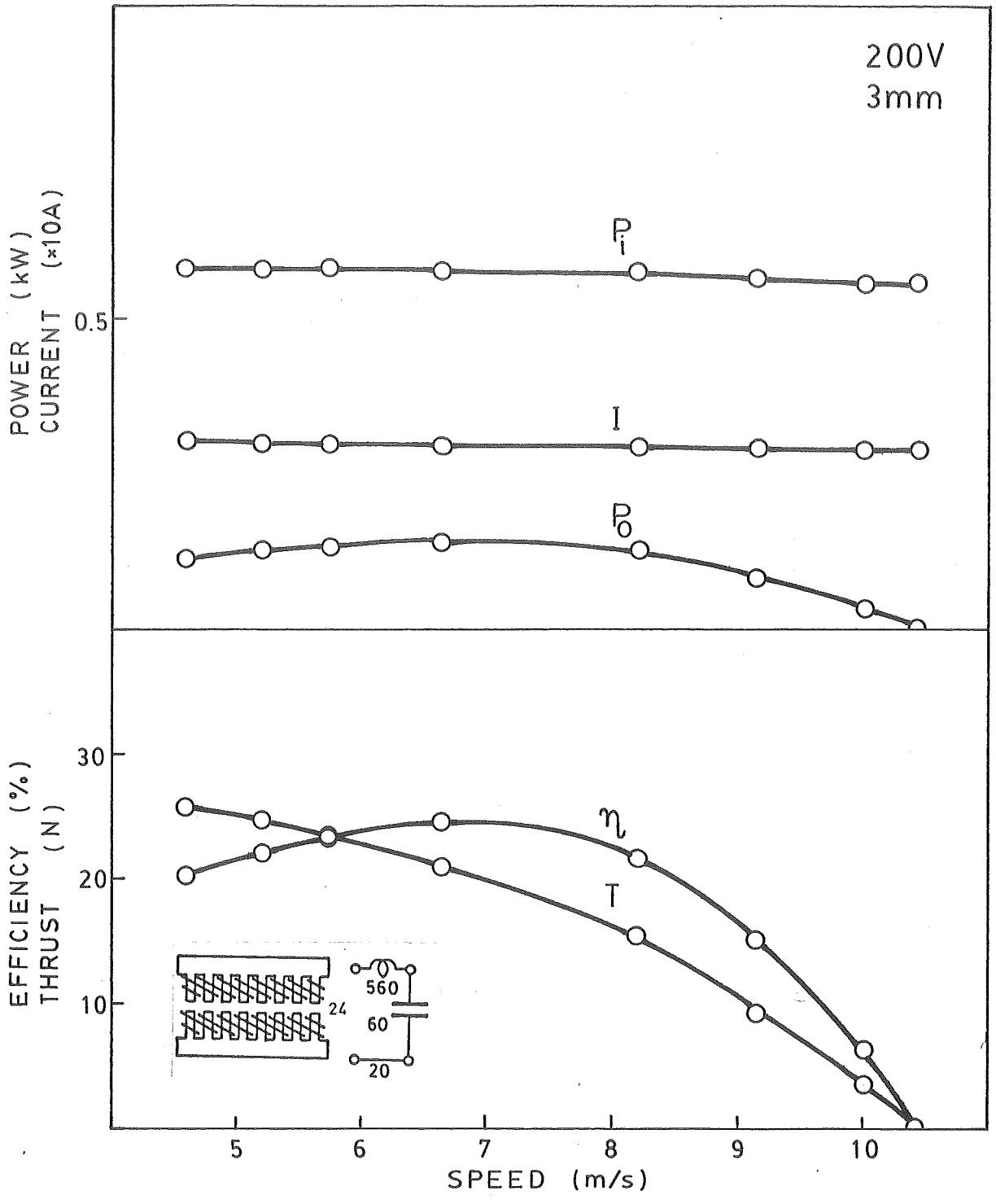
200V
3mm
POWER (kW)
CURRENT (×10A)
0.5
P_i
I
P_o
EFFICIENCY (%)
THRUST (N)
30
20
10
η
T
560
60
20
24
5
6
7
8
9
10
SPEED (m/s)

Fig. A124

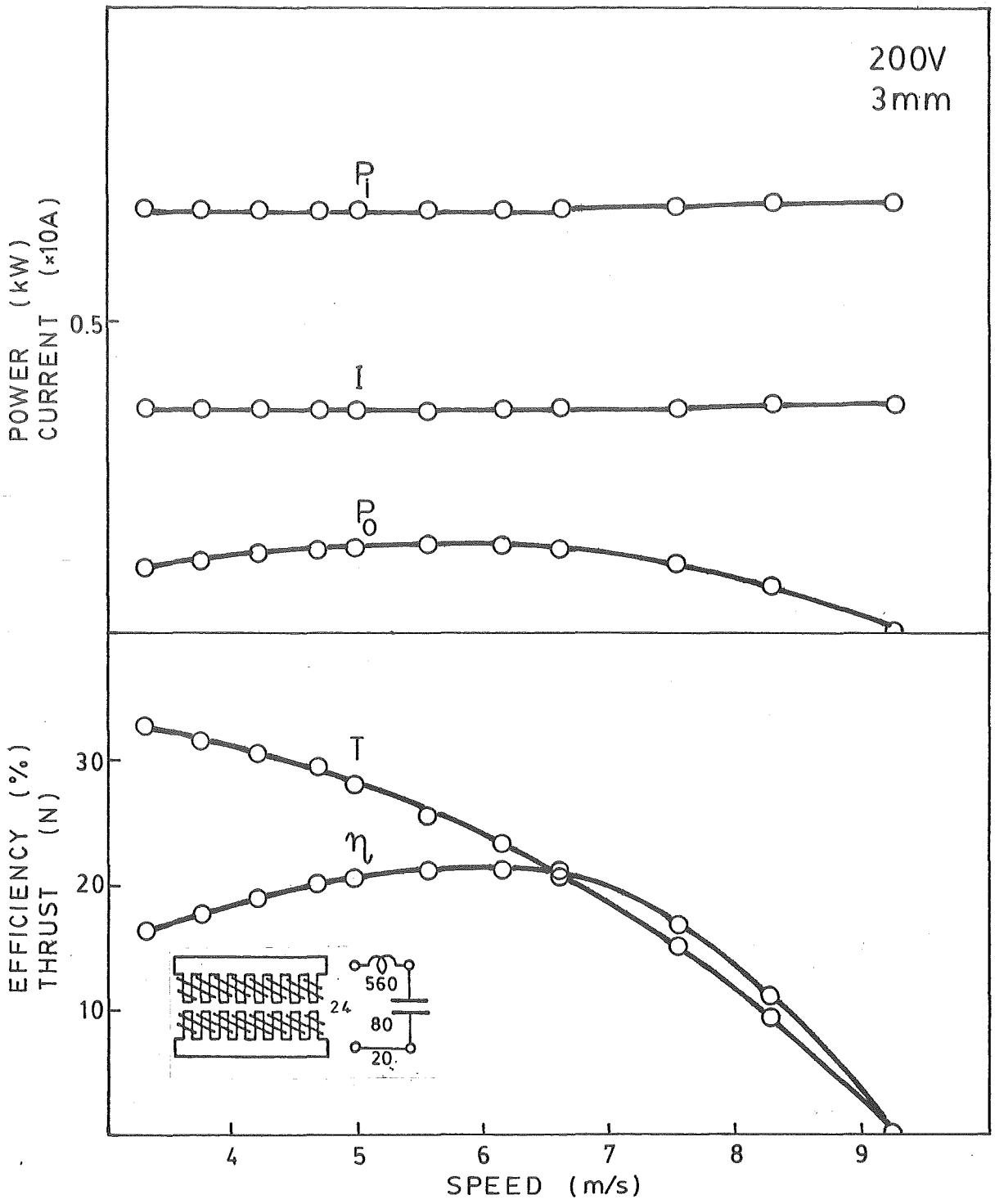
200V
3mm
P_i
I
P_o
POWER (kW)
CURRENT (×10A)
0.5
T
η
EFFICIENCY (%)
THRUST (N)
30
20
10
560
80
20
24
4
5
6
7
8
9
SPEED (m/s)

Fig. A·125

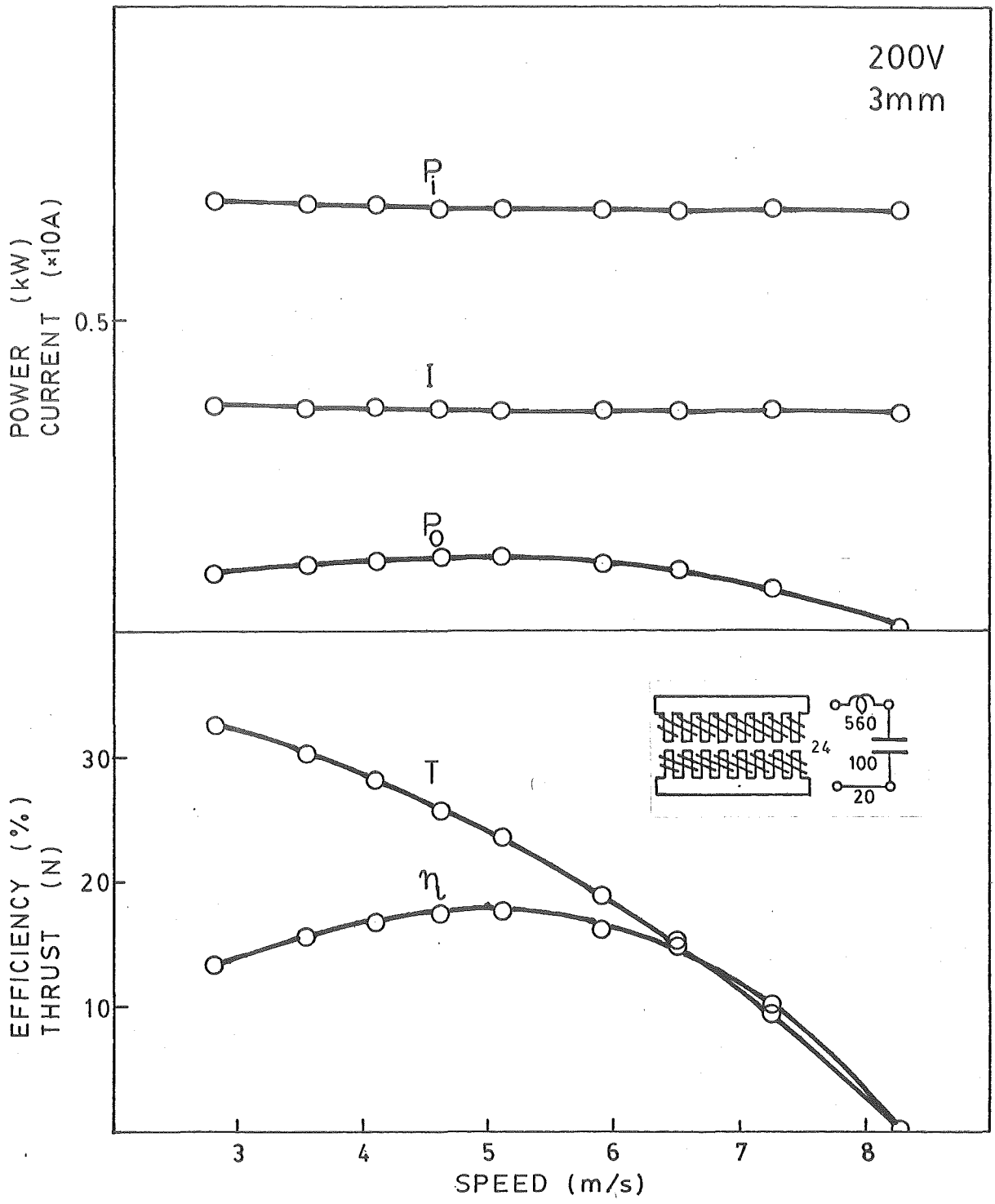
200V
3mm
POWER (kW)
CURRENT (×10A)
0.5
P_i
I
P_o
EFFICIENCY (%)
THRUST (N)
30
20
10
T
η
24
560
100
20
3
4
5
6
7
8
SPEED (m/s)

Fig. A126

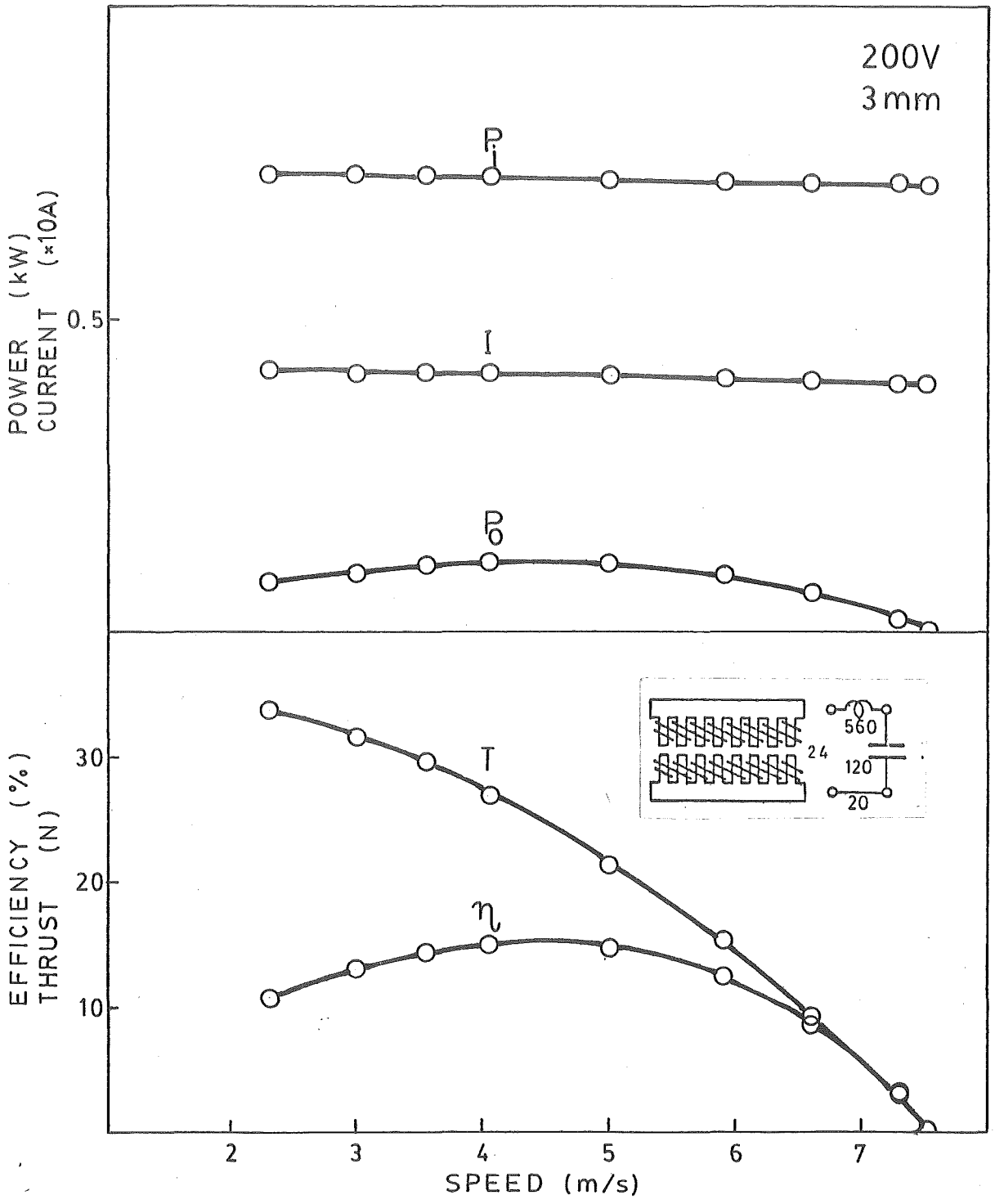
200V
3mm
P_i
I
P_o
POWER (kW)
CURRENT (×10A)
0.5
T
η
EFFICIENCY (%)
THRUST (N)
30
20
10
24
560
120
20
2
3
4
5
6
7
SPEED (m/s)

Fig. A127

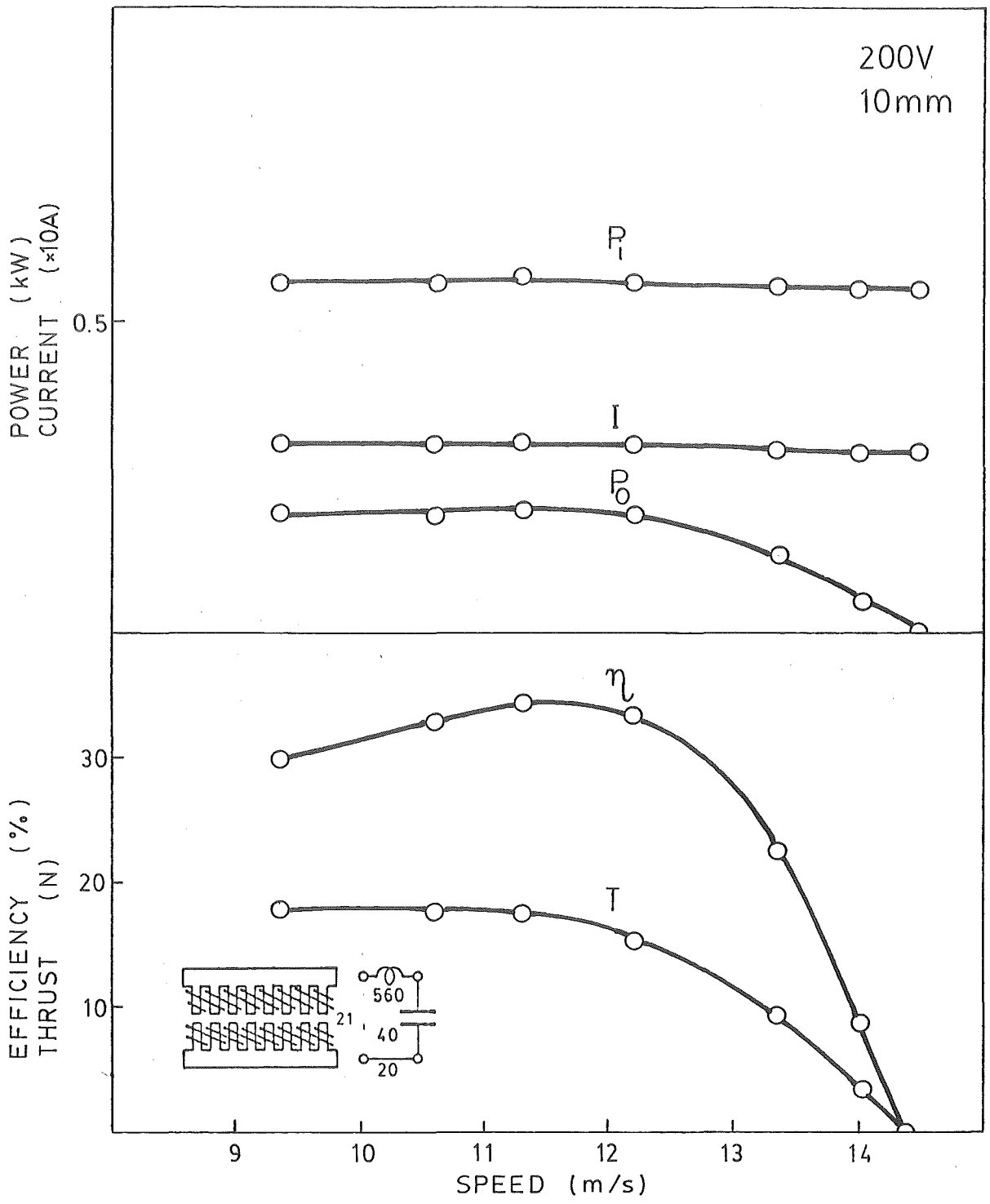
200V
10mm
POWER (kW)
CURRENT (×10A)
0.5
P_i
I
P_o
EFFICIENCY (%)
THRUST (N)
30
20
10
η
T
560
40
20
21
9
10
11
12
13
14
SPEED (m/s)

Fig. A128

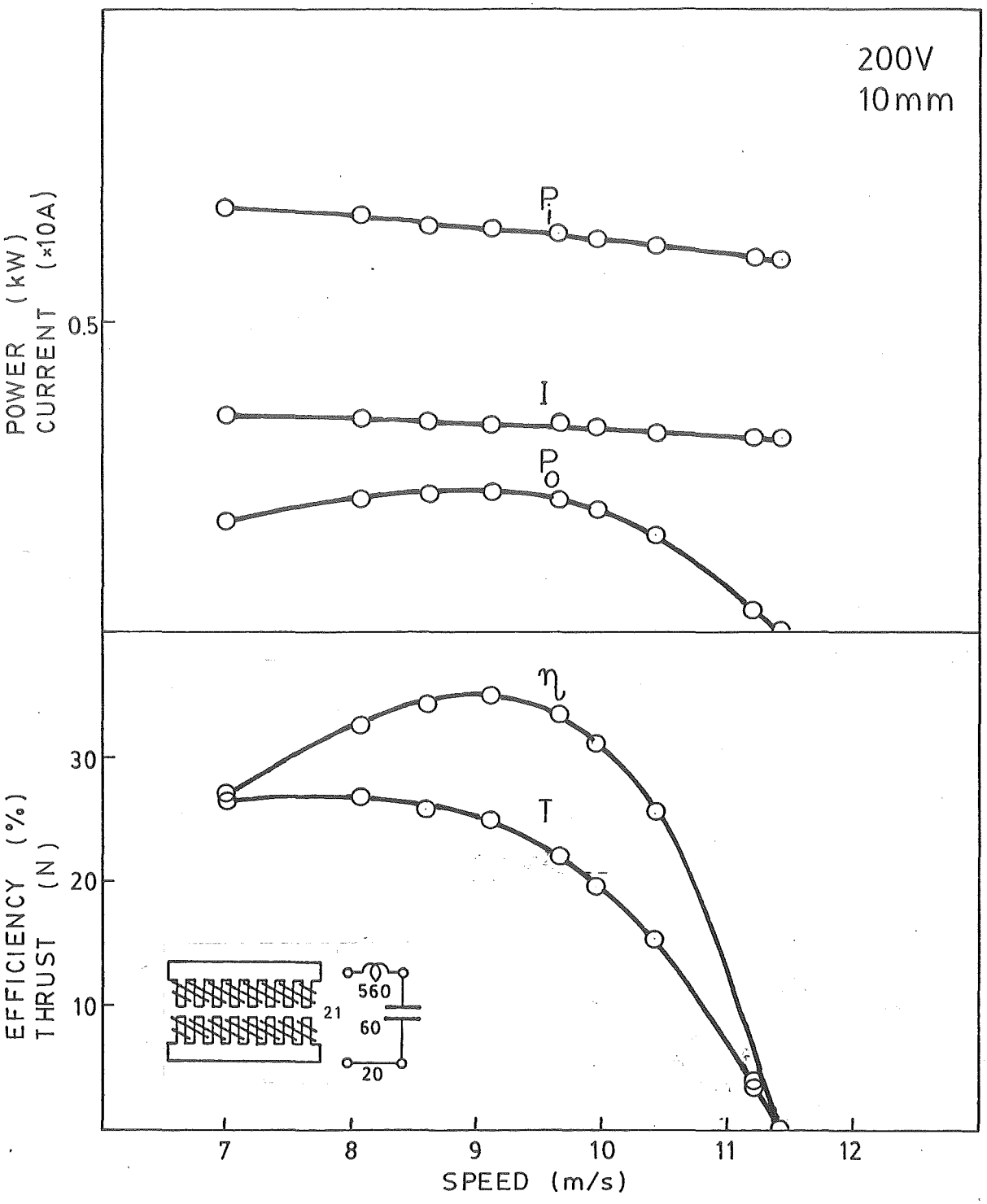
200V
10mm
POWER (kW)
CURRENT (×10A)
0.5
P
I
Po
η
T
30
20
10
EFFICIENCY (%)
THRUST (N)
560
60
20
21
7
8
9
10
11
12
SPEED (m/s)

Fig. A129

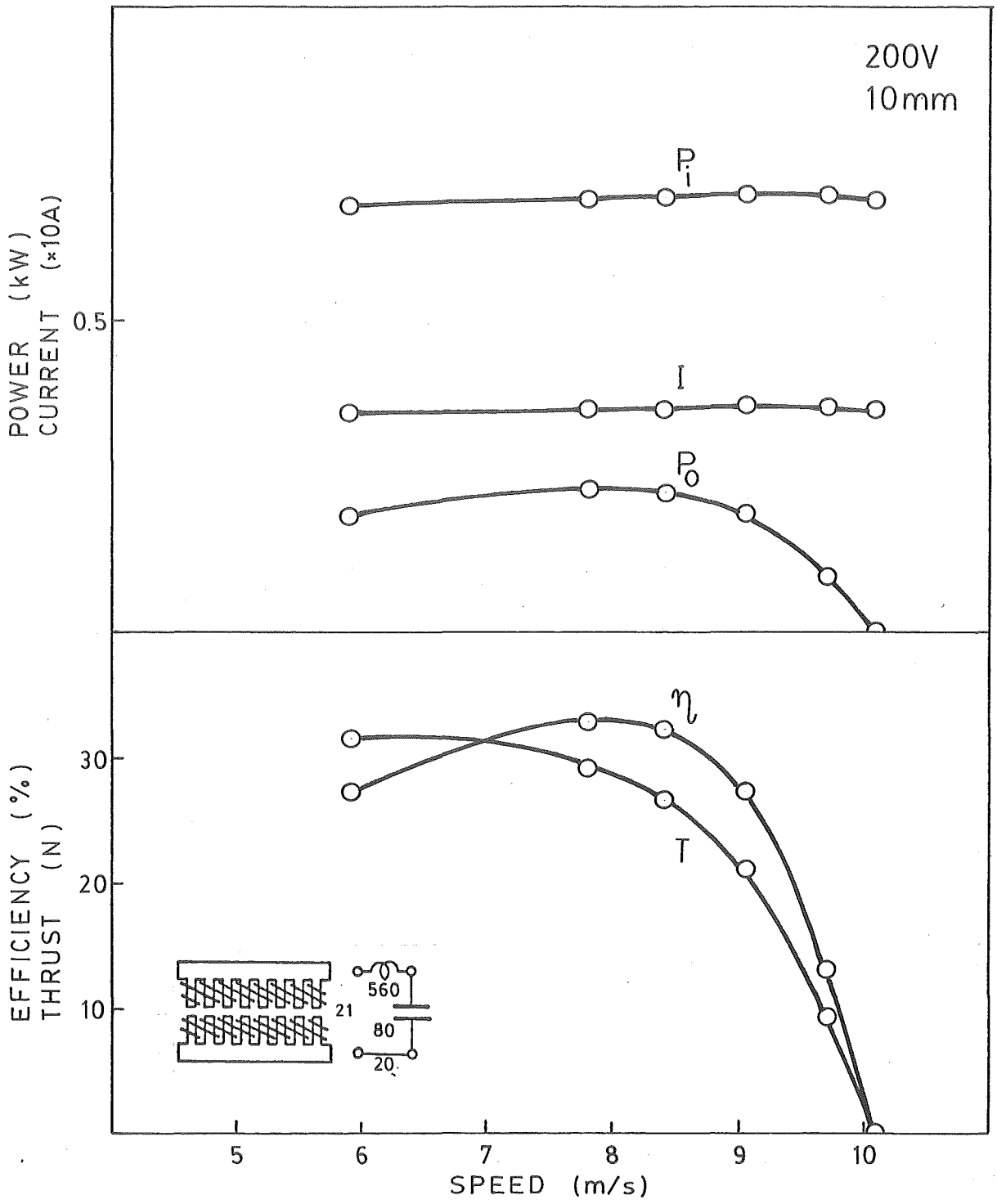
200V
10mm
POWER (kW)
CURRENT (×10A)
0.5
P_i
I
P_o
EFFICIENCY (%)
THRUST (N)
30
20
10
η
T
560
21
80
20
5
6
7
8
9
10
SPEED (m/s)

Fig. A130

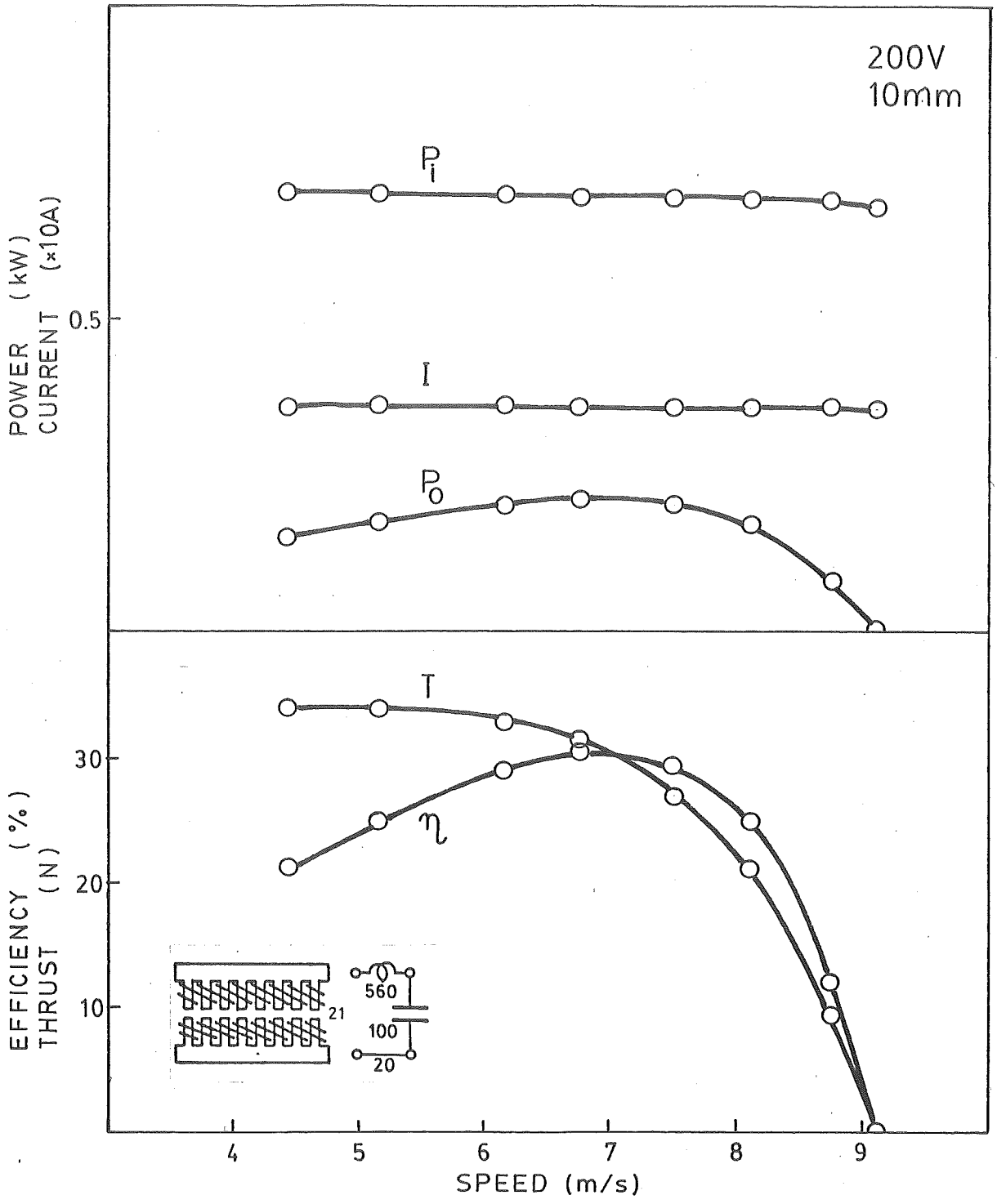
200V
10mm
POWER (kW)
CURRENT (×10A)
0.5
P_i
I
P_o
EFFICIENCY (%)
THRUST (N)
30
20
10
T
η
560
100
20
21
4
5
6
7
8
9
SPEED (m/s)

Fig. A131

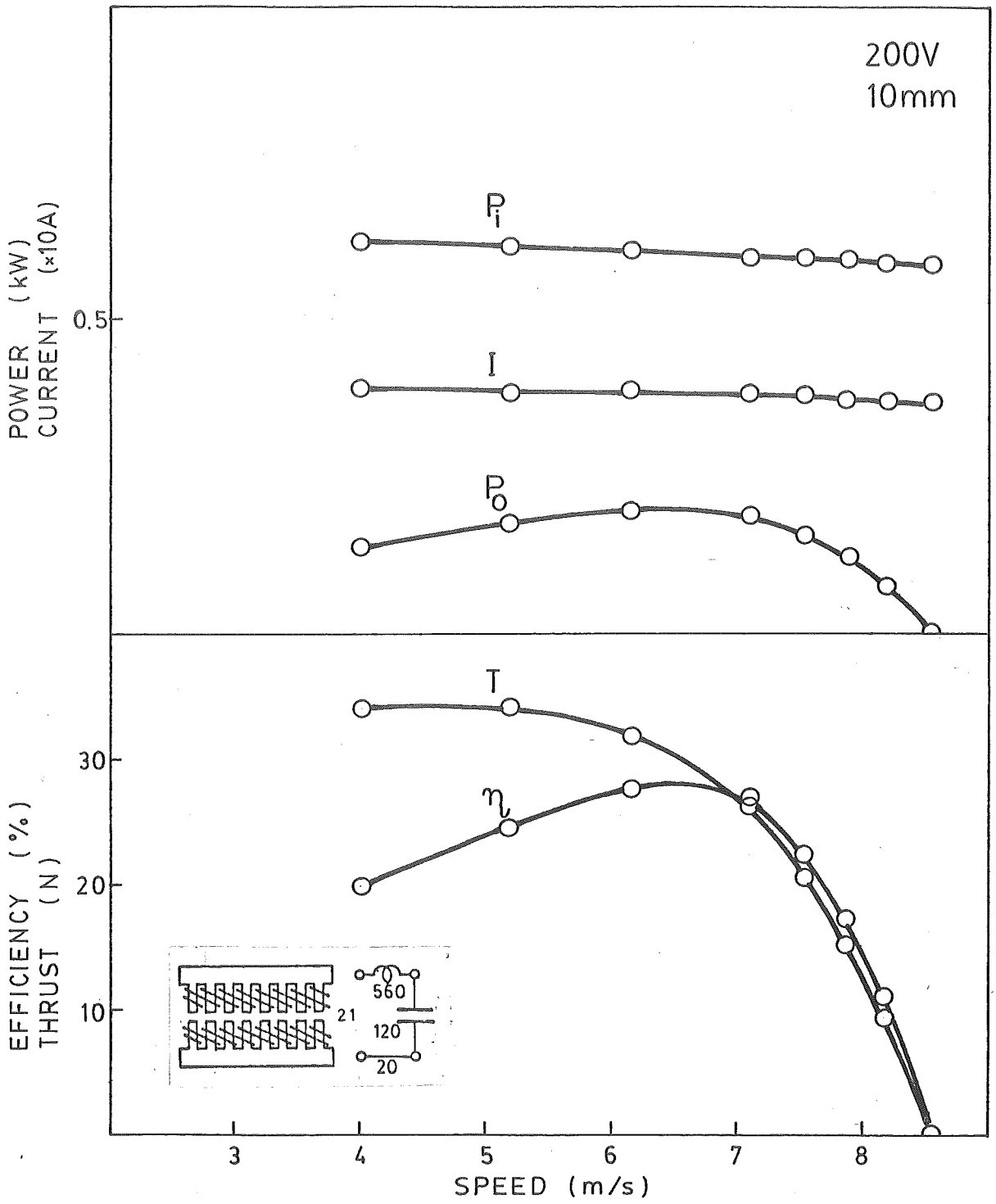
200V
10mm
POWER (kW)
CURRENT (×10A)
0.5
P_i
I
P_o
EFFICIENCY (%)
THRUST (N)
30
20
10
T
η
560
120
20
21
3
4
5
6
7
8
SPEED (m/s)

Fig. A132

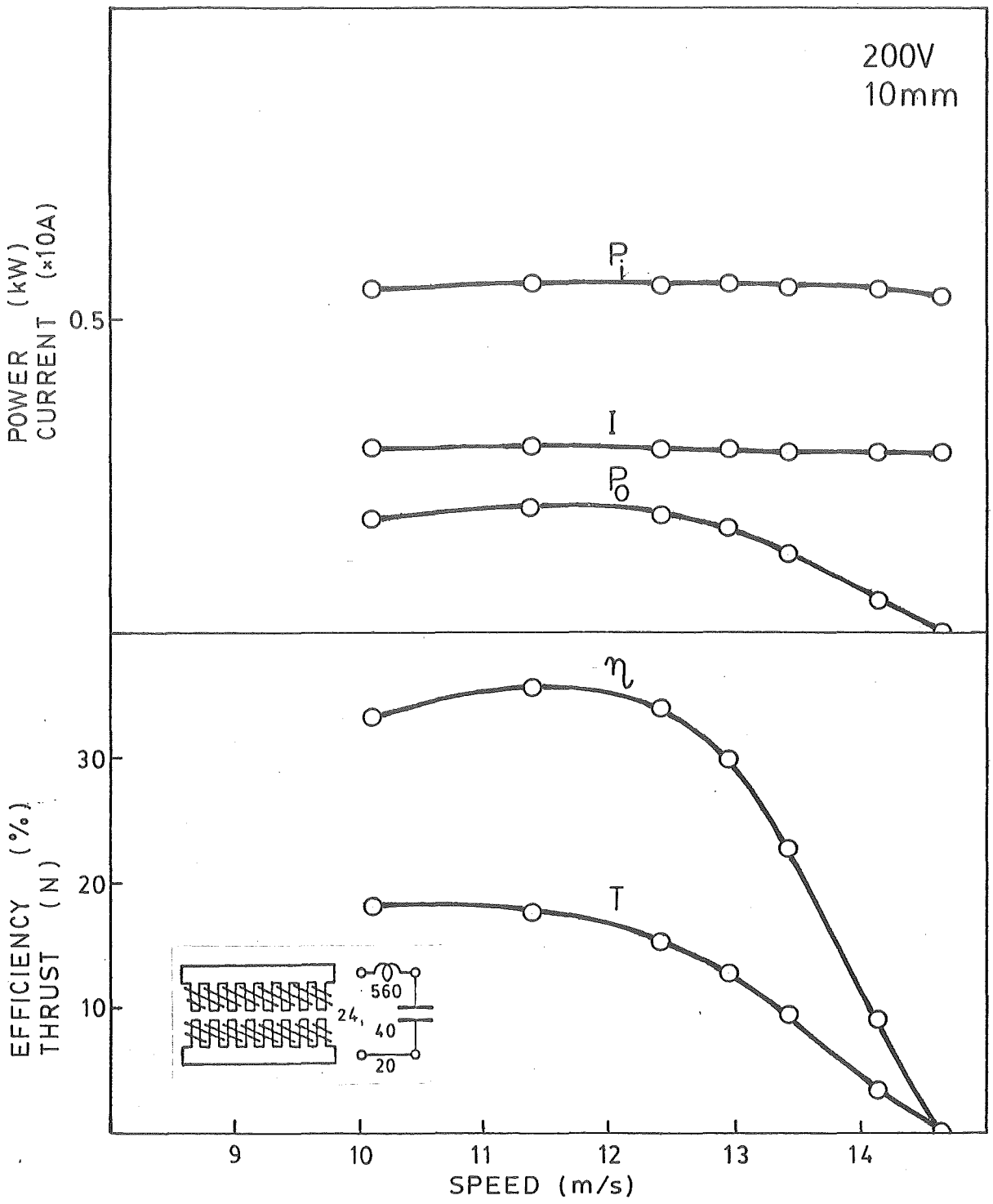
200V
10mm
POWER (kW)
CURRENT (×10A)
0.5
P_i
I
P_o
EFFICIENCY (%)
THRUST (N)
30
20
10
η
T
560
24
40
20
9
10
11
12
13
14
SPEED (m/s)

Fig. A133

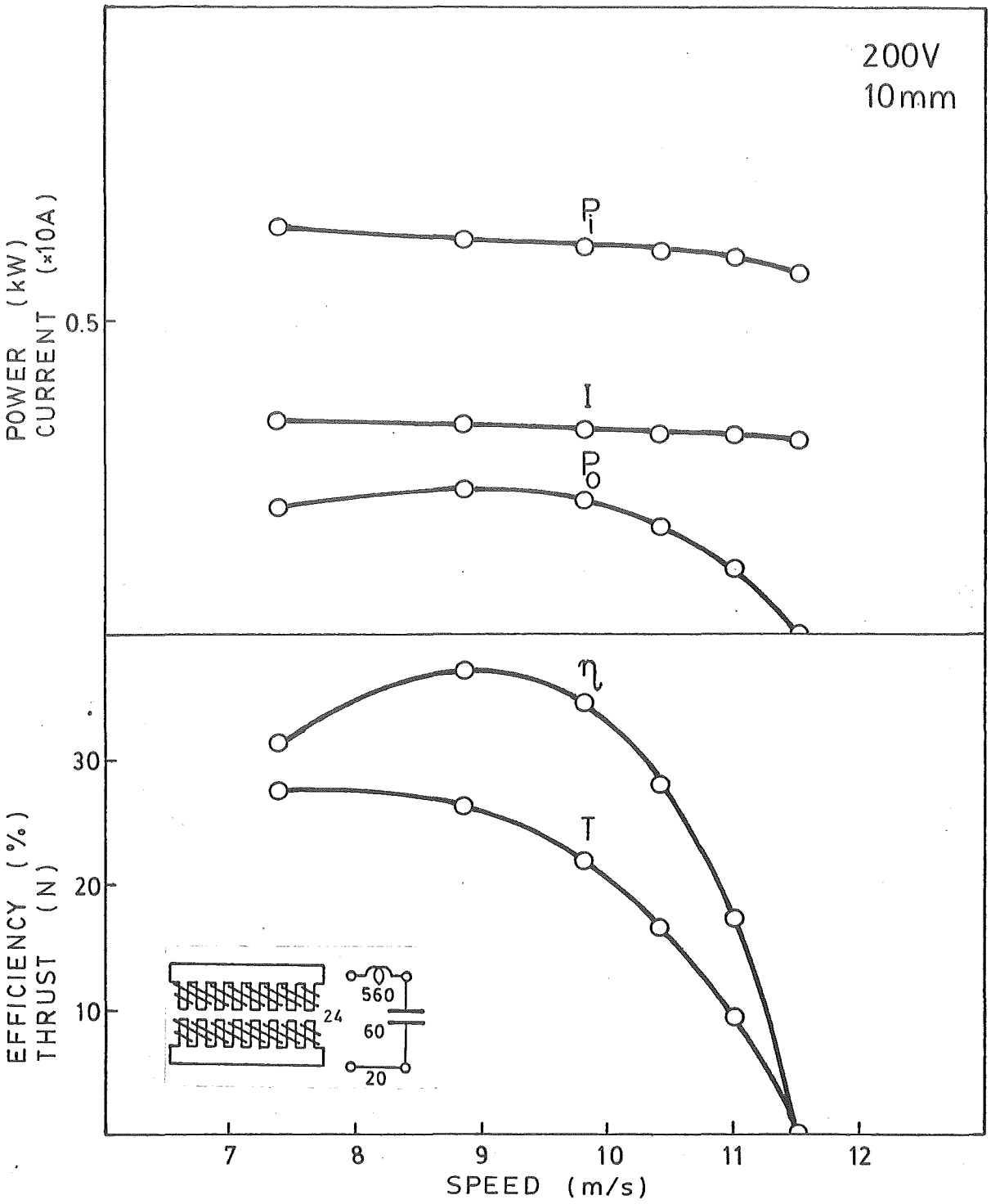
200V
10mm
POWER (kW)
CURRENT (×10A)
0.5
P_i
I
P_o
EFFICIENCY (%)
THRUST (N)
30
20
10
η
T
24
560
60
20
7
8
9
10
11
12
SPEED (m/s)

Fig. A134

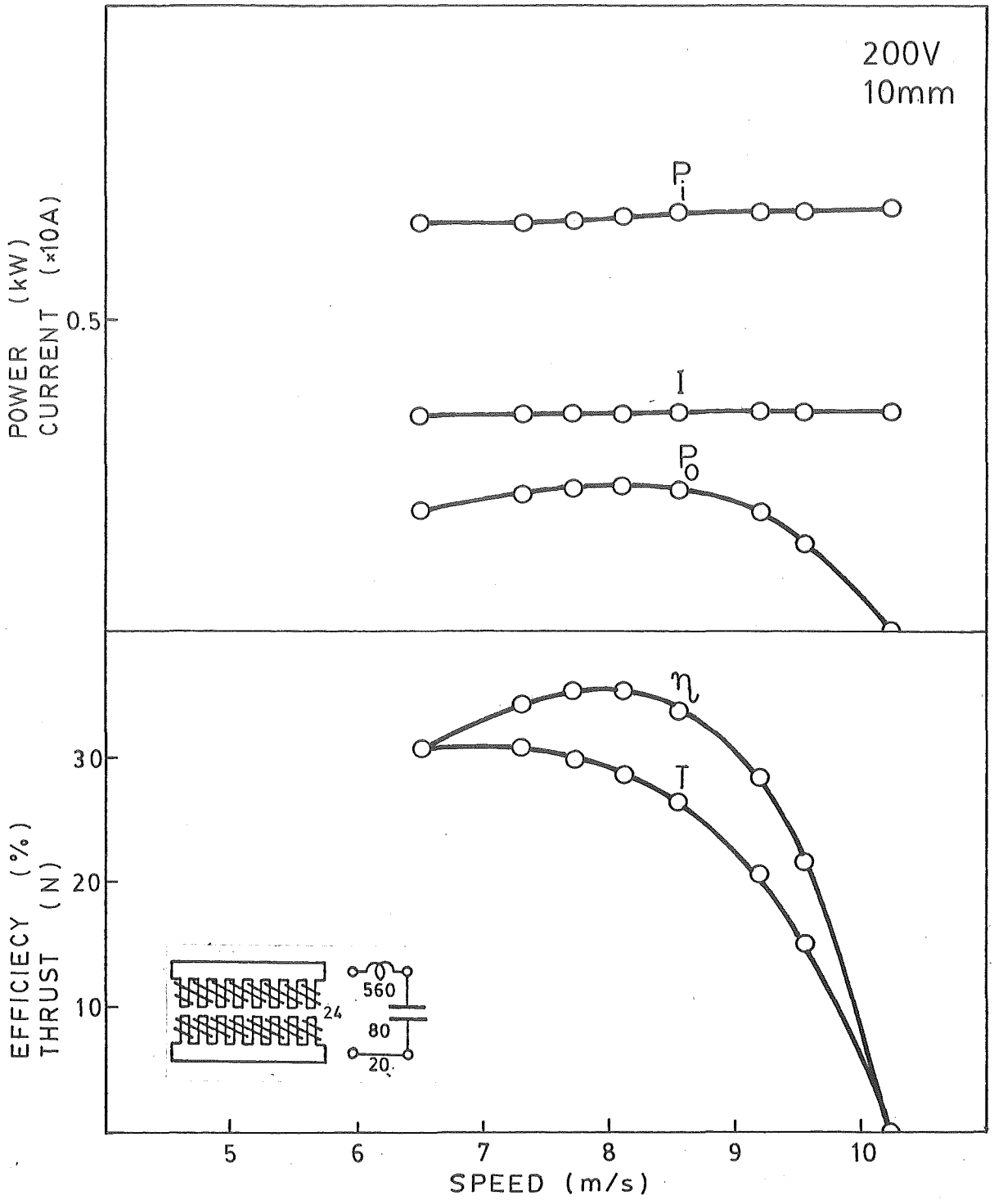
200V
10mm
POWER (kW)
CURRENT (×10A)
0.5
P_i
I
P_o
EFFICIECY (%)
THRUST (N)
30
20
10
η
T
560
80
20
24
5
6
7
8
9
10
SPEED (m/s)

Fig. A135

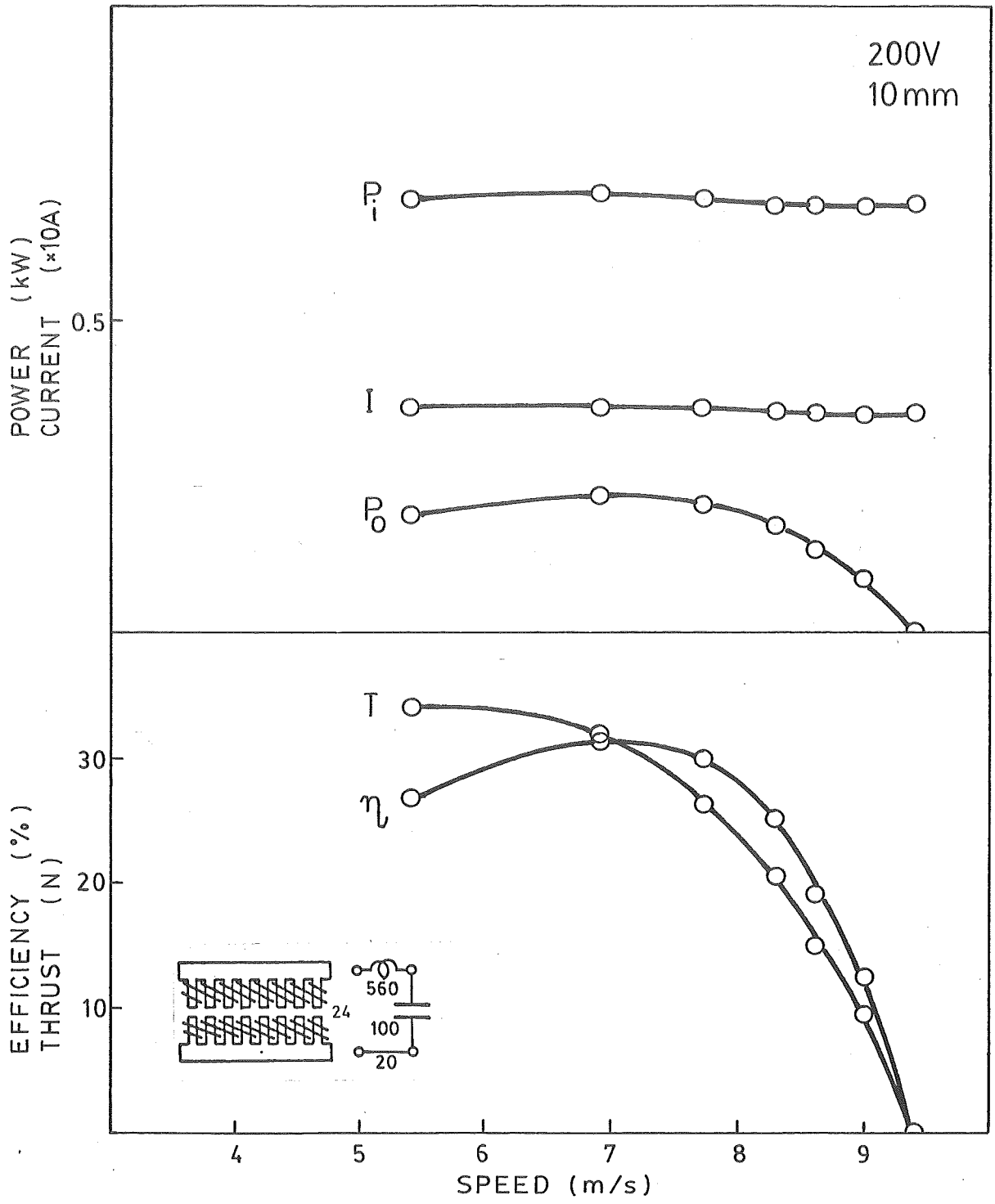
200V
10mm
POWER (kW)
CURRENT (×10A)
0.5
P_i
I
P_o
EFFICIENCY (%)
THRUST (N)
30
20
10
T
η
560
100
20
24
4
5
6
7
8
9
SPEED (m/s)

Fig.A136

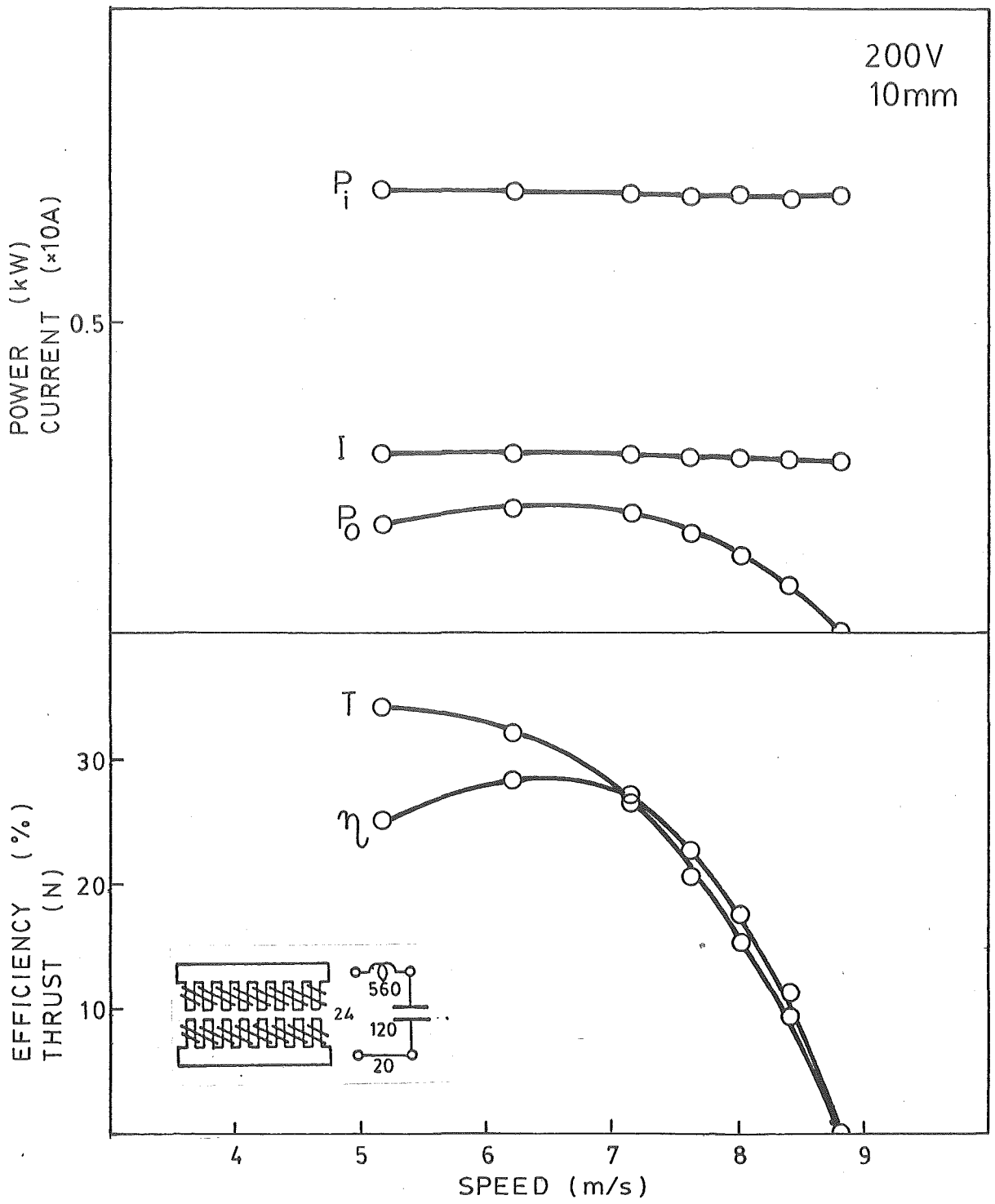
200V
10mm
POWER (kW)
CURRENT (×10A)
0.5
P_i
I
P_o
EFFICIENCY (%)
THRUST (N)
30
20
10
T
η
560
120
20
24
4
5
6
7
8
9
SPEED (m/s)

Fig.A137

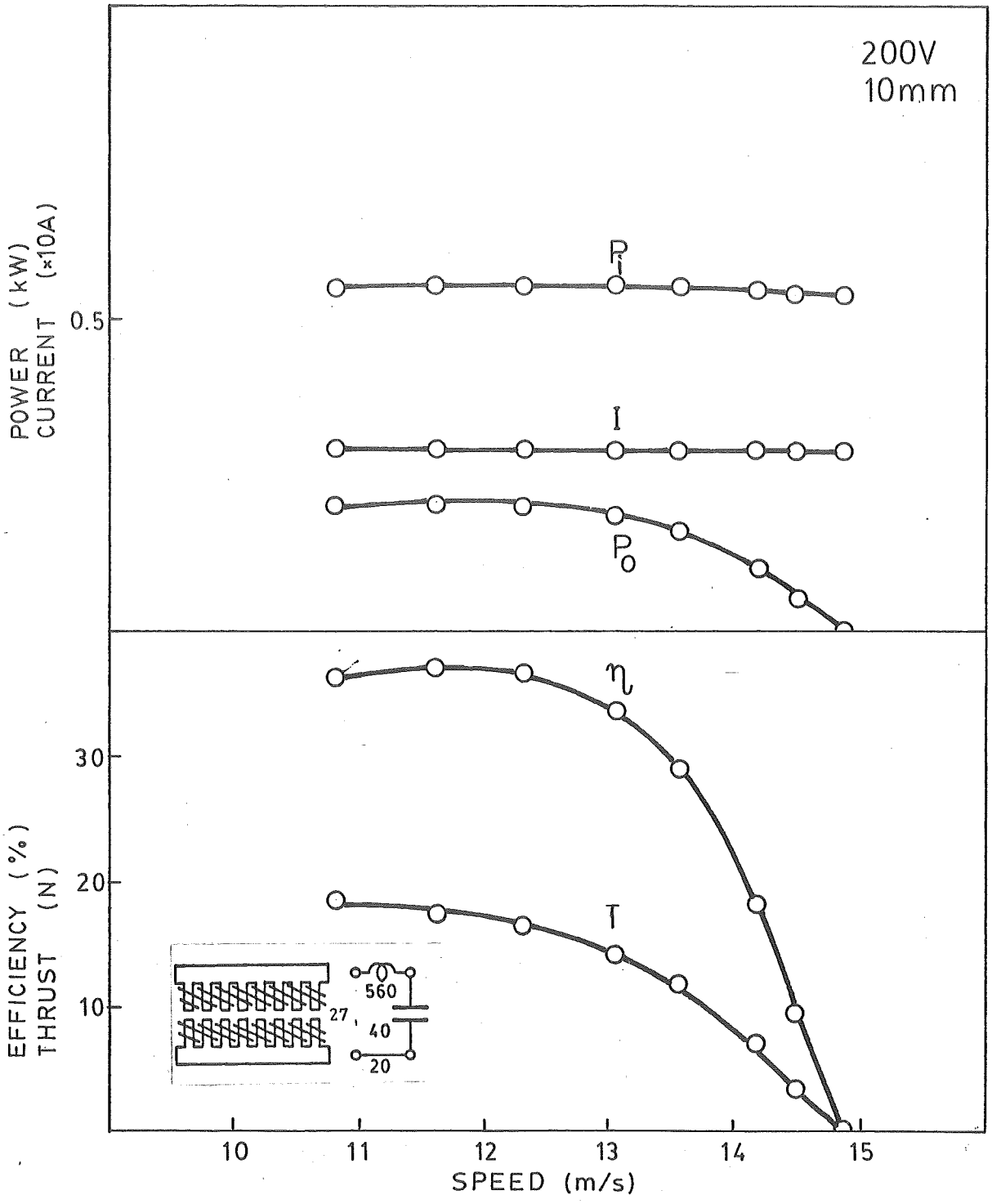
200V
10mm
POWER (kW)
CURRENT (×10A)
0.5
P
I
Po
η
T
30
20
10
EFFICIENCY (%)
THRUST (N)
560
27
40
20
10
11
12
13
14
15
SPEED (m/s)

Fig. A138

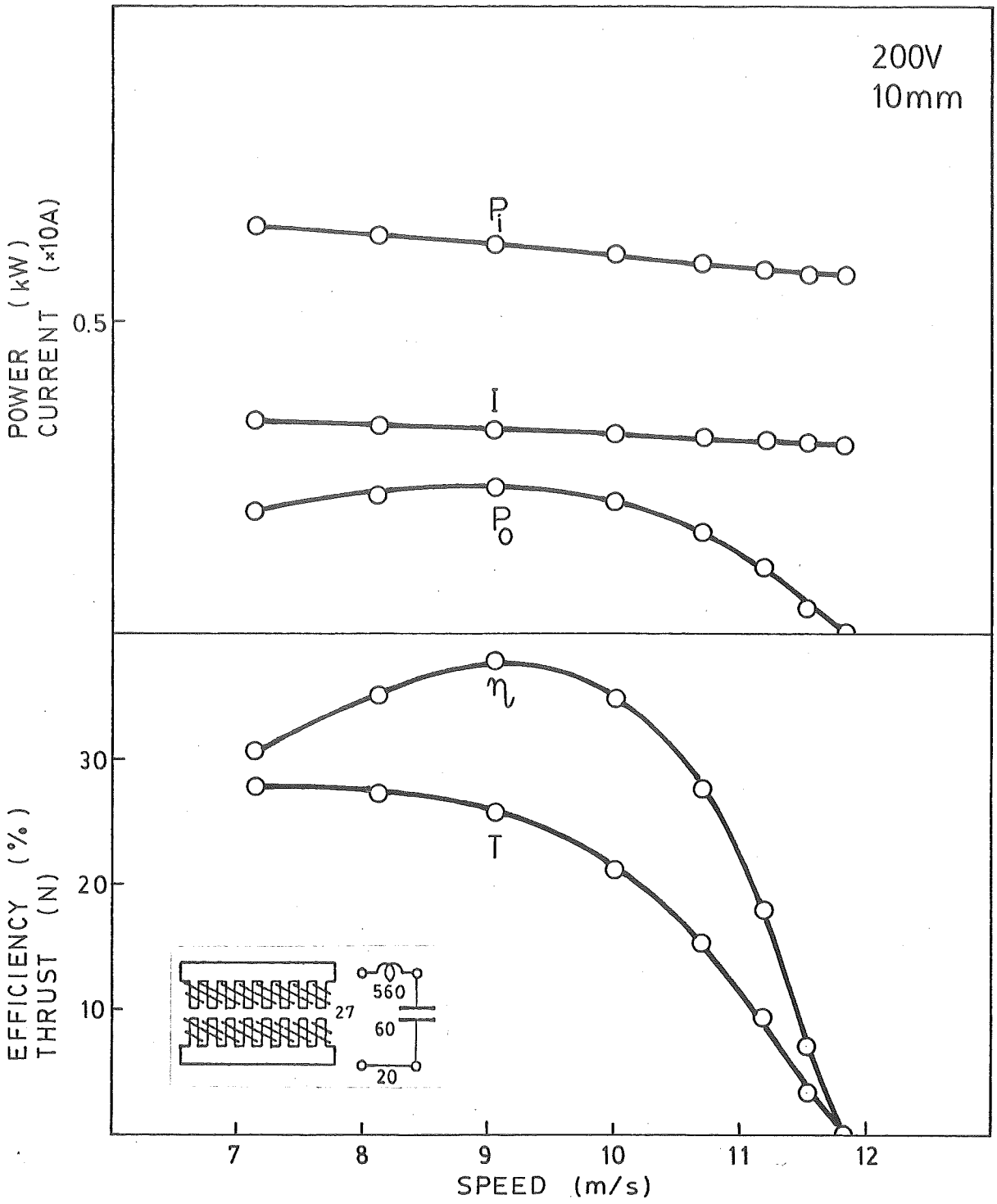
200V
10mm
POWER (kW)
CURRENT (×10A)
0.5
P_i
I
P_o
EFFICIENCY (%)
THRUST (N)
30
20
10
η
T
560
60
20
27
7
8
9
10
11
12
SPEED (m/s)

Fig. A139

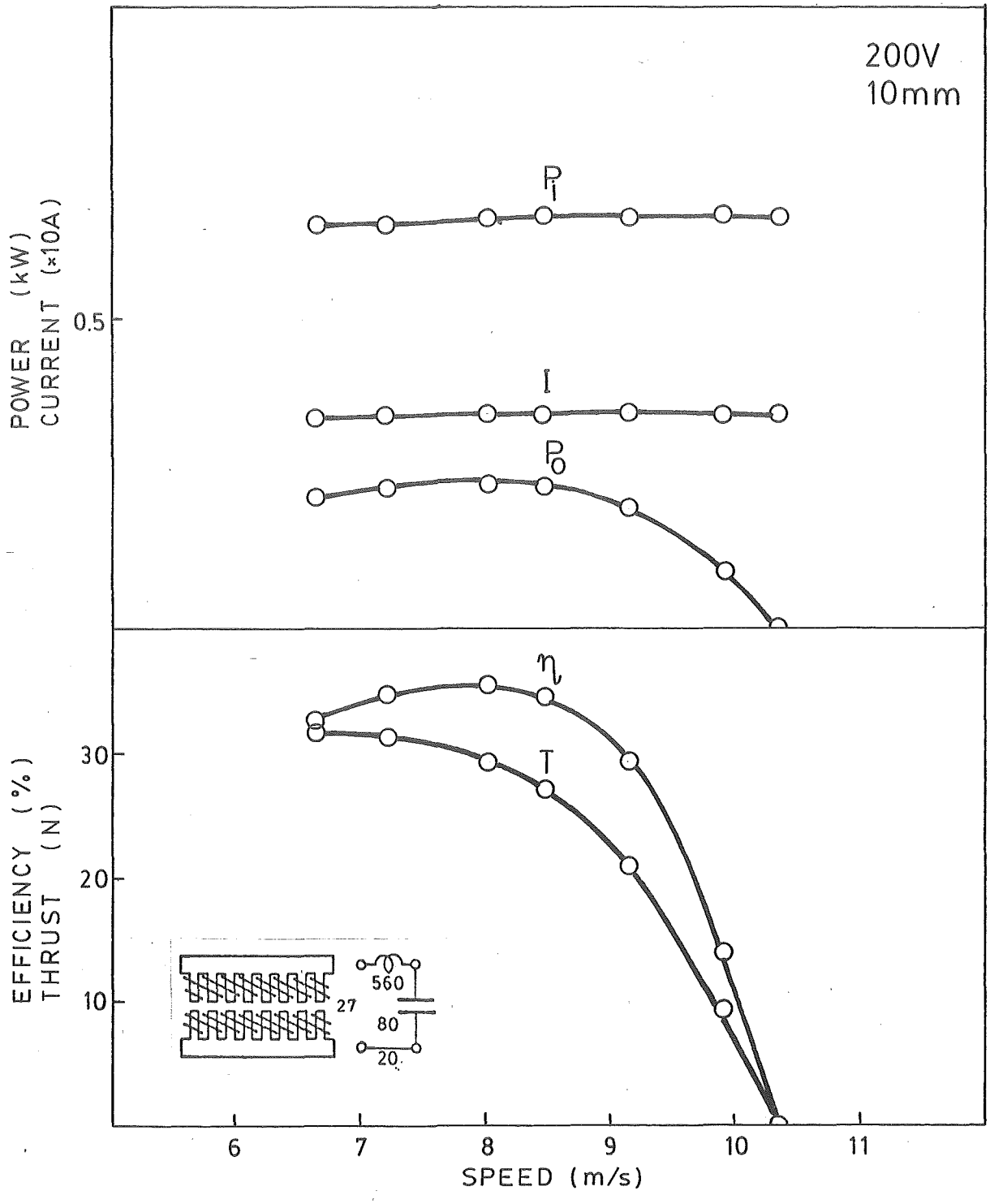
200V
10mm
POWER (kW)
CURRENT (×10A)
0.5
P_i
I
P_o
EFFICIENCY (%)
THRUST (N)
30
20
10
η
T
560
27
80
20
6
7
8
9
10
11
SPEED (m/s)

Fig. A140

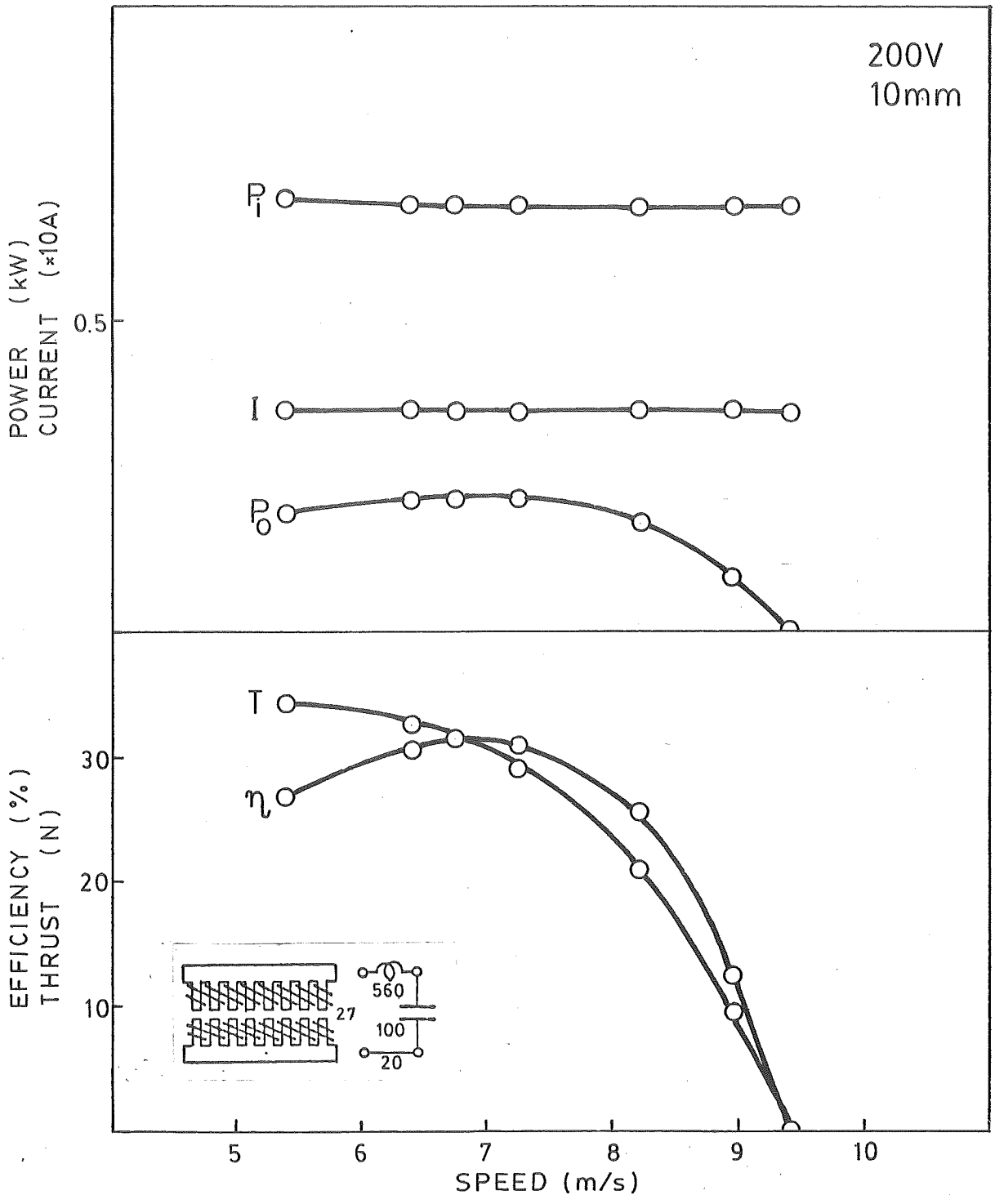
200V
10mm
POWER (kW)
CURRENT (×10A)
P_I
I
P_O
0.5
EFFICIENCY (%)
THRUST (N)
T
η
30
20
10
560
27
100
20
5
6
7
8
9
10
SPEED (m/s)

Fig. A141

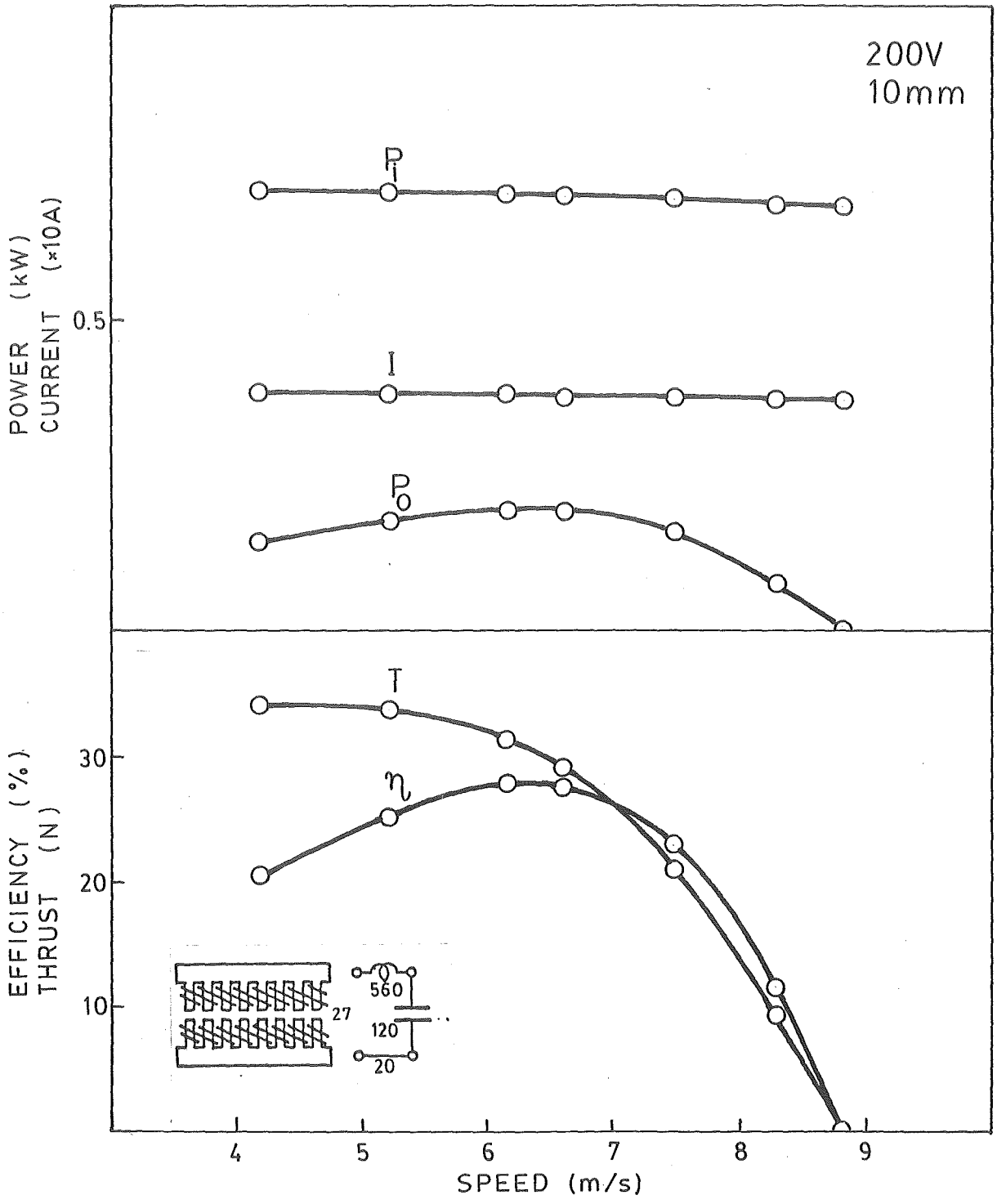
200V
10mm
POWER (kW)
CURRENT (×10A)
0.5
P_I
I
P_O
EFFICIENCY (%)
THRUST (N)
30
20
10
T
η
560
27
120
20
4
5
6
7
8
9
SPEED (m/s)

Fig. A142

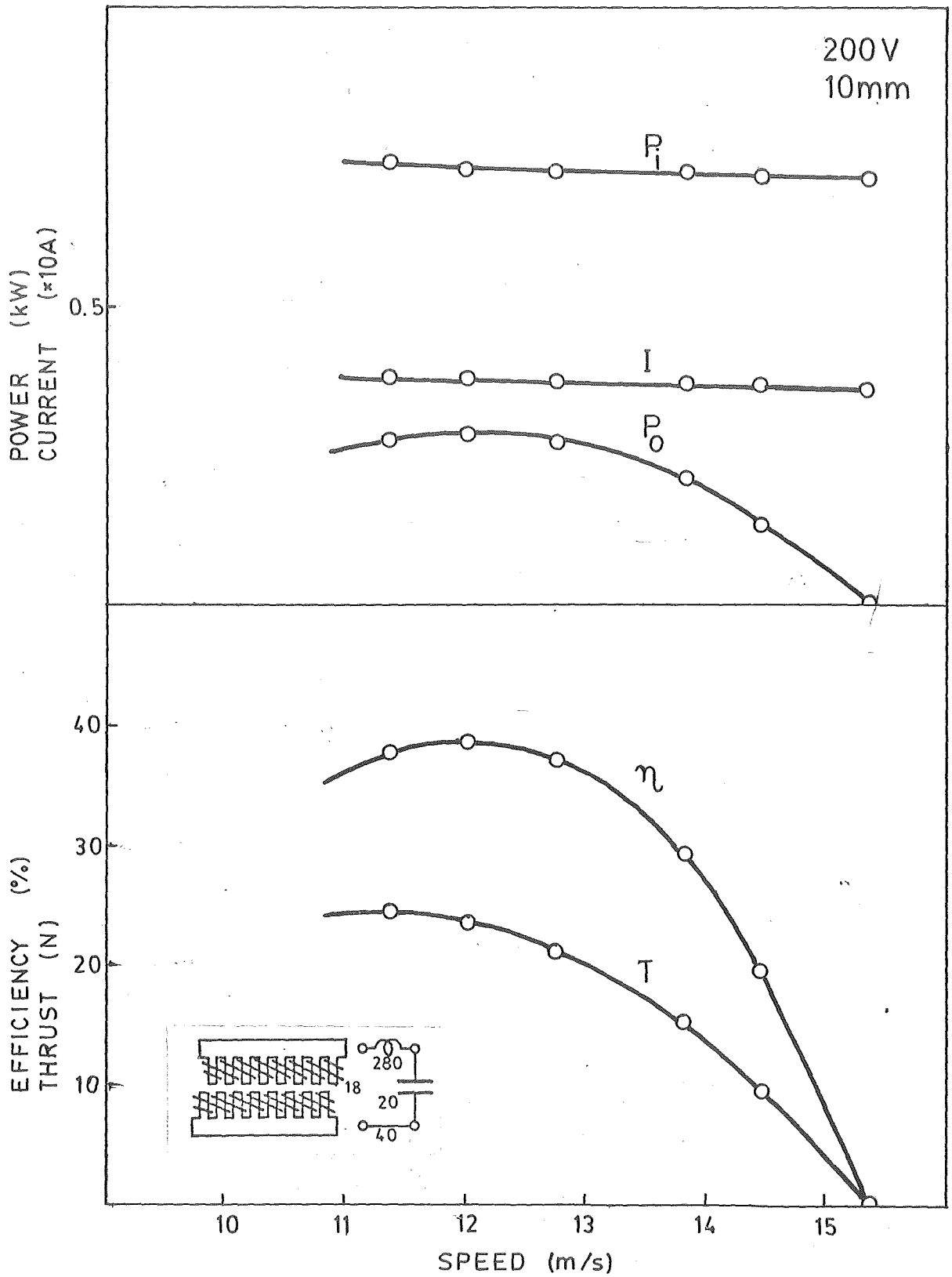
200V
10mm
P_i
I
P_o
POWER (kW)
CURRENT (×10A)
0.5
η
T
EFFICIENCY (%)
THRUST (N)
40
30
20
10
280
18
20
40
10
11
12
13
14
15
SPEED (m/s)

Fig. A143

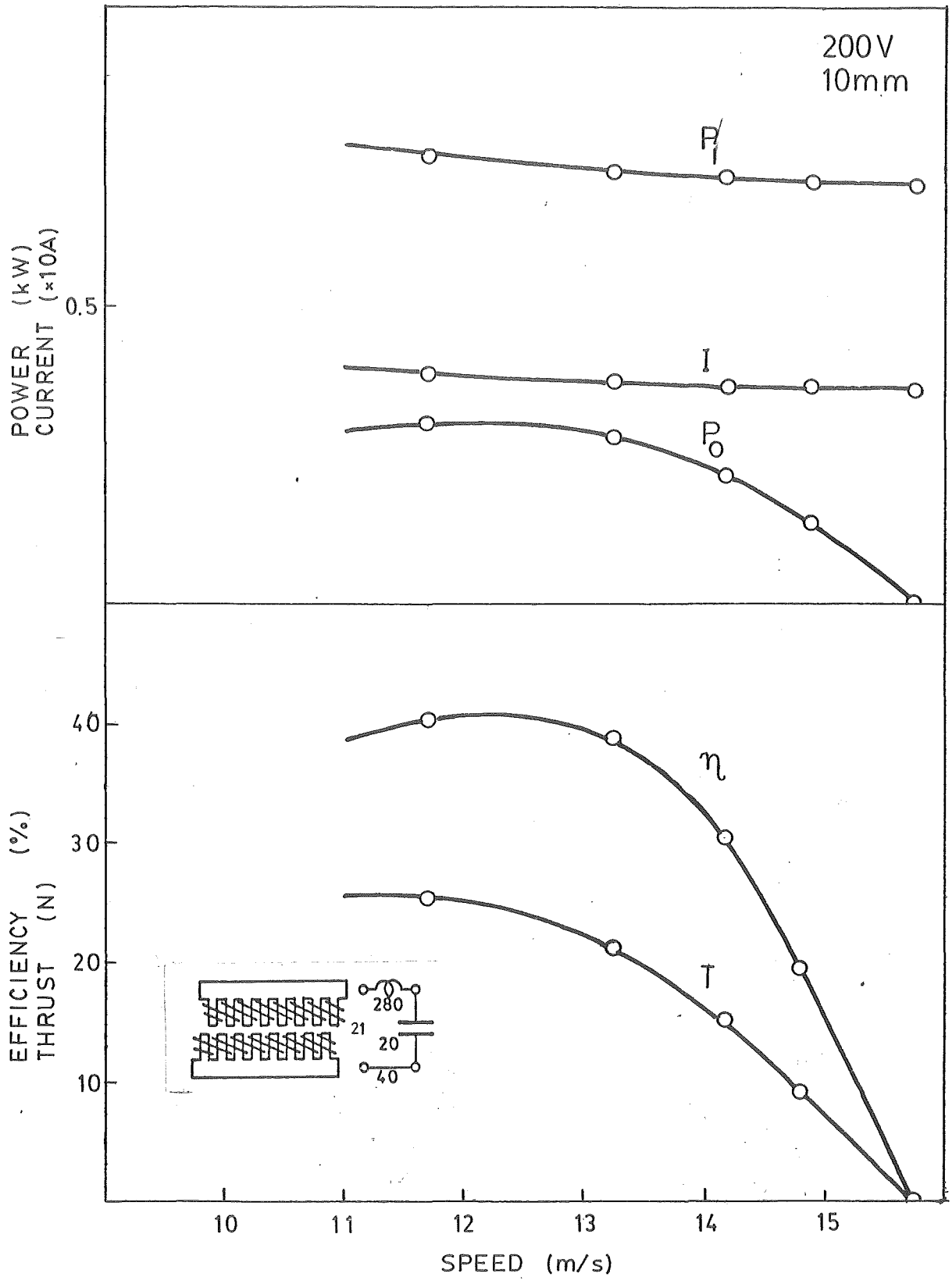
200V
10mm
P_I
I
P_O
POWER (kW)
CURRENT (×10A)
0.5
η
T
EFFICIENCY (%)
THRUST (N)
40
30
20
10
280
21
20
40
10
11
12
13
14
15
SPEED (m/s)

Fig. A144

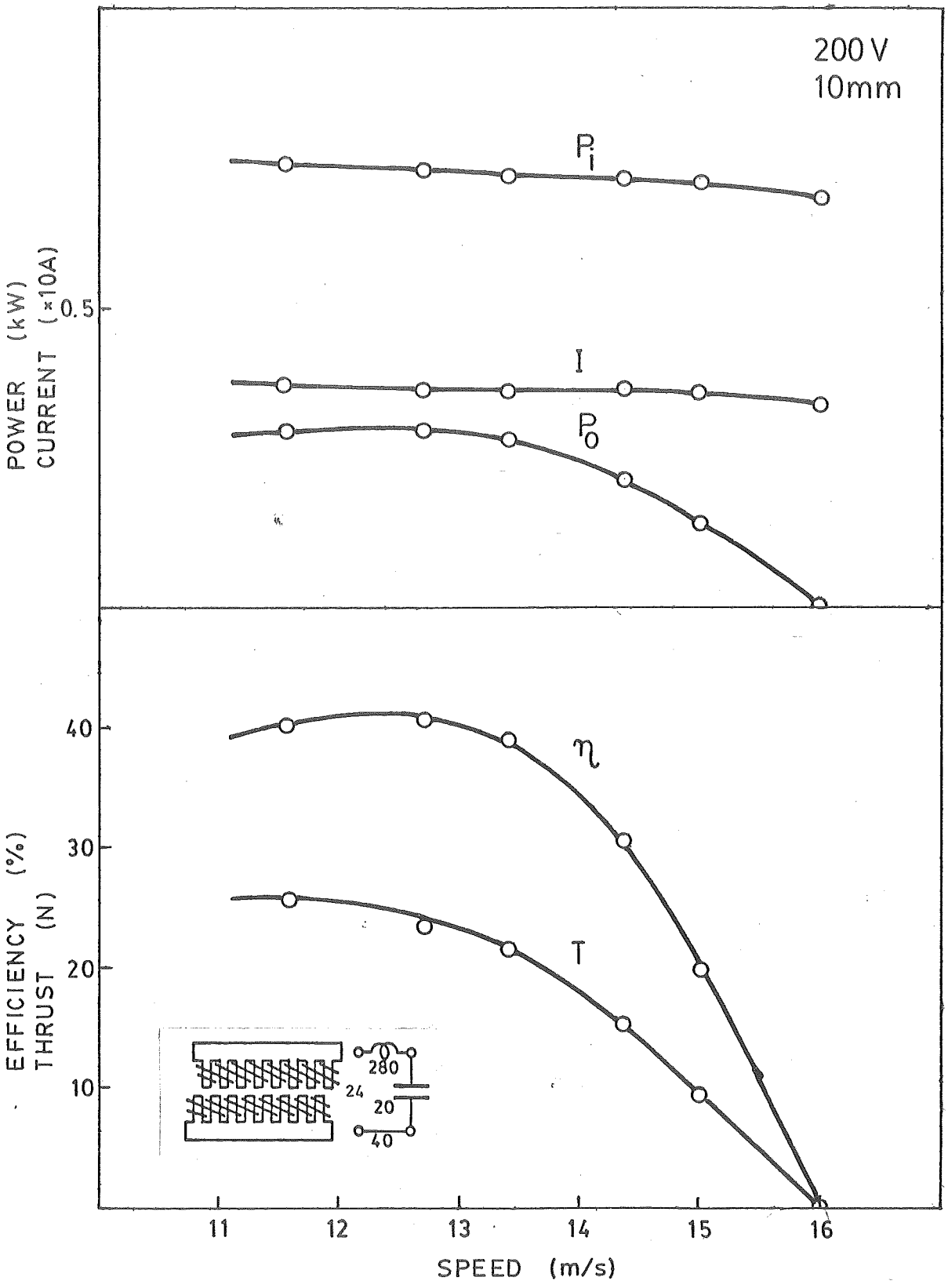
200 V
10mm
P_i
I
P_o
POWER (kW)
CURRENT (×10A)
0.5
η
T
EFFICIENCY (%)
THRUST (N)
40
30
20
10
280
24
20
40
11
12
13
14
15
16
SPEED (m/s)

Fig. A145

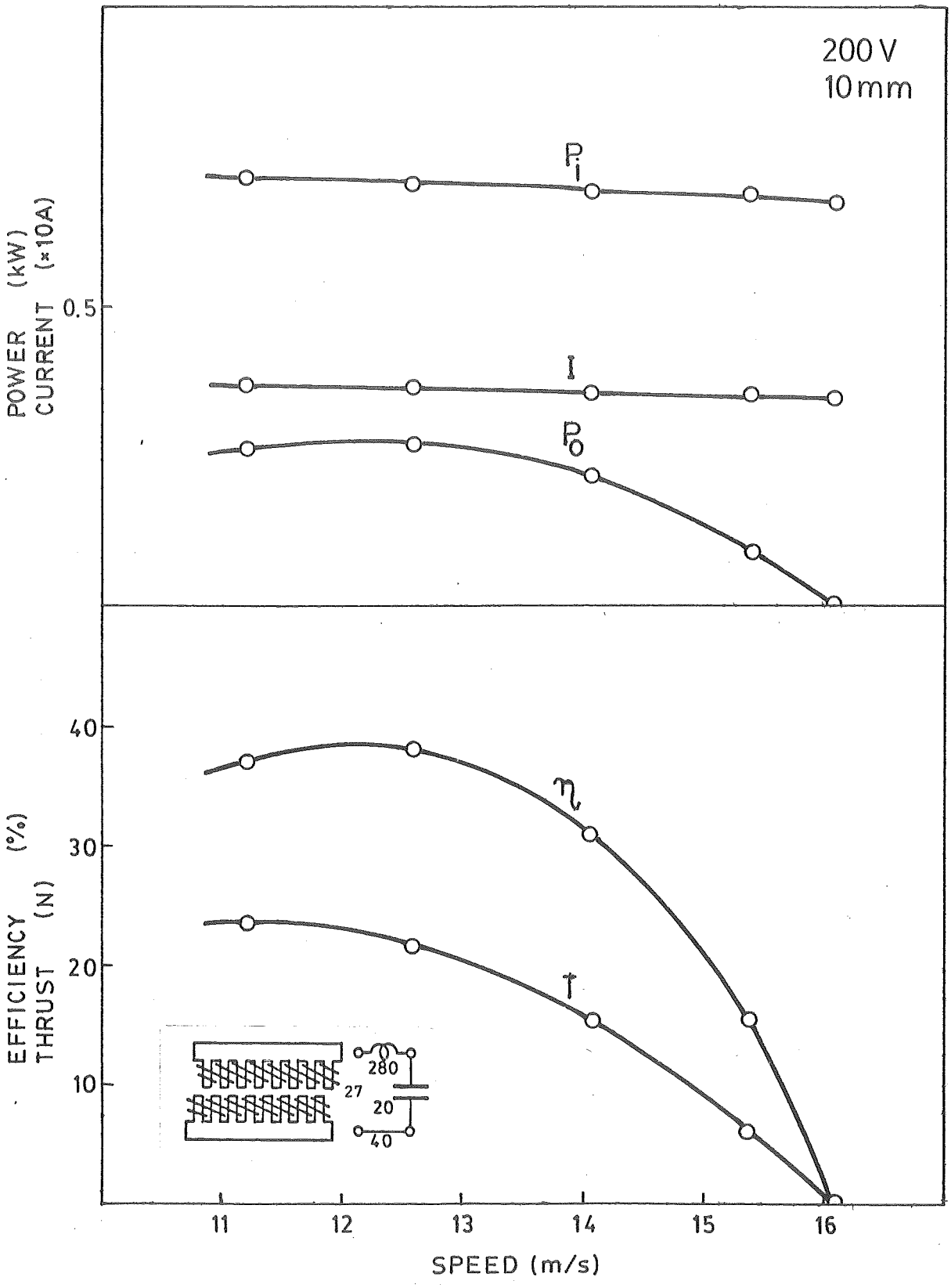
200 V
10 mm
POWER (KW)
CURRENT (×10A)
0.5
P_i
I
P_o
EFFICIENCY (%)
THRUST (N)
40
30
20
10
η
T
280
27
20
40
11
12
13
14
15
16
SPEED (m/s)

Fig. A146

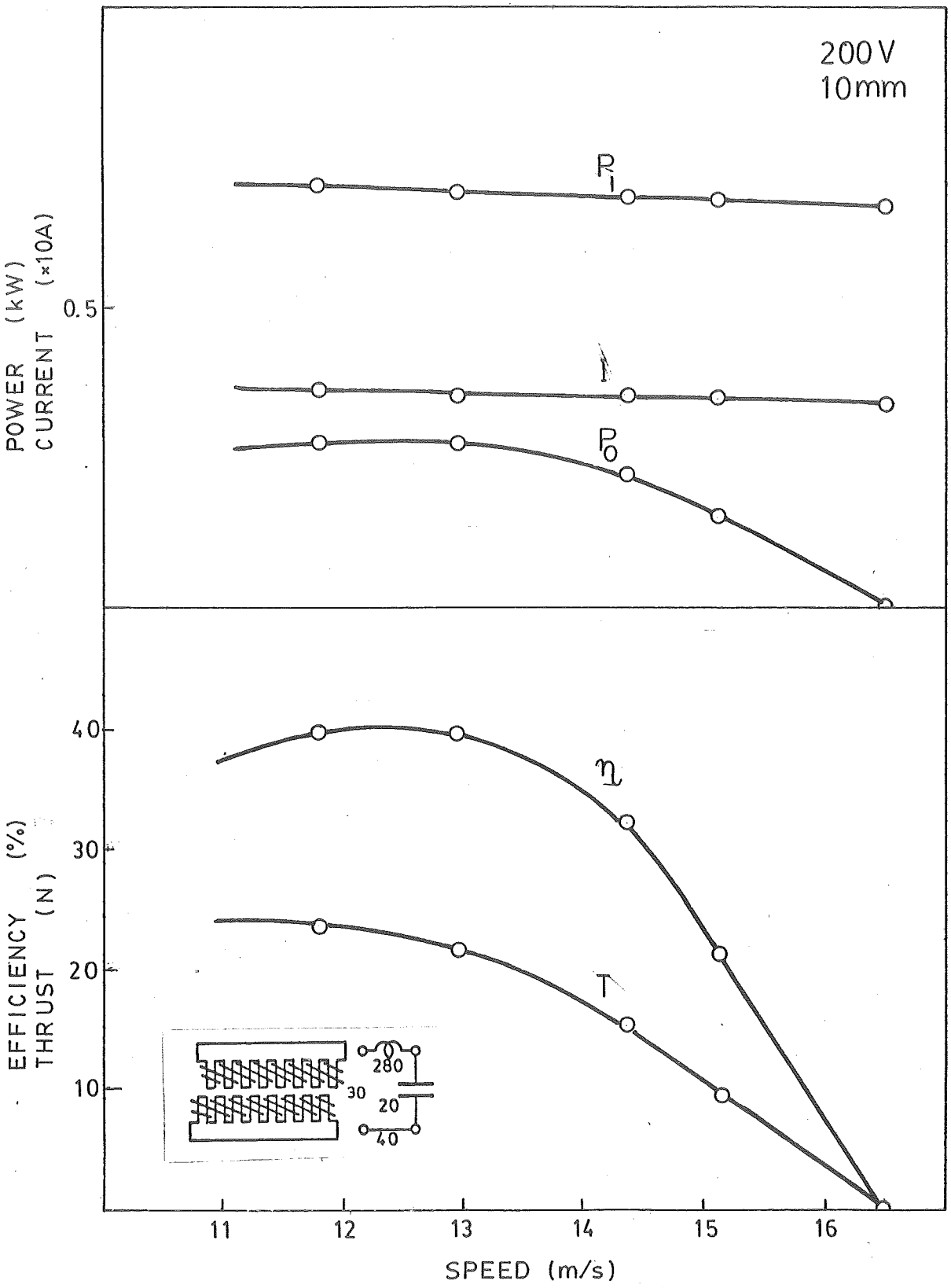
200V
10mm
POWER (kW)
CURRENT (×10A)
0.5
R
I
Po
EFFICIENCY (%)
THRUST (N)
40
30
20
10
η
T
280
30
20
40
11
12
13
14
15
16
SPEED (m/s)

Fig.A147

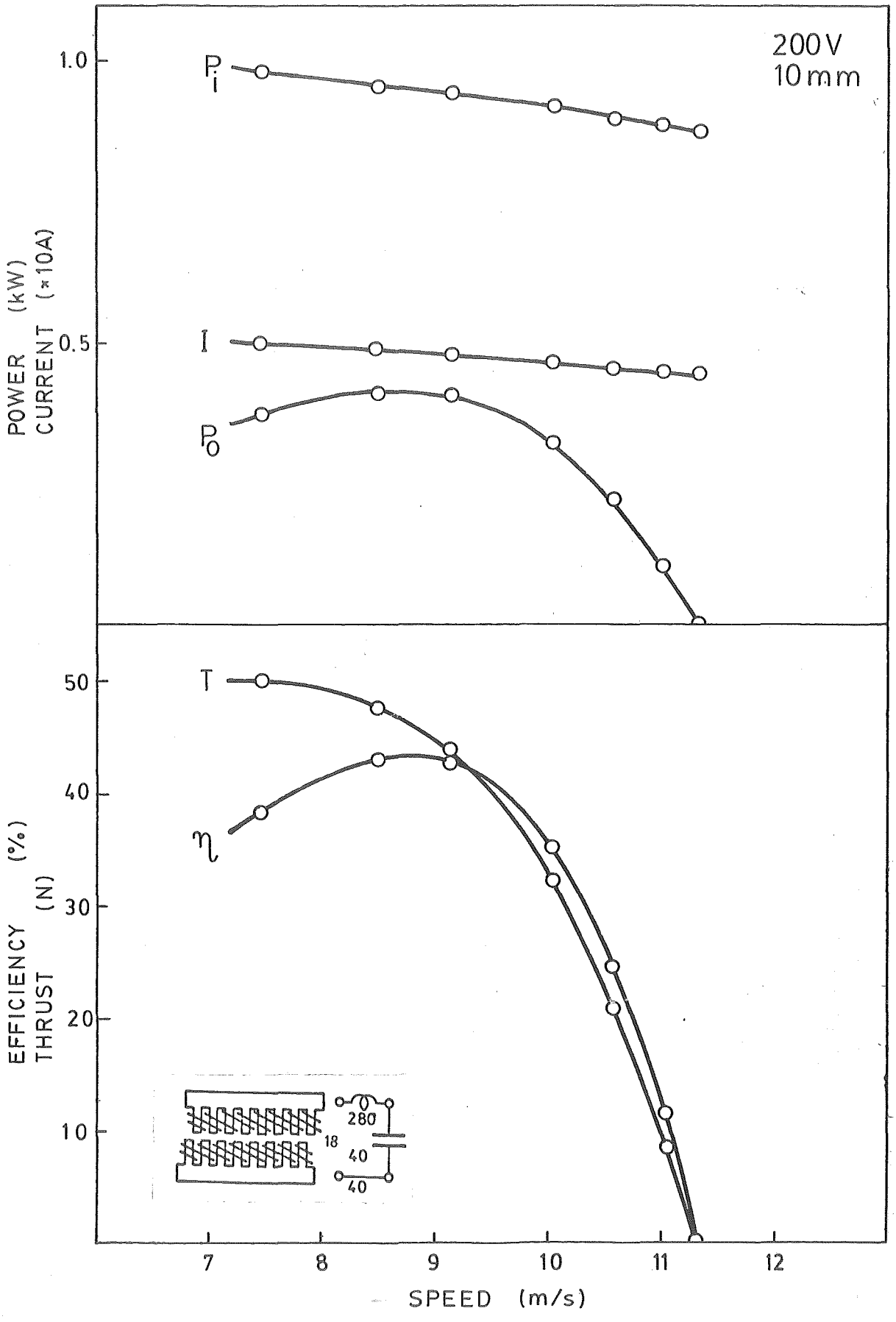
200V
10mm
1.0
0.5
POWER (kW)
CURRENT (×10A)
P_i
I
P_0
50
40
30
20
10
EFFICIENCY (%)
THRUST (N)
T
η
280
18
40
40
7
8
9
10
11
12
SPEED (m/s)

Fig. A148

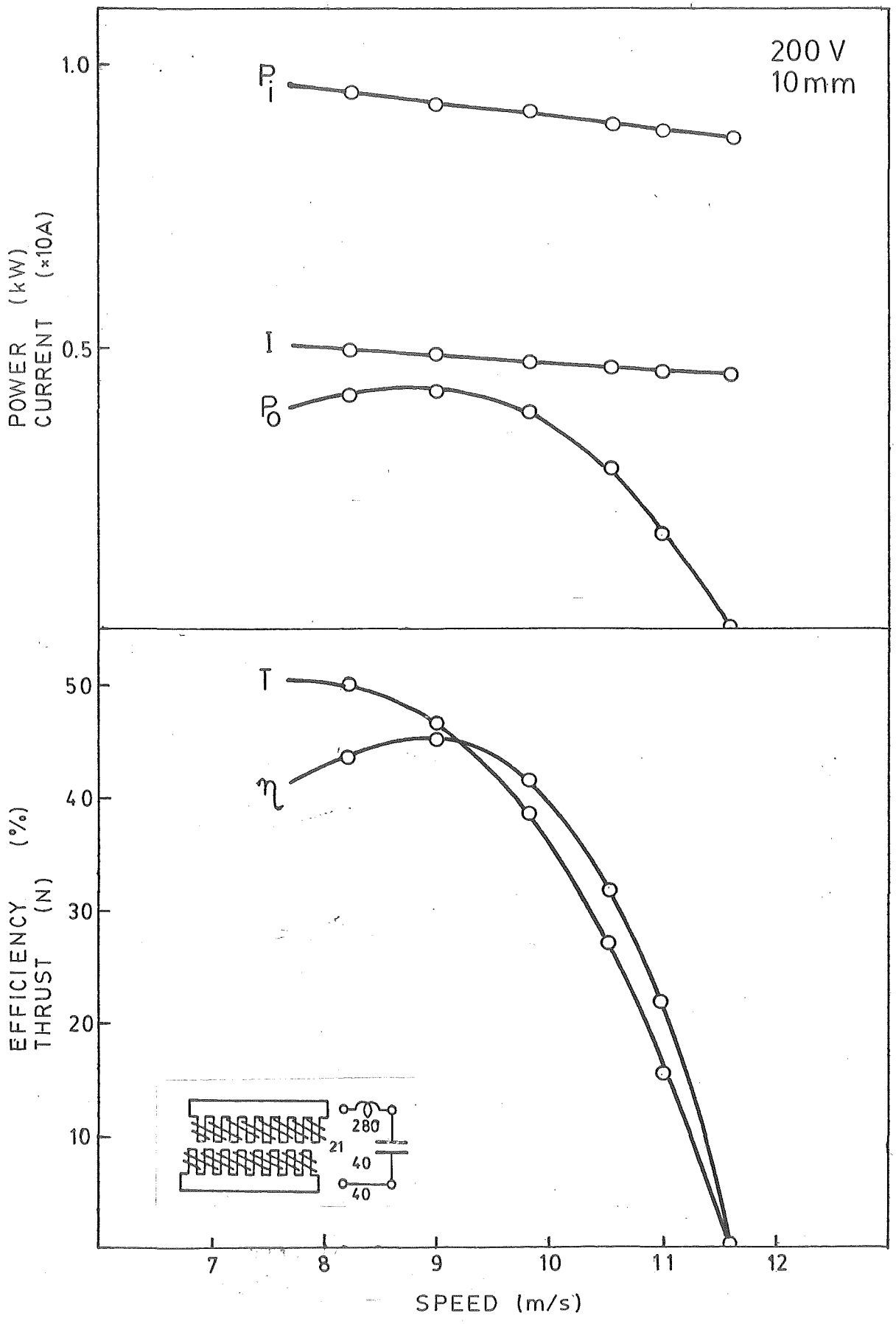
200 V
10 mm
POWER (kW)
CURRENT (×10A)
1.0
0.5
P_i
I
P_o
EFFICIENCY (%)
THRUST (N)
50
40
30
20
10
T
η
280
21
40
40
7
8
9
10
11
12
SPEED (m/s)

Fig. A149

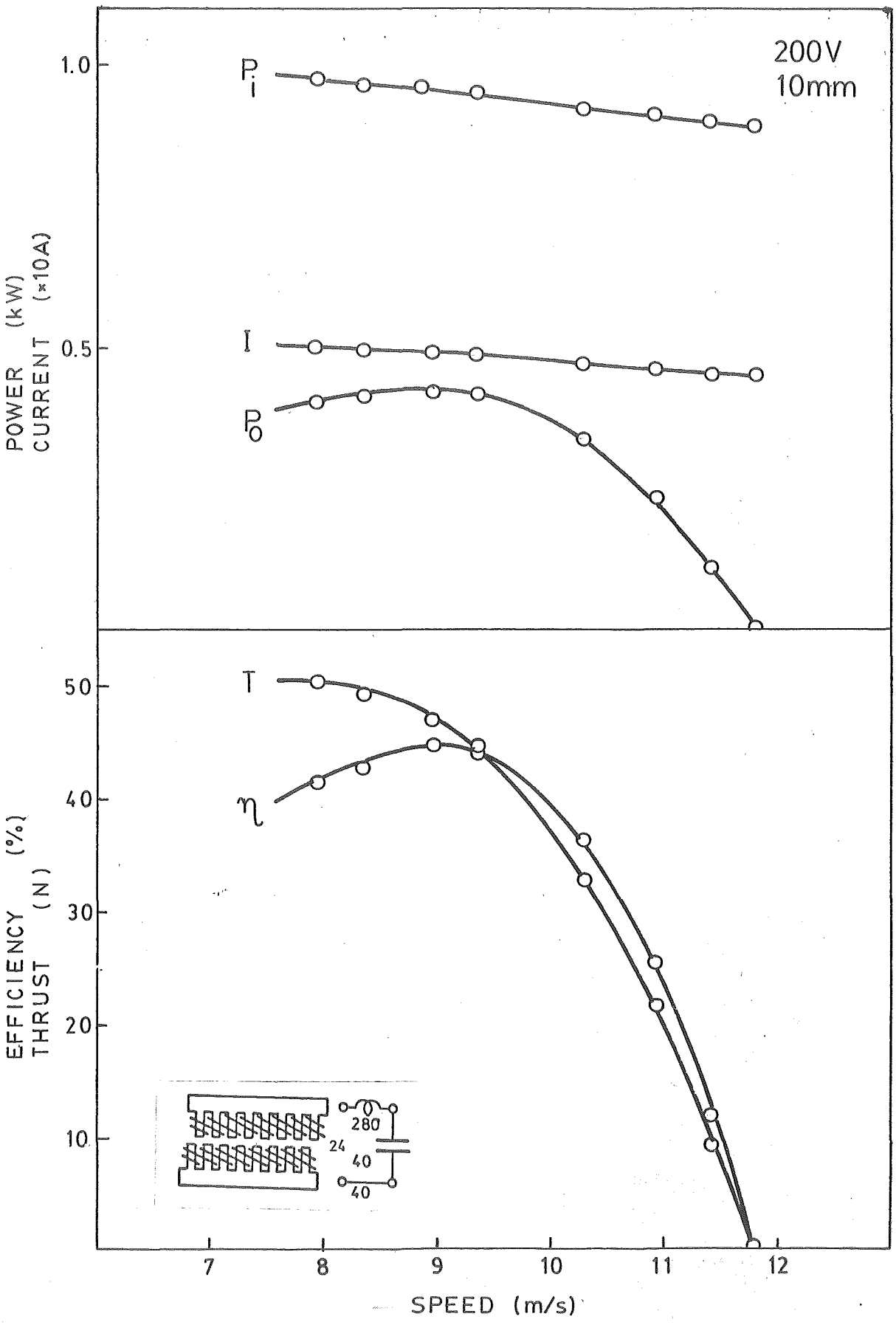
200V
10mm
P_i
I
P_o
POWER (kW)
CURRENT (×10A)
1.0
0.5
T
η
EFFICIENCY (%)
THRUST (N)
50
40
30
20
10
280
24
40
40
7
8
9
10
11
12
SPEED (m/s)

Fig. A150

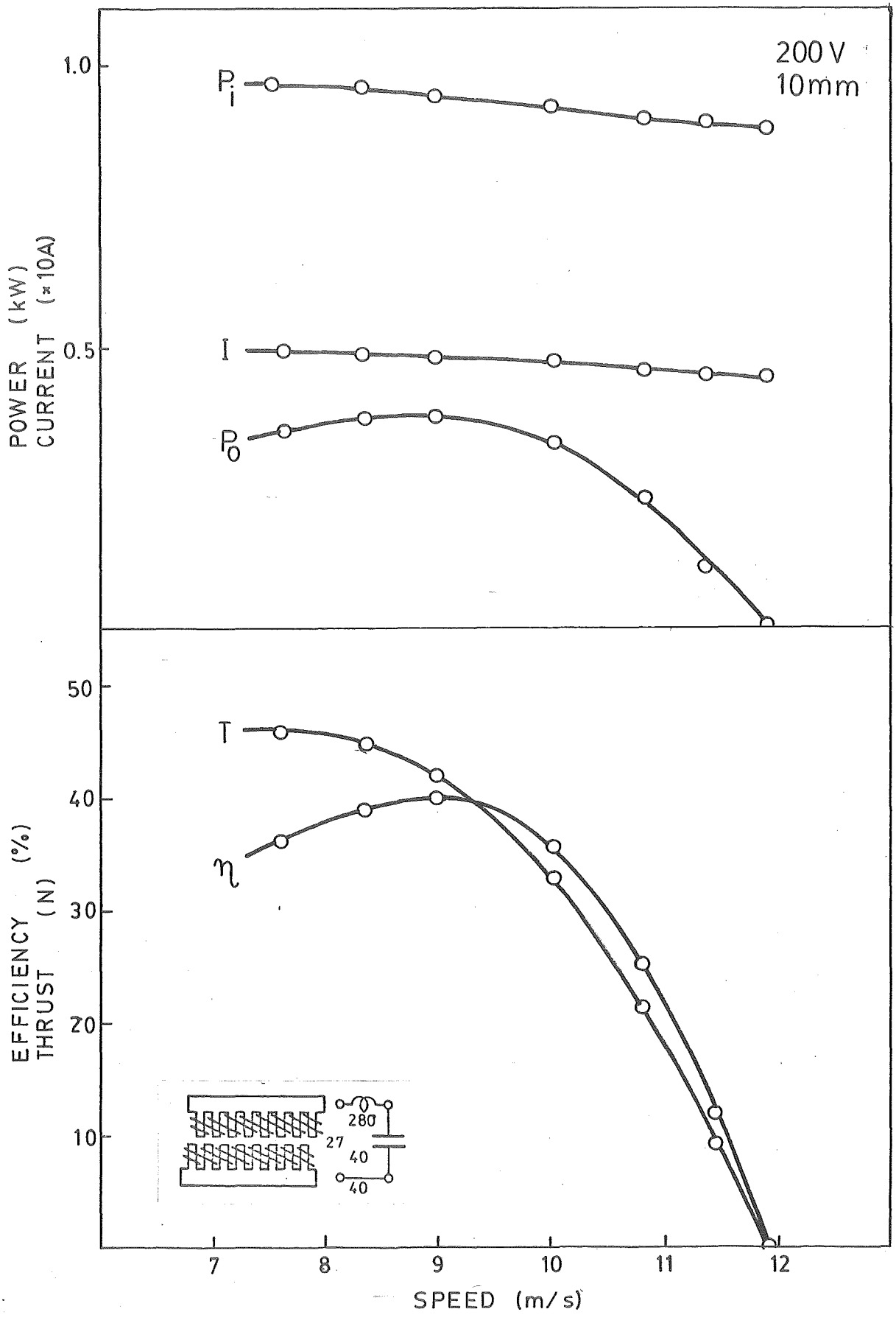
200 V
10mm
1.0
0.5
POWER (kW)
CURRENT (×10A)
P_i
I
P_0
50
40
30
20
10
EFFICIENCY (%)
THRUST (N)
T
η
280
27
40
40
7
8
9
10
11
12
SPEED (m/s)

Fig. A151

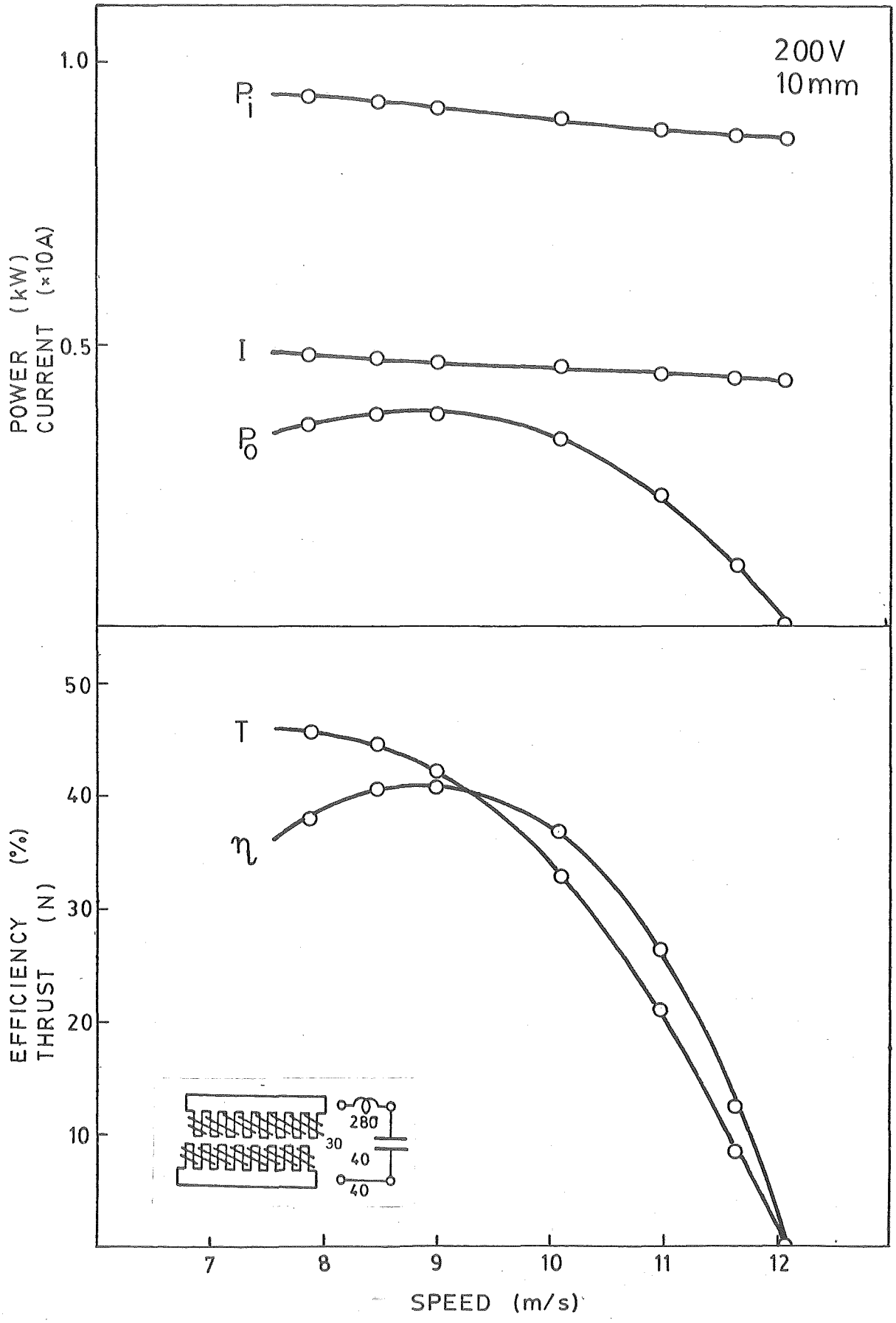
200V
10mm
P1
I
P0
POWER (kW)
CURRENT (×10A)
1.0
0.5
T
η
EFFICIENCY (%)
THRUST (N)
50
40
30
20
10
280
30
40
40
7
8
9
10
11
12
SPEED (m/s)

Fig. A152

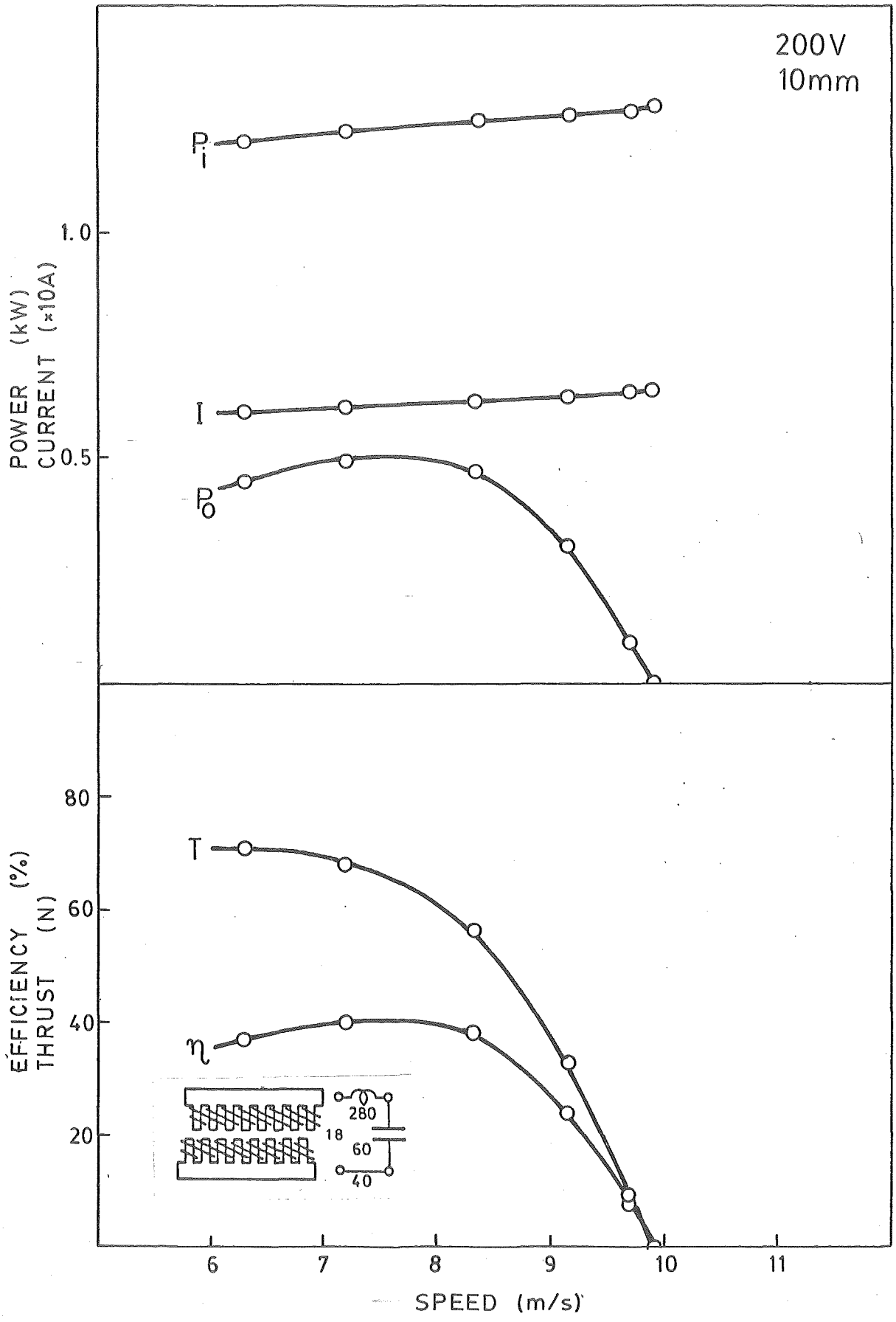
200V
10mm
P_i
I
P_o
POWER (kW)
CURRENT (×10A)
1.0
0.5
T
η
EFFICIENCY (%)
THRUST (N)
80
60
40
20
280
18
60
40
6
7
8
9
10
11
SPEED (m/s)

Fig. A153

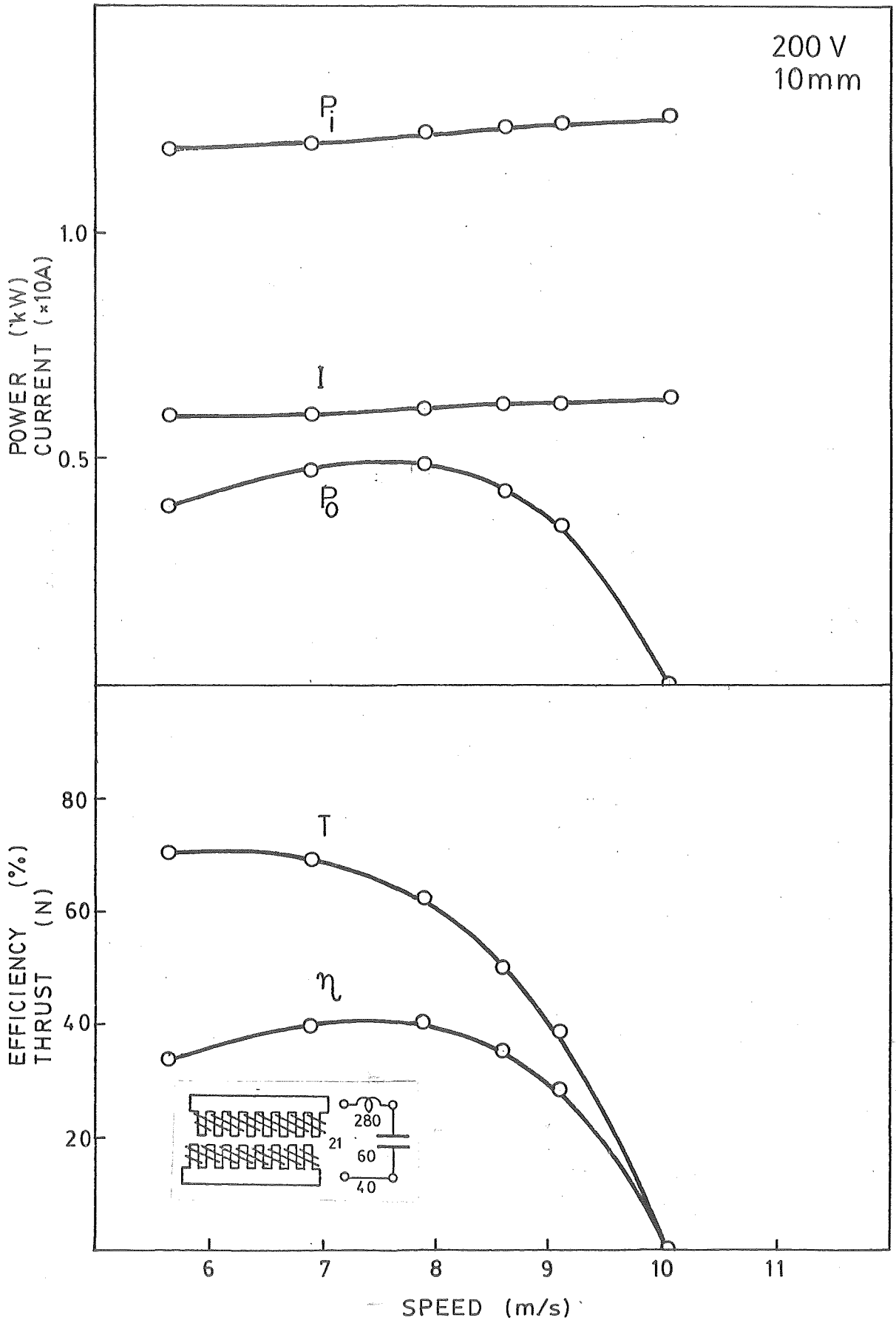
200 V
10mm
P_i
I
P_o
POWER (1kW)
CURRENT (×10A)
1.0
0.5
T
η
EFFICIENCY (%)
THRUST (N)
80
60
40
20
280
21
60
40
6
7
8
9
10
11
SPEED (m/s)

Fig. A154

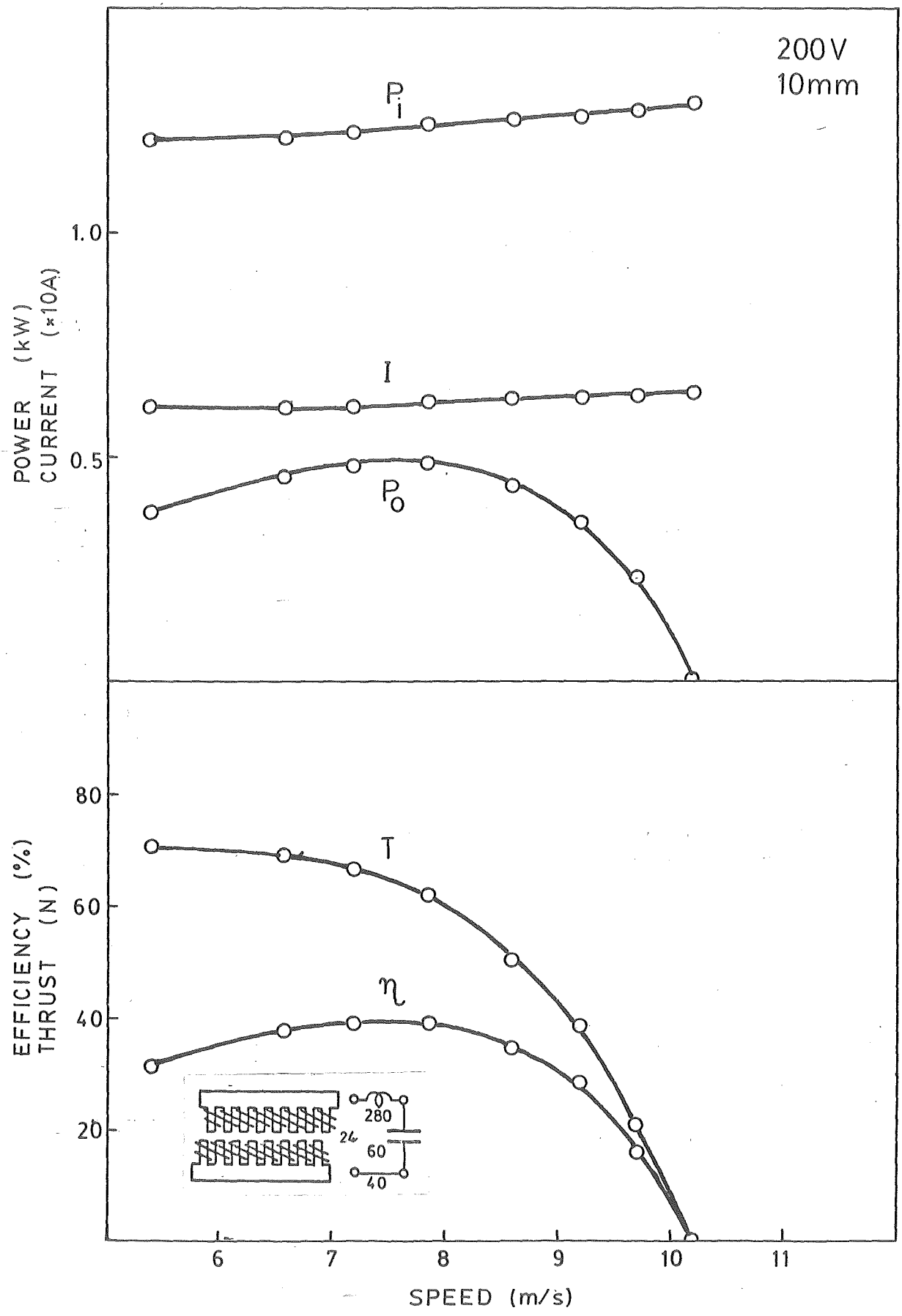
200V
10mm
P_i
I
P_o
POWER (kW)
CURRENT (×10A)
1.0
0.5
80
60
40
20
T
η
EFFICIENCY (%)
THRUST (N)
280
24
60
40
6
7
8
9
10
11
SPEED (m/s)

Fig. A155

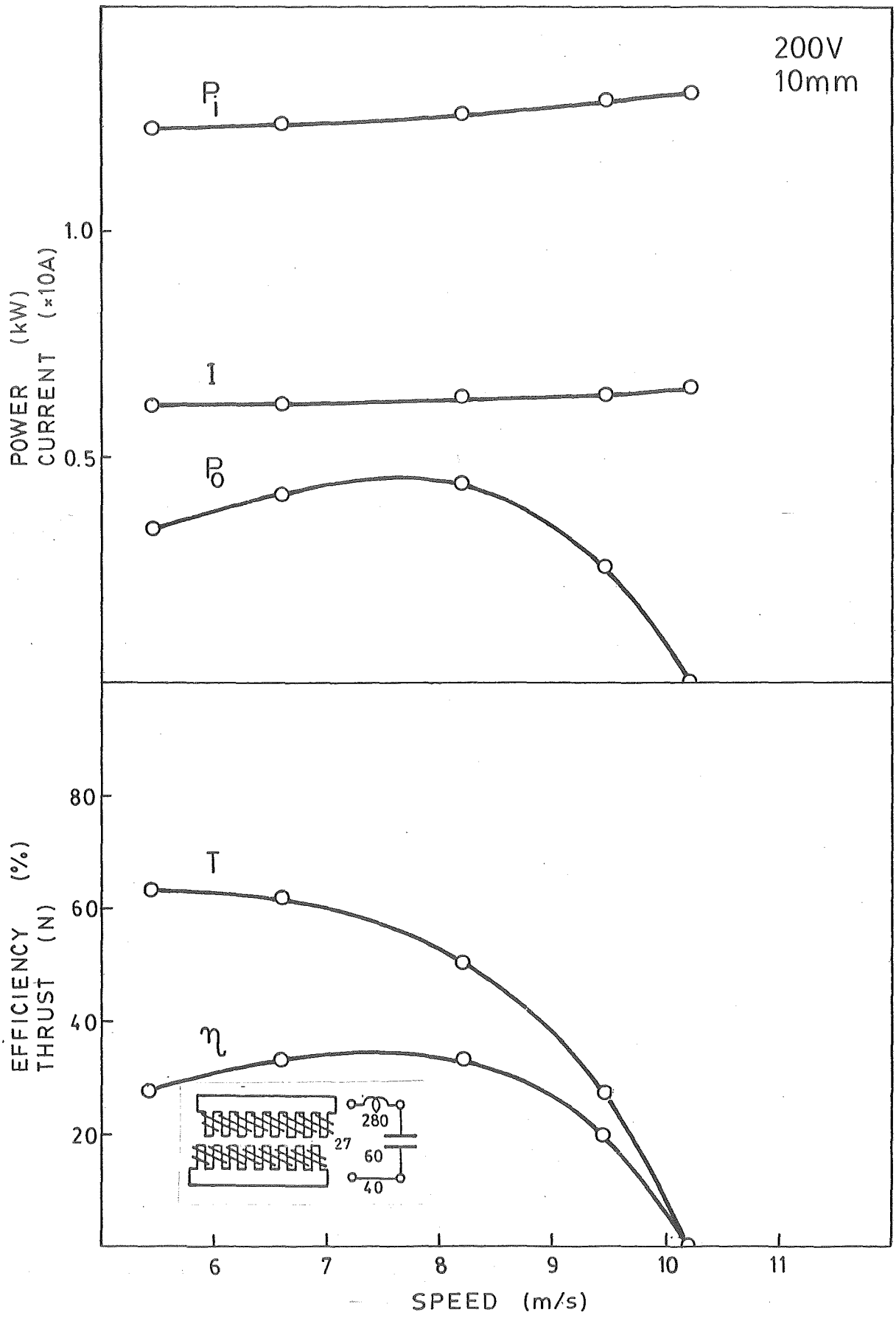
200V
10mm
P_i
I
P_o
POWER (kW)
CURRENT (×10A)
1.0
0.5
T
η
EFFICIENCY (%)
THRUST (N)
80
60
40
20
280
27
60
40
6
7
8
9
10
11
SPEED (m/s)

Fig. A156

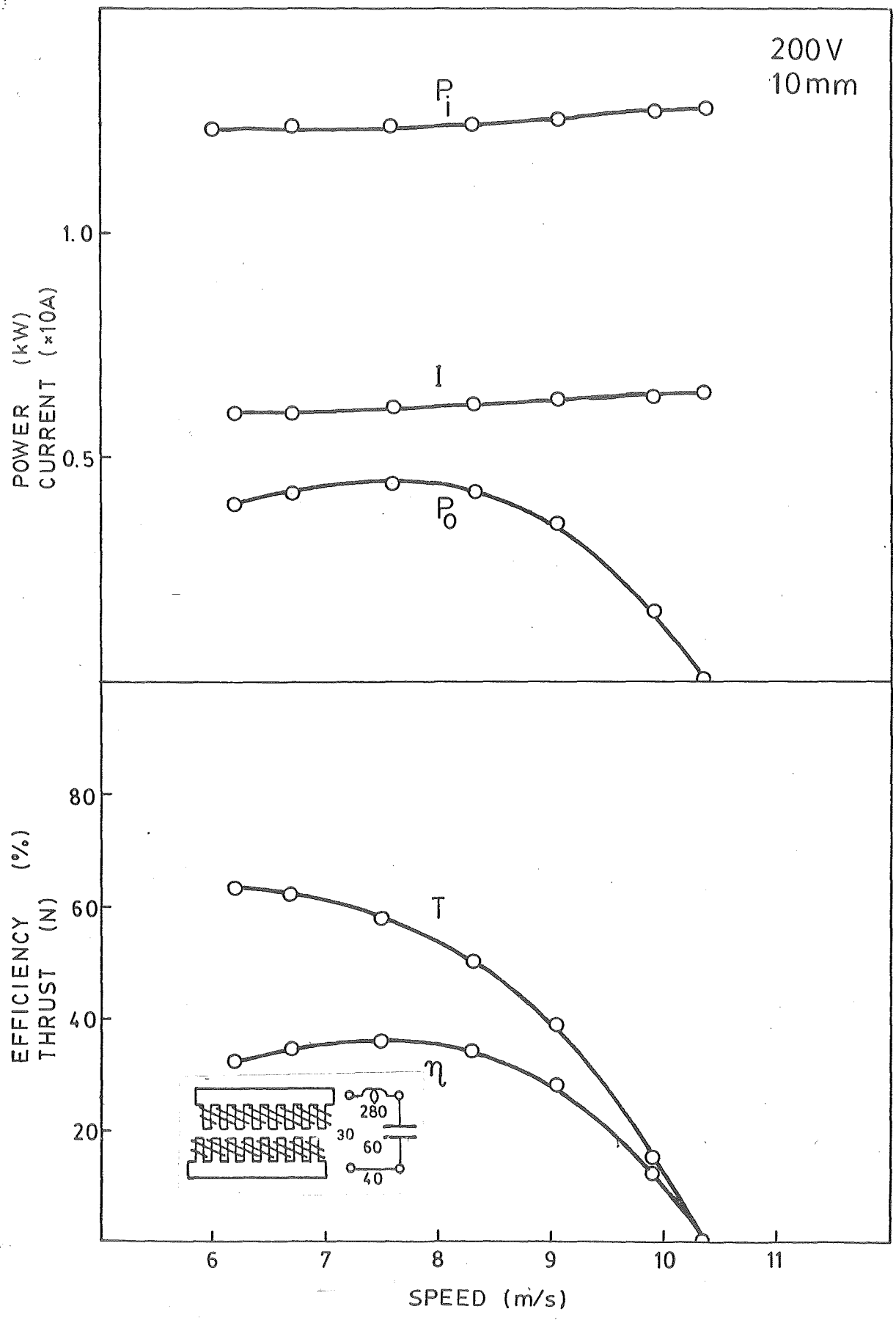
200V
10mm
P_i
I
P_o
1.0
0.5
POWER (kW)
CURRENT (×10A)
T
η
80
60
40
20
EFFICIENCY (%)
THRUST (N)
280
30
60
40
6
7
8
9
10
11
SPEED (m/s)

Fig. A157

APPENDIX 4

THE ALTERNATIVE CONNECTION MODE OF STLIM

THE ALTERNATIVE CONNECTION MODE OF STLIM[9]

The travelling wave machine utilises coils and capacitors to set up a travelling flux wave. When connected as in Figure 1b and energised from a single phase supply, the field travels away from the source at speed $U = 1/\sqrt{LC}$. Here L and C are the inductance and capacitance per meter respectively. This field can be used to drive a conducting metal sheet by induction motor action as described in this thesis. In this mode the speed is independent of frequency, but it can be varied by changing the capacitance or inductance. However, the thrust developed is also the function of capacitance. Increasing the speed by reducing C brings about a reduction in thrust and so the machine tends to have a constant power characteristic.

In this appendix we discuss the alternative mode of connection of Figure 1a Here the coils are shunt connected and the capacitors form the series elements. The first aspect of interest is that the travelling flux wave now moves toward the source i.e. in the opposite direction to that of Figure 1b. Secondly the speed is $U = \omega^2\sqrt{LC}$ which means that it is very sensitive to frequency, but at fixed frequency the speed now increases as the capacitance is increased. Figure 2 shows that the measured no-load speed of the motor varies approximately as frequency square for both thick and thin secondaries. It should be noted that for the same coil inductance L', and unit shunt capacitor C', the capacitance and inductance per unit length are now $L = \Delta L'$ and $C = \Delta C'$ instead of $L = L'/\Delta$ and $C = C'/\Delta$ as obtained from the normal STLIM arrangement.

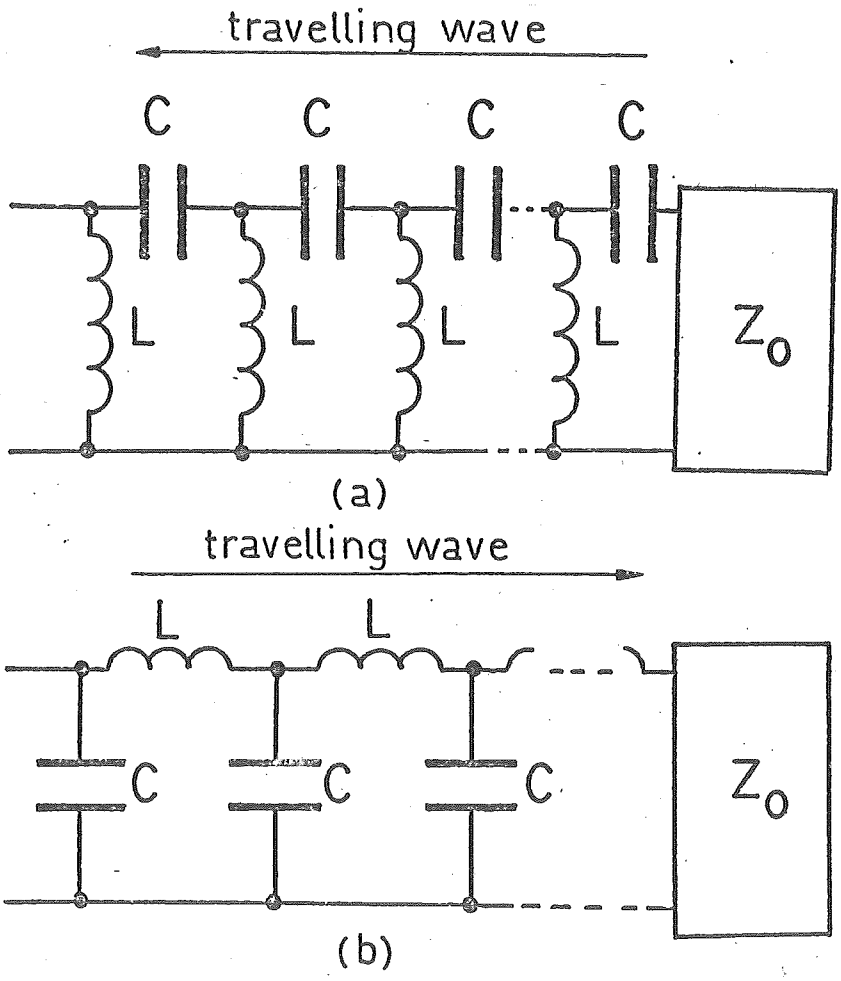

FIGURE 1 Arrangement of coils and capacitors on stator.
(a) Series capacitors.
(b) Shunt capacitors.

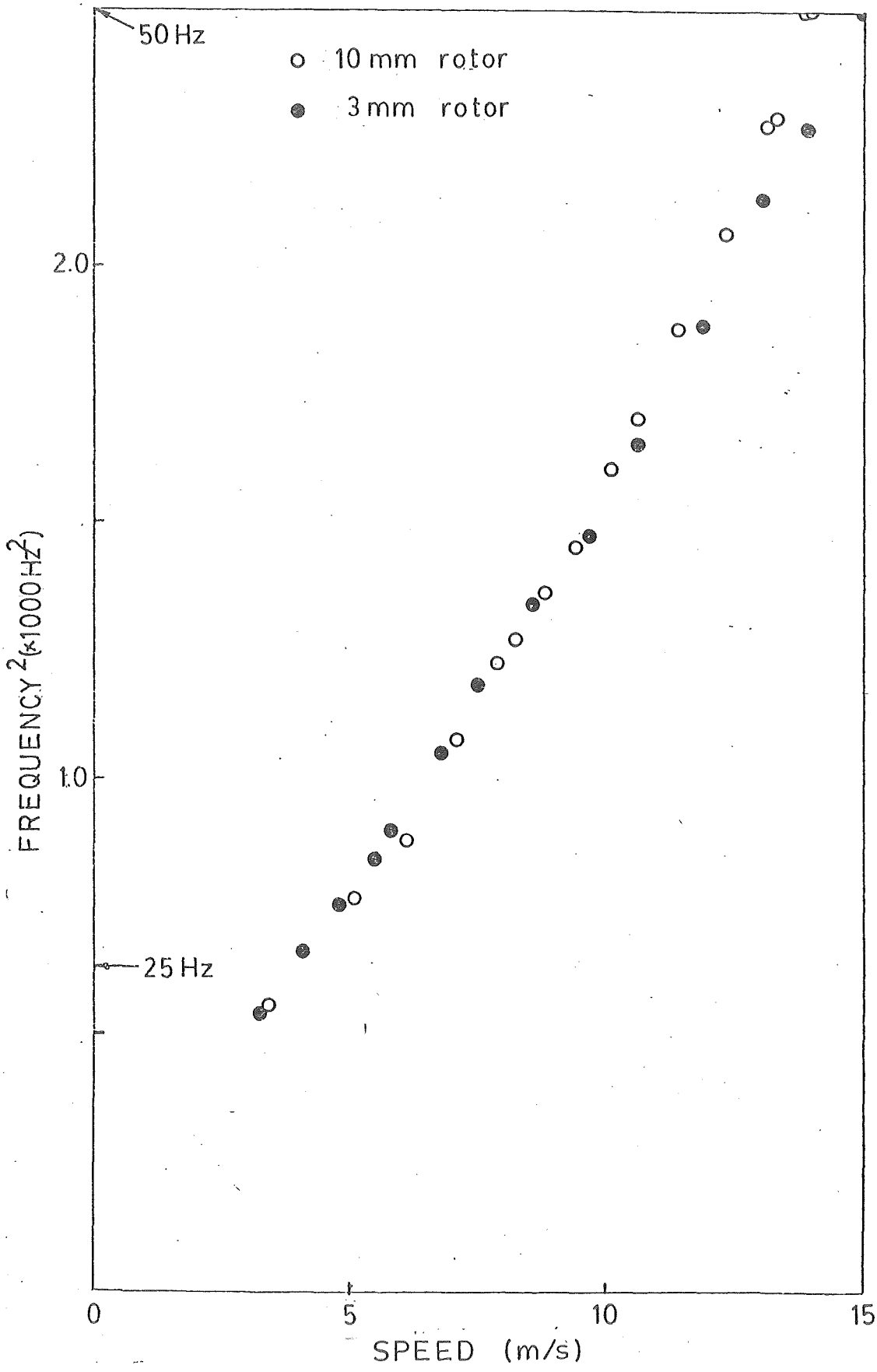

FIGURE 2 The no-load speed of the motor.
g = 18 mm, V = 220 V, Non-overlap coil STLIM
T = 600 turns/coil, C = 100 uF/coil.

To get an idea of how thrust might vary with capacitance we first note that the characteristic impedance is $Z_0 = \sqrt{L/C}$ and hence at constant voltage the power input is substantially $V^2\sqrt{C/L}$. Ignoring losses, and taking power to be the product of thrust and speed, we find that basically the thrust is $F = V^2/\omega^2 L$. We therefore expect in this case that the thrust is not affected by changes in C.

An experimental comparison of the two modes of operation has been made using non-overlap coil STLIM as described in Chapter 5. Details of the machine are: length of stator block 40 cm; width 9 cm; number of teeth 8; tooth width 2 cm; disc diameter 120 cm; secondary thickness 3 mm; airgap 24 mm;distance from center of disc to center-line of stator block 47 cm. Each coil of 600 turns spanned one tooth.

The force-speed characteristic of Figure 3 and Figure 4 were obtained for an applied voltage of 200 V, 50 Hz. The two modes of connection give similar magnitudes of speed and thrust but there are some remarkable differences. As expected, the new mode (Figure 1a) causes the disc to rotate toward the supply end, the speed increases as the capacitance is increased, and the thrust is almost unaffected by change in capacitance. Probably the most significant difference occurs when, with 100 uF capacitors, the mode of connection is changed: shunt connected capacitors (Figure 1b) give the no-load speed of 9 m/s while the corresponding speed for series connection (Figure 1a) is 17 m/s. Thus the simple switching can produce a 2:1 speed change. A higher value of C could give a wider speed change.

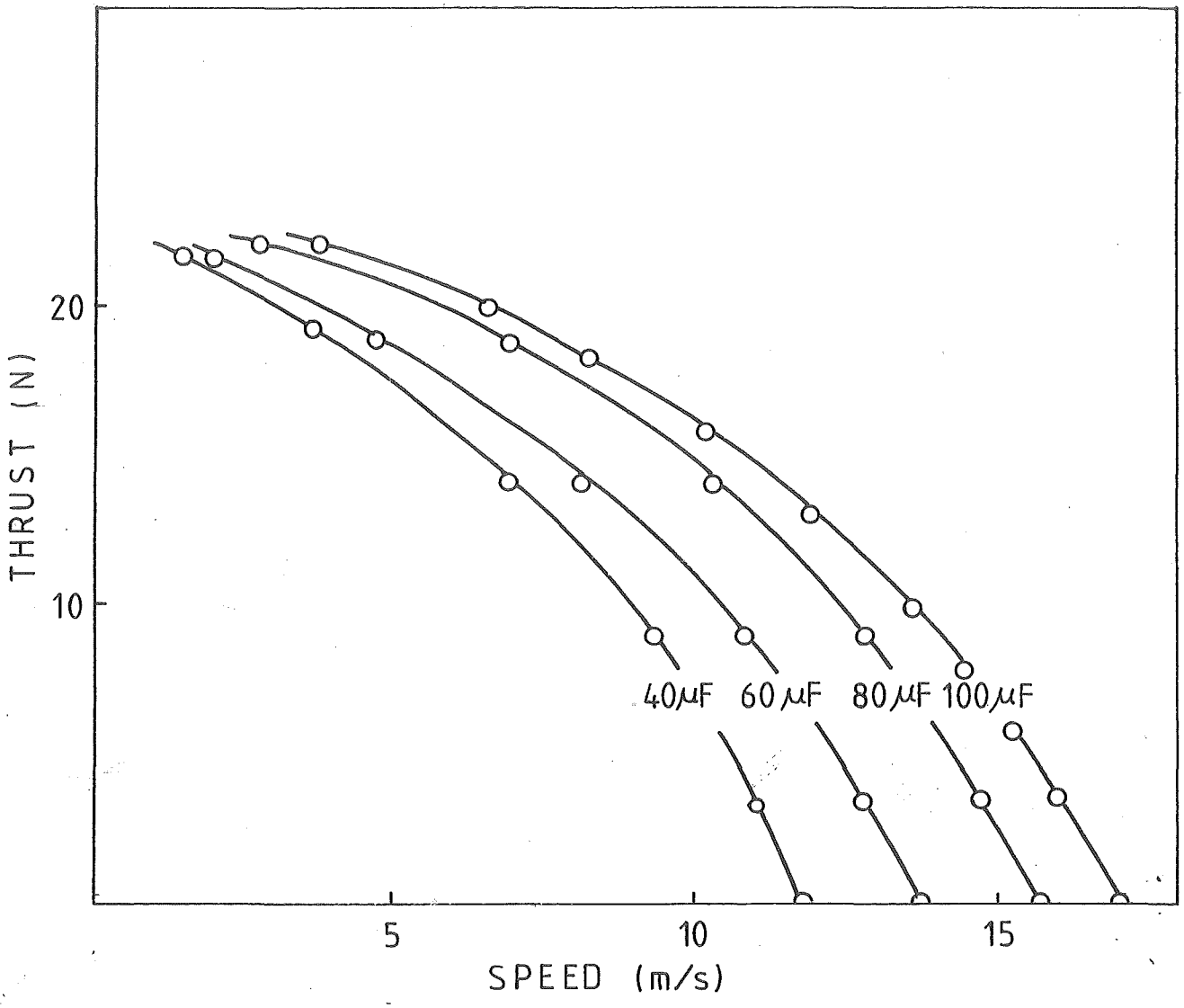

FIGURE 3 Thrust speed characteristic for series capacitors type at constant supply voltage of 200 V, 50 Hz.

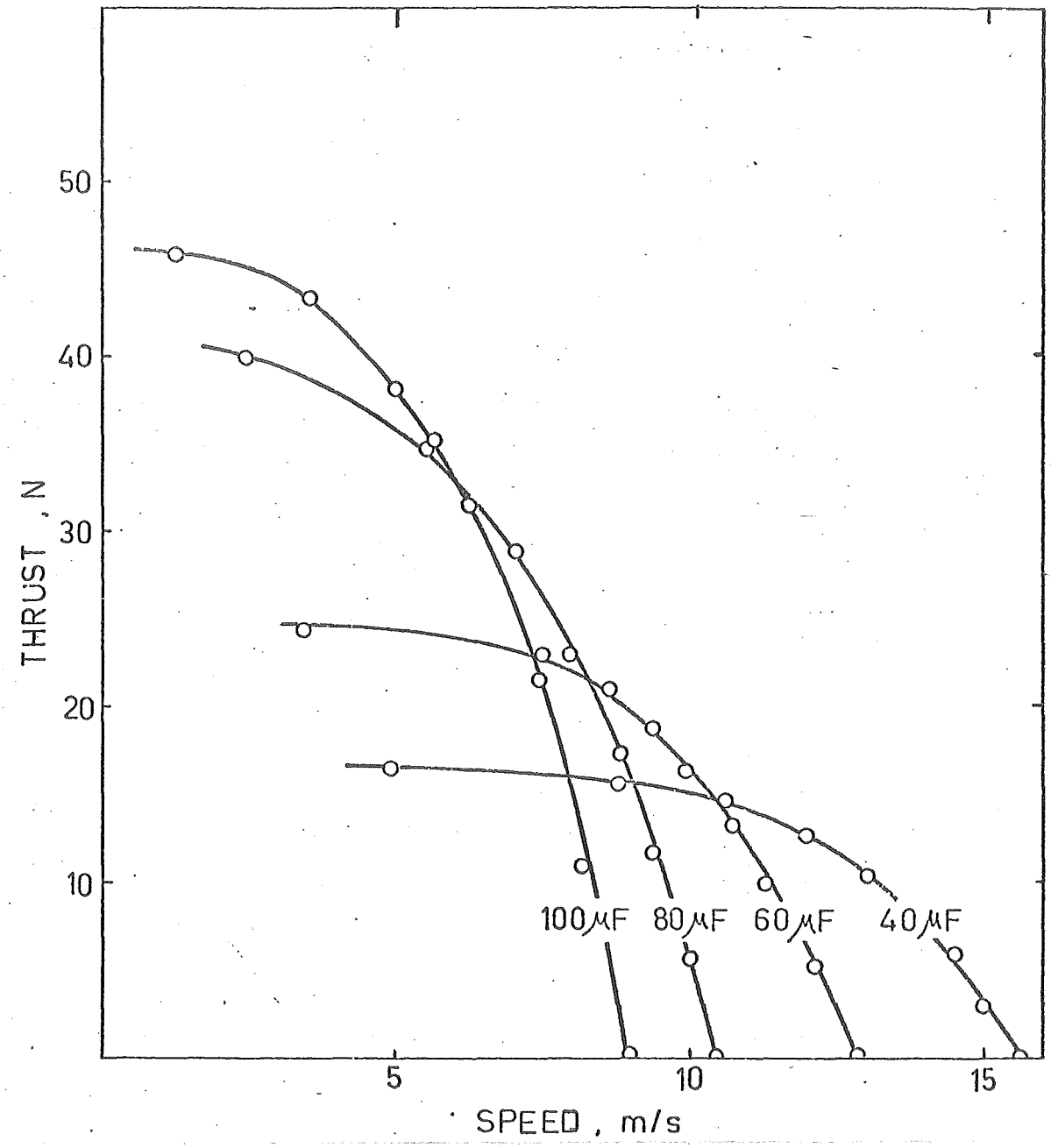

FIGURE 4 Thrust speed characteristic for conventional shunt capacitors type at constant supply voltage of 200 V, 50 Hz.

Finally by using STLIM conventional winding and alternative winding at both ends of a conventional LIM, the entry and exit end-effects, which often account for a low power factor and efficiency in low number pole pair LIMs, could be reduced. To fully utilise the material, the STLIMs compensation regions can be as short as two poles, and have a graded design in both winding and magnetic circuit. With good design, the STLIMs end winding losses can be controlled to a minimum. This is one possibility in improving the overall performance of a 2 pole LIM. The envisaged system is shown in Figure 5.

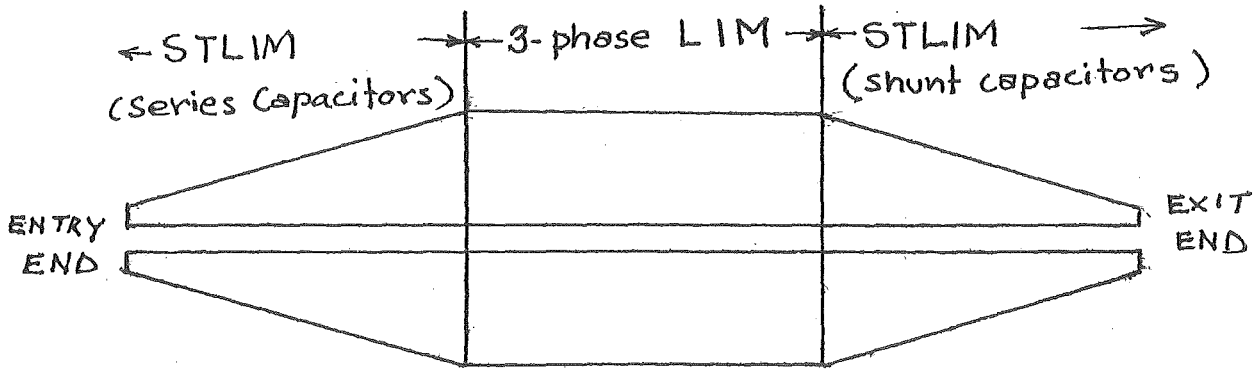

FIGURE 5 Two connection modes of STLIM for end-effects compensation of 3-phase LIM.

APPENDIX 5

ELECTROMAGNETIC BRAKING OF STLIM

ELECTROMAGNETIC BRAKING OF STLIM

In this Appendix, the preliminary investigation has been made into various methods of electromagnetic braking of STLIM. All results were obtained from the overlap coil motor with offset stator blocks as described in Part 2 of the thesis. The chosen parameters were fixed airgap of 21 mm, shunt capacitance of 2000 μF/m and 3 mm secondary thickness.

The simplest method of braking is to switch the supply from one end of the machine to the other, thereby reversing the thrust. In this method the stored energy is mainly dissipated in the rotor. Effective braking by this method requires a high resistance rotor since the slip exceed unity. Low resistance rotors would provide little reverse thrust.

Another method of braking is available which does not require reversal of supply terminals. It is based on the observation that when the rotor is moving faster than the synchronous speed the machine operates as a power amplifier. This was first investigated by Putman [6]. A reduced excitation at the supply terminals initiates a field travelling in the normal forward direction. The rotor, moving faster than the field, injects power into the stator windings which causes the voltage to increase with distance from the supply end. ($A= +\alpha - j\beta$) As a power amplifier the power in the terminating resistor can be controlled from the supply terminals: used as an electromagnetic brake the energy of the moving parts is dissipated in the terminating resistor. The results of input and output power are shown in Table 1.

A rather drastic method of limiting the speed which could be used in a run-away situation with failure of the

supply voltage is to simply connect the stator output terminals to the input terminals. The machine then operates as a positive feedback amplifier resulting in self excitation with accompanying very high braking torques. Energy is dissipated in rotor, stator winding, and terminating resistor. Table 2 gives some indication of the power levels attained. Self excitation of the model under test occurred at a disc velocity of 310 rev/min(15.5 m/s). When the terminating resistor was removed. The effect of re-connecting the terminating resistor is to increase the self excitation speed. The self excited mode is characterised by a kind of synchronous torque; it was not possible to drive the STLIM through its self excitation speed.

Speed rev/min	Input Power Watt	Output Power Watt
400	50	70
450	50	100
510	50	145
550	50	160
590	60	190
660	70	225

TABLE 1 Power amplification
Input voltage 40 V, terminating resistor 90 Ω.

Speed rev/min	V Volt	I Amp	P Watt
310	96	2.4	200
310	160	4.0	590
310	210	5.2	1010
310	220	5.5	1100

TABLE 2a Self excitation - open circuit

Speed rev/min	V Volt	I Amp	P(LOAD) Watt
362	73	2.7	59
362	100	3.7	111
362	120	4.4	160
362	148	5.5	243

TABLE 2b Self excitation - 90 ohm load

The most sophisticated braking method is to utilise the power amplification characteristic of the machine to feed energy back into the power supply. Such regenerative braking can only be achieved if the Thevenin open circuit terminal voltage at the terminating end of the stator winding is approximately in phase with the supply voltage, the Thevenin impedance of the winding being predominantly resistive. In our experimental machine the open circuit voltage leads the supply voltage by about 60 degrees; an inductive reactance was therefore connected in series at the input terminals (Figure 1) to move the supply voltage at that point back by

60 degrees. This put the terminal open circuit voltage in phase with the supply voltage. The results of a preliminary investigation are shown in Table 3. A power gain of about 2.2 is attained with a resultant power regeneration of about 300 W at 500 rev/min(25 m/s). The output voltage and current were maintained at 200 V and 3 A throughout.

Preliminary results of electromagnetic braking experiments have been presented. Although much further investigation is required, these initial results are very encouraging. Rheostatic braking can be achieved, self excitation can be used as an emergency speed limiting technique, and the possibility of power regeneration has been demonstrated. These characteristics appear potentially useful in the field of electromagnetic transportation.

Speed rev/min	INPUT V_1 Volt	I_1 Amp	P_1 Watt	OUTPUT V_1 Volt	I_2 Amp	P_2 Watt	Regenerated Power Watt
380	140	4.0	500	200	3	570	70
405	128	3.5	440	200	3	600	160
430	120	3.3	380	200	3	600	220
470	105	3.1	320	200	3	600	280
500	94	3.0	250	200	3	550	300
550	90	2.95	240	200	3	520	280
570	76	3.9	200	200	3	430	230
610	65	2.9	140	200	3	290	150

TABLE 3 Power regeneration.

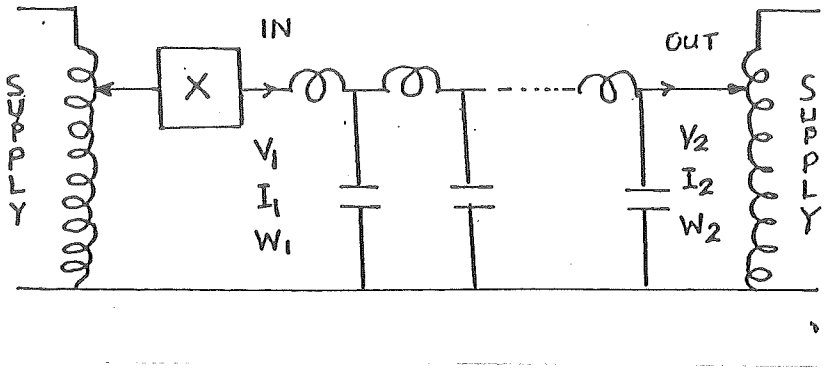

FIGURE 1 Experimental regenerative braking circuit.

APPENDIX 6

PUBLICATION ABSTRACTS

THE TRAVELLING WAVE MACHINE

ABSTRACT: The paper describes the characteristics of an experimental single phase linear induction motor. This machine has series connected windings and shunt connected capacitors which, as in an artificial transmission line, produce a travelling magnetic field. The speed of this field can be controlled by varying the capacitance. A current-sheet method of analysis is presented, leading to a simple equivalent circuit, and an expression for the thrust is deduced. Experimental results are compared with those obtained from the analytical model.

REFERENCE: WATSON, D.B., and VARASUNDHAROSOTH, B. The Travelling Wave Machine. Elec. Engg. Trans., I.E.Aust., Vol. EE 14, No. 1, 1978, pp. 25-30.

VARIABLE-SPEED SINGLE PHASE LINEAR INDUCTION MOTOR

ABSTRACT: A single phase travelling wave machine with series connected capacitors and shunt connected windings is described. Unlike the conventional travelling wave machine it produces a backward moving mmf wave, the speed increases as the capacitance is increased, and the thrust is not affected by change in capacitance.

REFERENCE: VARASUNDHAROSOTH, B., and WATSON, D.B. Variable-speed Single Phase Linear Induction Motor. Proc.I.E.E., Vol. 125, No. 11, 1978, pp. 1273-1274.

A SINGLE PHASE LINEAR TRAVELLING WAVE INDUCTION MACHINE

ABSTRACT: A simplified analysis of a single phase linear travelling wave induction machine is described. The analysis shows that the design goodness factor is independent of variation in the width of airgap, and predicts that the performance of the machine will not be degraded by an increase in airgap. A machine designed and constructed on the basis of the analysis, was used to investigate the possibility of varying the airgap to control the speed. The results of these investigations are fully discussed.

REFERENCE: VARASUNDHAROSOTH, B., and WATSON, D.B. A Single Phase Linear Travelling Wave Induction Machine. Electric Machines and Electromechanics, Vol. 3, No. 1, 1978, pp. 75-88.

NOVEL LINEAR DRIVE FOR LOW SPEED TRANSPORTATION

ABSTRACT: A variable speed single phase linear drive system is proposed for medium size low speed ground transportation. Such a device has series connected windings and shunt connected capacitors which, as in an artificial transmission line, produce a travelling magnetic field. The speed of the travelling field can be controlled by varying the shunt capacitors or the airgap. Control of torque, direction of travel, braking and regeneration of power can be achieved. A small model of such a machine has been investigated.

REFERENCE: WATSON, D.B. and VARASUNDHAROSOTH, B. Novel Linear Drive for Low Speed Transportation. To be presented at the Joint Intermag-MMM Conference, The Statler Hilton-New York, July 17-20, 1979.

To be withdrawn - due to travelling difficulties.
B.V.


KMIT MAGLEV